UTILIZATION OF ENDOPHYTIC FUNGI AND THEIR ENZYMES FOR TRANSFORMATION TO OBTAIN BIOACTIVE COMPOUNDS

A Thesis Submitted to
The Graduate School of Engineering and Sciences of
İzmir Institute of Technology
in Partial Fulfillment of the Requirements for the Degree of

DOCTOR OF PHILOSOPHY

in Bioengineering

by
Melis KÜÇÜKSOLAK

December 2022
İZMİR

ACKNOWLEDGMENTS

I would like to express my gratitude to my supervisor Prof. Dr. Erdal BEDİR, for his guidance, support, patience, encouragement, immense knowledge, and motivation throughout my thesis studies.

I would like to thank my co-advisor Assoc. Prof. Dr. Duygu SAĞ WINGENDER for all her support. I wish to show my appreciation to Prof. Dr. Petek BALLAR KIRMIZIBAYRAK for opening her laboratory and supporting bioactivity studies. I would like to thank Dr. Hasan Buğra ÇOBAN for his contribution to optimization and bioreactor studies. I would like to express my gratitude to the members of my thesis monitoring and dissertation committee, Assoc. Prof. Dr. Nur Başak SÜRMELİ ERALTUĞ, Assoc. Prof. Dr. Sinan GÜVEN, Prof. Dr. Gaye ÖNGEN ÖZGEN, and Prof. Dr. Derya GÜLCEMAL for giving valuable time, comments, and contributions to this thesis.

I am very thankful to Dr. Özgür TAĞ, Dr. Güner EKİZ DİNÇMAN, and Dr. Özge ÖZÇINAR for their support and mentoring. I would like to thank my dear friends Göklem ÜNER, Sinem YILMAZ, and Ünver KURT for exchanging ideas, fun, solace, help, and support. I would like to express my gratitude to all Bedir Group members, particularly Eyüp BİLGİ, Gamze DOĞAN, Gülten KURU, and Yiğit Ege ÇÖMLEKÇİ for their friendships and support.

I wish to extend my special thanks to my beloved family, Seyhan KÜÇÜKSOLAK and Mustafa KÜÇÜKSOLAK. Without your support, this thesis would not have been completed.

I am very grateful to Bionorm Natural Products for providing cyclocephagenol, cycloastragenol, and astragenol. I would like to thank the Biotechnology and Bioengineering Research Center (Izmir Institute of Technology) and the Pharmaceutical Sciences Research Center (Ege University) for equipment support. I am very thankful to Prof. Dr. Ahmet Ceyhan GÖREN for his help in mass spectrometry and Central Research Laboratory Application and Research Center (Çankırı Karatekin University) and Assoc. Prof. Dr. Salih GÜNNAZ for obtaining NMR spectra.

This study was supported by The Scientific and Technological Research Council of Turkey with a scholarship under 2211/A National Ph.D. Scholarship Program (Grant No: 1649B031600136). I wish to acknowledge the financial support provided by The Scientific and Technological Research Council of Turkey (119Z870), Izmir Institute of Technology Research Fund (2017İYTE63), and Ege University Research Fund (GAP-23729).

ABSTRACT

UTILIZATION OF ENDOPHYTIC FUNGI AND THEIR ENZYMES FOR TRANSFORMATION TO OBTAIN BIOACTIVE COMPOUNDS

Biotransformation is a chemical reaction performed by biological systems or their components to modify molecules and has many applications in the pharmaceutical industry. In our previous project, biotransformation studies were carried out on *Astragalus* cycloartanes using endophytic fungi isolated from the tissues of *Astragalus* species, and the effects of the metabolites on telomerase activation were investigated. Among the isolated endophytic fungi, *Alternaria eureka* and *Camarosporium laburnicola* were identified as potent biocatalysts in developing molecule libraries and producing potent telomerase activators.

This thesis aims to demonstrate the potential use of endophytic fungi in the production of bioactive metabolites. In the first part, biotransformation studies were performed on cyclocephagenol, a novel cycloartane-type sapogenin with tetrahydropyran unit, using *Alternaria eureka* and *Camarosporium laburnicola*, and twenty-eight new metabolites were obtained. According to the results of bioactivity studies, *Alternaria eureka* and *Camarosporium laburnicola* were found to be responsible for producing potent neuroprotective agents and potent telomerase activators, respectively. In parallel, biotransformation conditions were statistically optimized to afford potential telomerase activators, discovered in our previous studies (E-CG-01, E-AG-01 and E-AG-02). For this, nine parameters were screened by Plackett-Burman Design, and three significant parameters were optimized using Central Composite Design. As a result, production yields were increased by 1.95-fold for E-CG-01, 70-fold for E-AG-01, and 19-fold for E-AG-02. In the last part, the partial purification and characterization of alcohol dehydrogenase, Baeyer-Villiger monooxygenase, and lactone hydrolase enzymes, which were catalyzing the modifications in the production of telomerase activators, from *Camarosporium laburnicola* were performed.

ÖZET

ENDOFİTİK FUNGUSLARIN VE ENZİMLERİNİN BİYOAKTİF BİLEŞİKLERİN ELDESİ İÇİN TRANSFORMASYONDA KULLANILMASI

Biyotransformasyon, molekülleri modifiye etmek için biyolojik sistemler veya bileşenleri tarafından gerçekleştirilen kimyasal reaksiyonlardır ve ilaç endüstrisinde birçok uygulamaya sahiptir. Önceki projemizde, *Astragalus* türlerinin dokularından izole edilen endofitik funguslar kullanılarak *Astragalus* sikloartanları üzerinde biyotransformasyon çalışmaları yapılmış ve elde edilen metabolitlerin telomeraz aktivasyonu üzerine etkileri araştırılmıştır. İzole edilen endofitik funguslar arasında *Alternaria eureka* ve *Camarosporium laburnicola*, molekül kütüphanesinin geliştirilmesi ve potent biyoaktif metabolitlerin üretimi açısından güçlü biyokatalizörler olarak tanımlanmıştır.

Bu tezde, biyoaktif metabolitlerin üretiminde endofitik fungusların kullanım potansiyelinin ortaya konulması amaçlanmıştır. Birinci bölümde, tetrahidropiran ünitesine sahip yeni bir sikloartan tipi sapogenin olan siklosefagenol üzerinde *Alternaria eureka* ve *Camarosporium laburnicola* kullanılarak biyotransformasyon çalışmaları yapılmış ve yirmi sekiz yeni metabolit elde edilmiştir. Biyoaktivite çalışmalarının sonuçlarına göre, *Alternaria eureka* ve *Camarosporium laburnicola* sırasıyla potent nöroprotektif ajanlar ve potent telomeraz aktivatörleri üretmede başarılı bulunmuştur. Buna paralel olarak, önceki çalışmalarımızda keşfedilen potansiyel telomeraz aktivatörlerini (E-CG-01, E-AG-01 ve E-AG-02) üretmek için biyotransformasyon koşulları istatistiksel olarak optimize edilmiş ve üretim verimleri artırılmıştır. Bunun için, Plackett-Burman Design ile dokuz parametre taranmış ve Central Composite Design kullanılarak üç önemli parametre optimize edilmiştir. Son bölümde ise, telomeraz aktivatörlerinin üretimindeki modifikasyonlardan sorumlu olan alkol dehidrogenaz, Baeyer-Villiger monooksigenaz ve lakton hidrolaz enzimlerinin *Camarosporium laburnicola*'dan kısmi saflaştırılması ve karakterizasyonu gerçekleştirilmiştir.

TABLE OF CONTENTS

LIST OF FIGURES

Figure **Page**

Figure **Page**

Figure **Page**

Figure **Page**

Figure **Page**

Figure **Page**

LIST OF TABLES

Table **Page**

Table **Page**

LIST OF SPECTRA

Spectrum **Page**

Spectrum **Page**

Spectrum **Page**

Spectrum **Page**

Spectrum **Page**

Spectrum **Page**

LIST OF CHROMATOGRAMS

Chromatogram **Page**

Chromatogram **Page**

Chromatogram **Page**

ABBREVIATIONS

^{13}C-NMR	Carbon Nuclear Magnetic Resonance
1D-NMR	One-Dimensional Nuclear Magnetic Resonance
^{1}H-NMR	Proton Nuclear Magnetic Resonance
2D-NMR	Two-Dimensional Nuclear Magnetic Resonance
6-OHDA	6-hydroxydopamine
ACN	Acetonitrile
ADH	Alcohol Dehydrogenase
AG	Astragenol
AHL	N-Acyl Homoserine Lactone
AP	Ammonium Persulfate
BCA	Bicinchoninic Acid
BM	Biotransformation Medium
BVMO	Baeyer Villiger Monooxygenase
C_5D_5N	Deuterated Pyridine
CCD	Central Composite Design
CD_3Cl	Deuterated Chloroform
CD_3OD	Deuterated Methanol
CG	Cycloastragenol
$CHCl_3$	Chloroform
clogP	Calculated Partition Coefficient
CO_2	Carbondioxide
COSY	Correlation Spectroscopy
CV	Column Volume
DAD	Diode Array Detector
DCM	Dichloromethane
DEAE	Diethylaminoethanol
DMEM	Dulbecco's Modified Eagle Medium
DMSO	Dimethyl Sulfoxide

DTT	Dithiothreitol
ELISA	Enzyme-Linked ImmunoSorbent Assay
ESI	Electrospray Ionisation
EtOAc	Ethyl Acetate
EtOH	Ethanol
FAD	Flavin adenine dinucleotide
FMN	Flavin mononucleotide
FR	Fraction
GAPDH	Glyceraldehyde-3-phosphate Dehydrogenase
H_2O	Water
H_2O_2	Hydrogen Peroxide
H_2SO_4	Sulfuric Acid
HCl	Hydrochloric Acid
HEKn	Human Epidermal Keratinocytes, Neonatal
HIC	Hydrophobic Interaction Chromatography
HMBC	Heteronuclear Multiple Bond Coherence
HPLC	High Performance Liquid Chromatography
HR	High Resolution
HSQC	Heteronuclear Single Quantum Coherence
hTERT	Human Telomerase Reverse Transcriptase
IEC	Ion Exchange Chromatography
IPA	Isopropyl Alcohol
K_2HPO_4	Di-Potassium Hydrogen Phosphate Anhydrous
LH	Lactone Hydrolase
MeOH	Methanol
MM2	Molecular Mechanics
MS	Mass Spectrometry
MTT	3-[4,5-Dimethylthiazol-2-yl]-2,5-diphenyltetrazolium bromide
Na_2HPO_4	Sodium Phosphate Dibasic Anhydrous
NaCl	Sodium Chloride
NADH	Nicotinamide Adenine Dinucleotide

NADPH	Nicotinamide Adenine Dinucleotide Phosphate
NaH_2PO_4	Sodium Phosphate Monobasic Monohydrate
NaOH	Sodium Hydroxide
NaPi	Sodium Phosphate Buffer
NOESY	The Nuclear Overhauser Effect
OFAT	One Factor at a Time
PBD	Plackett Burman Design
PBS	Phosphate Buffered Saline
PCR	Polymerase Chain Reaction
PDA	Potato Dextrose Agar
PDB	Potato Dextrose Broth
PMSF	Phenylmethylsulfonyl Fluoride
PTFE	Polytetrafluoroethylene
PVDF	Polyvinylidene Fluoride
rpm	Revolutions per Minute
Q	Quaternary Ammonium
QS	Quorum Sensing
RNA	Ribonucleic acid
ROS	Reactive Oxygen Species
RP	Reversed Phase
RSM	Response Surface Methodology
SAR	Structure Activity Relationship
SDS-PAGE	Sodium Dodecyl Sulphate-Polyacrylamide Gel Electrophoresis
SEC	Size Exclusion Chromatography
TEMED	Tetramethyl Ethylenediamine
tert-BuOH	Tertiary Butanol
TLC	Thin Layer Chromatography
TMB	3,3′,5,5′-tetramethylbenzidine
TOSCY	Total Correlation Spectroscopy
UPW	UltraPure Water
ZEN	Zearalenone

CHAPTER 1

INTRODUCTION

Triterpenoids are the largest group of natural products, and it is estimated that more than 20,000 triterpenoids are found in nature. Triterpenoids are composed of isopentenyl pyrophosphate units and are biosynthesized in plants by the cyclization of squalene, the precursor of all steroids. This natural product group includes more than 100 different skeletons[1–4]. The most common triterpenoids in nature and medicinal plants are tetracyclic and pentacylic triterpenoids. Tetracyclic triterpenoids include the dammarane, cucurbitane, cycloartane, lanostane and protostane groups, while pentacyclic triterpenoids comprise the oleanane, ursane and lupane groups[5,6].

Cycloartane-type triterpenoids (9,19-cyclolanostane) are produced only by photosynthetic eukaryotes. In the plant kingdom, these metabolites are not as common as other triterpenoids (oleanane, ursane, steroidal triterpenoids). The plants richest in cycloartane-type of compounds are *Astragalus* species[7]. Nearly 650 cycloartane-type metabolites have been identified so far, and nearly half of them were obtained from *Astragalus* species[8–10]. Cycloartanes constitute one of the two groups that carry the 9,19-cyclopropane and steroidal nuclei together among natural compounds (other group: *Buxus* alkaloids)[11].

Cycloartane-type triterpenoids have been classified based on the side chains, which extend from C-17 of the steroidal nuclei: 20,24-epoxy-, acyclic, and 20,25-epoxy side chains[12]. Cycloastragenol and cyclocanthogenol are the most common cycloartane skeletons, possessing 20,24-epoxy (tetrahydrofuran) and acyclic side chains on C-17, respectively, while cyclocephagenol is the less common group represented by 20,25-epoxy side chain[12].

Cycloartane-type triterpenoids have an important position among low molecular weight bioregulators as they are produced only by photosynthetic organisms and play a key role in the biosynthesis of different phytosterols (cucurbitacins, cholesterol, steroids,

cardenolides). The elucidation of this pathway and the broad biological effect has led to increased interest in cycloartanes[9,13].

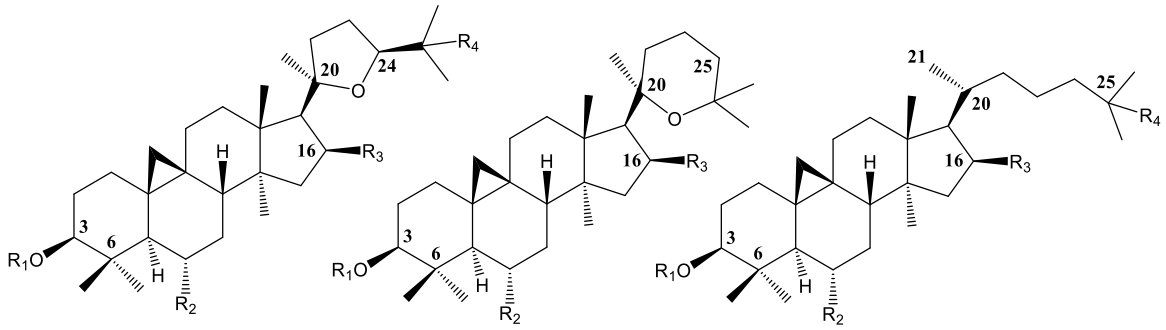

Figure 1.1. Main structures of cycloartane-type saponins: a) 20,24-epoxy side chain, b) 20,25-epoxy side chain, c) acyclic side chain.

The biological activities of cycloartanes and their semi-synthetic derivatives indicate their wide range of bioactivity, including immunostimulating[14–16], anti-protozoal[17], antiviral[18], cytotoxic[19,20], cardiotonic[21], wound healing[22] and adjuvant[23–25] activities.

The most important development in the last ten years for cycloartanes was the discovery of cycloastragenol as a potent telomerase activator by Geron Corporation in 2004[26]. Since 2007, cycloastragenol, present only in *Astragalus* species, has been in the market as an anti-aging dietary supplement with the trade name TA-65.

Telomerase activation is a potential target for treating diseases associated with telomere loss, as telomere shortening is a consequence of the biological aging process and is also considered a risk factor for many age-related diseases. In addition, diseases associated with telomere shortening are not only age-related. Hence, telomerase activation *in vivo* has significant potential for treating many chronic and degenerative diseases. Thus, cycloastragenol and its derivatives have been at the center of nature-based regenerative medicine research as well its utilization in degenerative diseases is a hot topic[27–32]. Two clinical trials were completed for the use of compound in metabolic syndrome and Alzheimer's disease (NCT number: 02531334 and 02530255, respectively), which is also an indication of the potential of telomerase activators. Additionally, two clinical trials are

recruiting for cognitive impairment and parkinsonism (NCT numbers: 05578443 and 05506891).

Bedir Group is one of the most experienced groups in cycloartane chemistry by introducing about two hundred new compounds[33–39]. Upon finding that cycloartane-type triterpenoids were potent telomerase activators, the group has focused on derivatization of cycloartanes to develop a compound library for screening towards telomerase activation (TÜBİTAK 1001 projects: 109S345 and 114Z958).

Modification of natural products occurs either by chemical reactions or by biotransformation reactions. Biotransformation is the biochemical reactions of living systems or their components (enzymes) to alter molecules. It is an effective tool in obtaining molecules that are difficult to prepare by conventional synthetic methods and has a wide range of uses. In the pharmaceutical industry, microbial biotransformation has been utilized in enzymatic transformation to synthesize chiral intermediates and end products[40–47].

Within the scope of the 114Z958-TÜBİTAK project, biotransformation studies were carried out on cycloartanes using endophytic fungi isolated from the tissues of *Astragalus* species, and effects of the metabolites on telomerase activation were investigated. Cycloastragenol, cyclocanthogenol and semi-synthetic derivatives astragenol and 20(27)-octanor cycloastragenol, the main triterpenoids in *Astragalus*, were used as starting molecules. In the telomerase activation screening panel using obtained metabolites, 16 compounds showed activity ranging from 1.2 to 11.3-fold at doses of 0.5 to 300 nM compared to the control cells treated with DMSO[48–50]. The national and international patent applications have been made for the active molecules, and their registration is awaited[51].

From this point of view, within the scope of this thesis, we decided to carry out further studies to demonstrate the potential use of *Astragalus* endophytic fungi and their enzymes in the production of bioactive compounds.

In Chapters 2 and 3, biotransformation studies were performed on cyclocephagenol, one of the cycloartane-type triterpenoids of *Astragalus* plant with tetrahydropyran unit, using *Astragalus* originating endophytic fungi to obtain bioactive metabolites and to investigate structure-activity relationship studies. While we focused on the neuroprotective activities of biotransformation products in Chapter 2, we aimed to develop potent telomerase activators and to examine the effect of tetrahydropyran unit on telomerase activation in Chapter 3.

In Chapter 4, we performed optimization studies on the biotransformation conditions of *C. laburnicola* to produce our newly discovered molecules, which have excellent growth potential for the market of telomerase activators in the future. In our previous project, no effort was made to increase metabolite production and/or to search for alternative methods for high efficiency and productivity. Thus, we decided to optimize the biotransformation conditions to increase the production efficiency of these potent telomerase activators.

In Chapter 5, the major enzyme system, composed of alcohol dehydrogenase (ADH), Baeyer Villiger monooxygenase (BVMO) and lactone hydrolase (LH), responsible for the modification of our target molecules were partially purified from *C. laburnicola*, and characterization studies were performed on these enzymes. The most important reason we want to elucidate the enzyme system is that this fungus is newly discovered, and its biocatalyst potential has never been evaluated apart from the study of our group.

CHAPTER 2

BIOTRANSFORMATION OF CYCLOCEPHAGENOL BY THE ENDOPHYTIC FUNGUS *ALTERNARIA EUREKA* AND NEUROPROTECTIVE ACTIVITY OF METABOLITES

2.1. Background

Neurodegeneration refers to the loss of structure/function of the central or peripheral nervous system. The most common neurodegenerative diseases are Alzheimer's, Parkinson's, Huntington's, Multiple Sclerosis, Amyotrophic Lateral Sclerosis, and Spinal Cord Injury. Since neurodegeneration relates to multifactorial pathological mechanisms, multiple action mechanisms are promising for preventing and treating neurodegenerative diseases[52,53].

The discovery of novel therapeutics against neurodegenerative diseases has been an area of intense research, as neurodegenerative diseases are a considerable burden on society and the economy[54]. Numerous studies reported that natural products have the potential for the prevention and treatment of neurodegeneration. Luteolin, quercetin, resveratrol, apigenin, genistein, hesperidin, and numerous medicinal plant extracts have possible therapeutic effects for combating neurodegenerative diseases. Astragaloside IV (AST-IV), a cycloartane-type saponin from *Astragalus* species, efficiently attenuated hydrogen peroxide (H_2O_2)-induced neuronal cell death[55]. Moreover, the aglycone of AST-IV, viz. cycloastragenol (CG), diminished amyloid-beta mediated neurogenic dysfunction[56].

Based on the potential of cycloartane-type saponins, herein, we also focused on the neuroprotective activity of cyclocephagenol (**1**), a novel cycloartane-type sapogenin from *Astragalus microcephalus*. As **1** demonstrated significant protection, we further performed a

modification study on **1** utilizing microbial transformation and examined the neuroprotective potential of metabolites in H_2O_2-induced injury in SH-SY5Y cells.

2.1.1. Biotransformation

Biotransformation is the biochemical reactions of living systems or their components (enzymes) to alter molecules. Significant advantages of this methodology are; i) stereo-, regio- and enantioselective catalysis; ii) transformation at non-reactive sites of the substrates; iii) mild reaction conditions (optimum pH, non-toxic atmospheres, atmospheric pressure, etc.); iv) transformation of complex molecules without the need of protection/deprotection steps; v) waste minimization[47,57–61].

There are many applications of biotransformation in drug discovery and development studies, including the synthesis of drug metabolites for estimation of mammalian metabolism, lead optimization, and the development of metabolite libraries from highly diverse lead compounds for structure-activity relationship (SAR) and bioactivity screening studies[62].

Biotransformation of natural products can provide a wide range of structural diversity and improved biological activity. With the transition to microbial applications, the multi-step and costly reactions that require high temperature and pressure conditions in the production processes of these active substances have been replaced by environmentally friendly and economical bioproduction. For example, chemical steroid synthesis involves 31 reaction steps to obtain 1 g of cortisone from 615 g of deoxycholic acid purified from bovine bile. Instead, transforming the simple natural precursor molecule using *Rhizopus arrhizus* ATCC 11145 and *Aspergillus niger* ATCC 9142 reduced cortisone production costs from $200 to $1 for 1 g of cortisone and reduced 31 chemical steps to 11 steps[42,43].

In addition to overcoming the difficulties encountered in chemical synthesis, microbial biotransformation is effectively used to increase/reduce the bioactivity/toxicity profiles of drug precursor molecules and to create molecular libraries for structure-activity studies with their highly diverse enzyme systems[40–47].

Research groups focusing on biocatalysts are pursuing the discovery of new microorganisms and/or enzyme/s obtained from those microorganisms to be developed as industrial biocatalysts. In this regard, endophytes are powerful biocatalysts because of their capability to produce enzymes necessary for their colonization; therefore, they have recently begun to take their place in biotransformation studies. It is anticipated that the endophytic biocatalysts will match chemical reactions even as powerful as conventional chemical methods in the near future[58,63–65].

2.1.2. Endophytic Fungi

Endophytic fungi are microorganisms that live in the inner tissues of plants, do not cause any visible signs of disease, and can colonize the leaf, root, and stem tissues of host plants. Both parties benefit from the interaction between the host plant and endophytic fungi. In this interrelationship, endophytes synthesize a wide variety of bioactive natural products that will create low toxicity for the plant to provide protection and survival conditions to the host plant, and to create a selective environment for different microorganisms. This situation requires continuous reactions by the endophyte against the defense mechanism of the host plant, and this will make selection pressure for the development of new metabolic pathways[63,66–68].

On the other hand, endophytic microorganisms must produce enzymes necessary for colonization in plant tissues. Therefore, they are considered powerful biocatalysts that can be evaluated in chemical modifications. The use of endophytic microorganisms as biocatalysts in biotransformation studies is very limited in the literature, and studies in this area have been increasing in recent years. Therefore, it is not currently used in industrial processes. Studies on endophytic microorganisms have focused on their isolation and investigation of secondary metabolite contents. In recent years, studies on the optimization of secondary metabolite production and enzyme production of endophytic fungi have begun to be reported[66,69,70]. The isolation of these microorganisms is usually given in the procedures such as temperature, pH, and nutrient medium[71]. Secondary metabolite screening and use as

a biocatalyst after isolation are carried out under similar process conditions for the isolated fungi. However, it should be noted that each endophyte's growth conditions may differ. Therefore, optimization studies of process conditions are essential, mainly to produce therapeutically valuable molecules and enzymes. Thus, product/enzyme formation or biotransformation studies will be possible with affordable cost and high efficiency[58,63–65].

2.1.3. Biotransformation Studies Using Endophytic Fungi Isolated from *Astragalus* sp.

Our research group has isolated endophytes from *Astragalus angustifolius* ssp. *angustifolius* and *A. condensatus* to perform biotransformation studies with the plants' own endophytes. Root, leaf and stem tissues of *Astragalus* species were used to obtain endophytes. As a result of subculturing studies, endophytic fungi were isolated, and molecular methods based on ITS sequence analysis were used to identify endophytic fungi. As a result of these studies, 15 different endophytes were obtained: *Alternaria alternata* 1E2L1 (Accession No. KU866390.1), *Podospora* sp. 1E4CR-1 (LC109288.1), *Fusarium torulosum* 1E2L-1 (JX534258.1), *Leptosphaeria* sp. 1E2R1 (KT269871.1), *Fusarium* sp. 1E4AS-1 (KT269061.1), *Fusarium acuminatum* 1E3AS1-1 (JX534294.1), *Alternaria eureka* 1E1BL-1 (FR799468.1), *Allophaeosphaeria cytisi* 1E4AL (KT306947.1), *Neosartorya hiratsukae* 1E2AR1-1 (FR733873.1), *Fusarium solani* 1E1BR2 (KT583204.1), *Fusarium* sp. 1E4CS (KT323109.1), *Penicillium roseopurpureum* 1E4BS1 (KJ775658.1), *Phaeosphaeria* sp. 1E4CS-1 (KJ188706.1), *Penicillium* sp. 1E4BR2-2 (JQ781815.1), *Camarosporium laburnicola* 1E4BL1 (KY497784)[72].

Cyclocanthogenol, cycloastragenol and its semi-synthetic derivatives astragenol and 20(27)-octanor cycloastragenol, the main sapogenins in the *Astragalus* genus, were used as substrates in biotransformation studies. In these studies, production yields of endophytic fungi were evaluated by analytical scale biotransformation studies, and *Alternaria eureka*, *Neosartorya hiratsukae*, *Penicillium roseopurpureum*, and *Camarosporium laburnicola* were selected for further studies. As a result of biotransformation studies on sapogenins, a

total of forty-one metabolites were isolated. Hydroxylation, oxidation, epoxidation, *O*-methylation, ring expansion, methyl migration, Baeyer-Villiger oxidation, and ring-opening reactions took place in the metabolites obtained (Figure 2.1)[48–50,73].

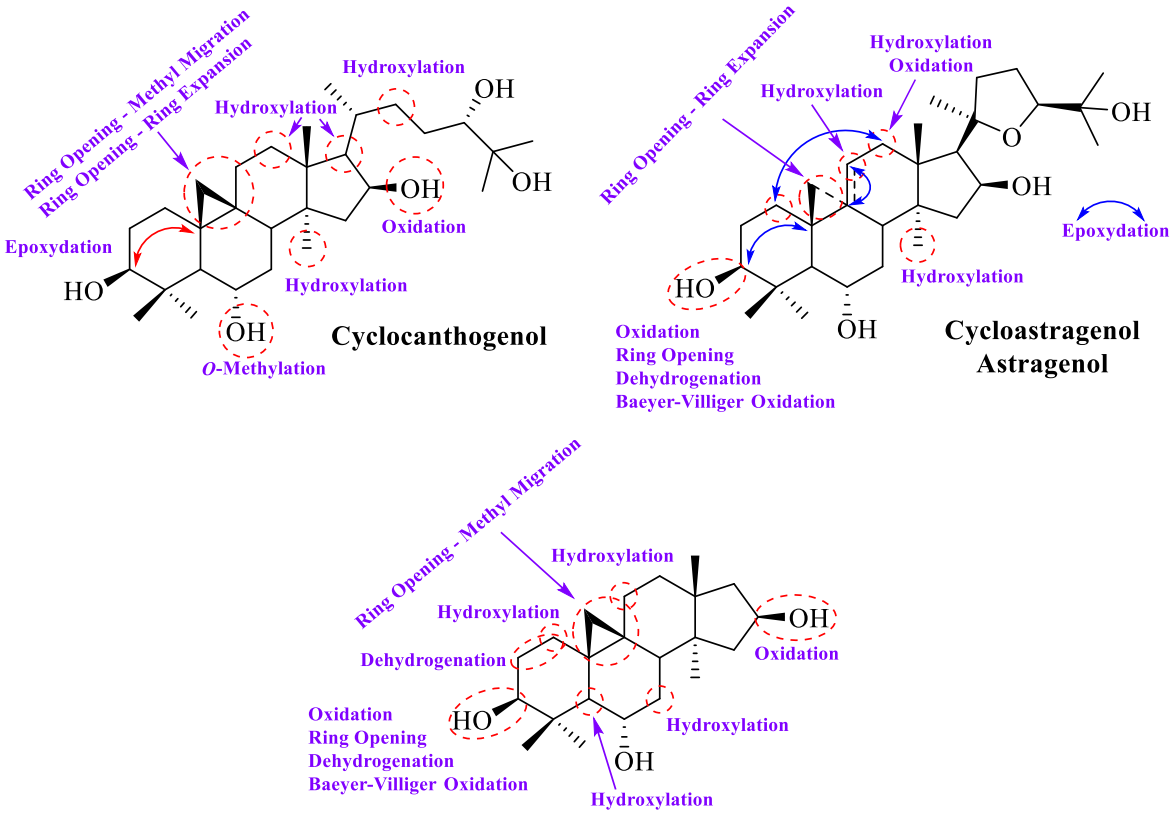

Figure 2.1. Transformations observed in biotransformation studies on cyclocanthogenol, cycloastragenol, astragenol and 20(27)-octanor cycloastragenol.

The hydroxylation reactions (C-1, C-7, C-5, C-11, C-12, C-17, C-19, C-22, C-30) on sapogenin skeletons are catalyzed by cytochrome P450 monooxygenase enzymes of endophytic fungi. In addition, these enzyme systems can also perform hydroxylation at inactive sites. Microbial biotransformation-mediated C-5, C-17 and C-22 hydroxylation reactions were reported in the cycloartane skeleton for the first time in our studies.

In addition to hydroxylation reactions, *A. eureka* performed ring expansion, epoxidation, and methyl migration reactions. According to the literature, these transformations are not catalyzed by a single fungus. So, the diversity of the metabolite library produced by *A. eureka* reveals the potential of this fungus[74–77].

Oxidation, Baeyer-Villiger oxidation and ring-opening reactions were observed on the A ring of the sapogenin skeletons as a result of biotransformation with *C. laburnicola*. Baeyer-Villiger oxidation, which can also be carried out chemically, has begun to be replaced by biological applications, including enzymatic or microbial, due to its high chemo-, regio- and enantioselectivity, wide substrate range, and no need to use strong acids[78]. In the biotransformation studies of cycloastragenol and astragenol with *Glomerella fusarioides* ATCC 9552, lactone formation and subsequent opening of the A ring were also observed in the biotransformation studies performed by our group[74,76]. Although the metabolites obtained from biotransformation with *C. laburnicola* are the same as *G. fusarioides*, the metabolite diversity of *C. laburnicola* is less than that of *G. fusarioides*. This means higher efficiency, easier isolation, and significant advantage in scale-up.

Biotransformation studies on the *Astragalus* cycloartanes-type sapogenins by *Astragalus* endophytes resulted in highly diverse metabolite pool. From this point of view, studies have been conducted to investigate the biocatalytic features of these endophytes on starting molecules with different skeletons.

The first of these studies was carried out on neoruscogenin, a steroidal sapogenin. Neoruscogenin is one of the major bioactive steroidal sapogenins of *Ruscus aculeatus* (Butcher's broom, Rusci rhizome, Asparagaceae)[79]. Ruscogenins (neoruscogenin and ruscogenin) are included in many pharmaceutical preparations used in the treatment of chronic venous insufficiency, varicose veins, hemorrhoids, and orthostatic hypotension due to their pharmacological activities[80–82].

Although a few biotransformation studies have been found in the literature, there were no *in vitro* or *in vivo* studies on the metabolism of ruscogenins. Since fungal biotransformation studies are also used to predict mammalian metabolism, our team decided to perform biotransformation studies on neoruscogenin with *N. hiratsukae* and *A. eureka*. Oxidation, hydroxylation, epoxidation, glycosidation, and opening of the spiroketal system

on the steroidal sapogenin skeleton were determined, and seventeen metabolites were isolated (Figure 2.2)[83,84].

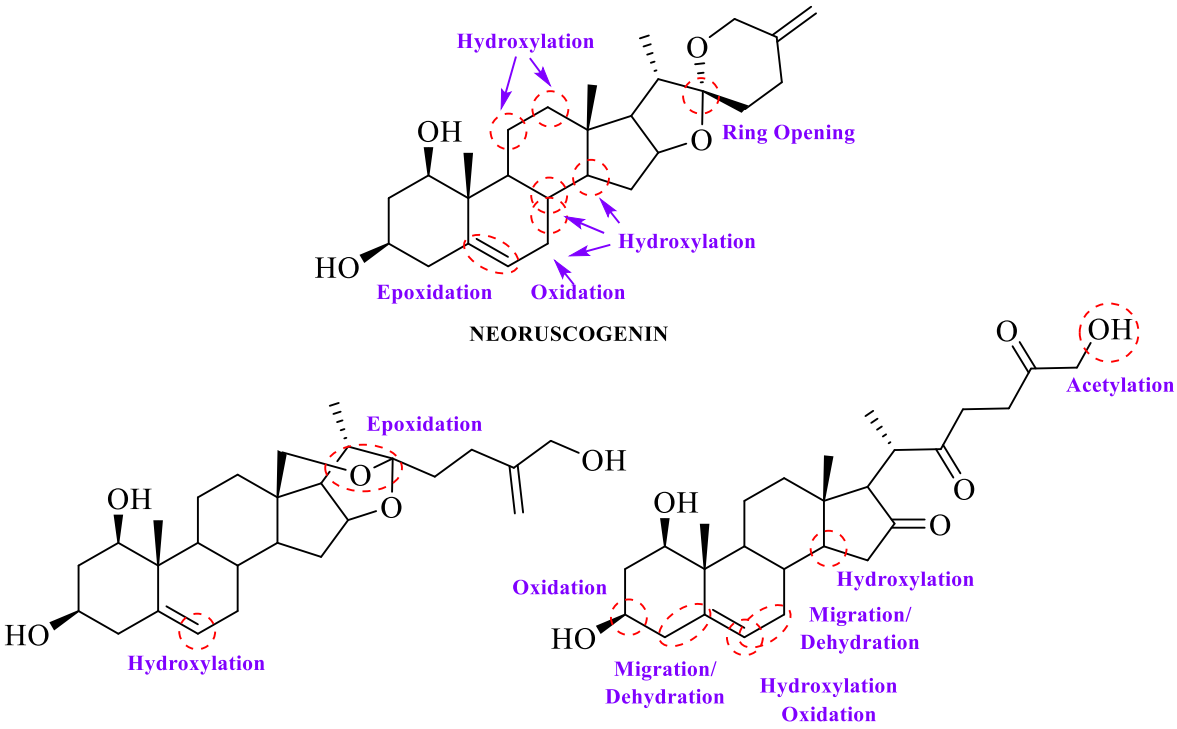

Figure 2.2. Transformations observed in biotransformation studies on neoruscogenin using *N. hiratsukae* and *A. eureka*.

N. hiratsukae catalyzed phase I and phase II reactions on the steroid ring of the spirostanol structure. Cytochrome P450 enzymes of *N. hiratsukae* performed hydroxylation at C-7 and C-12 and further oxidation reactions at C-12. As a phase II reaction, glycosidation was observed. In the literature, glycosidation reaction is rarely encountered in biotransformation studies in which microorganisms are used as the whole cell system[85].

In the biotransformation study of neoruscogenin with *A. eureka*, hydroxylation (C-7, C-8, C-11, C-12 and C-14), oxidation (C-7), epoxidation and ring opening reactions were determined. In the literature, hydroxylation and advanced oxidation reactions at C-7, C-11 and C-12 are frequently observed, while hydroxylation of the less active C-14 is very rare[86–88]. The hydroxylation at the stereocenter C-8 was only yielded in the biotransformation of

steroidal compounds using *Alternaria alternata* and *Corynespora cassiicada* in previous studies[89,90]. One of the interesting reactions was epoxidation, which we encountered in various semi-synthesis and microbial biotransformation studies. In this study, microbial enzyme system-mediated C-5(6) double-bond epoxidation of a steroid compound was reported for the first time.

One of the most significant transformations was the cleavage of the C-22/C-26 oxygen bridge yielding a furostanol-type steroidal framework. This modification resulted in the formation of a C-18(O)C-22 epoxide ring system. These cleavages and further epoxide ring formation were encountered for the first time in steroid chemistry. While spiroketal hydrolysis has been observed for the first time in a microbial system, this reaction is an important reaction for producing potent cytotoxic metabolites (such as OSW-1) under mild conditions.

Another application of biotransformation studies is obtaining metabolites with improved bioactivity compared to the starting molecules. For this purpose, biotransformation studies with *Astragalus* endophytes (*A. eureka* and *Phaeosphaeria* sp.) were performed on the major metabolites of *Nerium oleander* leaves (cardiac glycosides: oleandrin and nerigoside; cardenolide: gitoxigenin).

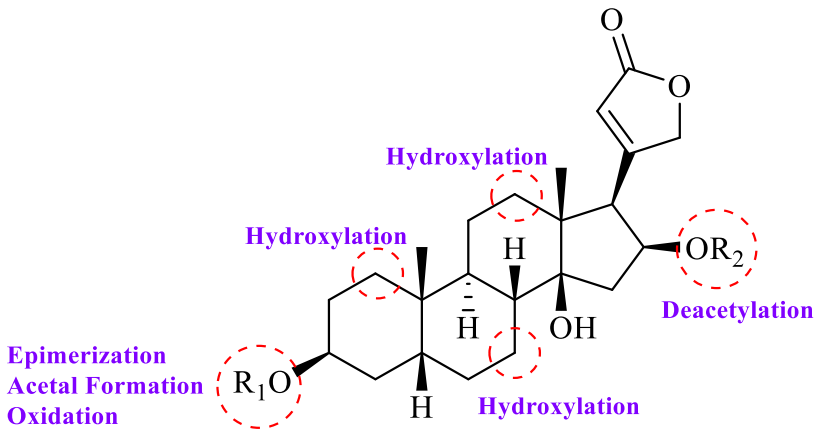

Figure 2.3. Transformations observed in biotransformation studies on oleandrin, nerigoside and gitoxigenin using *A. eureka* and *Phaeosphaeria* sp.

As a result of these studies, fourteen biotransformation products were obtained, and hydroxylation, oxidation, epimerization, dimethyl acetal formation and deacetylation transformations were observed on the starting compounds (Figure 2.3)[91,92]. The epimerization and dimethyl acetal formation by *A. eureka* are fascinating reactions for biotransformation studies. Epimerization reactions are infrequent in biotransformation studies. The formation of dimethyl acetal using a microbial system was reported for the first time.

2.2. Materials and Methods

2.2.1. Microorganism and Starting Compound

Cyclocephagenol (**1**) was donated by Bionorm Natural Products, Ltd. (İzmir, Turkey) (Figure 2.4).

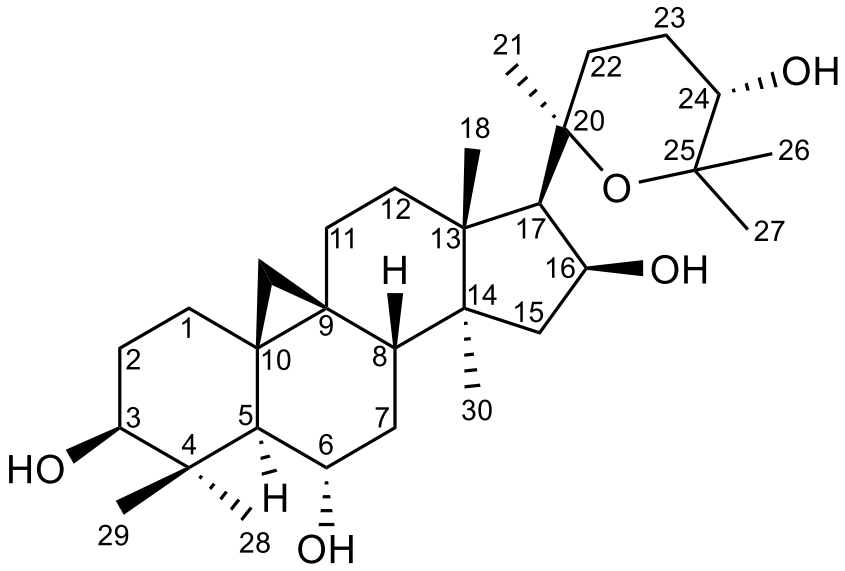

Figure 2.4. Structure of cyclocephagenol.

A. eureka, the fungal endophyte, was isolated from fresh and healthy leaves of *Astragalus angustifolius* (Figure 2.5). The original strain was deposited at the Bedir Laboratory with the deposit number 20131E1BL1[73]. The culture was maintained on potato dextrose agar (PDA) slants and stored at 4 °C until use. Prior to biotransformation, the fungus was pre-cultivated on PDA in Petri dishes for 10 days at 25 °C.

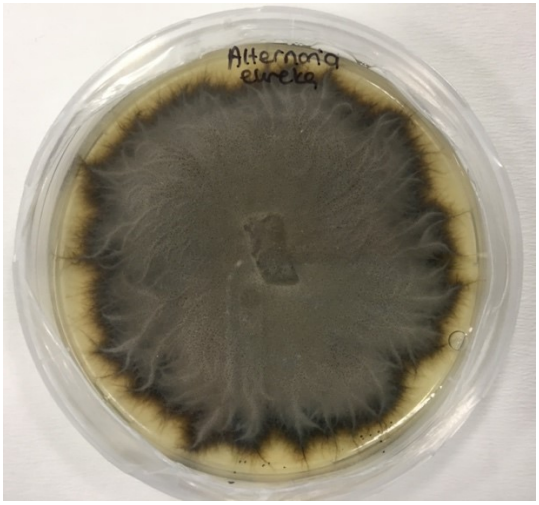

Figure 2.5. *Alternaria eureka*

2.2.2. Microbial Biotransformation Procedures

Stock cultures stored at 4 °C in an agar slant were transferred to the fresh PDA medium and incubated at 25 °C for 10 days. Following incubation, Tween 80 (0.1%) was added to the fungi grown in the PDA medium and a spore solution was obtained by scraping with an inoculation loop. The spore suspension was inoculated to a biotransformation medium (BM: 2% glucose, 0.5% NaCl, 0.5% peptone, 0.5% yeast extract, 0.5% K_2HPO_4). After 3 days of incubation, the substrate (20 mg/mL in DMSO) was dosed at 1 % (v/v) of the medium. Preparative-scale biotransformation studies were performed employing 1850 mg of **1** with *A. eureka* for 13 days (25 °C and 180 rpm)[73].

2.2.3. Extraction and Isolation

After an incubation period, the fungal mycelia were filtered on a Buchner funnel, and the filtrate was extracted with EtOAc (×3). The organic phase evaporated under reduced dryness pressure (Chromatogram 2.1).

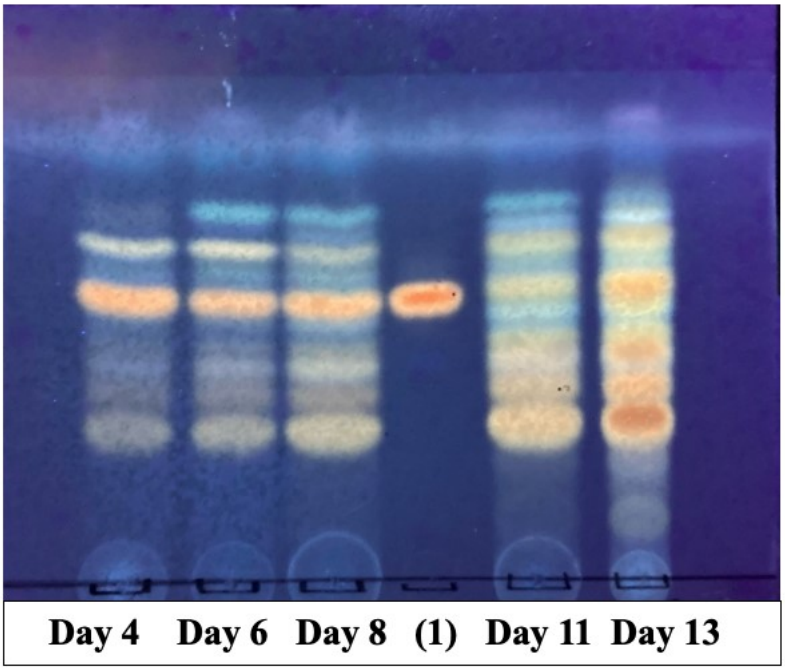

Chromatogram 2.1. Thin layer chromatogram of EtOAc extracts for different biotransformation time points (Day 4, 6, 8, 11 and 13) [Silica gel, Mobile phase: 87.5:12.5 ($CHCl_3$:MeOH)].

Compounds **2**-**22** were isolated from the EtOAc extract (3.05 g) of *A. eureka* and **1**. This crude extract was first chromatographed on a reversed-phase column (RP-C18, 80 g), using elution mixtures of MeOH:H_2O (25:75, 35:65, 45:55, 50:50, 55:45, 70:30, 80:20, 90:10, 100:0), yielding 12 fractions (A-L). Fraction B (19.3 mg) was submitted to silica gel column chromatography (10 g), eluting with $CHCl_3$:MeOH (90:10) to afford 2 mg of **18** (yield: 0.11%). Fraction D (175.3 mg) was applied to a silica gel column (52 g) using a

$CHCl_3$:MeOH gradient (95:5, 93:7), to yield **17** (3.5 mg, yield: 0.19%) and **2** (120.5 mg, yield: 6.51%). Fraction E (301.2 mg) was subjected to a silica gel column (52 g) using a $CHCl_3$:MeOH gradient (93:7, 92:8, 90:10) to give **3** (18.2 mg, yield: 0.98%) and four fractions (E1-4). Fraction E1 (7.6 mg) was further purified on a silica gel column (10 g) and eluted with *n*-hexane:EtOAc:MeOH (10:10:1) to give 2.8 mg of **14** (yield: 0.15%). To isolate metabolite **9** (8 mg, yield: 0.43%), fraction E2 (27.8 mg) was further purified on a silica gel column (15 g) using *n*-hexane:EtOAc:MeOH (10:10:1). Fraction E3 (50.1 mg) was subjected to a silica gel column (15 g) using $CHCl_3$:MeOH (95:5) to afford 15 mg of **13** (yield: 0.81%). Fraction E4 (21.7 mg) was subjected to a silica gel column (15 g), using $CHCl_3$:MeOH (95:5) for elution, to give **16** (4 mg, yield: 0.22%). Fraction F (192.9 mg) was further purified on a silica gel column (50 g) using $CHCl_3$:MeOH (97:3, 95:5, 93:7) for elution, to give metabolites **10** (6.3 mg, yield: 0.34%), **19** (31.1 mg, yield: 1.68%) and one impure fraction (F1). Fraction F1 was further purified by a silica gel column (10 g) with the solvent system *n*-hexane:EtOAc:MeOH (10:10:1), to provide 3.6 mg of **15** (yield: 0.19%). Fraction G (98.7 mg) was submitted to a silica gel column (53 g) using mixtures of $CHCl_3$:MeOH (95:5, 94:6, 93:7) to give **12** (3.5 mg, yield: 0.19%) and two fractions (G1-2). To isolate metabolite **11** (1.4 mg, yield: 0.075%), fraction G1 (23.3 mg) was subjected to a silica gel column (10 g), using *n*-hexane:EtOAc:MeOH (10:10:1). Fraction G2 (9 mg) was further fractionated over a silica gel column (10 g) with the solvent system *n*-hexane:EtOAc:MeOH (10:10:1, 10:10:2), to provide 4.6 mg of **4** (yield: 0.25%). Fraction H (275.1 mg) was submitted to a silica gel column (50 g) and eluted with a $CHCl_3$:MeOH gradient (95:5, 93:7, 92:8, 90:10) to afford two fractions (H1-2). Fraction H1 (18.3 mg) was purified by a silica gel column (10 g) and eluted with *n*-hexane:EtOAc:MeOH (10:10:1), to give 5.4 mg of **5** (yield: 0.29%). Fraction H2 (138.2 mg) was applied to VLC packed with reversed-phase silica gel (RP-C18, 30 g), using ACN:H_2O gradient (25:75, 30:70, 40:60, 50:50), to afford **6** (95.4 mg, yield: 5.16%). Fraction I (86.9 mg) was subjected a silica gel column (50 g) using $CHCl_3$:MeOH solvent system (95:5) to give **7** (16.9 mg, yield: 0.91%) and one impure fraction (I1). Fraction I1 (12.9 mg) was further purified on a silica gel column (10 g) and was eluted with a $CHCl_3$:MeOH gradient (99:1, 98:2) to give 1.1 mg of **22** (yield: 0.06%) and fraction I1a. To purify metabolite **8** (2.4 mg, yield: 0.13%), fraction I1a (7.4 mg) was subjected to silica gel column chromatography (10 g) with the solvent system *n*-hexane:EtOAc:MeOH (10:10:1).

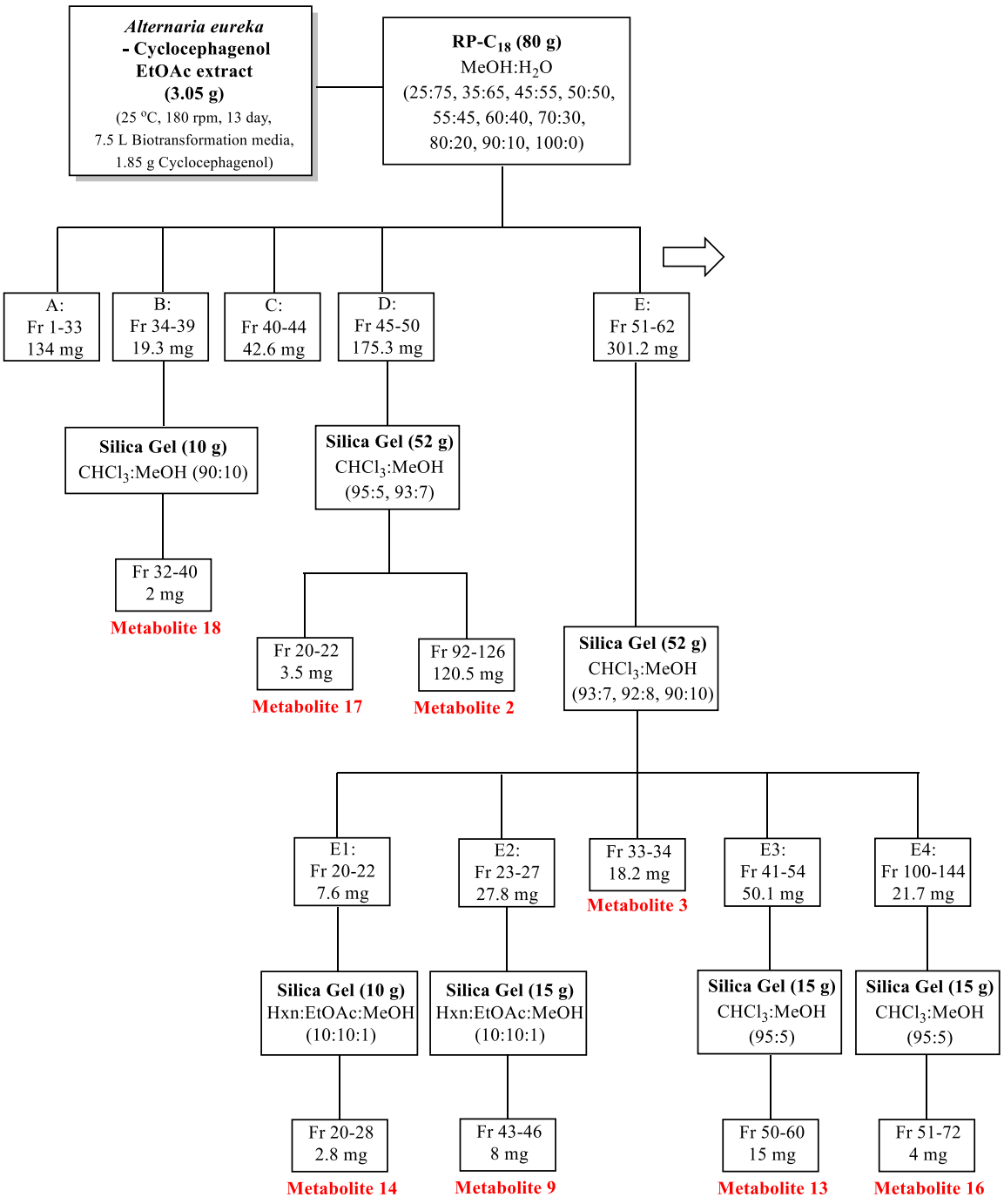

Figure 2.6. Isolation scheme of biotransformation products of cyclocephagenol by *A. eureka*

(cont. on next page)

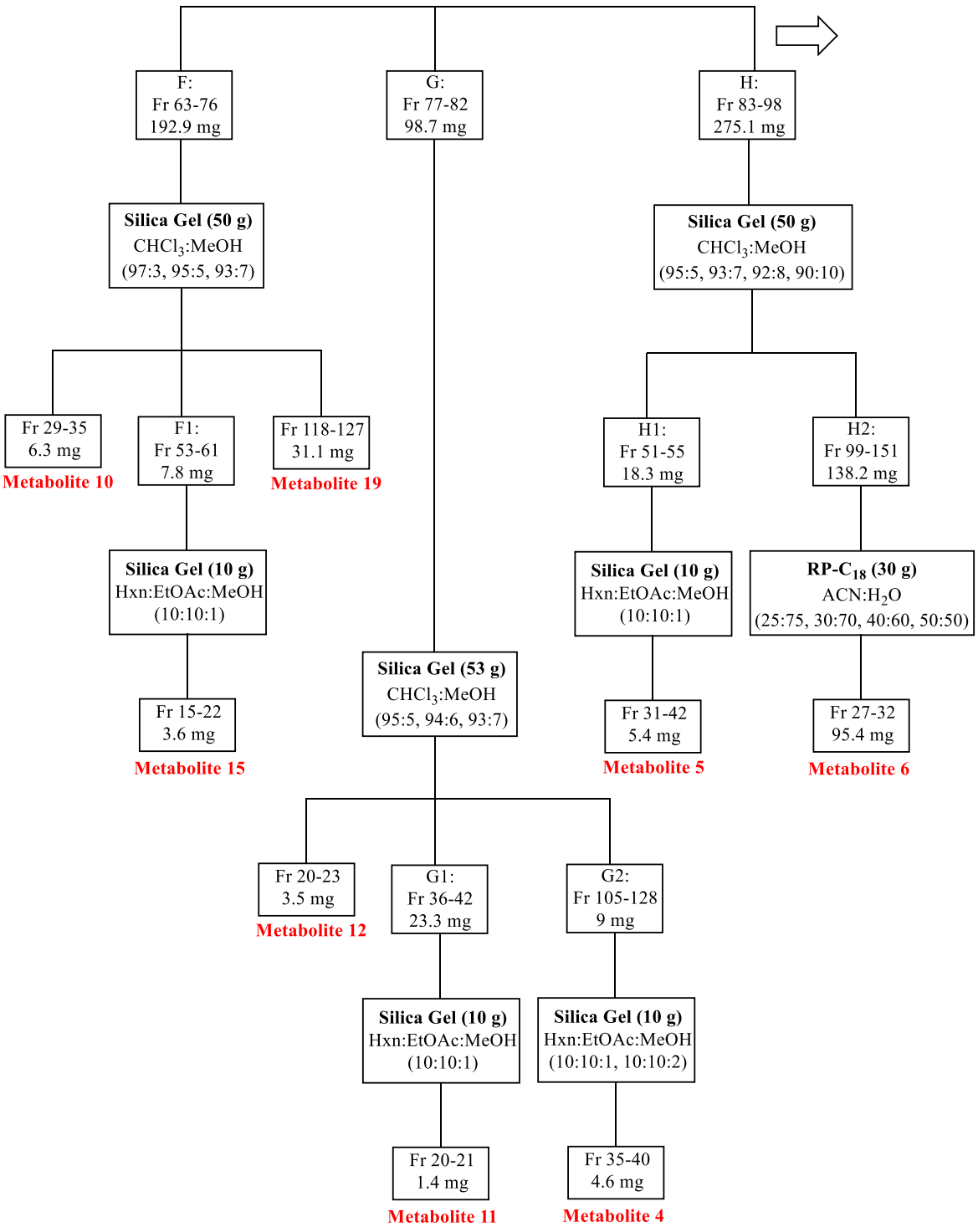

Figure 2.6. (cont.)

(cont. on next page)

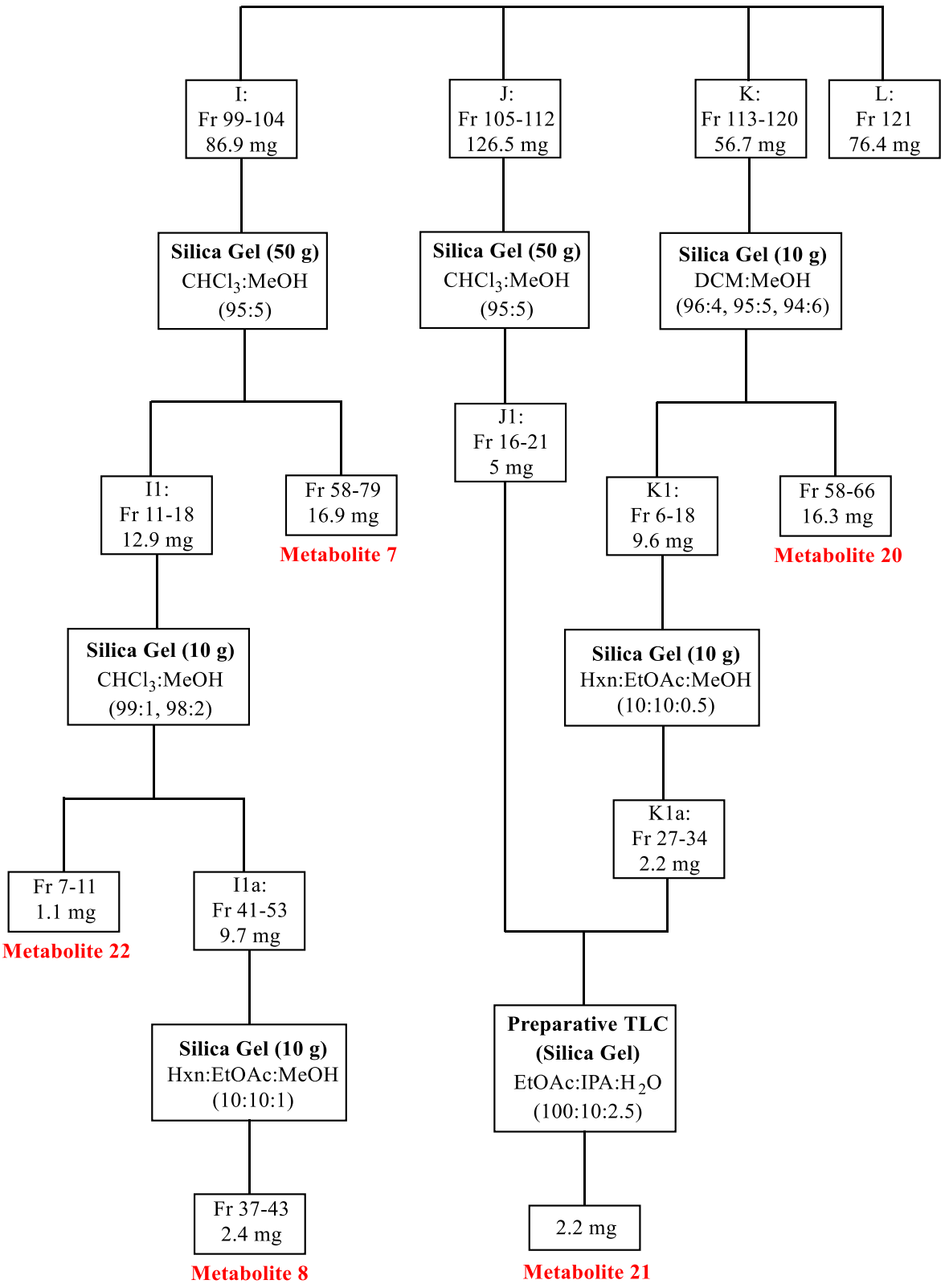

Figure 2.6. (cont.)

Fraction J (126.5 mg) was submitted to a silica gel column (50 g), eluted with $CHCl_3$:MeOH (95:5) to give fraction J1 (5 mg). Fraction K (56.7 mg) was subjected to silica gel column chromatography (10 g) to yield **20** (16.3 mg, yield: 0.88%) one impure fraction (K1) after elution with DCM:MeOH gradient (96:4, 95:5, 94:6). Fraction K1 (9.6 mg) was chromatographed on a silica gel column (10 g) using *n*-hexane:EtOAc:MeOH (10:10:0.5) to afford fraction K1a (2.1 mg). To isolate metabolite **21** (2.2 mg, yield: 0.12%), fractions K1a and J1 (7.1 mg) were combined and subjected to a preparative thin layer chromatography employed with EtOAc:IPA:H_2O (100:10:2.5) (Chromatogram 2.2 and Figure 2.6).

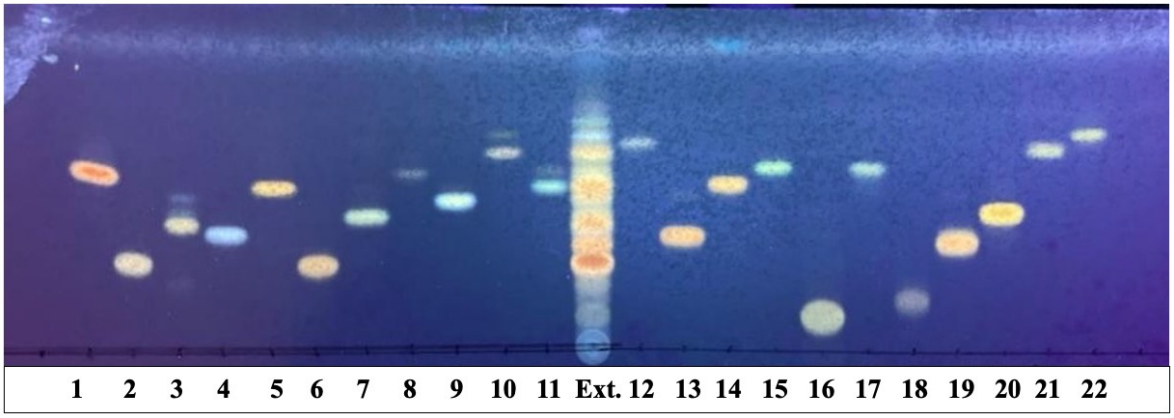

Chromatogram 2.2. Thin layer chromatogram of the isolated metabolites and the EtOAc extract [Silica gel, Mobile phase: 87.5:12.5 ($CHCl_3$:MeOH)].

2.2.4. Neuroprotection Studies for Biotransformation Products from *Alternaria eureka*

2.2.4.1. Determination of Cell Viability

SH-SY5Y cell line was maintained in high-glucose Dulbecco's modified Eagle medium (DMEM) containing 10% FBS at 37 °C, and 5% CO_2. The cells were homogenously

seeded in 96 well plate (20000 cells/well) and incubated for 24 h. Following 2 h incubation with compounds or vehicle (DMSO), the cells were treated with 70 µM H_2O_2. For the 6-OHDA mediated toxicity experiments, cells were treated with 50 µM 6-OHDA after 8 h of treatment with the compounds. For both experiments, cell viability was determined after 24 h via the MTT (3-[4,5-Dimethylthiazol-2-yl]-2,5-diphenyltetrazolium bromide) assay. Briefly, the cells were incubated with MTT (0.5 mg/ml final concentration) for 4 h. Then, all the media was pulled out, and DMSO was added to wells. Photometric absorbance was measured at a wavelength of 590/690 nm by using Varioscan flash spectrophotometer by Thermo Scientific. The statistical significance of differences between compounds and H_2O_2 or 6-OHDA treatments were assessed by one-way ANOVA using GraphPad Prism software.

2.2.4.2. Determination of ROS Levels

SH-SY5Y cells were seeded onto the 6 well plates and were treated with either compounds or the vesicle for 2 h. Then, cells were treated with 70 µM H_2O_2. After 24 h, cells were incubated with 10 µM 2',7'-Dichlorodihydrofluorescein diacetate (Enzo; ALX-610-022-M050) in PBS for 30 min at 37 °C. Cells were then detached from the surface by using trypsin and harvested in PBS, and part of the suspension was transferred to a 96-well black plate to measure absorbance at 495/520 nm (Varioscan, Thermo Fisher Scientific, US). To normalize fluorescence values, protein concentrations of the remaining suspension were determined by the bicinchoninic acid (BCA) protein assay (Thermo Fisher Scientific, US).

2.2.4.3. Determination of Mitochondrial Membrane Potential

SH-SY5Y cells were seeded onto the coverslip. After 2 h pretreatment with 100 nM each compound, cells were exposed to 70 µM H_2O_2. Following 24 h incubation, cells were treated with 100 nM MitoTracker® Red FM (Thermo Fisher Scientific, US) for 30 min at 37

°C. Then cells were washed with PBS. After mounting, cells were immediately observed using a fluorescence microscope (Olympus IX70).

All photographs were taken under the same conditions, and the fluorescence intensity of the mitochondria relative to the cell volume was calculated in 30 cells using the ImageJ software.

2.3. Results

2.3.1. Neuroprotective Activity of Cyclocephagenol

The neuroprotective activities of cyclocephagenol (**1**) and cycloastragenol (CG) were determined against H_2O_2 induced SH-SY5Y cell death.

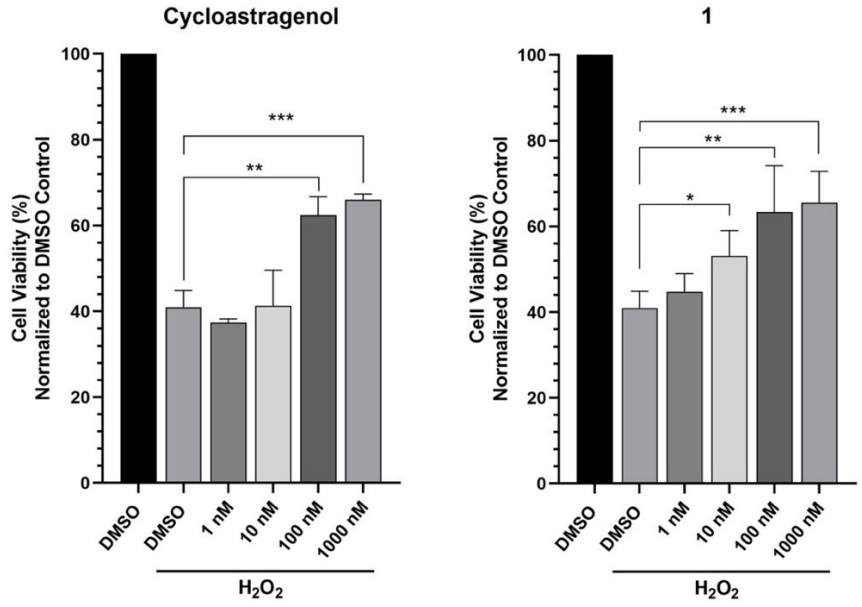

Figure 2.7. Neuroprotective activity of CG and **1** against H_2O_2 toxicity. Error bars are the standard deviations (n = 3). p-Values were calculated with respect to H_2O_2-treated cells (*p<0.05, **p<0.01, ***p< 0.001)

Results showed that both CG and **1** provided dose dependent protection against H_2O_2-induced cell death (Figure 2.7). However, protective activity of **1** started at lower concentrations compared to CG (Figure 2.7). Based on potent activity of **1**, a biotransformation study on **1** was carried out to develop a molecule library and to investigate structure-activity relationships by *A. eureka* affording notable chemical diversity[49,73,84,91,92].

2.3.2. Biotransformation of Cyclocephagenol by *Alternaria eureka*

Biotransformation of cyclocephagenol (**1**) using the endophytic fungus *A. eureka* for 13 days afforded twenty-one metabolites (**2** - **22**). Structural elucidation the compounds was performed based on spectroscopic methods (1D-NMR, 2D-NMR and HR-MS).

2.3.2.1. Structure Elucidation of Cyclocephagenol (1)

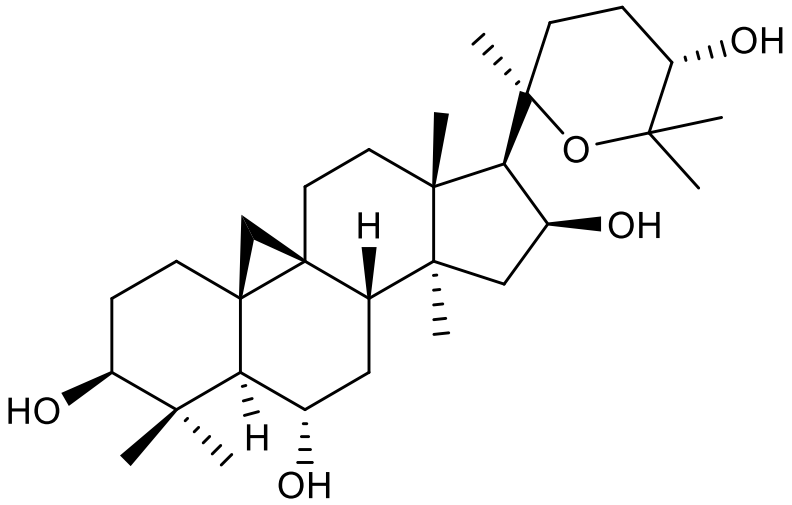

Figure 2.8. Chemical structure of compound **1**.

Compound **1** is a deglycosylated product of a known cycloartane diglycoside, namely cyclocephaloside I[93]. Since it has not been previously reported as a new sapogenin, herein, its structural elucidation is discussed.

The molecular formula of **1** was determined as $C_{30}H_{50}O_5$ due to the sodium adduct ion peak at *m/z* 513.35607 $[M+Na]^+$ by HR-ESI-MS. The ^{1}H-NMR spectrum showed characteristic signals of cyclopropane–methylene protons as an AX system at δ_H 0.30 and 0.58 (each d, J_{AX}=4.1 Hz, H-19a and J_{AX}=3.1 Hz H-19b) and seven tertiary methyl groups. Hence, compound **1** was a cycloartane-type triterpenoid, and this inspection was supported by the ^{13}C-NMR spectral data. The resonances for low-field carbon atoms indicated the presence of four oxymethine carbons (δ_C 78.1, C-3; δ_C 68.3, C-6; δ_C 73.8, C-16; δ_C 68.5, C-24) and two oxygenated singlet carbons (δ_C 78.8, C-20; δ_C 75.1, C-25) substantiated by HSQC. The ^{13}C and ^{1}H-NMR data substantiated with 1D- and 2D-NMR spectra showed that resonances arising from the triterpenoid skeleton were almost superimposable with those of cycloastragenol[94], which is one of the major aglycone constituents of *Astragalus* sp., except for the side chain signals. The HMBC experiment suggested that the 24-hydroxy-20,25-epoxy structure was intact in the side chain of **1**, as in cyclocephaloside I. The carbon resonances ascribed to the side chain consisting of a doublet (δ_C 68.5, C-24), two triplets (δ_C 26.4, C-22; 23.8, C-23), two singlets (δ_C 78.8, C-20; 75.1, C-25) and three quartets (δ_C 28.5, C-21; 28.4, C-26; 27.8; C-27). The HMBC spectrum displayed cross-peaks from H_3-18 and H_3-21 to C-17, H-17 and H_3-21 to C-20, H-17 and H_3-21 to C-22, H_3-26 and H_3-27 to C-24, and H_3-26 and H_3-27 to C-25 confirm this proposal. Thus, the structure of **1** was elucidated as 20,25-epoxy-3β,6α,16β,24α-tetrahydroxycycloartane, which is the aglycone of cyclocephaloside I[93]. Hence, **1** was named as cyclocephagenol.

Table 2.1. The ^{13}C and ^{1}H NMR data of **1** (100/400 MHz, δ ppm, in C_5D_5N).

Position	δ_C (ppm)	δ_H (ppm), *J* (Hz)
1	32.6	1.20 m, 1.61 m
2	31.2	1.92 m, 2.00 m
3	78.1	3.64 dd (8.6, 2.7)
4	42.2	-
5	53.8	1.70 m
6	68.3	3.78 t (8.7)
7	38.7	1.62 m, 1.79 m
8	47.1	1.94 m
9	21.1	-
10	29.6	-
11	26.2	1.14 m, 1.97 m
12	34.0	1.72 m, 1.87 m
13	46.6	-
14	45.7	-
15	47.8	1.79 m, 2.11 m
16	73.8	4.90 dtd (8.0, 5.7, 3.1)
17	60.7	2.10 d (5.9)
18	20.7	1.70 s
19	31.0	0.30 d (3.1), 0.58 d (4.1)
20	78.8	-
21	28.5	1.57 s
22	26.4	1.24 m, 3.09 td (11.2, 4.3)
23	23.8	1.88 m, 2.18 m
24	68.5	3.67 brs
25	75.1	-
26	28.4	1.45 s
27	27.8	1.29 s
28	29.2	1.88 s
29	15.9	1.34 s
30	20.2	0.97 s

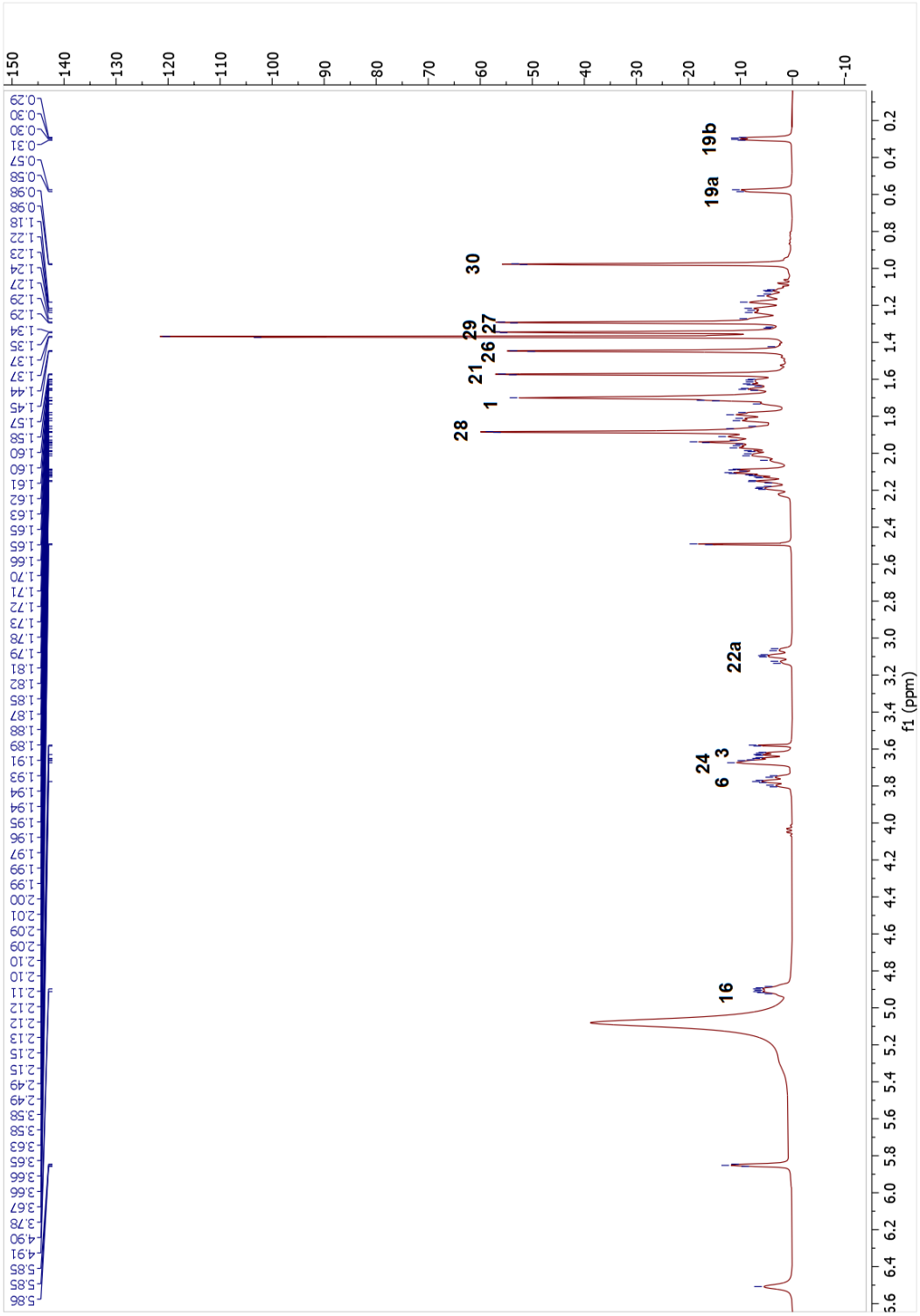

Spectrum 2.1. ^{1}H-NMR spectrum of compound **1**.

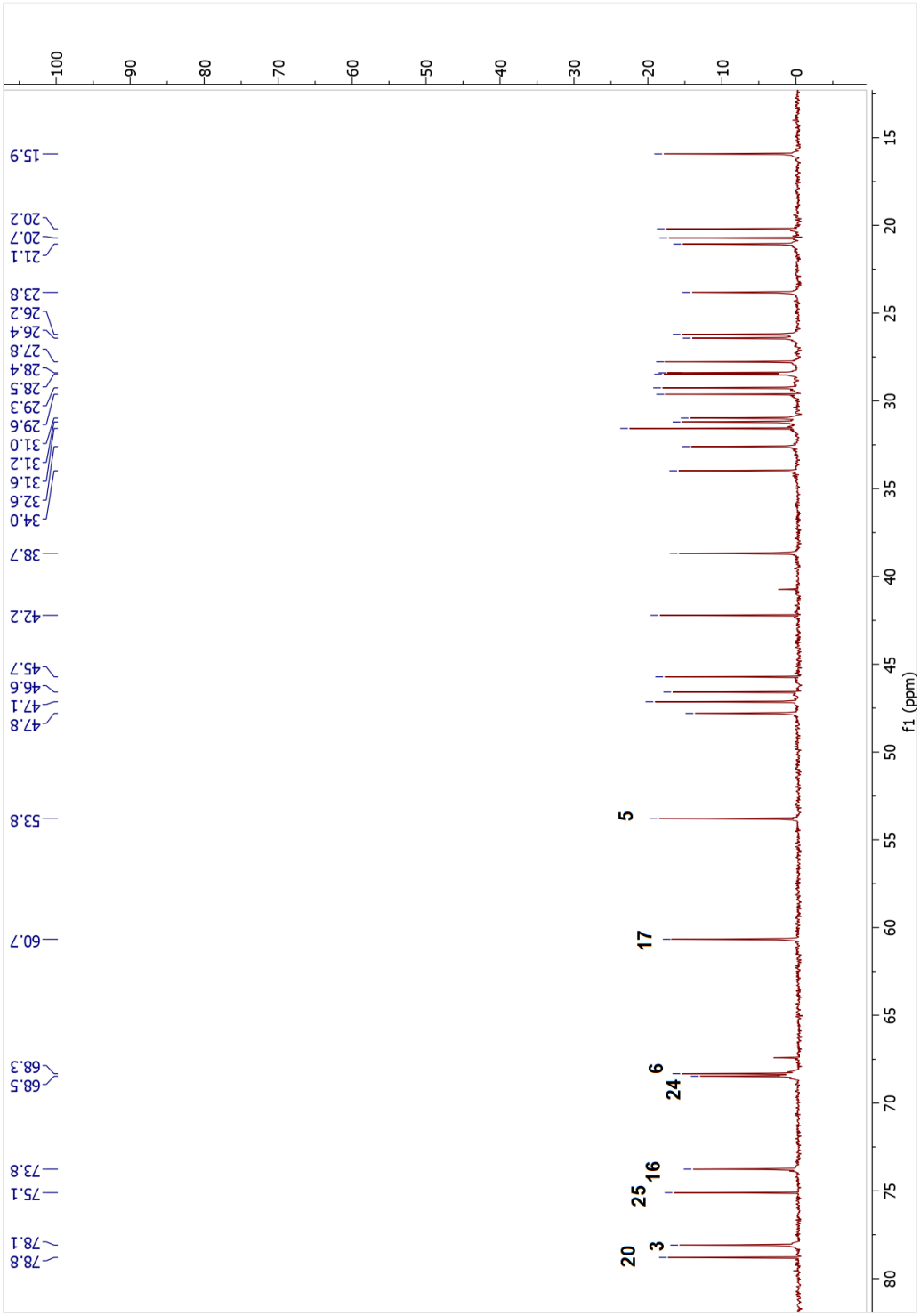

Spectrum 2.2. ^{13}C-NMR spectrum of compound **1**.

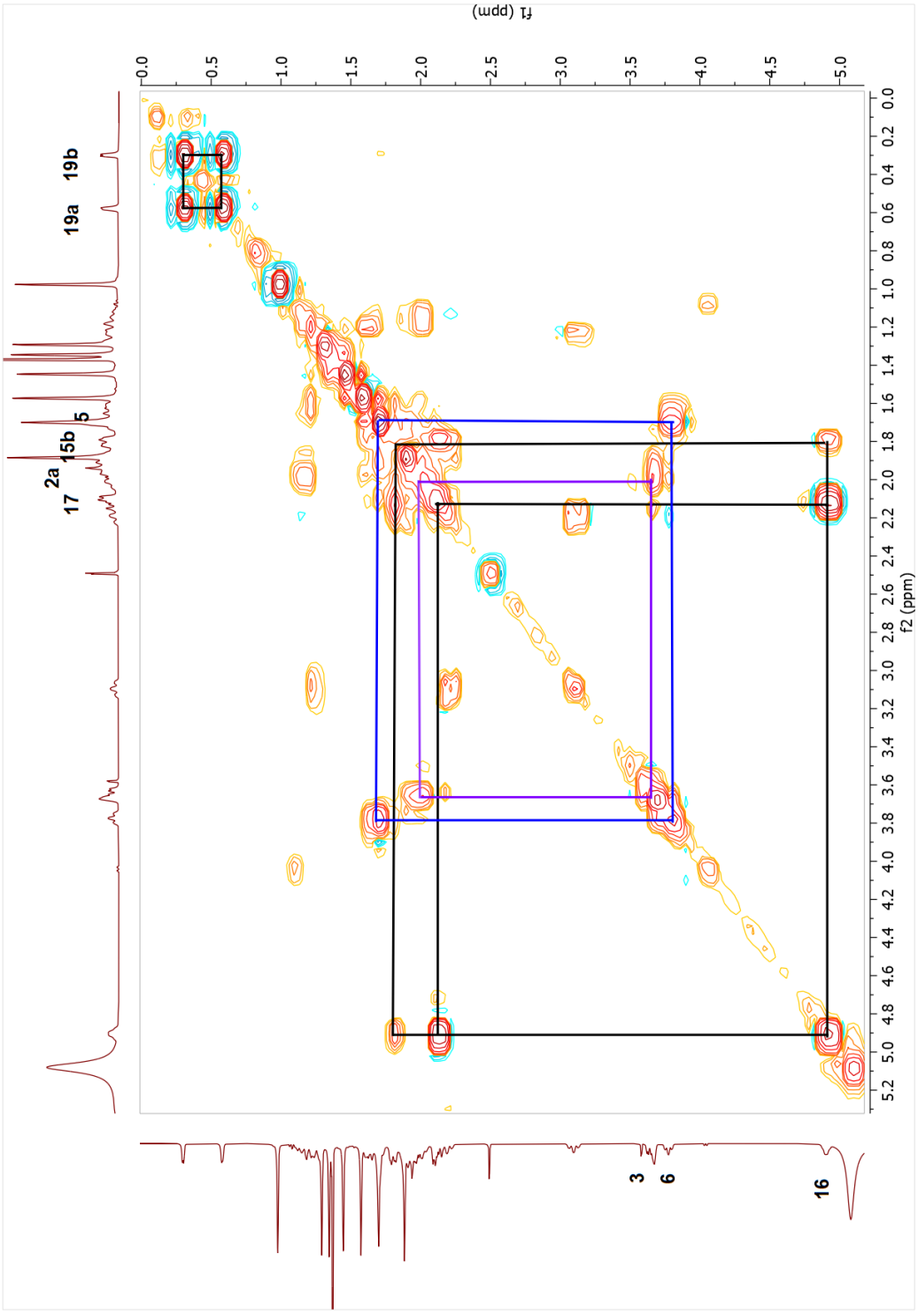

Spectrum 2.3. COSY spectrum of compound **1**.

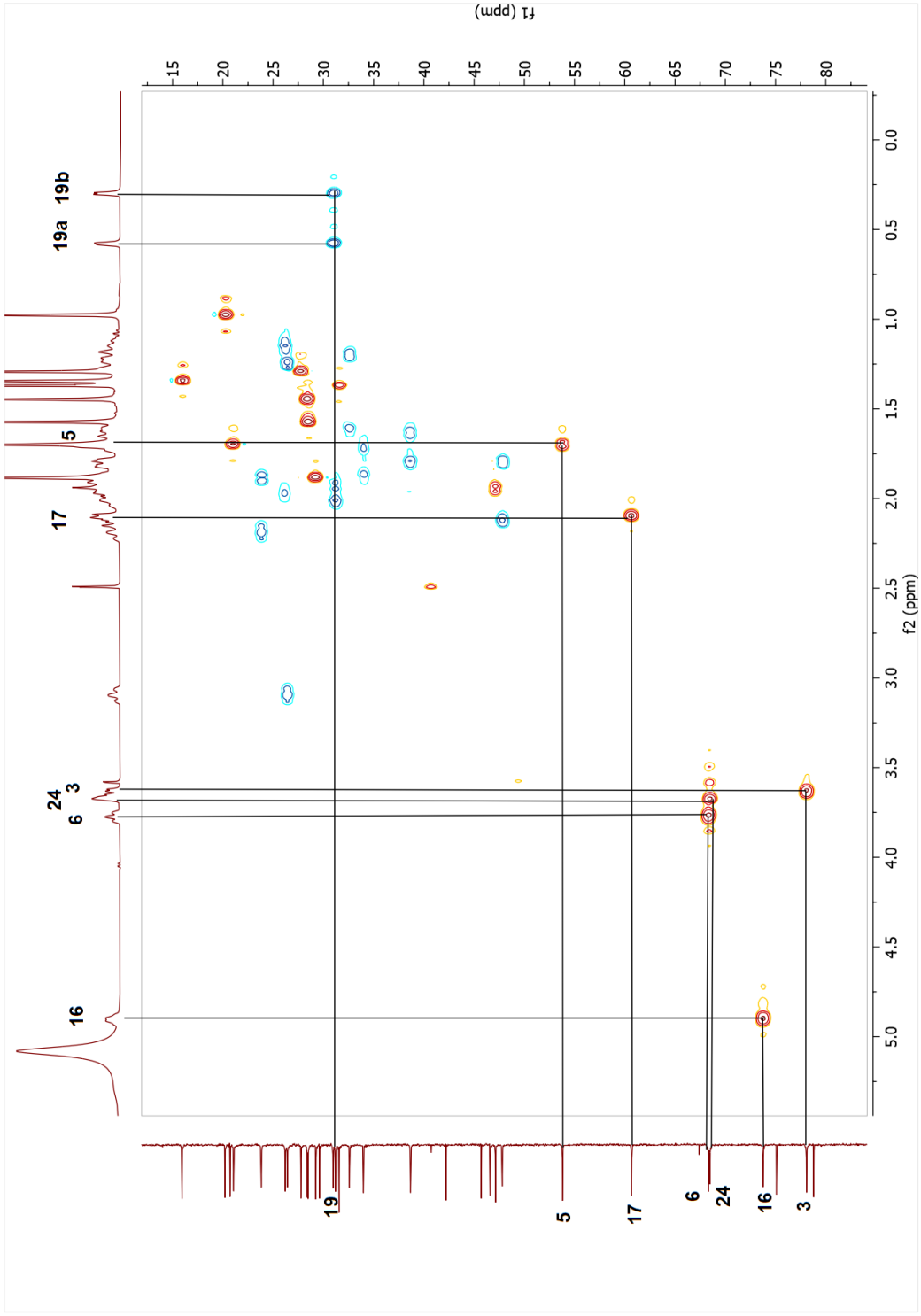

Spectrum 2.4. HSQC spectrum of compound **1**.

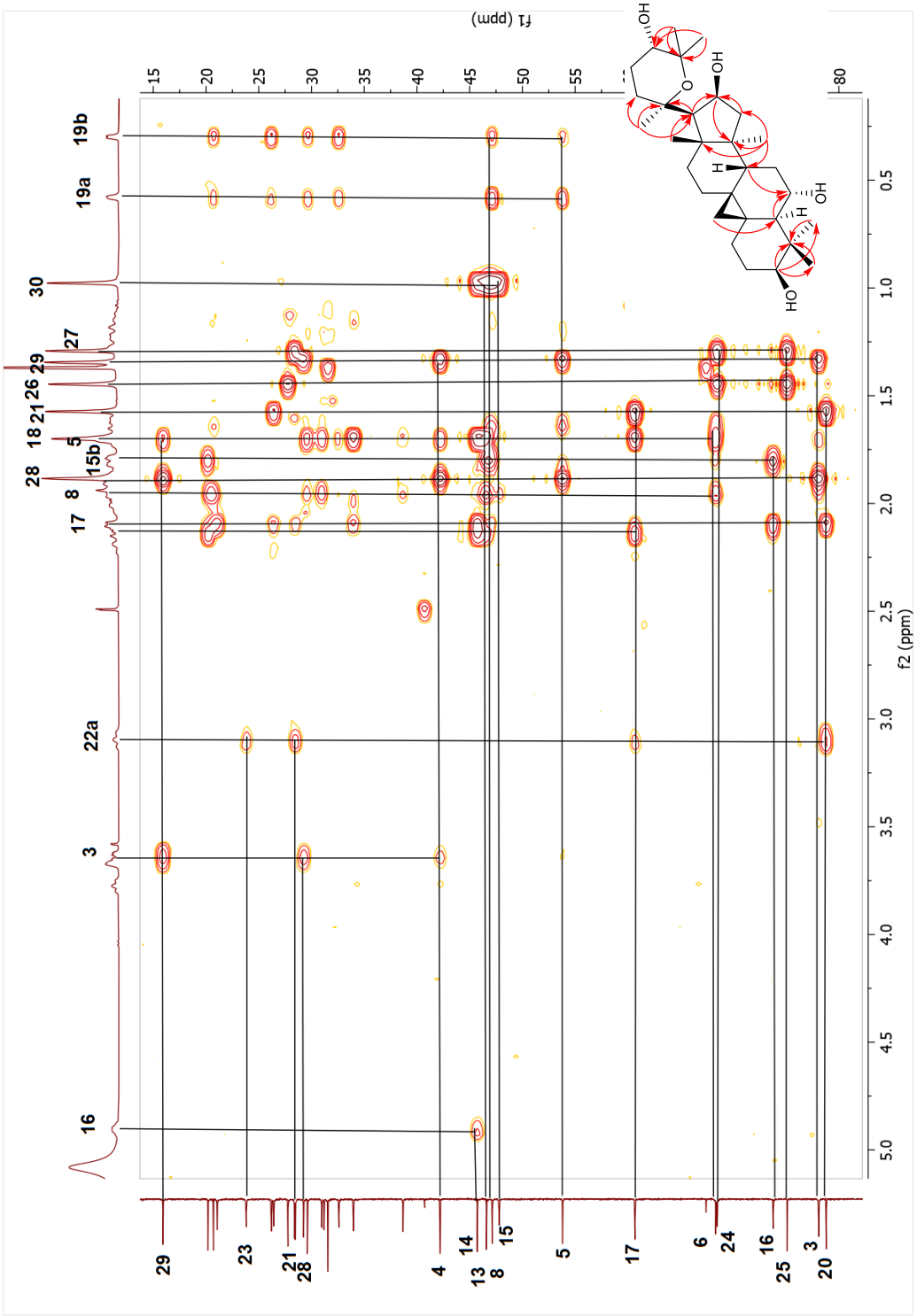

Spectrum 2.5. HMBC spectrum of compound **1**.

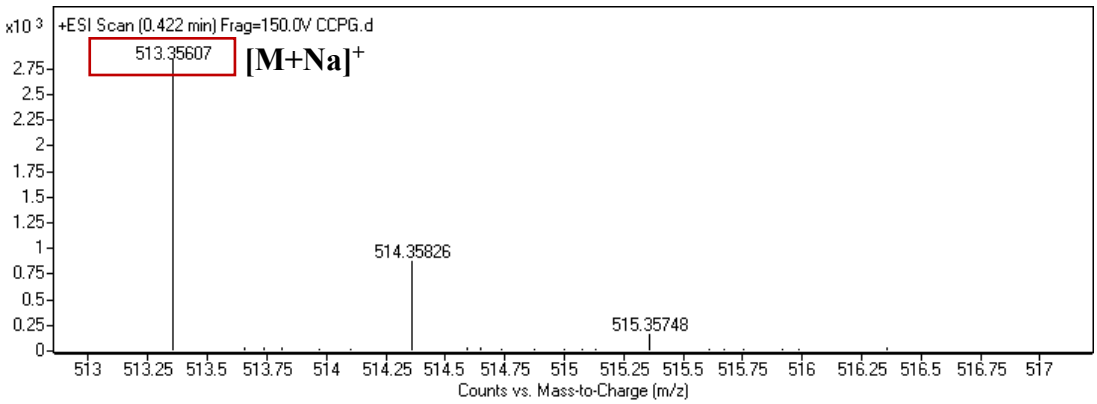

Spectrum 2.6. HR-ESI-MS spectrum of compound **1**.

2.3.2.2. Structure Elucidation of Compound 2

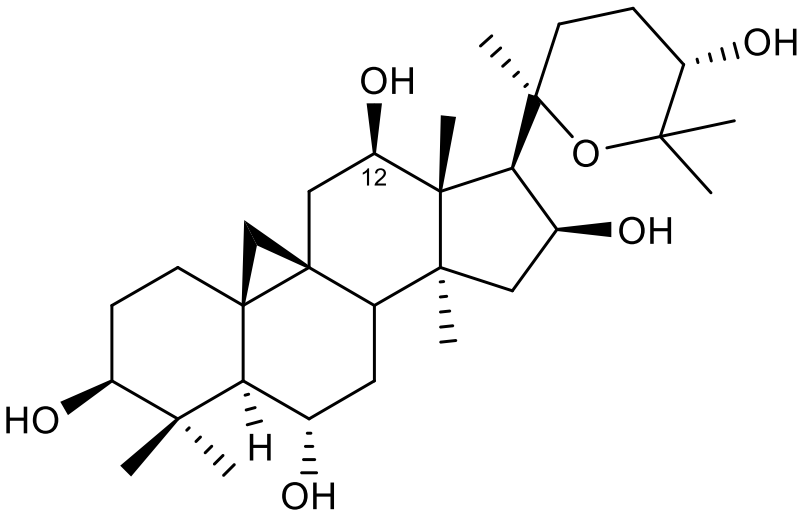

Figure 2.9. Chemical structure of compound **2**.

The HR-ESI-MS data of compound **2** (*m/z* 529.35165 $[M + Na]^+$, calcd for $C_{30}H_{50}NaO_6$, 529.35031) supported a molecular formula of $C_{30}H_{50}O_6$ implying a monooxygenation of **1** due to a +16 amu difference. In the ^{1}H-NMR spectrum, the AX system signals of cyclopropane ring, seven methyl groups in the up-field region, and the characteristic signals belonging to the H-3, H-6, H-16 and H-24 oxymethine protons in the

low-field displayed no significant discrepancy compared to **1**. Apart from the characteristic low-field signals, an additional oxymethine signal at δ_H 4.24 was observed corresponding to a carbon at δ_C 71.6 in the HSQC spectrum. The ^{13}C-NMR spectrum of **2** showed that C-11 (δ_C 36.4) and C-13 (δ_C 52.3) signals underwent a significant down-field shift (*ca*. 10.2 and 5.7 ppm, respectively) when compared to that of **1**, suggesting a hydroxylation at the C-12 position. This assumption was confirmed with the long-distance correlations in the HMBC spectrum from δ_H 4.24 to C-9, C-11, C-17, C-18, and H_2-11, H-17 and H_3-18 to δ_C 71.6. The hydroxy group at C-12 was deduced to be β-oriented on the basis of NOESY correlations of H-12 with α-oriented H_3-30 and H-17 protons. Thus, the structure of **2** was identified as 20,25-epoxy-3β,6α,12β,16β,24α-pentahydroxycycloartane.

Table 2.2. The ^{13}C and ^{1}H NMR data of **2** (100/400 MHz, δ ppm, in C_5D_5N).

Position	**δ_C (ppm)**	**δ_H (ppm), *J* (Hz)**	**Position**	**δ_C (ppm)**	**δ_H (ppm), *J* (Hz)**
1	32.3	1.37 m, 1.65 m	**16**	71.3	4.87 tt (8.1, 4.4)
2	31.0	1.94 m, 2.03 m	**17**	62.0	2.60 d (7.6)
3	78.0	3.66 dd (11.5, 4.5)	**18**	13.5	1.84 s
4	42.1	-	**19**	28.4	0.36 d (4.3), 0.71 d (4.4)
5	53.1	1.74 d (9.0)	**20**	78.5	-
6	66.9	3.89 dp (11.7, 3.9, 3.3)	**21**	27.0	2.04 s
7	37.2	1.67 m, 1.93 m	**22**	29.5	2.30 m, 2.66 m
8	44.4	2.25 m	**23**	23.7	1.95 m, 2.32 m
9	21.8	-	**24**	69.1	3.74 brs
10	29.2	-	**25**	75.7	-
11	36.4	1.72 m, 2.43 dd (15.2, 8.1)	**26**	28.4	1.41 s
12	71.6	4.24 t (7.2)	**27**	28.2	1.62 s
13	52.3	-	**28**	28.8	1.86 s
14	47.5	-	**29**	15.7	1.34 s
15	48.5	1.98 m, 2.20 m	**30**	19.7	1.04 s

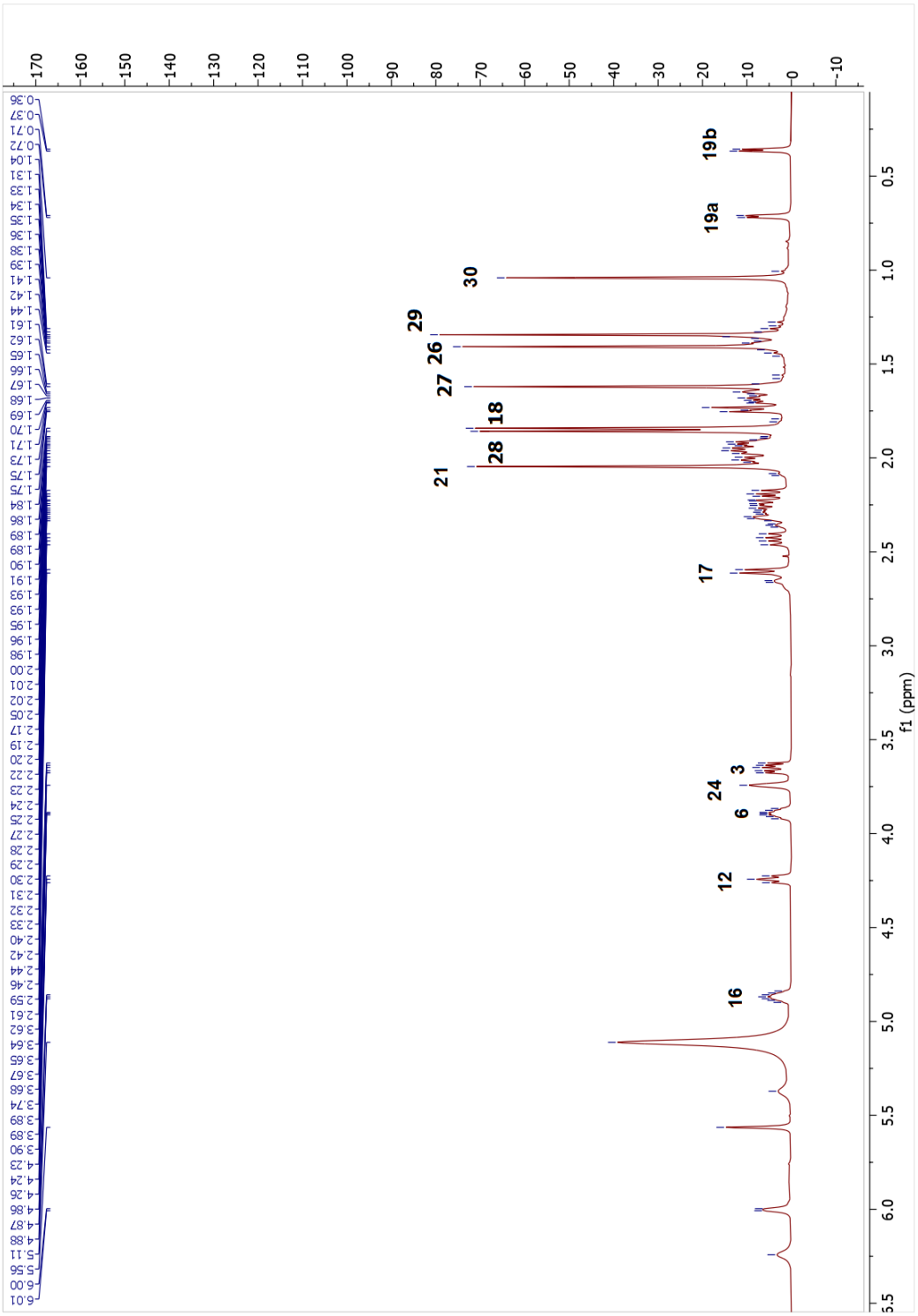

Spectrum 2.7. ^{1}H-NMR spectrum of compound **2**.

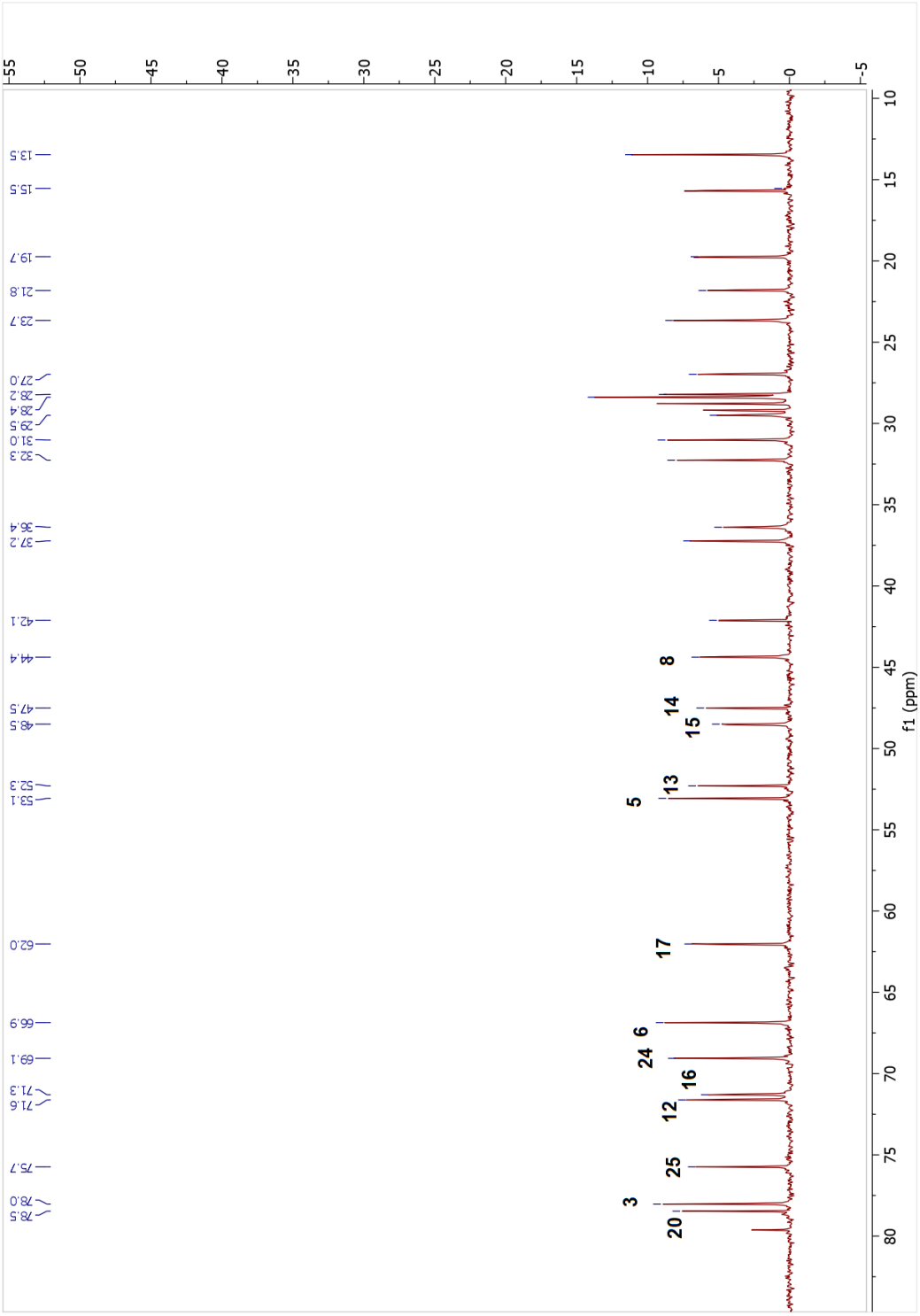

Spectrum 2.8. ^{13}C-NMR spectrum of compound **2**.

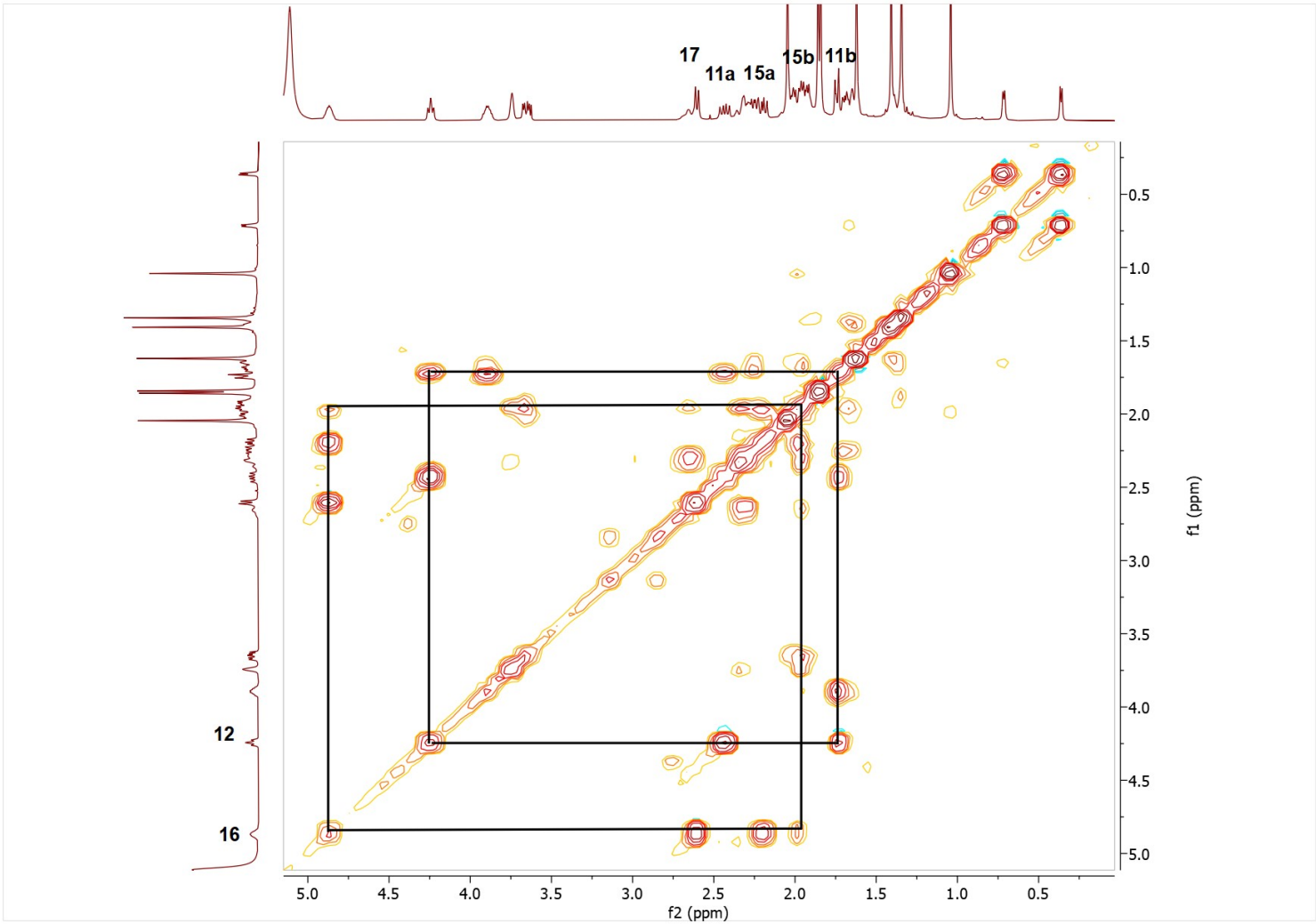

Spectrum 2.9. COSY spectrum of compound **2**.

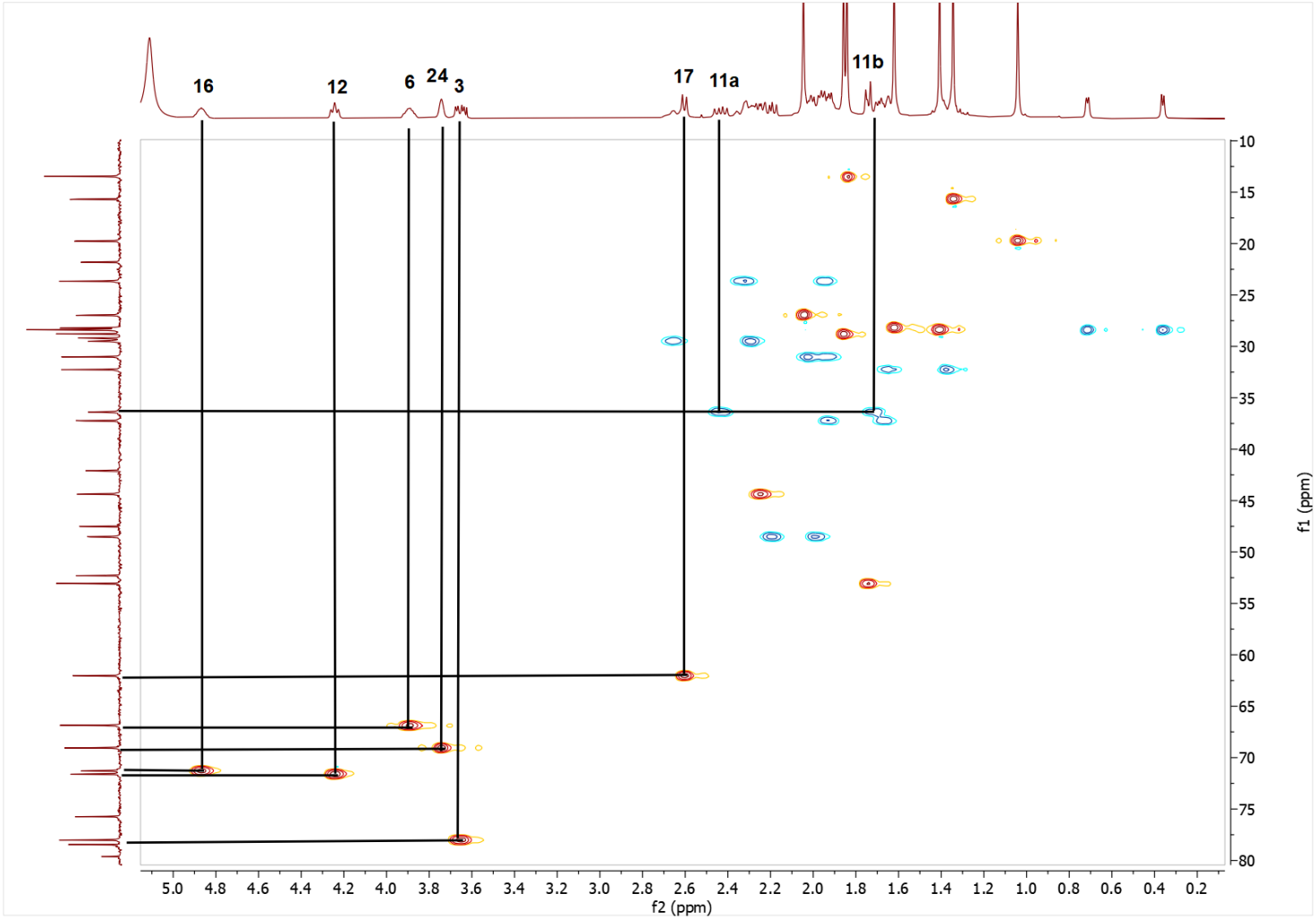

Spectrum 2.10. HSQC spectrum of compound **2**.

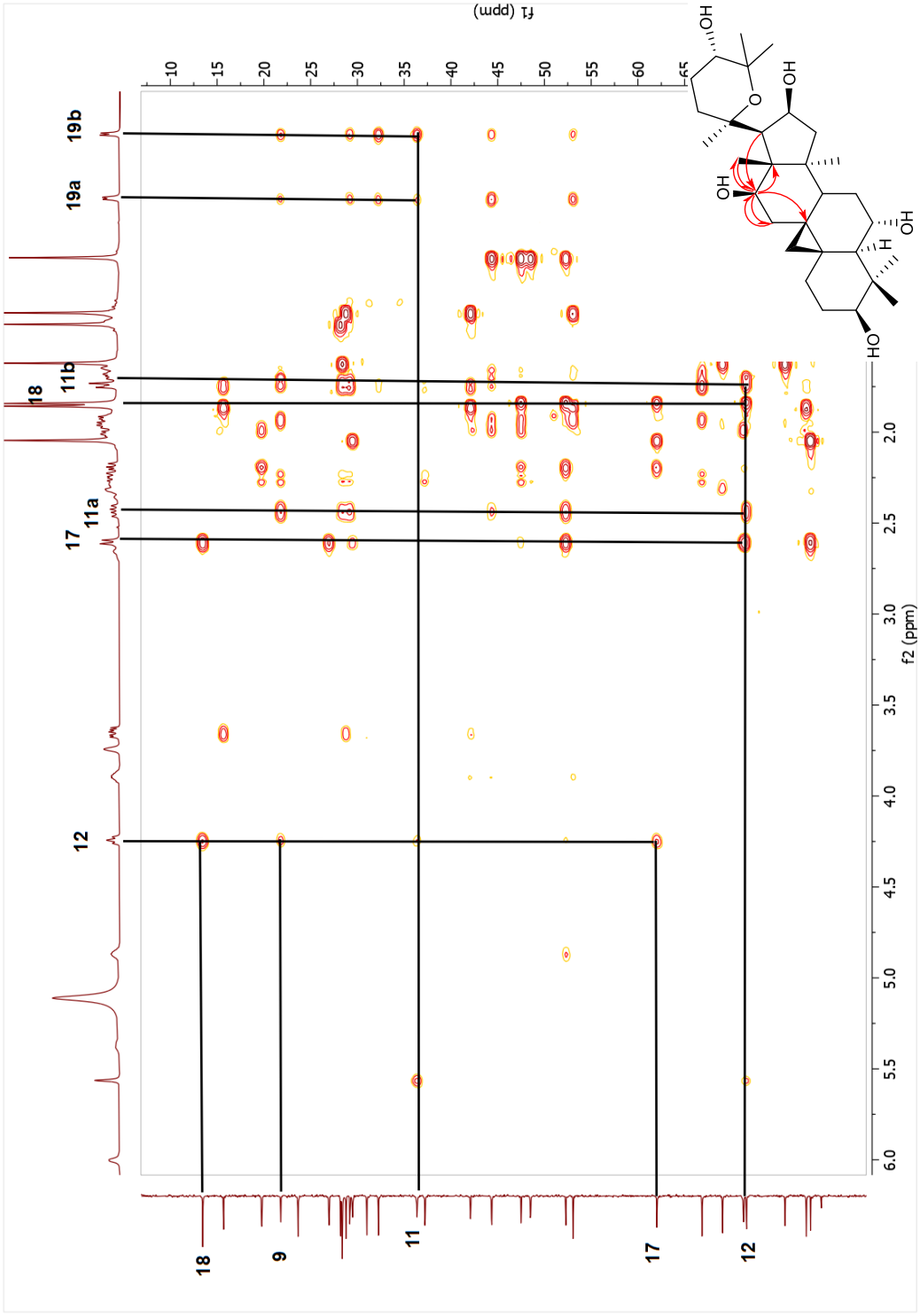

Spectrum 2.11. HMBC spectrum of compound **2**.

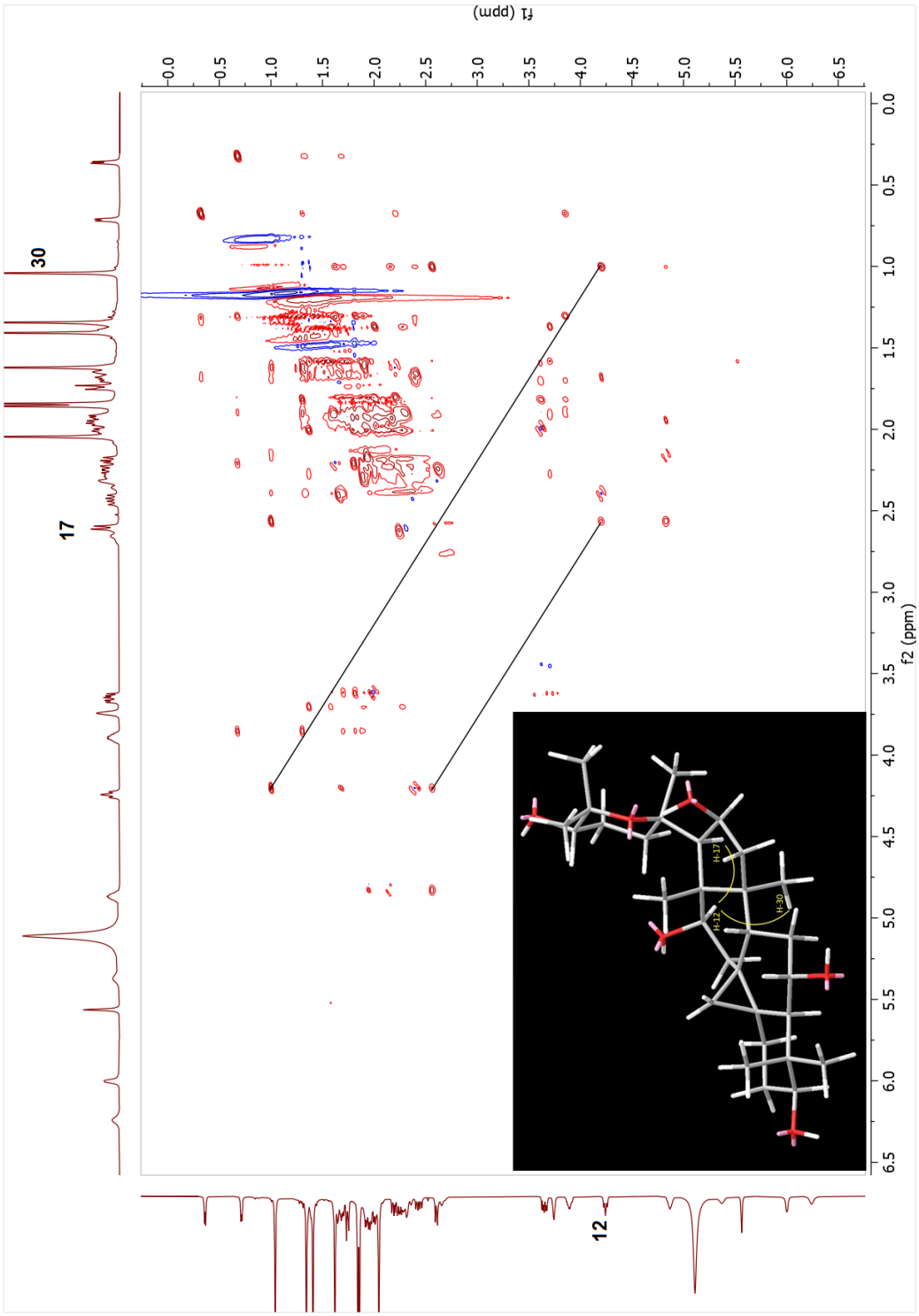

Spectrum 2.12. NOESY spectrum of compound **2**.

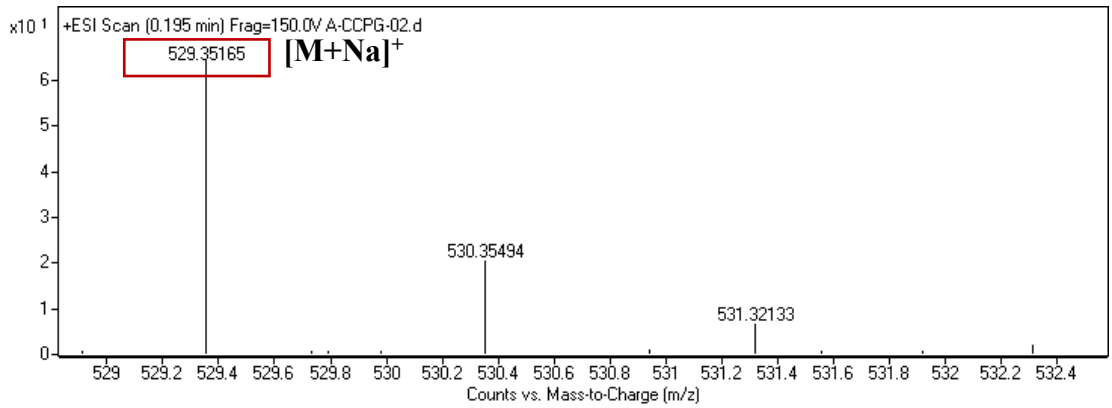

Spectrum 2.13. HR-ESI-MS spectrum of compound **2**.

2.3.2.3. Structure Elucidation of Compound 3

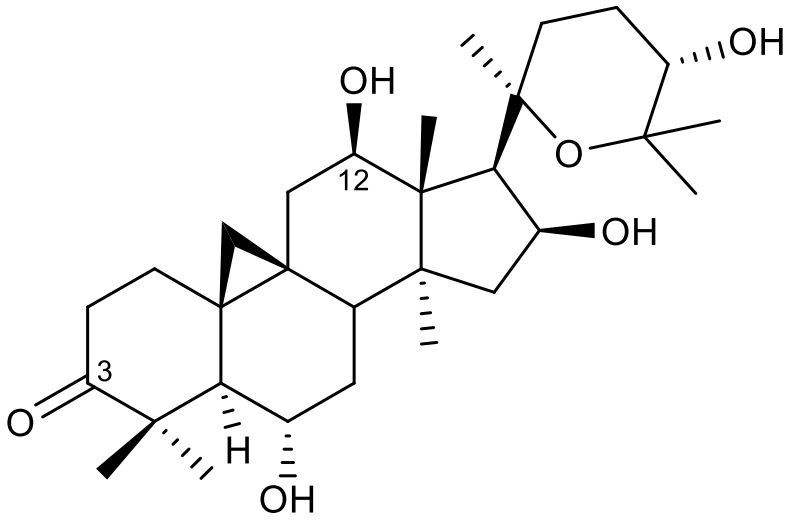

Figure 2.10. Chemical structure of compound **3**.

The HR-ESI-MS of **3** exhibited a sodium adduct ion at *m/z* 527.33685 $[M + Na]^+$ (calcd for $C_{30}H_{48}NaO_6$, 527.33486) supported a molecular formula $C_{30}H_{48}O_6$ with seven indices of hydrogen deficiency. The absence of low-field oxymethine signal of H-3 in the ^{1}H-NMR spectrum, together with the observation of a keto carbonyl carbon (δ_C 216.3) in the ^{13}C-NMR spectrum, suggested that the C-3 secondary alcohol had been oxidized. In the

HMBC spectrum, H_3-28, H_3-29, H_2-1 and H_2-2 displayed cross-peaks with the carbon signal at δ_C 216.3, confirming the presence of the carbonyl group at C-3. On the other hand, a new proton signal observed at δ_H 4.18 indicated an additional oxymethine group in the structure. Examination of COSY and HSQC spectra suggested oxygenation at C-12, as in **2**. This assumption was confirmed by the HMBC experiment, which showed a cross-peak between the H_3-18 and 71.6 ppm signal (C-12). The relative configuration was established via the 2D-NOESY data, in which correlations of H-12 and the α-oriented H-17 and H_3-30 revealed that the hydroxy group at C-12 is β-oriented. Consequently, the structure of **3** was determined as 20,25-epoxy-6α,12β,16β,24α-tetrahydroxycycloartan-3-one.

Table 2.3. The ^{13}C and ^{1}H NMR data of **3** (100/400 MHz, δ ppm, in C_5D_5N).

Position	δ_C (ppm)	δ_H (ppm), *J* (Hz)	Position	δ_C (ppm)	δ_H (ppm), *J* (Hz)
1	31.8	1.40 m, 1.94 m	**16**	71.3	4.82 tt (8.3, 4.6)
2	36.0	2.48 m, 2.60 m	**17**	62.1	2.49 m
3	216.3	-	**18**	13.8	1.80 s
4	50.3	-	**19**	30.1	0.45 d (4.3), 0.76 d (4.4)
5	53.2	2.11 d (9.2)	**20**	78.3	-
6	68.1	3.72 m	**21**	27.0	2.00 s
7	37.6	1.55 m, 1.77 m	**22**	29.3	2.22 d (16.4), 2.62 m
8	46.2	2.05 dd (11.5, 4.8)	**23**	23.6	1.89 m, 2.30 d (13.9)
9	22.1	-	**24**	68.9	3.69 m
10	28.6	-	**25**	75.6	-
11	36.6	1.46 dd (15.5, 4.3), 2.49 m	**26**	28.3	1.36 s
12	71.6	4.18 dd (6.7, 2.5)	**27**	28.2	1.56 s
13	52.3	-	**28**	27.7	1.72 s
14	47.3	-	**29**	20.5	1.38 s
15	48.9	1.93 m, 2.11 m	**30**	20.0	0.87 s

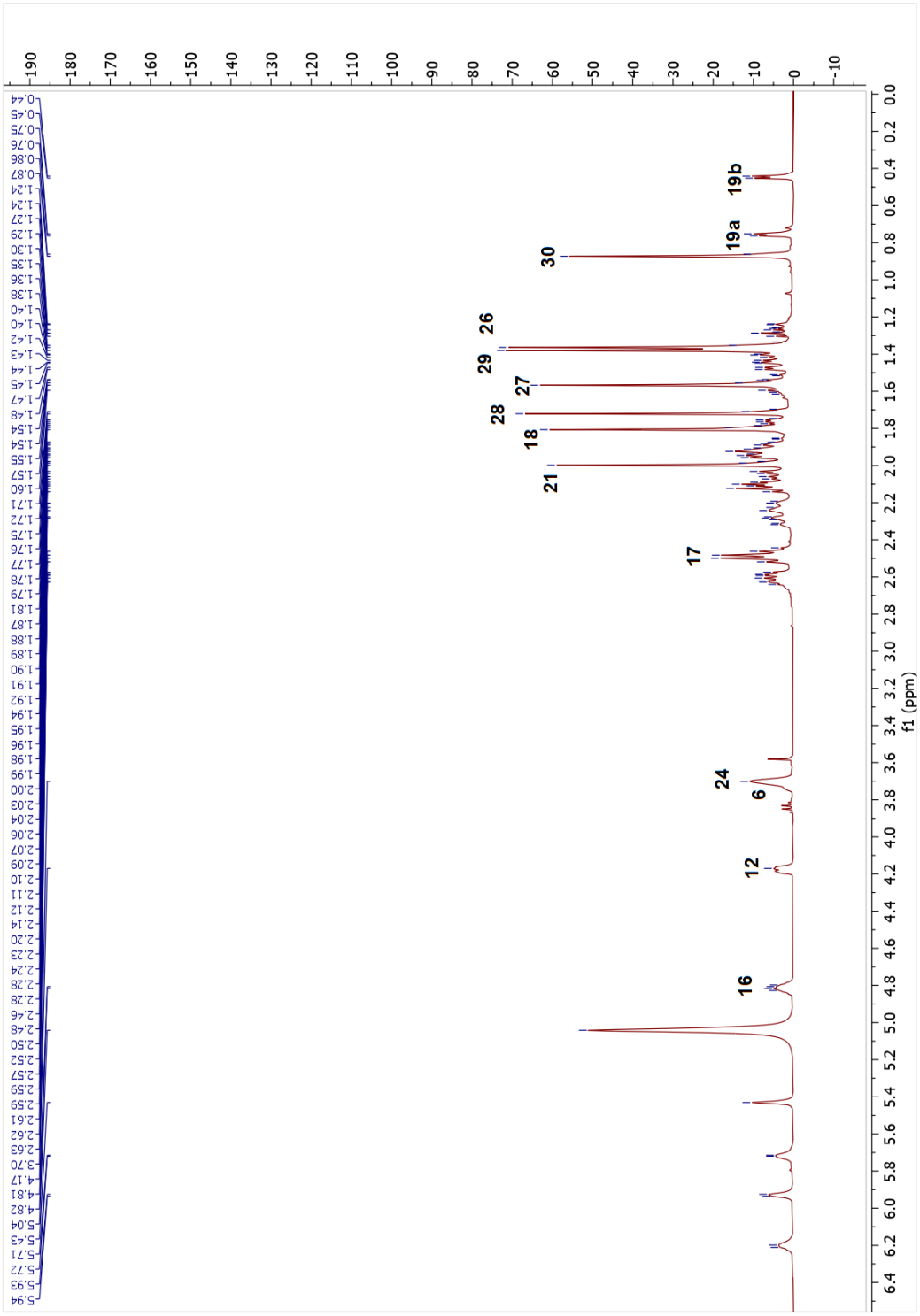

Spectrum 2.14. ^{1}H-NMR spectrum of compound **3**.

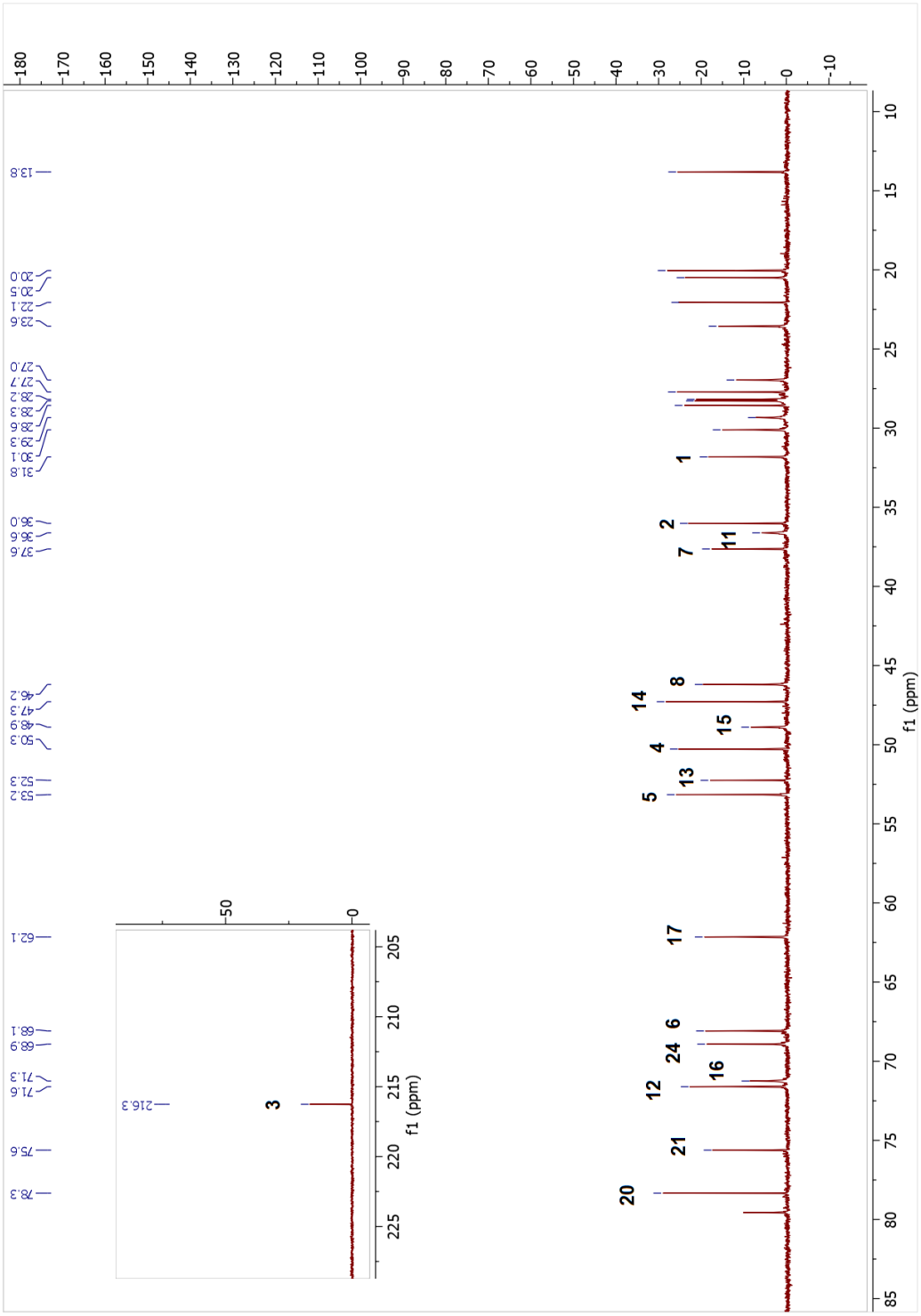

Spectrum 2.15. ^{13}C-NMR spectrum of compound **3**.

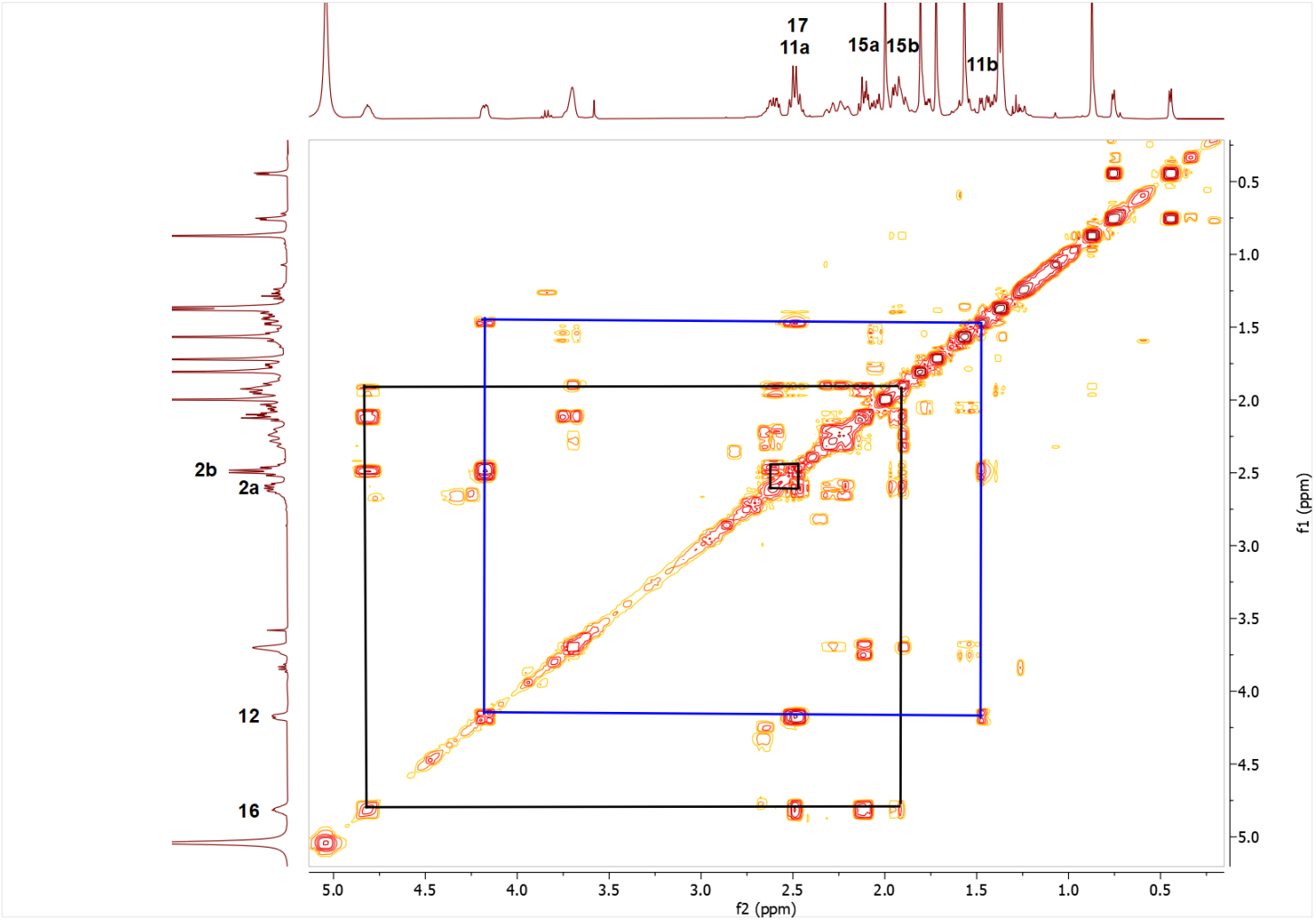

Spectrum 2.16. COSY spectrum of compound **3**.

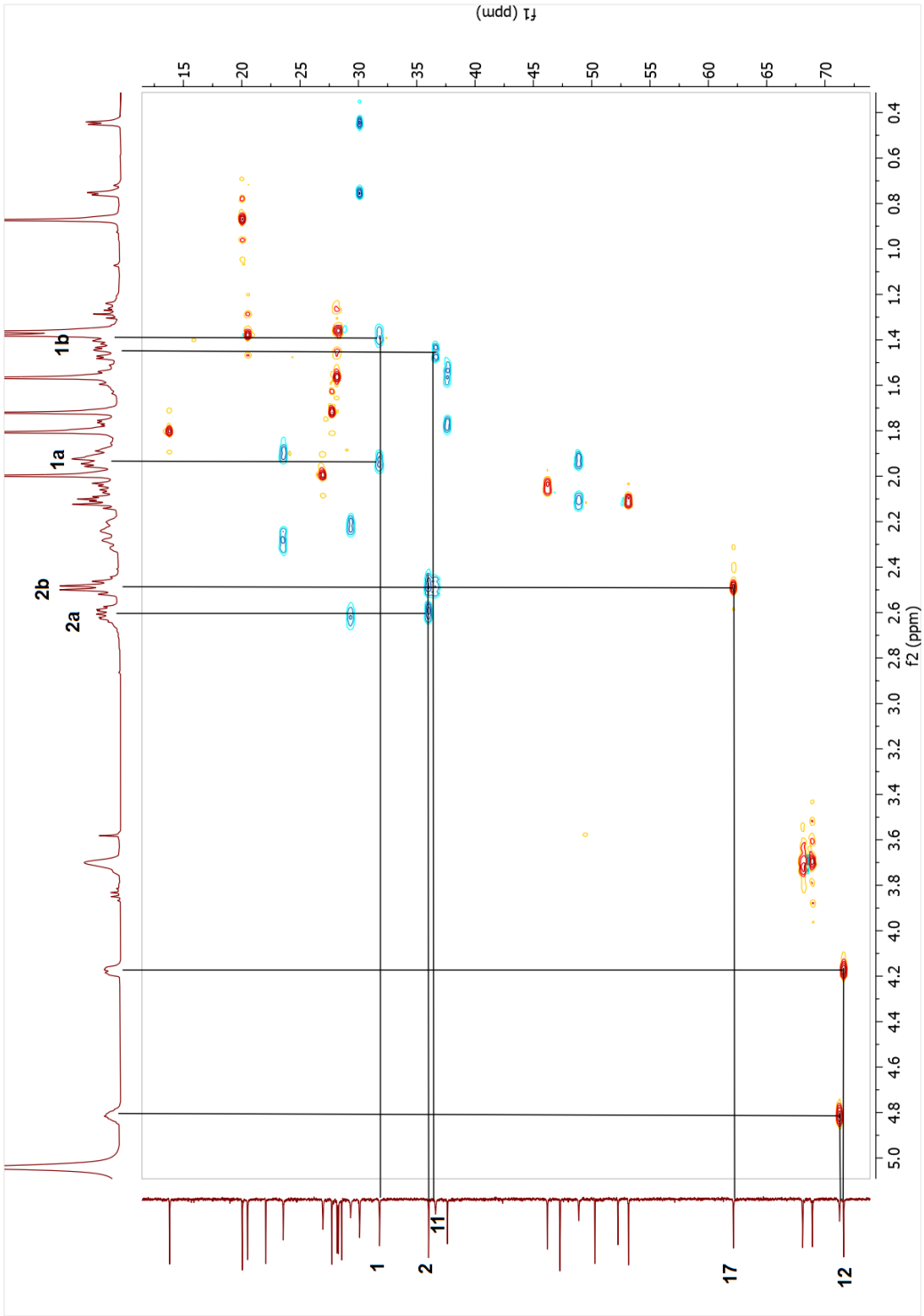

Spectrum 2.17. HSQC spectrum of compound **3**.

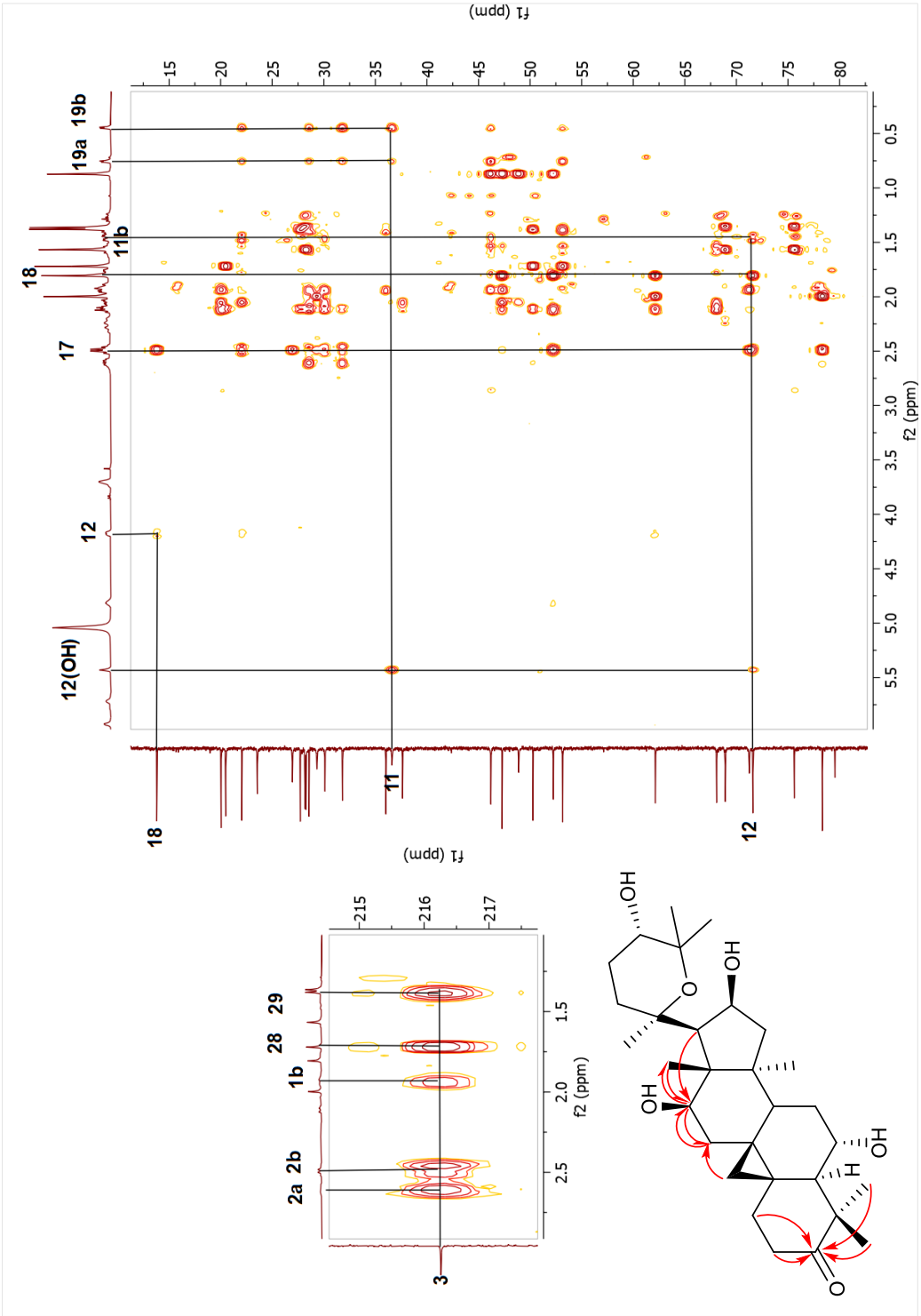

Spectrum 2.18. HMBC spectrum of compound **3**.

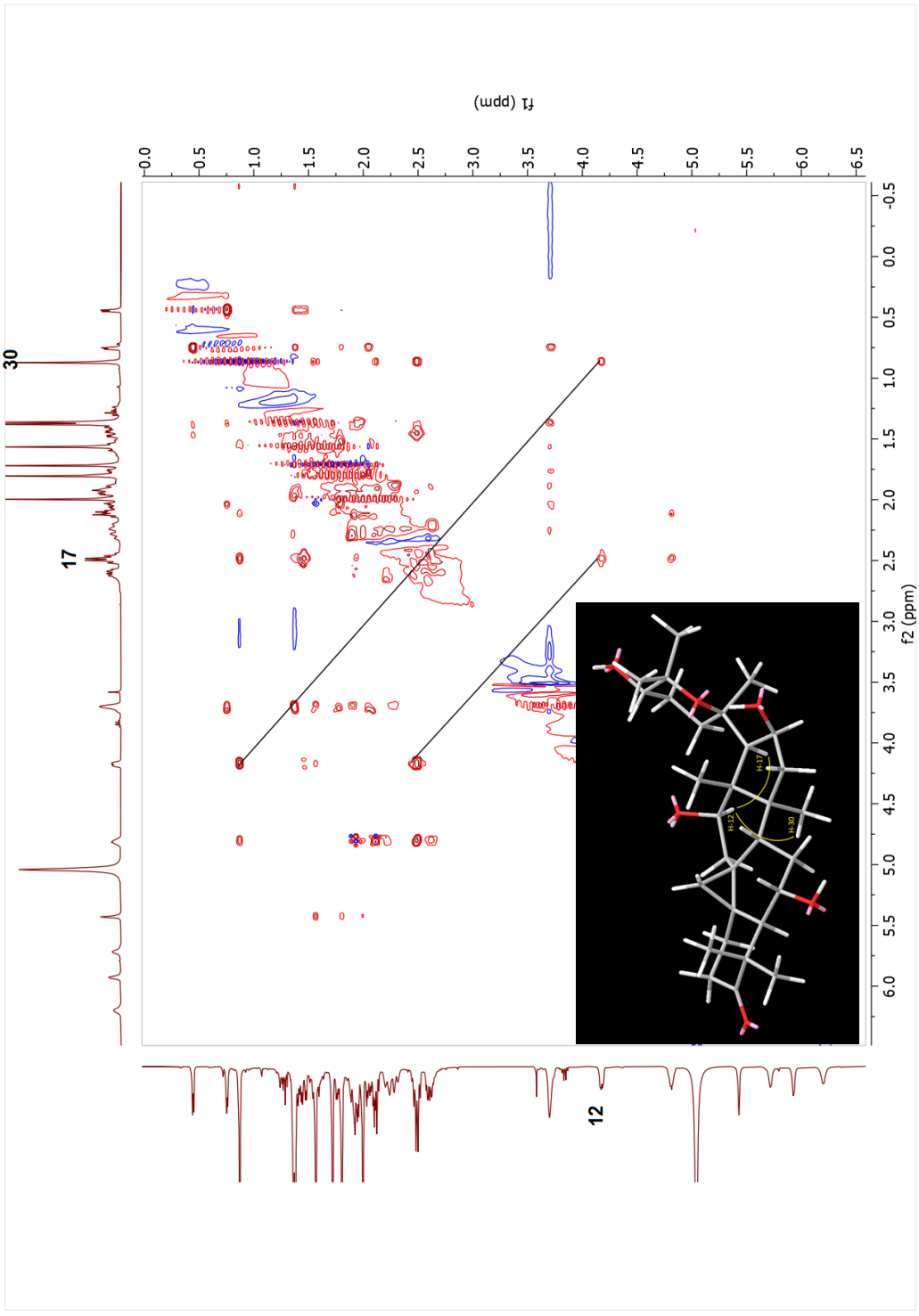

Spectrum 2.19. NOESY spectrum of compound **3**.

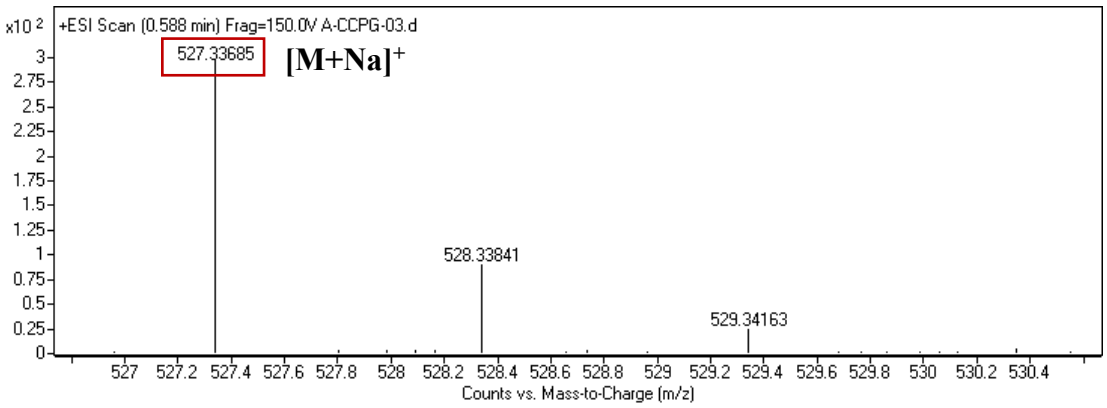

Spectrum 2.20. HR-ESI-MS spectrum of compound **3**.

2.3.2.4. Structure Elucidation of Compound 4

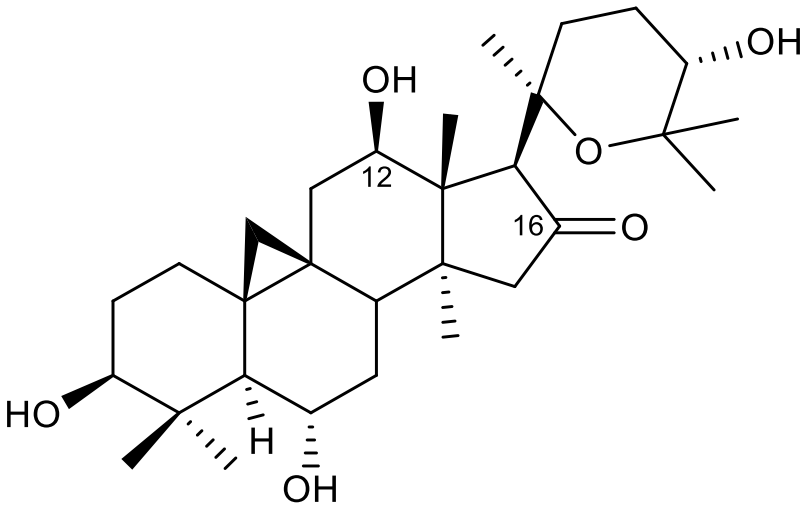

Figure 2.11. Chemical structure of compound **4**.

The HR-ESI-MS of **4** (*m/z* 527.33596 $[M + Na]^+$, calcd for $C_{30}H_{48}NaO_6$, 527.33486) was consistent with a molecular formula of $C_{30}H_{48}O_6$. When the ^1H and ^{13}C-NMR spectra of **4** inspected, signals at δ_C 215.8 and δ_H 4.16 suggested a keto carbonyl group and an additional oxymethine group in the structure as in **3**. The long-range correlations from H-17 and H_2-15 to δ_C 215.8 confirmed the location of the carbonyl group to be at C-16. A new hydroxy group

located at C-12 based on COSY correlation of H-12 (δ_H 4.16) with H_2-11 and the key long-range correlation between H_3-18 (δ_H 1.47) and δ_C 71.5. The relative configuration at C-12 was deduced based on the 2D-NOESY data, which showed a NOE correlation between H-12 and α-oriented H_3-30/H-17 and provided evidence for the β-orientation of the hydroxy group at C-12. Thus, metabolite **4** was characterized as 20,25-epoxy-3β,6α,12β,24α-tetrahydroxycycloartan-16-one.

Table 2.4. The ^{13}C and ^{1}H NMR data of **4** (100/400 MHz, δ ppm, in C_5D_5N).

Position	δ_C (ppm)	δ_H (ppm), *J* (Hz)
1	32.3	1.27 m, 1.58 m
2	31.0	1.88 m, 2.00 m
3	77.9	3.60 td (7.9, 1.7)
4	42.1	-
5	53.3	1.69 d (9.2)
6	67.2	3.80 q (7.7)
7	37.8	1.54 m, 1.74 m
8	44.1	1.96 d (5.7)
9	20.8	-
10	29.5	-
11	36.5	1.58 m, 2.49 dd (15.5, 8.6)
12	71.5	4.16 dd (8.8, 4.3)
13	52.4	-
14	42.8	-
15	50.9	2.10 d (17.6), 2.36 d (17.7)
16	215.8	-
17	71.2	3.06 s
18	14.0	1.47 s
19	29.9	0.44 d (4.3), 0.67 d (4.4)
20	76.5	-
21	23.3	1.44 s
22	31.9	2.64 dd (12.8, 5.1), 2.27 dd (14.2, 3.2)
23	23.3	1.82 m, 2.20 d (14.1)
24	68.5	3.64 brs
25	76.6	-
26	28.0	1.57 s
27	28.0	1.30 s
28	28.9	1.84 s
29	15.7	1.31 s
30	19.0	1.00 s

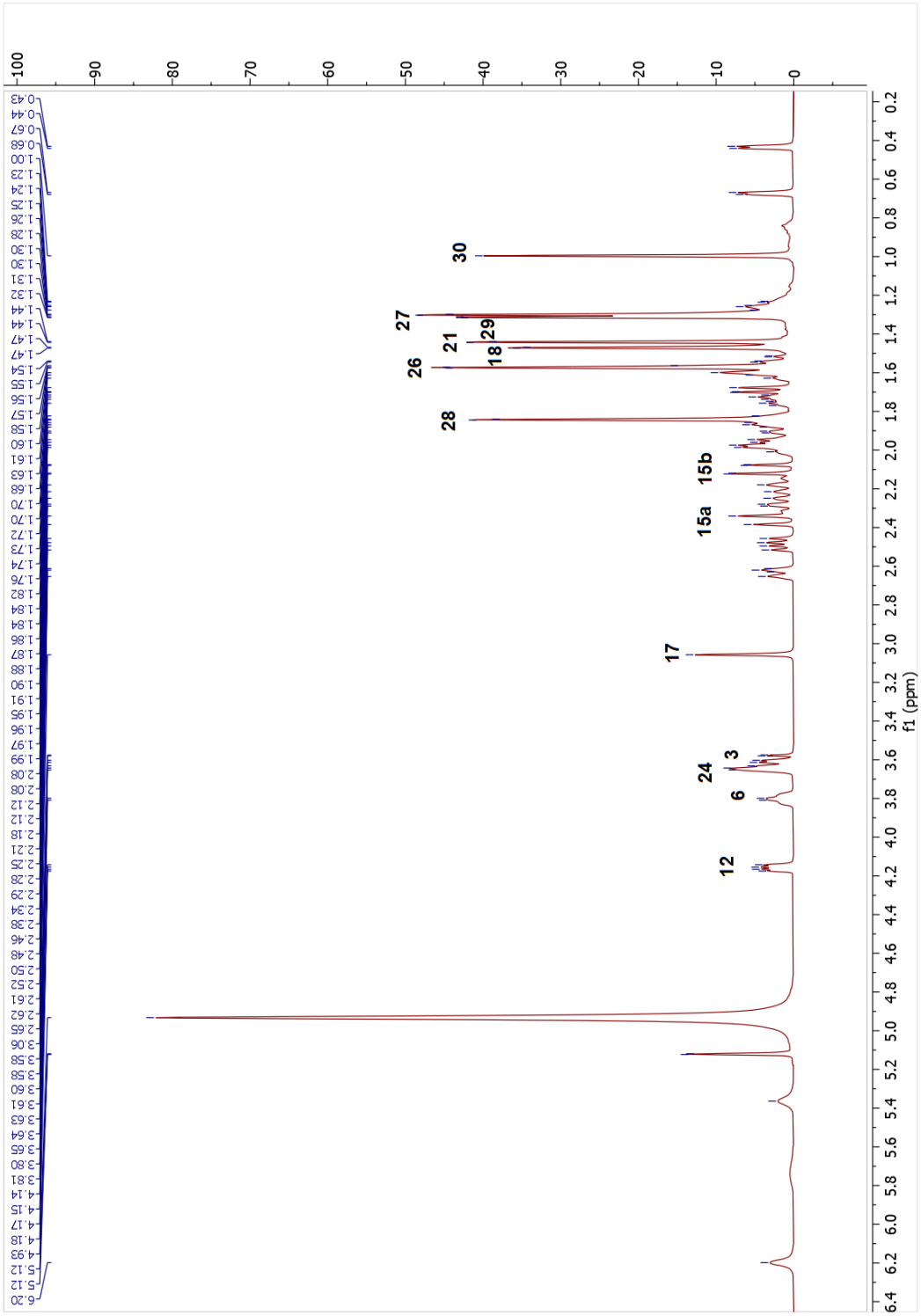

Spectrum 2.21. ^{1}H-NMR spectrum of compound **4**.

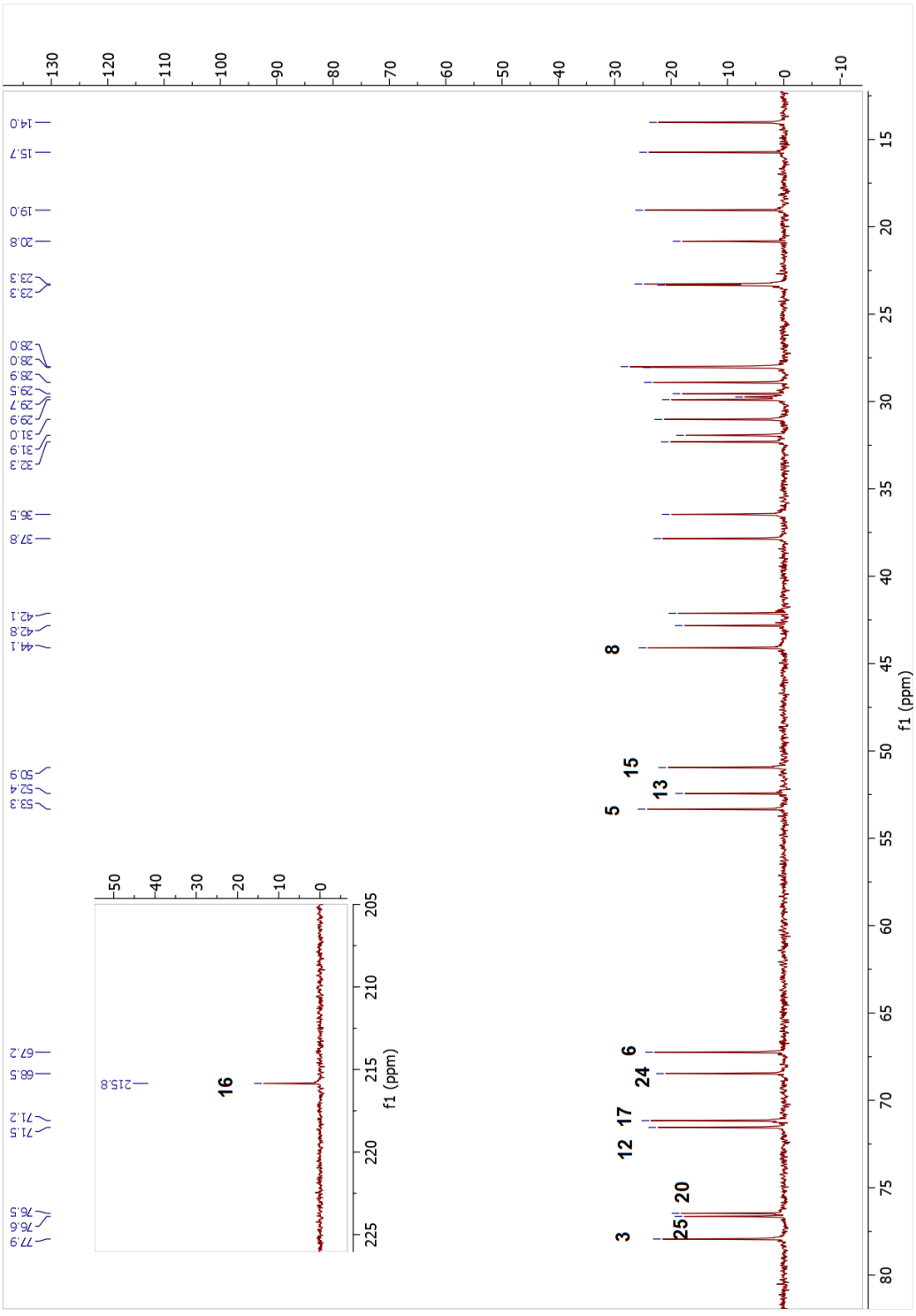

Spectrum 2.22. ^{13}C-NMR spectrum of compound **4**.

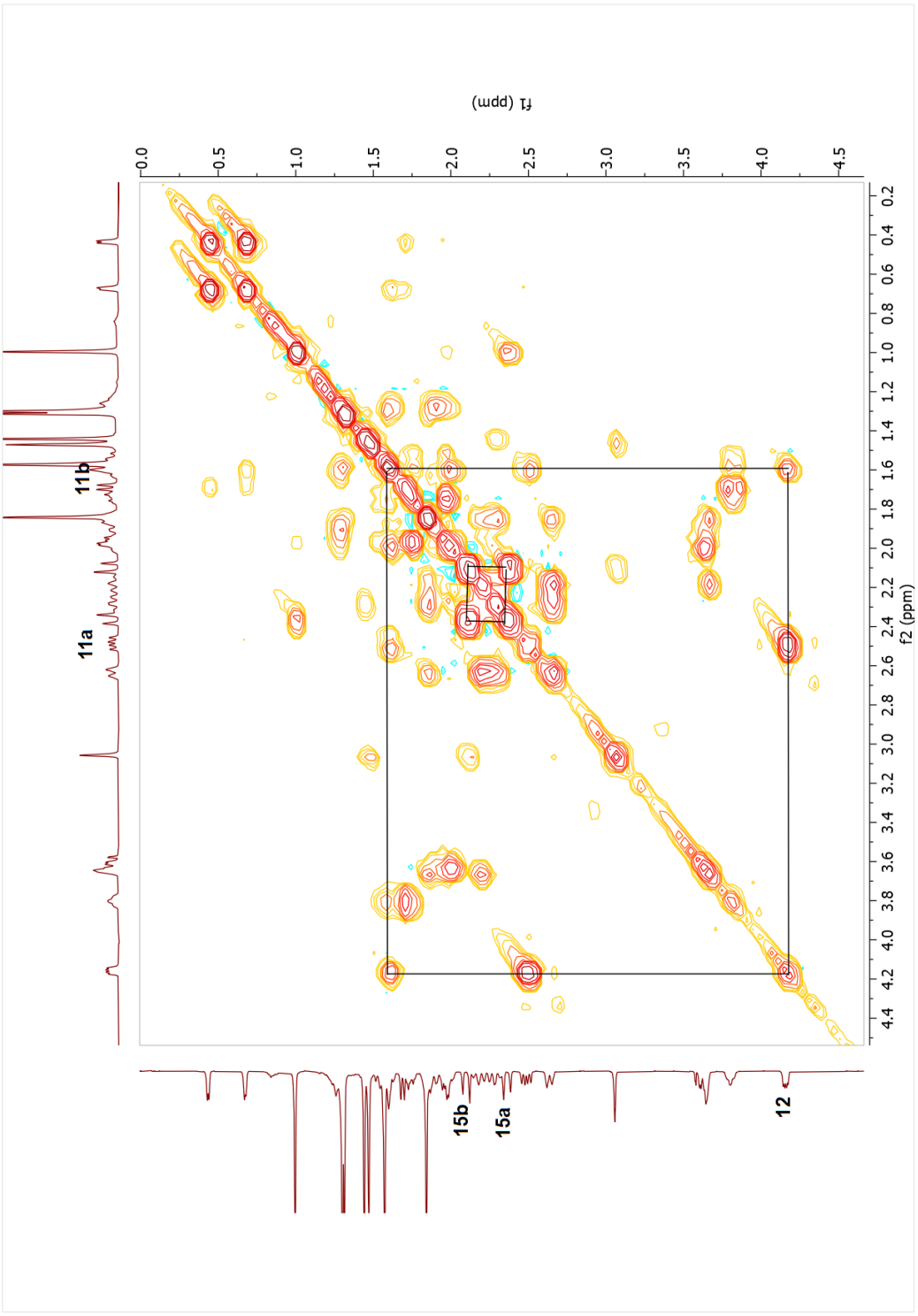

Spectrum 2.23. COSY spectrum of compound **4**.

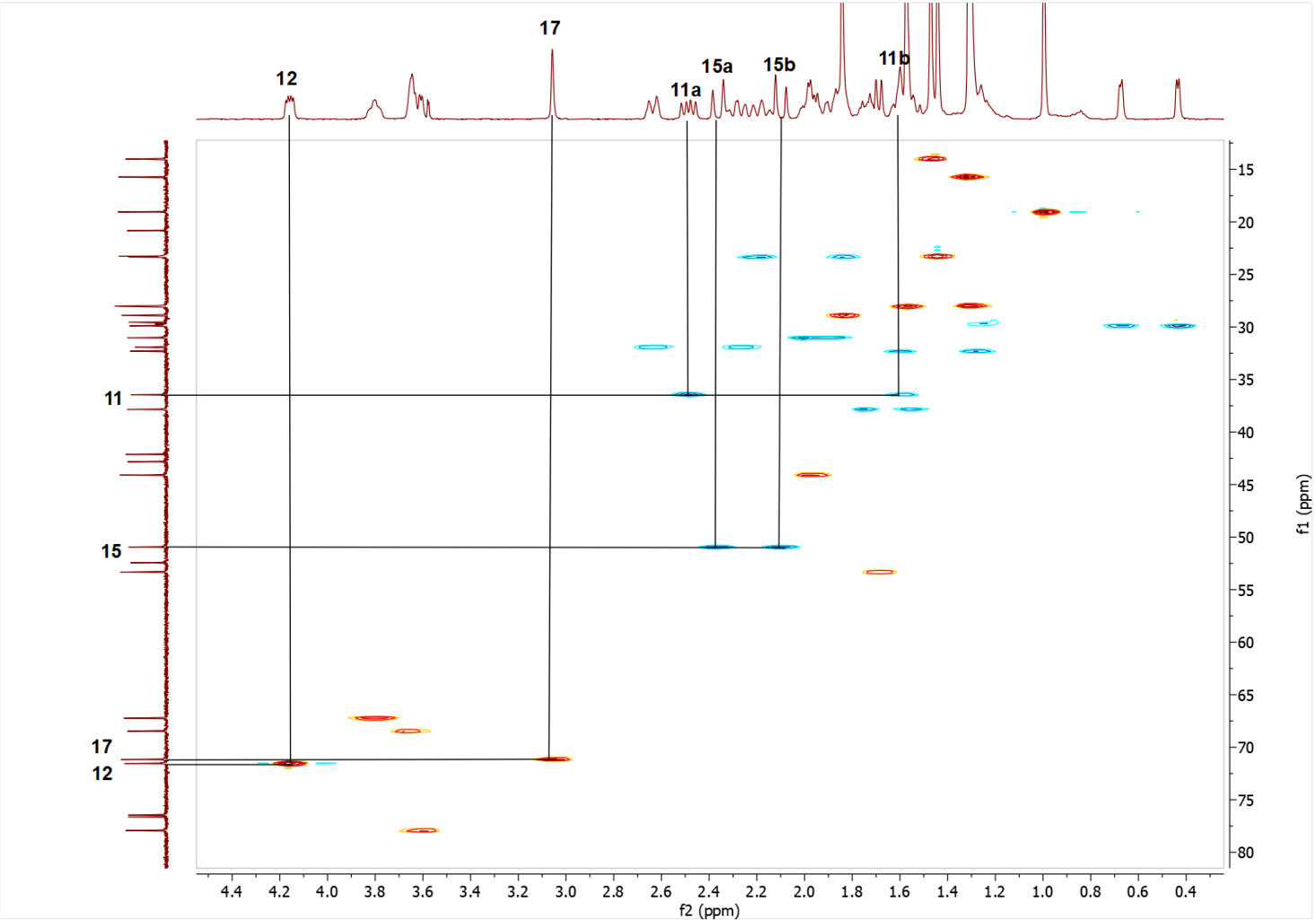

Spectrum 2.24. HSQC spectrum of compound **4**.

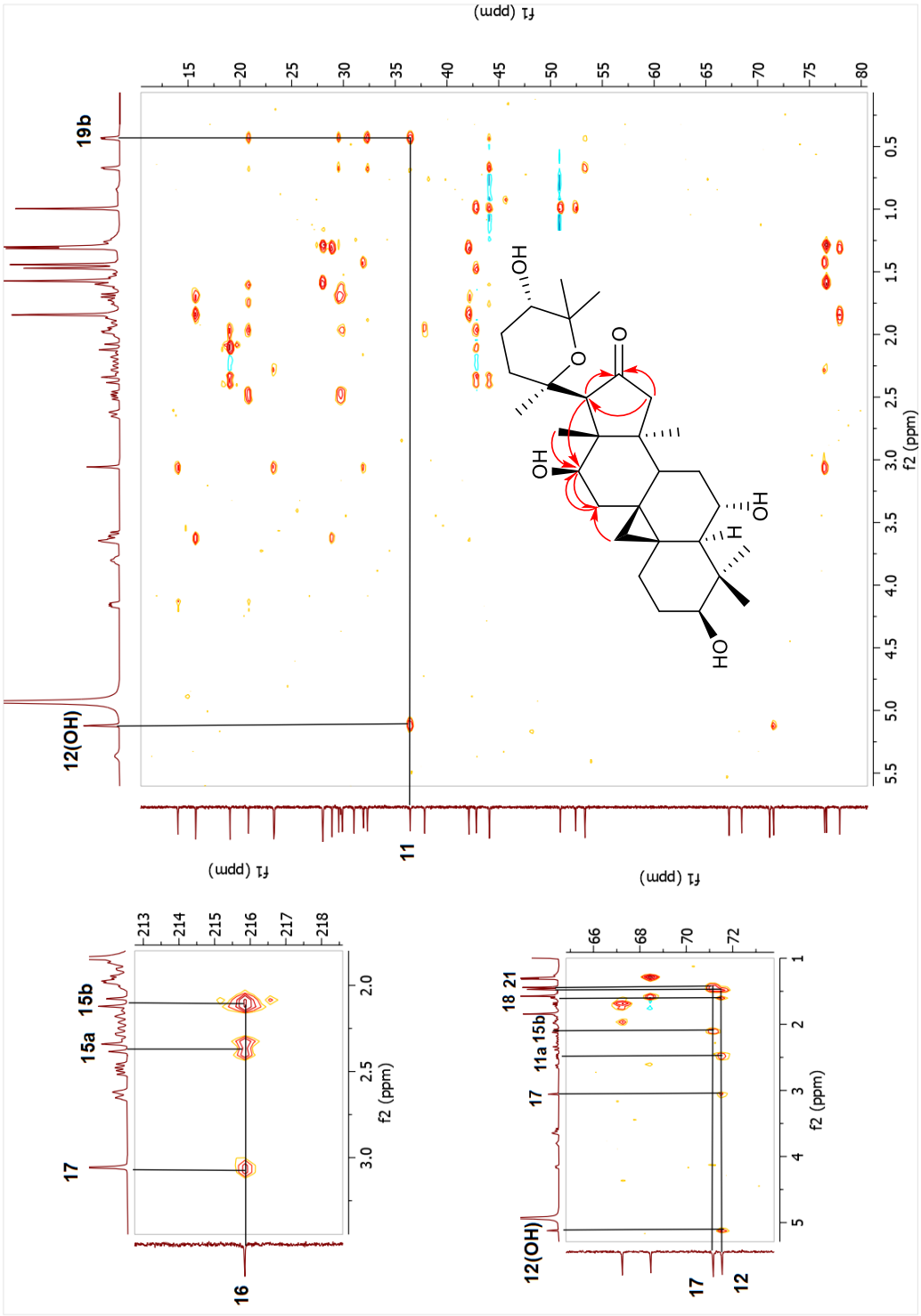

Spectrum 2.25. HMBC spectrum of compound **4**.

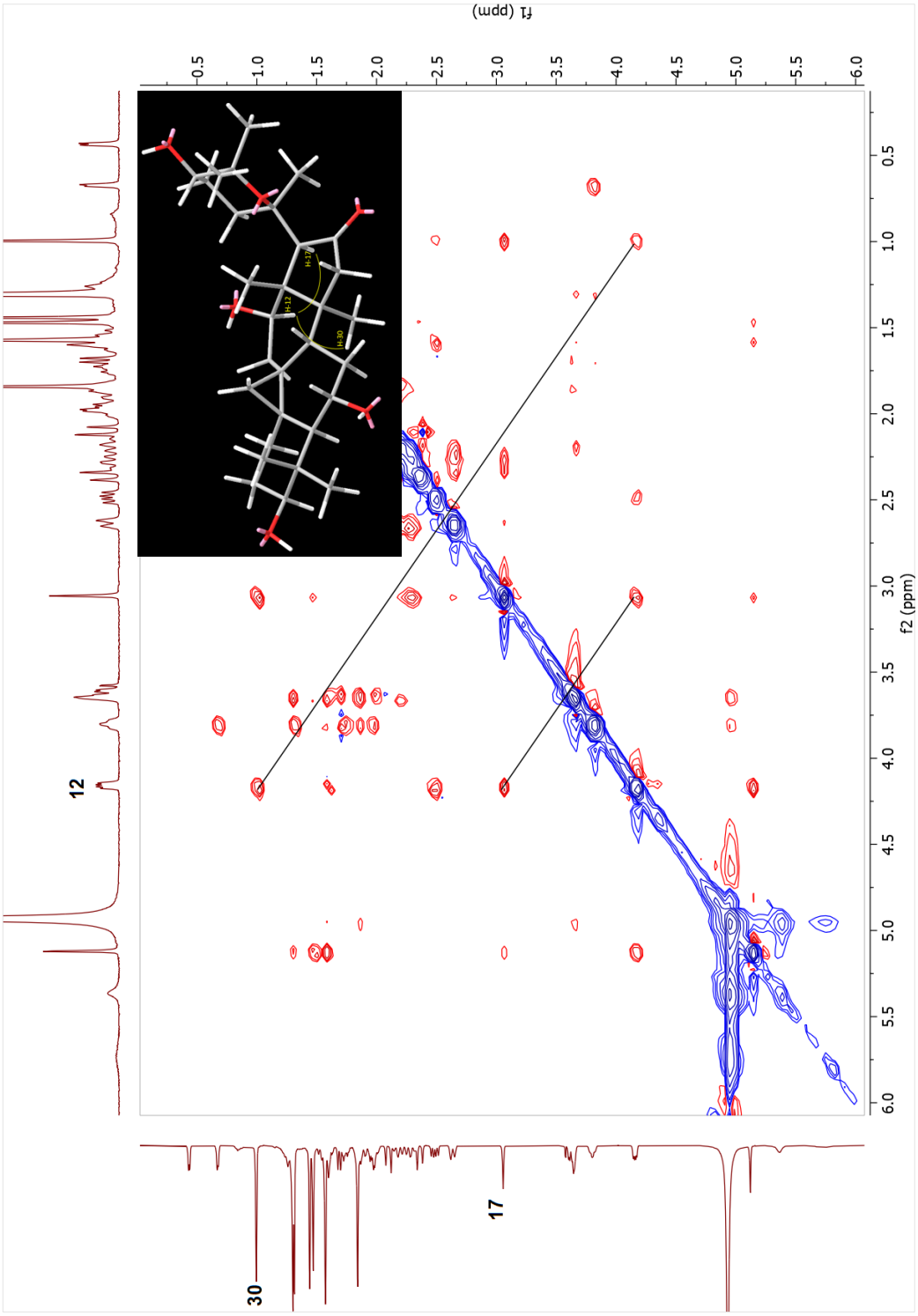

Spectrum 2.26. NOESY spectrum of compound **4**.

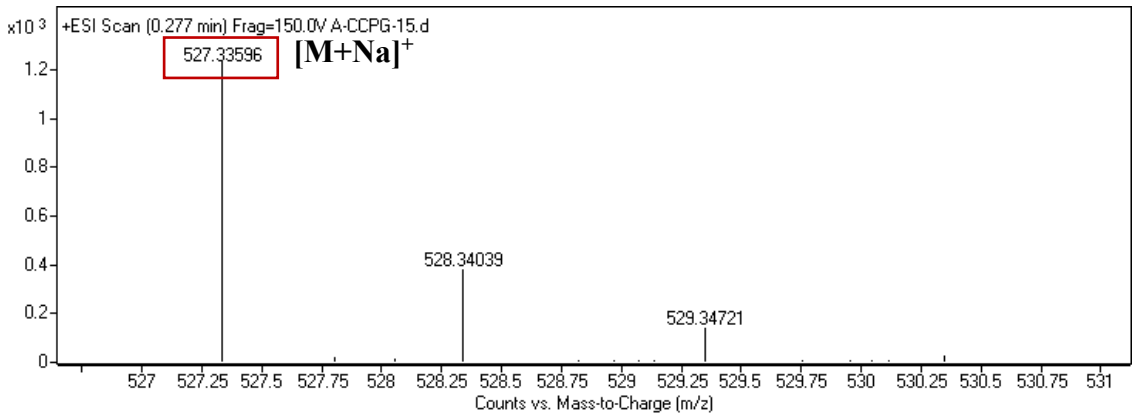

Spectrum 2.27. HR-ESI-MS spectrum of compound **4**.

2.3.2.5. Structure Elucidation of Compound 5

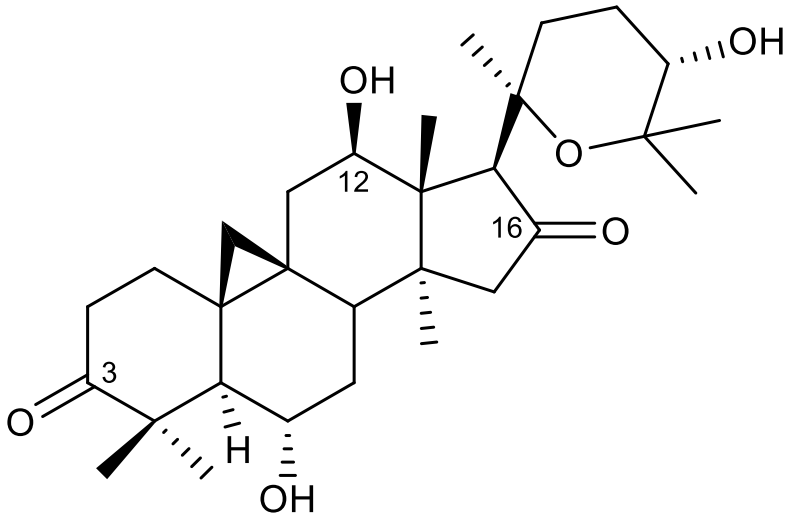

Figure 2.12. Chemical structure of compound **5**.

The HR-ESI-MS of **5** exhibited a sodium adduct ion peak at *m/z* 525.31989 [M + Na]$^+$ (calcd for $C_{30}H_{46}NaO_6$, 525.31921), supporting a molecular formula of $C_{30}H_{46}O_6$. The absence of a low-field oxymethine signal due to H-3 and H-16 in the ^{1}H-NMR spectrum, together with the observation of two keto carbonyl carbons (δ_C 215.6 and 216.1) in the ^{13}C-NMR spectrum, suggested the C-3 and C-16 secondary alcohols had been oxidized. The

carbon signal at δ_C 215.6 showed long-range correlations with H_2-15 and H-17, while the δ_C 216.1 signal displayed cross-peaks with H_3-28, H_3-29 and H_2-2, confirming the presence of the carbonyl groups at C-16 and C-3, respectively. Besides, in the ^{13}C-NMR spectrum, an extra down-field carbon signal at δ_C 71.6 was also noticed. Full assignments of the proton and carbon signals of **5** secured by the COSY and HSQC spectra implied the position of monooxygenation as C-12. In the HMBC spectrum, long-range correlations of H-17 (δ_H 3.02), H-11a (δ_H 2.56) and H_3-18 (δ_H 1.47) with the oxymethine carbon signal at δ_C 71.6 verified the proposed transformation. The stereochemistry of the hydroxy group at C-12 was determined by examining the NOESY spectrum, which exhibited a cross-peak from the α-oriented H_3-30 confirming the orientation of C-12(OH) as β. Based on this evidence, the structure of **5** was elucidated as 20,25-epoxy-6α,12β,24α-trihydroxycycloartan-3,16-dione.

Table 2.5. The ^{13}C and ^{1}H NMR data of **5** (100/400 MHz, δ ppm, in C_5D_5N).

Position	δ_C (ppm)	δ_H (ppm), *J* (Hz)	Position	δ_C (ppm)	δ_H (ppm), *J* (Hz)
1	31.5	1.29 m, 1.95 dt (14.7, 8.5)	**16**	215.6	-
2	35.8	2.45 m, 2.62 m	**17**	71.2	3.02 s
3	216.1	-	**18**	14.4	1.49 s
4	50.2	-	**19**	30.9	0.54 d (3.7), 0.76 d (4.1)
5	53.2	2.13 m	**20**	76.4	-
6	68.3	3.68 m	**21**	23.2	1.44 s
7	37.8	1.54 d (13.3), 1.66 dt (12.0, 3.6)	**22**	32.0	2.27 d (13.3), 2.62 m
8	45.5	1.85 m	**23**	23.3	1.84 m, 2.20 dd (13.9, 3.0)
9	21.0	-	**24**	68.4	3.66 brs
10	28.6	-	**25**	76.6	-
11	36.5	1.38 m, 2.56 dd (15.6, 9.0)	**26**	28.0	1.58 s
12	71.6	4.14 dd (9.1, 2.7)	**27**	28.0	1.31 s
13	52.4	-	**28**	28.0	1.74 s
14	42.6	-	**29**	20.3	1.41 s
15	51.2	2.11 d (17.6), 2.38 d (17.9)	**30**	19.3	0.92 s

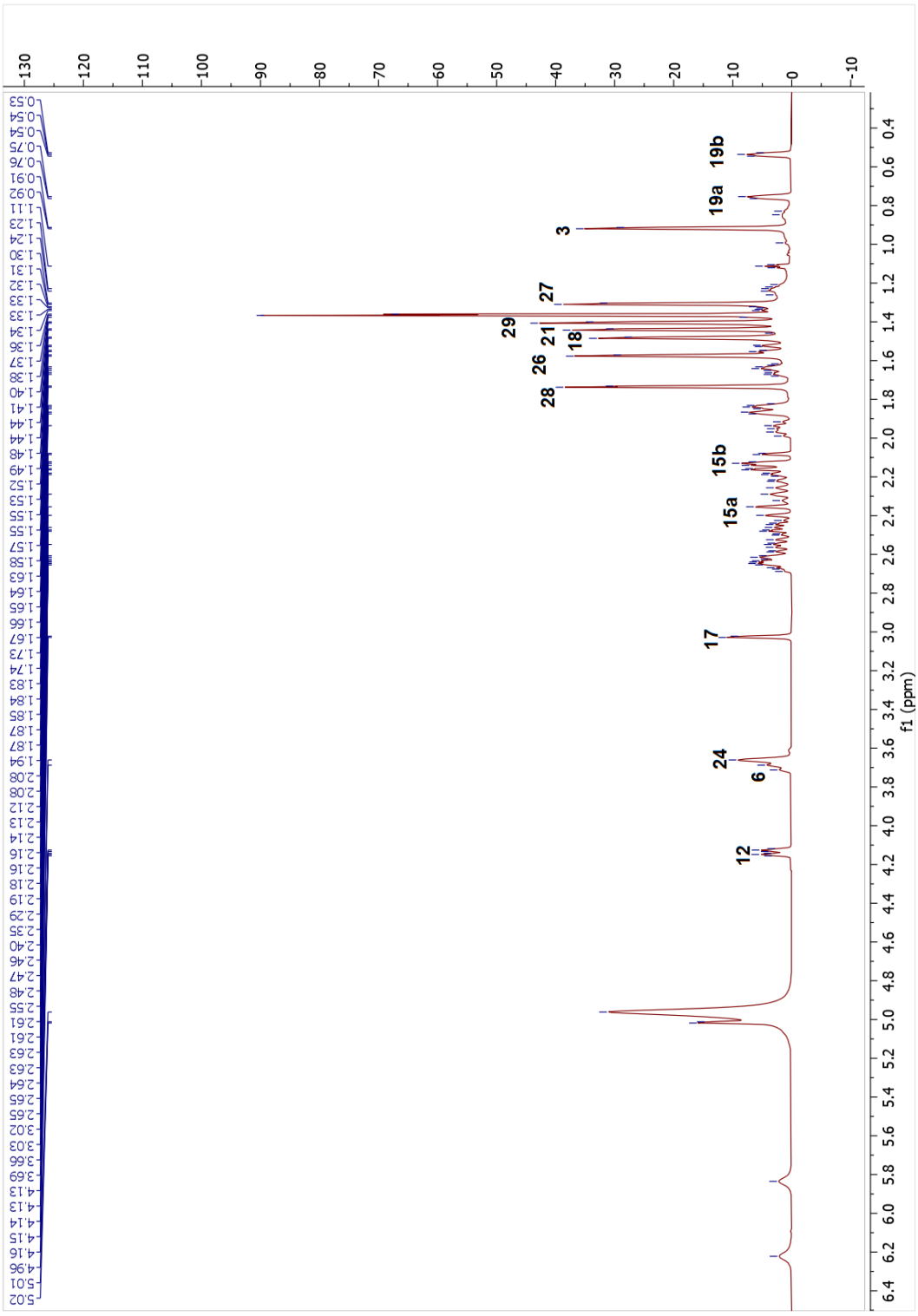

Spectrum 2.28. ^{1}H-NMR spectrum of compound **5**.

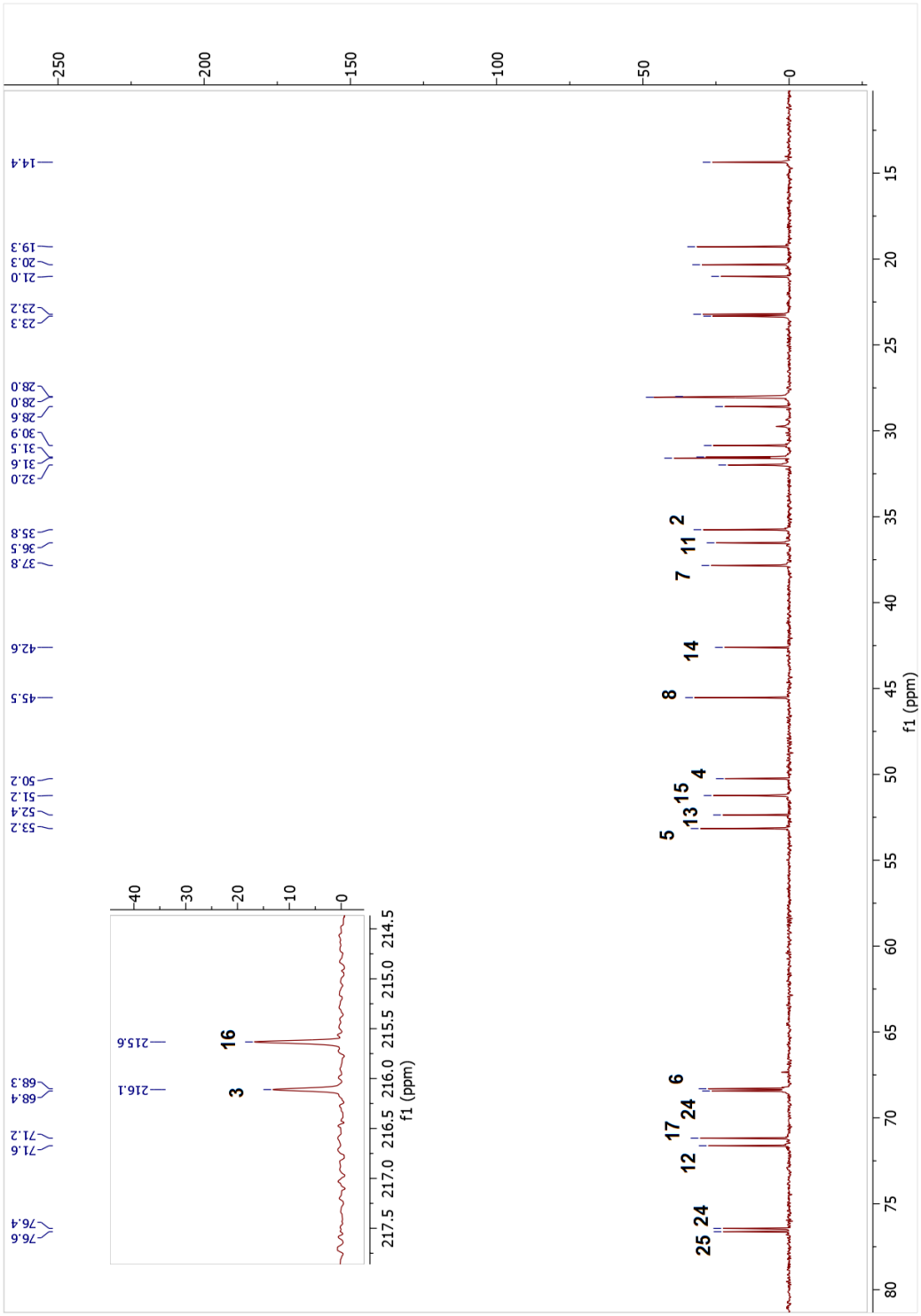

Spectrum 2.29. ^{13}C-NMR spectrum of compound **5**.

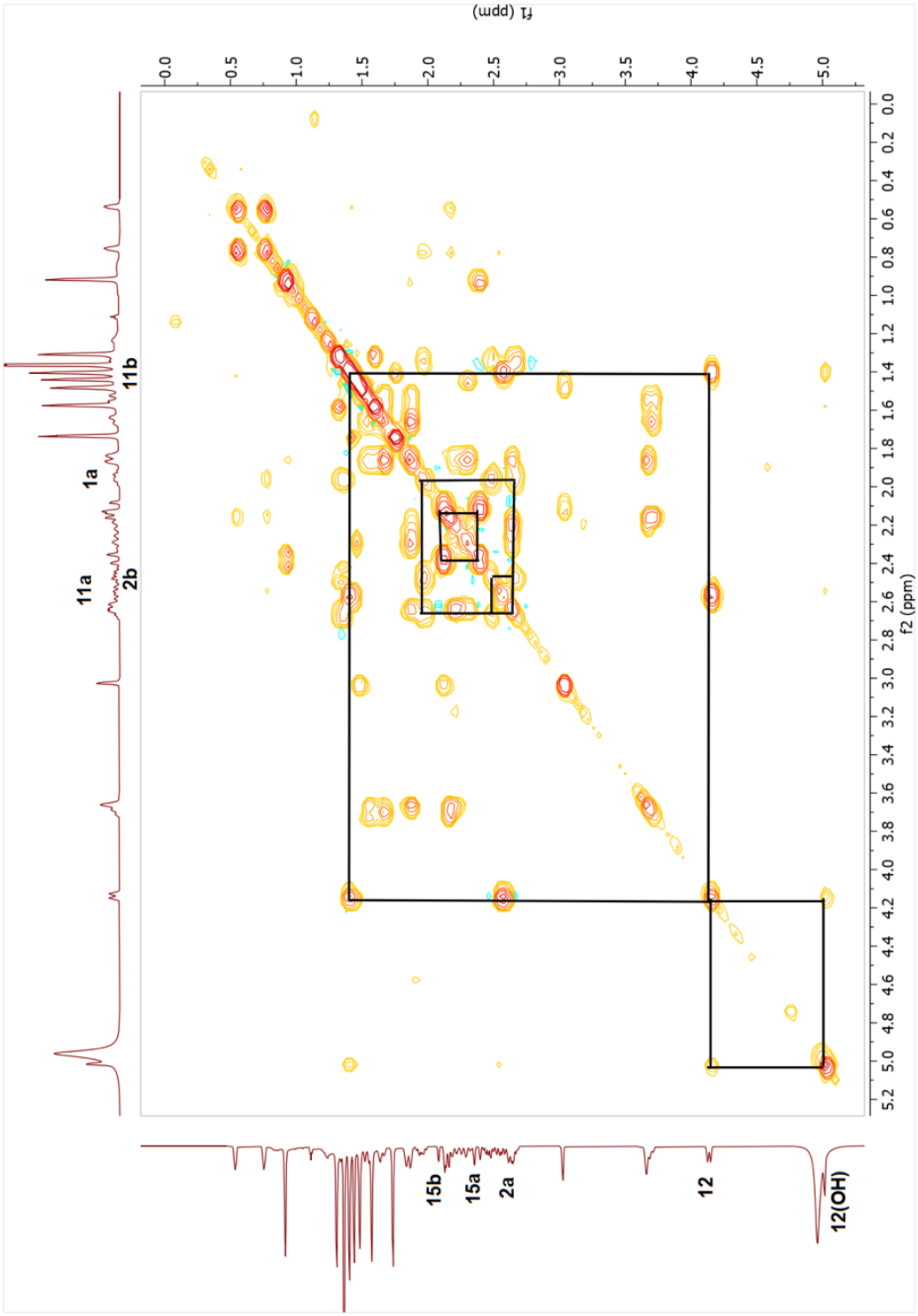

Spectrum 2.30. COSY spectrum of compound **5**.

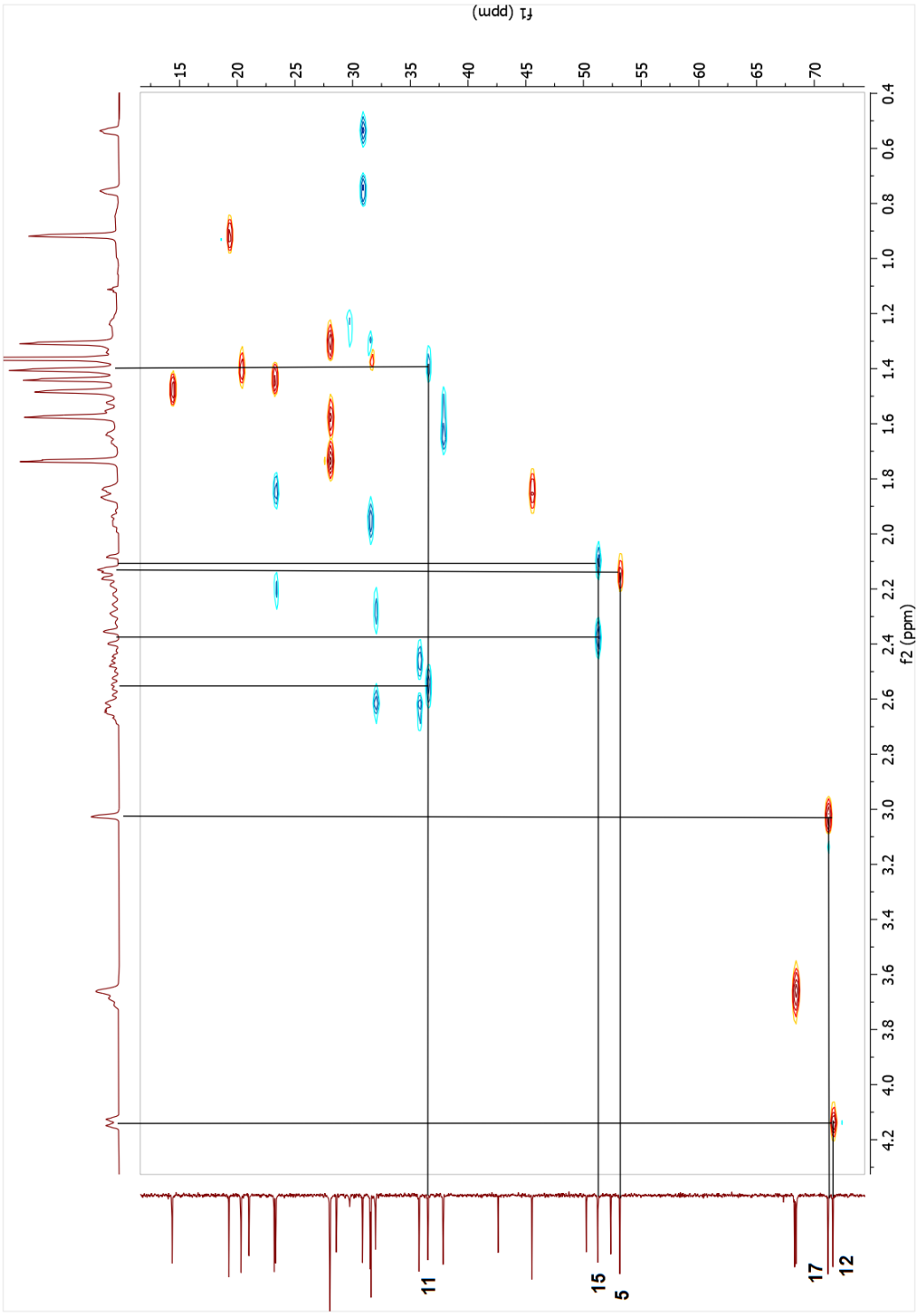

Spectrum 2.31. HSQC spectrum of compound **5**.

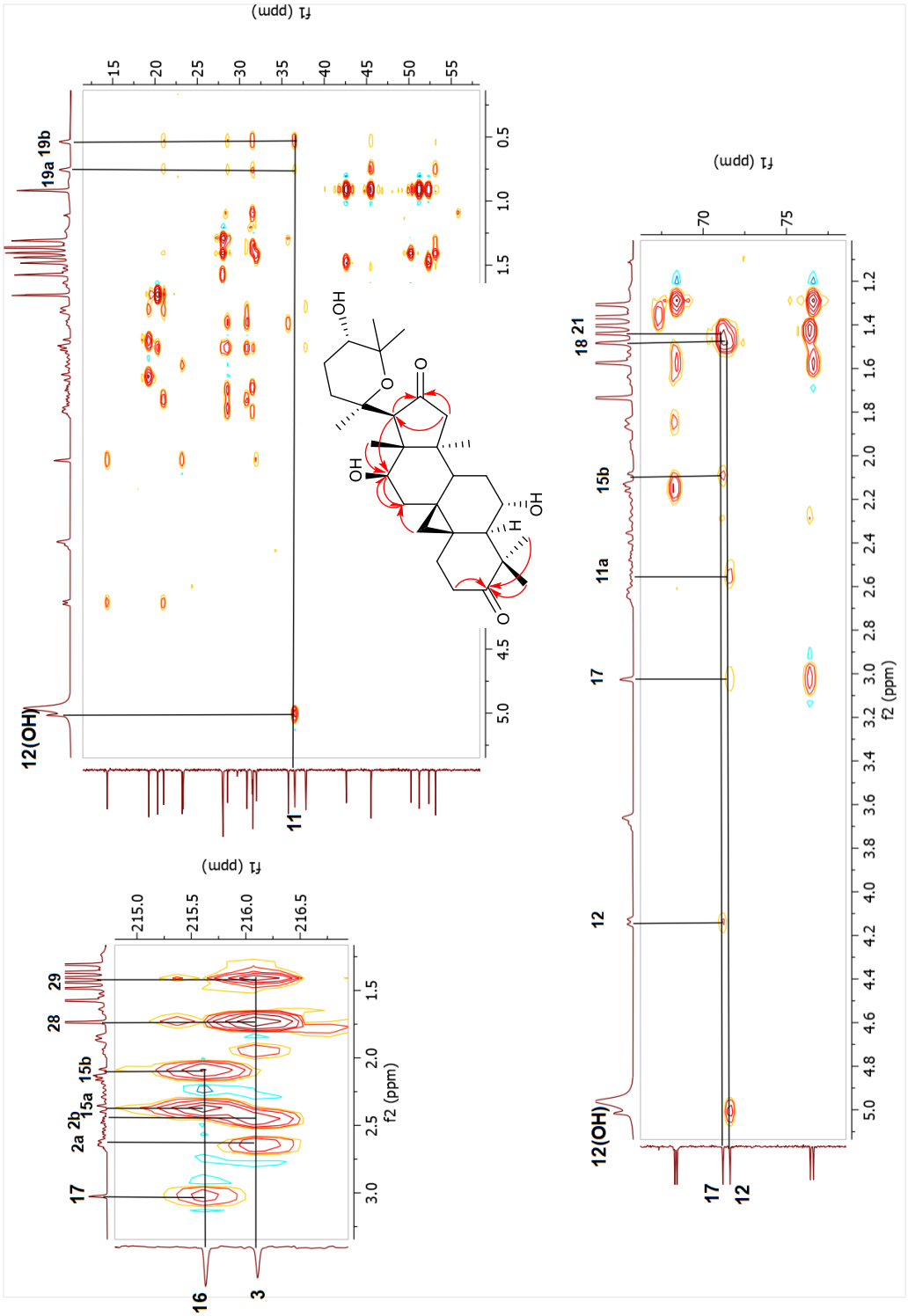

Spectrum 2.32. HMBC spectrum of compound **5**.

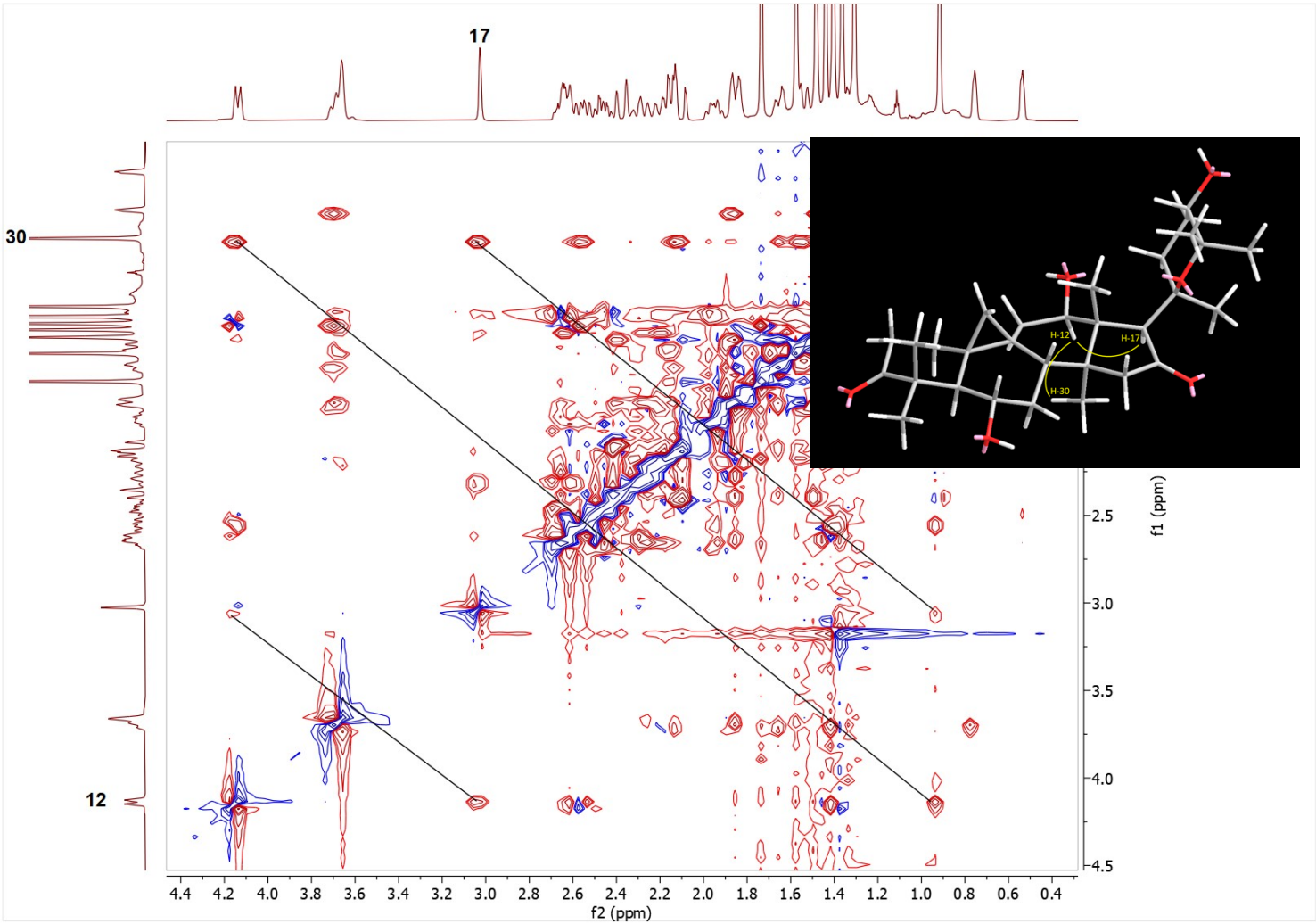

Spectrum 2.33. NOESY spectrum of compound **5**.

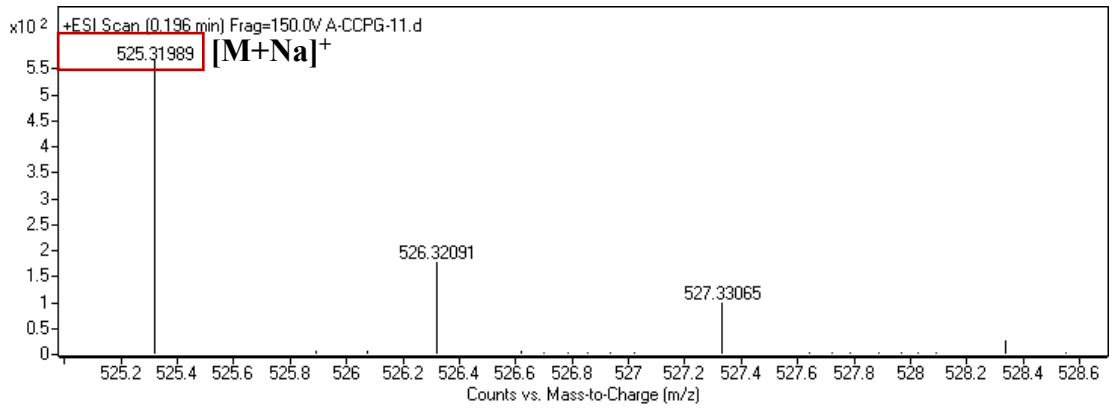

Spectrum 2.34. HR-ESI-MS spectrum of compound **5**.

2.3.2.6. Structure Elucidation of Compound 6

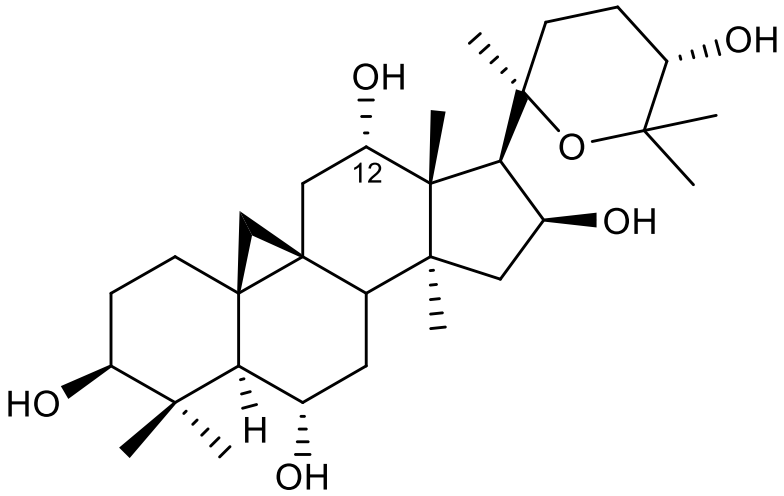

Figure 2.13. Chemical structure of compound **6**.

The HR-ESI-MS spectrum of compound **6** showed a major ion peak at *m/z* 529.35093 $[M + Na]^+$ ($C_{30}H_{50}NaO_6$). In the HMBC spectrum, the new oxymethine carbon signal observed at δ_H 73.0 showed long-range correlations with H-17, H_3-18 and H_2-11 as in **2**. A detailed inspection of the ^{13}C-NMR spectrum showed a down-field shift for C-17 and C-18 signals (*ca*. 9.2 and 7 ppm, respectively) when compared to that of **2**. The hydroxy group at

C-12 was readily deduced to be α-oriented on the basis of NOESY correlation of OH-12 with α-oriented H-17 (δ_H 2.93). Thus, the structure of **6** was determined as 20,25-epoxy-3β,6α,12α,16β,24α-pentahydroxycycloartane.

Table 2.6. The ^{13}C and ^{1}H NMR data of **6** (100/400 MHz, δ ppm, in C_5D_5N).

Position	δ_C (ppm)	δ_H (ppm), *J* (Hz)
1	32.9	1.32 m, 1.64 td (12.5, 4.5)
2	31.3	1.94 m (2H)
3	78.1	3.63 dt (10.7, 5.1)
4	42.2	-
5	54.2	1.72 m
6	69.0	3.76 tdd (9.5, 5.8, 3.0)
7	39.5	1.79 td (8.0, 3.5) (2H)
8	48.3	1.86 m
9	20.9	-
10	28.9	-
11	37.9	1.89 m, 2.37 dd (14.9, 5.8)
12	73.0	4.27 ddd (9.1, 5.9, 2.6)
13	51.2	-
14	46.2	-
15	50.6	1.86 m, 2.15 dd (12.6, 7.9)
16	71.9	4.88 tt (8.0, 5.0)
17	55.0	2.93 d (8.0)
18	20.5	1.71 s
19	31.6	0.48 d (4.2), 0.59 d (4.2)
20	79.3	-
21	27.2	1.94 s
22	28.6	2.08 dd (13.3, 3.5), 2.75 td (13.4, 4.1)
23	23.6	1.89 m, 2.28 dt (13.8, 3.4)
24	68.6	3.69 brs
25	75.6	-
26	28.4	1.52 s
27	28.0	1.35 s
28	29.5	1.91 s
29	16.0	1.37 s
30	21.8	1.26 s

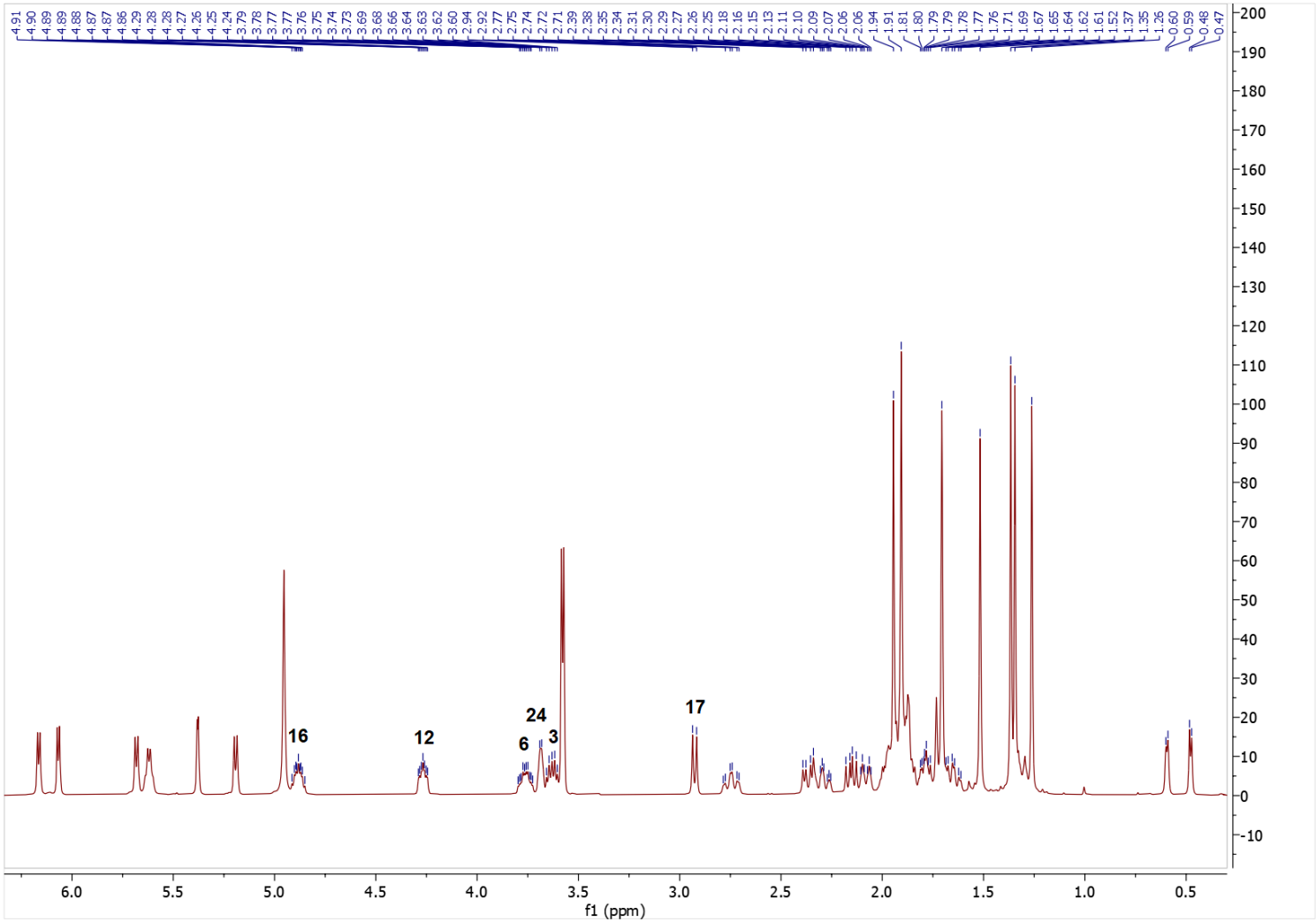

Spectrum 2.35. ^{1}H-NMR spectrum of compound **6**.

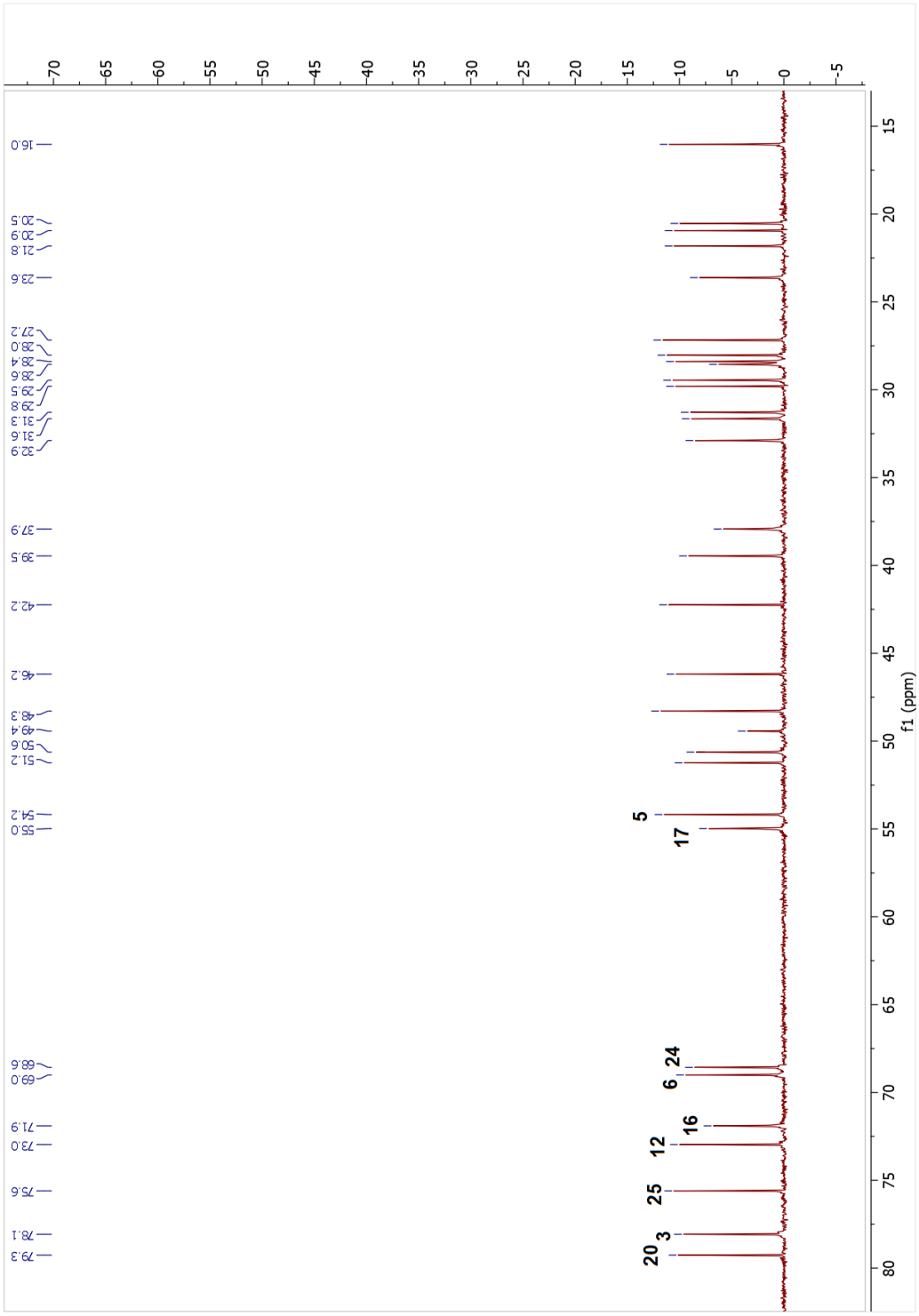

Spectrum 2.36. ^{13}C-NMR spectrum of compound **6**.

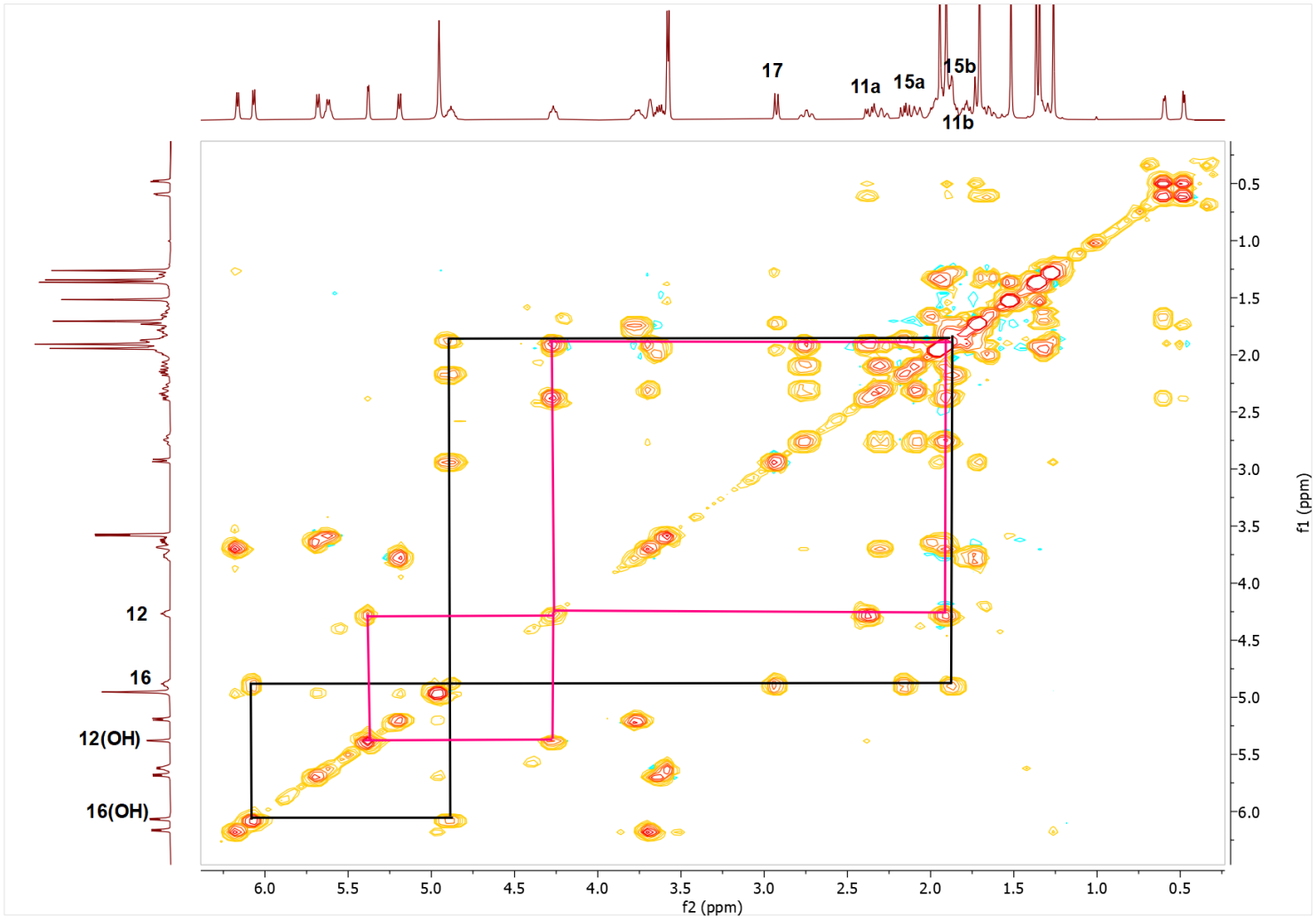

Spectrum 2.37. COSY spectrum of compound **6**.

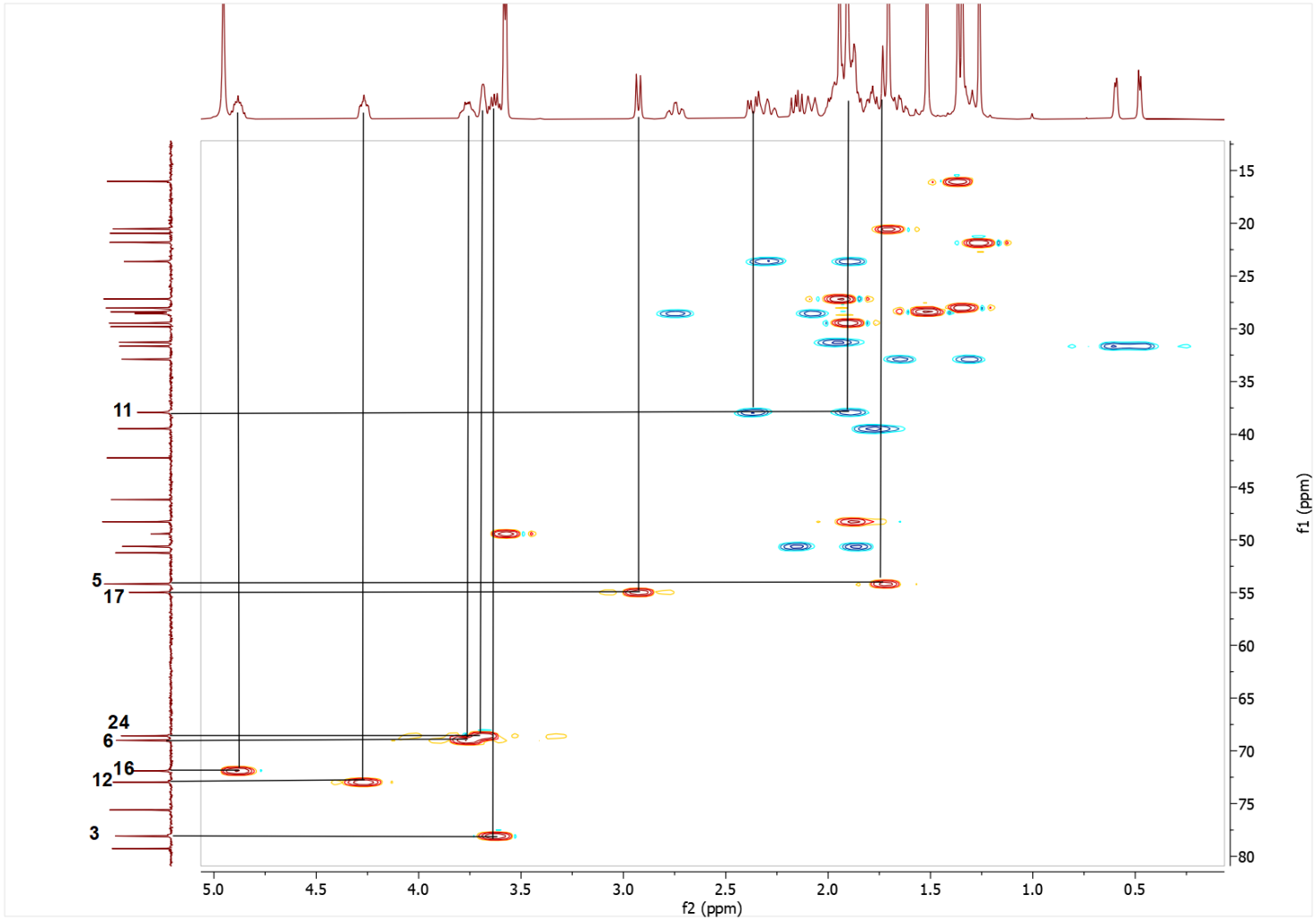

Spectrum 2.38. HSQC spectrum of compound **6**.

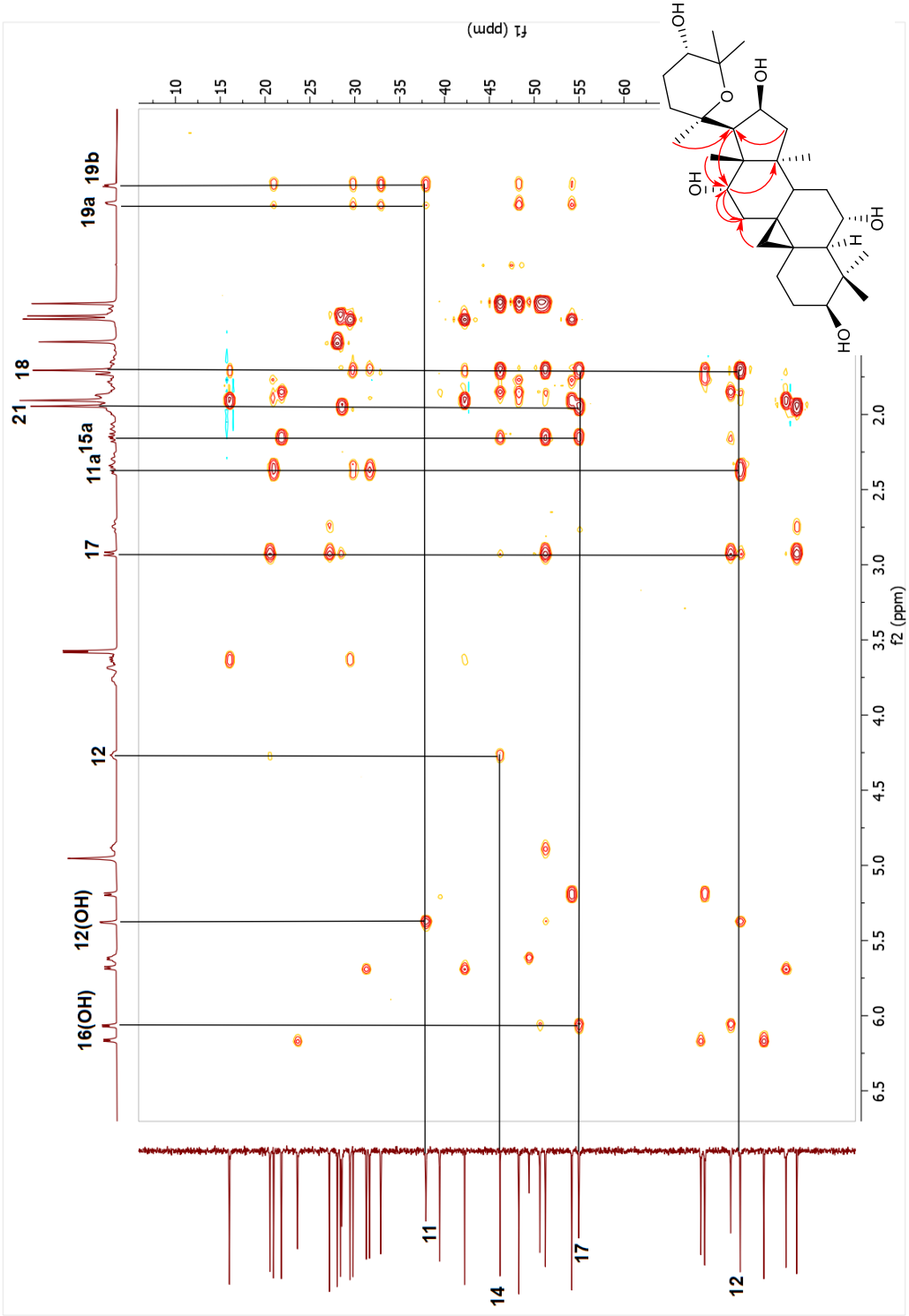

Spectrum 2.39. HMBC spectrum of compound **6**.

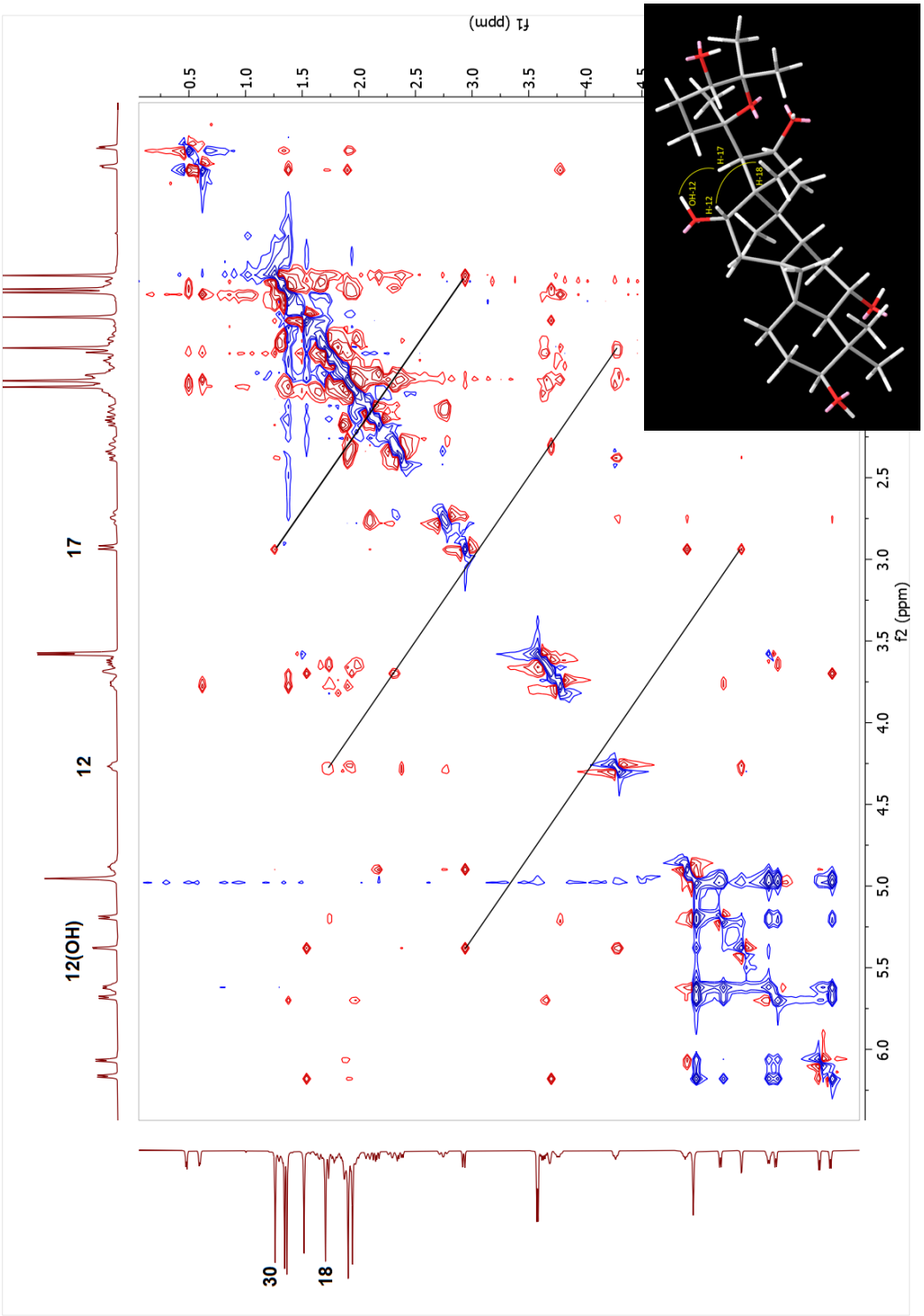

Spectrum 2.40. NOESY spectrum of compound **6**.

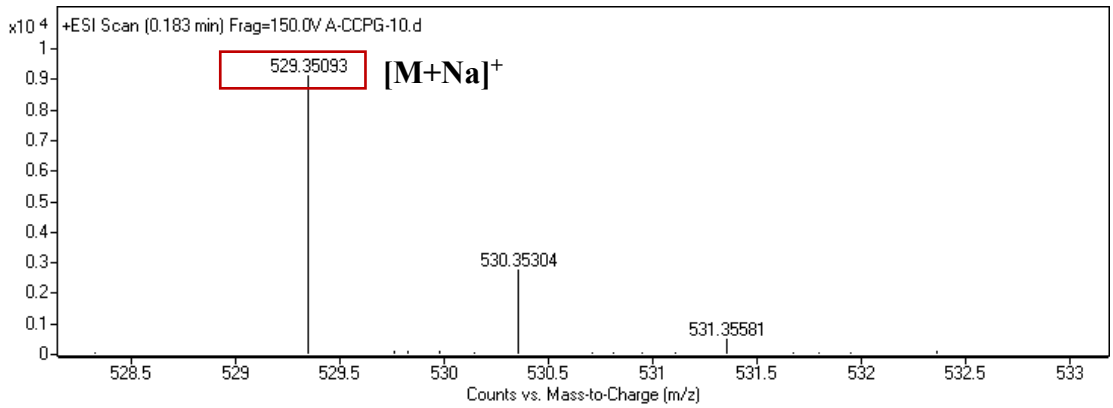

Spectrum 2.41. HR-ESI-MS spectrum of compound **6**.

2.3.2.7. Structure Elucidation of Compound 7

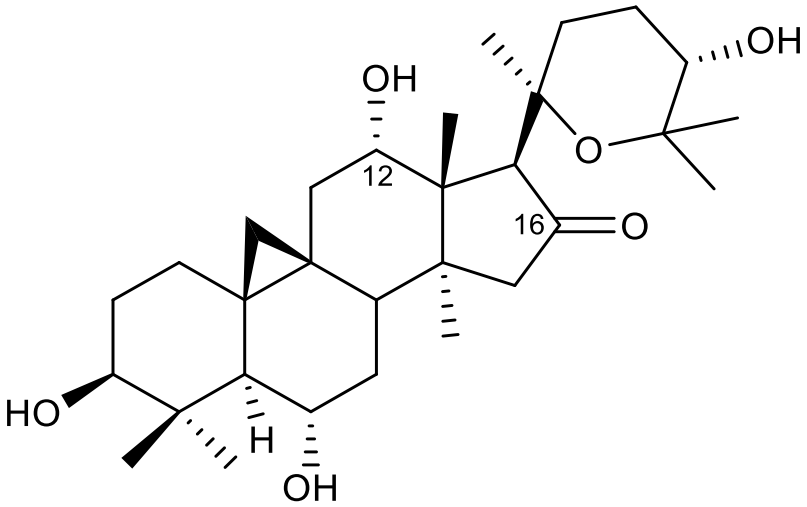

Figure 2.14. Chemical structure of compound **7**.

The molecular formula of **7** was determined to be $C_{30}H_{48}O_6$ by the HR-ESI-MS analysis (*m/z* 527.33594 $[M + Na]^+$, calcd for $C_{30}H_{48}NaO_6$, 527.33486). The disappearance of the low-field H-16 signal in the ^{1}H-NMR spectrum as well as the appearance of a carbonyl resonance at δ_C 216.6 in the ^{13}C-NMR spectrum implied oxidation of the secondary alcohol at C-16. Additionally, the new proton signal observed at δ_H 4.19, correlating with a carbon

at 72.7 ppm signal in the HSQC spectrum, indicated an additional monooxygenation in the structure. A new hydroxy group was located at C-12 on the basis of the COSY correlation of H-12 (δ_H 4.19) with H_2-11 (δ_H 1.85 and 2.33) and a long-range correlation between H_3-18 (δ_H 1.37) and δ_C 72.7. The stereochemistry of C-12(OH) was deduced as α by comparison of the NMR data with those of **4** and **6**. Consequently, metabolite **7** was deduced to be 20,25-epoxy-3β,6α,12α,24α-tetrahydroxycycloartan-16-one.

Table 2.7. The ^{13}C and ^{1}H NMR data of **7** (100/400 MHz, δ ppm, in C_5D_5N).

Position	δ_C (ppm)	δ_H (ppm), *J* (Hz)
1	32.6	1.27 m, 1.63 m
2	31.2	1.98 m (2H)
3	78.0	3.64 m
4	42.0	-
5	54.1	1.70 m
6	68.8	3.75 ddd (12.3, 8.9, 3.4)
7	39.4	1.66 m (2H)
8	46.9	1.76 m
9	20.1	-
10	29.8	-
11	36.1	1.85 td (8.3, 6.9, 3.5), 2.33 m
12	72.7	4.19 dt (9.5, 4.8)
13	51.7	-
14	42.0	-
15	52.7	2.09 d (17.4), 2.28 d (17.8)
16	216.6	-
17	65.6	3.56 s
18	20.1	1.37 s
19	31.0	0.53 d (4.5), 0.58 d (4.2)
20	76.4	-
21	23.5†	1.52 s
22	32.4	2.33 m (2H)
23	23.4†	1.81 m, 2.15 m
24	68.0	3.64 brs
25	75.5	-
26	27.8	1.47 s
27	27.5	1.30 s
28	29.5	1.92 s
29	16.1	1.37 s
30	20.5	1.32 s

†Overlapped signals

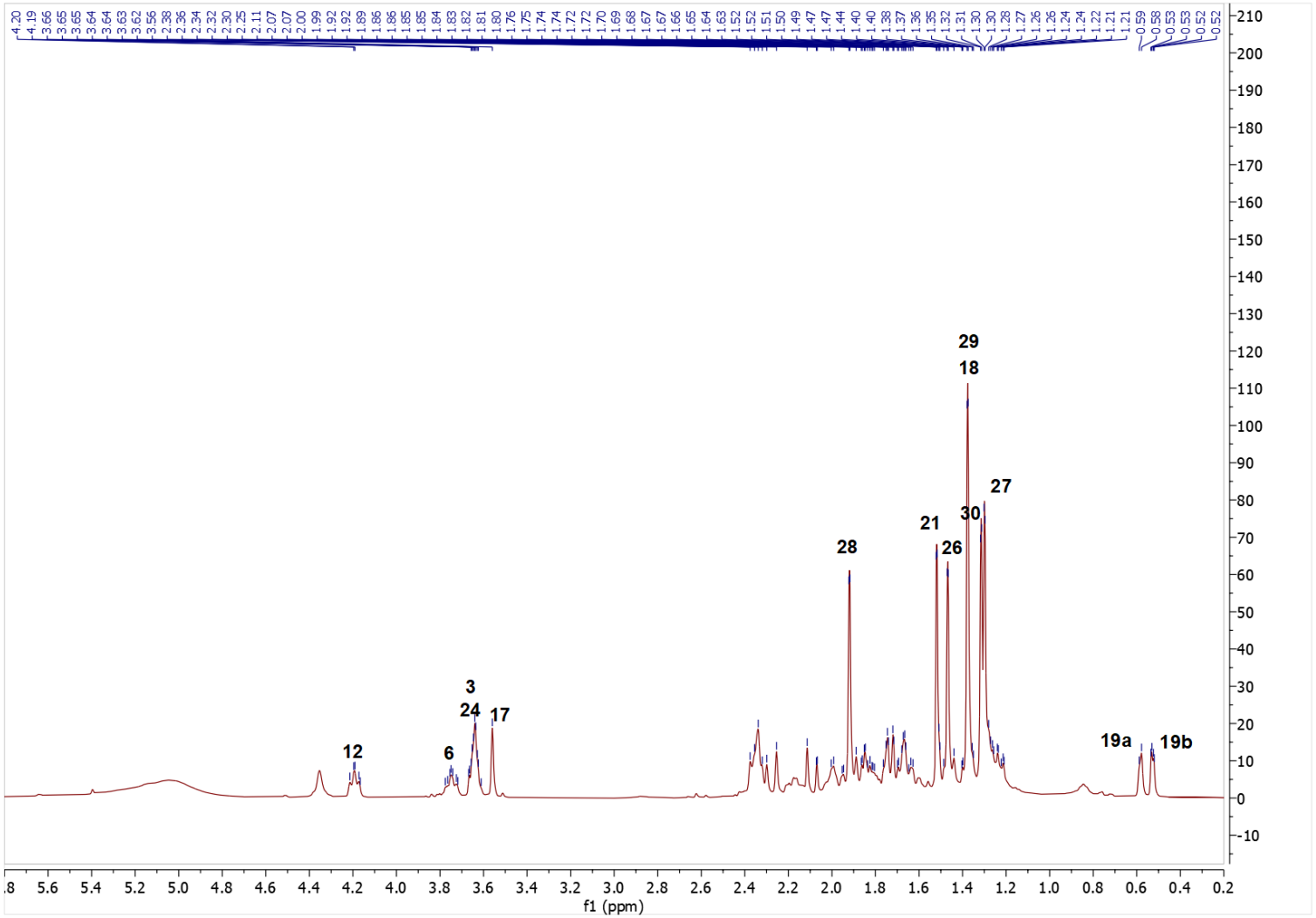

Spectrum 2.42. ^{1}H-NMR spectrum of compound **7**.

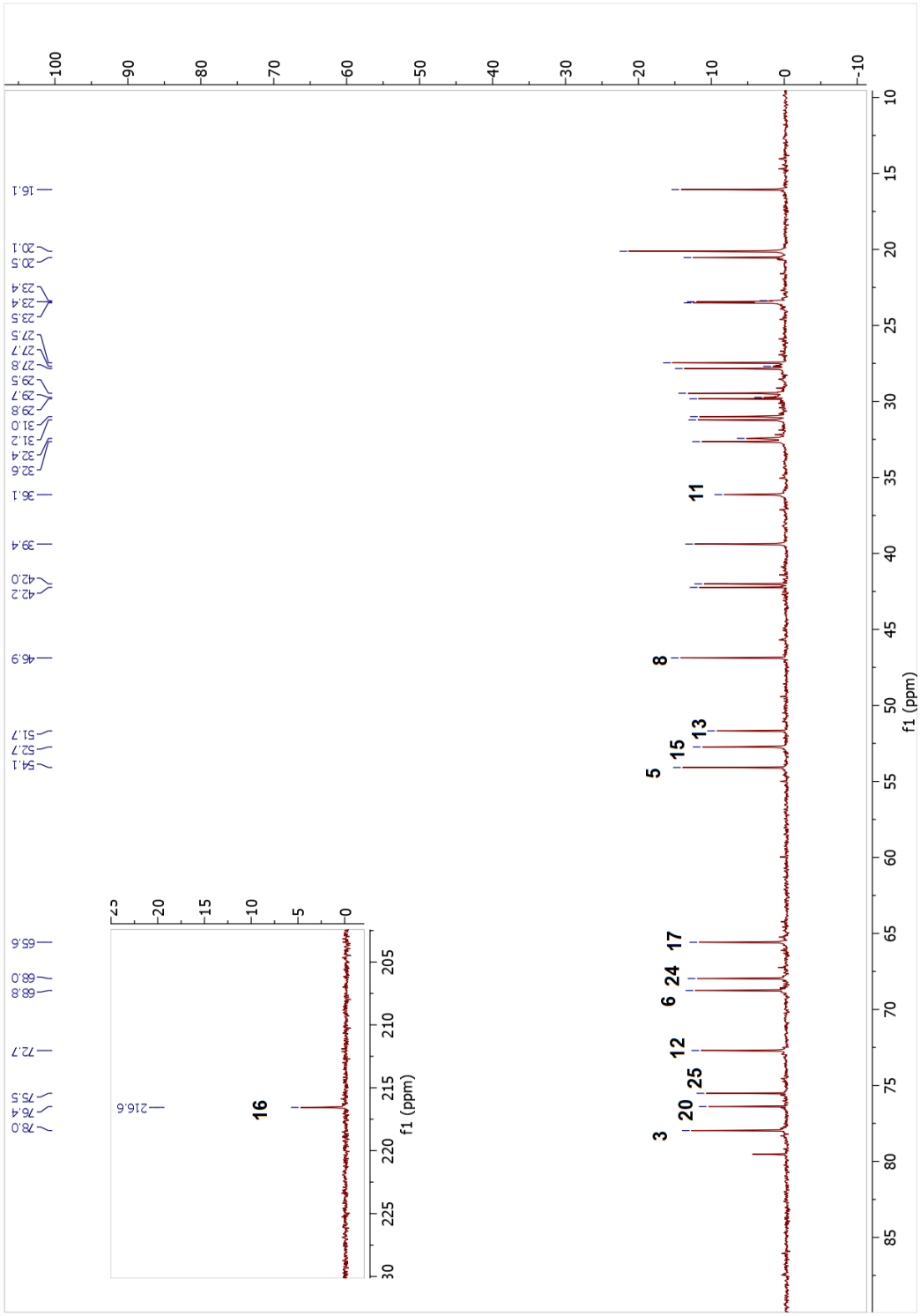

Spectrum 2.43. ^{13}C-NMR spectrum of compound **7**.

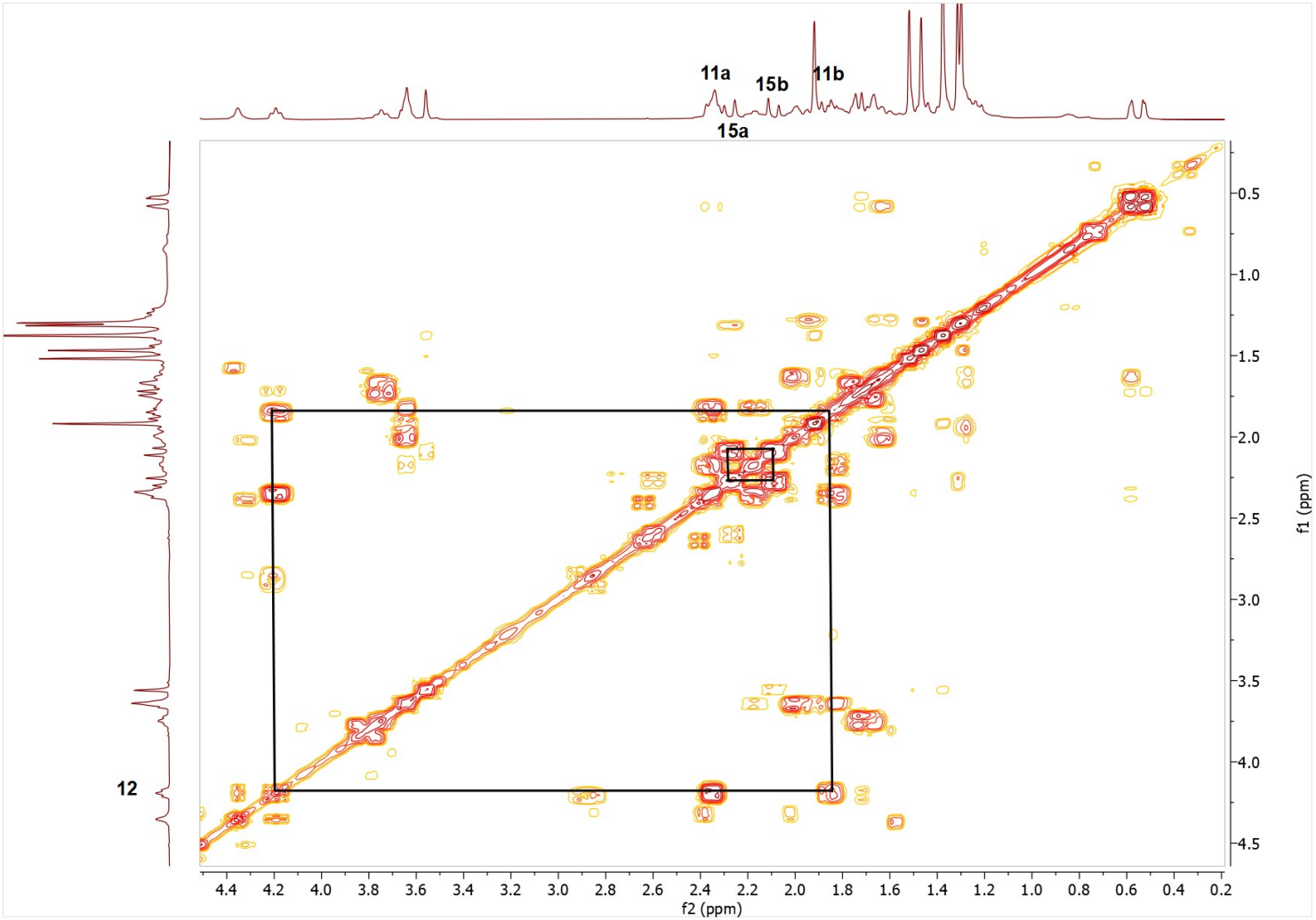

Spectrum 2.44. COSY spectrum of compound **7**.

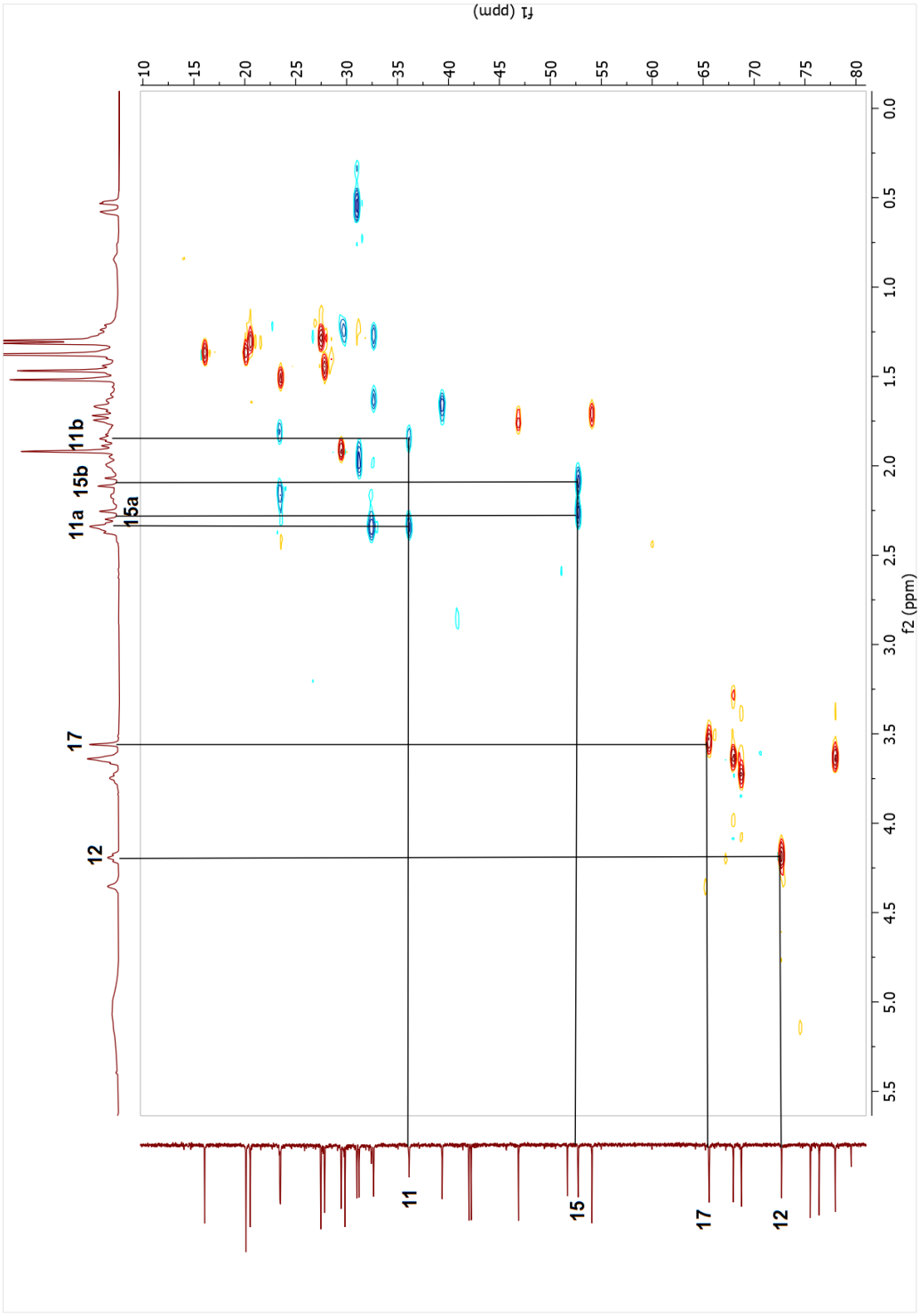

Spectrum 2.45. HSQC spectrum of compound **7**.

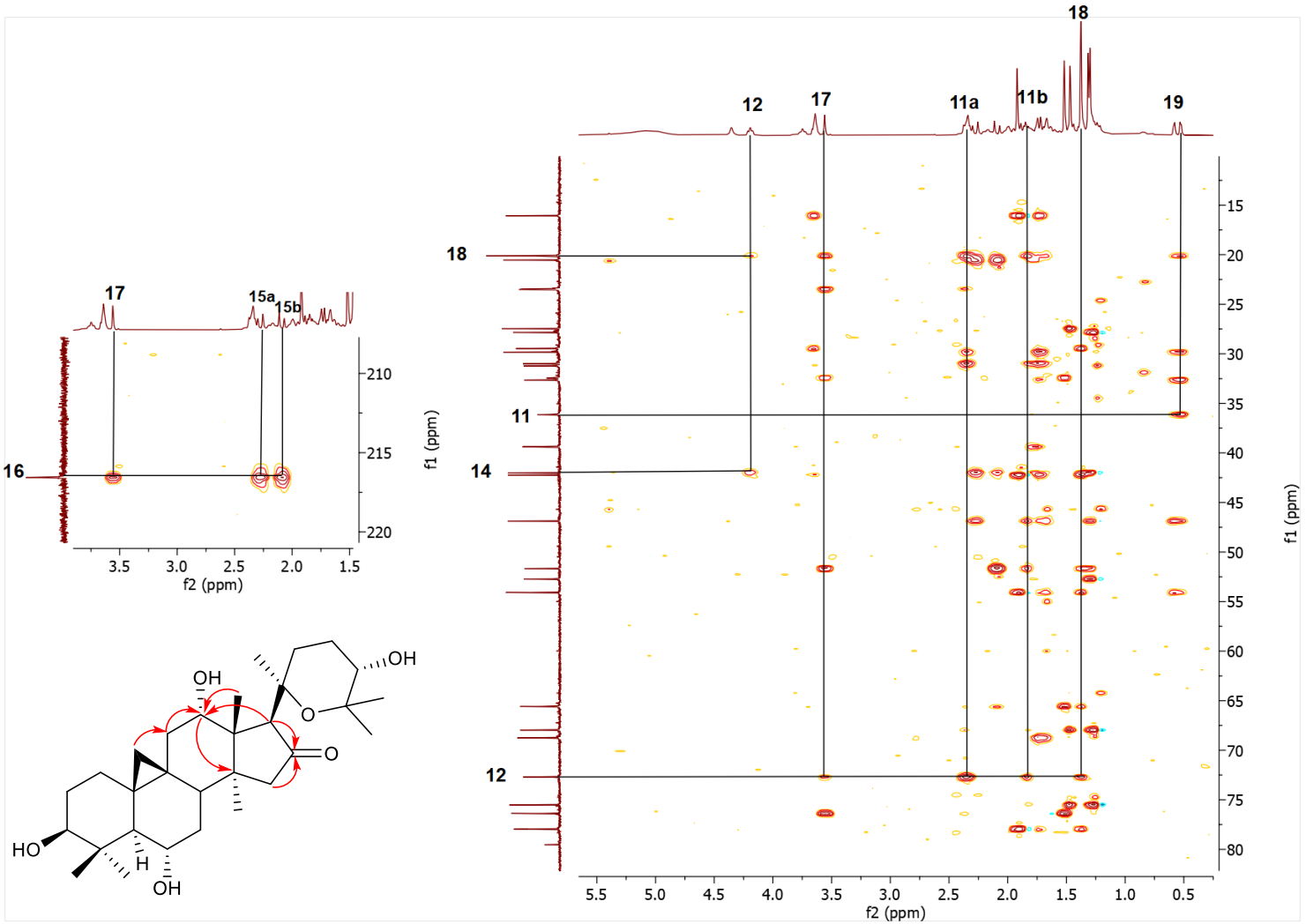

Spectrum 2.46. HMBC spectrum of compound **7**.

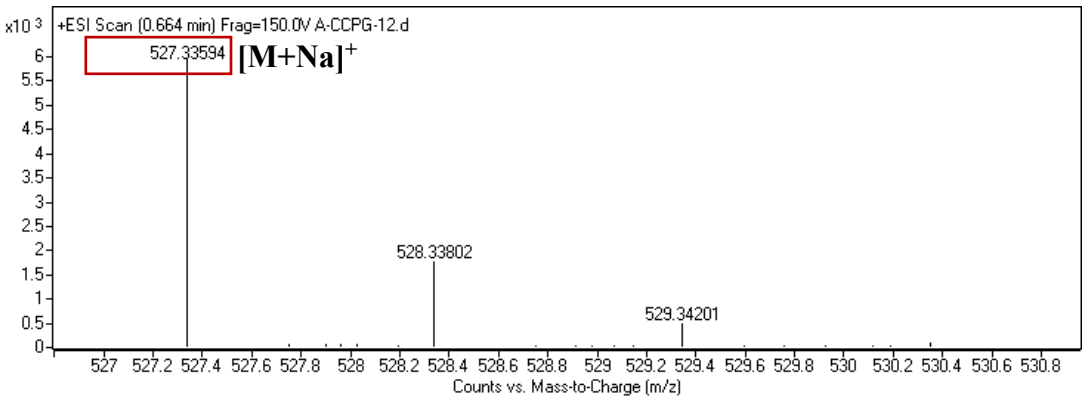

Spectrum 2.47. HR-ESI-MS spectrum of compound **7**.

2.3.2.8. Structure Elucidation of Compound 8

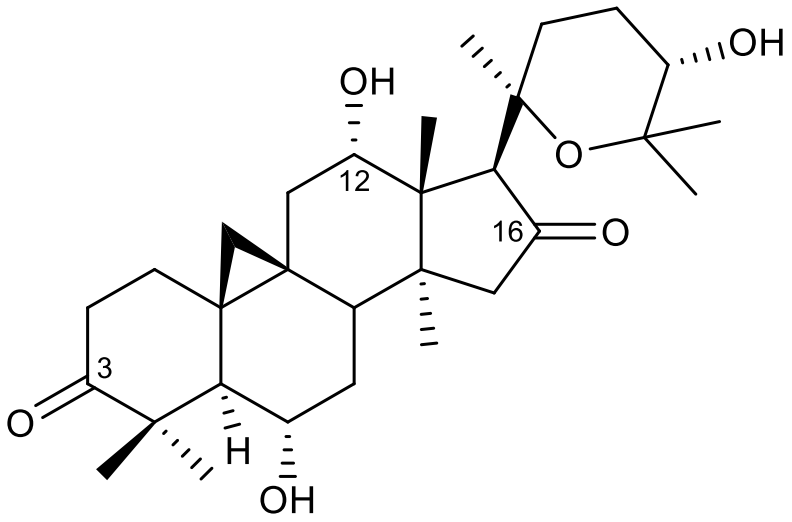

Figure 2.15. Chemical structure of compound **8**.

The HR-ESI-MS spectrum of **8** provided a major ion peak at *m/z* 547.3276 [M + FA - H]$^-$ ($C_{31}H_{47}O_8$). Apart from the oxymethine signals of C-3, resonances of **7** were present for **8**. In the ^{13}C-NMR spectrum, the resonance at 217.8 ppm was obvious, implying biotransformation of C-3 secondary alcohol to a ketone via an oxidation reaction. The HMBC cross-peaks from H_3-28 (δ_H 1.73), H_3-29 (δ_H 1.45) and H_2-2 (δ_H 2.38 and 2.75) to δ_C 217.8

justifying the assignment. Thus, the structure of **8** was deduced as 20,25-epoxy-6α,12α,24α-trihydroxycycloartan-3,16-dione.

Table 2.8. The ^{13}C and ^{1}H NMR data of **8** (100/400 MHz, δ ppm, in C_5D_5N).

Position	δ_C (ppm)	δ_H (ppm), *J* (Hz)
1	32.5	1.32 m, 2.04 m
2	36.3	2.38 m, 2.75 ddd (13.9, 9.2, 6.4)
3	217.8	-
4	51.3	-
5	54.2	2.26 m
6	70.2	3.65 m
7	39.4	1.62 m, 1.73 m
8	48.0	1.73 m
9	21.3	-
10	28.9	-
11	37.3	1.66 m, 2.31 m
12	73.7	4.15 ddd (9.7, 7.3, 2.6)
13	52.8	-
14	43.0	-
15	53.8	2.09 d (17.5), 2.27 d (16.2)
16	217.5	-
17	66.7	3.55 s
18	21.2	1.33 s
19	31.2	0.47 d (4.2), 0.65 d (4.2)
20	77.5	-
21	24.5	1.49 s
22	33.5	1.84 m, 2.34 m
23	24.5	1.85 m, 2.21 m
24	69.0	3.64 brs
25	76.7	-
26	28.9	1.45 s
27	28.5	1.28 s
28	29.9	1.73 s
29	21.0	1.45 s
30	21.7	1.27 s

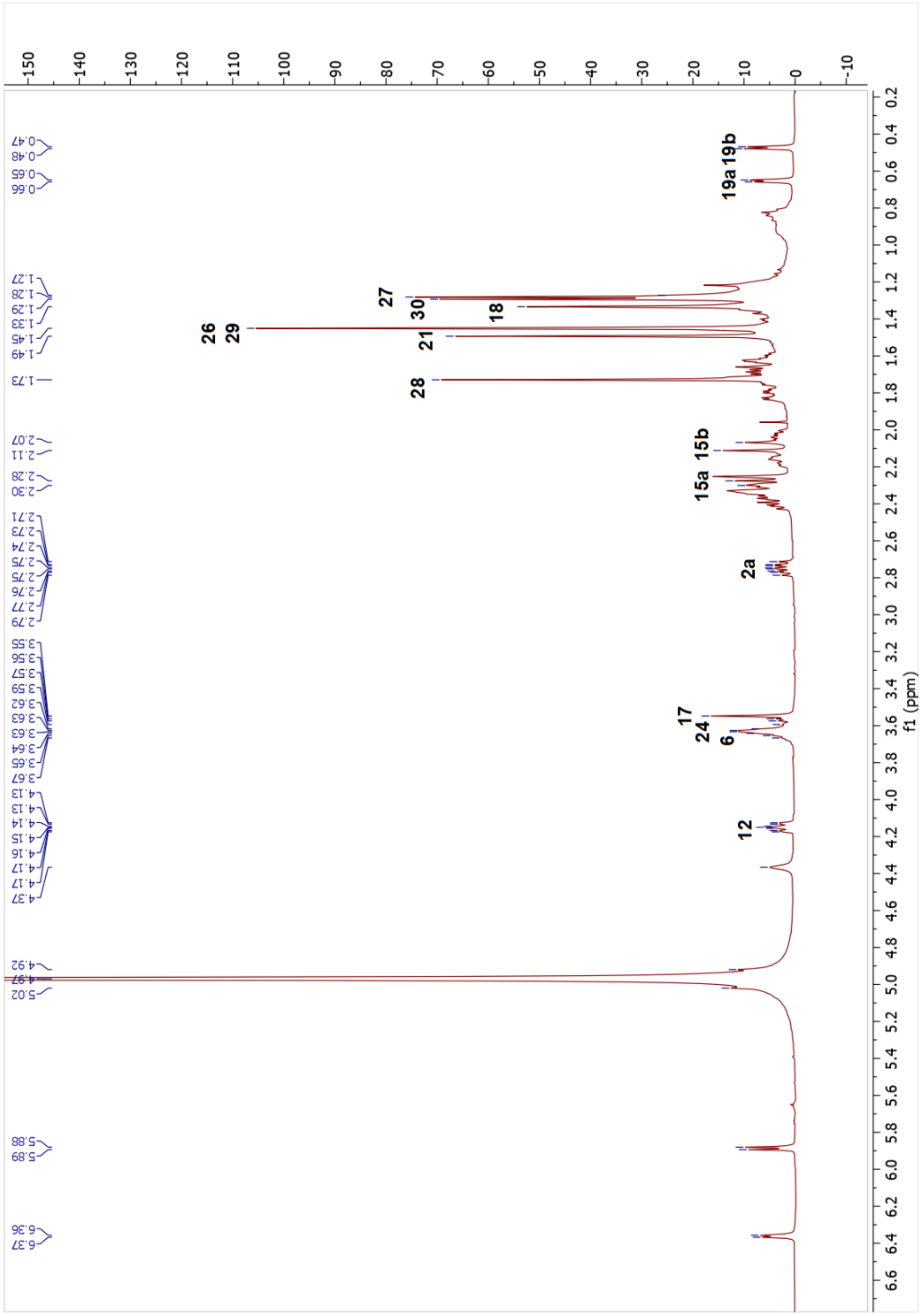

Spectrum 2.48. ^{1}H-NMR spectrum of compound **8**.

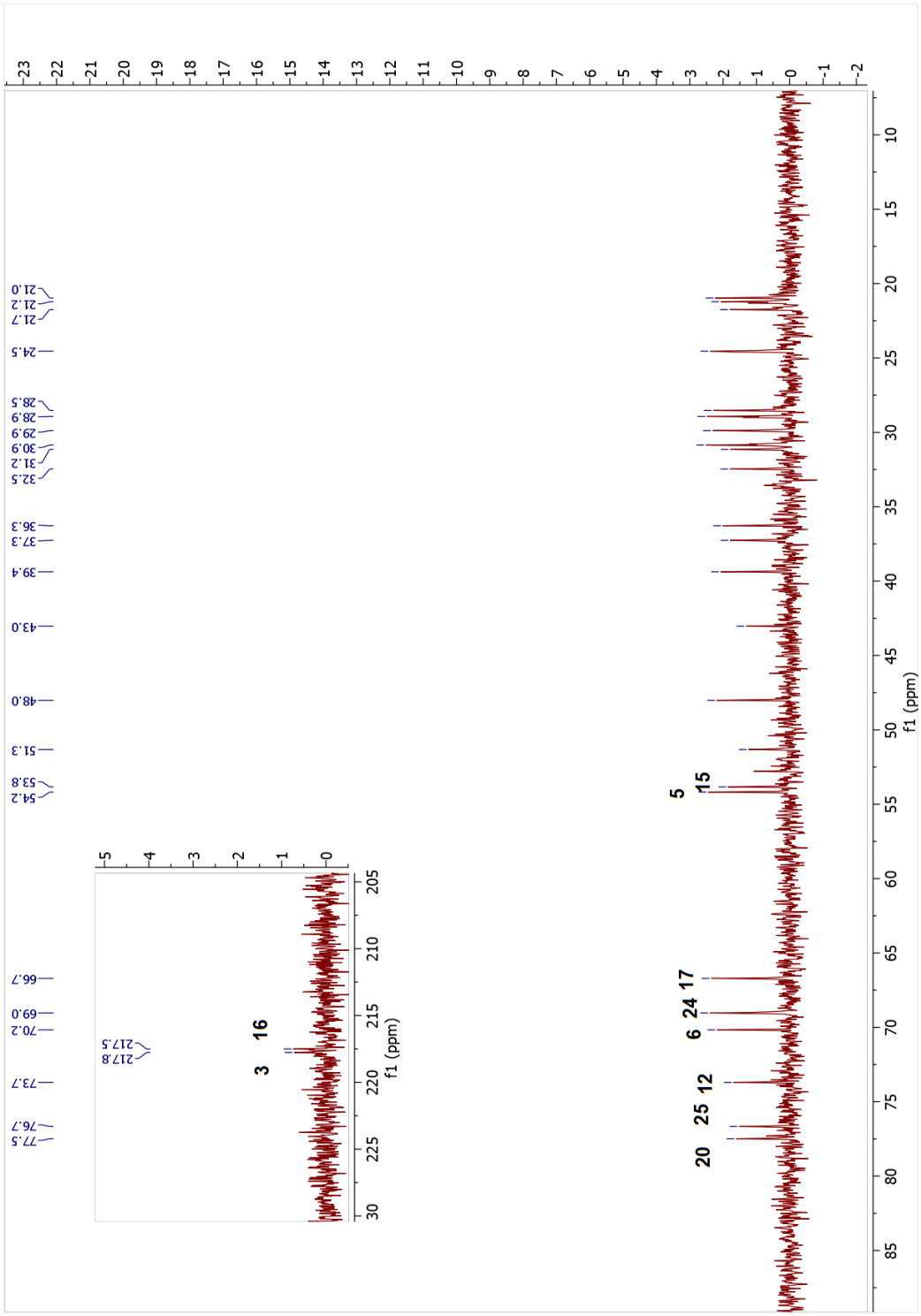

Spectrum 2.49. ^{13}C-NMR spectrum of compound **8**.

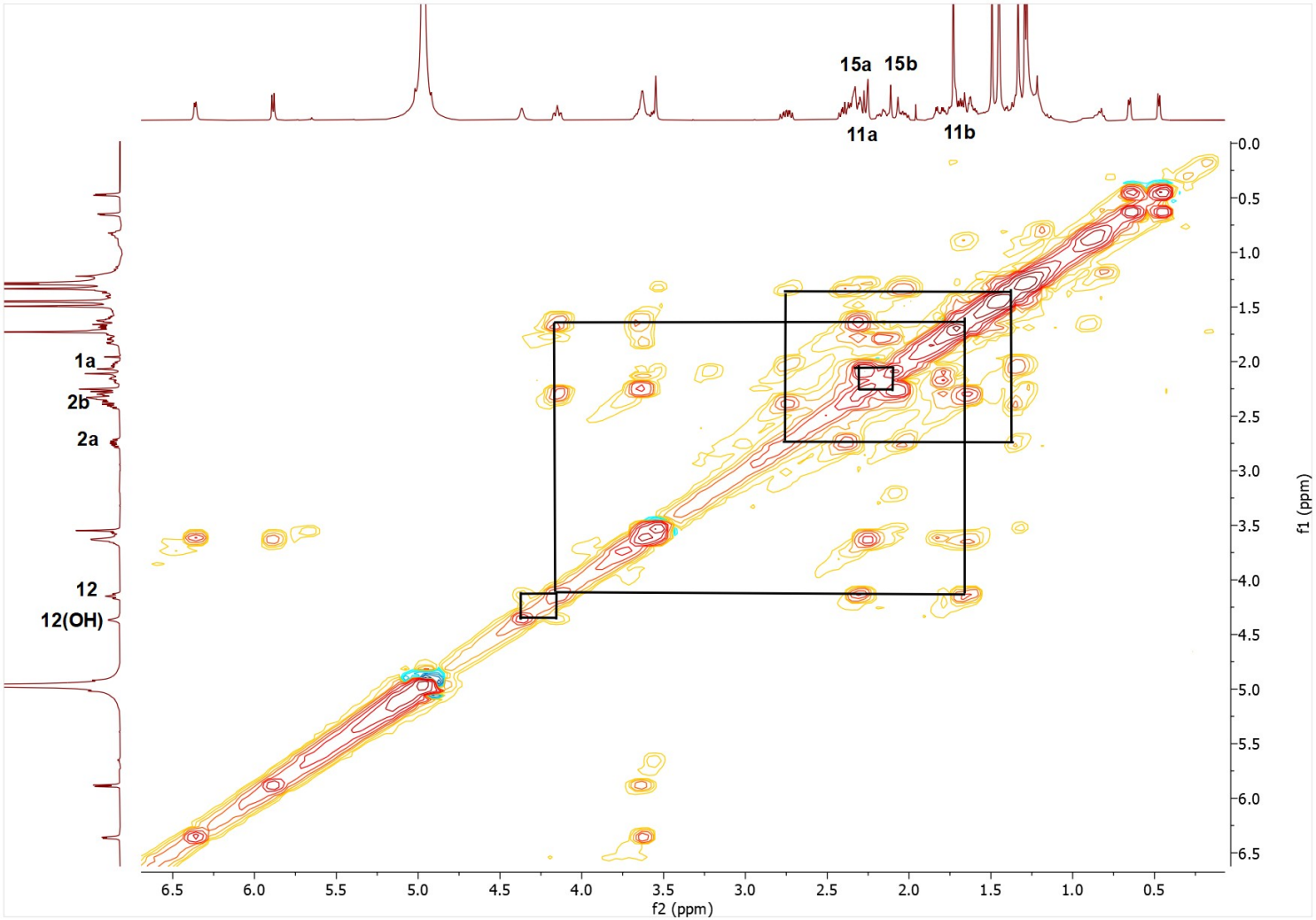

Spectrum 2.50. COSY spectrum of compound **8**.

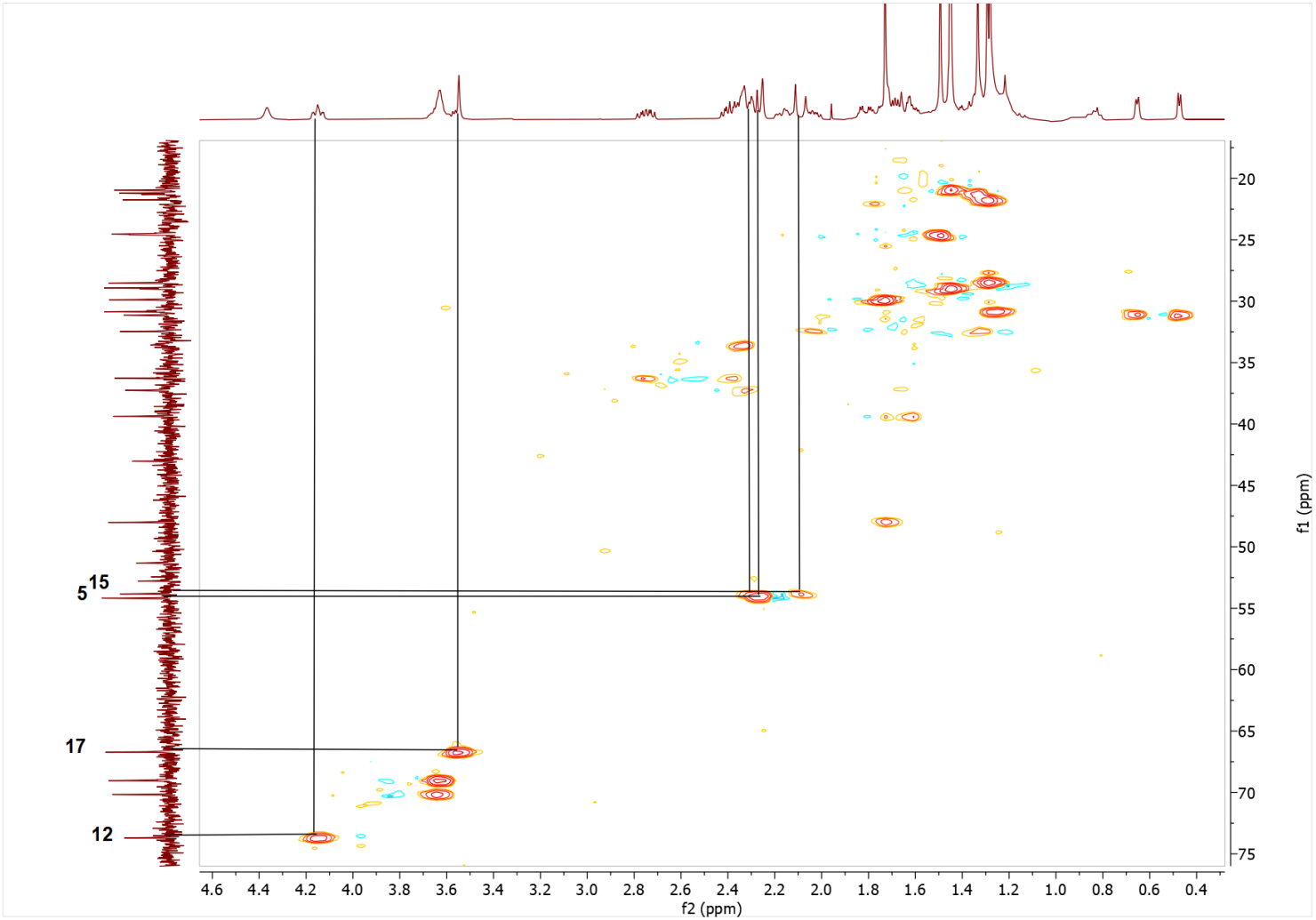

Spectrum 2.51. HSQC spectrum of compound **8**.

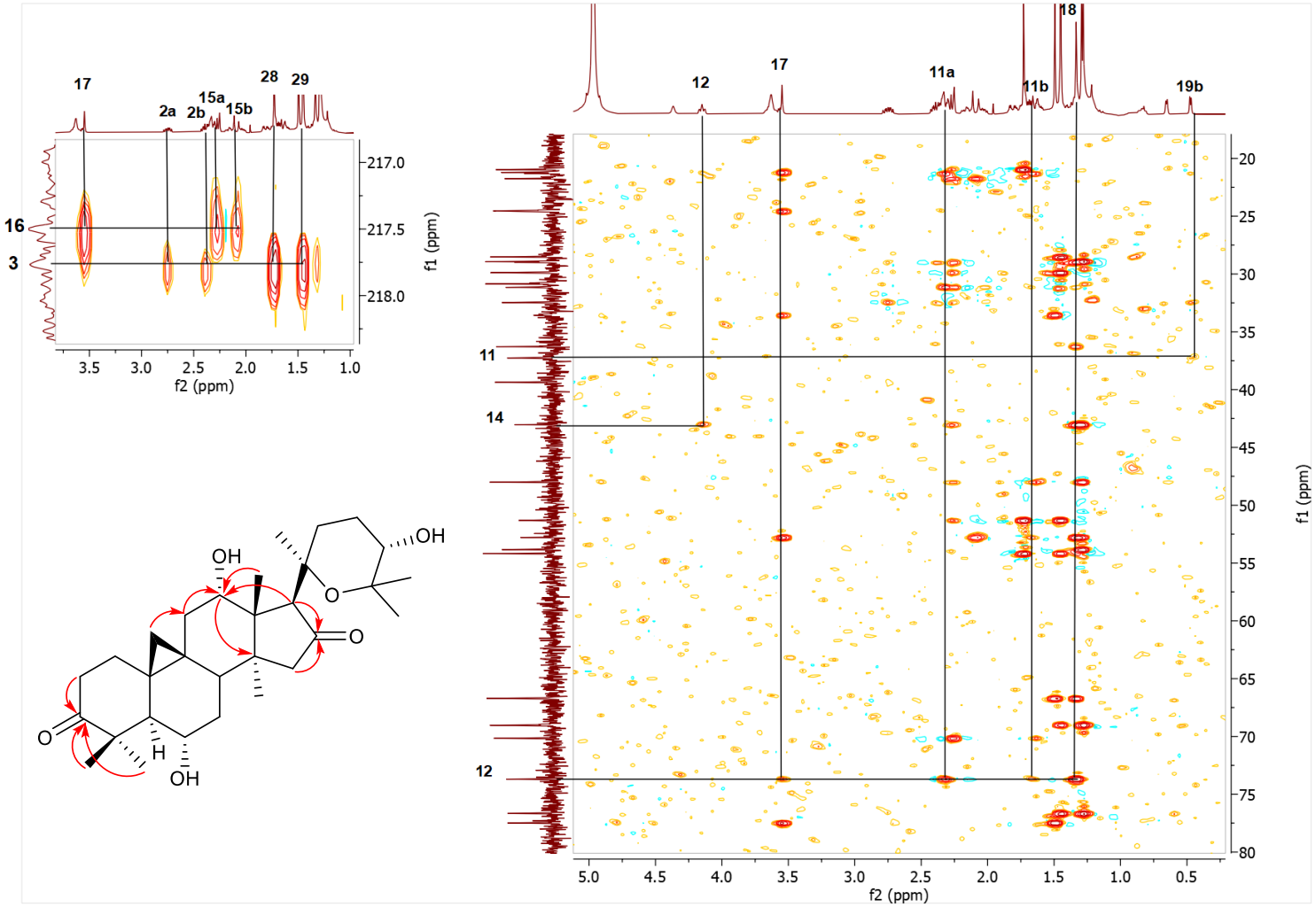

Spectrum 2.52. HMBC spectrum of compound **8**.

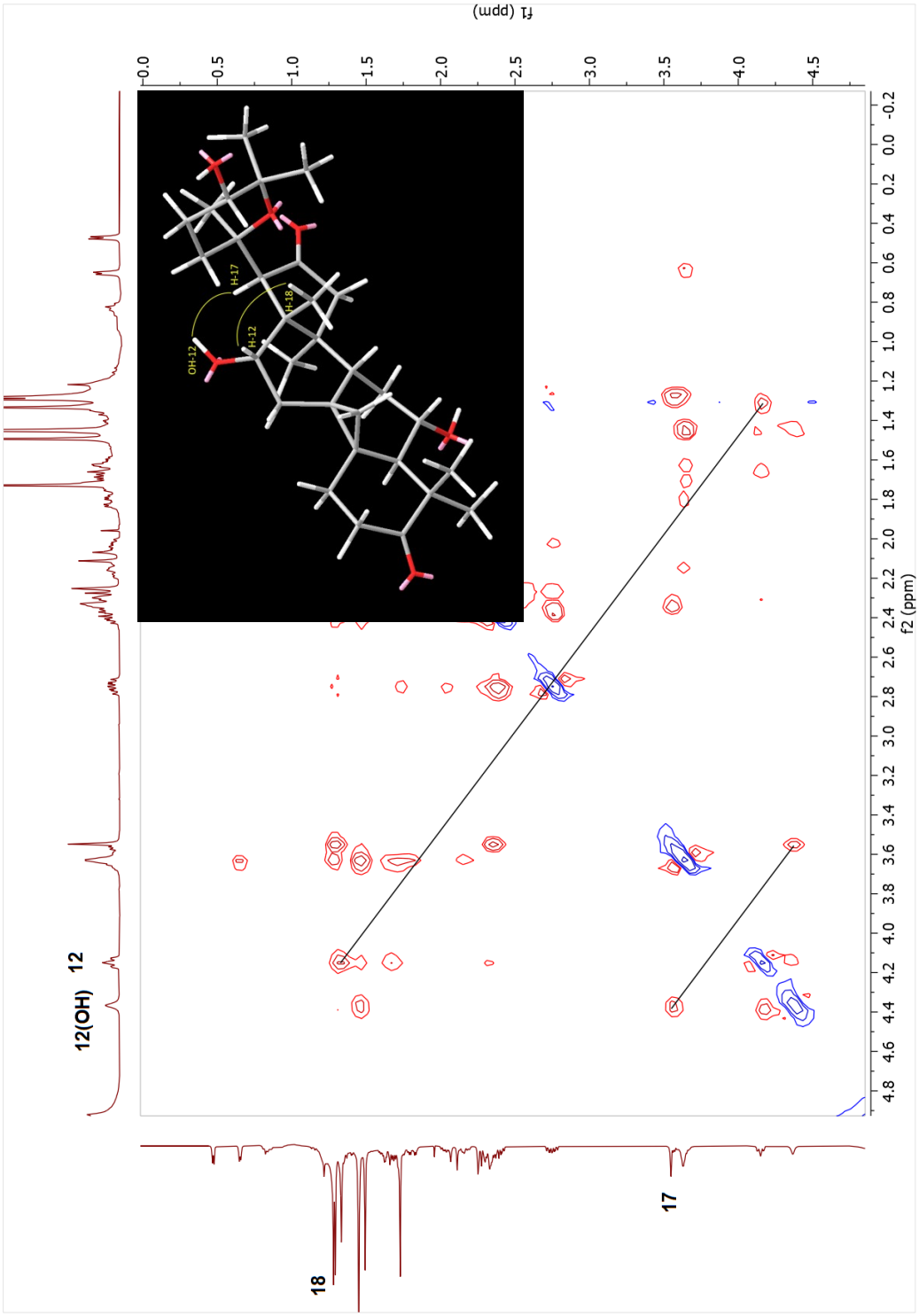

Spectrum 2.53. NOESY spectrum of compound **8**.

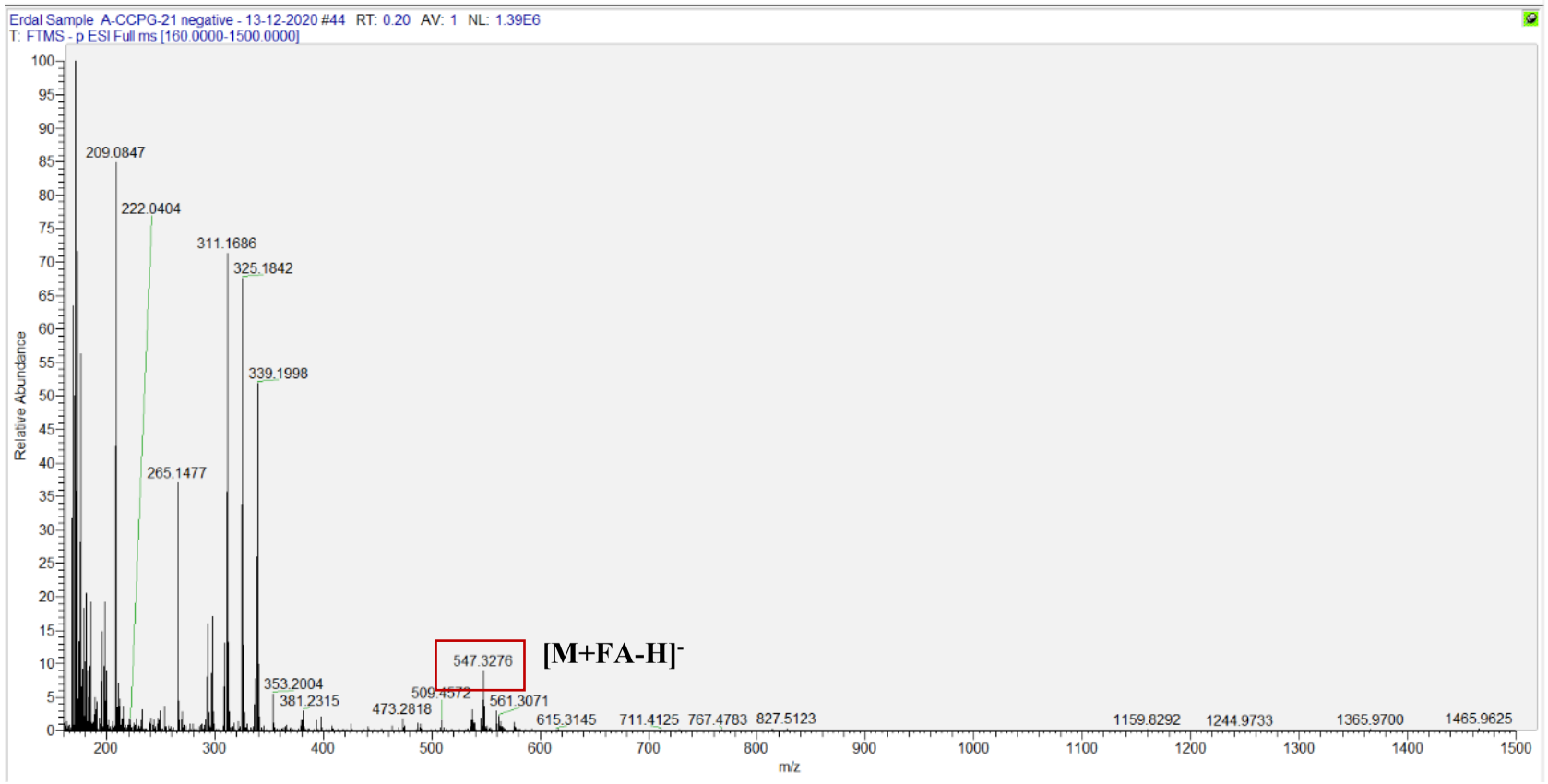

Spectrum 2.54. HR-ESI-MS spectrum of compound **8**.

2.3.2.9. Structure Elucidation of Compound 9

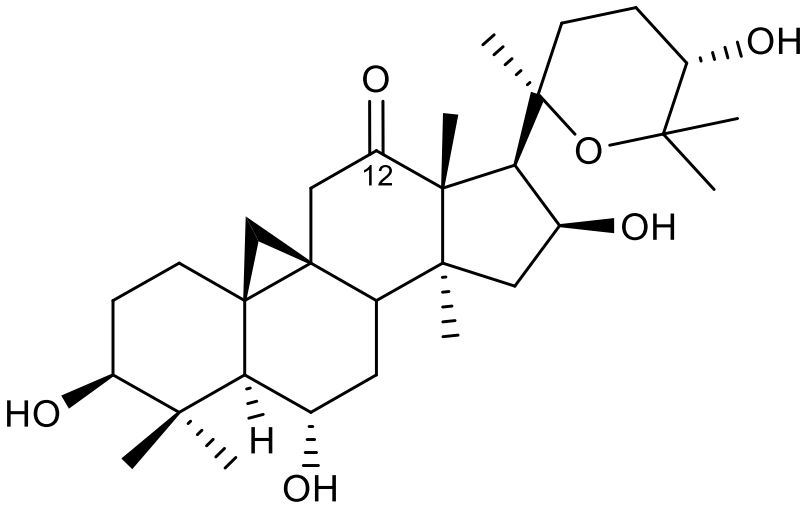

Figure 2.16. Chemical structure of compound **9**.

Compound **9** gave a major ion peak at *m/z* 527.33662 ([M + Na]$^+$, calcd for $C_{30}H_{48}NaO_6$, 527.33486). The molecular weight of **9** was 14 amu higher than **1**, suggesting a mono-hydroxylation and an additional unsaturation. When the ^{1}H-NMR spectrum of **9** was inspected, the characteristic signals belonging to H-3, H-6, H-16 and H-24 oxymethine protons were observed readily, suggesting that oxidation occurred in a new oxymethine carbon. In the HMBC spectrum, H_2-11 (δ_H 1.97 and 2.61), H_3-18 (δ_H 1.72) and H-17 (δ_H 2.36) showed cross-peaks with a carbon resonating at δ_C 212.0, confirming the location of the carbonyl group to be at C-12. Based on these results, the structure of **9** was elucidated as 20,25-epoxy-3β,6α,16β,24α-tetrahydroxycycloartan-12-one.

Table 2.9. The ^{13}C and ^{1}H NMR data of **9** (100/400 MHz, δ ppm, in $CDCl_3$).

Position	δ_C (ppm)	δ_H (ppm), *J* (Hz)
1	32.8	1.00 dd (9.0, 3.1), 1.60 m
2	30.0	1.60 m, 1.81 d (9.4)
3	77.9	3.29 m
4	41.3	-
5	52.9	1.31 d (9.6)
6	69.0	3.56 t (10.8)
7	38.1	1.47 m (2H)
8	47.3	2.00 m
9	21.0	-
10	30.9	-
11	45.7	1.97 d (19.6), 2.61 d (19.8)
12	212.0	-
13	61.0	-
14	47.8†	-
15	48.0†	1.68 m, 2.12 m
16	72.9	4.54 m
17	51.5	2.36 d (8.7)
18	13.1	1.72 s
19	32.8	0.49 d (4.6), 0.73 d (4.7)
20	79.3	-
21	27.0†	1.62 s
22	26.9†	1.39 m, 2.07 m
23	23.1	1.70 m, 2.17 m
24	69.4	3.49 brs
25	75.3	-
26	27.9	1.27 s
27	27.5	1.18 s
28	28.2	1.28 s
29	15.0	0.97 s
30	20.6	0.62 s

†Overlapped signals

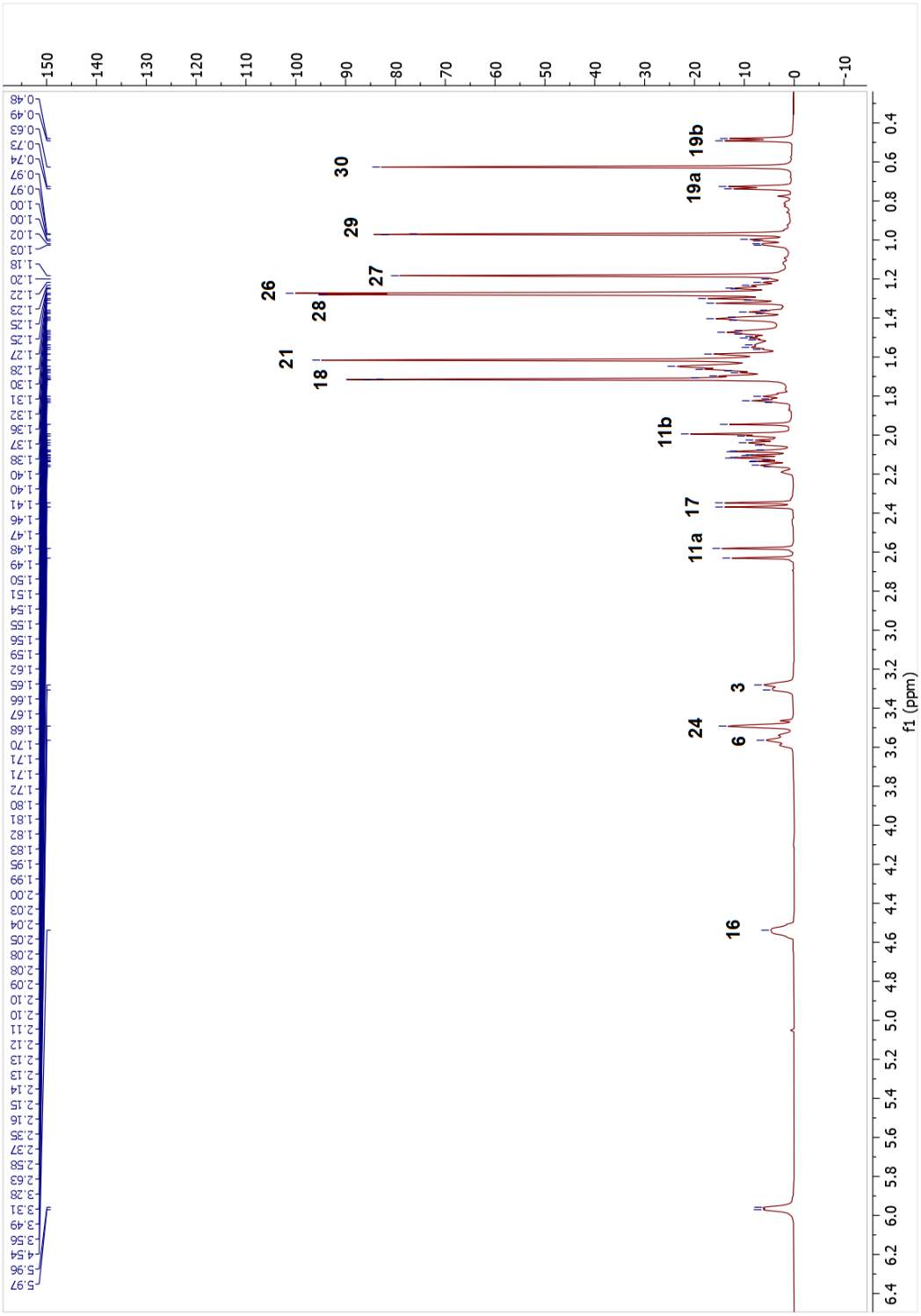

Spectrum 2.55. ^{1}H-NMR spectrum of compound **9**.

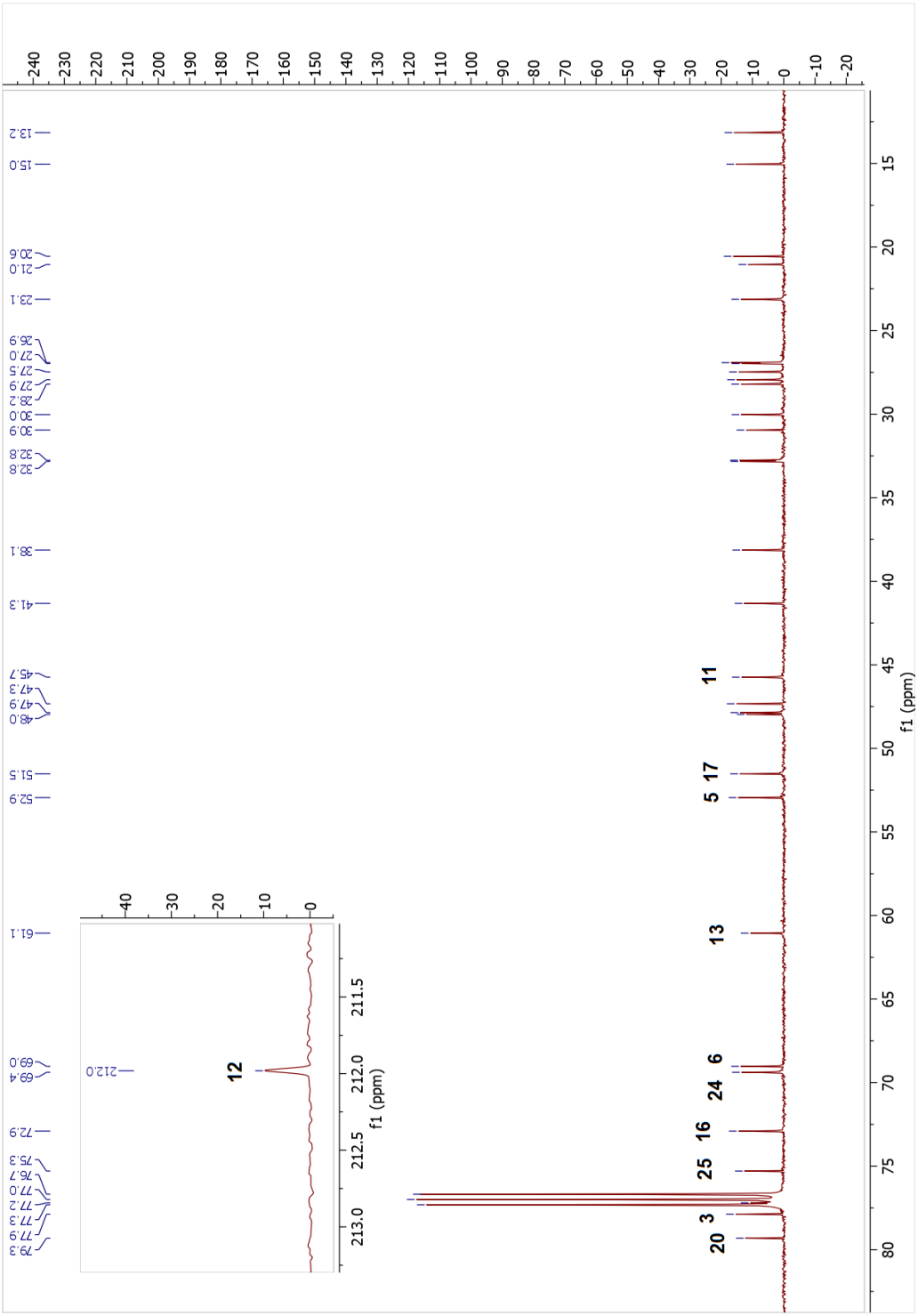

Spectrum 2.56. ^{13}C-NMR spectrum of compound **9**.

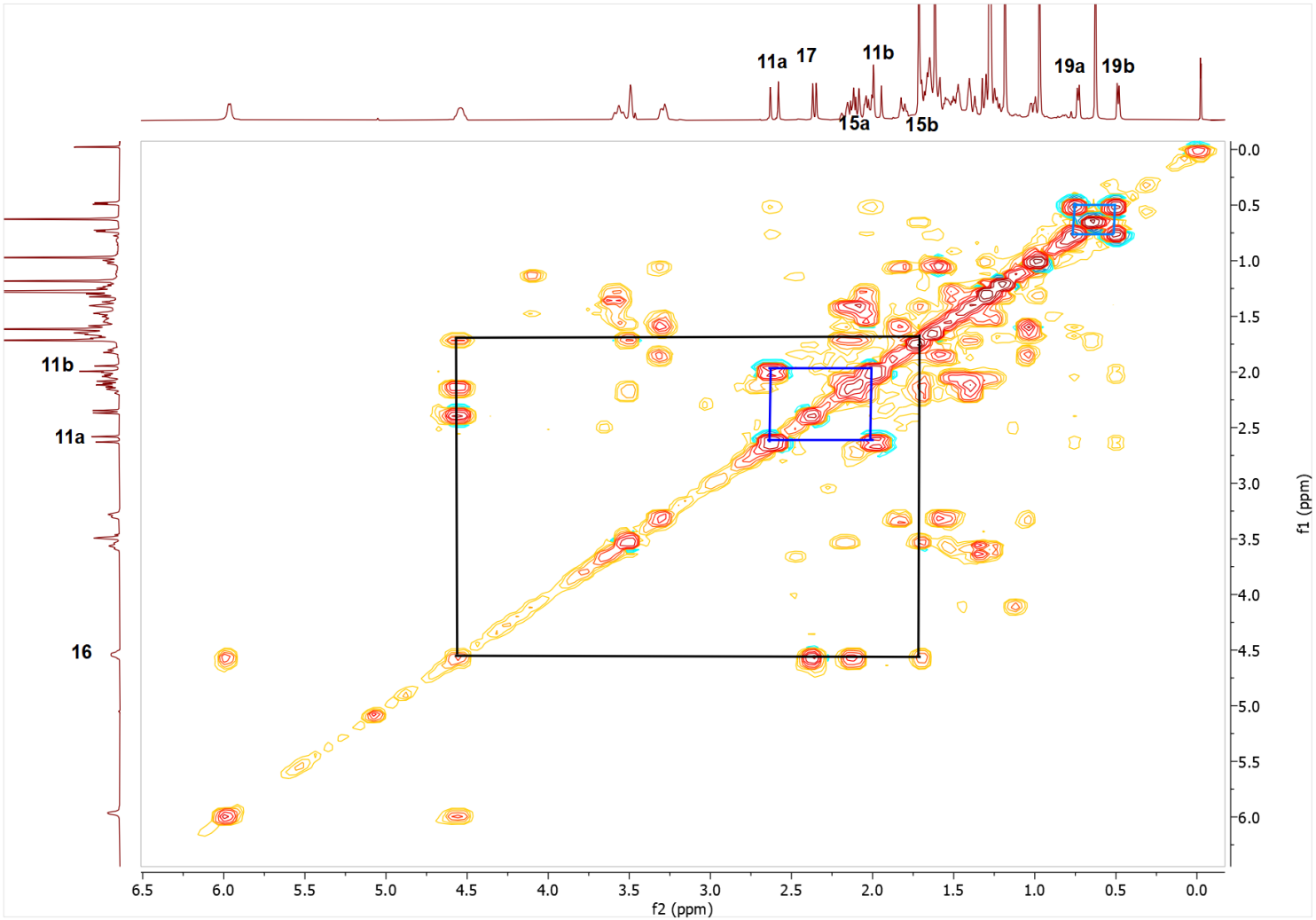

Spectrum 2.57. COSY spectrum of compound **9**.

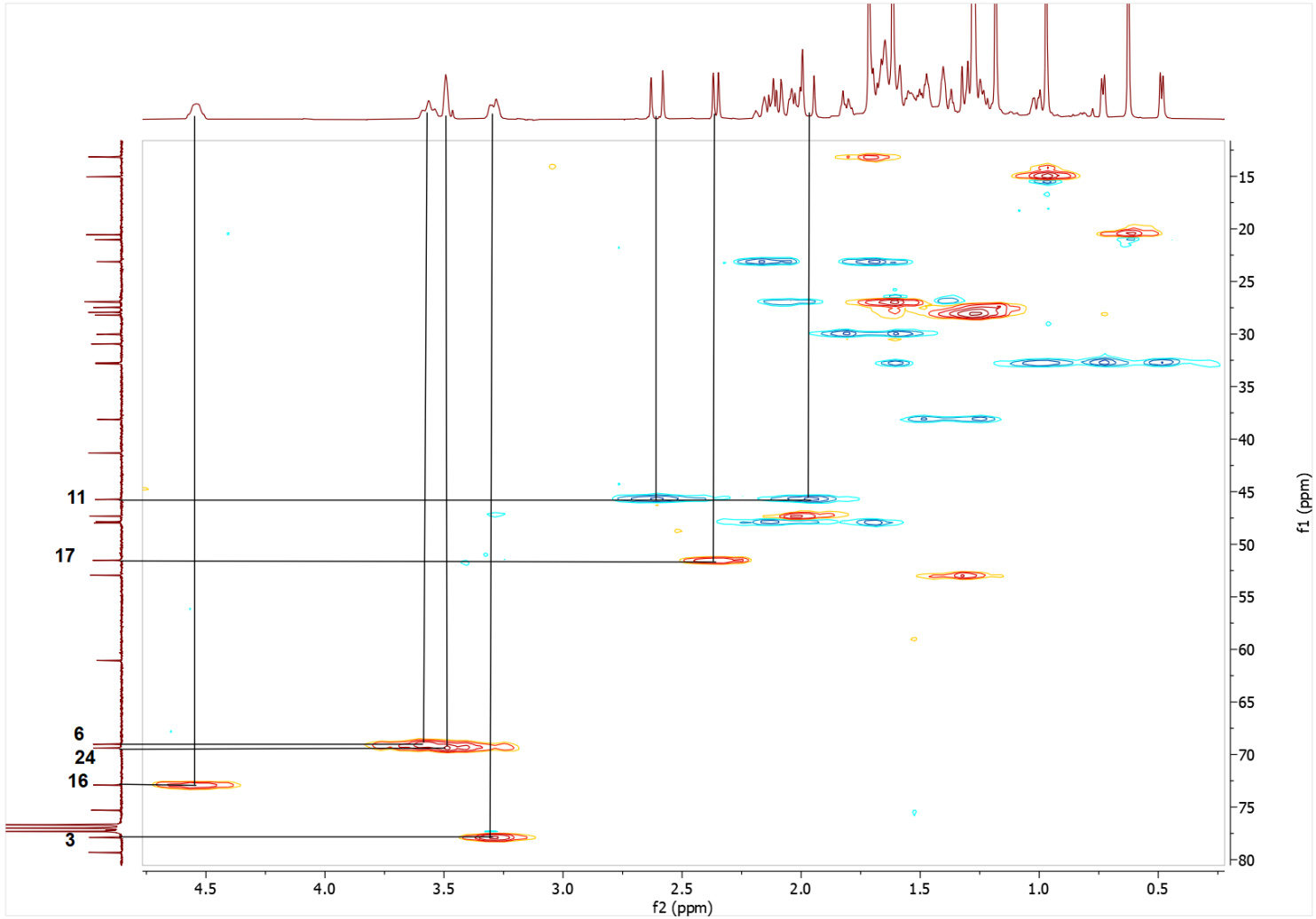

Spectrum 2.58. HSQC spectrum of compound **9**.

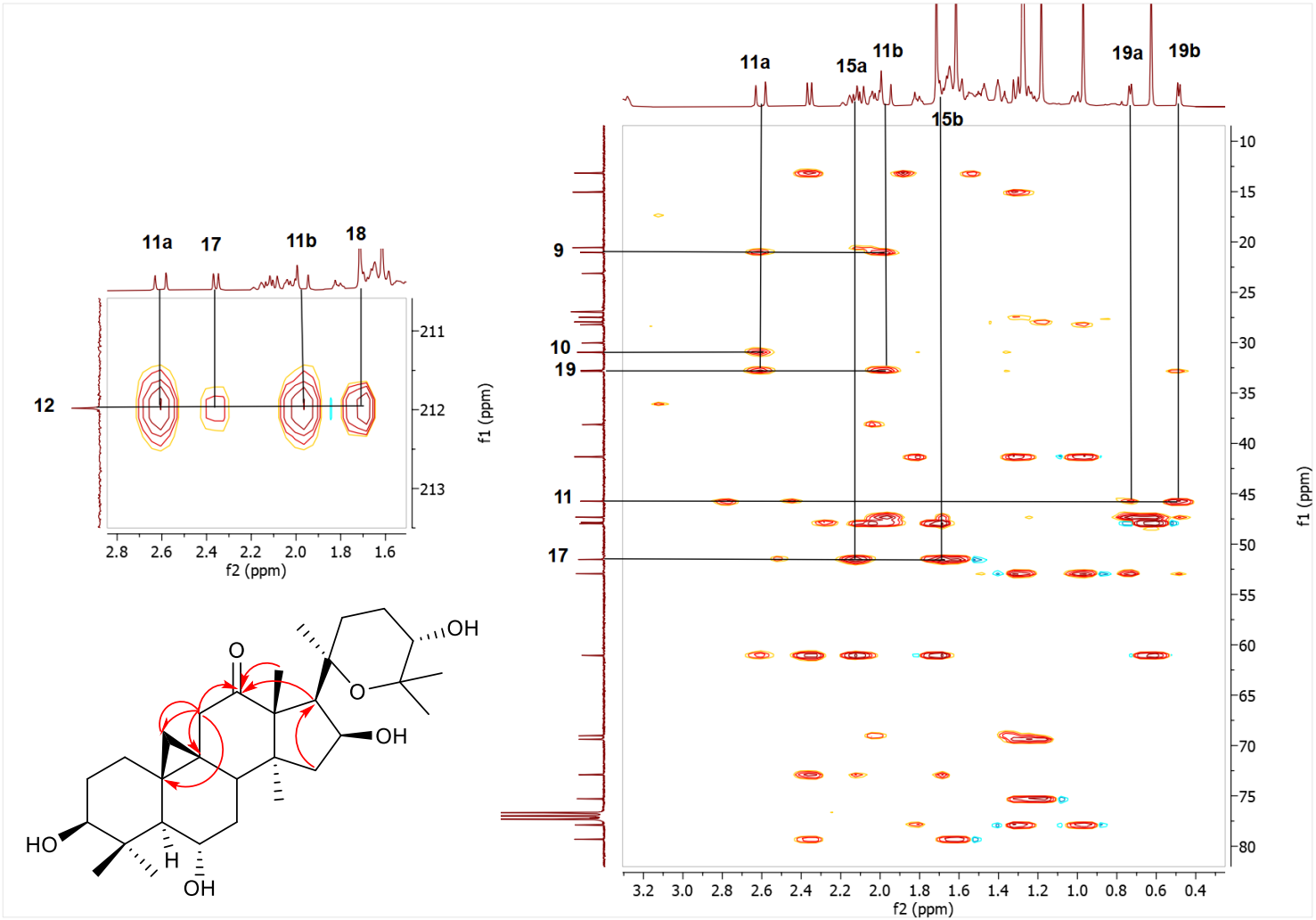

Spectrum 2.59. HMBC spectrum of compound **9**.

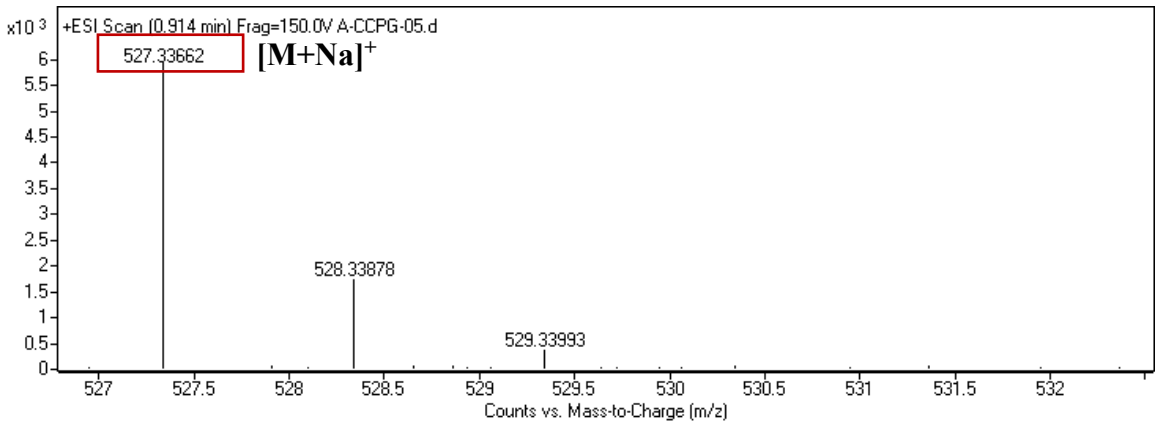

Spectrum 2.60. HR-ESI-MS spectrum of compound **9**.

2.3.2.10. Structure Elucidation of Compound 10

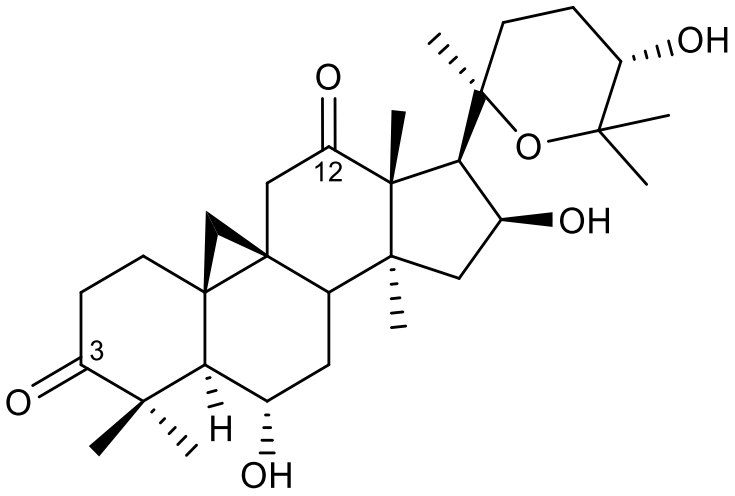

Figure 2.17. Chemical structure of compound **10**.

The molecular formula of compound **10** was established as $C_{30}H_{46}O_6$ by HR-ESI-MS (*m/z* 525.31890 ($[M + Na]^+$). When the ^{13}C-NMR and HMBC spectra of **10** was examined, signals at δ_C 210-220 range suggested two keto carbonyl groups in the structure. The HMBC correlations from H_2-11 (δ_H 1.96 and 2.64) and H_3-18 (δ_H 1.73) to δ_C 211.3 confirmed the location of the first ketone group to be at C-12. Moreover, the low-field signal of H-3 in **10**

was absent in the ^{1}H-NMR spectrum. The carbon signal δ_C 216.1 had long-range correlations with H_3-28 and H_3-29, readily assigned to C-3 in the HMBC spectrum of **10**. Thus, the structure of **10** was deduced as 20,25-epoxy-6α,16β,24α-trihydroxycycloartan-3,12-dione.

Table 2.10. The ^{13}C and ^{1}H NMR data of **10** (100/400 MHz, δ ppm, in $CDCl_3$).

Position	δ_C (ppm)	δ_H (ppm), *J* (Hz)
1	32.3	1.24 m, 2.08 m
2	35.6	2.49 m, 2.60 m
3	216.1	-
4	50.0	-
5	53.0	1.87 d (9.9)
6	69.2	3.58 t (10.3)
7	37.7	1.32 m, 1.50 m
8	47.5	2.04 m
9	21.5	-
10	29.9	-
11	45.4	1.96 d (19.8), 2.64 d (19.9)
12	211.3	-
13	61.1	-
14	47.8	-
15	47.9	1.68 m, 2.12 m
16	72.9	4.56 q (7.6)
17	51.6	2.37 d (8.7)
18	13.1	1.73 s
19	32.0	0.55 d (4.7), 0.89 d (4.8)
20	79.3	-
21	27.0	1.62 s
22	26.9	1.41 m, 2.03 m
23	23.1	1.70 m, 2.17 m
24	69.4	3.50 brs
25	75.3	-
26	27.9	1.27 s
27	27.5	1.18 s
28	27.6	1.36 s
29	20.4	1.22 s
30	20.7	0.65 s

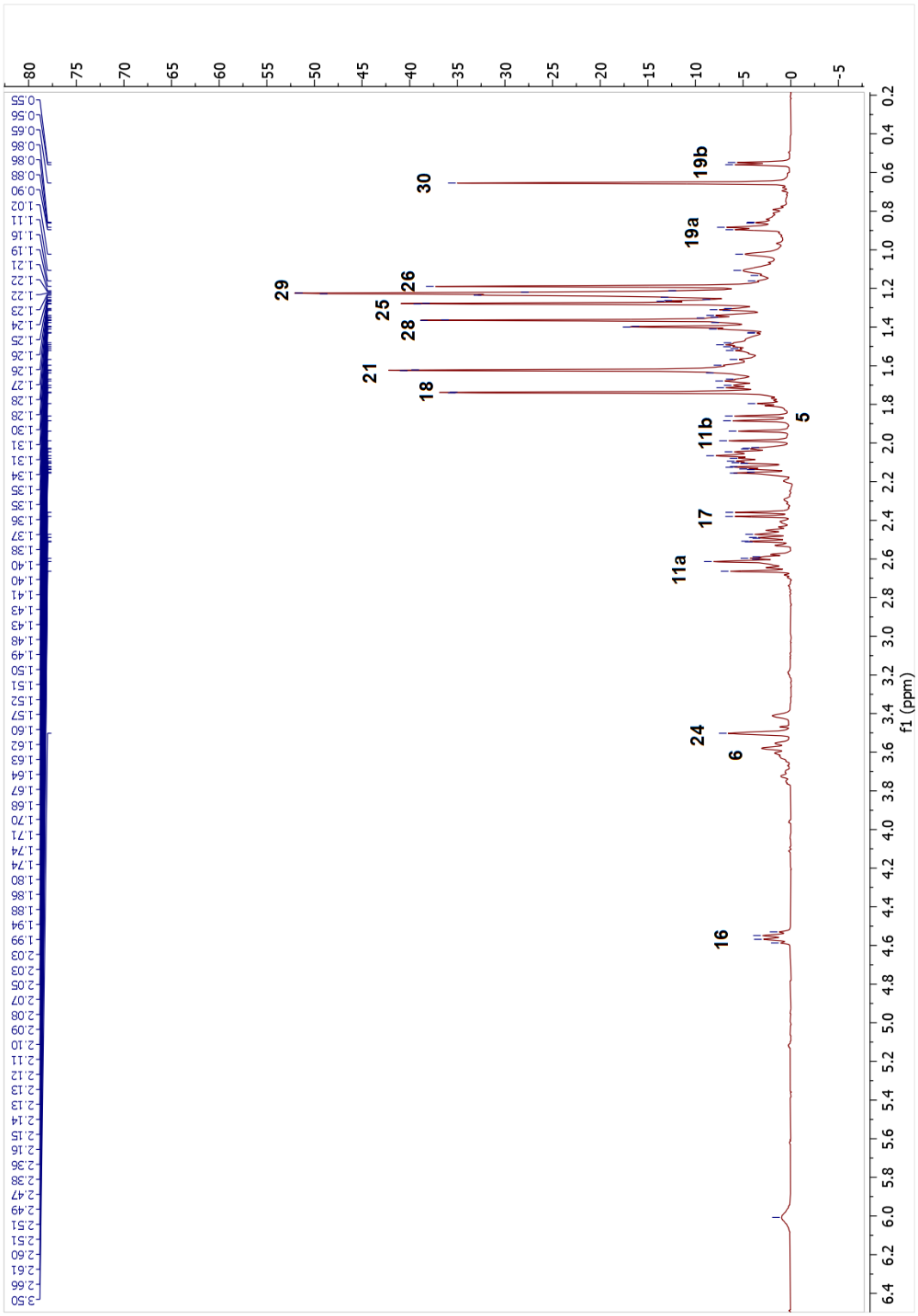

Spectrum 2.61. ^{1}H-NMR spectrum of compound **10**.

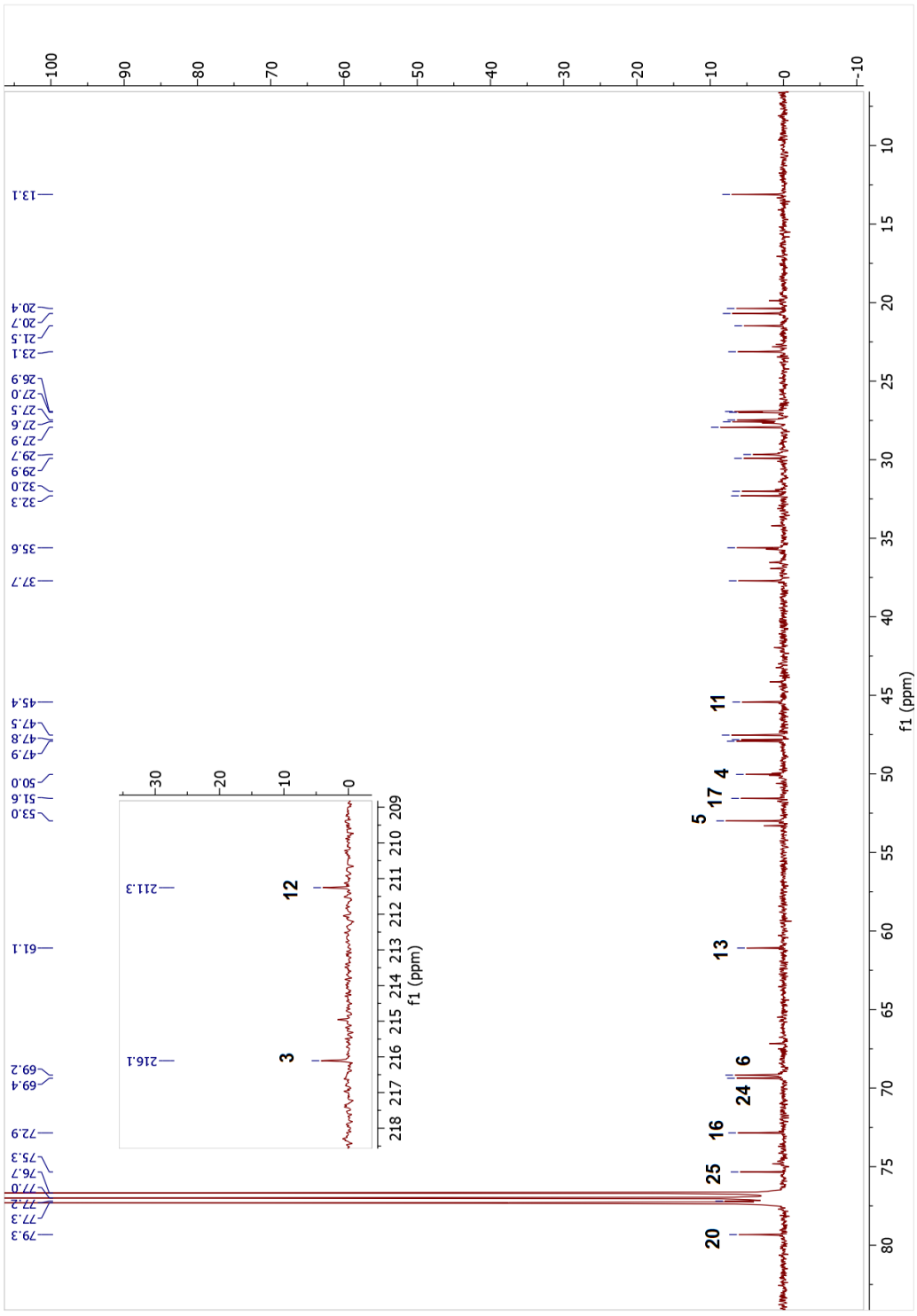

Spectrum 2.62. ^{13}C-NMR spectrum of compound **10**.

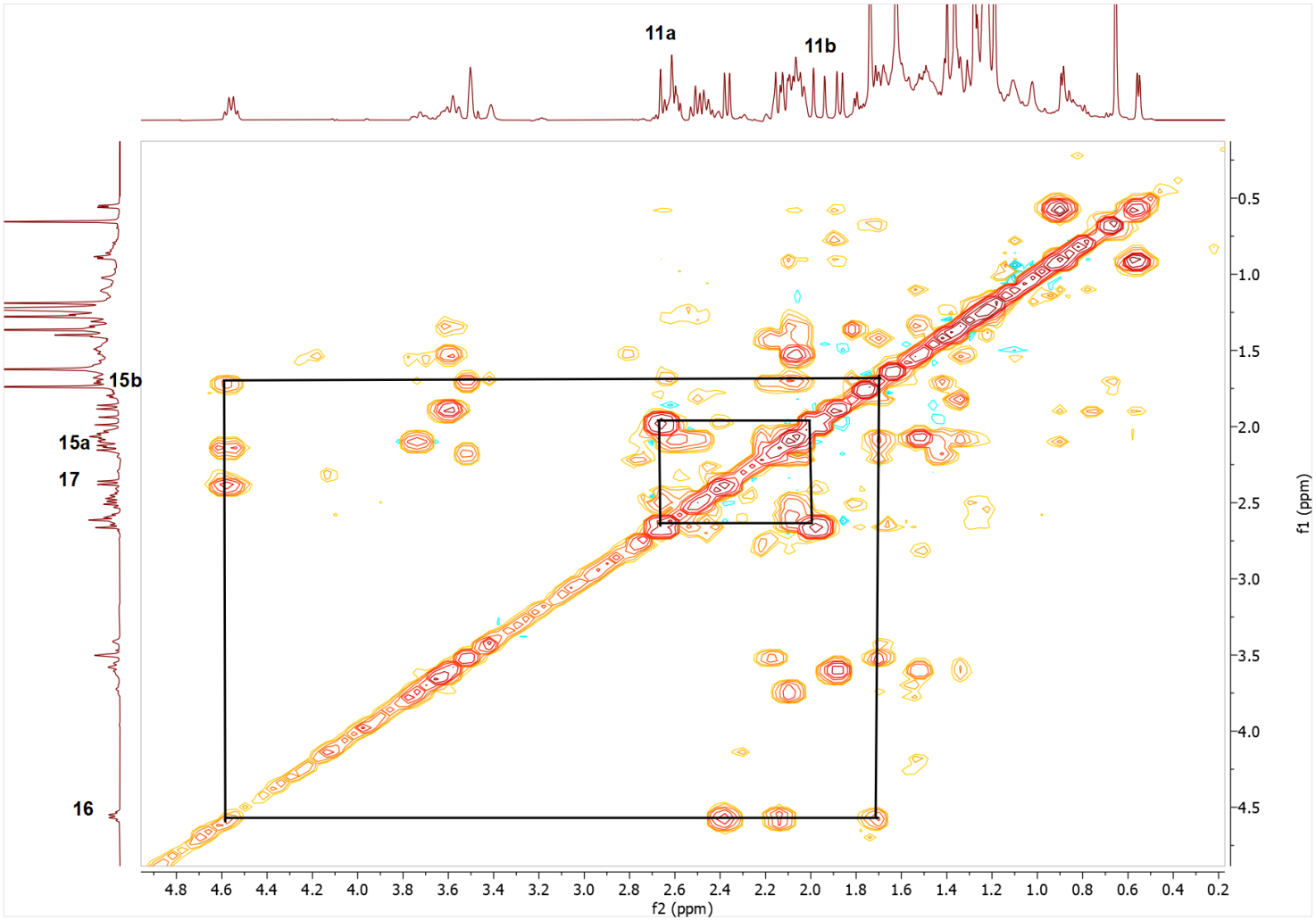

Spectrum 2.63. COSY spectrum of compound **10**.

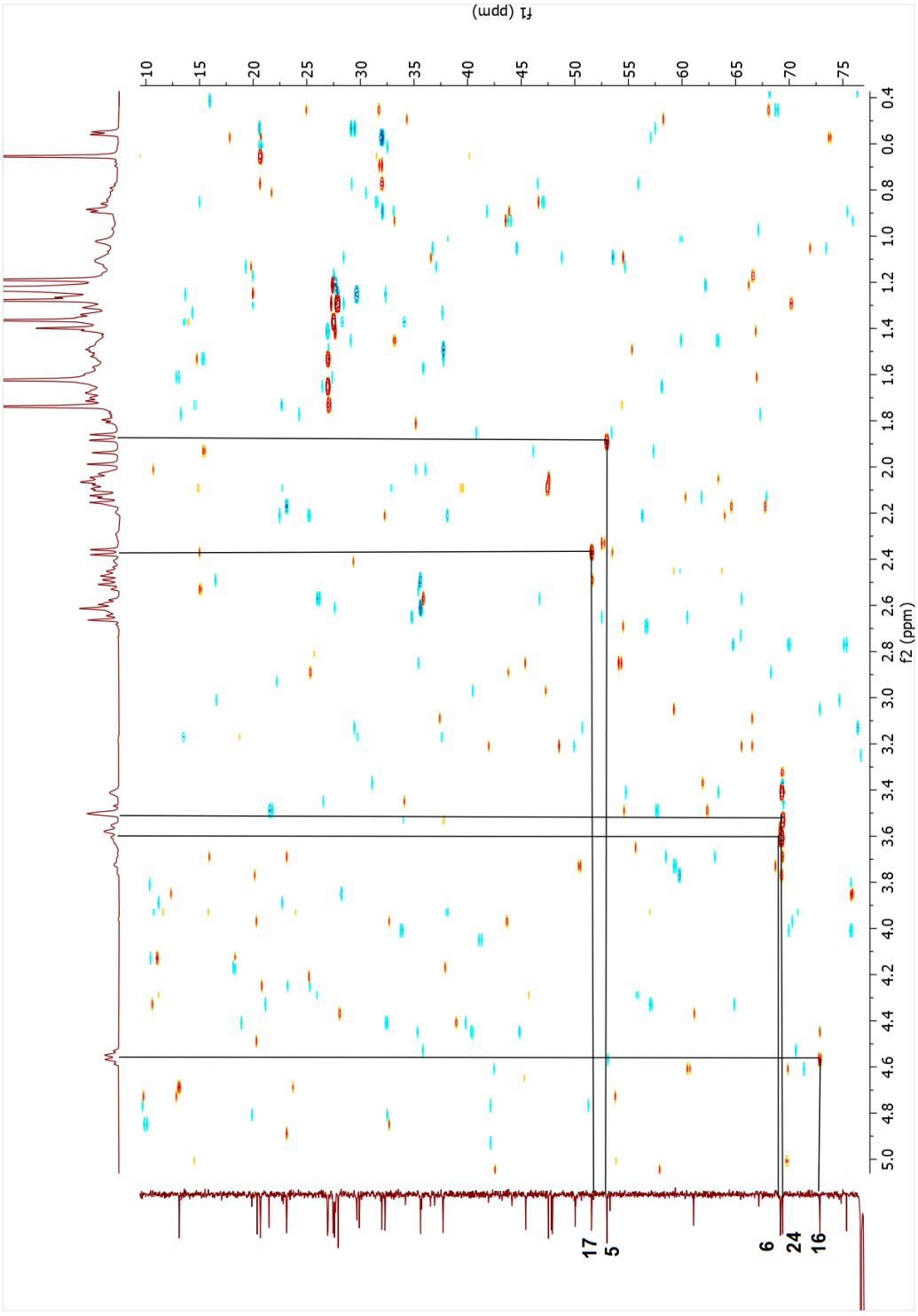

Spectrum 2.64. HSQC spectrum of compound **10**.

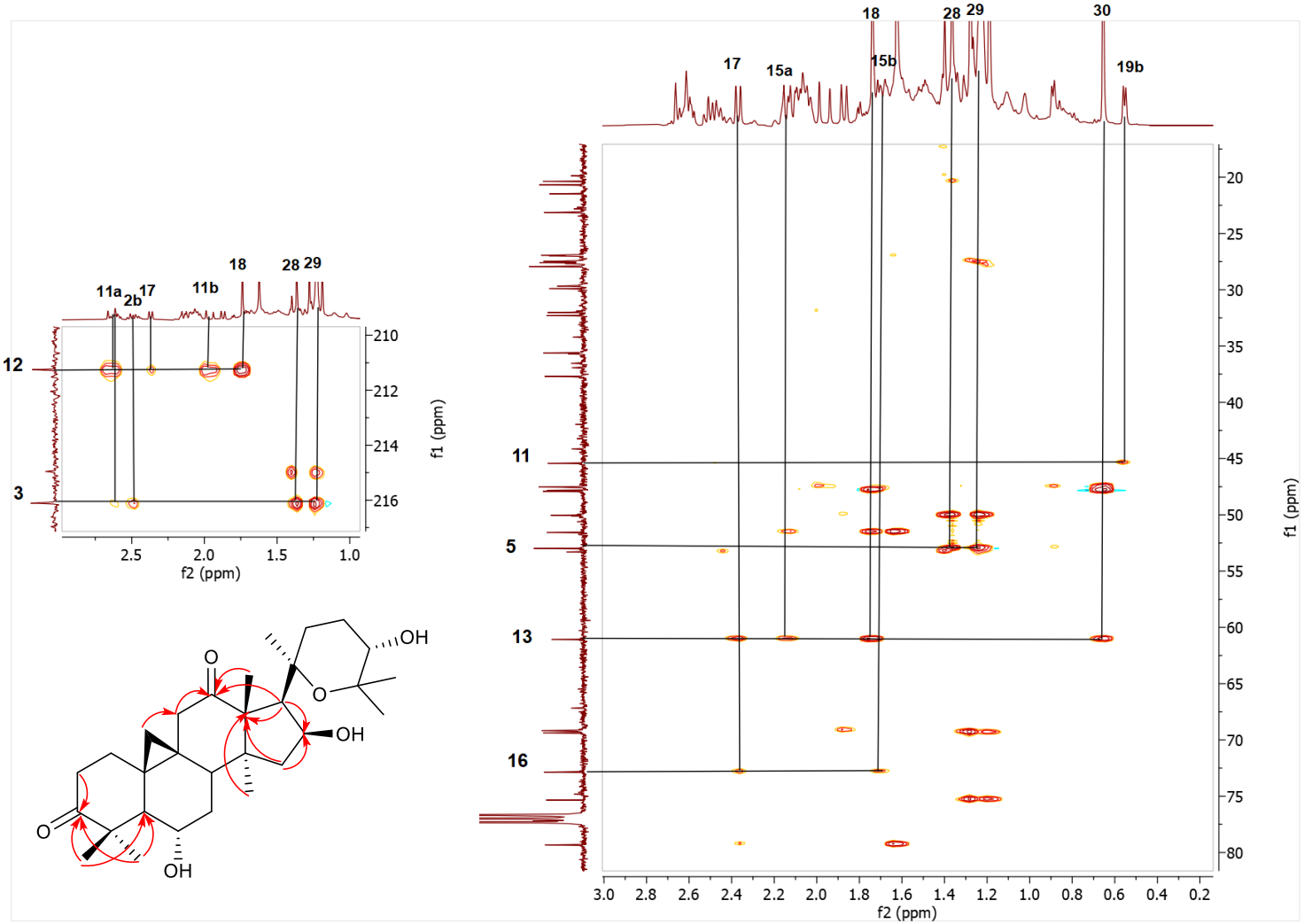

Spectrum 2.65. HMBC spectrum of compound **10**.

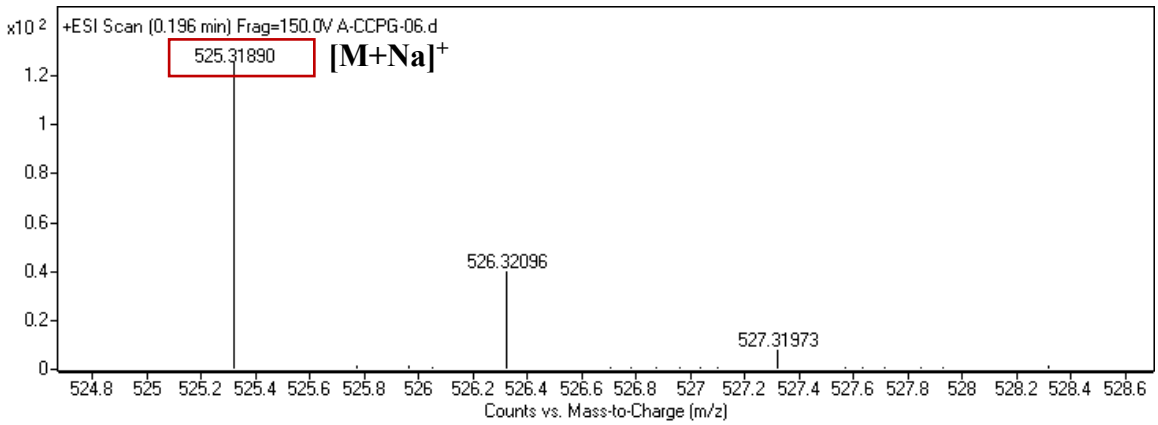

Spectrum 2.66. HR-ESI-MS spectrum of compound **10**.

2.3.2.11. Structure Elucidation of Compound 11

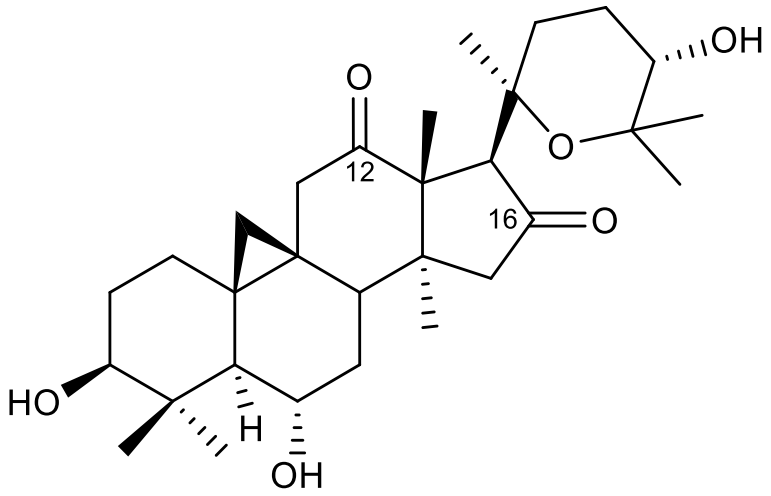

Figure 2.18. Chemical structure of compound **11**.

The molecular formula of compound **11** was established as $C_{30}H_{46}O_6$ by HR-ESI-MS (*m/z* 525.32125 ($[M + Na]^+$). When the ^{13}C-NMR and HMBC spectra of **11** were examined, signals at δ_C 210-220 range suggested two keto carbonyl groups in the structure, as in **10**. The HMBC correlations from H_2-11 (δ_H 2.09 and 2.83) and H_3-18 (δ_H 2.06) to δ_C 210.2 for **11** confirmed the location of the first ketone group to be at C-12. Moreover, the low-field

signal of H-16 signal disappeared in in the ^{1}H-NMR spectrum. The HMBC correlations of H-17 (δ_H 3.08) and H_2-15 (δ_H 2.18 and 2.52) with the carbonyl carbon at δ_C 214.4 confirmed the oxidation at C-16 to establish the structure of **11**. Thus, the structure of **11** was established as 20,25-epoxy-3β,6α,24α-trihydroxycycloartan-12,16-dione.

Table 2.11. The ^{13}C and ^{1}H NMR data of **11** (100/400 MHz, δ ppm, in C_5D_5N).

Position	δ_C (ppm)	δ_H (ppm), *J* (Hz)
1	33.0	0.99 d (13.5), 1.58 m
2	30.9	1.87 – 2.02 (2H)
3	77.6	3.60 td (12.6, 1.8)
4	42.1	-
5	53.1	1.64 d (10.0)
6	68.1	3.83 t (11.0)
7	39.0	1.56 m, 1.70 d (11.5)
8	46.2	2.12 m
9	20.5	-
10	31.3	-
11	45.4	2.09 m, 2.83 d (20.1)
12	210.2	-
13	60.3	-
14	43.7	-
15	51.0	2.18 d (18.1), 2.52 d (16.2)
16	214.4	-
17	60.1	3.08 s
18	12.7	2.06 s
19	32.2	0.40 d (4.9), 0.76 d (4.5)
20	75.8	-
21	27.6	1.88 s
22	27.2	1.58 m, 2.47 m
23	23.5	1.83 m, 2.22 m
24	68.5	3.63 brs
25	74.7	-
26	28.1	1.43 s
27	28.0	1.26 s
28	29.3	1.92 s
29	15.7	1.37 s
30	19.5	0.76 s

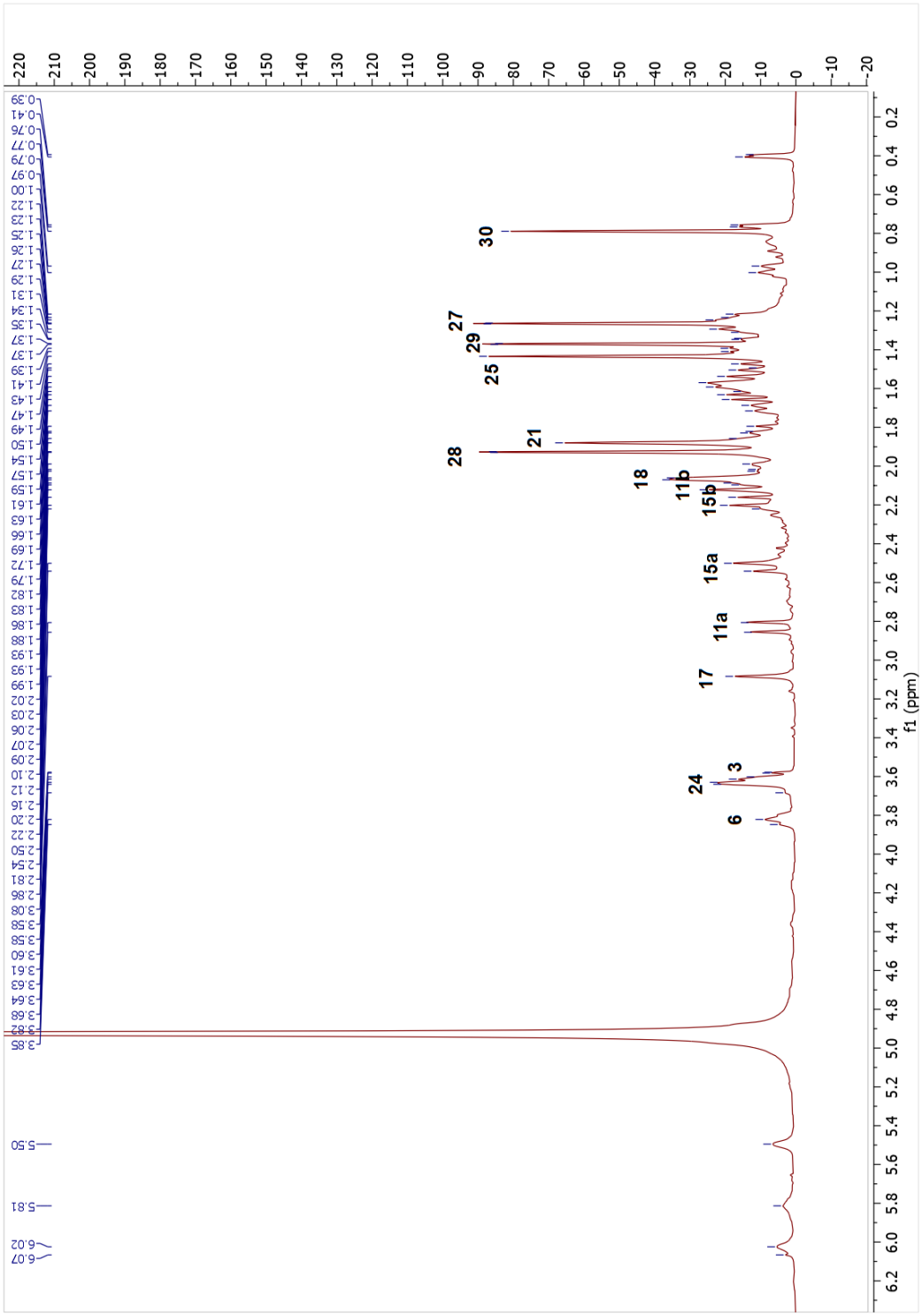

Spectrum 2.67. ^{1}H-NMR spectrum of compound **11**.

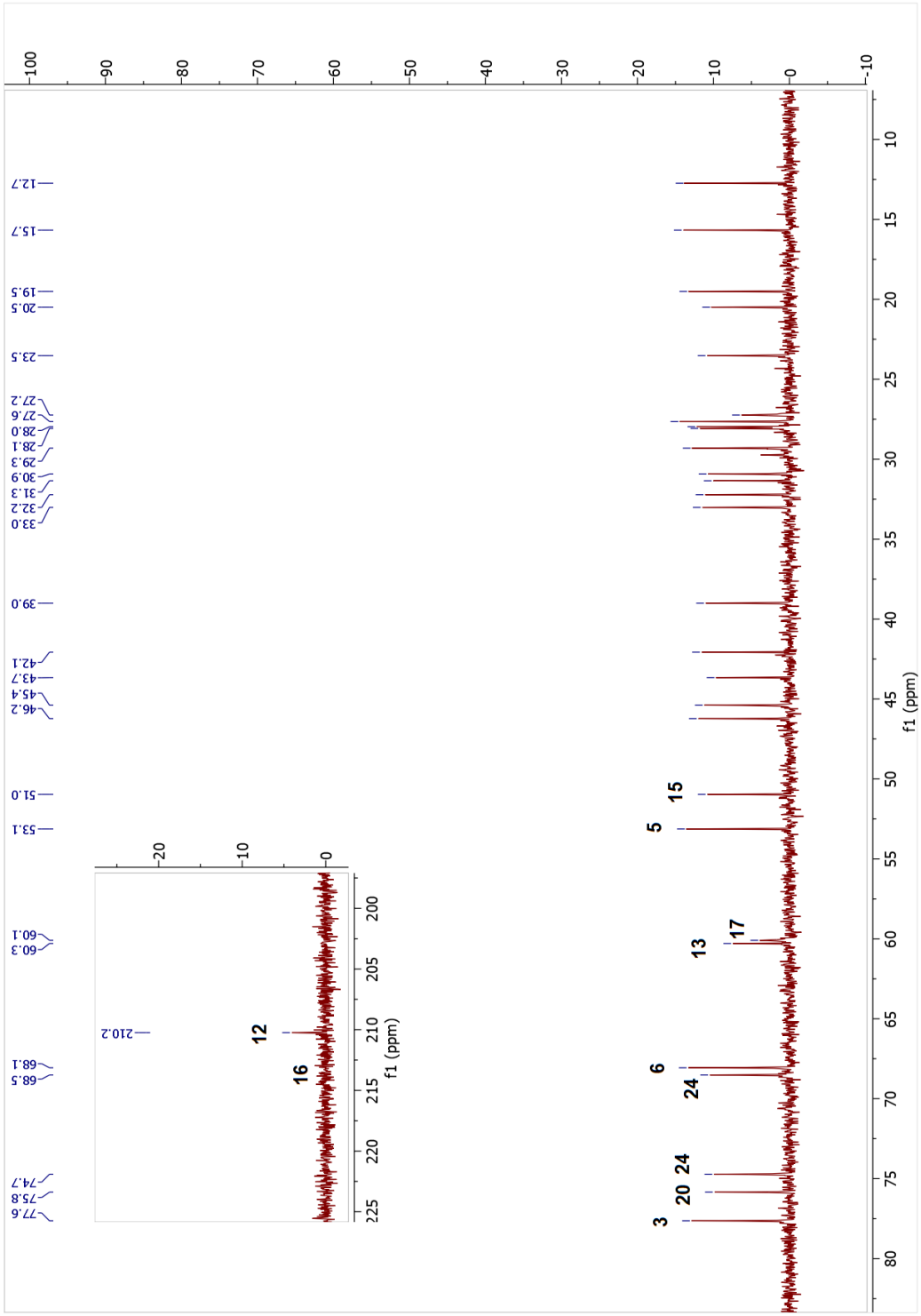

Spectrum 2.68. ^{13}C-NMR spectrum of compound **11**.

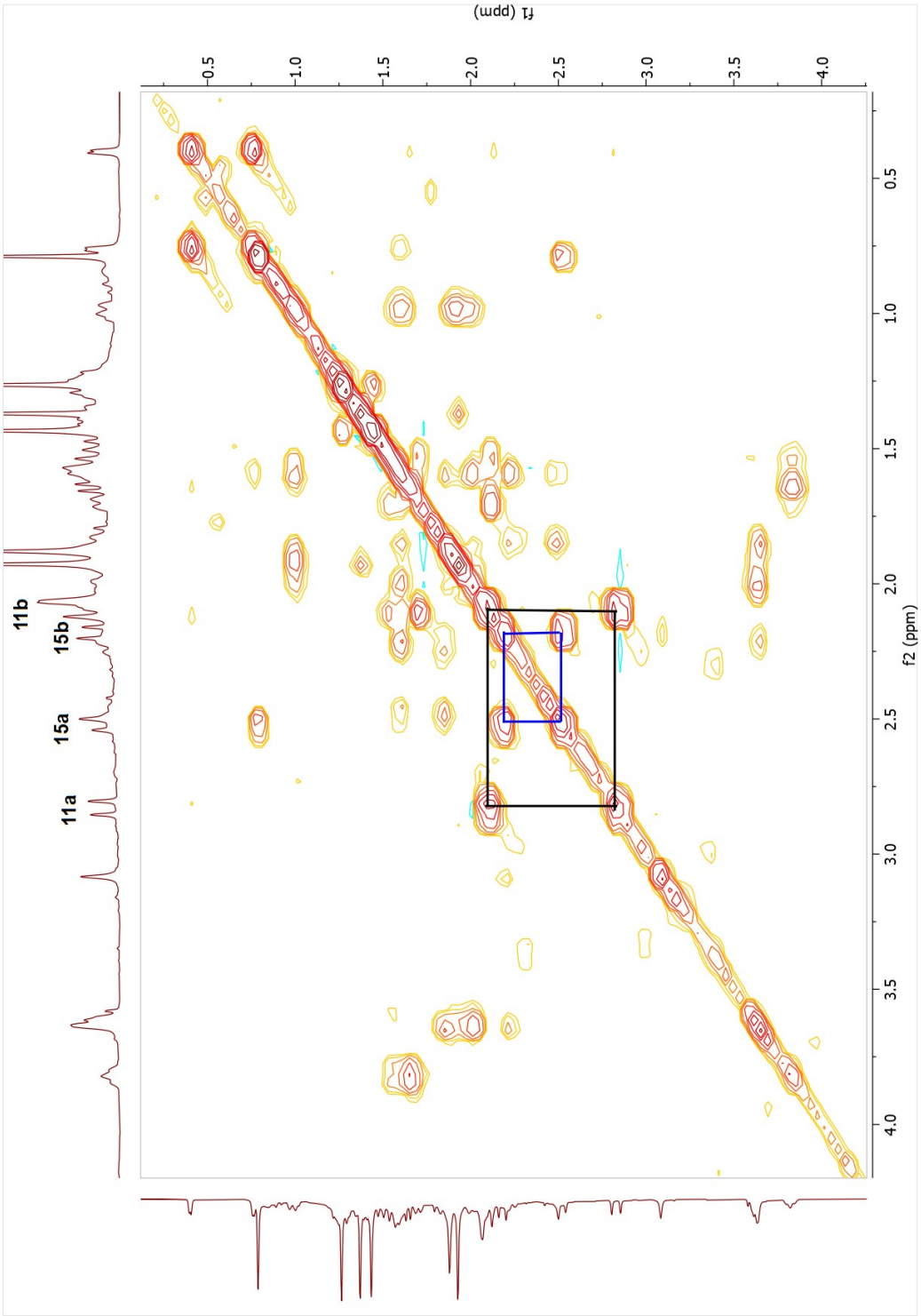

Spectrum 2.69. COSY spectrum of compound **11**.

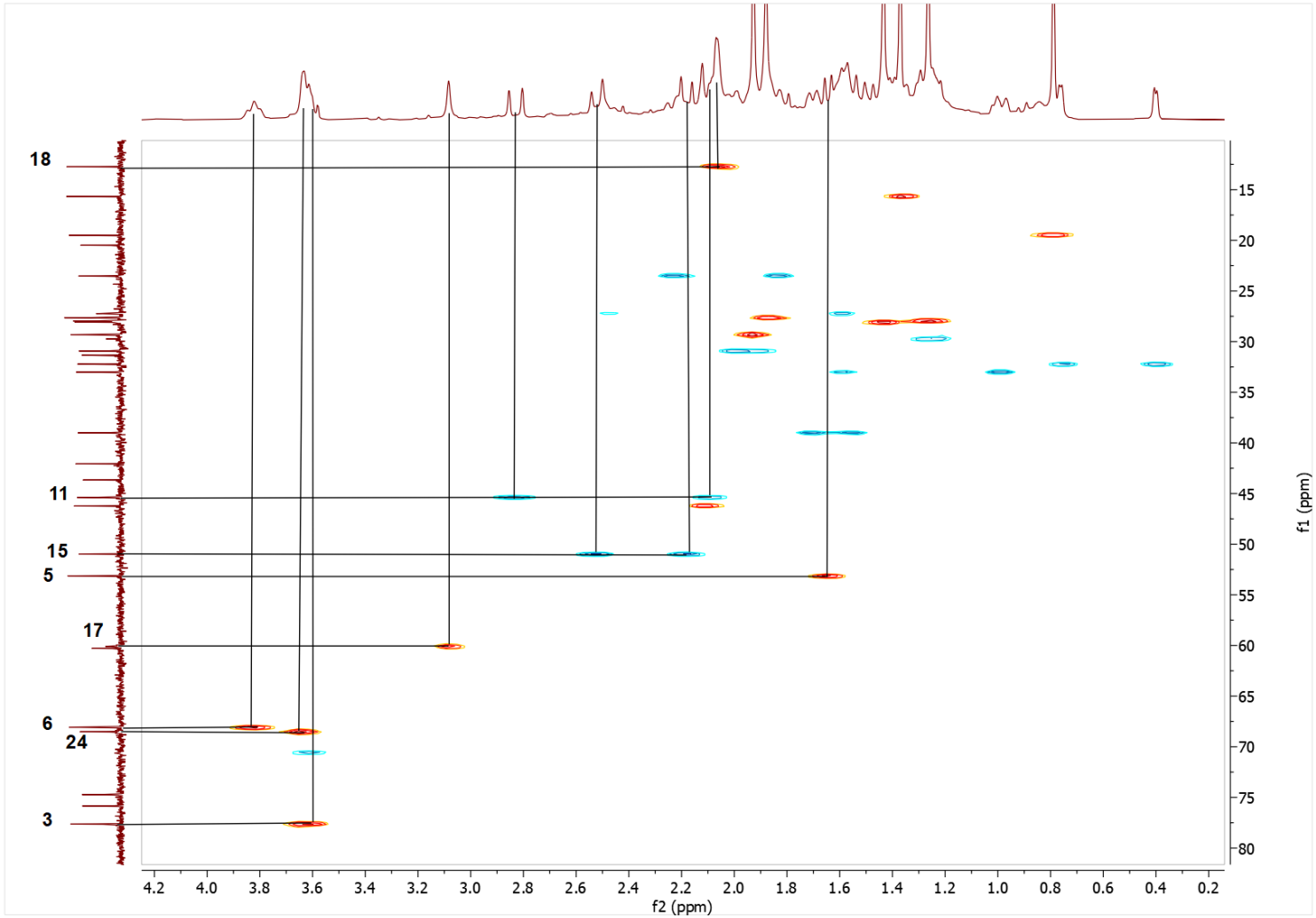

Spectrum 2.70. HSQC spectrum of compound **11**.

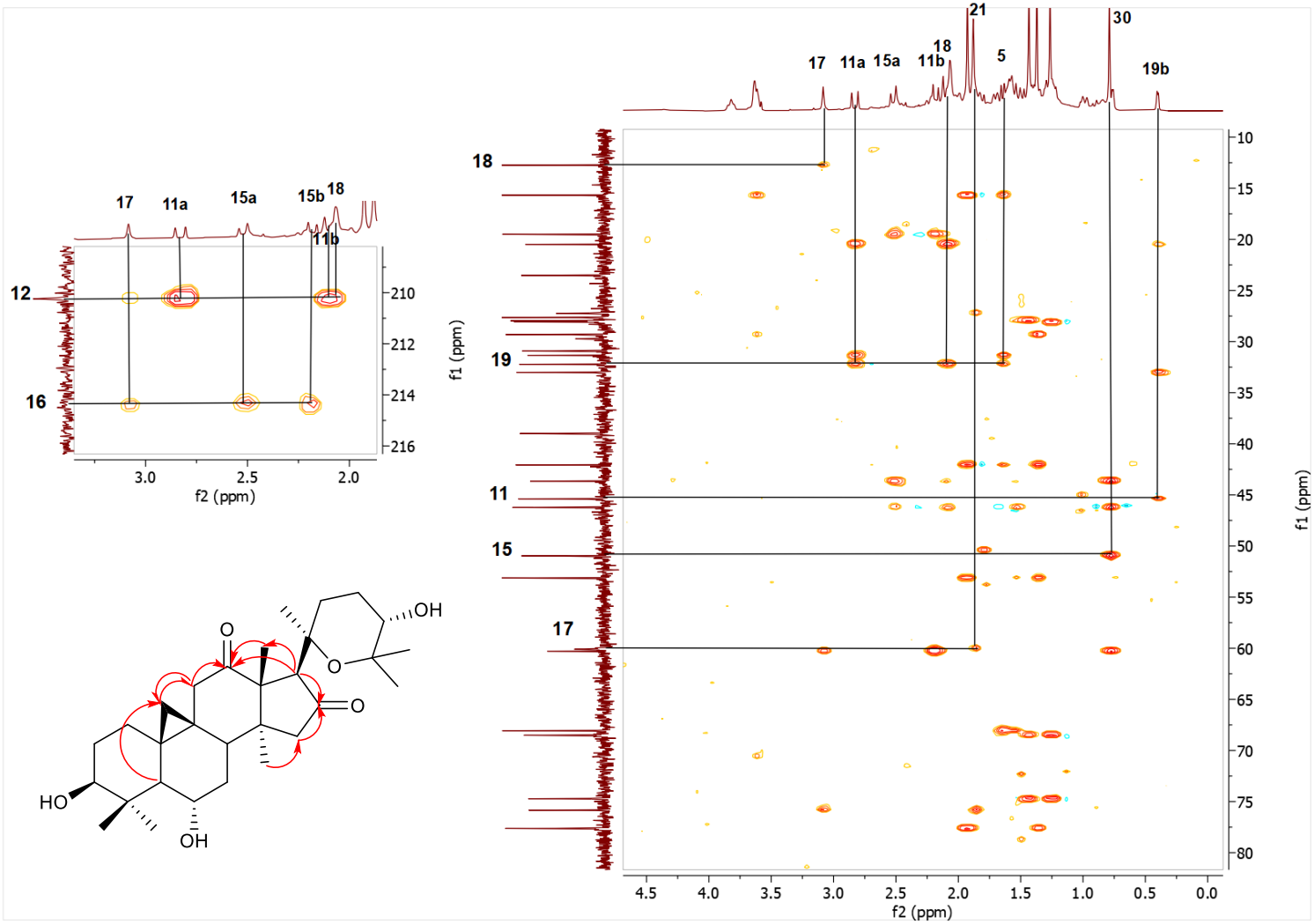

Spectrum 2.71. HMBC spectrum of compound **11**.

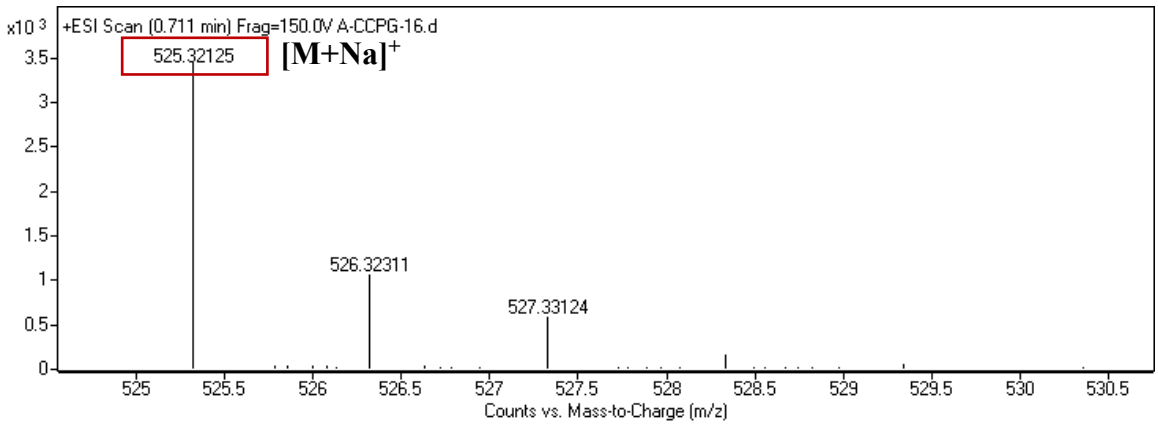

Spectrum 2.72. HR-ESI-MS spectrum of compound **11**.

2.3.2.12. Structure Elucidation of Compound 12

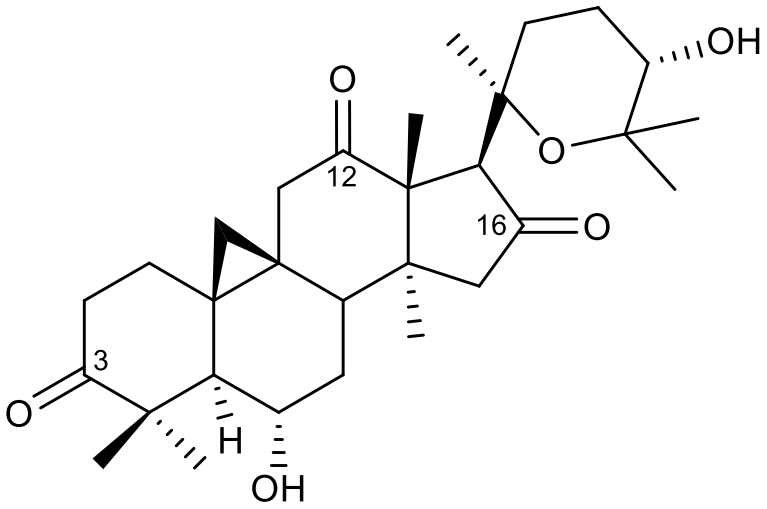

Figure 2.19. Chemical structure of compound **12**.

The metabolite **12** gave a molecular formula of $C_{30}H_{44}O_6$ based on the HR-ESI-MS data (*m/z* 523.30530 ($[M + Na]^+$, calcd for $C_{30}H_{44}NaO_6$, 523.30356) with nine indices of hydrogen deficiency. The absence of low-field oxymethine signals due to H-3 and H-16 in the ^{1}H-NMR spectrum, together with the observation of two keto carbonyl carbons in the ^{13}C-NMR and HMBC spectra, suggested that C-3 (δ_C 215.7) and C-16 (δ_C 214.1) secondary

alcohols had been oxidized, as in **5**. Also, the signal at δ_C 209.6 suggested an additional keto carbonyl group in structure, which showed cross-peaks with H_2-11 (δ_H 2.05 and 2.83), H-17 (δ_H 3.07) and H-18 (δ_H 2.06) in the HMBC spectrum, revealing the oxidation at C-12. Based on these results, the structure of **12** was elucidated as 20,25-epoxy-6α,24α-dihydroxycycloartan-3,12,16-trione.

Table 2.12. The ^{13}C and ^{1}H NMR data of **12** (100/400 MHz, δ ppm, in C_5D_5N).

Position	δ_C (ppm)	δ_H (ppm), *J* (Hz)
1	31.9	1.16 m, 1.97 m
2	35.7	2.49 m, 2.66 ddd (13.5, 7.9, 5.1)
3	215.7	-
4	50.2	-
5	52.7	2.14 d (9.8)
6	68.1	3.75 t (10.2)
7	38.2	1.53 m, 1.67 m
8	46.2	2.09 m
9	20.9	-
10	29.9	-
11	44.9	2.05 d (20.0), 2.83 d (20.0)
12	209.6	-
13	60.3	-
14	43.5	-
15	50.9	2.19 d (16.6), 2.53 d (17.5)
16	214.1	-
17	60.1	3.07 s
18	12.7	2.06 s
19	31.2	0.45 d (4.5), 0.87 d (4.7)
20	75.9	-
21	27.6	1.88 s
22	27.2	1.59 m, 2.47 m
23	23.5	1.85 m, 2.24 m
24	68.5	3.61 brs
25	74.7	-
26	28.1	1.42 s
27	28.0	1.26 s
28	28.1	1.76 s
29	20.4	1.44 s
30	19.6	0.79 s

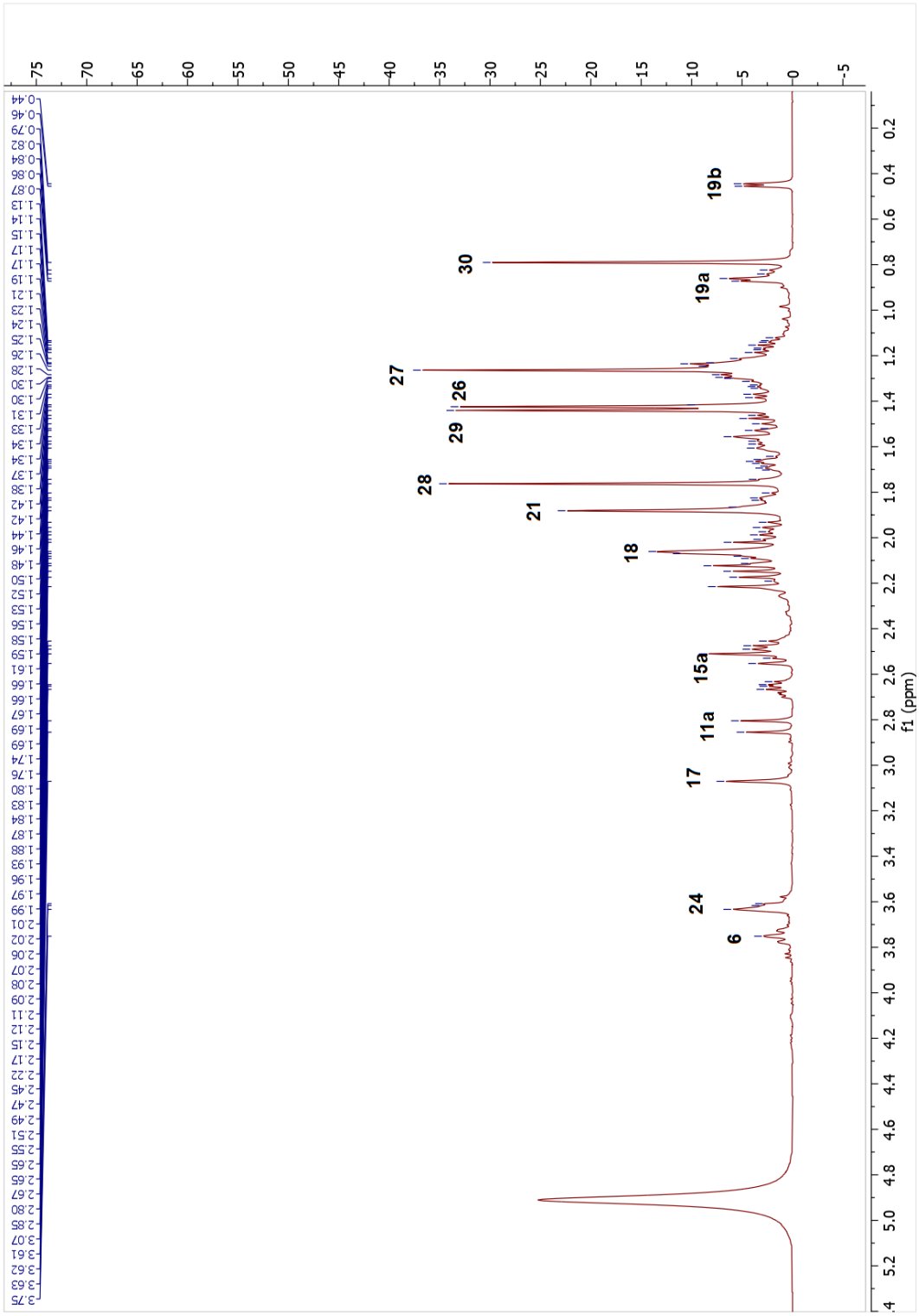

Spectrum 2.73. ^{1}H-NMR spectrum of compound **12**.

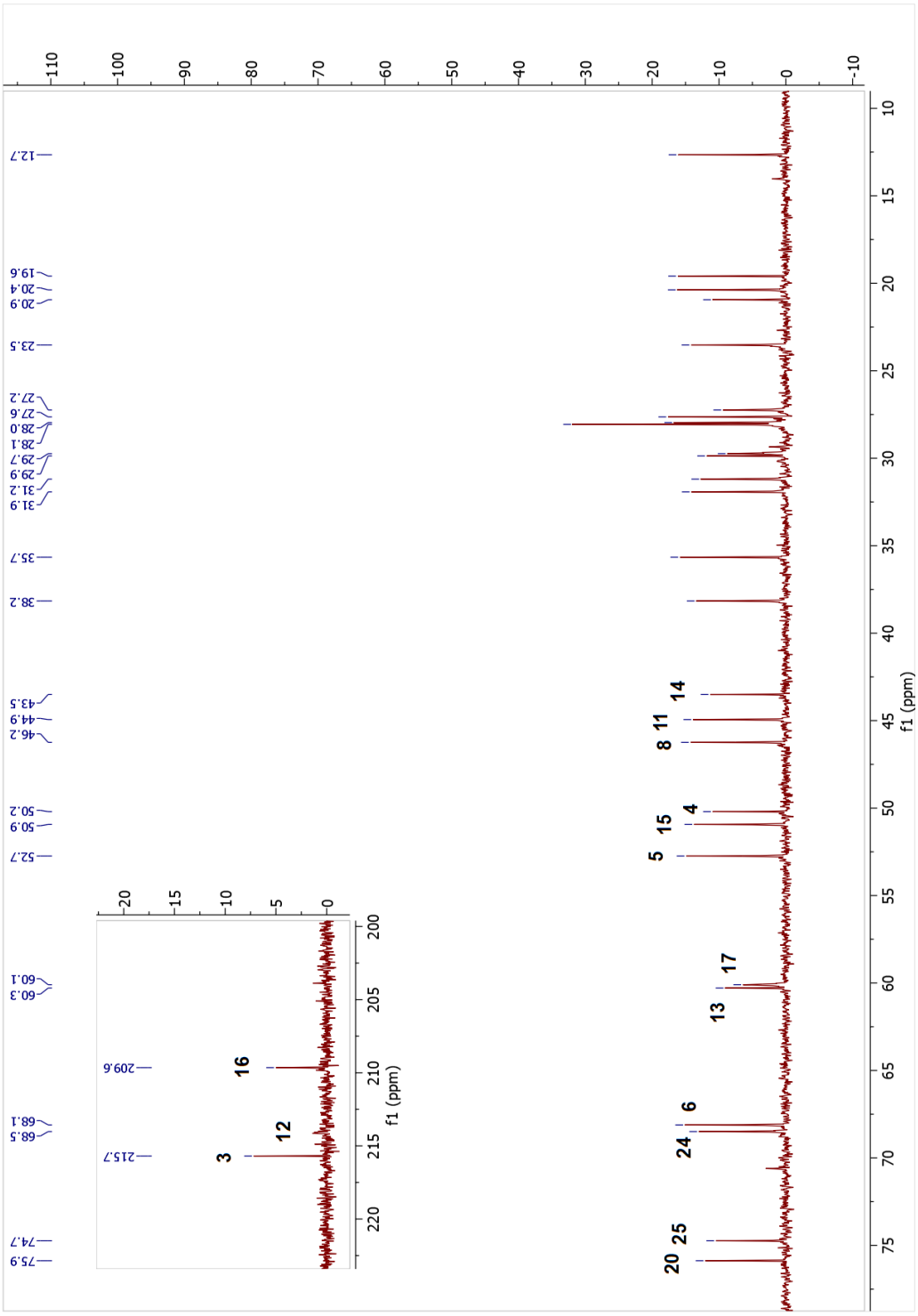

Spectrum 2.74. ^{13}C-NMR spectrum of compound **12**.

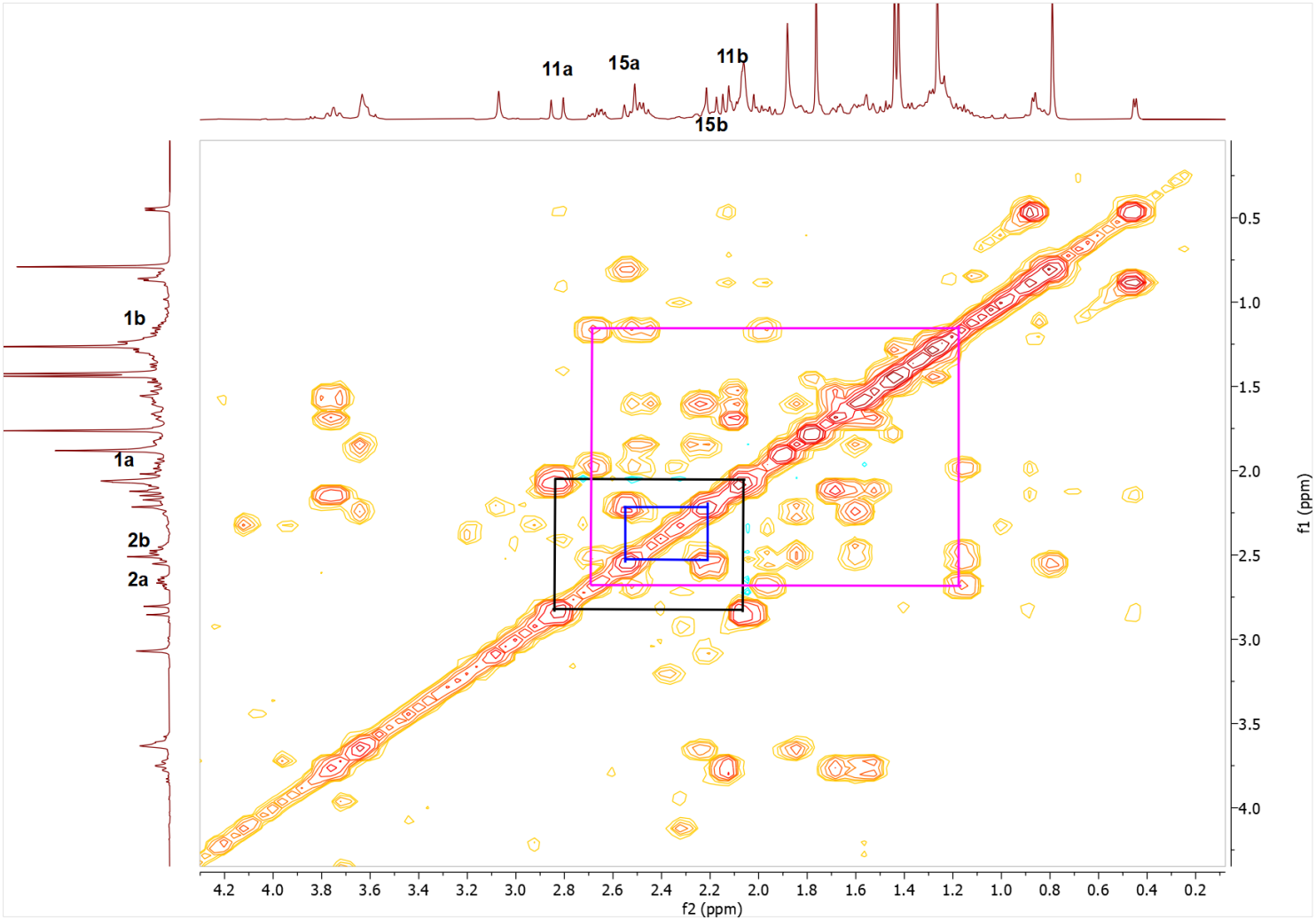

Spectrum 2.75. COSY spectrum of compound **12**.

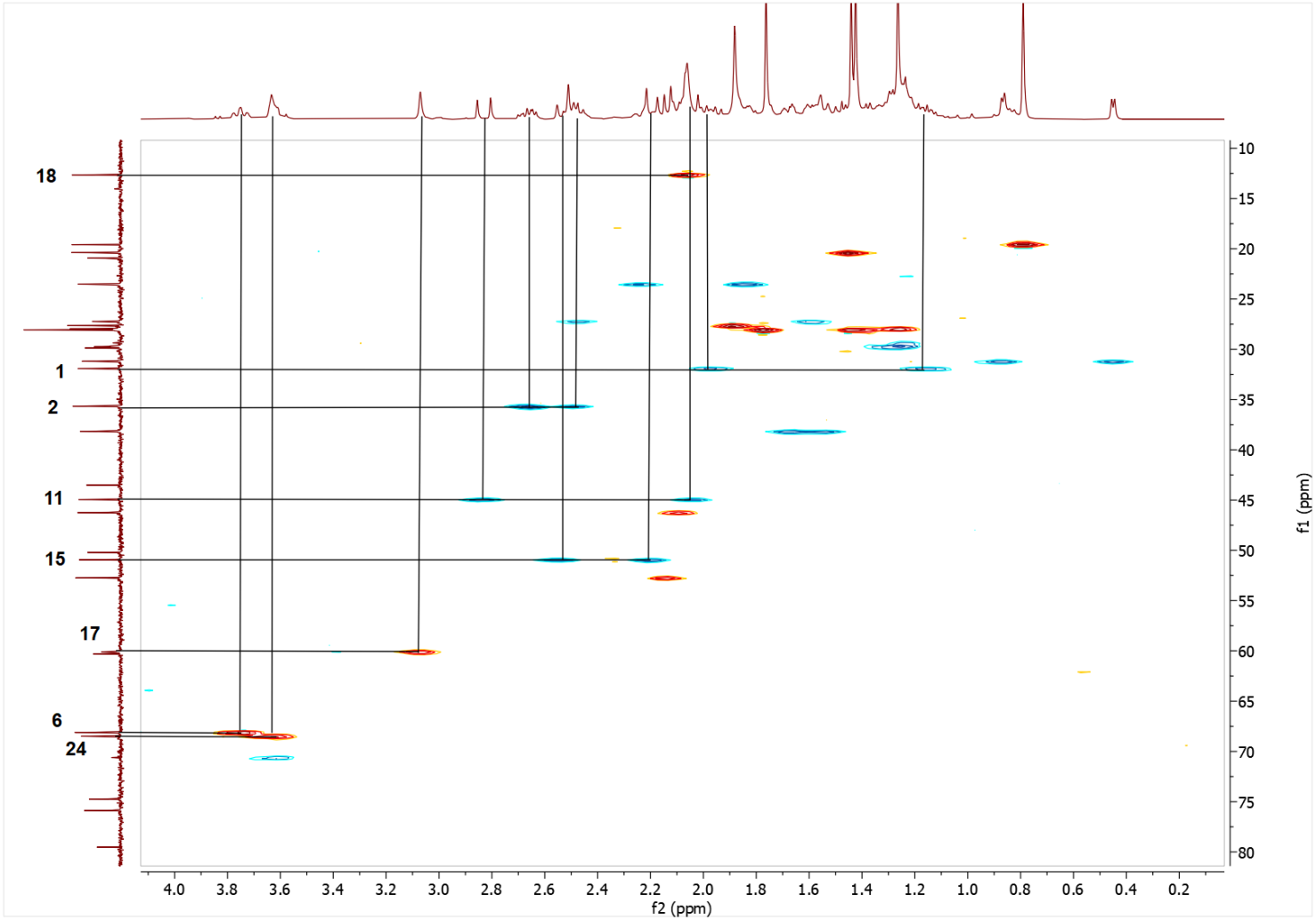

Spectrum 2.76. HSQC spectrum of compound **12**.

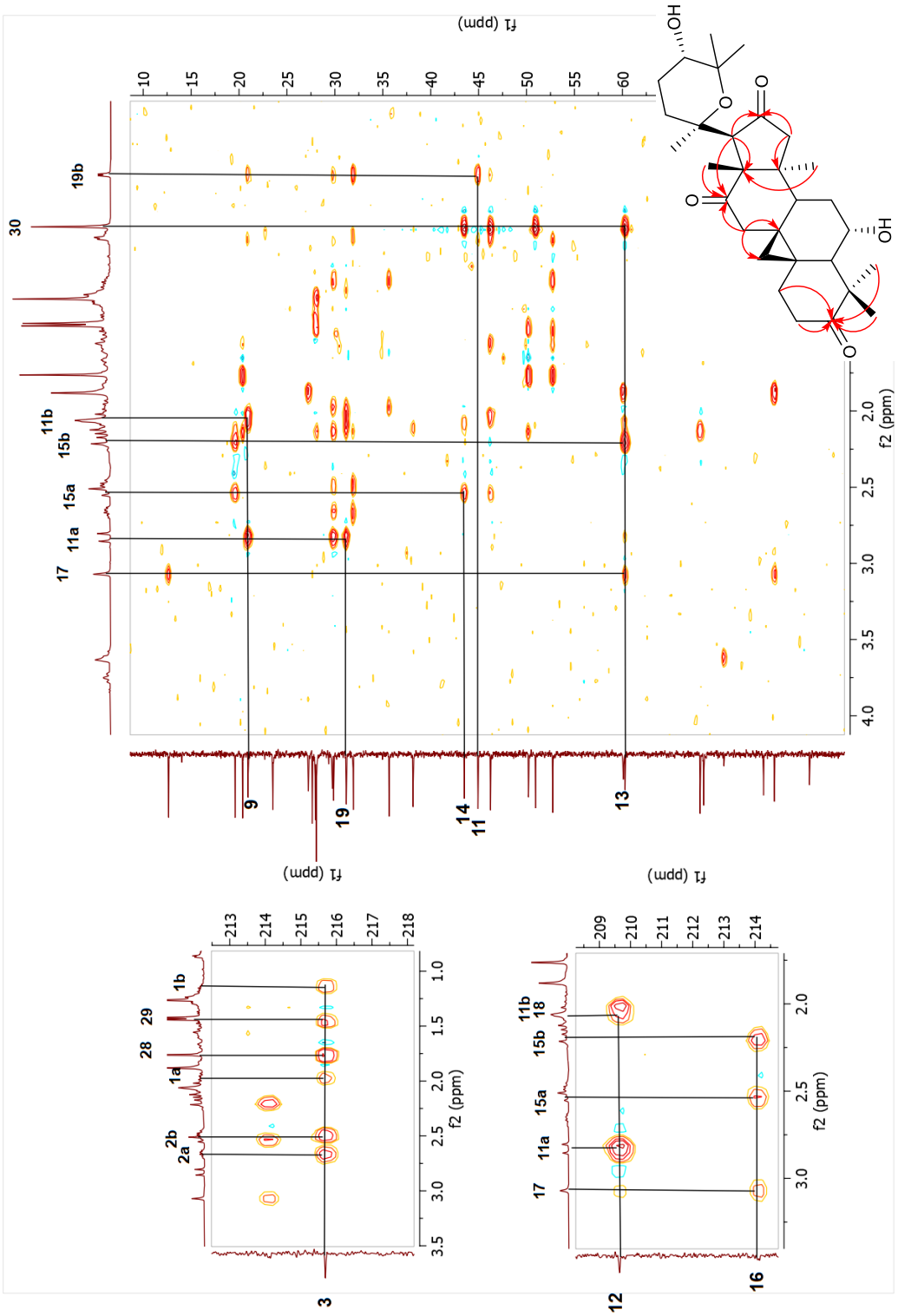

Spectrum 2.77. HMBC spectrum of compound **12**.

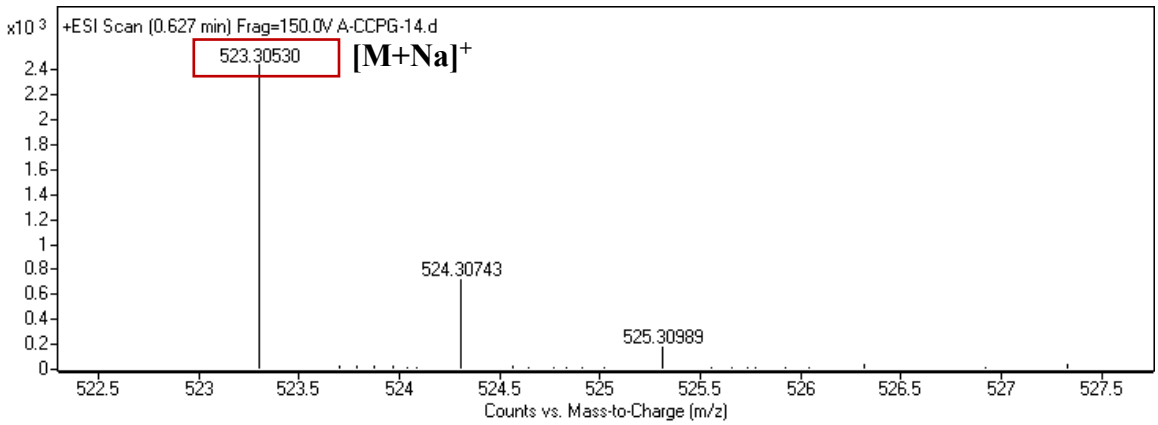

Spectrum 2.78. HR-ESI-MS spectrum of compound **12**.

2.3.2.13. Structure Elucidation of Compound 13

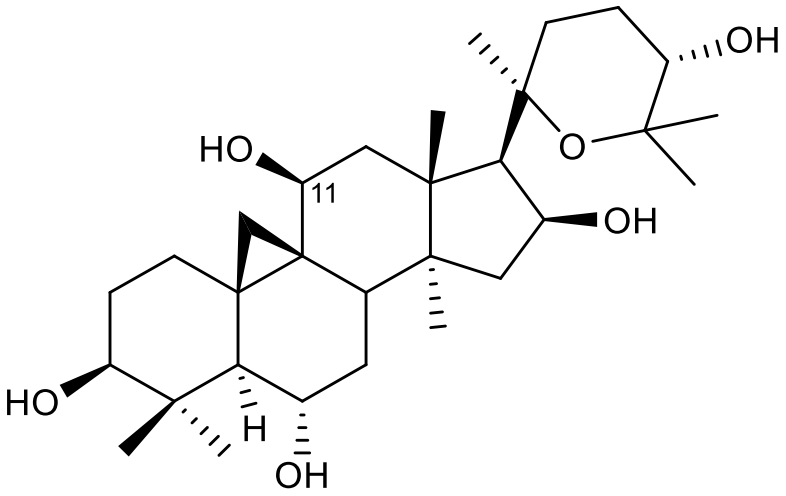

Figure 2.20. Chemical structure of compound **13**.

The molecular formula of metabolite **13** was determined as $C_{30}H_{50}O_6$ (*m/z* 529.35090 ([M + Na]$^+$, calcd for $C_{30}H_{50}NaO_6$, 529.35051). Apart from the characteristic low-field signals observed (H-3, H-6, H-16 and H-24), an additional oxymethine signal at δ_H 3.87 (dd, *J*= 8.7, 2.5 Hz) was observed, which correlated with a resonance at δ_C 65.4 in the HSQC spectrum. Furthermore, the ^{1}H-NMR spectrum of **13** revealed that one of the 9,19-

cyclopropane ring signals (δ_H 1.10, H-19a) had undergone a significant downfield shift when compared to that of **1**, indicating hydroxylation at the C-11 position[49,50,76]. The HMBC cross-peaks from H_2-12 (δ_H 1.86 and 2.31) and H_2-19 (δ_H 0.29 and 1.10) to δ_C 65.4 signal, and the down-field shifts of C-9 and C-12 signals (*ca*. 6.5 and 13.4 ppm, respectively) substantiated the assignment. The orientation of C-11(OH) was found to be β based on NOESY cross-peak between H-11 (δ_H 3.87) and α-oriented H_3-30 (δ_H 0.84). Thus, the structure of **13** was established as 20,25-epoxy-3β,6α,11β,16β,24α-pentahydroxycycloartane.

Table 2.13. The ^{13}C and ^{1}H NMR data of **13** (100/400 MHz, δ ppm, in CD_3OD and a drop of C_5D_5N).

Position	δ_C (ppm)	δ_H (ppm), *J* (Hz)	Position	δ_C (ppm)	δ_H (ppm), *J* (Hz)
1	29.7	1.32 m, 1.82 dt (12.7, 3.5)	**16**	74.2	4.59 td (7.7, 5.3)
2	30.2	1.58 dd (12.3, 3.8), 1.68 m	**17**	60.3	1.94 d (7.7)
3	78.5	3.22 dd (11.6, 4.6)	**18**	20.1	1.44 s
4	41.9	-	**19**	21.6	0.29 d (4.7), 1.10 d (4.7)
5	53.8	1.36 d (9.4)	**20**	79.5	-
6	67.7	3.54 td (9.5, 3.9)	**21**	27.8	1.47 s
7	37.6	1.36 m, 1.48 m	**22**	26.3	1.15 m, 2.63 dt (13.5, 6.9)
8	45.7	2.05 m	**23**	23.1	1.67 m, 2.14 t (13.5)
9	27.6	-	**24**	68.9	3.45 brs
10	29.9	-	**25**	75.6	-
11	65.4	3.87 dd (8.7, 2.5)	**26**	27.6	1.17 s
12	47.4	1.86 m, 2.31 dd (14.3, 8.6)	**27**	27.5	1.23 s
13	46.8†	-	**28**	27.9	1.26 s
14	46.1	-	**29**	15.1	0.96 s
15	46.8†	1.49 m, 1.93 m	**30**	20.5	0.84 s

†Overlapped signals

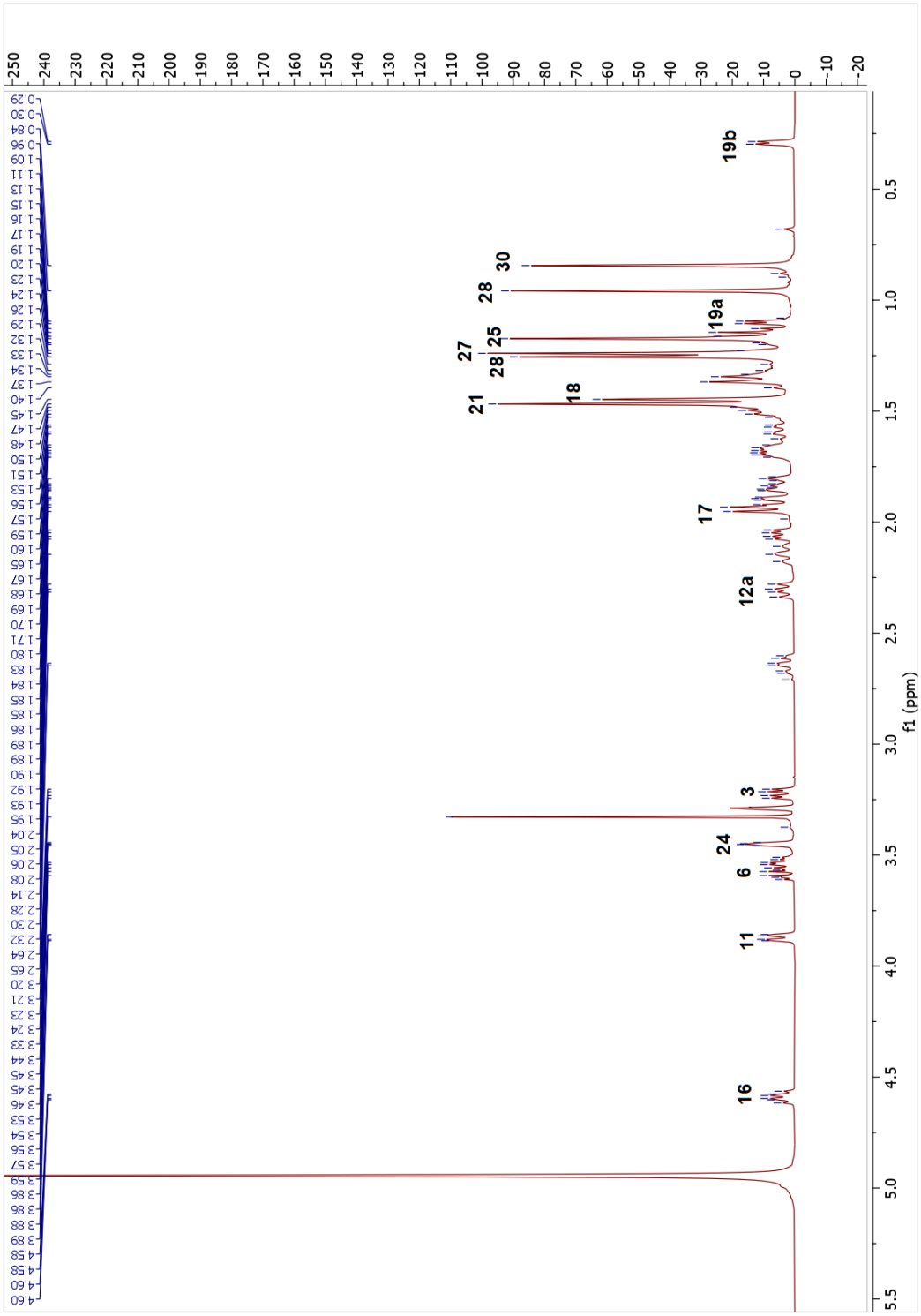

Spectrum 2.79. ^{1}H-NMR spectrum of compound **13**.

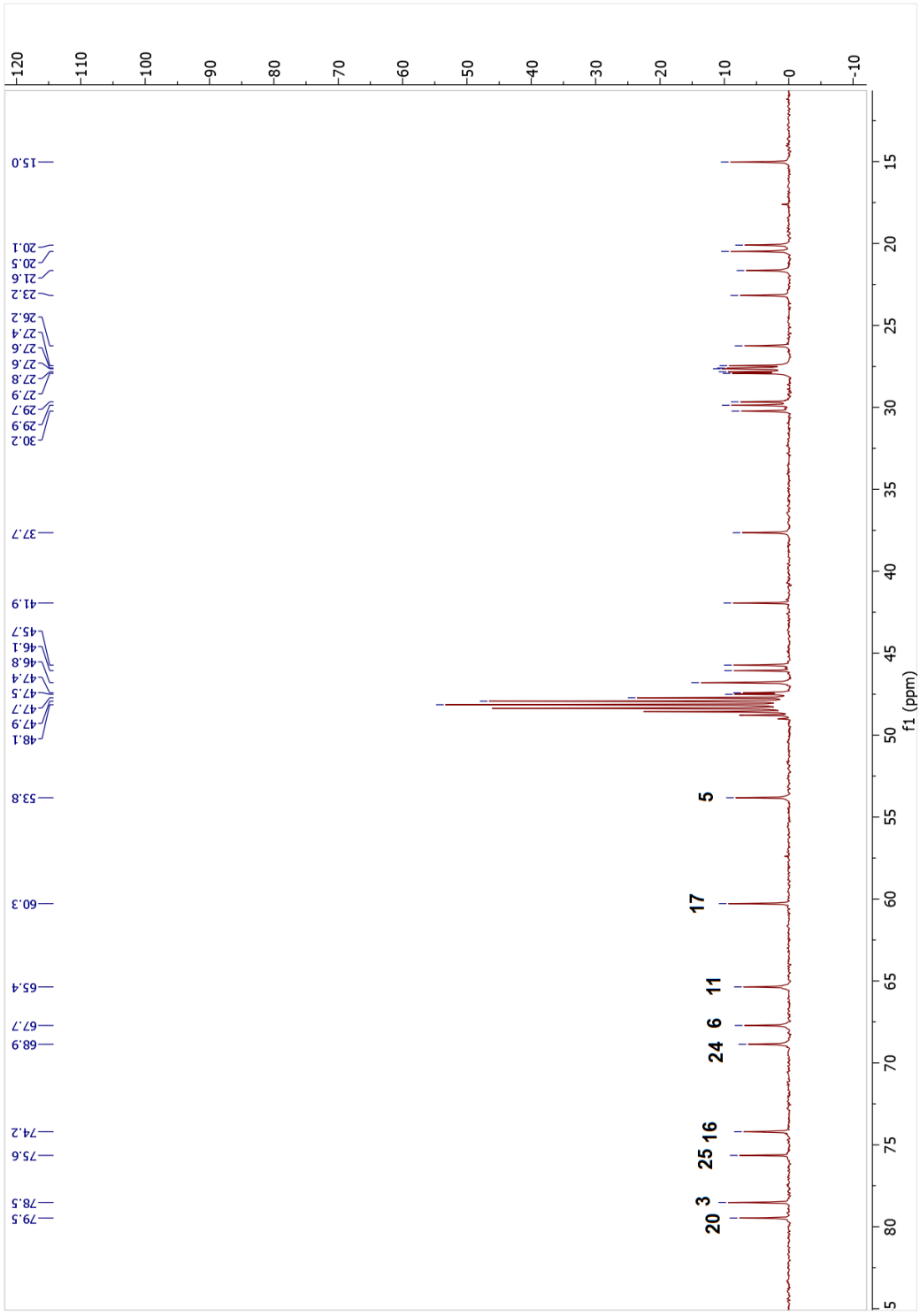

Spectrum 2.80. ^{13}C-NMR spectrum of compound **13**.

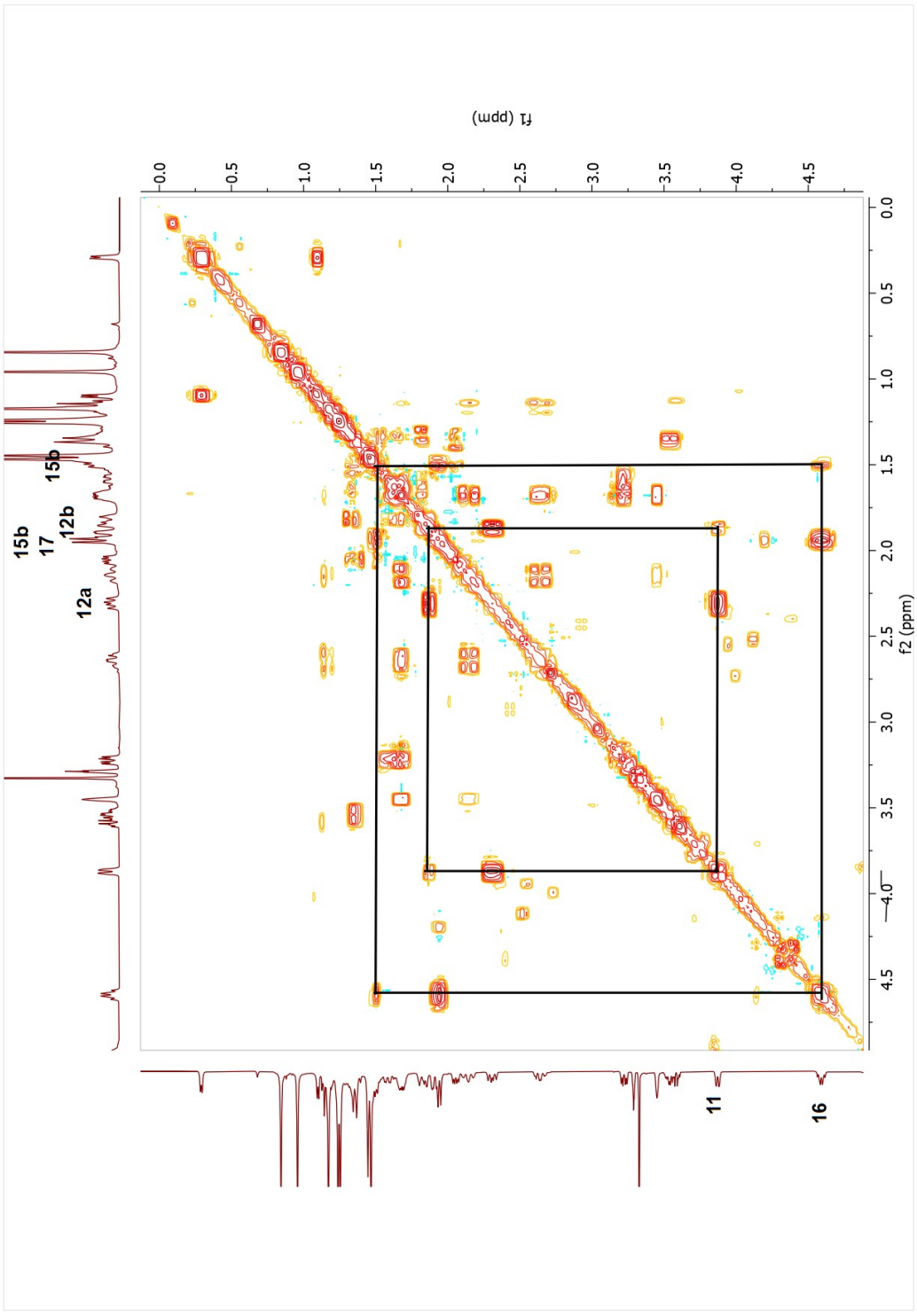

Spectrum 2.81. COSY spectrum of compound **13**.

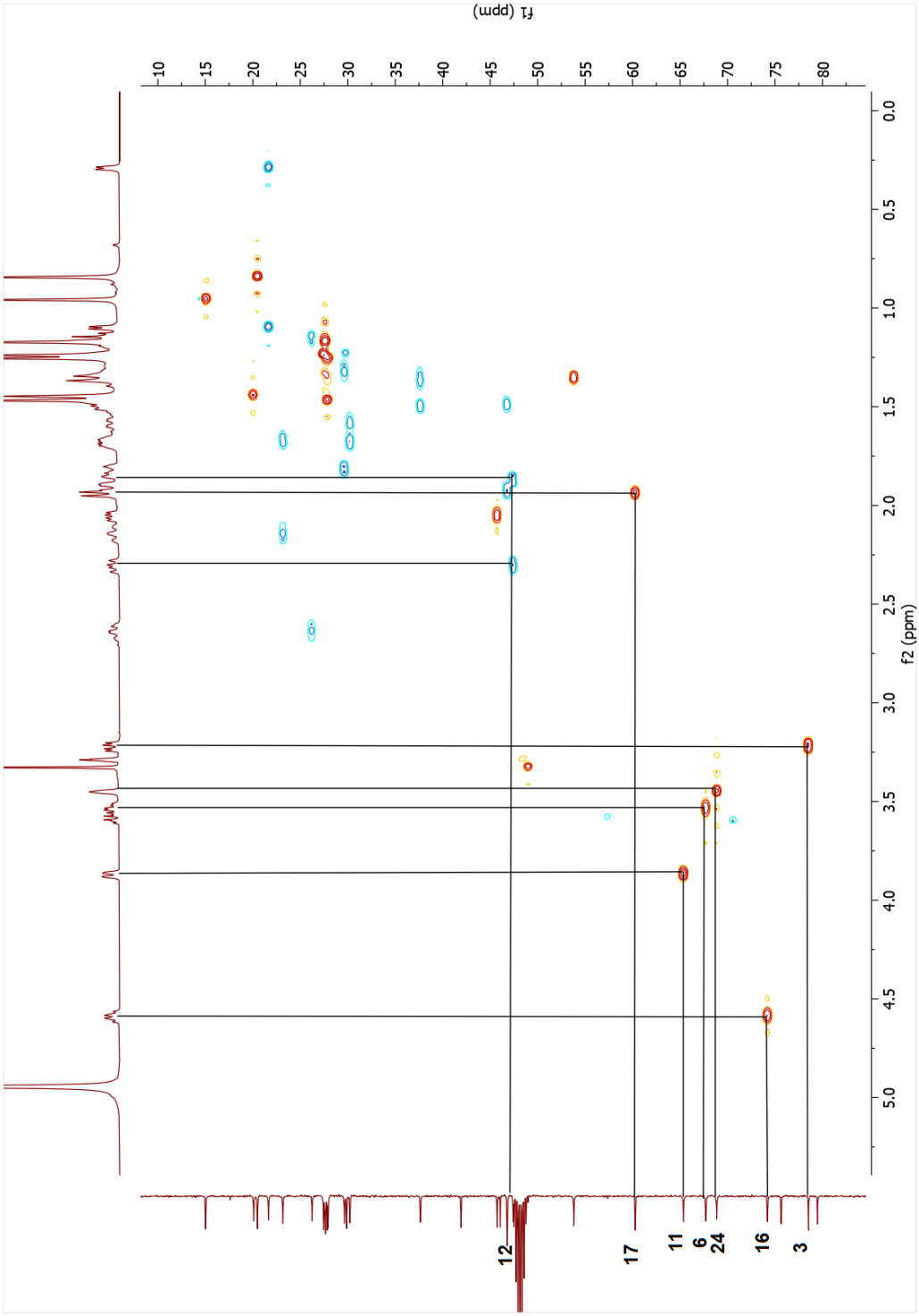

Spectrum 2.82. HSQC spectrum of compound **13**.

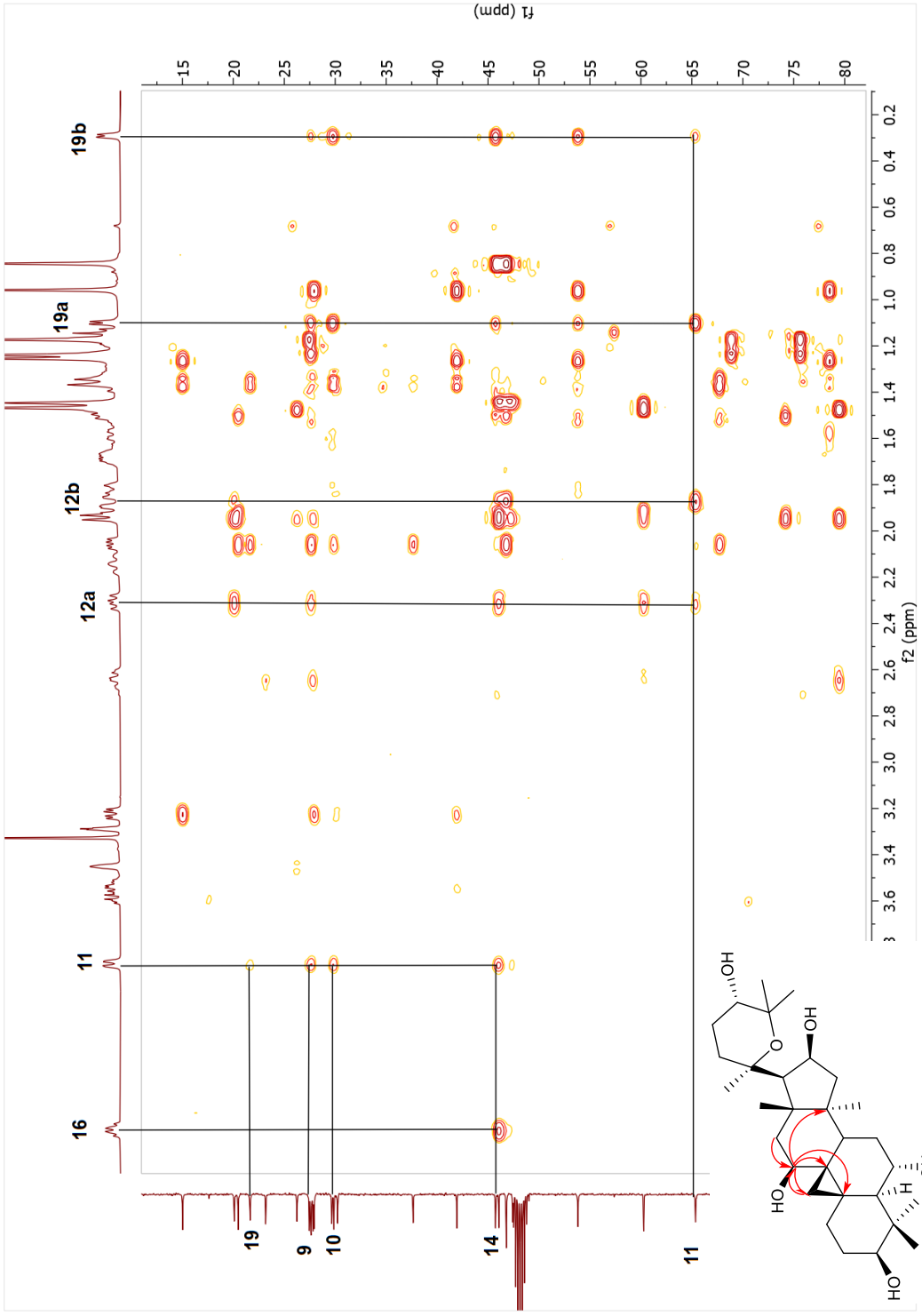

Spectrum 2.83. HMBC spectrum of compound **13**.

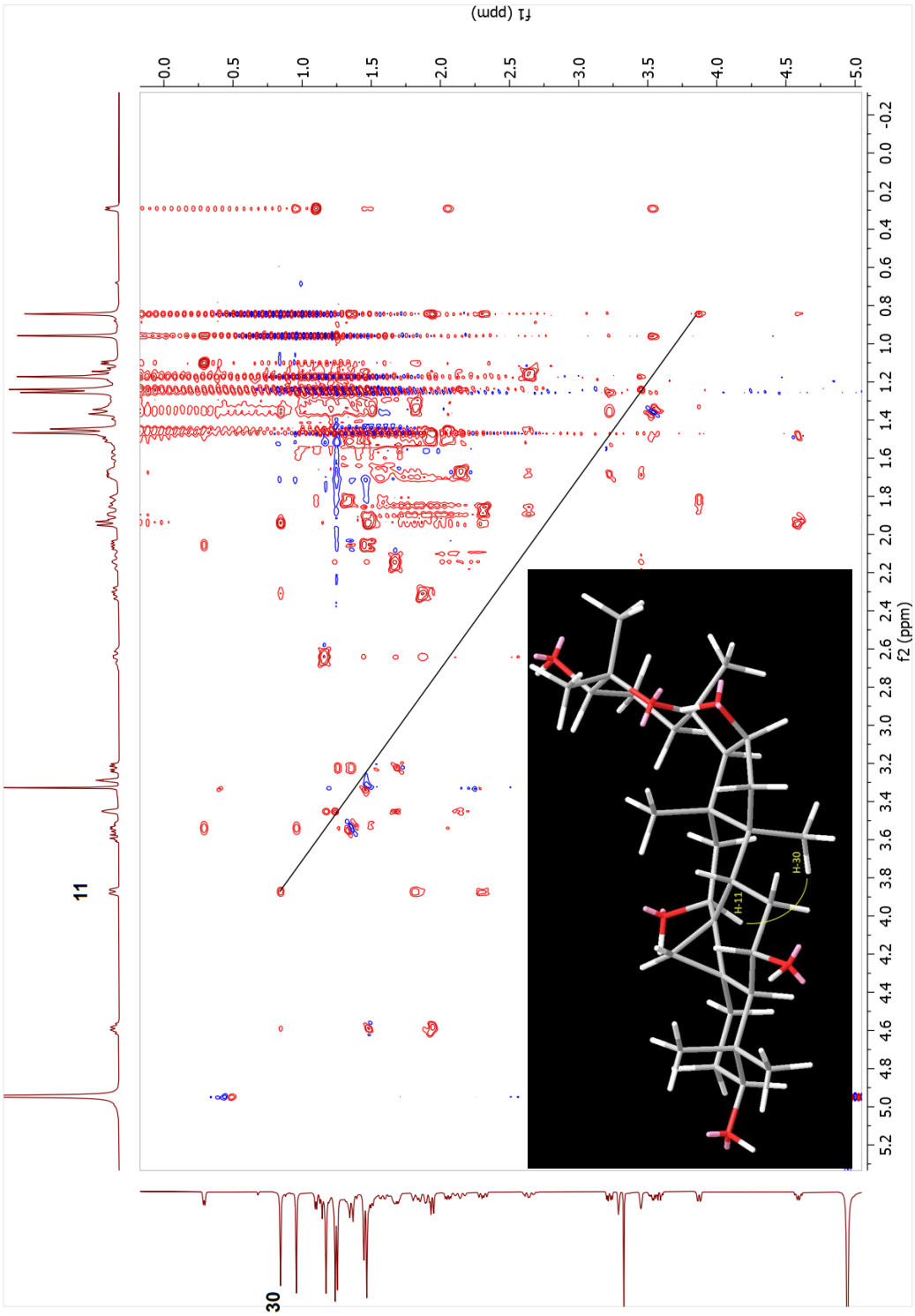

Spectrum 2.84. NOESY spectrum of compound **13**.

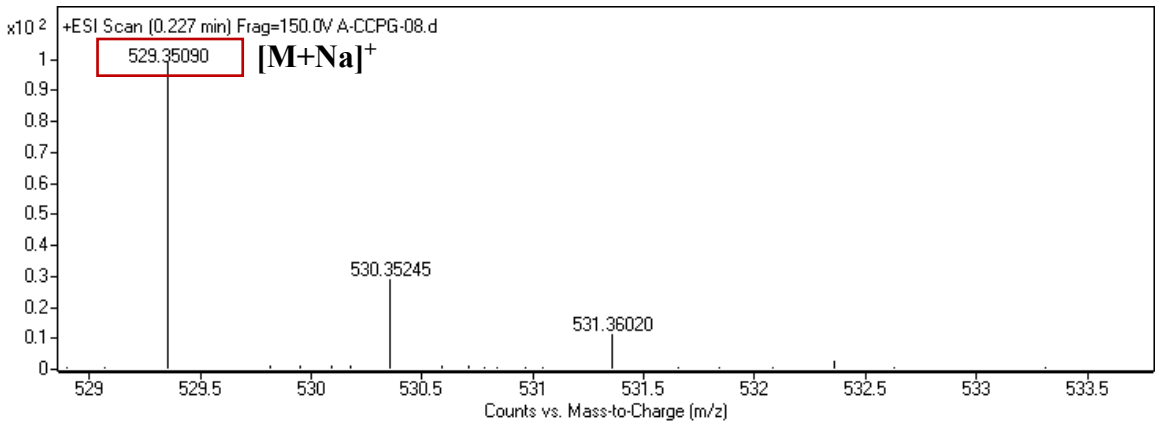

Spectrum 2.85. HR-ESI-MS spectrum of compound **13**.

2.3.2.14. Structure Elucidation of Compound 14

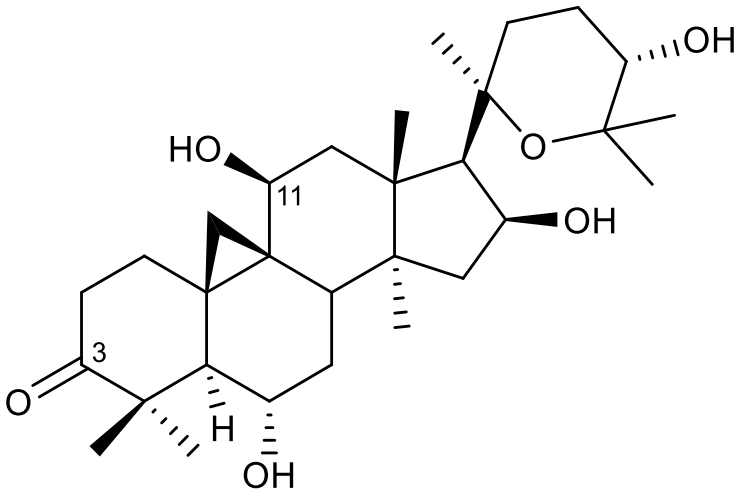

Figure 2.21. Chemical structure of compound **14**.

In the HR-ESI-MS spectrum of **14**, a major ion peak was observed at *m/z* 527.33574 (calcd for $C_{30}H_{48}NaO_6$, 527.33486) indicating a molecular formula of $C_{30}H_{48}O_6$. The characteristic oxymethine proton at C-3 was absent in the ^{1}H-NMR spectrum, together with the keto carbonyl signal (δ_C 217.2) in the ^{13}C-NMR spectrum. The long-range correlations from H_3-28 and H_3-29 to δ_C 217.2 in the HMBC spectrum, verified the location of the

carbonyl group to be at C-3. A broad singlet proton observed at 4.34 ppm, correlated in the HSQC spectrum with the carbon signal at δ_C 63.8, was suggestive of monohydroxylation. A detailed examination of 1D and 2D-NMR spectra suggested oxygenation at C-11, as in **13**. This assumption was confirmed by the HMBC experiment, which showed a cross-peak between H-19a (δ_H 1.70) and 63.8 ppm (C-11). The relative configuration was established via the 2D-NOESY data, correlations of H-11 and the α-oriented H_3-30 (δ_H 0.93) revealed that the hydroxy group at C-11 was β-oriented. Consequently, the structure of **14** was determined as 20,25-epoxy-6α,11β,16β,24α-tetrahydroxycycloartan-3-one.

Table 2.14. The ^{13}C and ^{1}H NMR data of **14** (100/400 MHz, δ ppm, in C_5D_5N).

Position	δ_C (ppm)	δ_H (ppm), *J* (Hz)	Position	δ_C (ppm)	δ_H (ppm), *J* (Hz)
1	29.3	2.02 dd (13.2, 5.1), 2.56 m	**16**	73.7	4.91 m
2	36.1	2.55 m, 2.75 dd (13.0, 4.7)	**17**	60.7	2.10 d (7.6)
3	217.2	-	**18**	21.3	1.80 s
4	50.5	-	**19**	21.6	0.52 d (4.1), 1.70 d (4.1)
5	54.4	2.30 d (9.9)	**20**	78.8	-
6	68.6	3.81 td (10.3, 2.9)	**21**	28.3	1.57 s
7	38.6	1.69 m, 1.81 m	**22**	26.4	1.22 m, 3.09 td (13.6, 4.5)
8	47.8	2.16 m	**23**	23.8	1.82 m, 2.15 m
9	27.9	-	**24**	68.4	3.64 brs
10	28.3	-	**25**	75.2	-
11	63.8	4.34 dd (9.4, 3.4)	**26**	28.5	1.42 s
12	49.3	2.26 dd (10.8, 3.4), 2.67 dd (13.9, 9.4)	**27**	27.8	1.26 s
13	46.6	-	**28**	28.5	1.79 s
14	46.3	-	**29**	20.3	1.50 s
15	47.9	1.85 m, 2.10 m	**30**	21.5	0.93 s

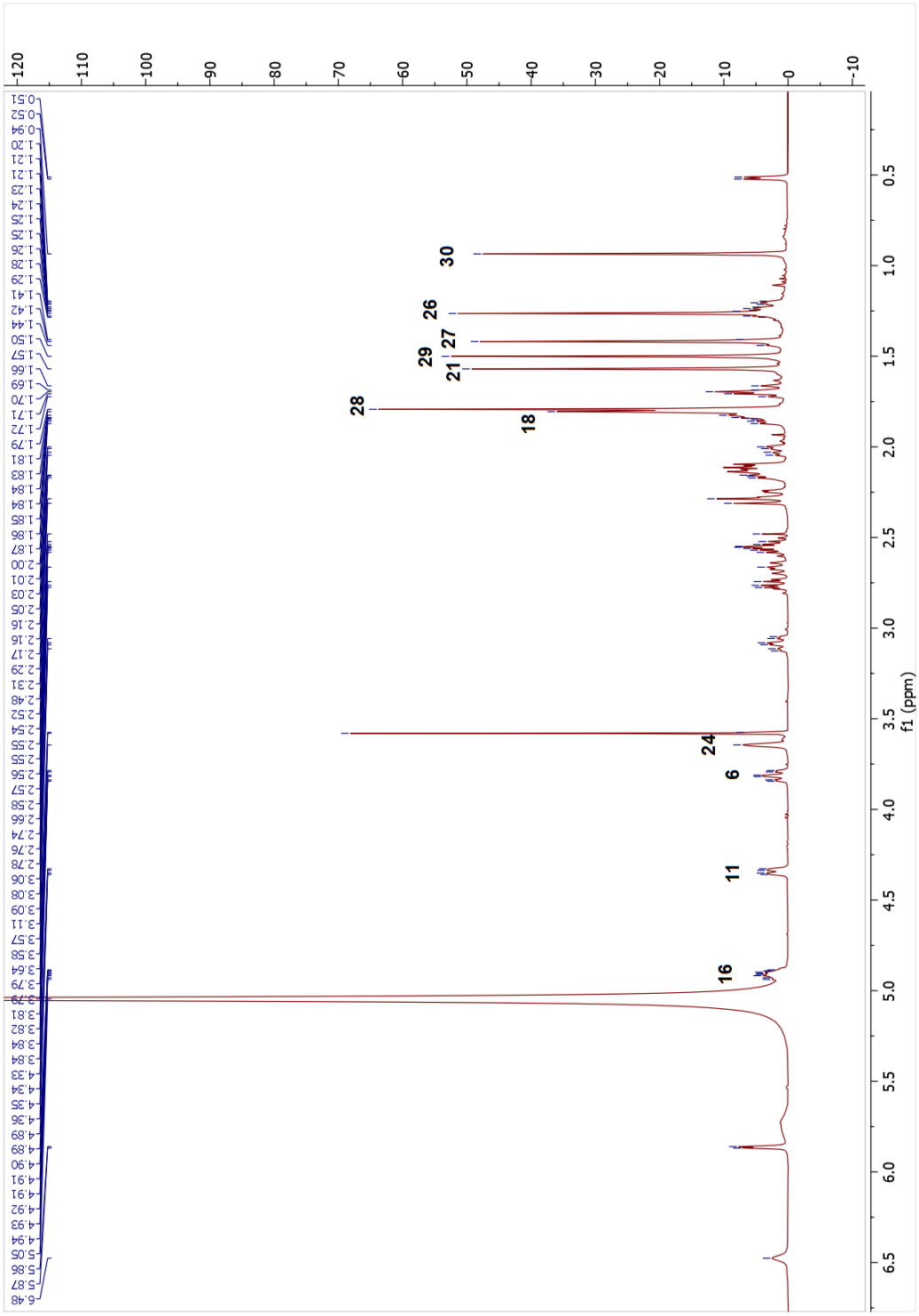

Spectrum 2.86. ^{1}H-NMR spectrum of compound **14**.

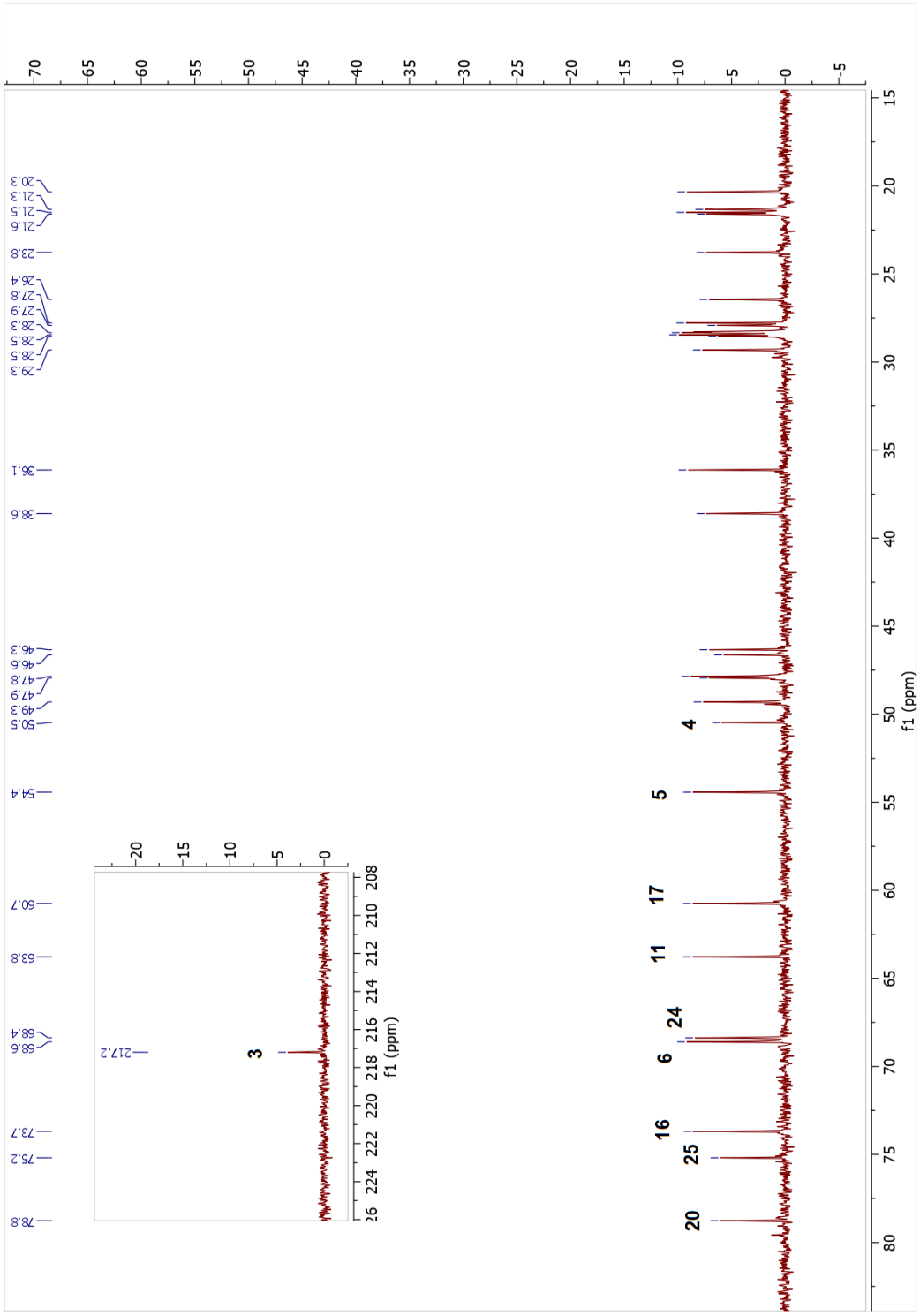

Spectrum 2.87. ^{13}C-NMR spectrum of compound **14**.

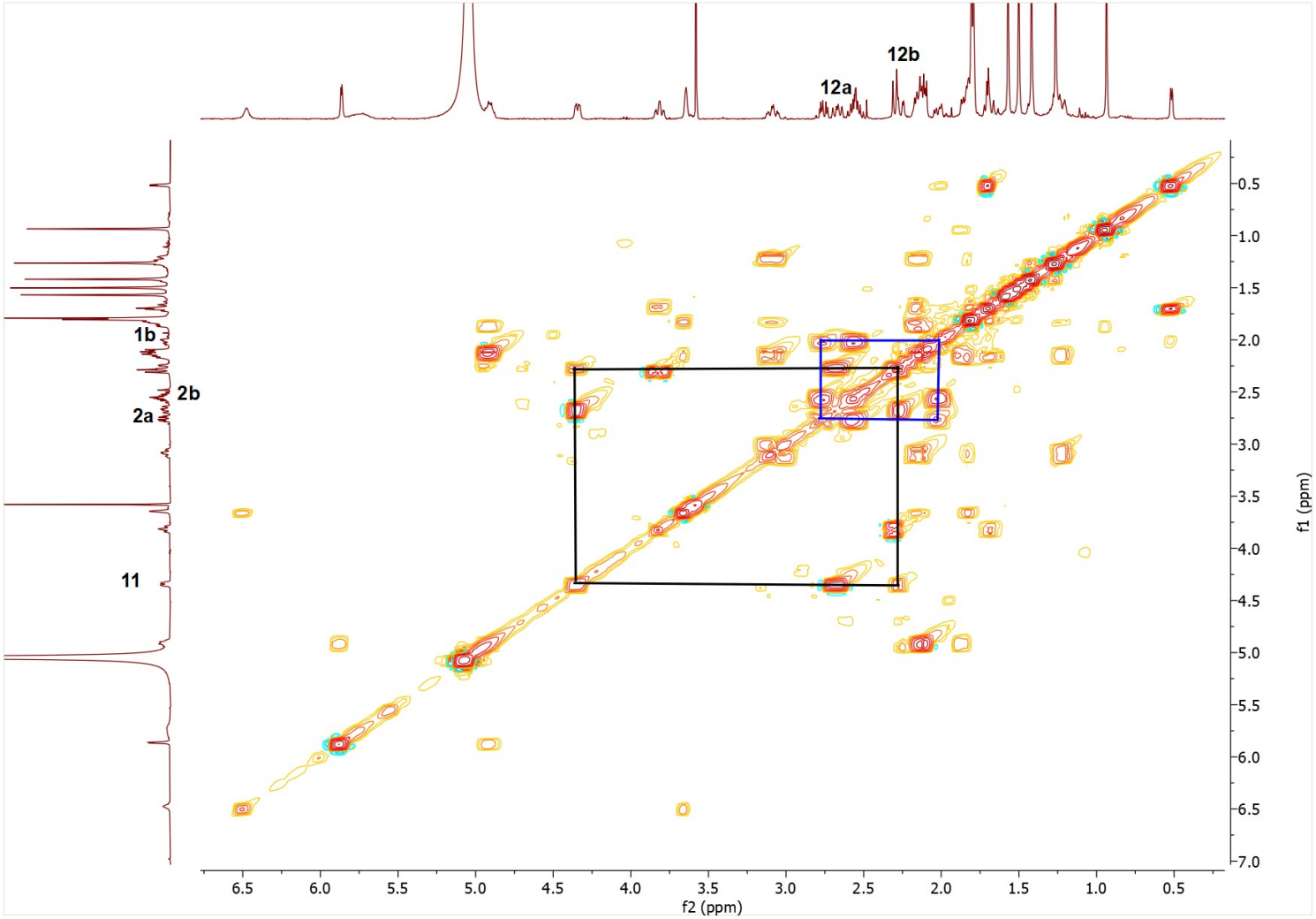

Spectrum 2.88. COSY spectrum of compound **14**.

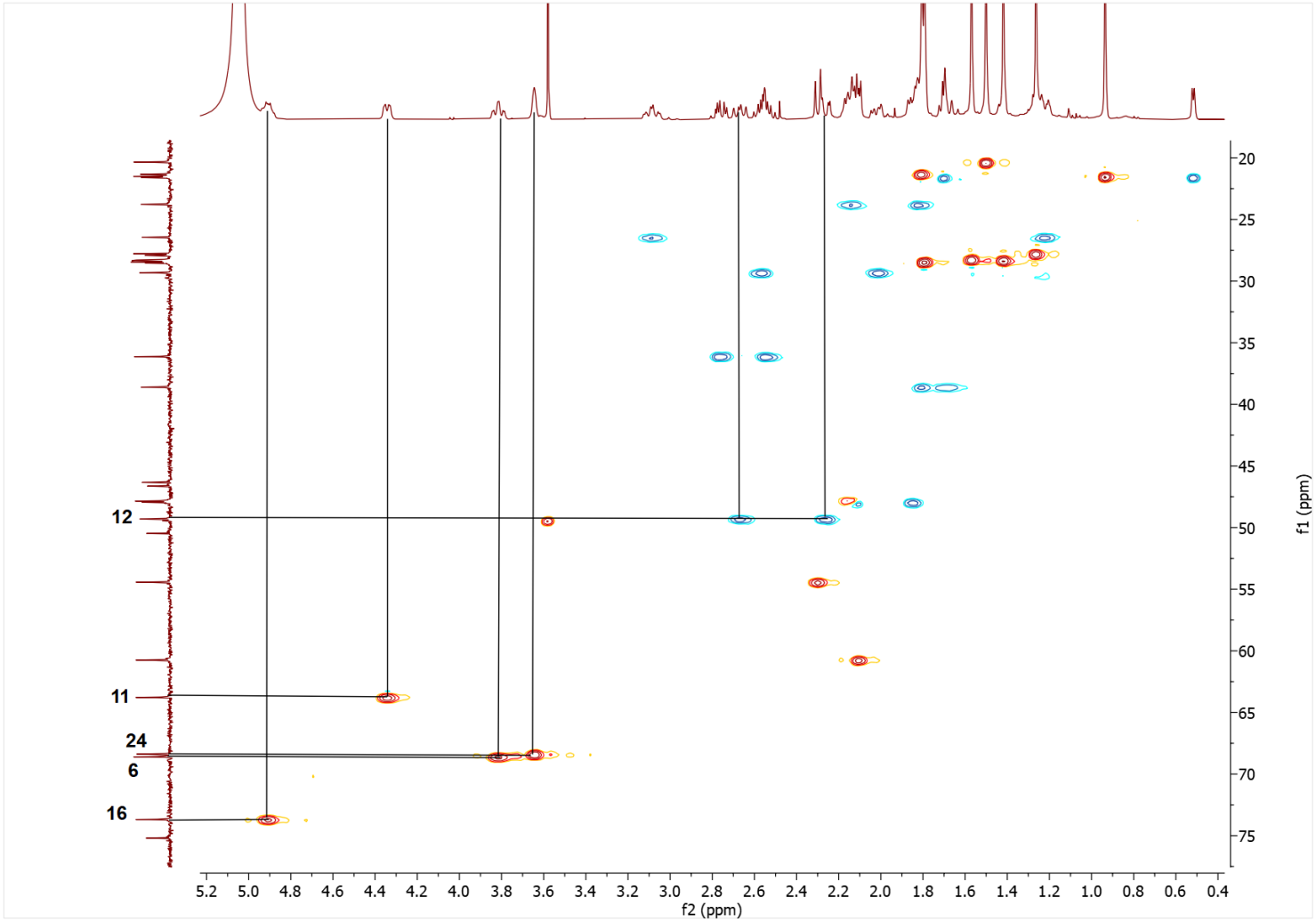

Spectrum 2.89. HSQC spectrum of compound **14**.

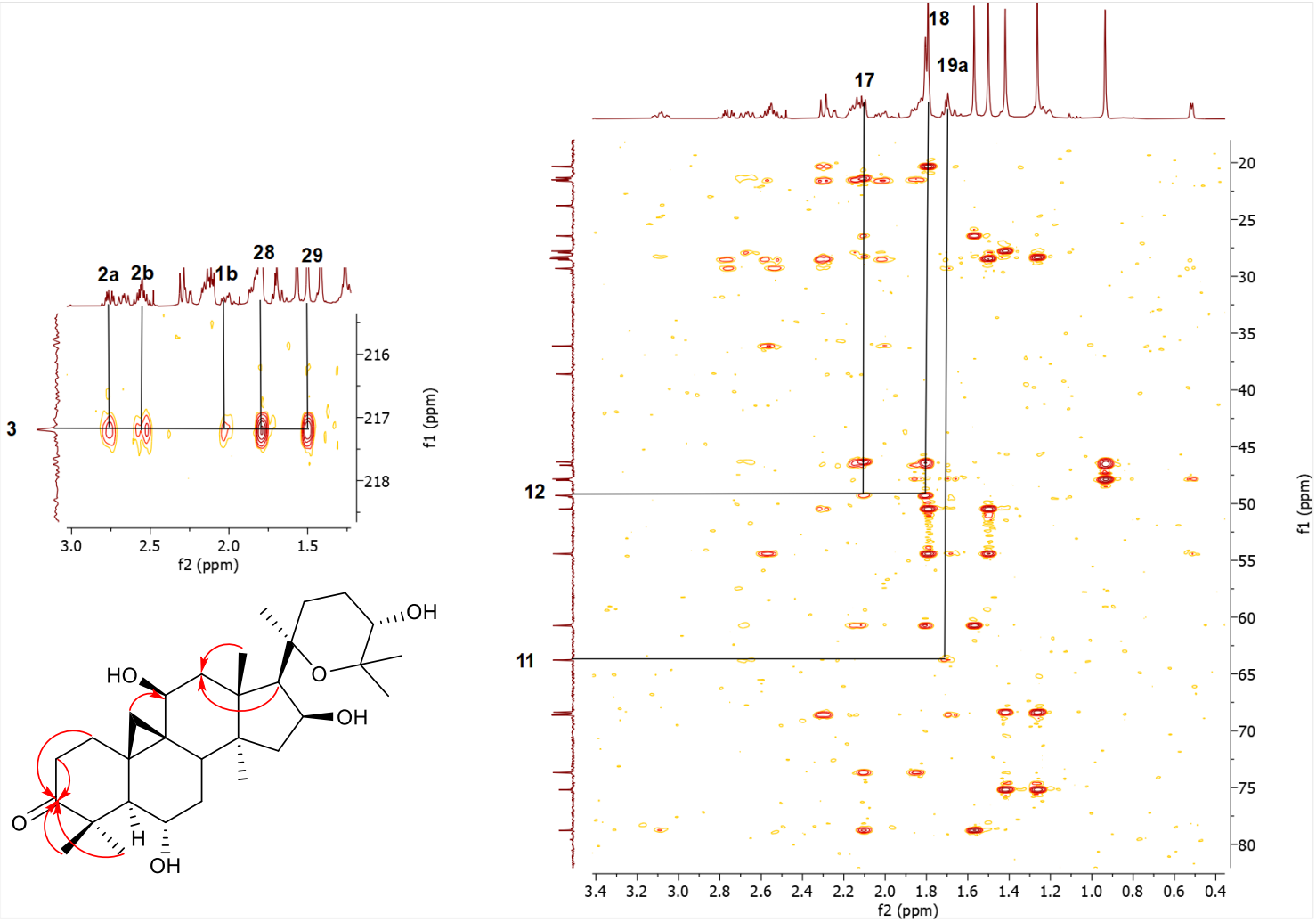

Spectrum 2.90. HMBC spectrum of compound **14**.

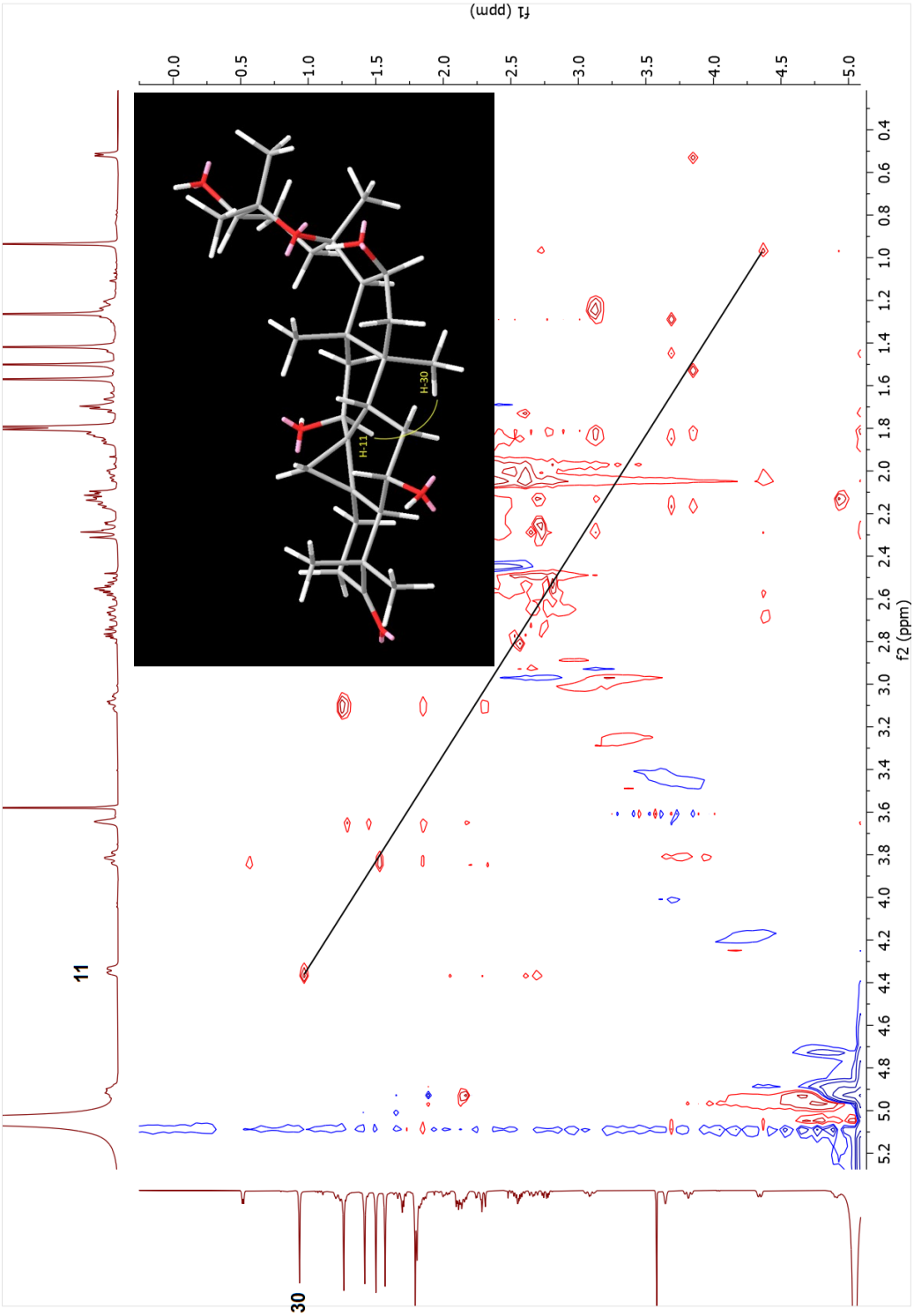

Spectrum 2.91. NOESY spectrum of compound **14**.

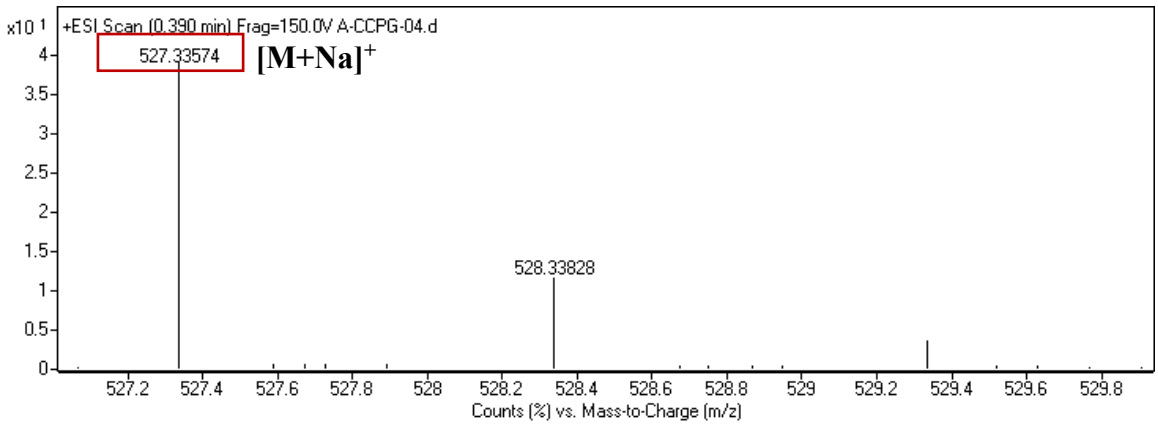

Spectrum 2.92. HR-ESI-MS spectrum of compound **14**.

2.3.2.15. Structure Elucidation of Compound 15

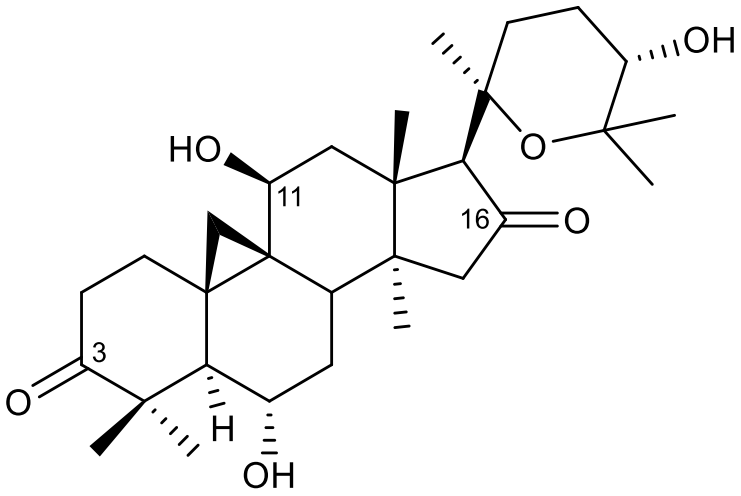

Figure 2.22. Chemical structure of compound **15**.

In the HR-ESI-MS spectrum of **15**, the major ion peak was observed at *m/z* 525.3170 $[M + Na]^+$ (calcd. 525.31921 for $C_{30}H_{46}NaO_6$). The ^1H- and ^{13}C-NMR spectra of **15** were similar to those of **14**, except for the absence of H-16 resonance, the signals deriving from an additional carbonyl resonance (δ_C 219.2) and those in its close proximity. The downfield shift for C-17 (ca. 10.2 ppm at δ_C 70.9) in the ^{13}C-NMR spectrum and the isolated C-15

methylene protons in the COSY and ^{1}H-NMR spectra indicated functionalization at C-16. This assumption was confirmed by the HMBC experiment, which showed a cross-peak between H-17 (δ_H 2.86), H_2-15 (δ_H 2.13 and 2.30) and 219.2 ppm (C-16). As a result, metabolite **15** was established as 20,25-epoxy-6α,11β,24α-trihydroxycycloartan-3,16-dione.

Table 2.15. The ^{13}C and ^{1}H NMR data of **15** (125/500 MHz, δ ppm, in C_5D_5N).

Position	δ_C (ppm)	δ_H (ppm), *J* (Hz)
1	29.9	2.00 m, 2.56 m
2	36.8	2.59 m, 2.79 m
3	218.7	-
4	51.2	-
5	55.0	2.32 m
6	69.0	3.86 m
7	39.3	1.70 m (2H)
8	47.7	2.13 m
9	28.5	-
10	29.6	-
11	64.0	4.34 m
12	48.3	2.48 dd (14.6, 3.1), 2.84 m
13	51.2	-
14	47.1	-
15	51.8	2.13 m, 2.30 m
16	219.2	-
17	70.9	2.86 m
18	21.2†	1.60 s
19	22.3	0.58 d (4.3), 1.80 d (4.2)
20	76.3	-
21	25.5	1.49 s
22	30.5	1.33 m, 2.31 m
23	24.3	1.86 m, 2.17 m
24	69.5	3.64 brs
25	75.3	-
26	29.1	1.42 s
27	28.8	1.28 s
28	29.1	1.83 s
29	21.1†	1.55 s
30	21.4	1.00 s

†Overlapped signals

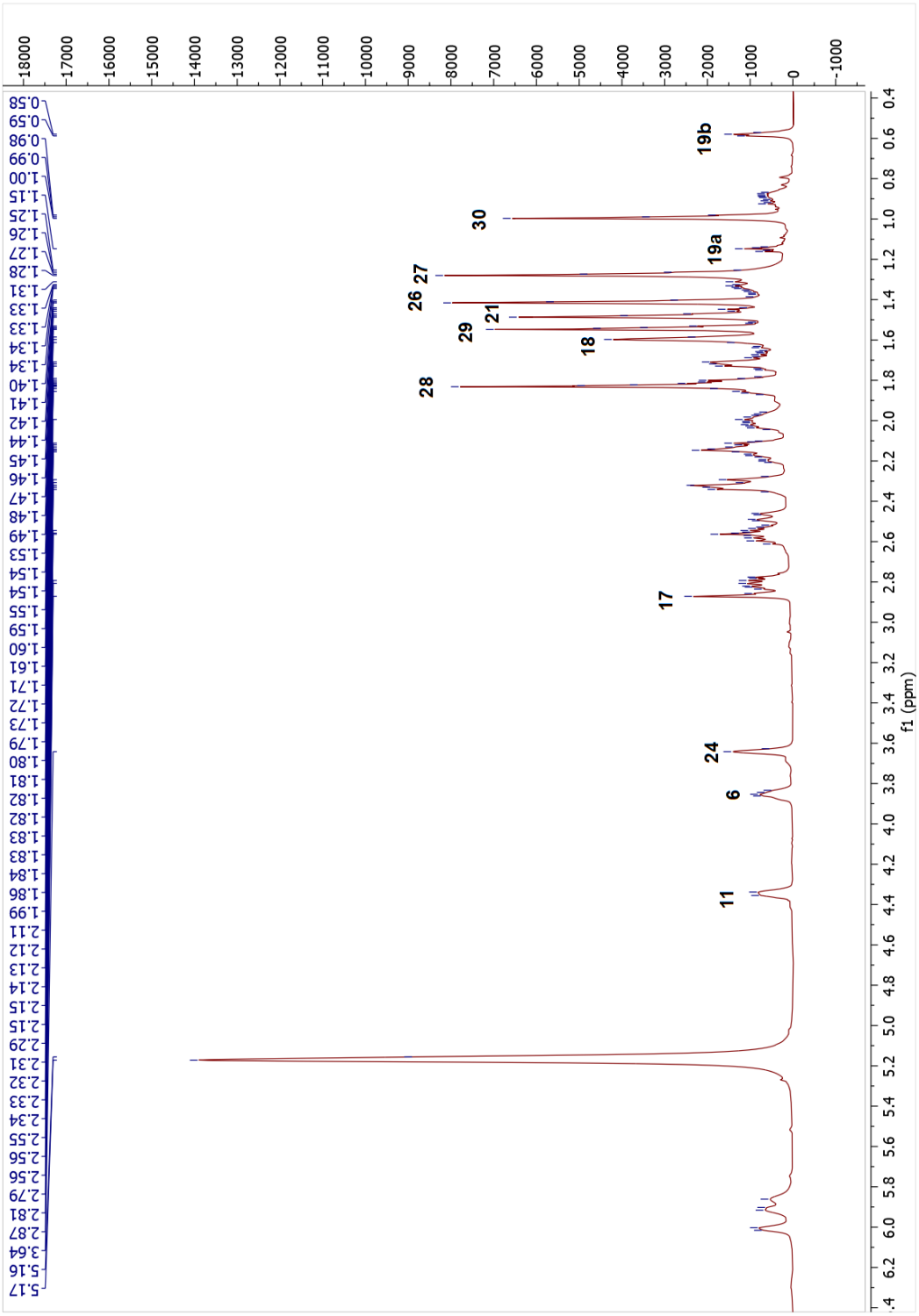

Spectrum 2.93. ^{1}H-NMR spectrum of compound **15**.

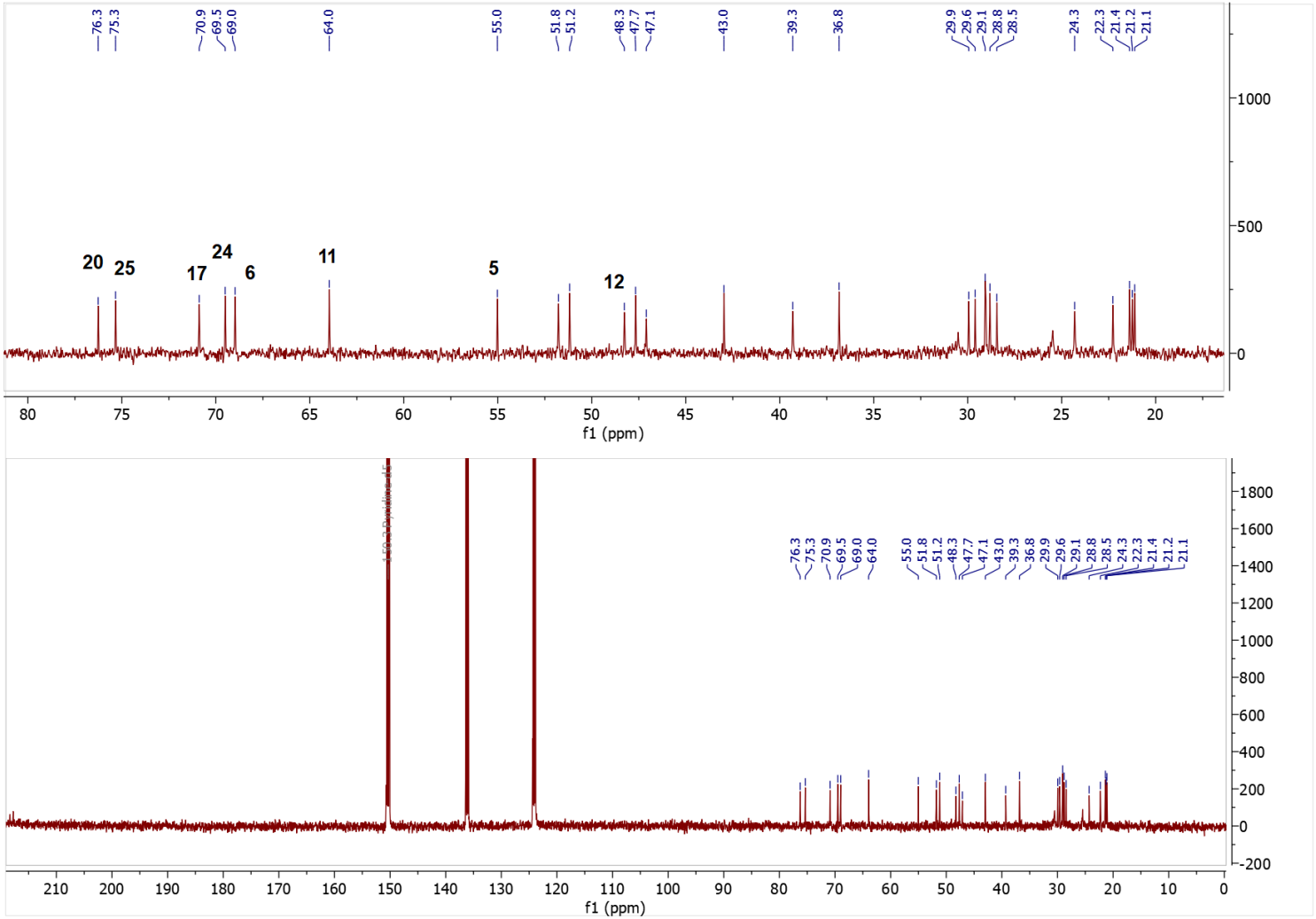

Spectrum 2.94. ^{13}C-NMR spectrum of compound **15**.

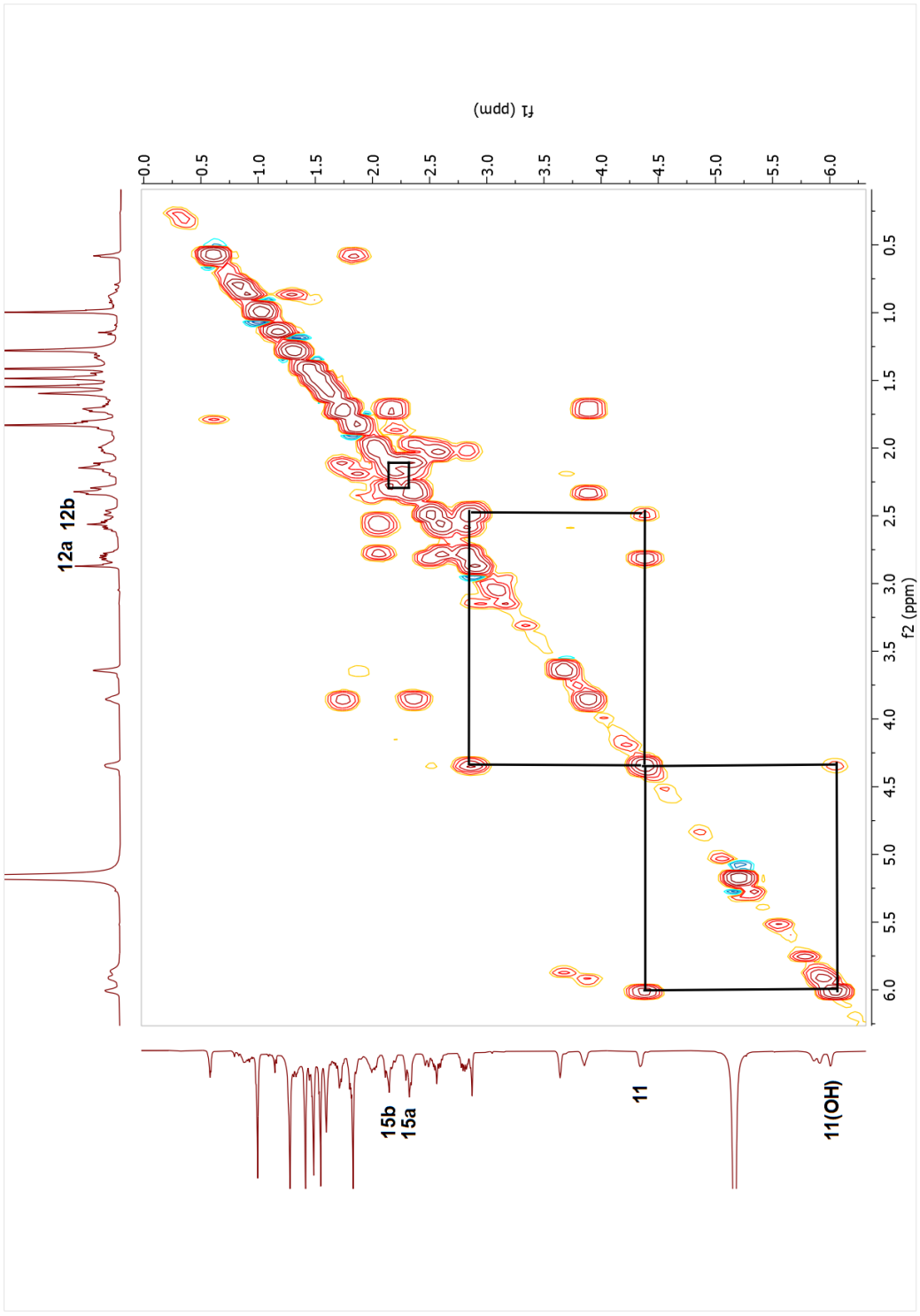

Spectrum 2.95. COSY spectrum of compound **15**.

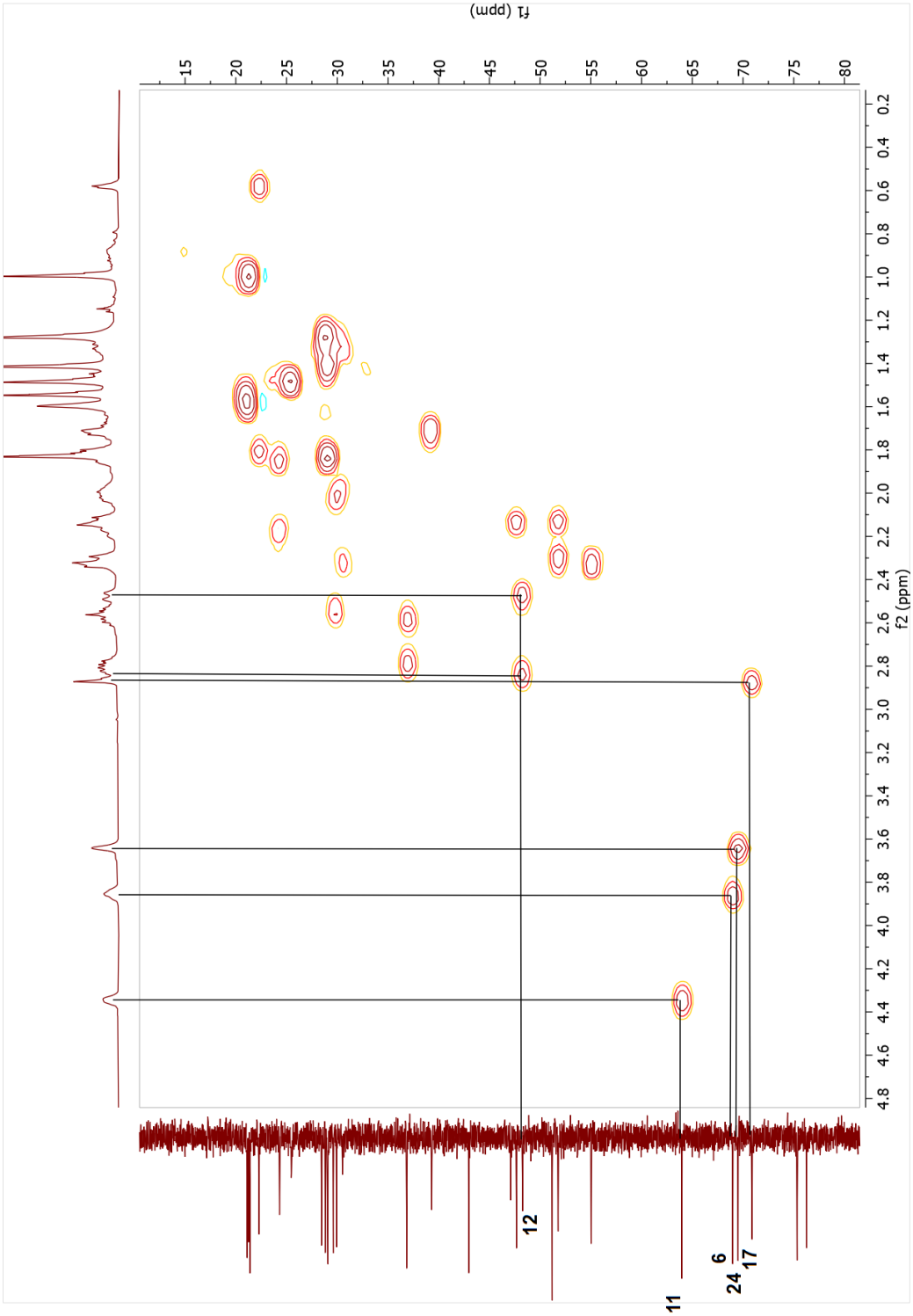

Spectrum 2.96. HSQC spectrum of compound **15**.

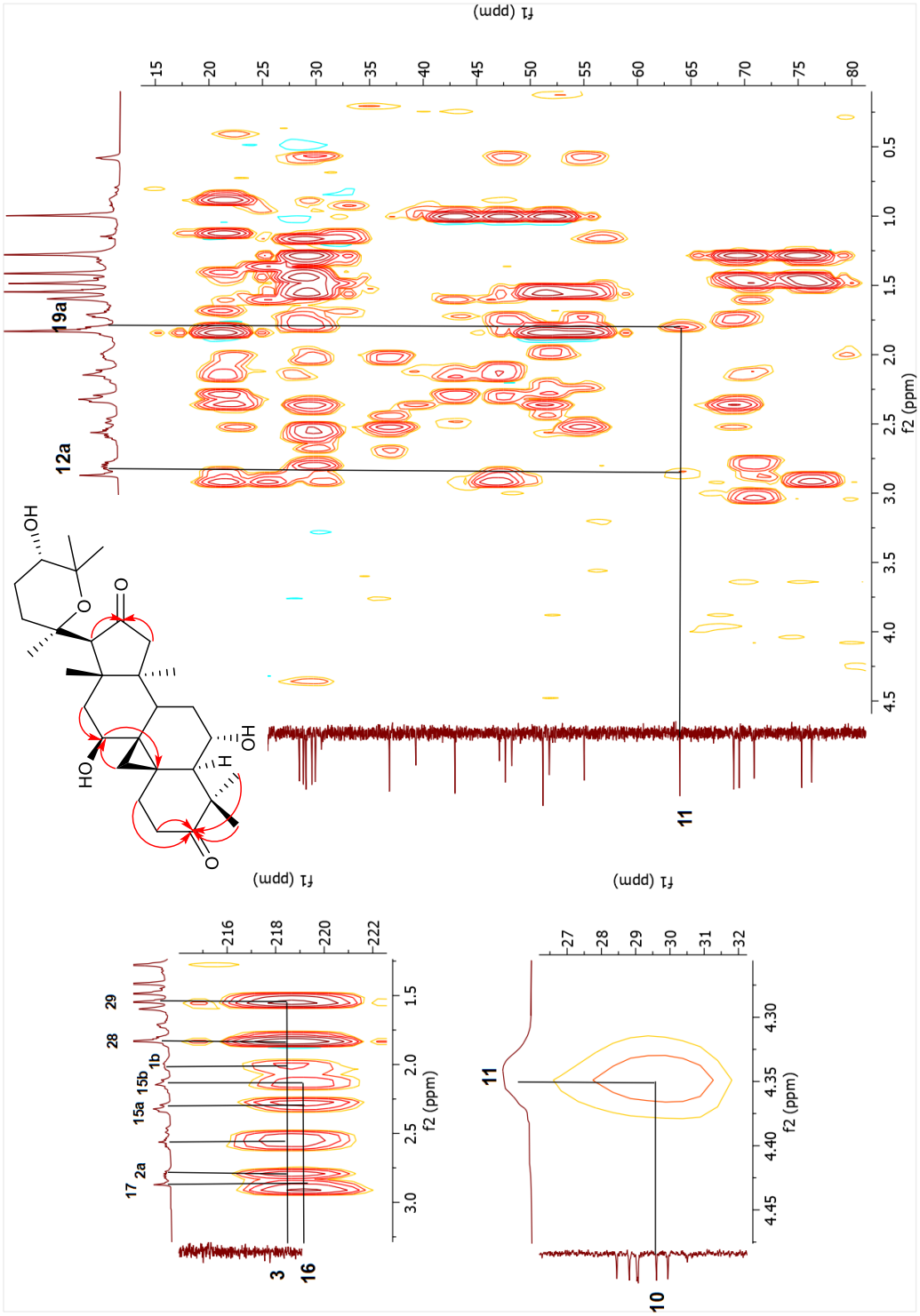

Spectrum 2.97. HMBC spectrum of compound **15**.

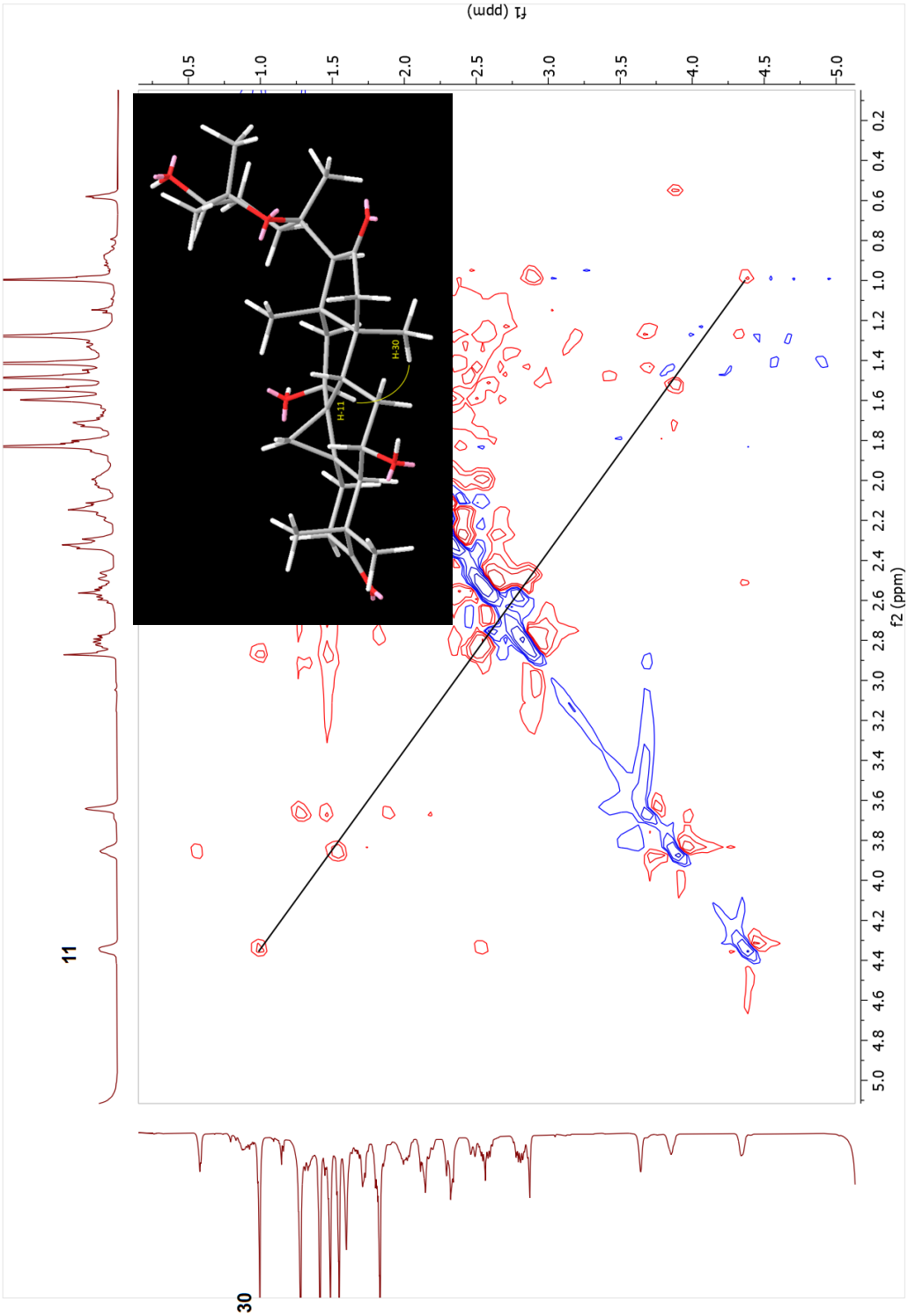

Spectrum 2.98. NOESY spectrum of compound **15**.

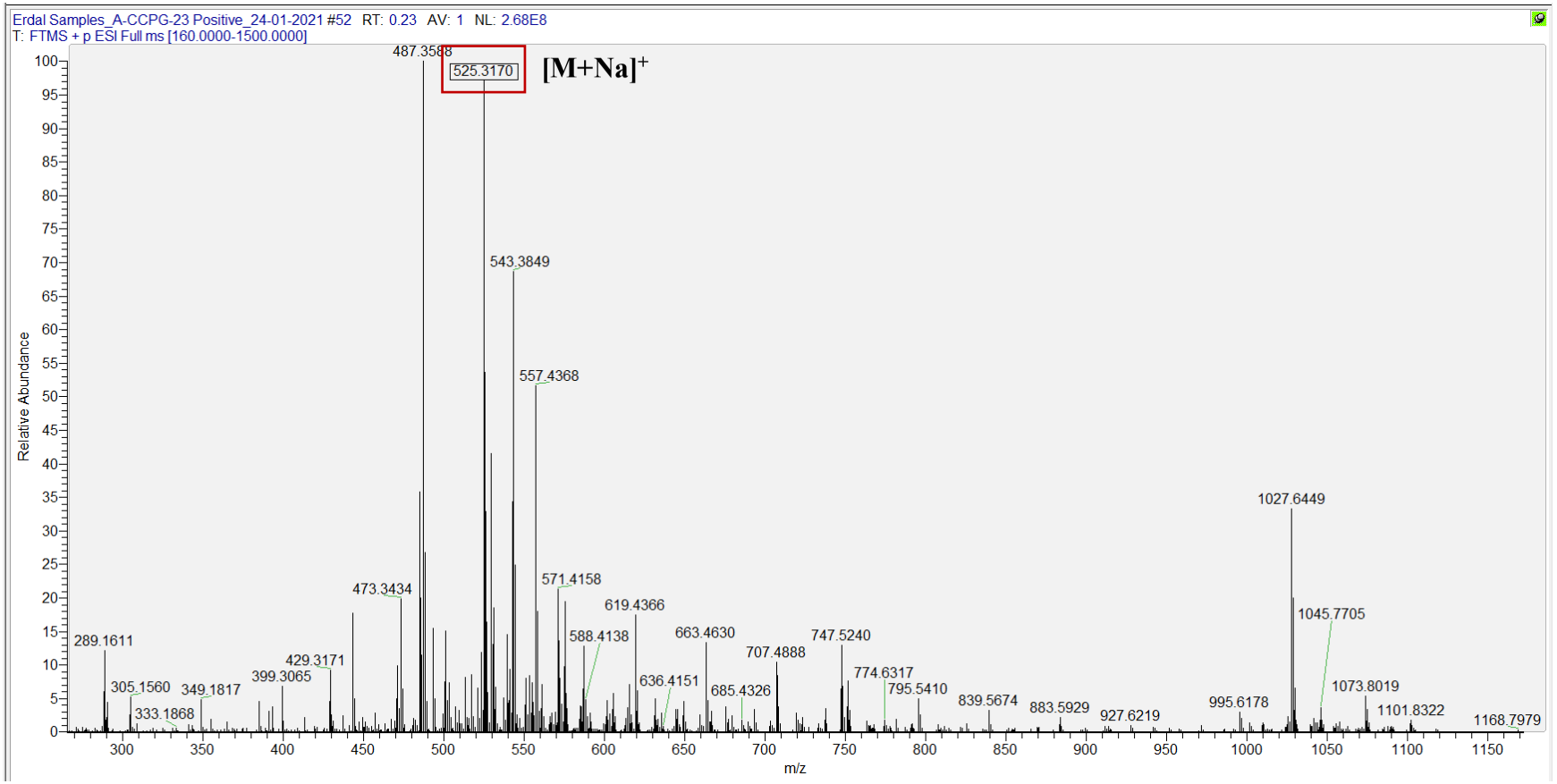

Spectrum 2.99. HR-ESI-MS spectrum of compound **15**.

2.3.2.16. Structure Elucidation of Compound 16

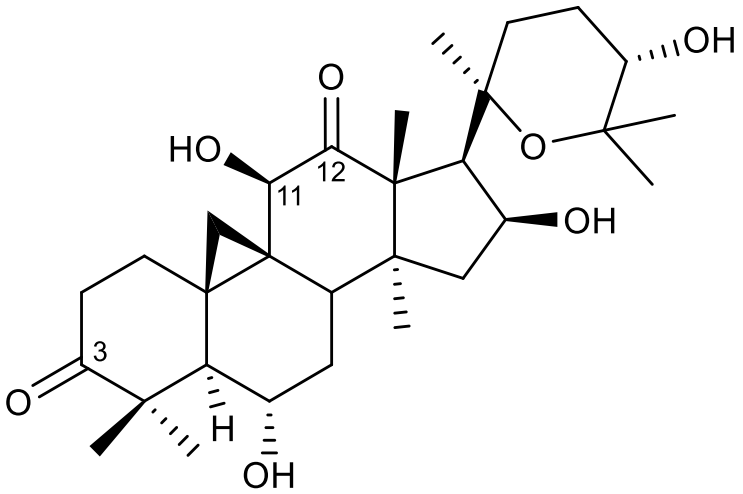

Figure 2.23. Chemical structure of compound **16**.

The major ion peak at *m/z* 545.34597 $[M + Na]^+$ (calcd. 545.34542 for $C_{30}H_{50}NaO_7$) in the HR-ESI-MS spectrum of **16** displayed a 32 amu increase over **1**, suggesting a dihydroxy analog. In the low-field region of the ^{1}H-NMR spectrum, two additional low-field protons (δ_H 3.35 and 3.93) were observed. Besides, in the ^{13}C-NMR spectrum, two extra down-field carbon signals at δ_C 81.0 and 83.4 were also noted. To deduce oxidation positions, the 2D-NMR spectra were inspected in detail. In the HMBC spectrum, key long-range correlations from H_3-18 (δ_H 1.35) and H-17 (δ_H 2.32) to 83.4 ppm substantiated that one of the hydroxy groups was located at C-12. The second hydroxy group was located at C-11 (δ_C 81.0) based on the COSY correlation of H-11 (δ_H 3.35) with H-12 (δ_H 3.93) as well as the $^3J_{H\text{-}C}$ correlations from H_2-19 (δ_H 0.57 and 0.83) and H-12 (δ_H 3.93) to C-11. The relative configurations at C-11 and C-12 were determined based on the 2D-NOESY data. The orientation of C-12(OH) was found to be β based on NOESY cross-peak between H-12 (δ_H 3.93) and α-oriented H_3-30. The strong correlation of H-11 with one of the β-oriented C-19 protons ($\delta_{H\text{-}19a}$ 0.83) revealed that the hydroxy group at C-11 was α-oriented. On the basis of

these evidence, the structure of compound **16** was elucidated as 20,25-epoxy-3β,6α,11α,12β,16β,24α-hexahydroxycycloartane.

Table 2.16. The ^{13}C and ^{1}H NMR data of **16** (100/400 MHz, δ ppm, in CD_3OD and a drop of C_5D_5N).

Position	δ_C (ppm)	δ_H (ppm), *J* (Hz)
1	35.1	1.28 m, 1.96 m
2	30.2	1.70 m (2H)
3	78.0	3.26 m
4	41.5	-
5	53.0	1.54 d (9.8)
6	69.5	3.42 m
7	38.8	1.42 m (2H)
8	48.9	1.53 m
9	28.9	-
10	31.9	-
11	81.0	3.35 brs
12	83.4	3.93 brs
13	51.4	-
14	46.5	-
15	49.2	1.57 m, 2.02 m
16	71.1	4.51 q (7.4, 7.0)
17	61.5	2.32 d (7.8)
18	13.2	1.35 s
19	35.6	0.57 d (4.2), 0.83 m
20	78.3	-
21	25.8	1.65 s
22	28.8	1.88 d (12.9), 2.04 d (7.6)
23	22.3	1.64 m, 2.17 t (13.5)
24	68.8	3.45 brs
25	75.3	-
26	27.5	1.26 s
27	27.0	1.21 s
28	27.9	1.31 s
29	14.7	0.97 s
30	18.4	1.11 s

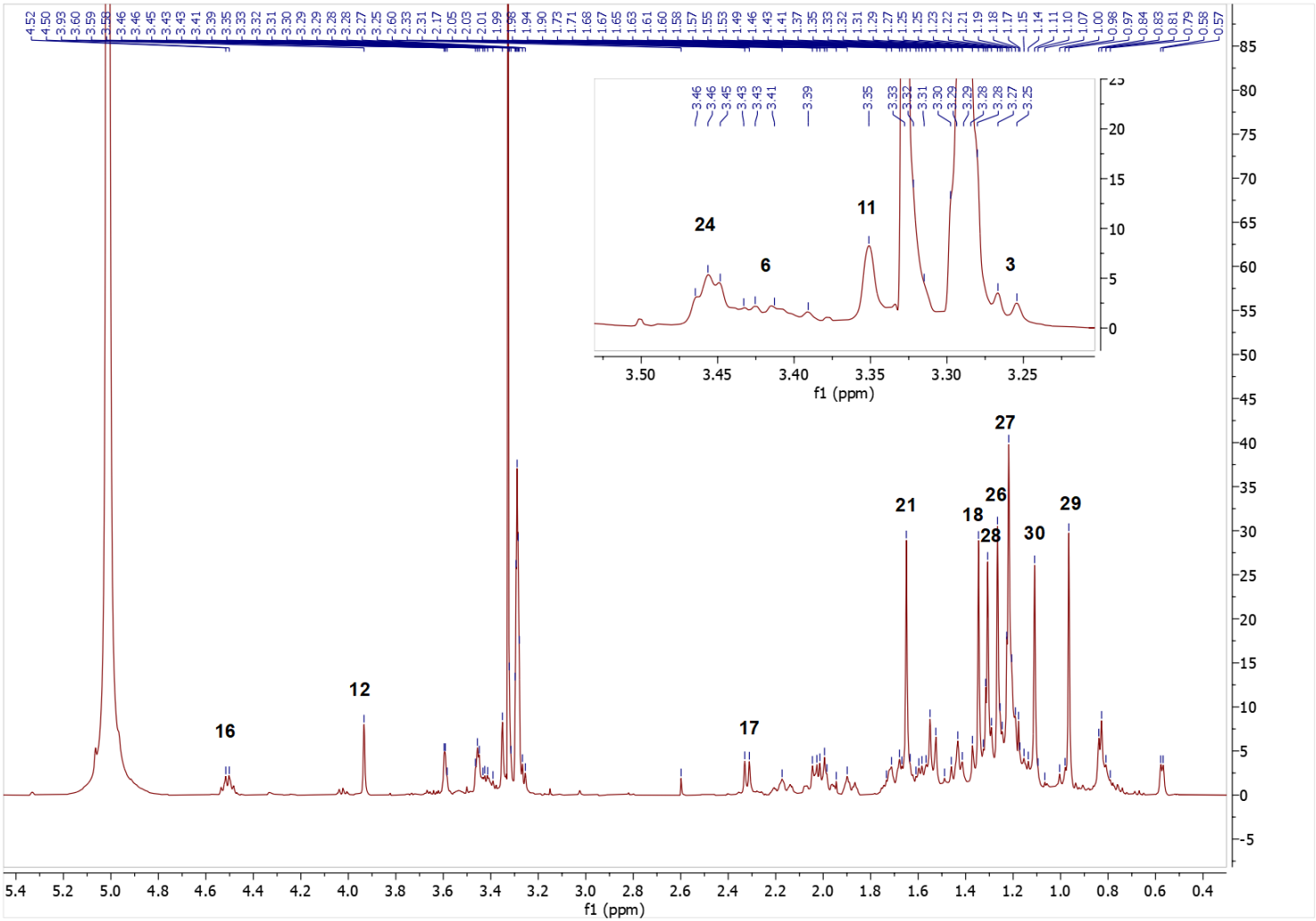

Spectrum 2.100. ^{1}H-NMR spectrum of compound **16**.

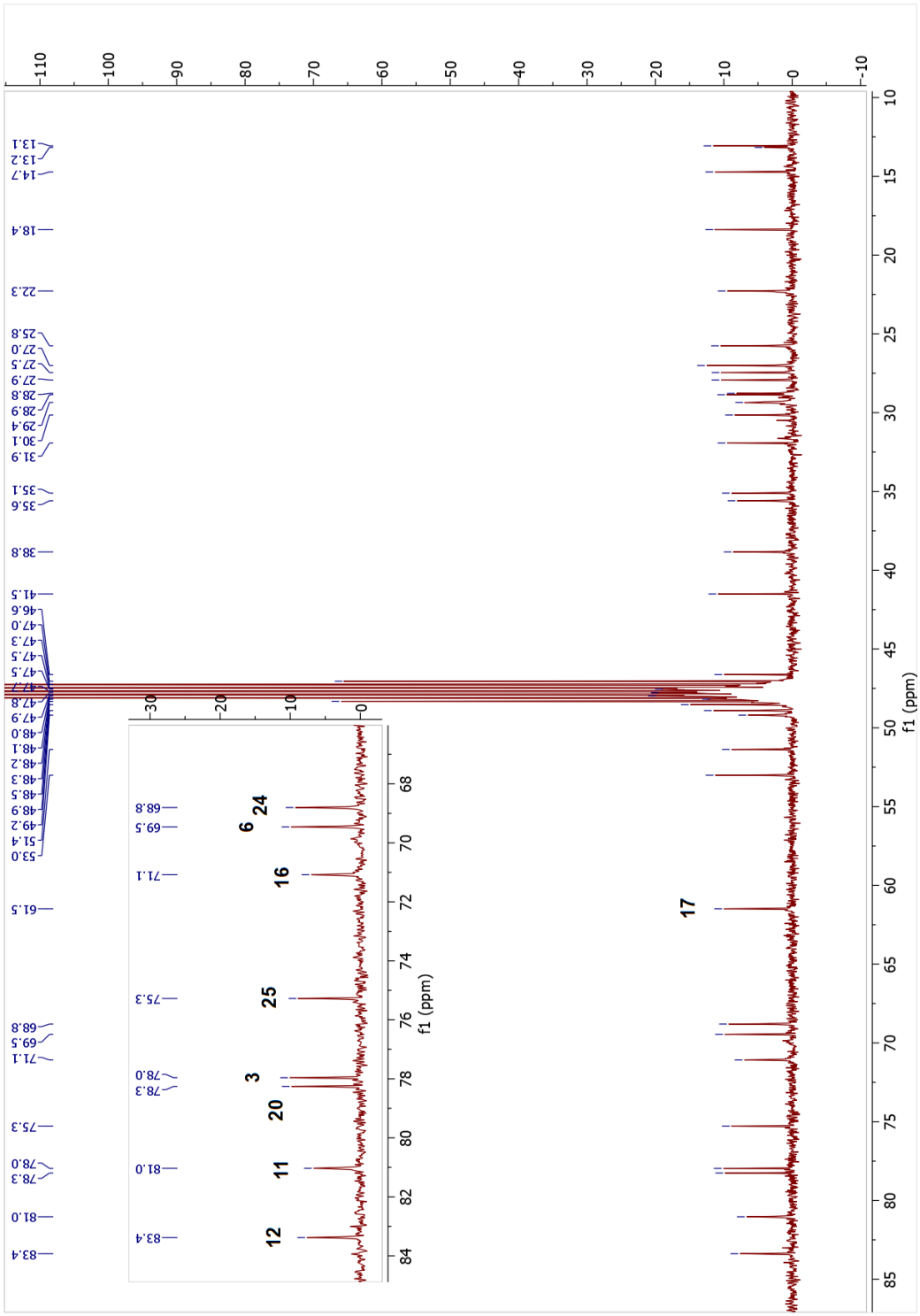

Spectrum 2.101. ^{13}C-NMR spectrum of compound **16**.

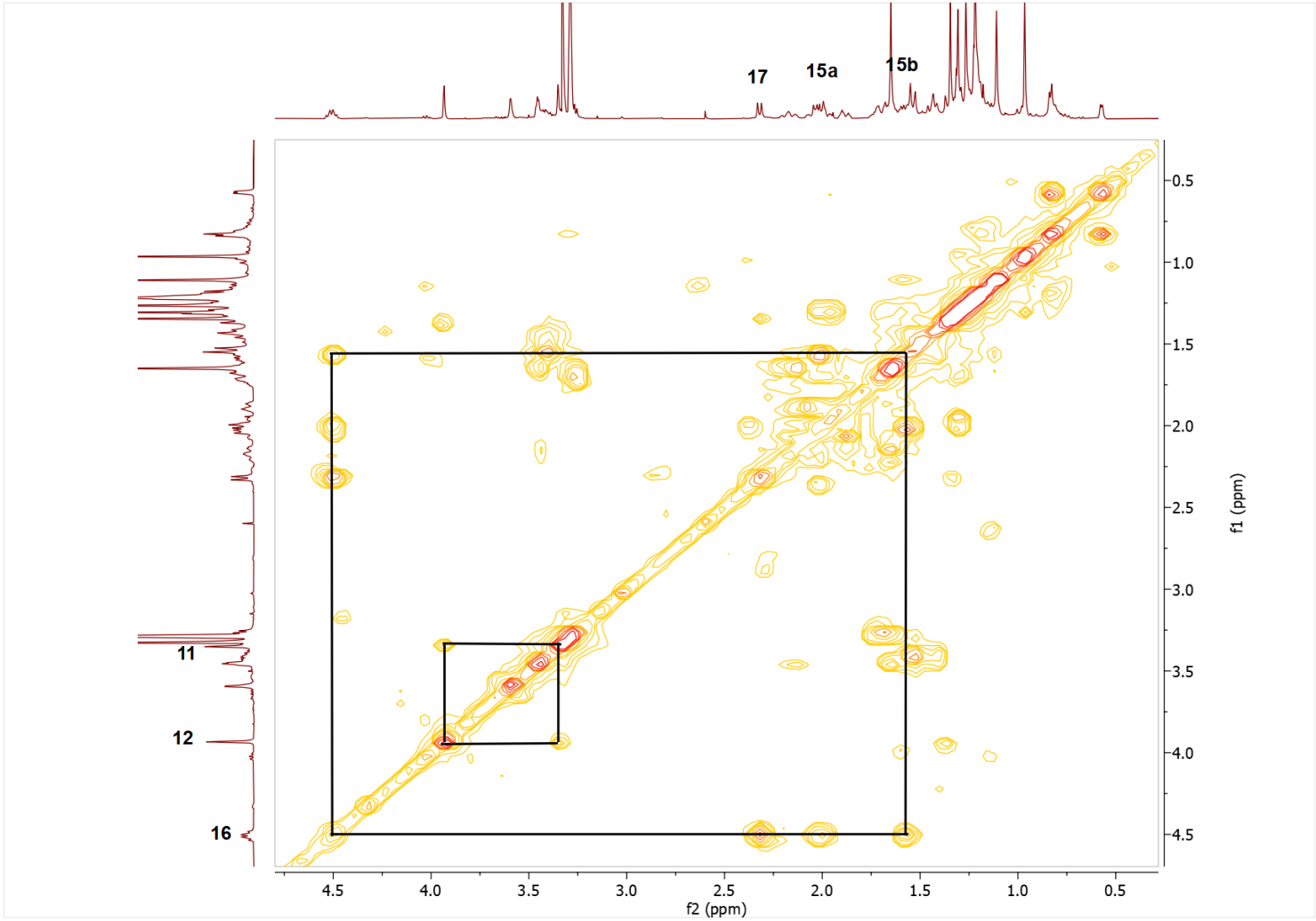

Spectrum 2.102. COSY spectrum of compound **16**.

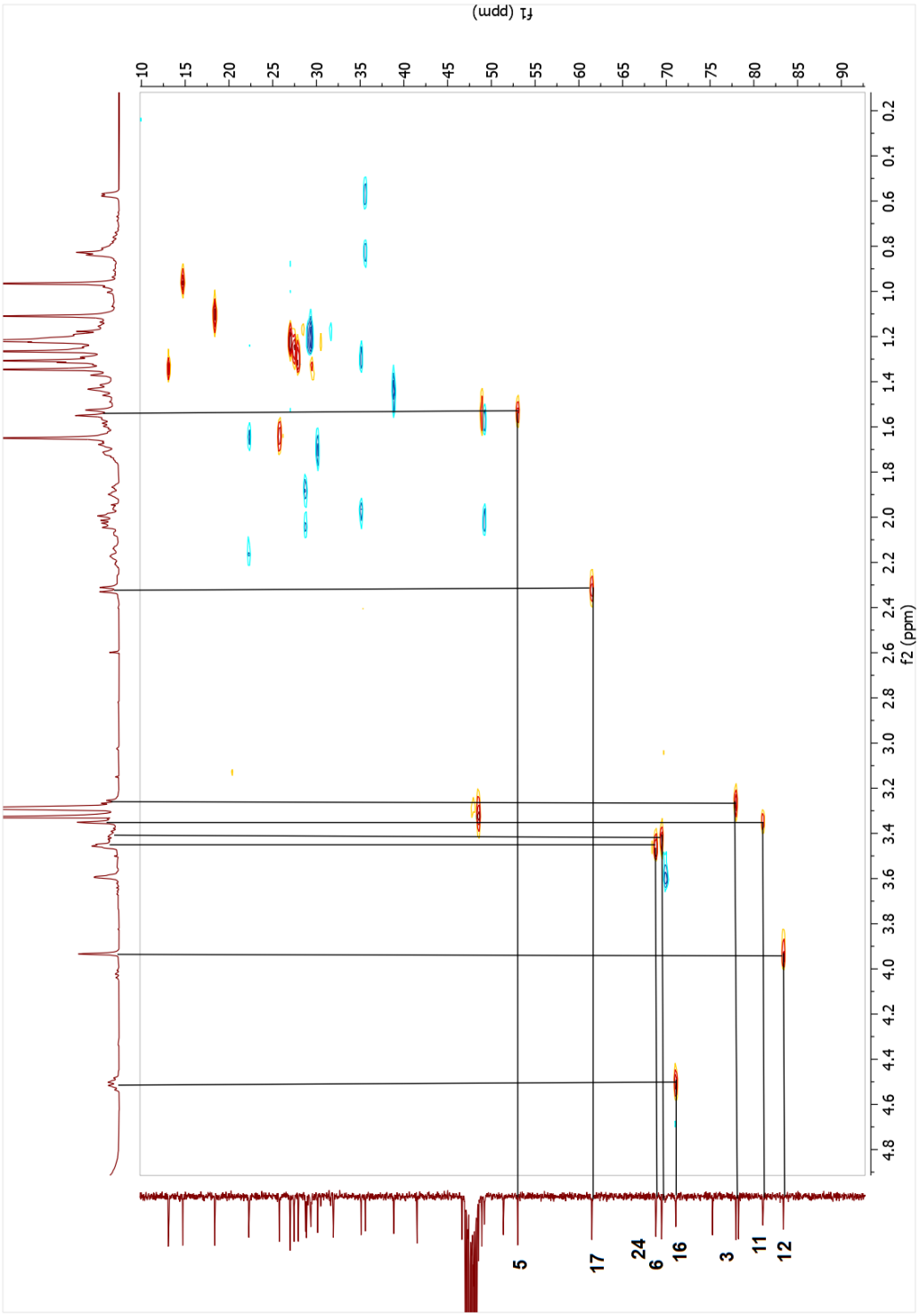

Spectrum 2.103. HSQC spectrum of compound **16**.

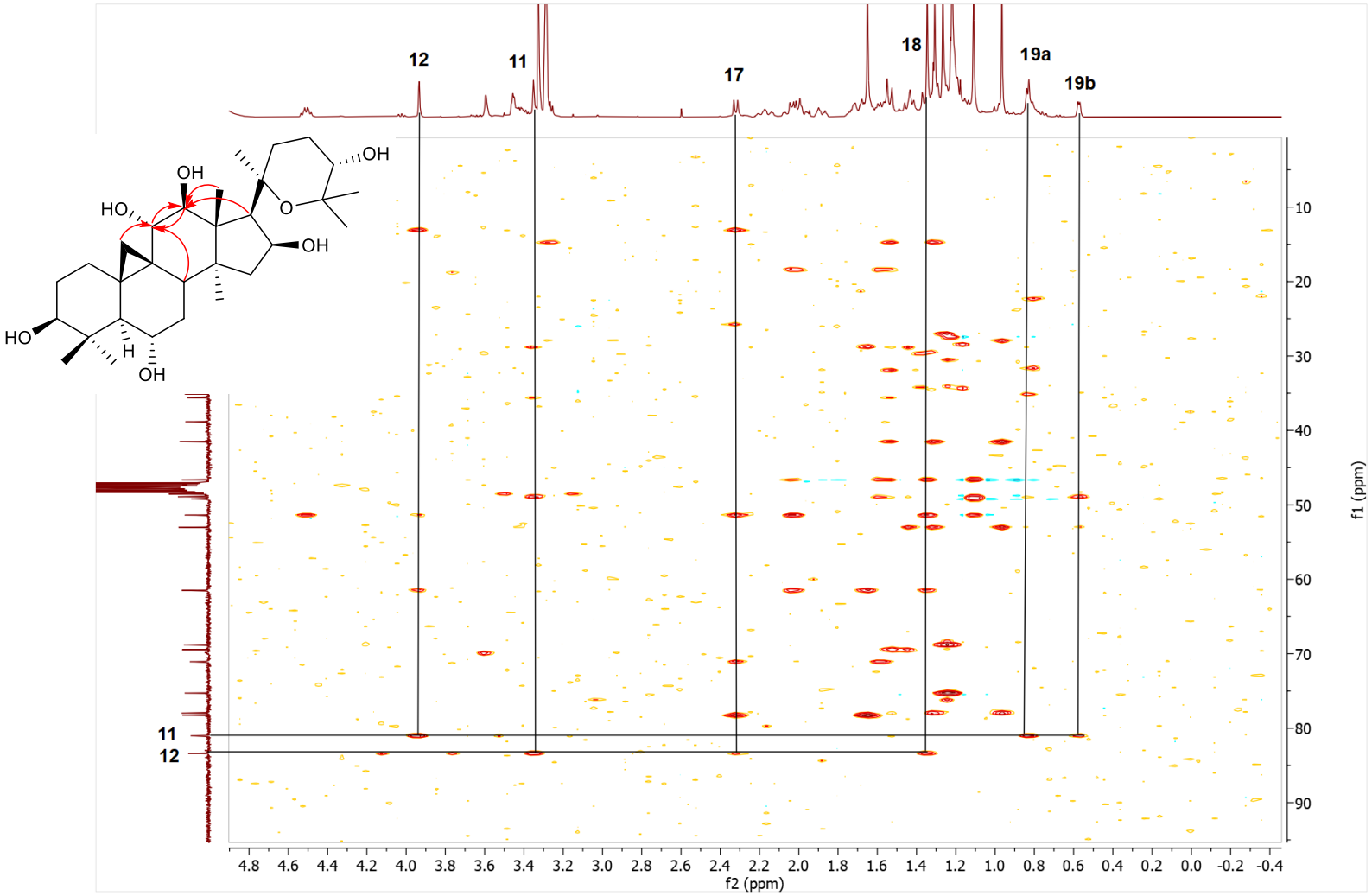

Spectrum 2.104. HMBC spectrum of compound **16**.

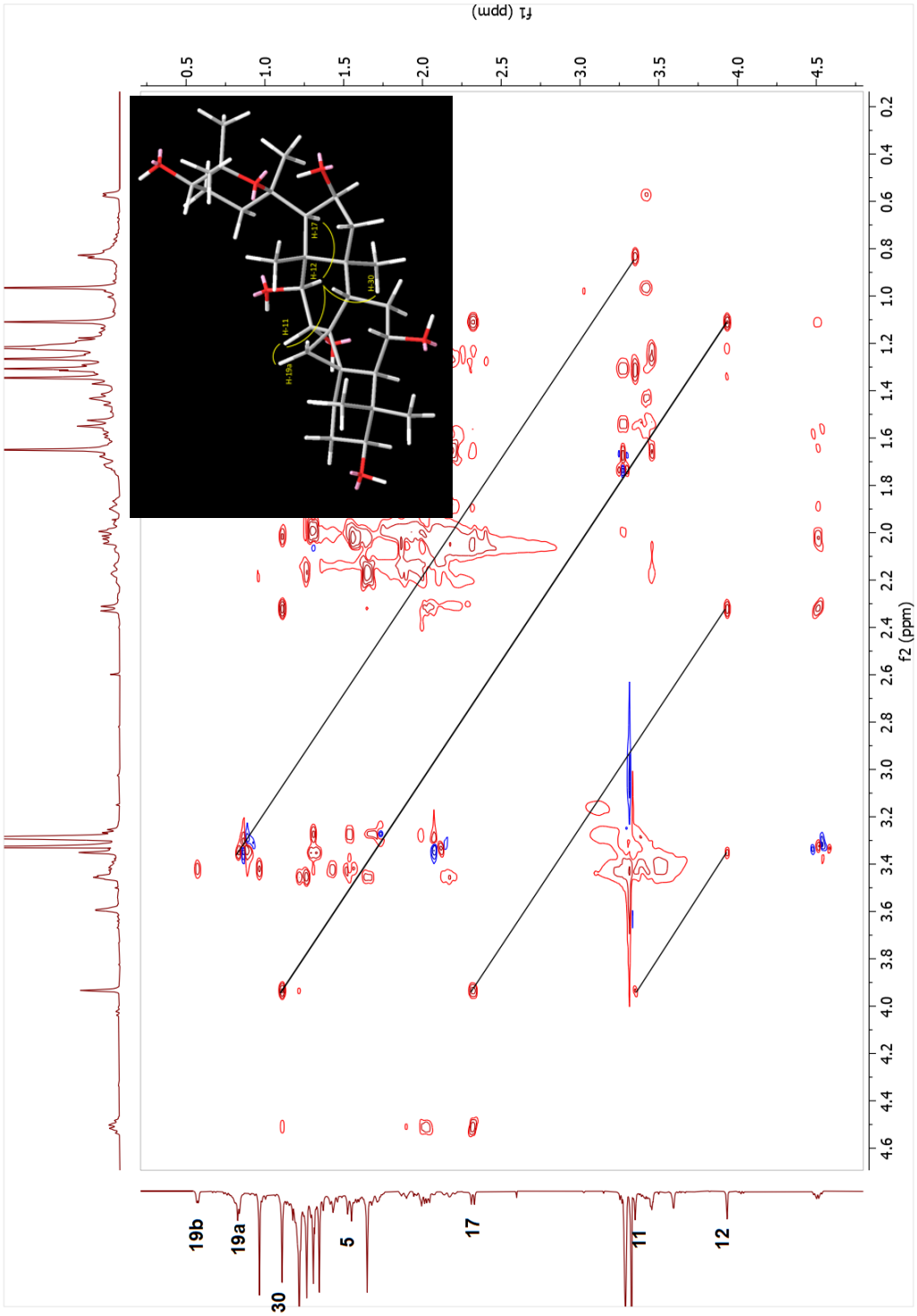

Spectrum 2.105. NOESY spectrum of compound **16**.

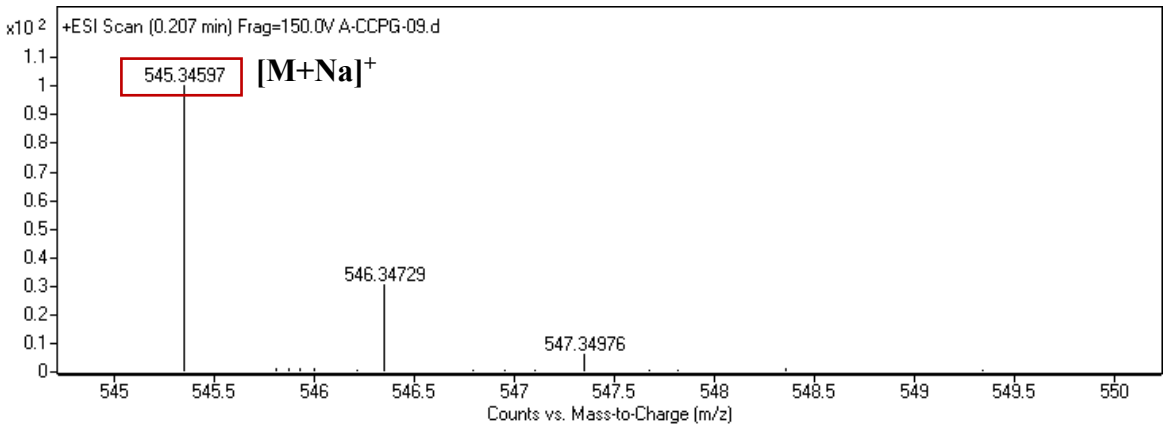

Spectrum 2.106. HR-ESI-MS spectrum of compound **16**.

2.3.2.17. Structure Elucidation of Compound 17

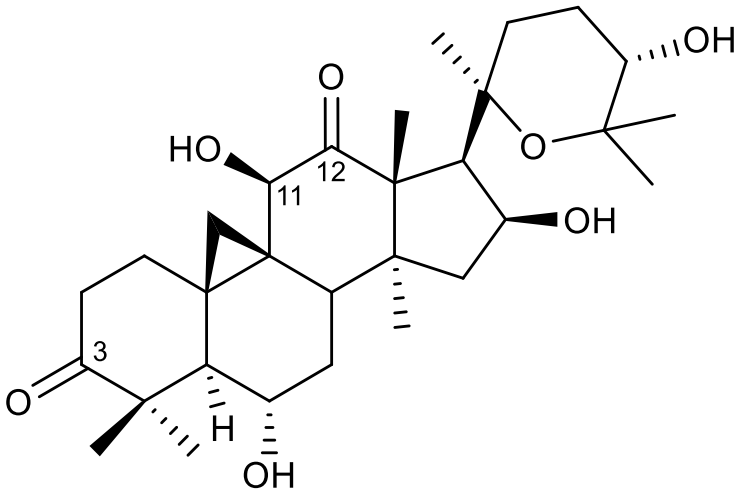

Figure 2.24. Chemical structure of compound **17**.

The HR-ESI-MS spectrum of **17** showed a major ion peak at *m/z* 541.31528 [M + Na]$^+$ ($C_{30}H_{46}NaO_7$). The oxymethine proton at C-3 was lost in the ^{1}H-NMR spectrum. A detailed inspection of ^{13}C-NMR and HMBC spectra suggested that the C-3 (δ_C 216.3) secondary alcohol had been oxidized. Additionally, the signal at δ_C 211.4 suggested an additional keto carbonyl group in **17**, which showed cross-peaks with H-17 (δ_H 2.33) and H-

18 (δ_H 1.72) in the HMBC spectrum, revealing oxidation at C-12. A broad singlet observed at δ_H 3.71 displaying a long-distance correlation with the C-12 (δ_C 211.4) indicated an additional oxymethine group. With these findings, a monooxygenation at C-11 was suggested. The configuration of C-11(OH) was deduced based on the 2D-NOESY data. The correlation of H-11 with α-oriented H_3-30 (δ_H 0.66) revealed that the configuration of the OH group at C-11 was β-oriented. Consequently, the structure of **17** was determined to be 20,25-epoxy-6α,11β,16β,24α-tetrahydroxycycloartan-3,12-dione.

Table 2.17. The ^{13}C and ^{1}H NMR data of **17** (100/400 MHz, δ ppm, in $CDCl_3$).

Position	δ_C (ppm)	δ_H (ppm), *J* (Hz)	Position	δ_C (ppm)	δ_H (ppm), *J* (Hz)
1	29.5†	1.24 m, 1.80 m	**16**	72.8	4.56 d (7.8)
2	36.1	2.54 t (6.6) (2H)	**17**	52.0	2.33 d (8.7)
3	216.3	-	**18**	13.9	-
4	50.2	-	**19**	22.0	0.51 d (4.8), 1.47 d (5.1)
5	53.6	1.86 d (9.9)	**20**	79.2	-
6	68.8	3.65 m	**21**	27.0	1.62 s
7	37.9	1.34 m, 1.52 m	**22**	26.9	1.42 m, 2.16 m
8	47.9†	2.23 m	**23**	23.1	1.72 m, 2.18 m
9	26.5	-	**24**	69.3	3.51 brs
10	29.7†	-	**25**	75.4	-
11	71.3	3.71 brs	**26**	27.9	1.28 s
12	211.4	-	**27**	27.5	1.19 s
13	59.8	-	**28**	27.2	1.38 s
14	46.5	-	**29**	20.7	1.24 s
15	47.9†	1.68 m, 2.12 m	**30**	21.7	0.66 s

†Overlapped signals

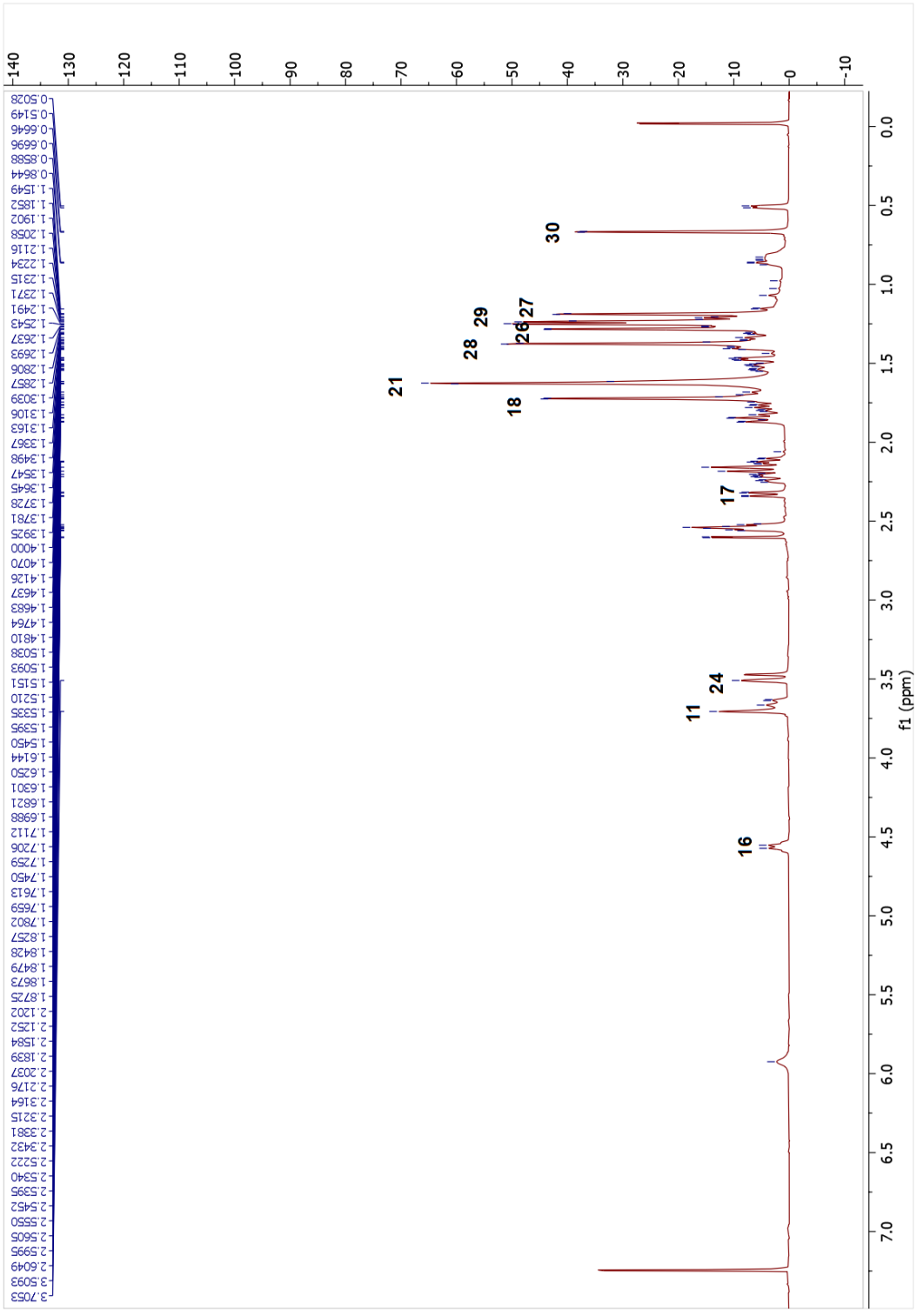

Spectrum 2.107. ^{1}H-NMR spectrum of compound **17**.

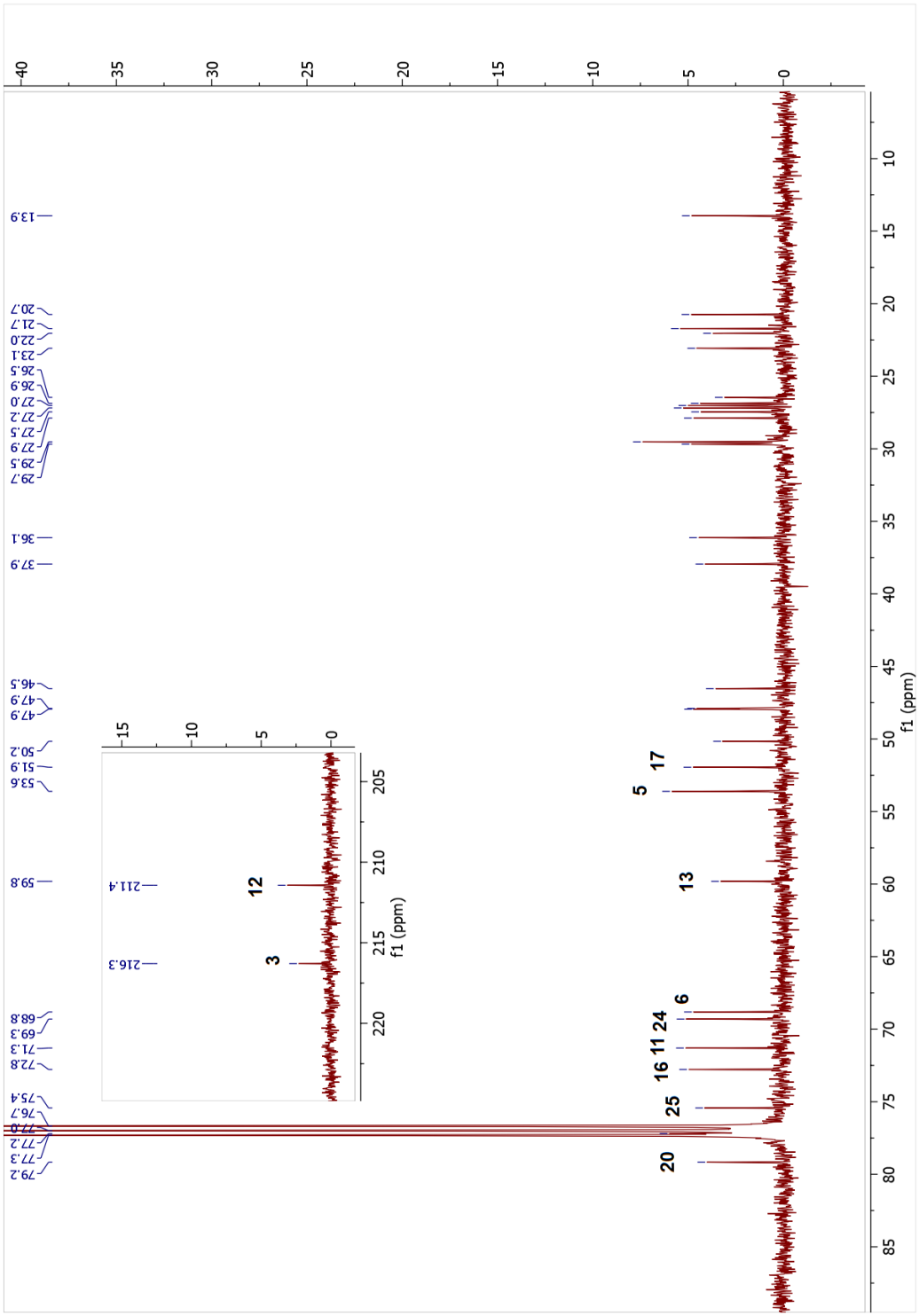

Spectrum 2.108. ^{13}C-NMR spectrum of compound **17**.

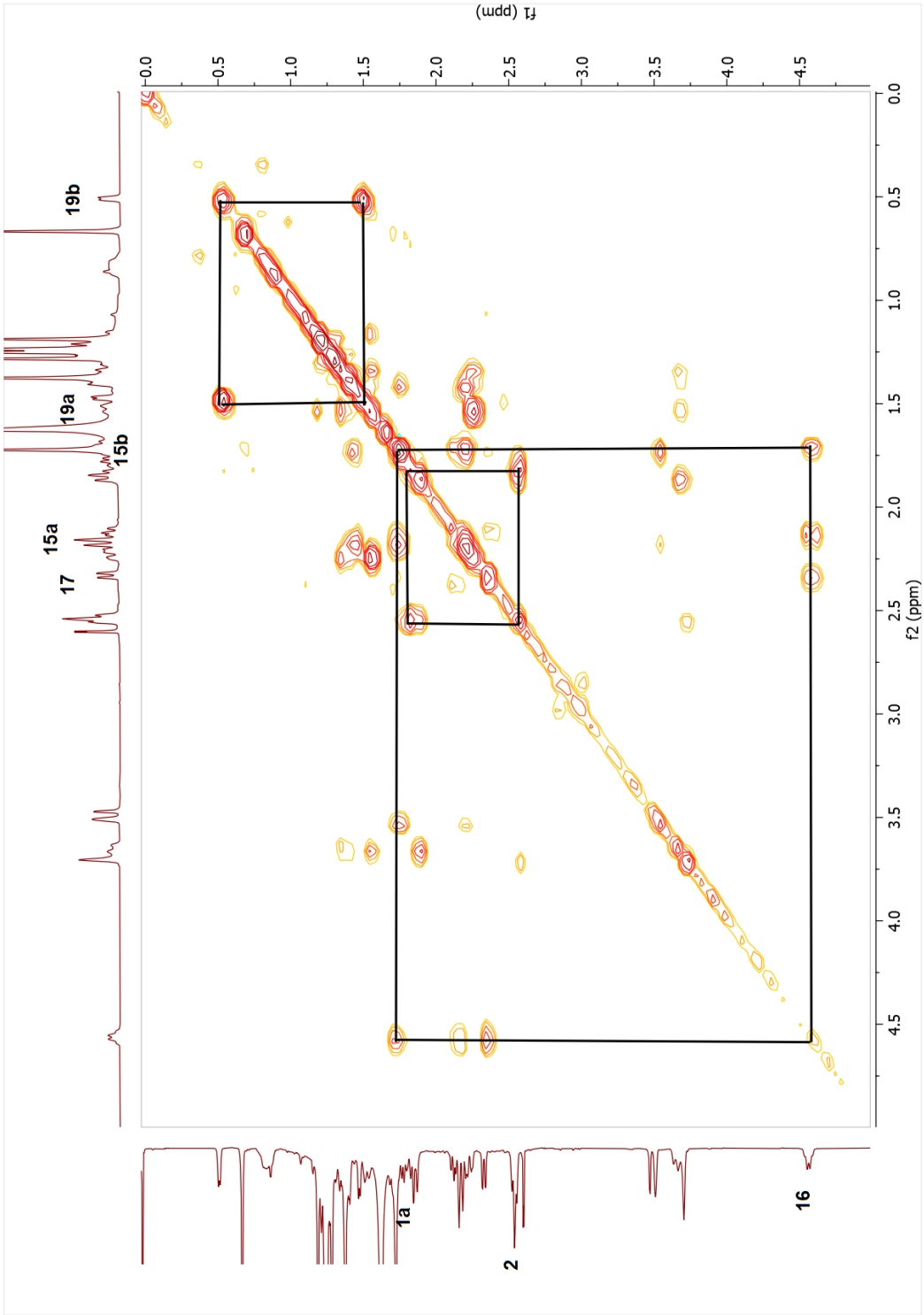

Spectrum 2.109. COSY spectrum of compound **17**.

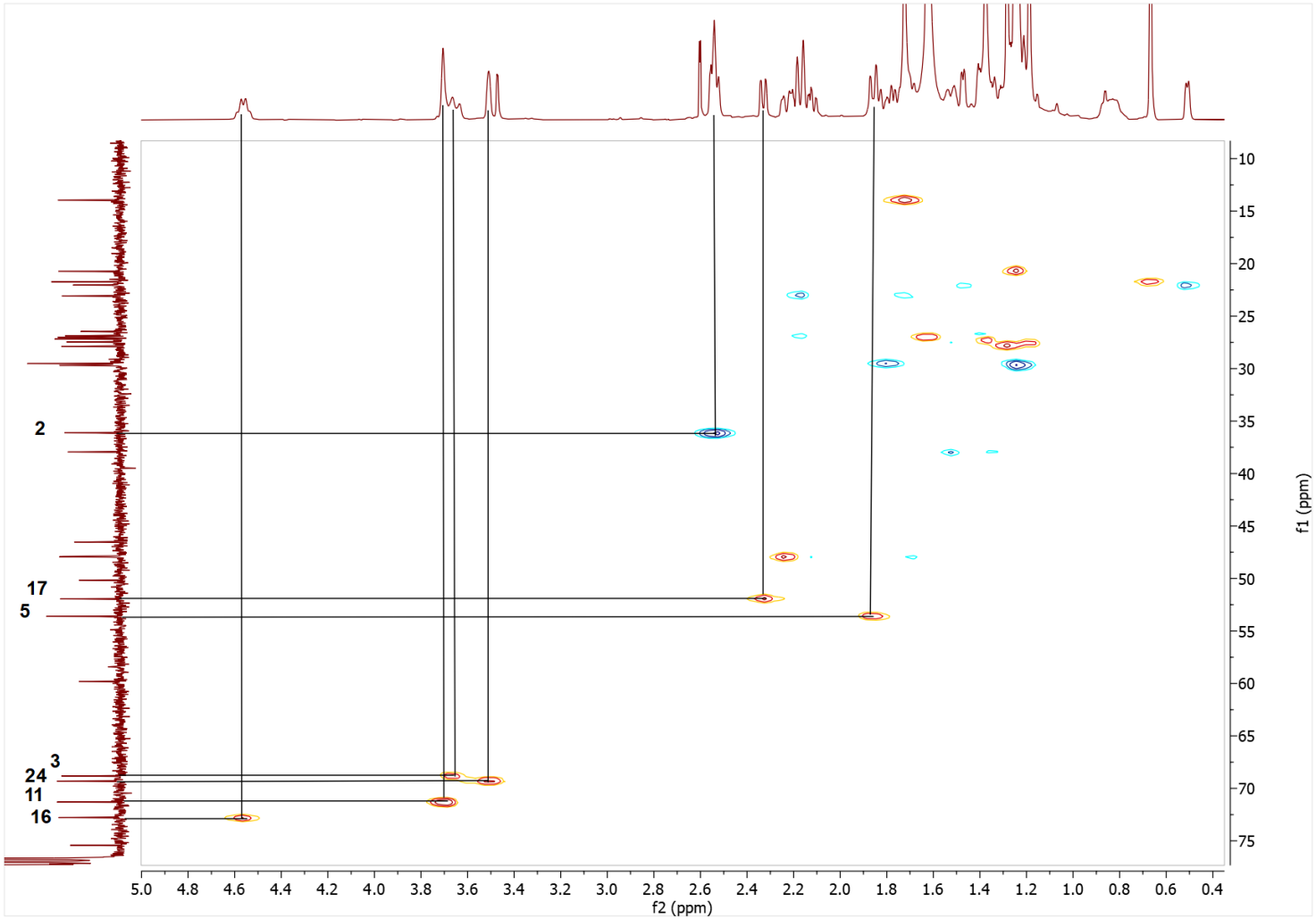

Spectrum 2.110. HSQC spectrum of compound **17**.

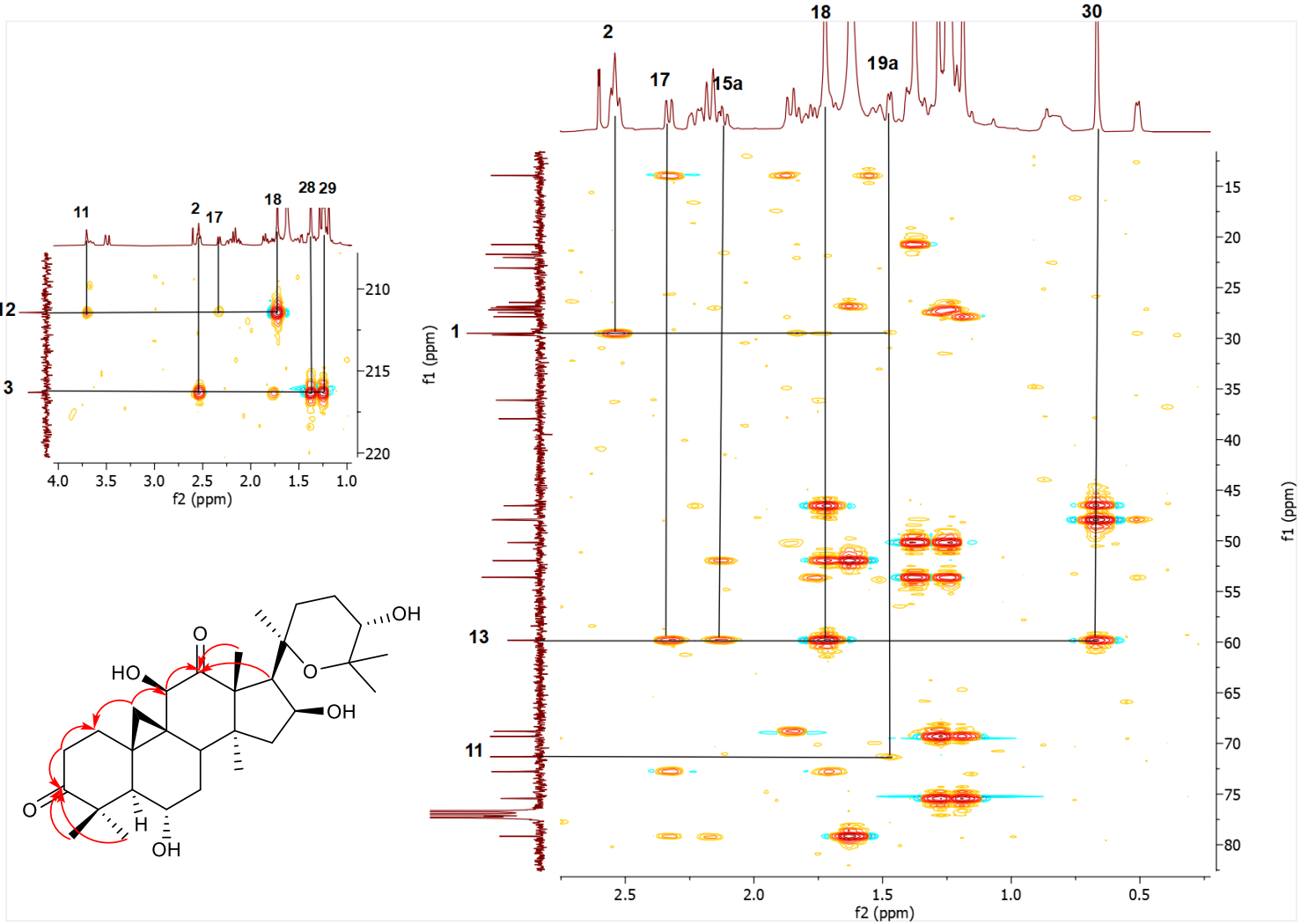

Spectrum 2.111. HMBC spectrum of compound **17**.

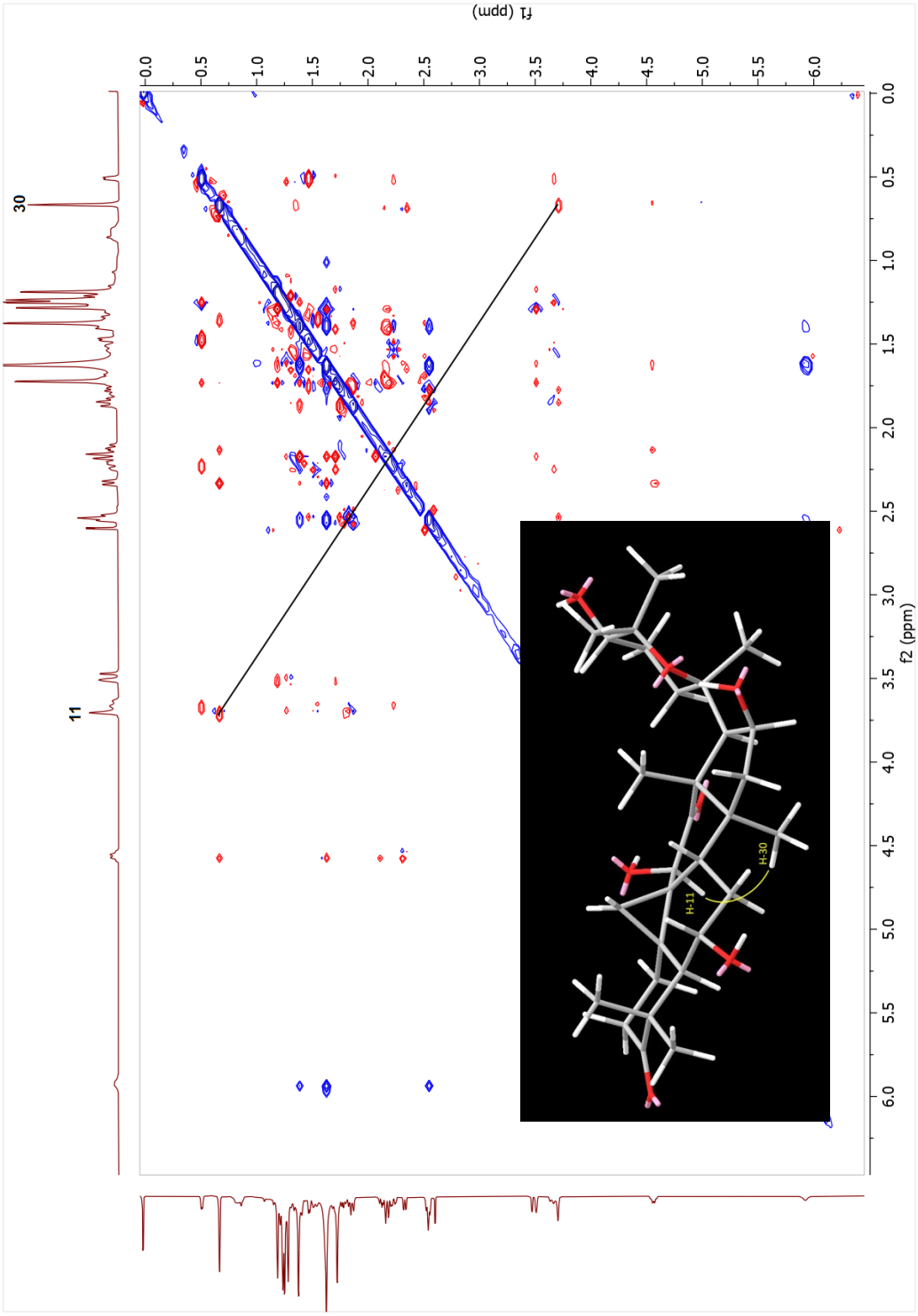

Spectrum 2.112. NOESY spectrum of compound **17**.

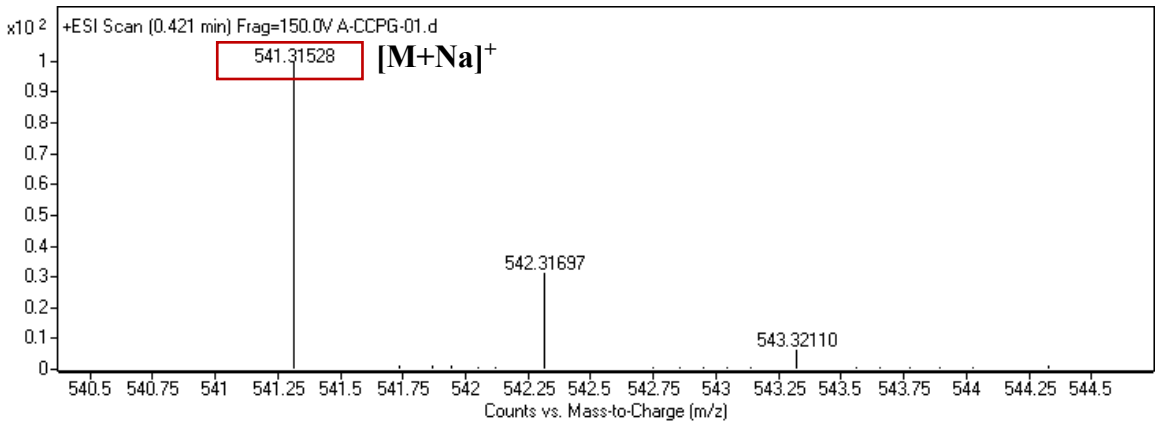

Spectrum 2.113. HR-ESI-MS spectrum of compound **17**.

2.3.2.18. Structure Elucidation of Compound 18

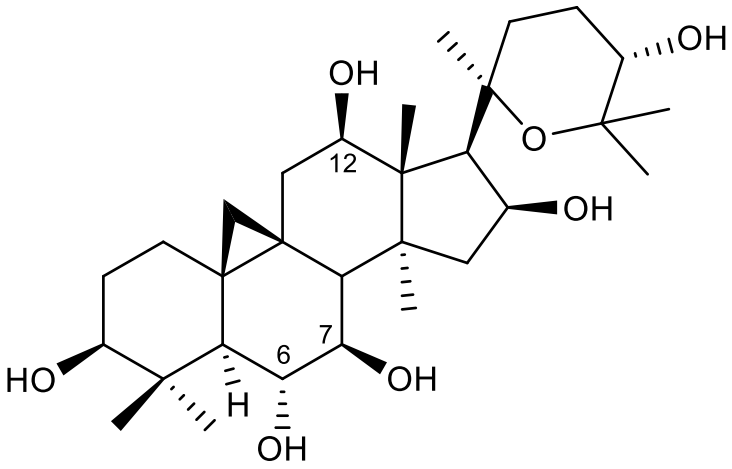

Figure 2.25. Chemical structure of compound **18**.

The HR-ESI-MS data of metabolite **18** displayed a sodium adduct ion at *m/z* 545.34775 $[M + Na]^+$ (calcd. 545.34542 for $C_{30}H_{50}NaO_7$). The mass data exhibited a 32 amu increase over **1**, and an appearance of two additional carbon signals at 71.4 and 73.2 ppm suggested a dihydroxy analog. In the HMBC spectrum, the $^3J_{H\text{-}C}$ correlations from the characteristic H-17 (δ_H 2.53) and H_3-18 (δ_H 1.88) resonances to the new signal at δ_C 71.4 (C-

12) verified the position of the first hydroxylation at C-12. The ^{13}C-NMR spectrum of **18** showed that C-6 (δ_C 73.2) and C-8 (δ_C 52.4) signals underwent a significant down-field shift (ca. 4.9 and 5.3 ppm, respectively) when compared to **1**, suggesting the second hydroxylation at C-7. In the COSY spectrum, identification of the spin system starting from H-5 [H-5 (δ_H 1.80 d, J = 9.3 Hz) → H-6 (δ_H 3.74) → H-7 (δ_H 3.71 s) → H-8 (δ_H 2.40 d, J = 6.9 Hz)], together with long-range correlations from H-6 and H-8 to C-7 (δ_C 75.7) in the HMBC spectrum verified the location of the transformation. In the 2D-NOESY spectrum, the correlations of H-12 with α-oriented H_3-30 (δ_H 1.03)/H-17 (δ_H 2.53), and cross-peaks between H-7 and α-oriented H_3-30/H-5 (δ_H 1.80) revealed the configurations of OH groups. Consequently, metabolite **18** was elucidated as 20,25-epoxy-3β,6α,7β,12β,16β,24α-hexahydroxycycloartane.

Table 2.18. The ^{13}C and ^{1}H NMR data of **18** (100/400 MHz, δ ppm, in C_5D_5N).

Position	δ_C (ppm)	δ_H (ppm), *J* (Hz)	Position	δ_C (ppm)	δ_H (ppm), *J* (Hz)
1	32.1	1.34 m, 1.61 m	**16**	71.5	4.84 m
2	30.9	1.88 m, 1.97 m	**17**	61.8	2.53 d (7.5)
3	77.8	3.61 m	**18**	13.4	1.88 s
4	42.0	-	**19**	29.8	0.40 d (4.5), 0.92 d (4.4)
5	50.8	1.80 d (9.3)	**20**	78.5	-
6	73.2	3.74 m	**21**	26.9	2.02 s
7	75.7	3.71 m	**22**	29.5	2.29 m, 2.63 m
8	52.4	2.40 d (6.9)	**23**	23.7	1.90 m, 2.29 m
9	20.9	-	**24**	69.0	3.70 brs
10	29.1	-	**25**	75.7	-
11	36.7	1.67 m, 2.43 d (5.6)	**26**	28.4	1.37 s
12	71.4	4.21 m	**27**	28.1	1.58 s
13	52.5	-	**28**	28.8	1.86 s
14	47.9	-	**29**	15.4	1.32 s
15	50.4	2.45 m, 2.69 d (8.3)	**30**	19.5	1.03 s

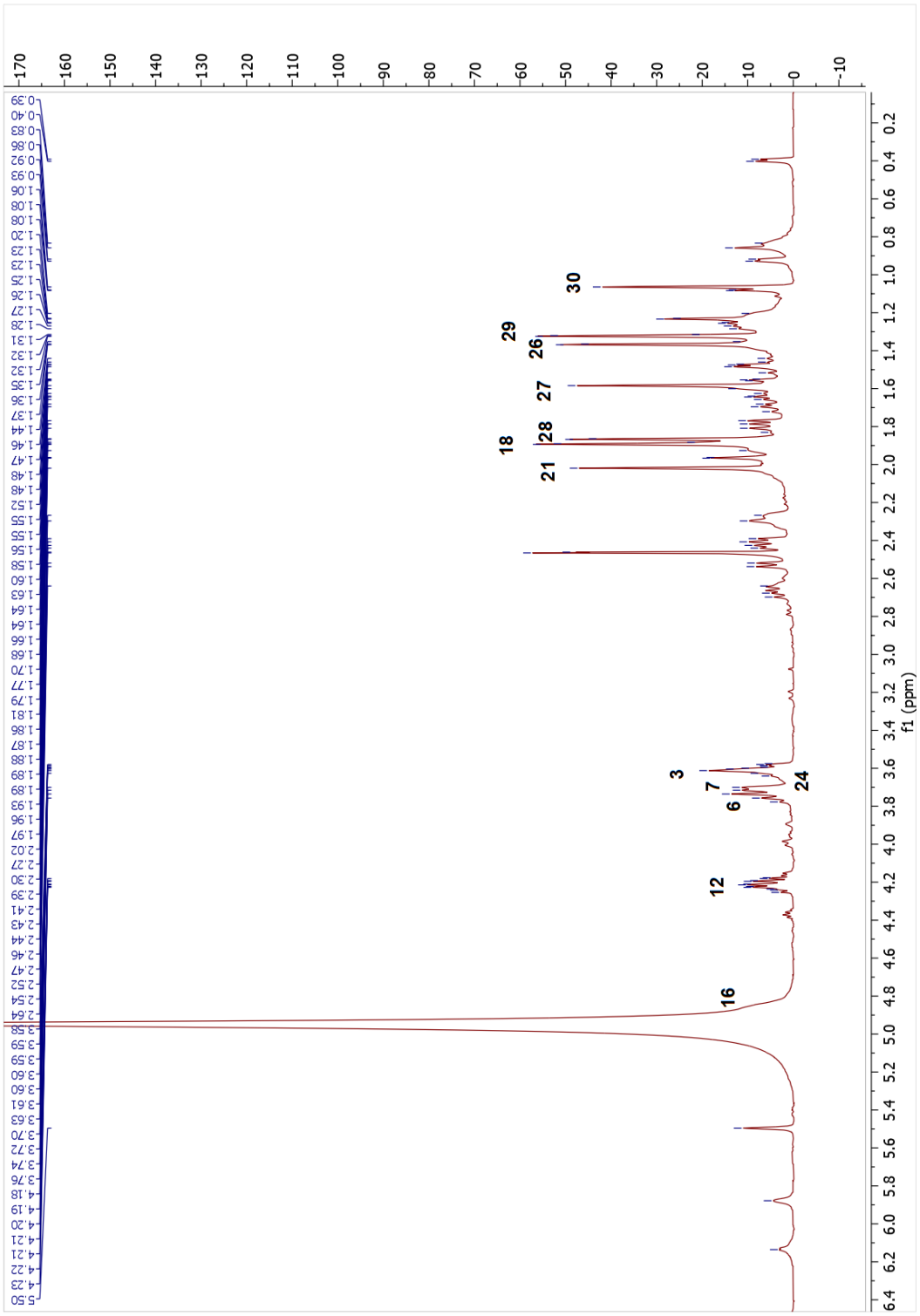

Spectrum 2.114. ^{1}H-NMR spectrum of compound **18**.

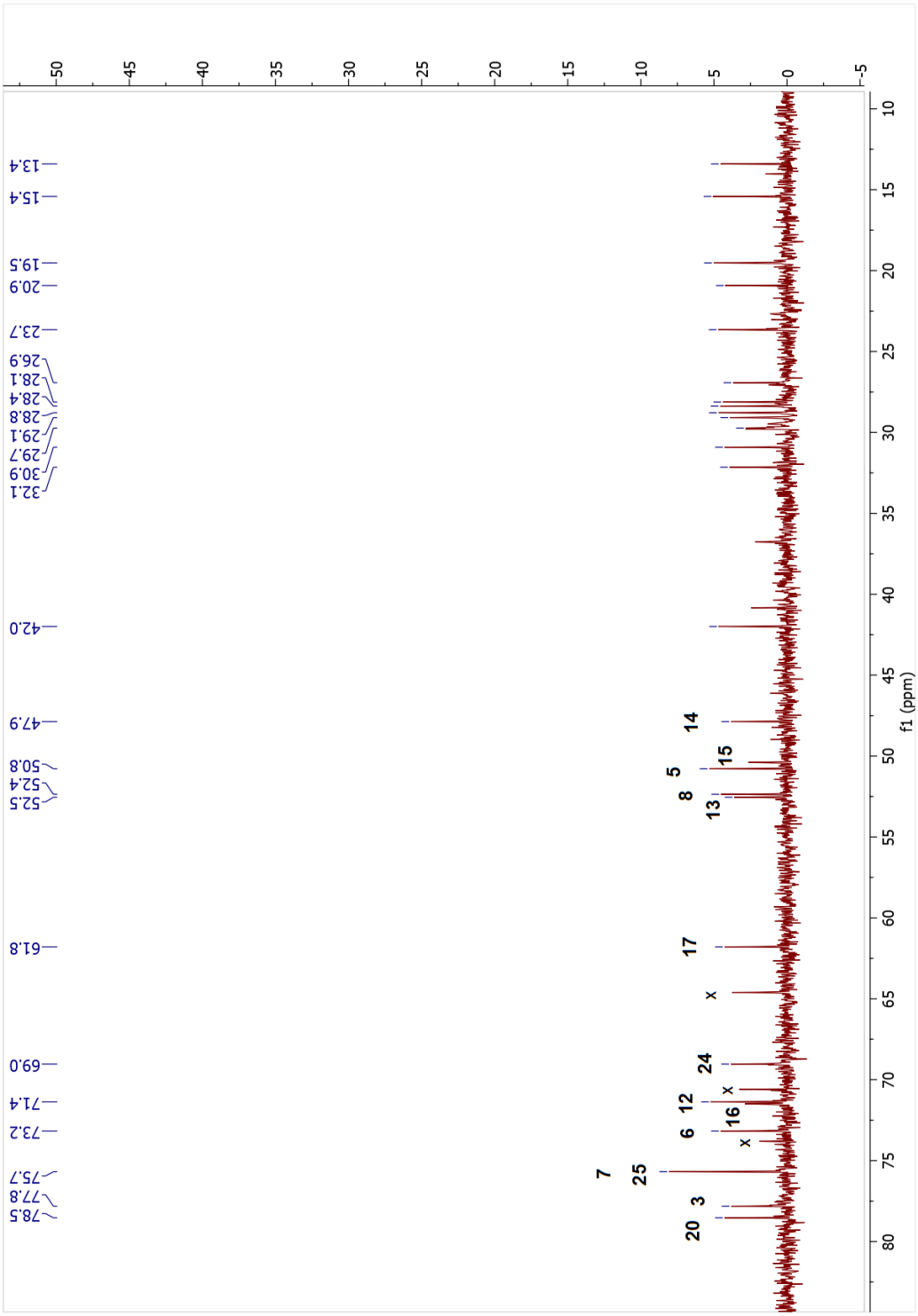

Spectrum 2.115. ^{13}C-NMR spectrum of compound **18**.

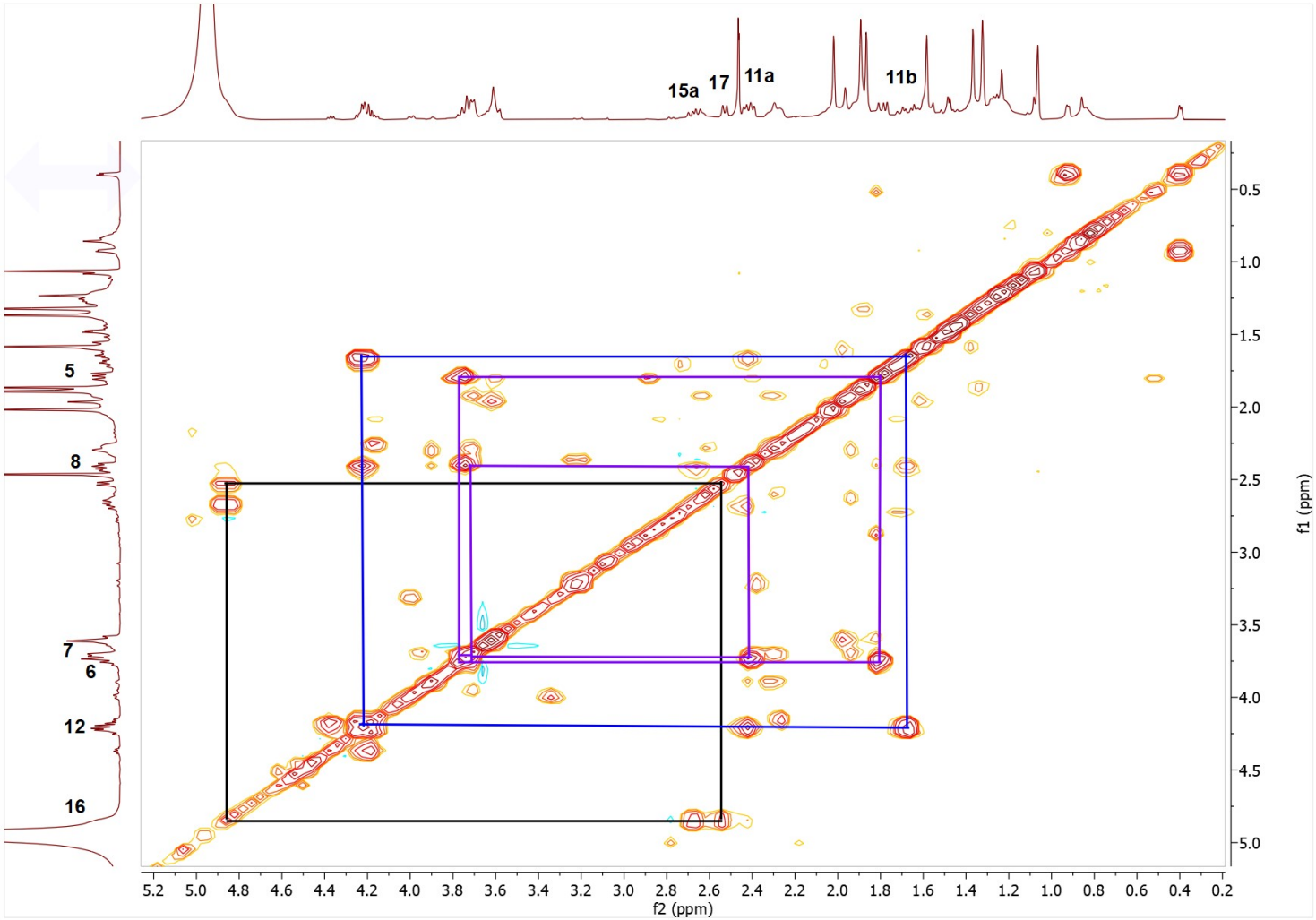

Spectrum 2.116. COSY spectrum of compound **18**.

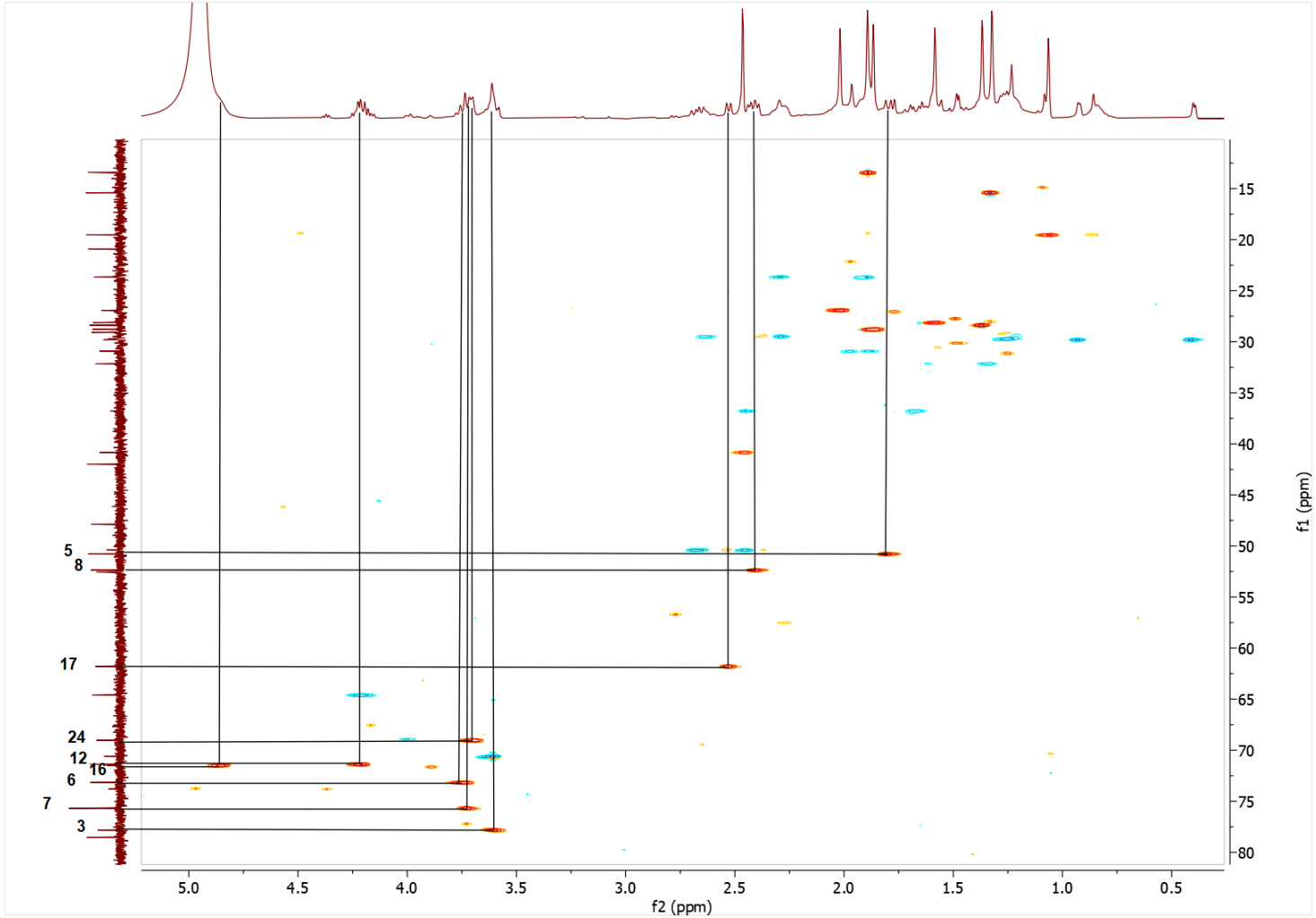

Spectrum 2.117. HSQC spectrum of compound **18**.

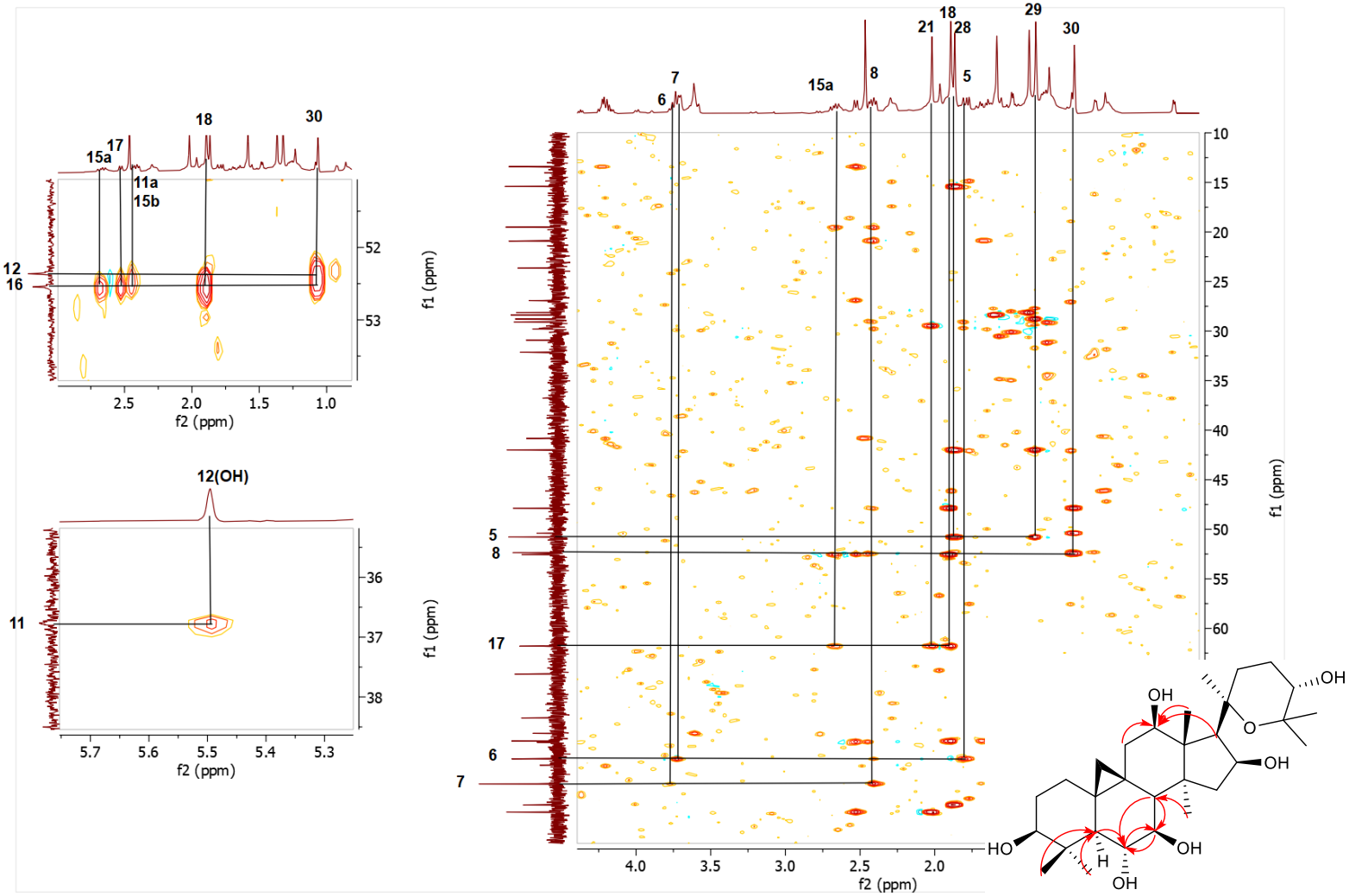

Spectrum 2.118. HMBC spectrum of compound **18**.

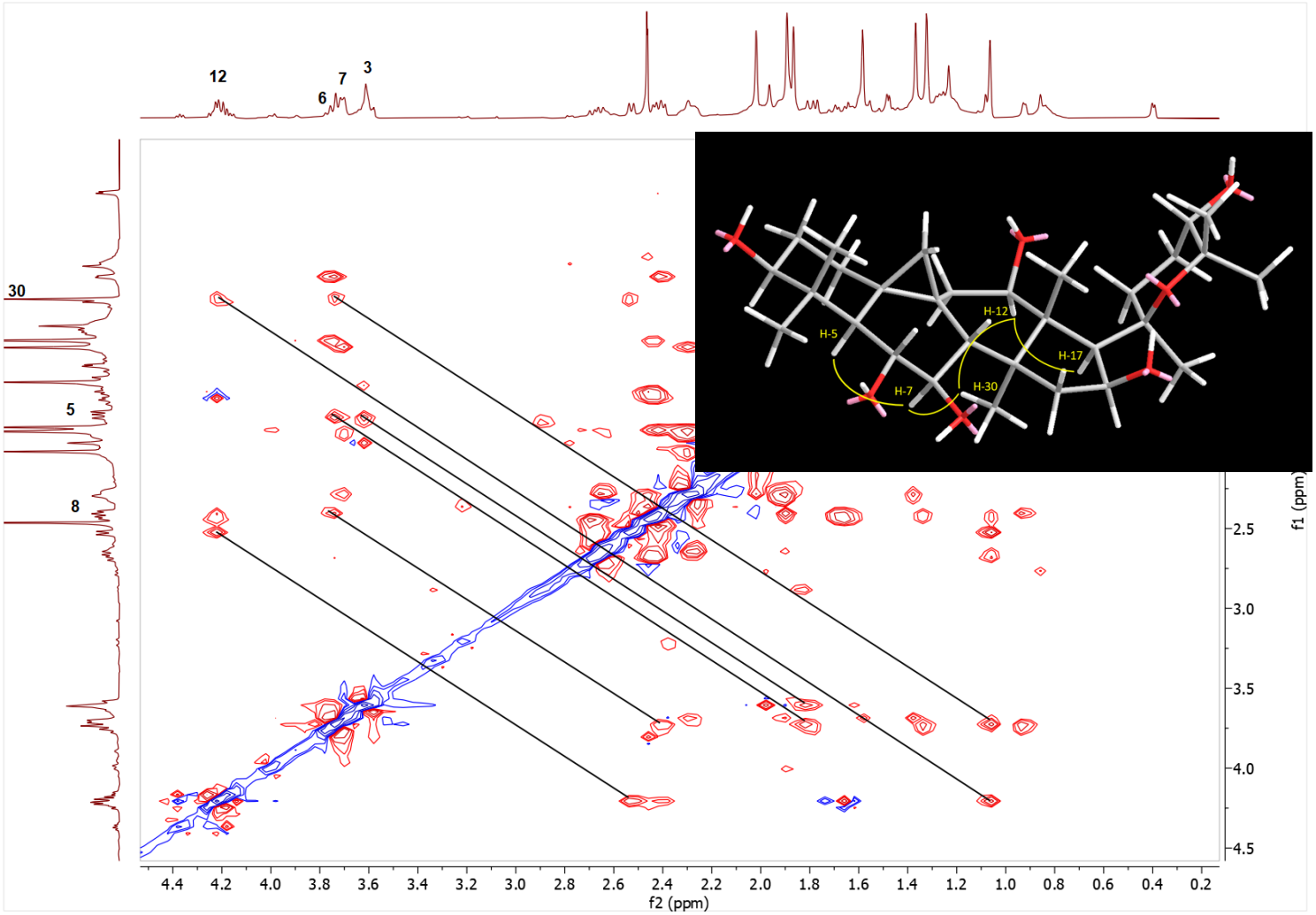

Spectrum 2.119. NOESY spectrum of compound **18**.

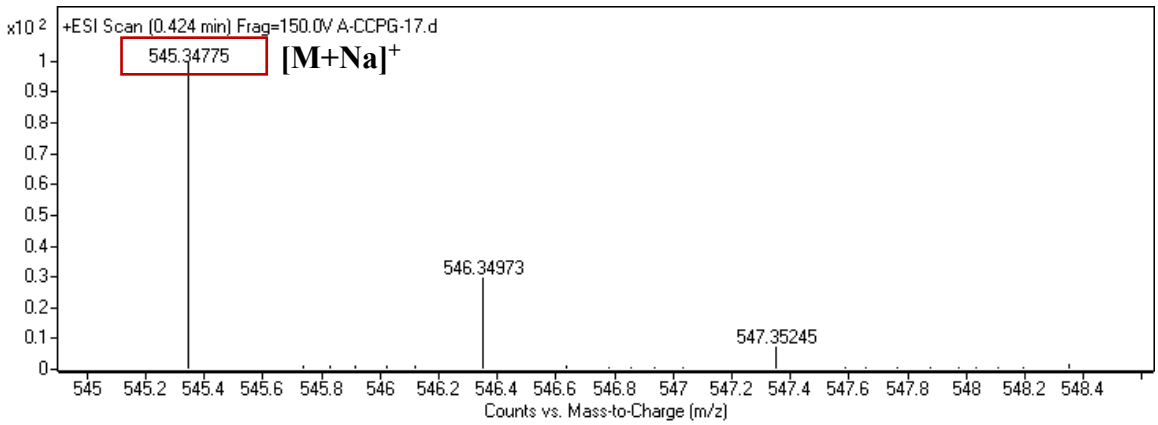

Spectrum 2.120. HR-ESI-MS spectrum of compound **18**.

2.3.2.19. Structure Elucidation of Compound 19

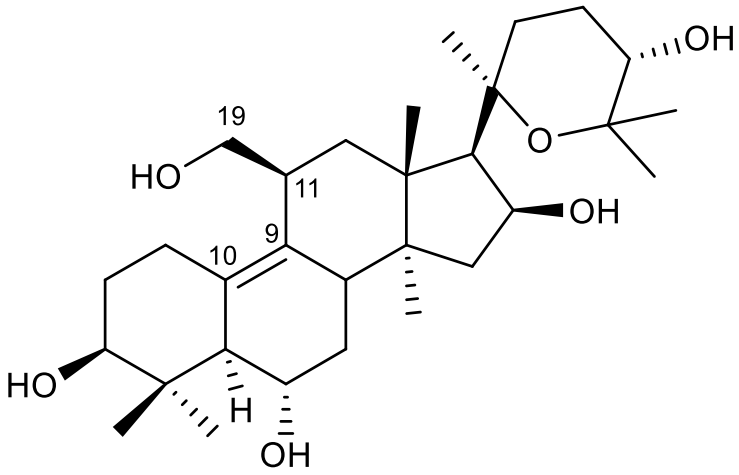

Figure 2.26. Chemical structure of compound **19**.

The metabolite **19** gave a molecular formula of $C_{30}H_{50}O_6$ based on the HR-ESI-MS data (*m/z* 529.35144 $[M + Na]^+$, calcd for $C_{30}H_{50}NaO_6$, 529.35051) indicating a 16 amu increase over **1**, suggesting being a monohydroxy derivative. In the ^{1}H-NMR spectrum of **19**, the absence of the AX system signals deriving from the characteristic 9,19-cyclopropane ring implied a ring cleavage. In the ^{13}C-NMR spectrum, an additional oxymethylene group at δ_C

68.5 and two olefinic carbon signals (δ_C 134.5, 132.7) were observed in the low field. In the HSQC spectrum, no correlation of double bond carbons with any proton indicated a tetrasubstituted olefinic system. The structure of **19** was proposed to have a C-9(10) double bond with a primary alcohol substitution at C-11 based on our previous biotransformation studies[49,73,74,76]. This assumption was confirmed with the $^{2}J_{H\text{-}C}$ and $^{3}J_{H\text{-}C}$ correlations in the HMBC spectrum (H-5 to C-9 and C-10; H_2-12 to C-9, C-11 and C-19). The orientation of C-19 extending from C-11 was deduced as β based on the correlation from H-11 (δ_H 3.32) to α-oriented H_3-30 (δ_H 0.81). In conclusion, the structure of metabolite **19** was determined to be 20,25-epoxy-3β,6α,16β,19,24α-pentahydroxy-ranunculan-9(10)-ene.

Table 2.19. The ^{13}C and ^{1}H NMR data of **19** (100/400 MHz, δ ppm, in C_5D_5N).

Position	δ_C (ppm)	δ_H (ppm), *J* (Hz)	Position	δ_C (ppm)	δ_H (ppm), *J* (Hz)
1	29.0	1.86 m, 2.91 d (9.1)	**16**	73.7	4.94 t (6.9)
2	32.8	1.85 m, 2.02 m	**17**	60.7	2.20 d (7.7)
3	77.2	3.73 m	**18**	19.8	1.61 s
4	42.0	-	**19**	68.5	3.91 m, 3.97 m
5	57.5	2.72 d (7.2)	**20**	78.4	-
6	67.5	4.14 t (8.4)	**21**	29.2	1.55 s
7	37.1	1.70 d (11.8), 2.02 m	**22**	26.4	1.22 d (14.0), 3.26 d (13.9)
8	40.7	2.65 d (11.7)	**23**	23.7	1.83 m, 2.11 m
9	132.7	-	**24**	68.6	3.65 brs
10	134.5	-	**25**	74.7	-
11	39.4	3.32 m	**26**	28.6	1.44 s
12	33.8	1.85 m, 2.78 d (13.9)	**27**	27.7	1.29 s
13	45.7	-	**28**	27.3	1.77 s
14	45.3	-	**29**	15.0	1.08 s
15	45.3	1.90 d (14.3), 2.09 d (12.7)	**30**	19.3	0.81 s

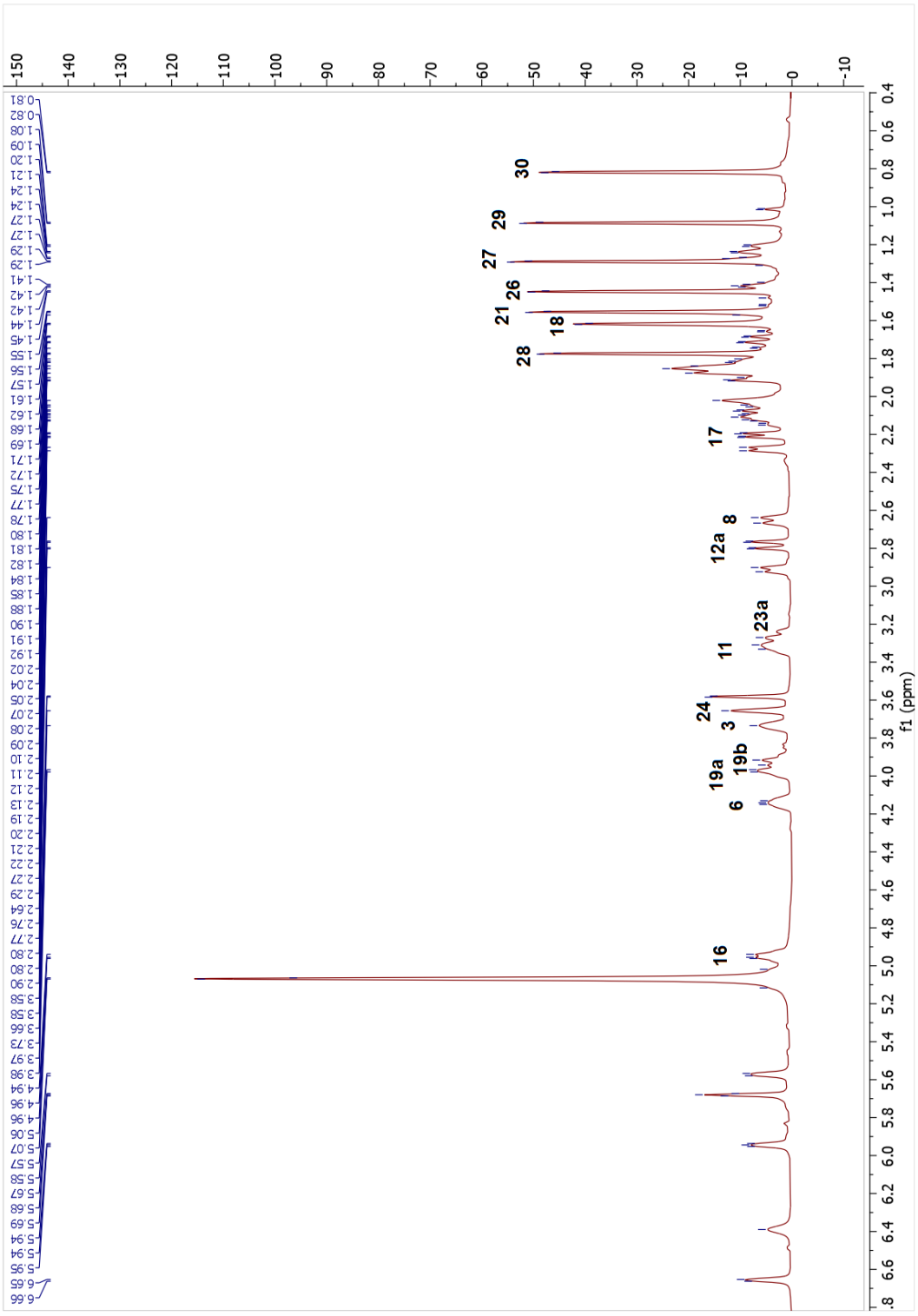

Spectrum 2.121. ^{1}H-NMR spectrum of compound **19**.

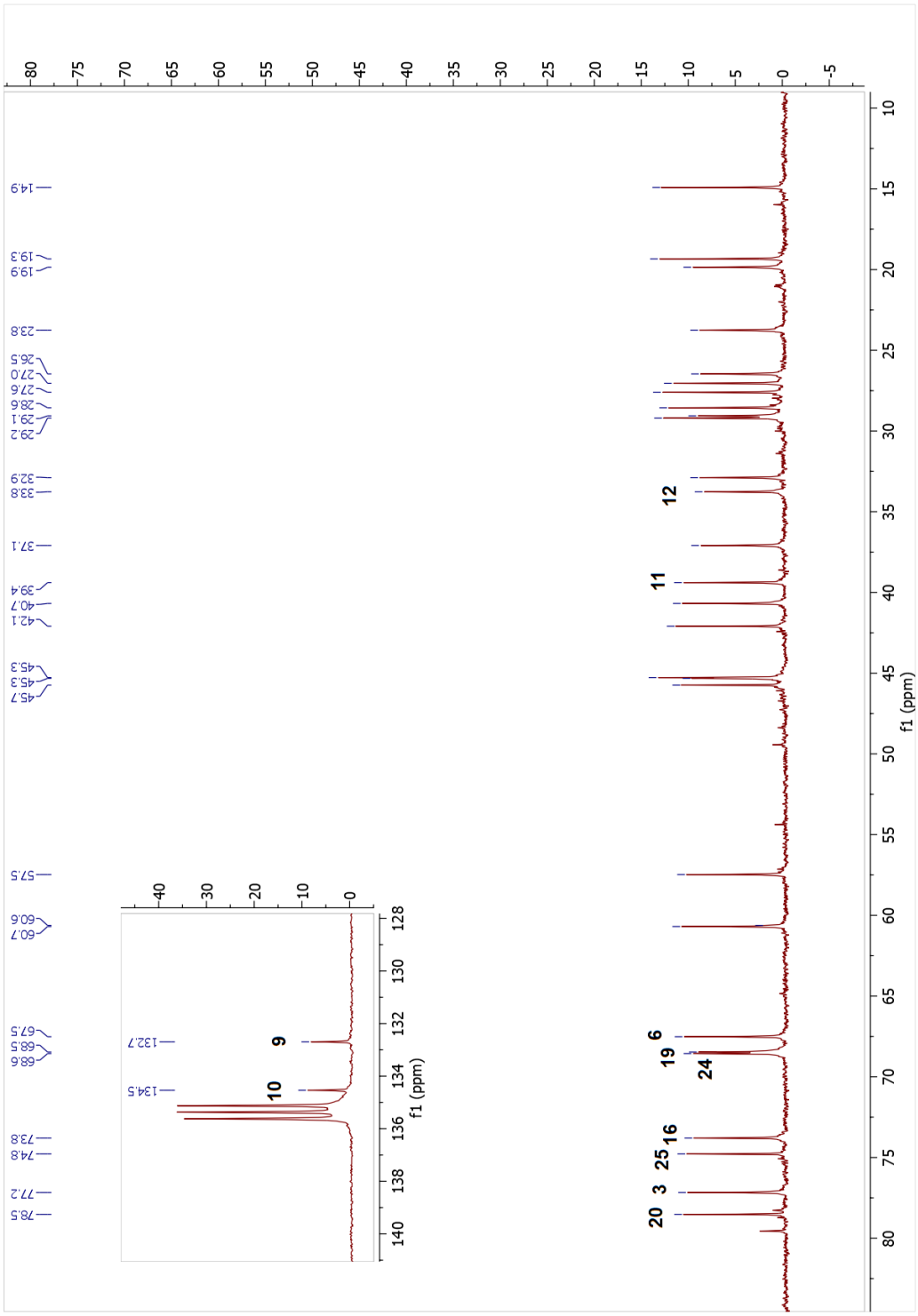

Spectrum 2.122. ^{13}C-NMR spectrum of compound **19**.

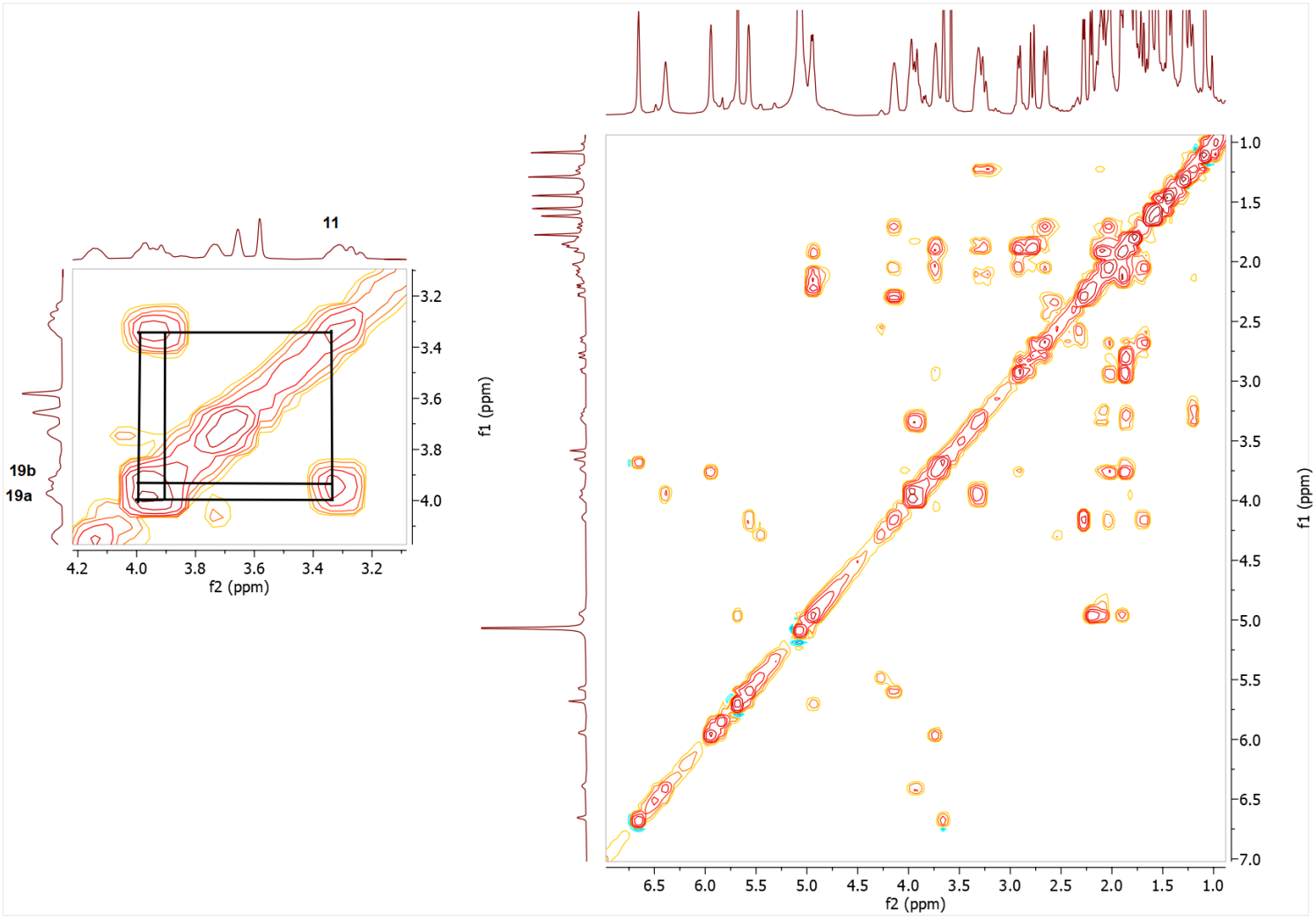

Spectrum 2.123. COSY spectrum of compound **19**.

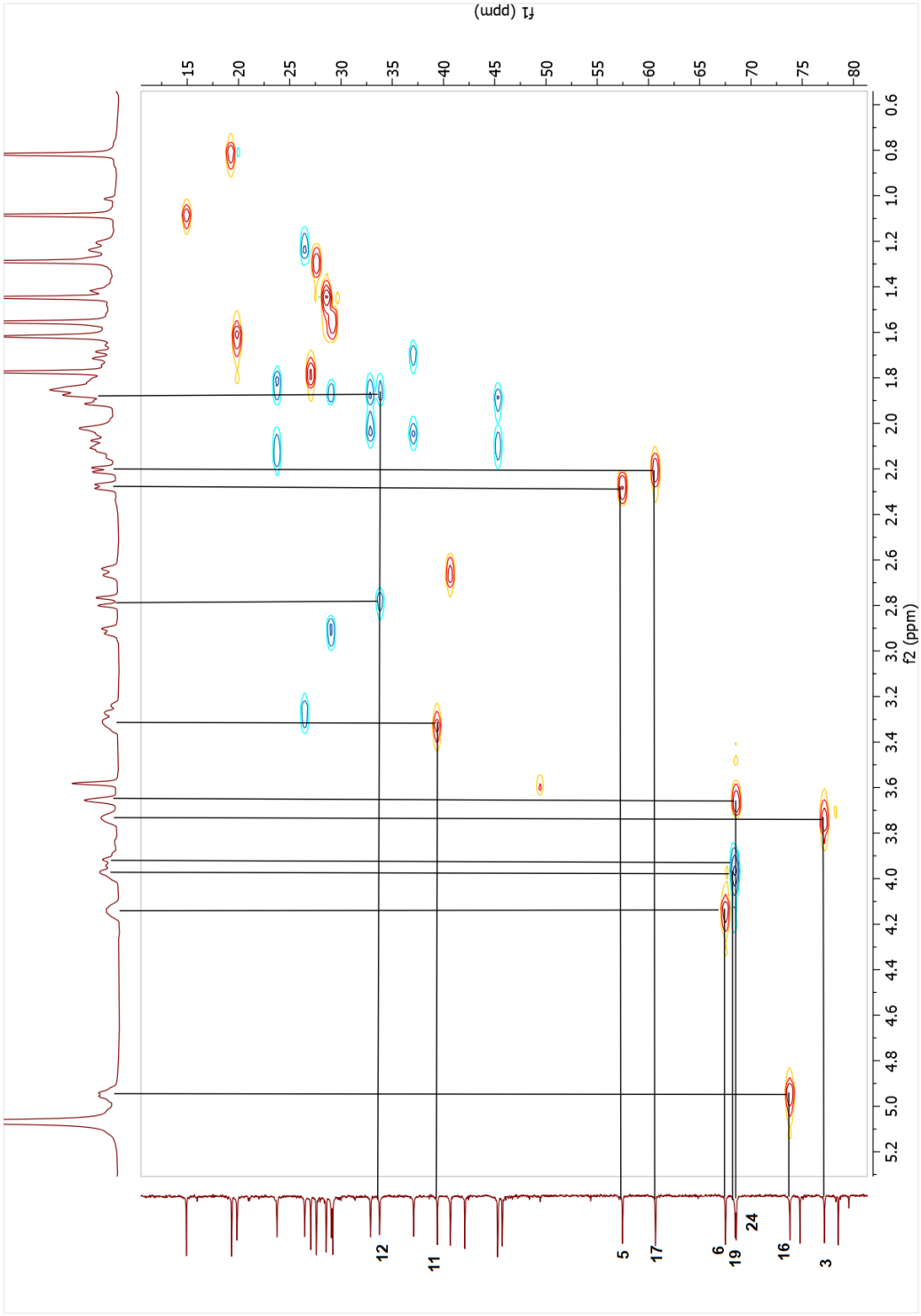

Spectrum 2.124. HSQC spectrum of compound **19**.

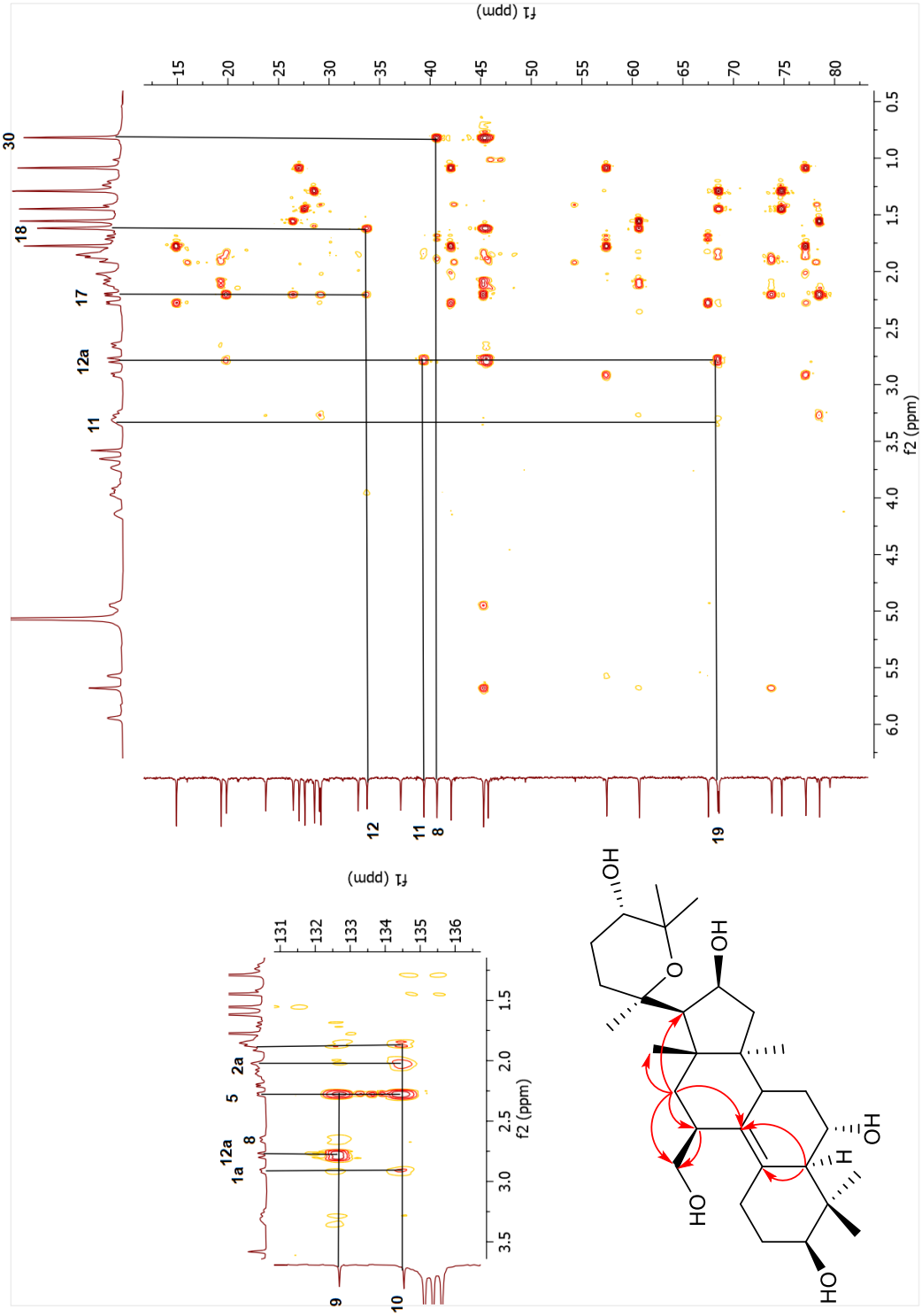

Spectrum 2.125. HMBC spectrum of compound **19**.

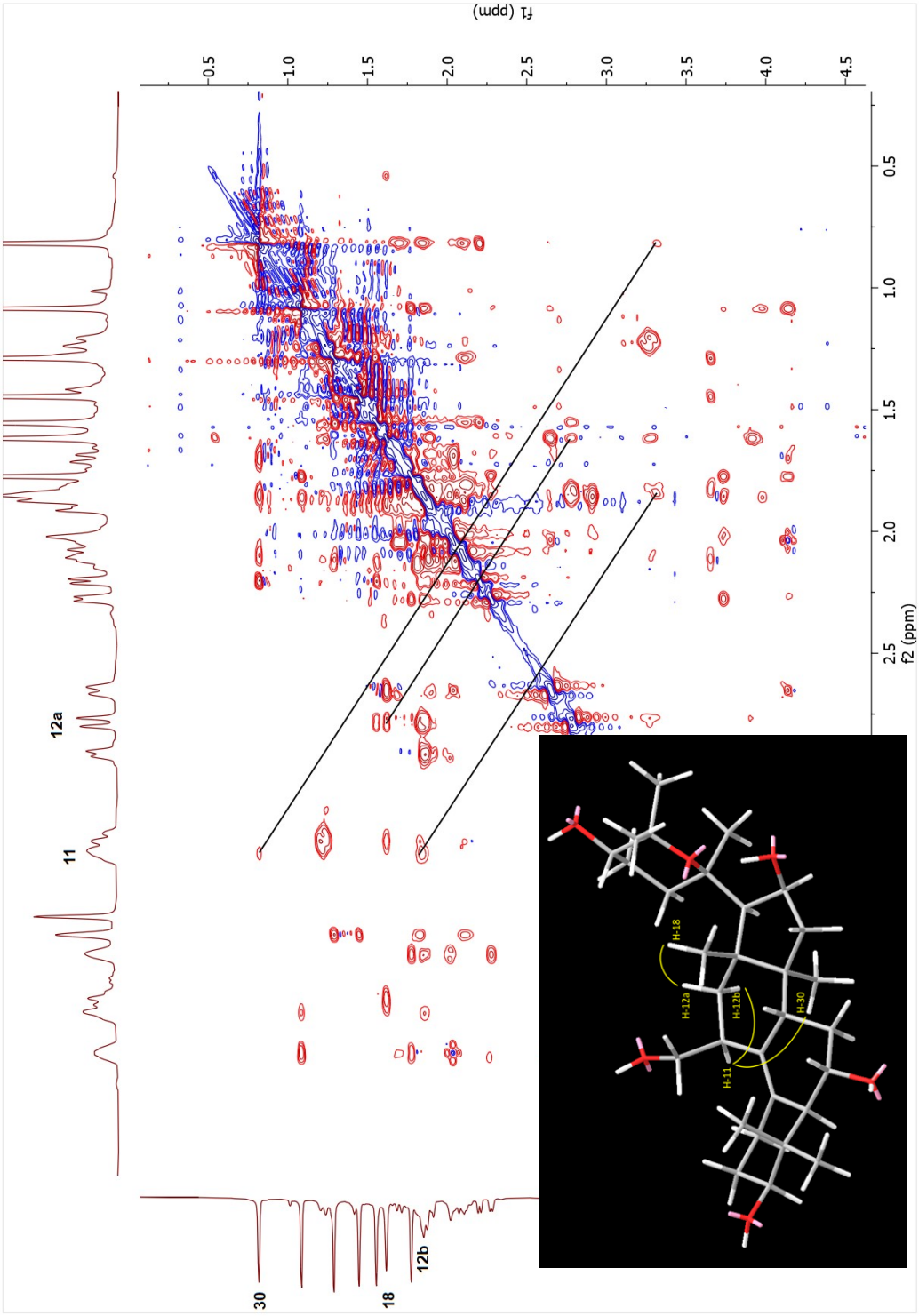

Spectrum 2.126. NOESY spectrum of compound **19**.

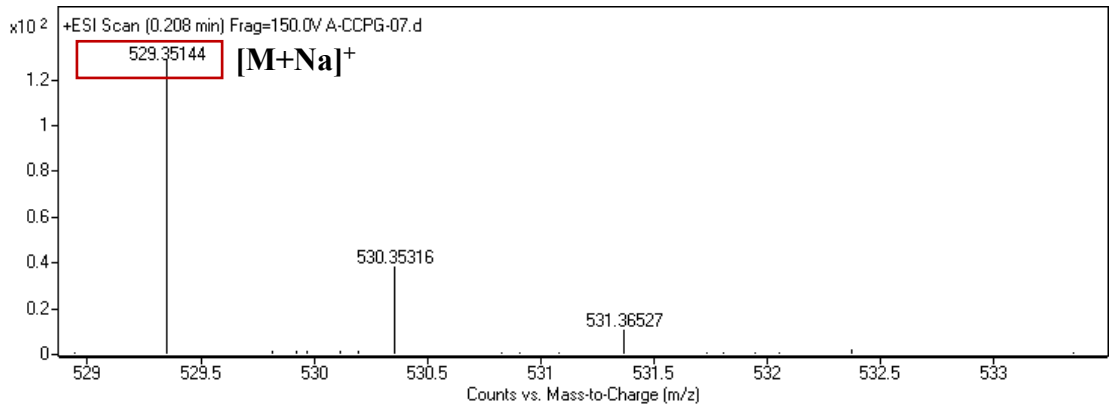

Spectrum 2.127. HR-ESI-MS spectrum of compound **19**.

2.3.2.20. Structure Elucidation of Compound 20

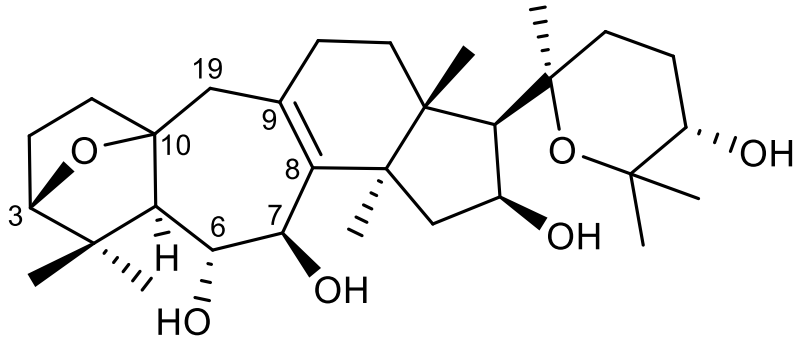

Figure 2.27. Chemical structure of compound **20**.

The molecular formula of **20** was established as $C_{30}H_{48}O_6$ by HR-ESI-MS analysis (*m/z* 527.33874 $[M + Na]^+$, calcd for $C_{30}H_{48}NaO_6$, 527.33486). In the ^{1}H-NMR spectrum, the disappearance of the 9,19-cyclopropane ring signal suggested a ring cleavage. In the ^{13}C-NMR spectrum, apart from the C-3, C-6, C-16 and C-24 oxygen-bearing methine carbons, two additional signals at δ_C 80.2 and 88.7 were detected. The ^{13}C-NMR spectrum of **20** also exhibited two olefinic carbon resonances at δ_C 126.7 and 139.5. In the HSQC spectrum, no correlation of these carbons with any proton indicated the tetra-substituted nature of the double bond. The δ_C 126.7 and 139.5 resonances were assigned to C-9 and C-8, respectively,

based on the long-distance correlations in the HMBC spectrum (C-9 to H_2-12; C-8 to H_2-12 and H_3-30). The signal observed at δ_H 4.39 suggested an additional oxymethine group corresponding to a carbon at δ_C 80.2 in the HSQC spectrum. A detailed inspection of the ^1H and ^{13}C NMR spectra showed down-field shifts for H-6 and C-6 signals (ca. 0.64 and 8.6 ppm, respectively) when compared to that of **1**, therefore, a hydroxylation at C-7 was suggested. The COSY and HSQC spectra revealed a spin system of H-5 (δ_H 1.47) → H-6 (δ_H 4.42) → H-7 (δ_H 4.39), justifying this assignment. The carbon signal at 86.3 ppm was readily assigned to C-3 because of its correlations with H_3-28 and H_3-29 in the HMBC spectrum. The HMBC spectrum also showed a long-range correlation between H-3 (δ_H 3.82) and C-10 (δ_C 88.7), indicative of an oxygen bridge between C-3 and C-10. Based on these evidence and previous biotransformation studies[73,75], ring B was deduced as a seven-membered ring [δ_C 55.5 (C-5), 76.9 (C-6), 80.2 (C-7), 139.5 (C-8), 126.7 (C-9), 36.3 (C-19), 88.7 (C-10)], and the δ_H 3.17 and 1.91 signals were assigned to H_2-19. In the 2D-NOESY spectrum, the orientation of C-7(OH) was found to be β based on NOESY cross-peaks between H-7 (δ_H 4.39) and the α-oriented H_3-30 and H-5. Consequently, the structure of **20** was established as 3β,10β;20,25-diepoxy-6α,7β,16β,24α-tetrahydroxy-9,10-seco-cycloartan-8-ene.

Table 2.20. The ^{13}C and ^1H NMR data of **20** (100/400 MHz, δ ppm, in C_5D_5N).

Position	δ_C (ppm)	δ_H (ppm), *J* (Hz)	Position	δ_C (ppm)	δ_H (ppm), *J* (Hz)
1	37.1	1.33 m, 1.58 m	**16**	74.1	4.97 m
2	24.8	1.68 m, 1.93 m	**17**	59.6	2.10 d (7.6)
3	86.3	3.82 dd (5.6, 1.7)	**18**	19.5	1.60 s
4	46.9	-	**19**	36.3	1.91 m, 3.17 m
5	55.5	1.47 d (12.0)	**20**	78.1	-
6	76.9	4.42 m	**21**	29.3	1.51 s
7	80.2	4.39 m	**22**	26.5	1.26 m, 3.23 td (13.7, 4.4)
8	139.5	-	**23**	23.9	1.86 m, 2.16 m
9	126.7	-	**24**	68.6	3.65 brs
10	88.7	-	**25**	74.6	-
11	30.8	1.74 m, 2.14 m	**26**	28.7	1.42 s
12	32.4	1.77 m, 2.16 m	**27**	27.6	1.31 s
13	49.1	-	**28**	24.1	1.66 s
14	44.3	-	**29**	25.7	1.31 s
15	41.6	2.14 m, 2.94 m	**30**	25.9	0.92 s

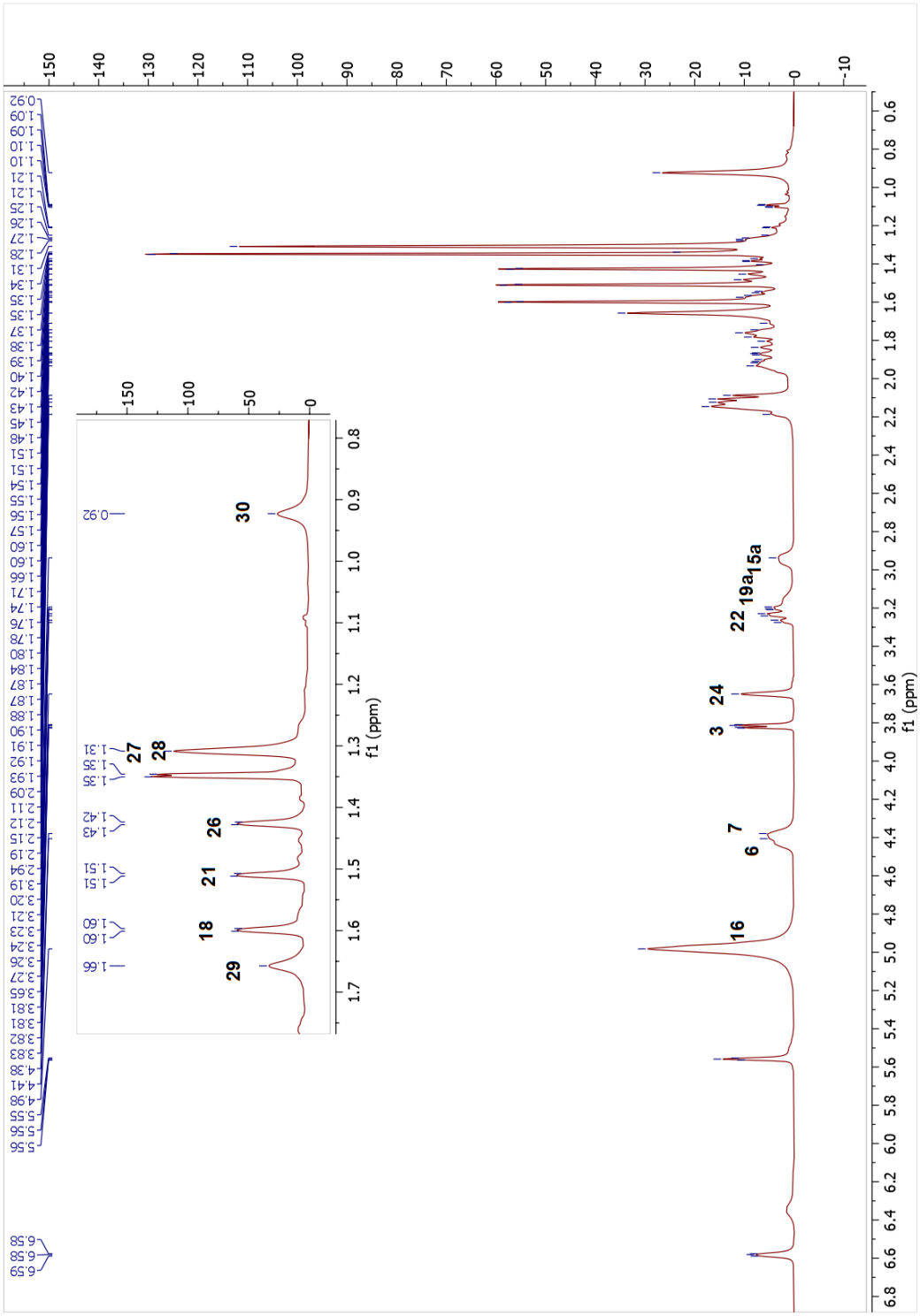

Spectrum 2.128. ^{1}H-NMR spectrum of compound **20**.

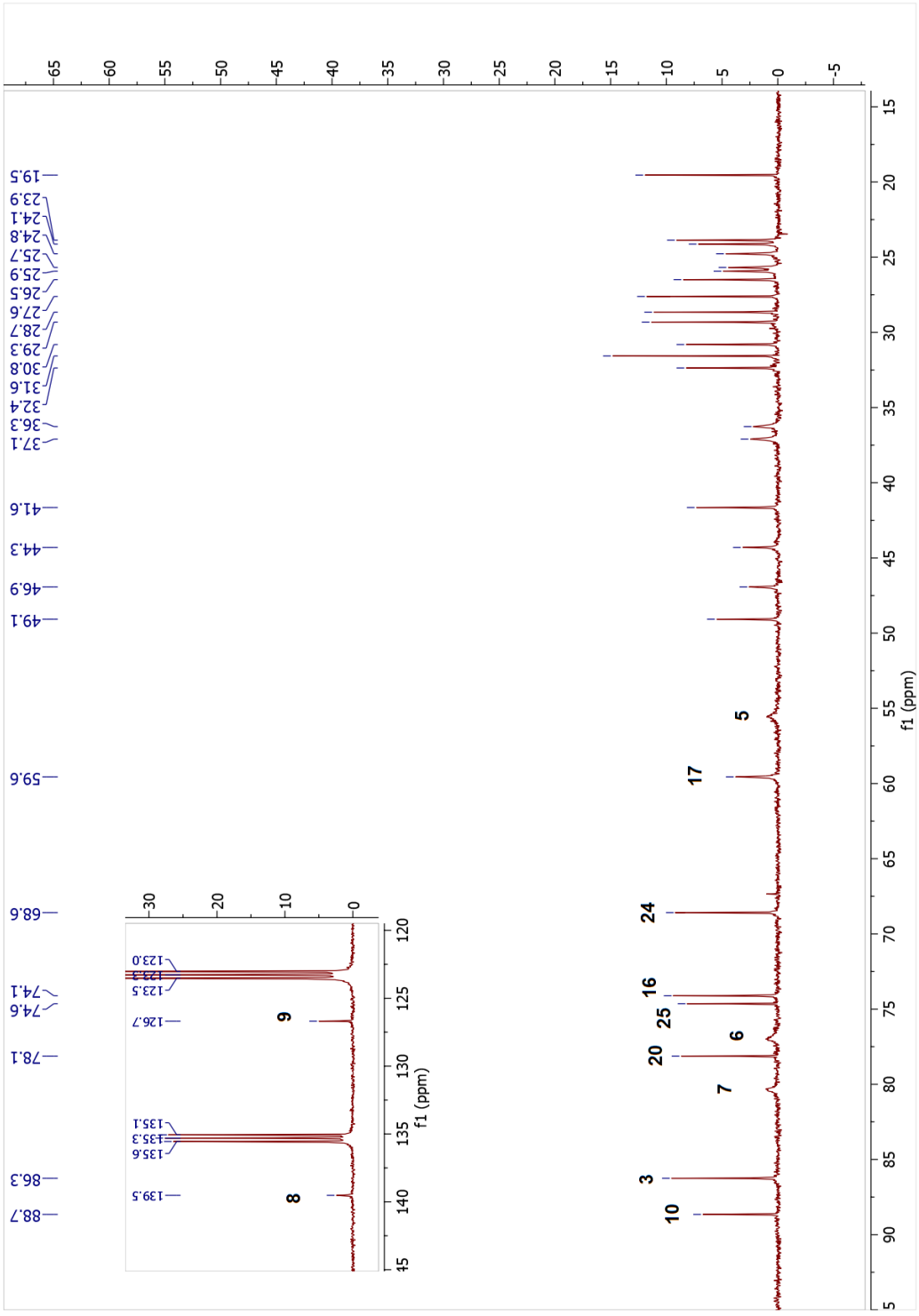

Spectrum 2.129. ^{13}C-NMR spectrum of compound **20**.

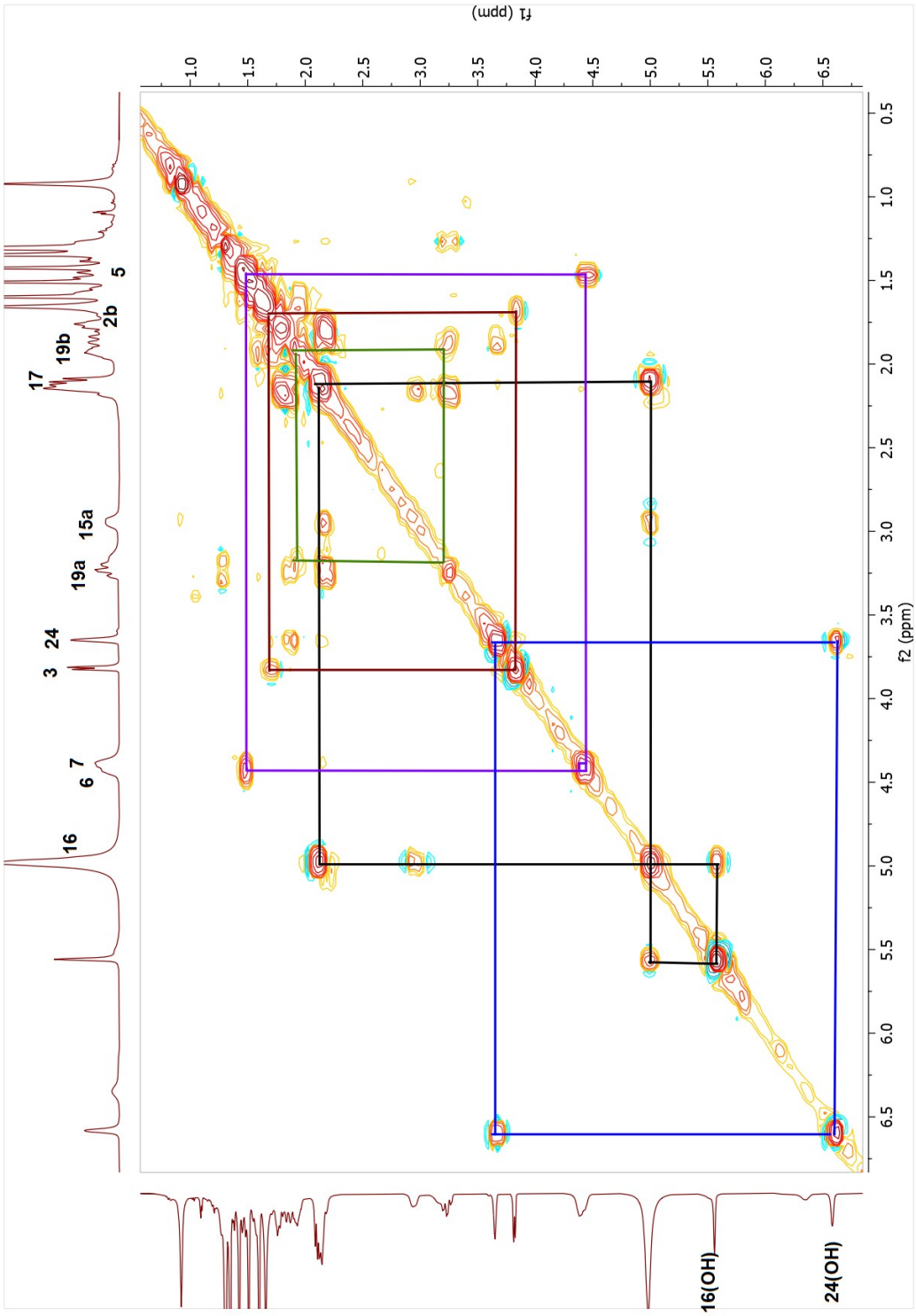

Spectrum 2.130. COSY spectrum of compound **20**.

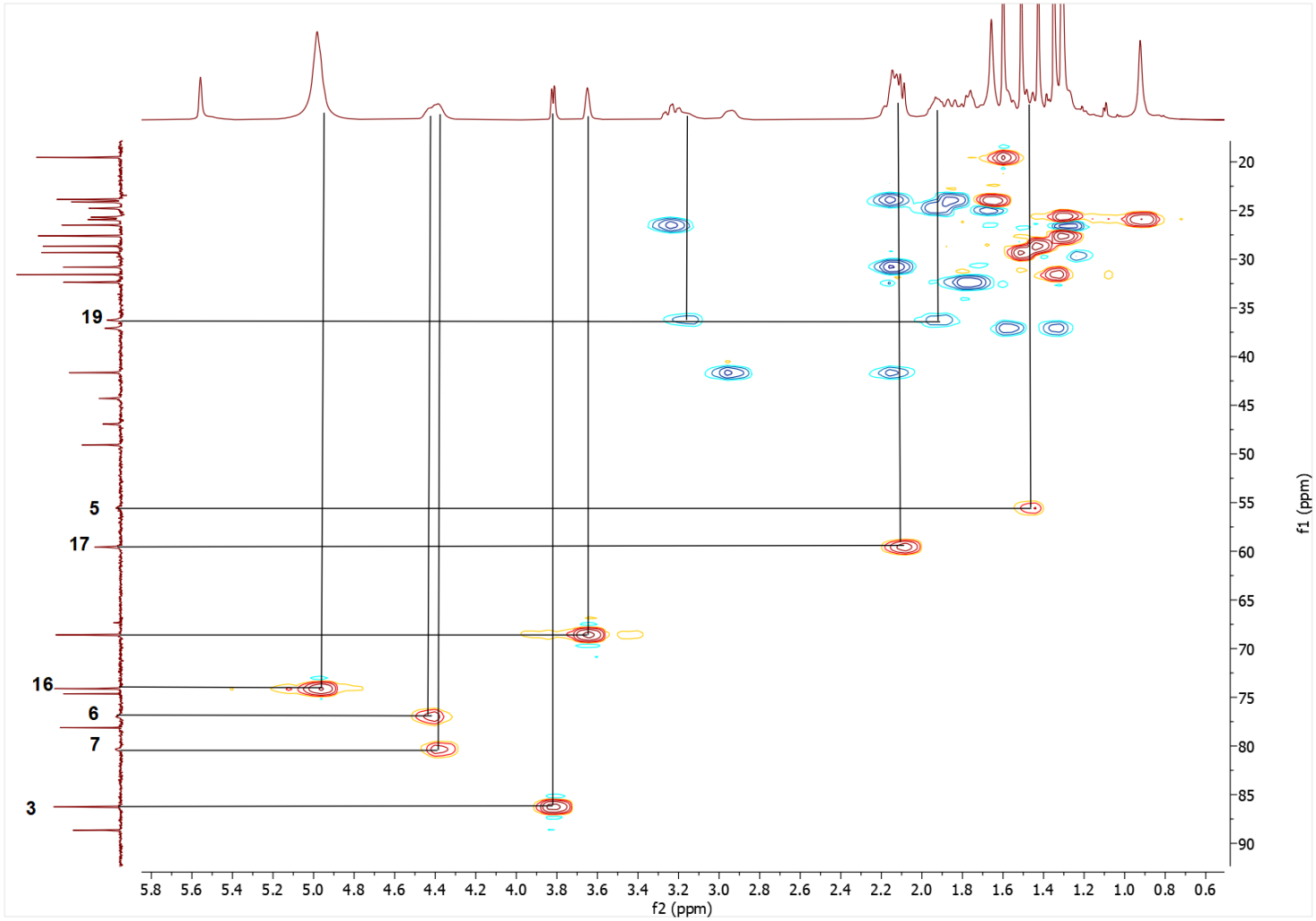

Spectrum 2.131. HSQC spectrum of compound **20**.

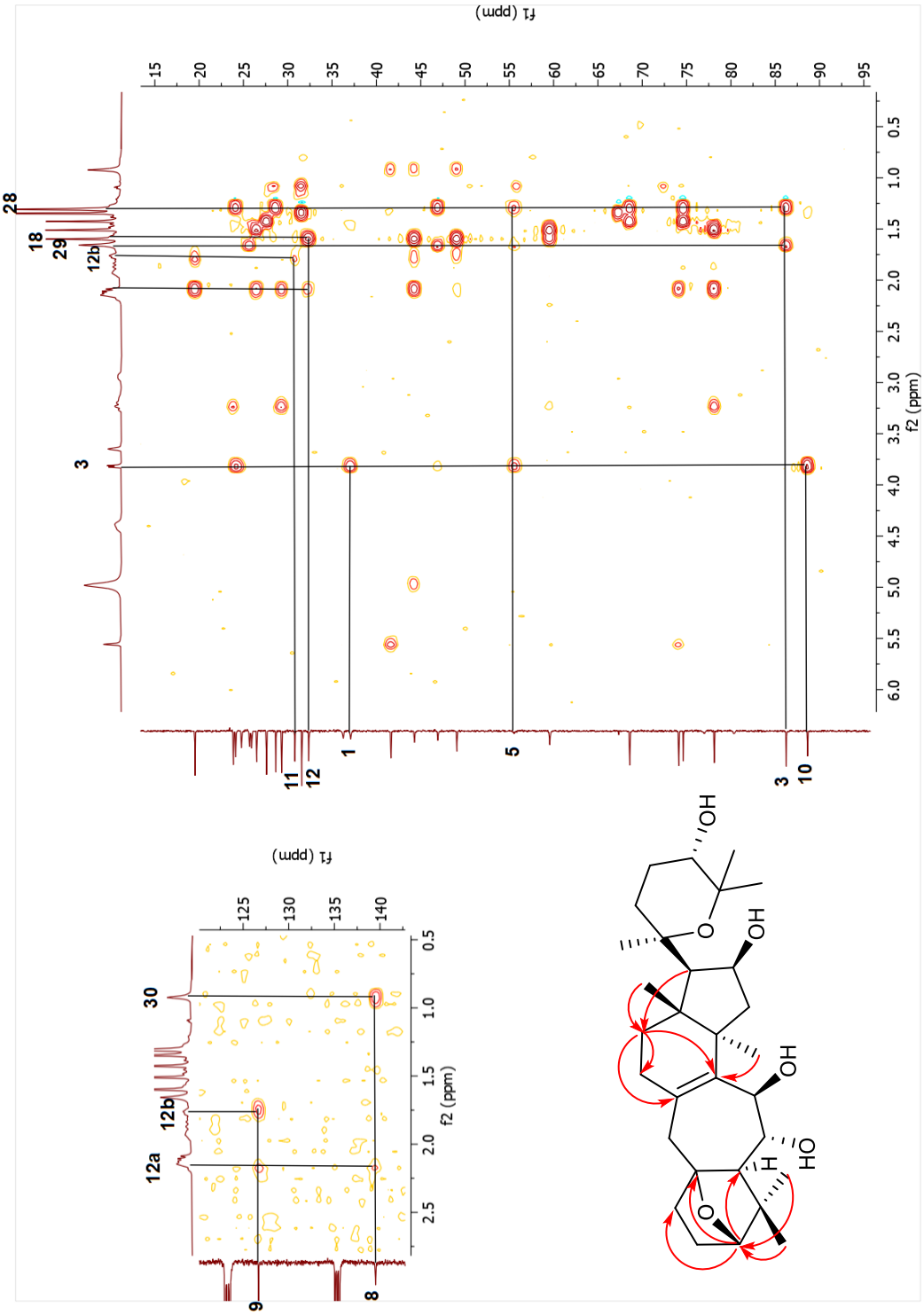

Spectrum 2.132. HMBC spectrum of compound **20**.

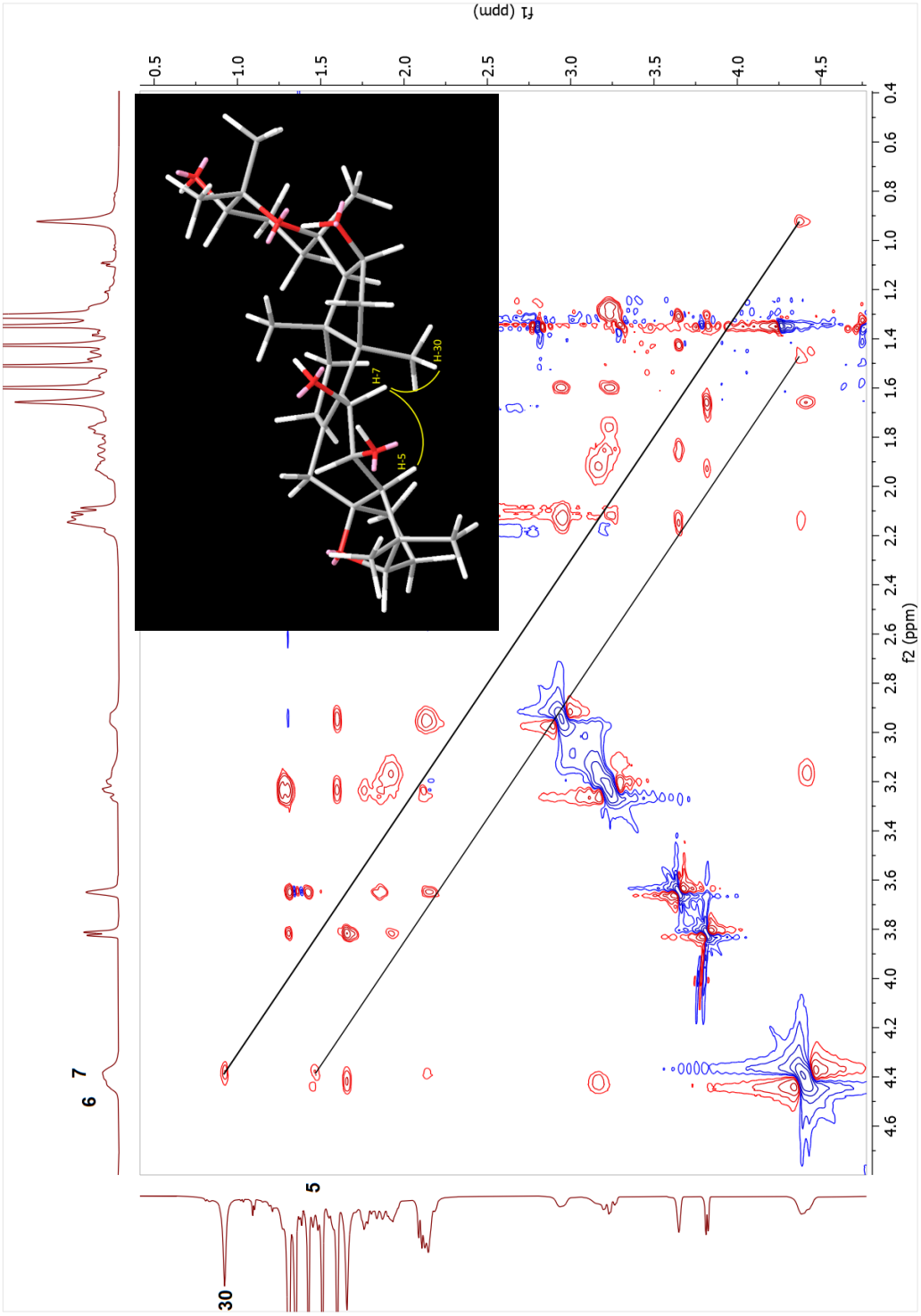

Spectrum 2.133. NOESY spectrum of compound **20**.

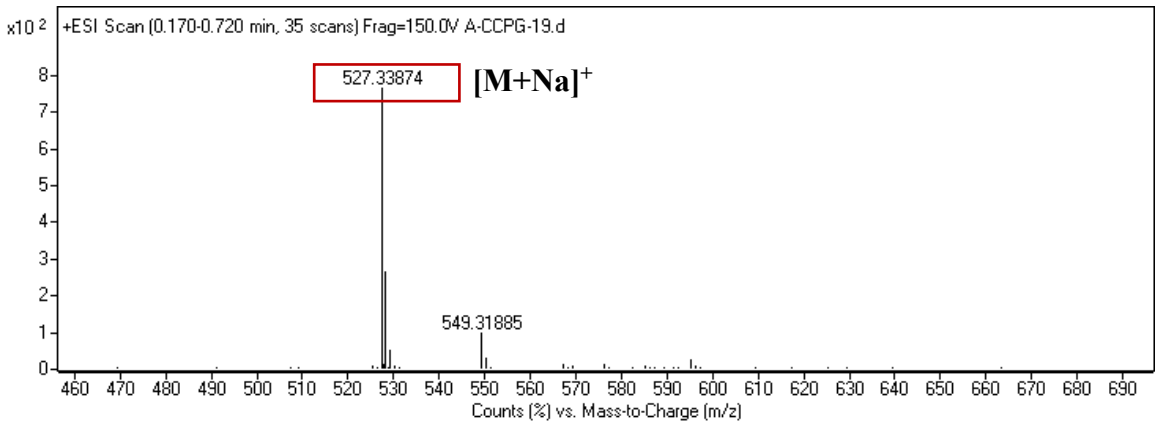

Spectrum 2.134. HR-ESI-MS spectrum of compound **20**.

2.3.2.21. Structure Elucidation of Compound 21

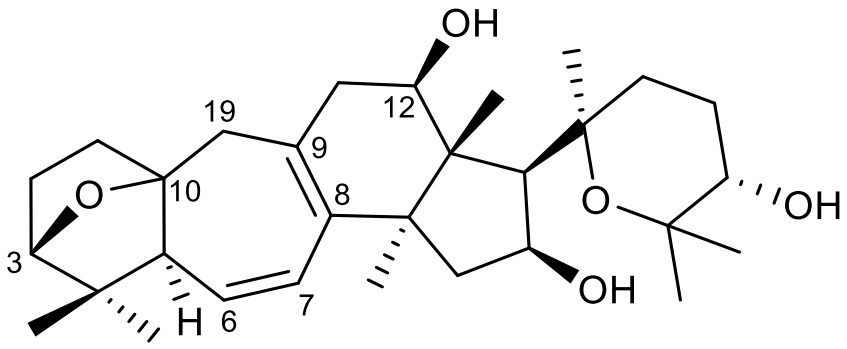

Figure 2.28. Chemical structure of compound **21**.

The HR-ESI-MS data of metabolite **21** displayed a sodium adduct ion at *m/z* 509.32640 $[M + Na]^+$ (calcd. 509.32429 for $C_{30}H_{46}NaO_5$). The absence of two signals deriving from 9,19-cyclopropane ring in the ^{1}H-NMR spectrum suggested a ring cleavage as in **20**. The hydroxymethine proton at C-6 was not present in the ^{1}H-NMR spectrum. Also, an additional oxymethine signal at δ_H 4.45 was observed corresponding to a carbon at δ_C 70.1 in the HSQC spectrum. The ^{13}C-NMR spectrum of **21** exhibited four olefinic carbon resonances (δ_C 128.7, 131.8, 132.1 and 138.5). Locations of the olefinic double bonds were

assigned from the correlations in the HMBC spectrum and with the combined use of COSY, HSQC and HSQC-TOCSY spectra. The spin system of B ring included a methine proton at δ_H 1.96 (m, H-5) which showed a correlation with the olefinic methine proton at C-6 (δ_H 5.88 m) and from there to an olefinic methine proton at δ_H 5.98 (m, H-7). The long-distance correlation from H-5 to the olefinic methine carbon at δ_C 128.7 confirmed the location of the double bond between C-6 and C-7. The other tetrasubstituted double bond was positioned between C-8 and C-9 based on the HMBC correlations from H_2-11a to the olefinic carbon at δ_C 131.8 (C-9), and H_2-11a and H_3-30 to the second double bond carbon at 138.5 ppm (C-8). The ^3J-HMBC correlations of the oxymethine proton at δ_H 4.45 with the C-18 signal revealed the position of oxygenation at C-12. Additionally, an oxygen bridge between C-3 and C-10 was evident as in **20** due to the HMBC correlation between H-3 (δ_H 3.78) and C-10 (δ_C 100.1). The hydroxy group at C-12 was deduced to be β-oriented based on NOESY correlation of H-12 (δ_H 4.45) with the α-oriented H_3-30 (δ_H 0.94). As a result, metabolite **21** was established as 3β,10β;20,25-diepoxy-12β,16β,24α-trihydroxy-9,10-seco-cycloartan-6,8-diene.

Table 2.21. The ^{13}C and ^1H NMR data of **21** (125/500 MHz, δ ppm, in C_5D_5N).

Position	δ_C (ppm)	δ_H (ppm), *J* (Hz)	Position	δ_C (ppm)	δ_H (ppm), *J* (Hz)
1	39.1	1.39 m, 1.64 m	**16**	72.0	4.89 m
2	26.1	1.65 m, 1.83 m	**17**	61.0	2.57 m
3	85.3	3.78 m	**18**	13.9	1.80 s
4	46.4	-	**19**	39.1	2.42 m, 2.54 m
5	58.1	1.96 m	**20**	79.3	-
6	132.1	5.88 m	**21**	27.2	2.01 s
7	128.7	5.98 m	**22**	30.1	2.38 m, 2.67 m
8	138.5	-	**23**	24.6	1.99 m, 2.32 m
9	131.8	-	**24**	70.1	3.75 brs
10	100.1	-	**25**	76.8	-
11	41.0	2.65 m, 2.91 m	**26**	29.3	1.42 s
12	70.1	4.45 m	**27**	28.6	1.65 s
13	51.4	-	**28**	26.6	0.96 s
14	46.5	-	**29**	26.0	1.08 s
15	45.2	2.20 m (2H)	**30**	25.4	0.94 s

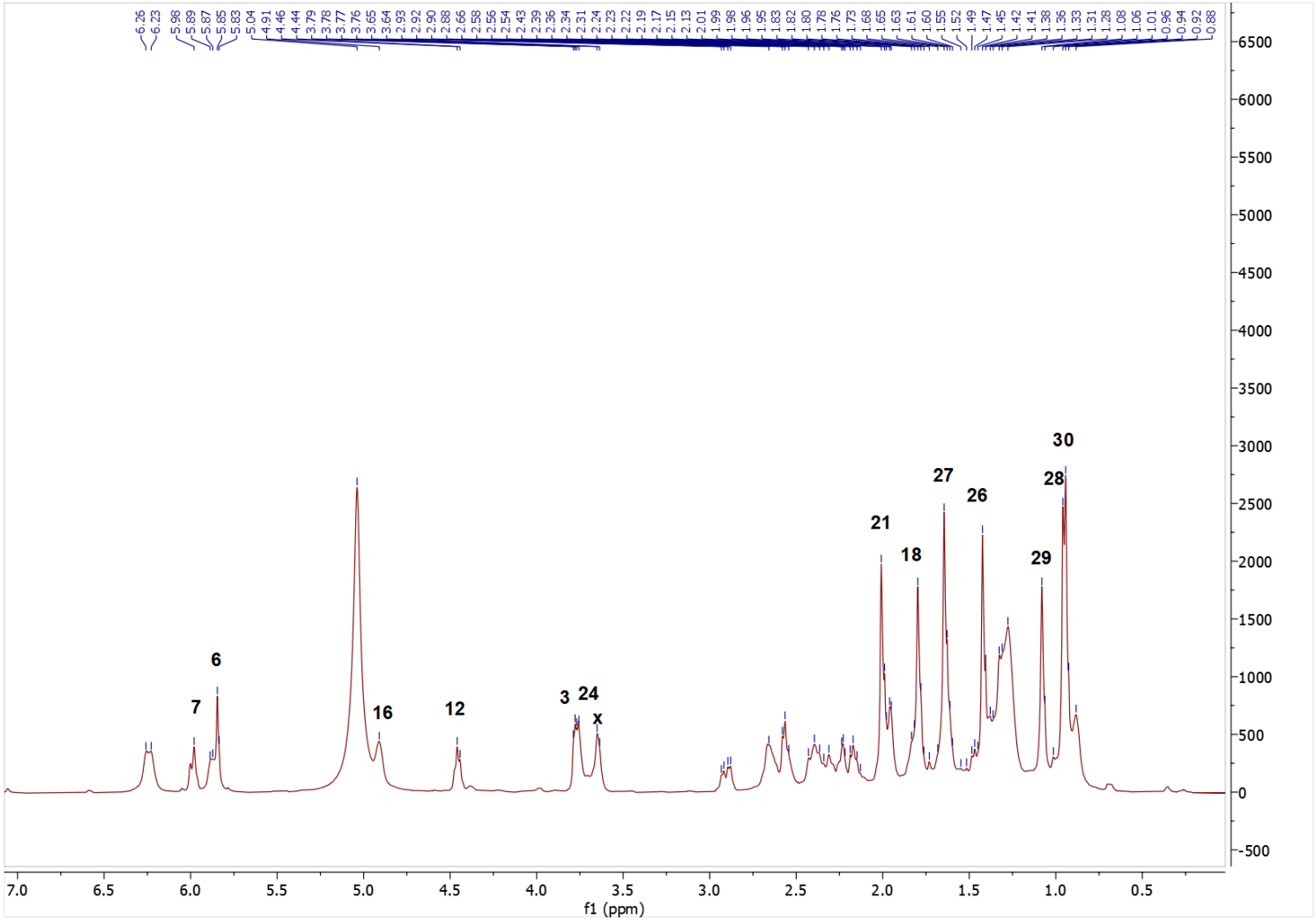

Spectrum 2.135. ^{1}H-NMR spectrum of compound **21**.

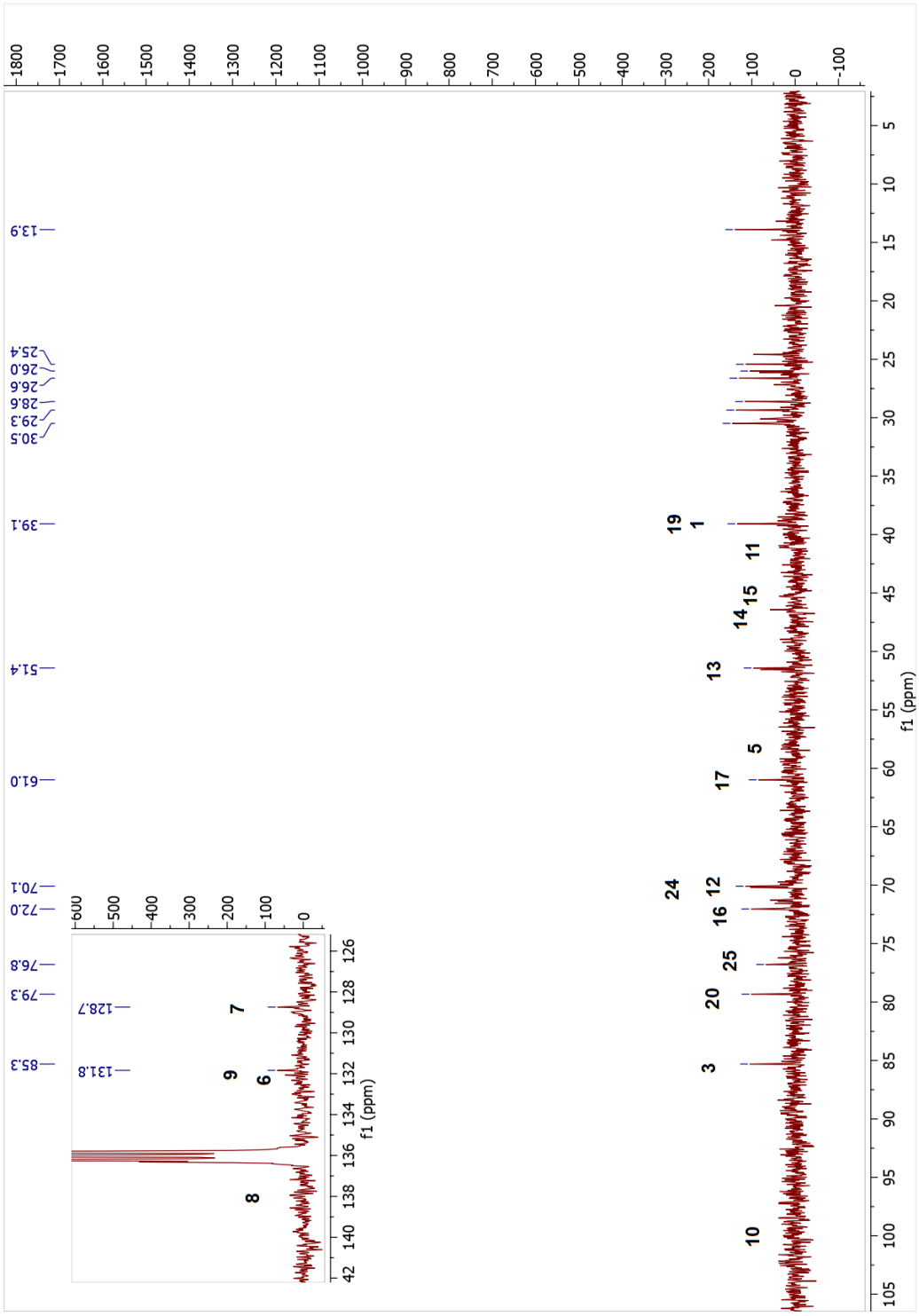

Spectrum 2.136. ^{13}C-NMR spectrum of compound **21**.

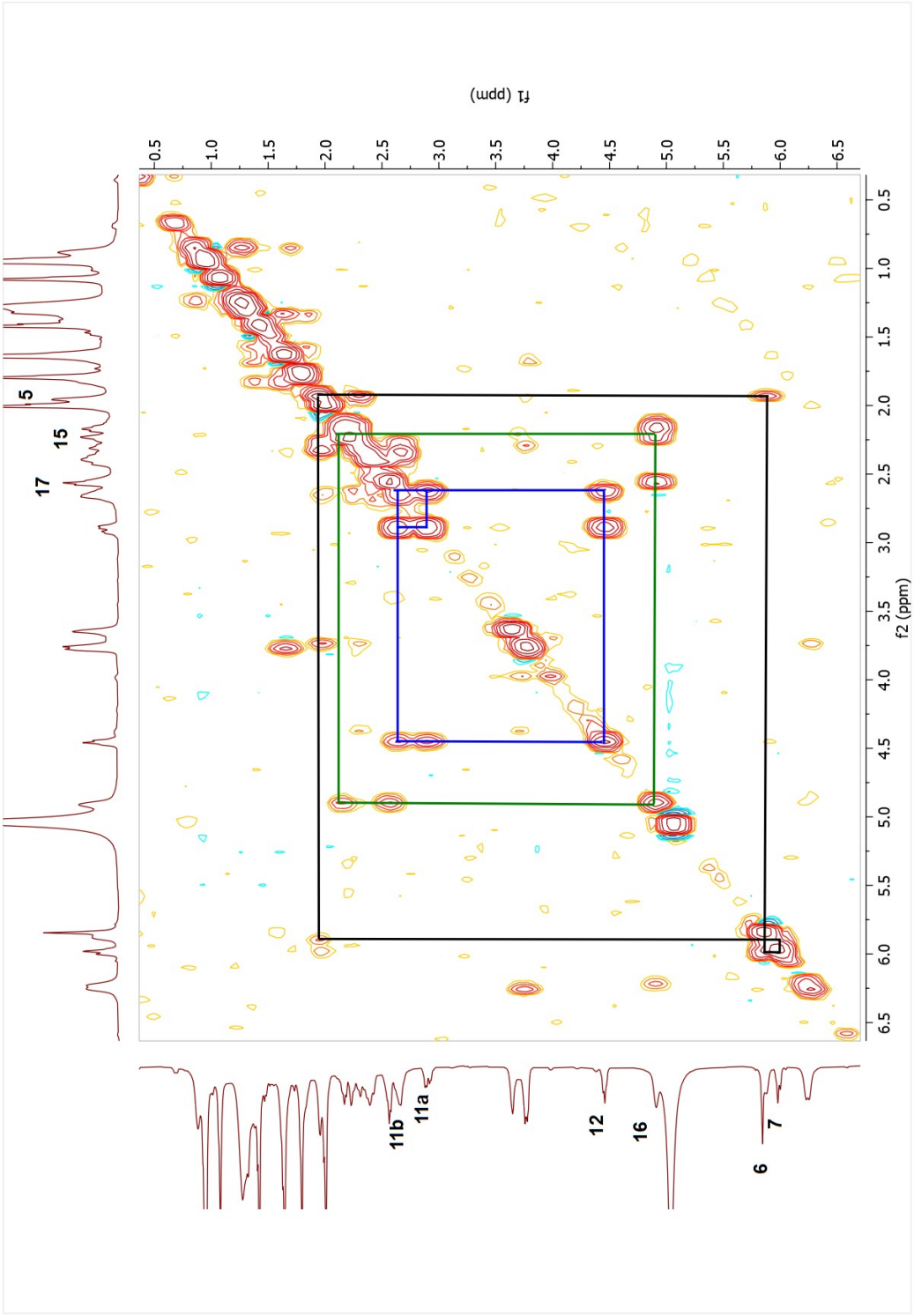

Spectrum 2.137. COSY spectrum of compound **21**.

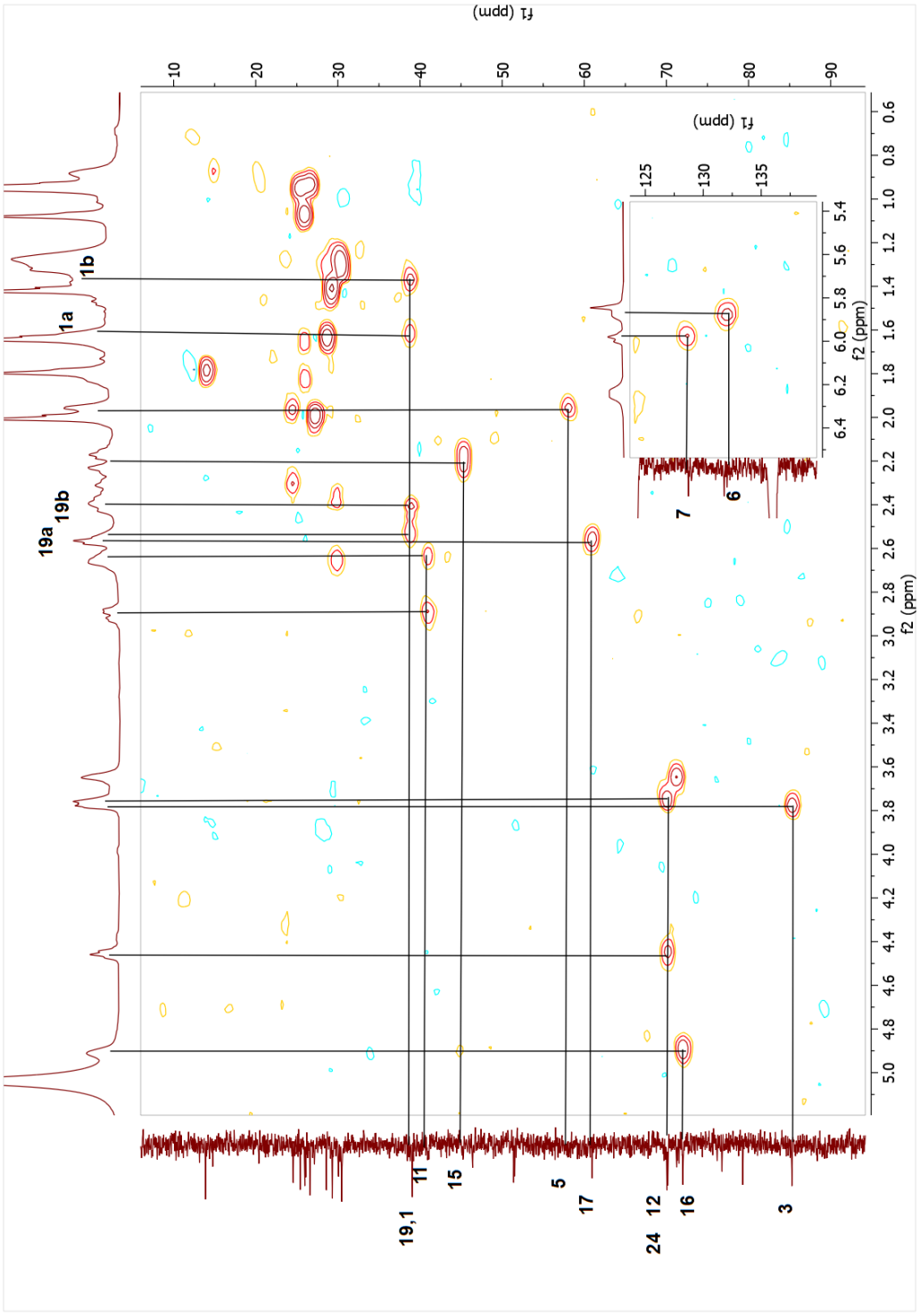

Spectrum 2.138. HSQC spectrum of compound **21**.

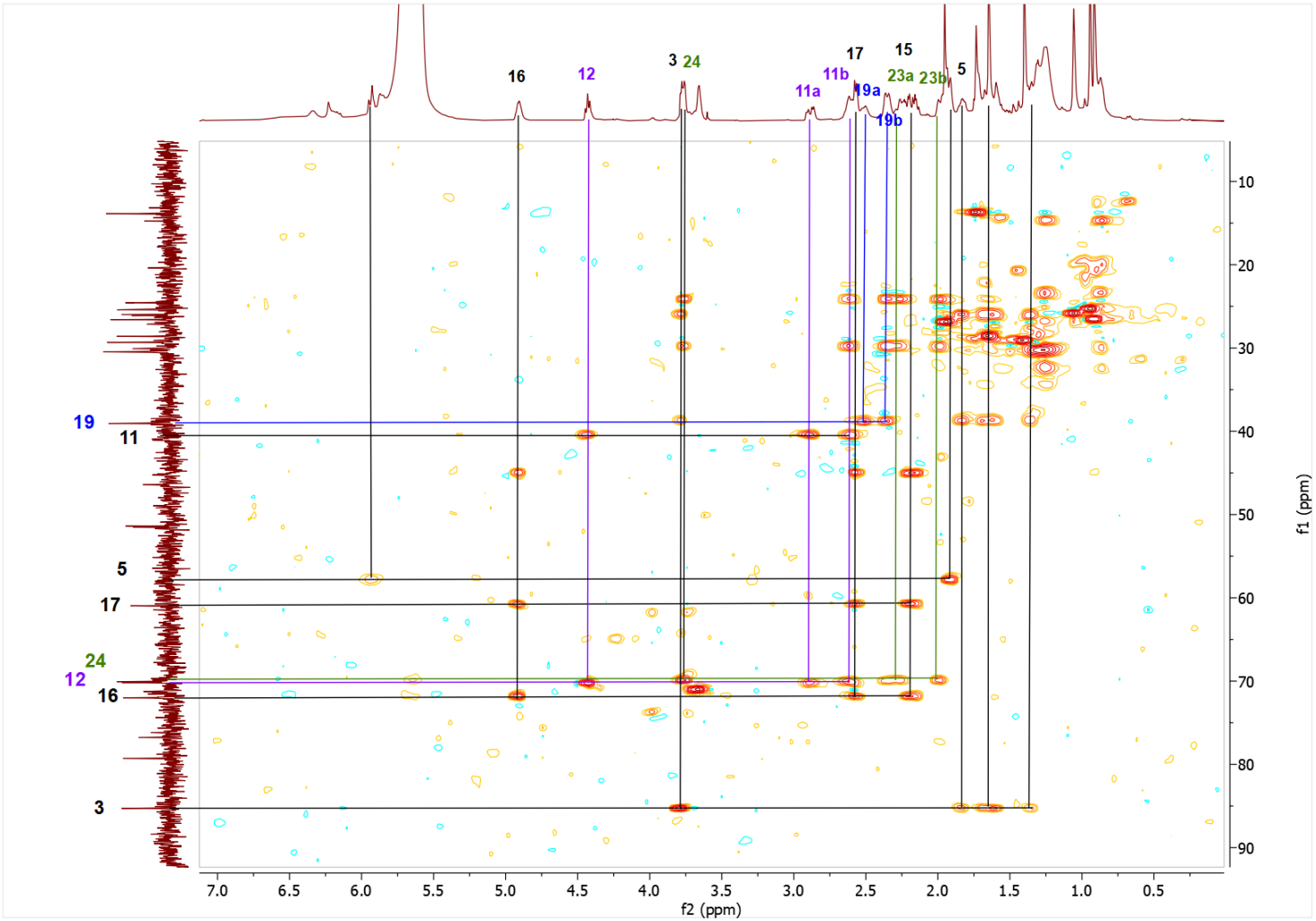

Spectrum 2.139. HSQC-TOCSY spectrum of compound **21**.

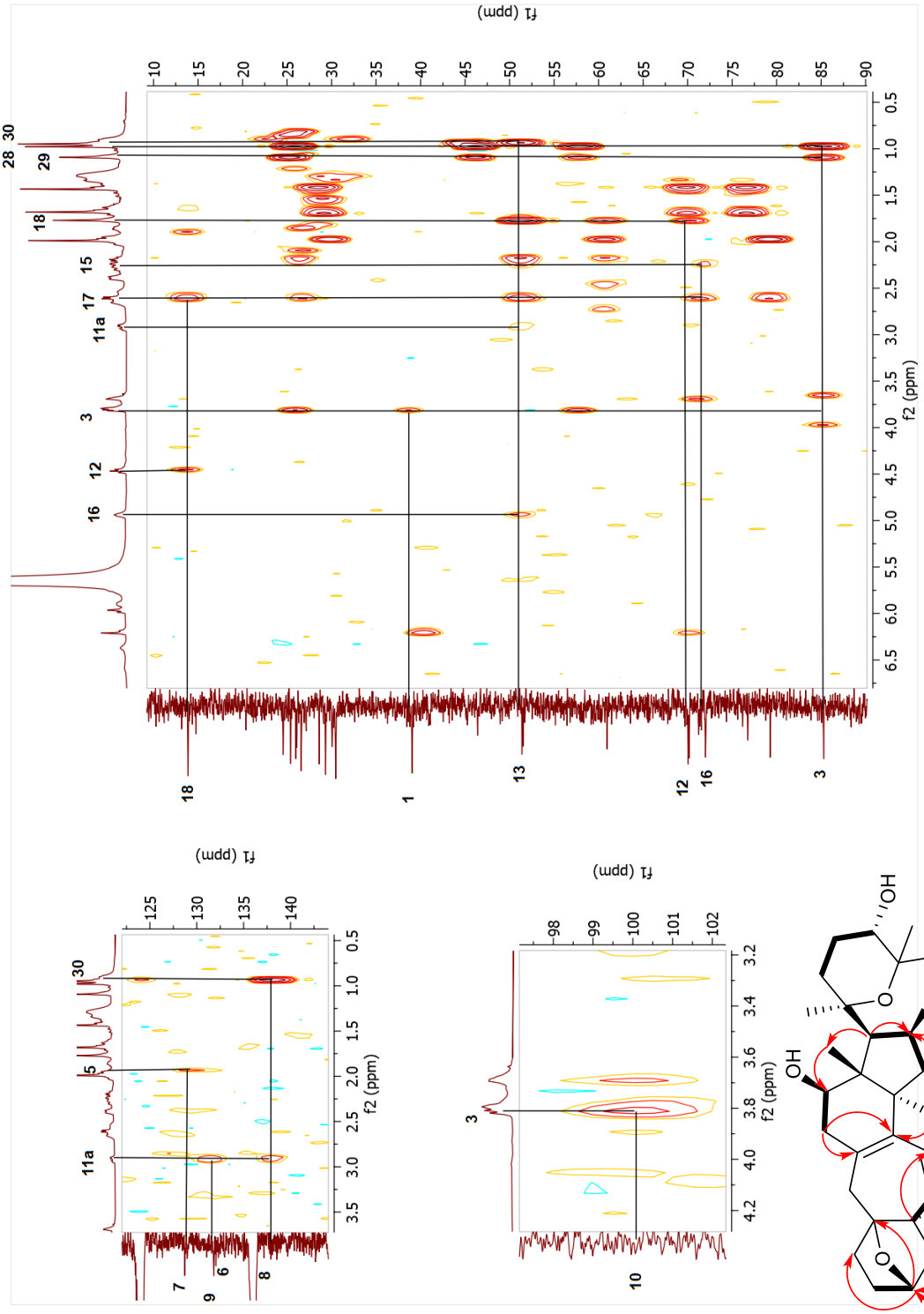

Spectrum 2.140. HMBC spectrum of compound **21**.

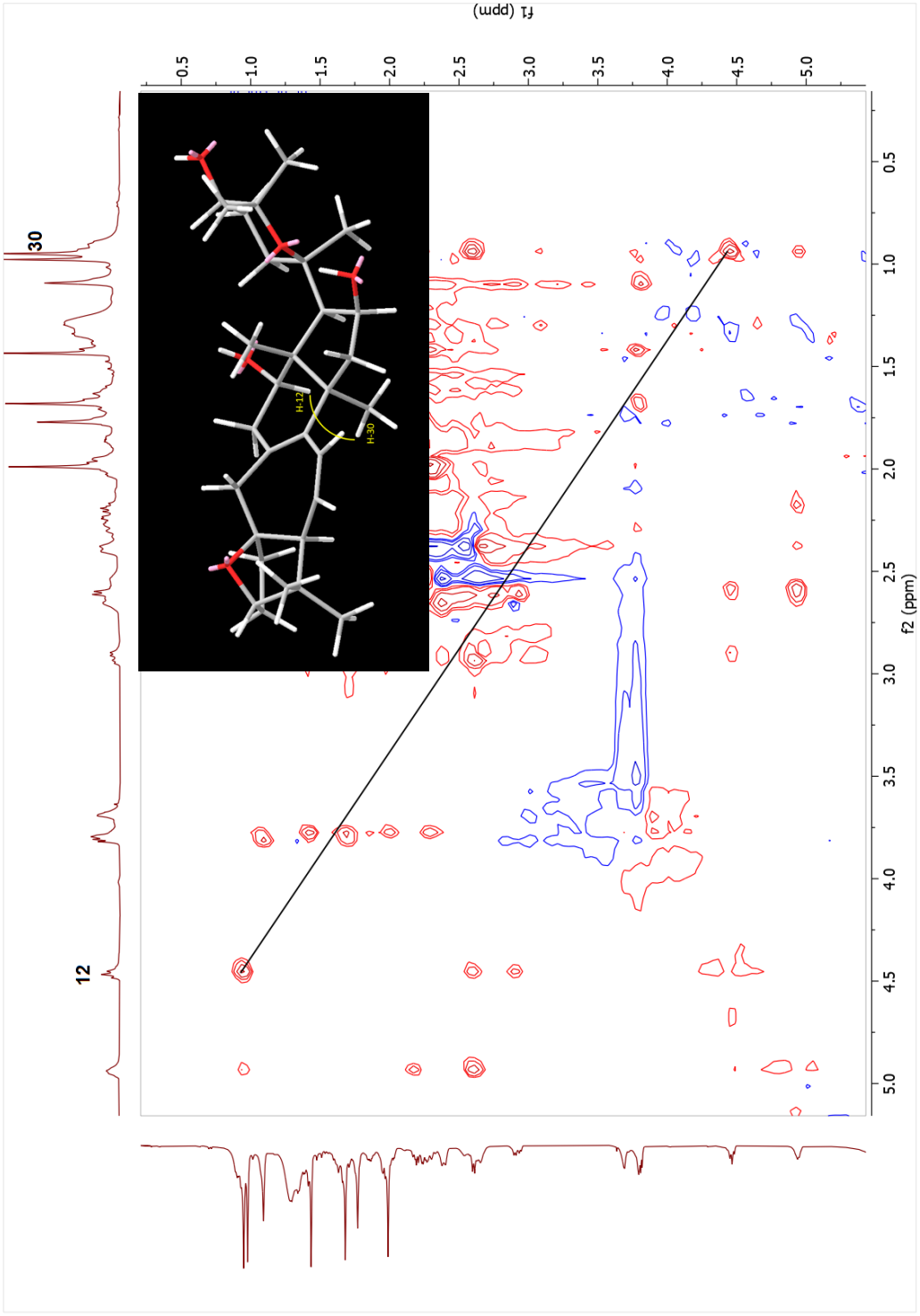

Spectrum 2.141. NOESY spectrum of compound **21**.

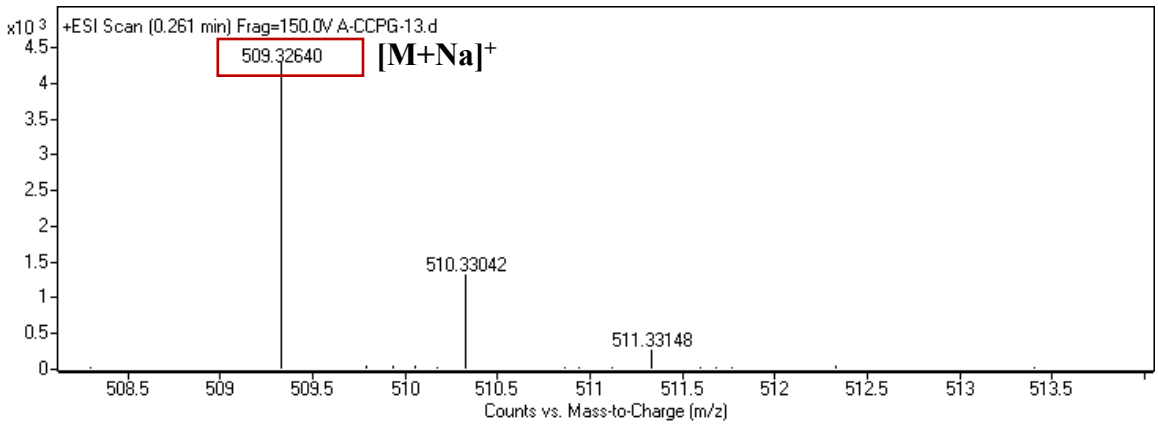

Spectrum 2.142. HR-ESI-MS spectrum of compound **21**.

2.3.2.22. Structure Elucidation of Compound 22

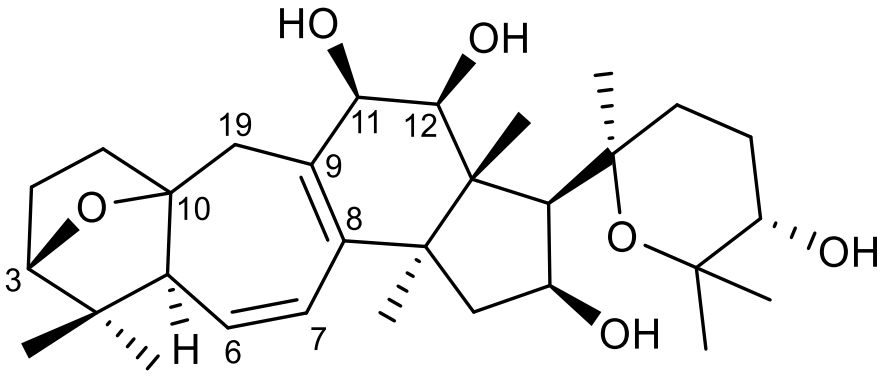

Figure 2.29. Chemical structure of compound **22**.

The molecular formula of **22** was established as $C_{30}H_{46}O_6$ by HR-ESI-MS analysis (*m/z* 525.3166 ([M + Na]$^+$, calcd for $C_{30}H_{46}NaO_6$, 525.31921; *m/z* 1027.6445 ([2M + Na]$^+$, calcd for $C_{60}H_{92}NaO_{12}$, 1027.6486). Its NMR spectra were very similar to those of **21**, except for the resonances corresponding to ring C. In the low-field region of the ^{1}H-NMR spectrum, an additional low-field proton (δ_H 4.73) was observed. Besides, in the ^{13}C-NMR spectrum, an extra down-field carbon signal at δ_C 70.8 was noted. In the COSY and HSQC-TOCSY spectra, the δ_H 4.73 proton coupled with an oxymethine proton at C-12 (δ_H 4.36), which had

long range correlation with C-18 (δ_H 16.1) in the HMBC spectrum. Based on these data, a new hydroxy group was undoubtedly located at C-11. The NOE correlation between H-11 and α-oriented H-12 indicated the β-configuration of 11-OH. Consequently, the structure of **22** was determined to be 3β,10β;20,25-diepoxy-11β,12β,16β,24α-tetrahydroxy-3(10)β-epoxy-9,10-seco-cycloartan-6,8-diene.

Table 2.22. The ^{13}C and ^{1}H NMR data of **22** (125/500 MHz, δ ppm, in C_5D_5N).

Position	δ_C (ppm)	δ_H (ppm), *J* (Hz)
1	38.1	1.53 m, 1.72 m
2	26.0	1.68 m, 1.84 m
3	85.6	3.79 m
4	45.9	-
5	56.8	1.94 m
6	134.1	6.09 m
7	128.8	6.05 d (10.4)
8	141.9	-
9	116.7	-
10	-[d]	-
11	70.8	4.73 m
12	72.3	4.36 d (6.7)
13	52.5	-
14	49.1	-
15	44.6	2.16 dd (12.3, 7.7), 2.25 m
16	72.5	4.96 m
17	60.6	2.57 d (7.4)
18	16.1	1.78 s
19	35.9	2.95 d (11.8), 3.13 m
20	79.6	-
21	27.3	1.99 s
22	29.3	2.33 m, 2.68 m
23	24.4	1.98 m, 2.32 m
24	70.0	3.78 brs
25	77.0	-
26	29.0	1.48 s
27	28.8	1.70 s
28	26.1	1.16 s
29	25.3	0.97 s
30	26.7	0.94 s

[d]Not detected

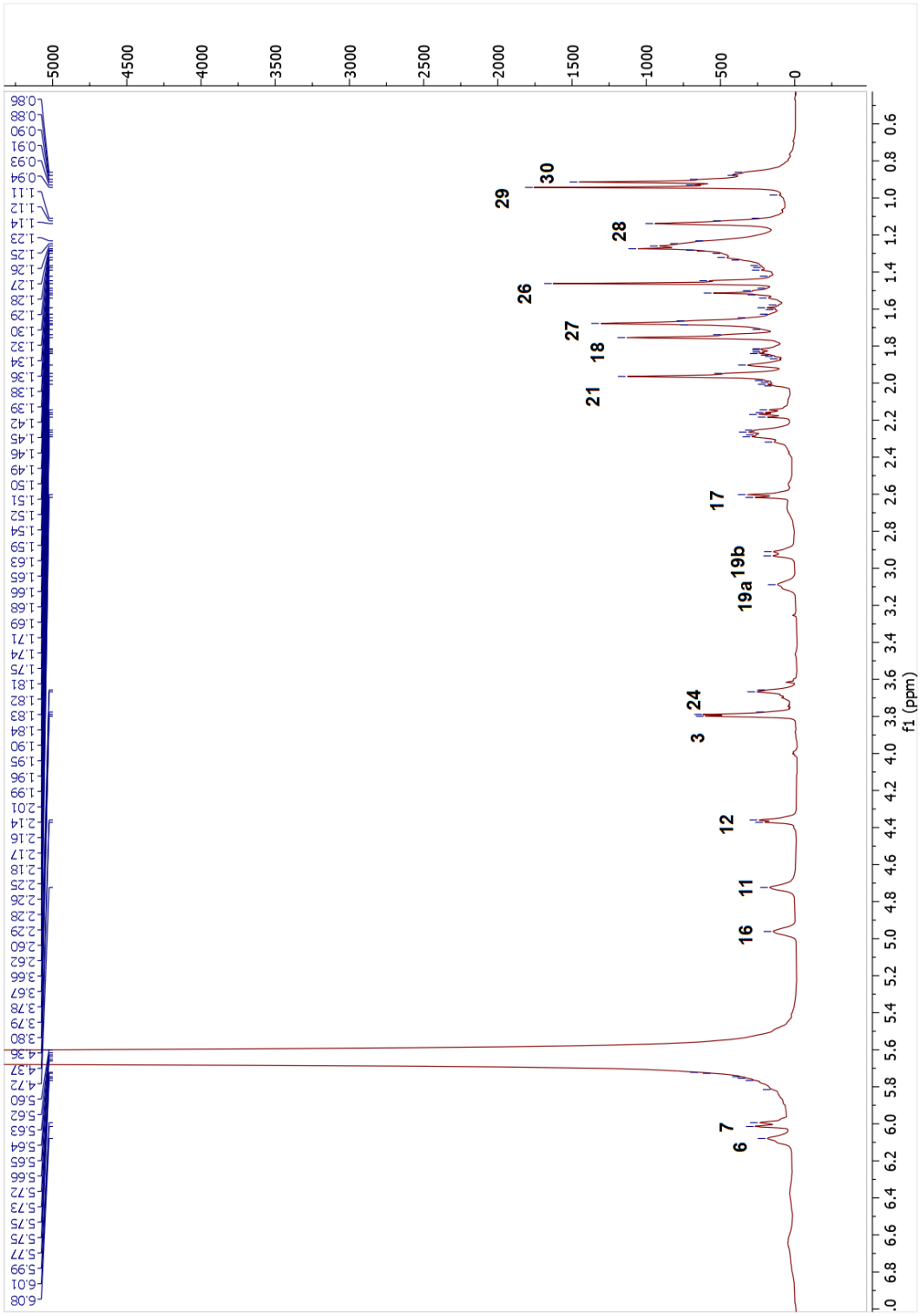

Spectrum 2.143. ^{1}H-NMR spectrum of compound **22**.

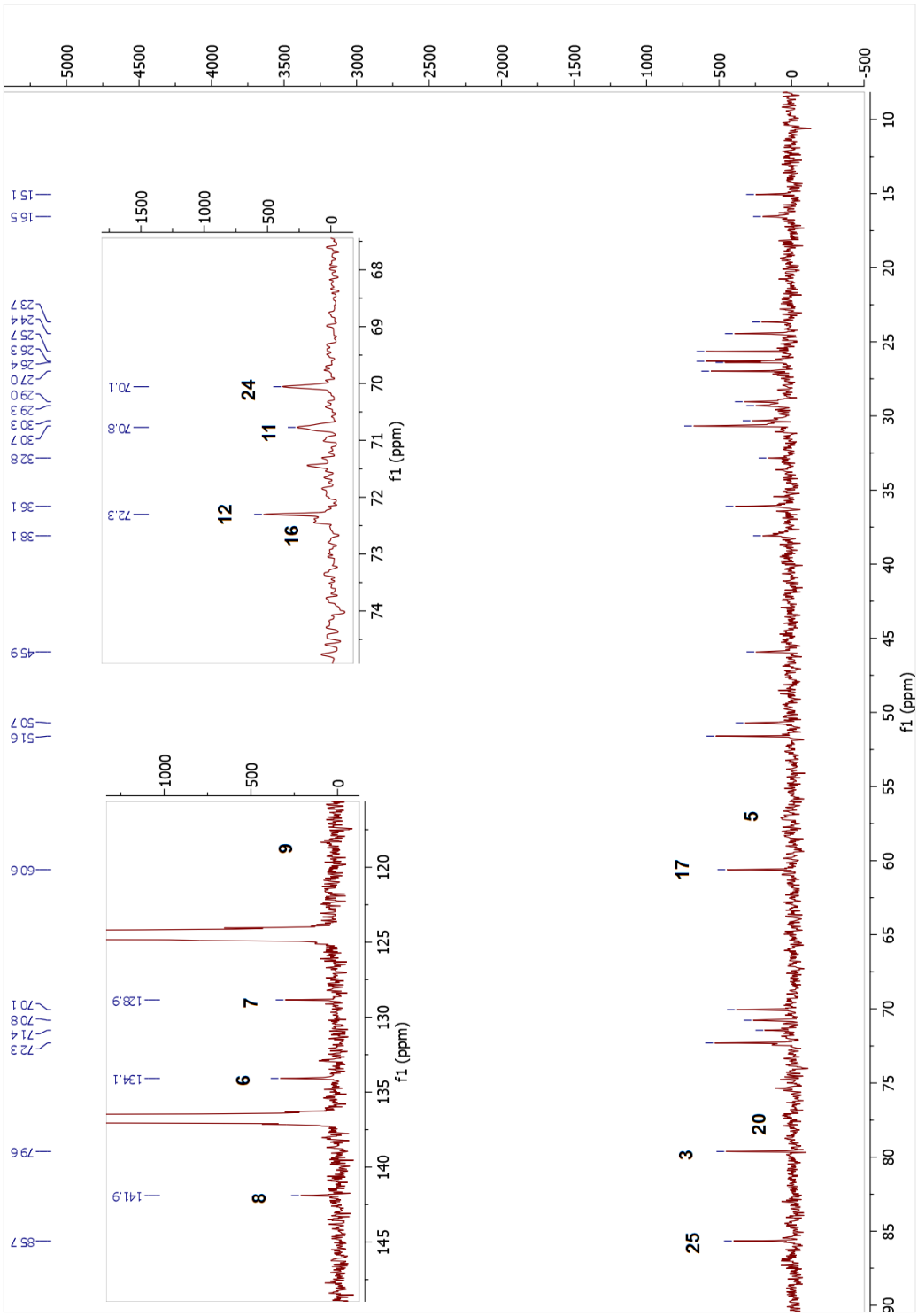

Spectrum 2.144. ^{13}C-NMR spectrum of compound **22**.

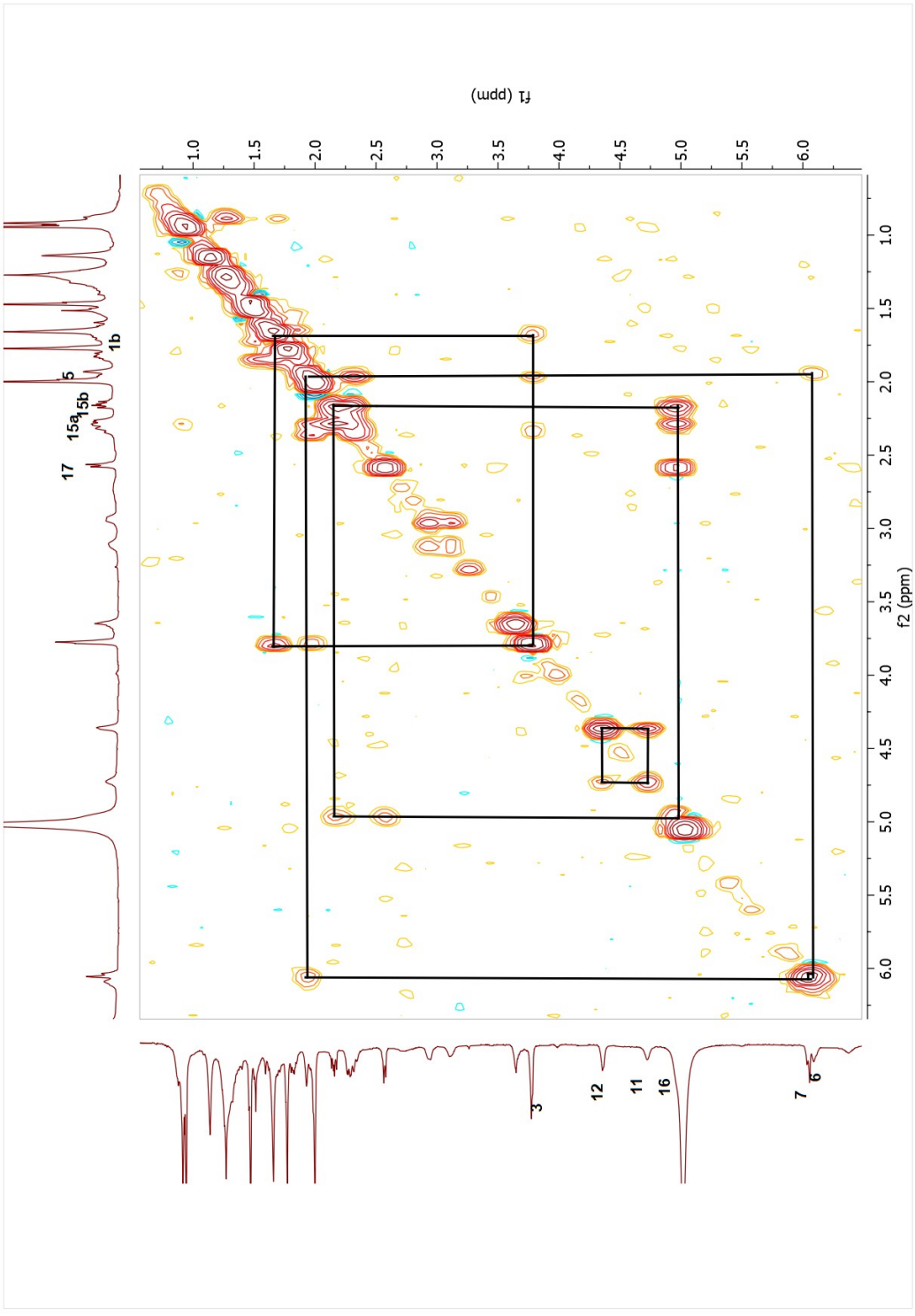

Spectrum 2.145. COSY spectrum of compound **22**.

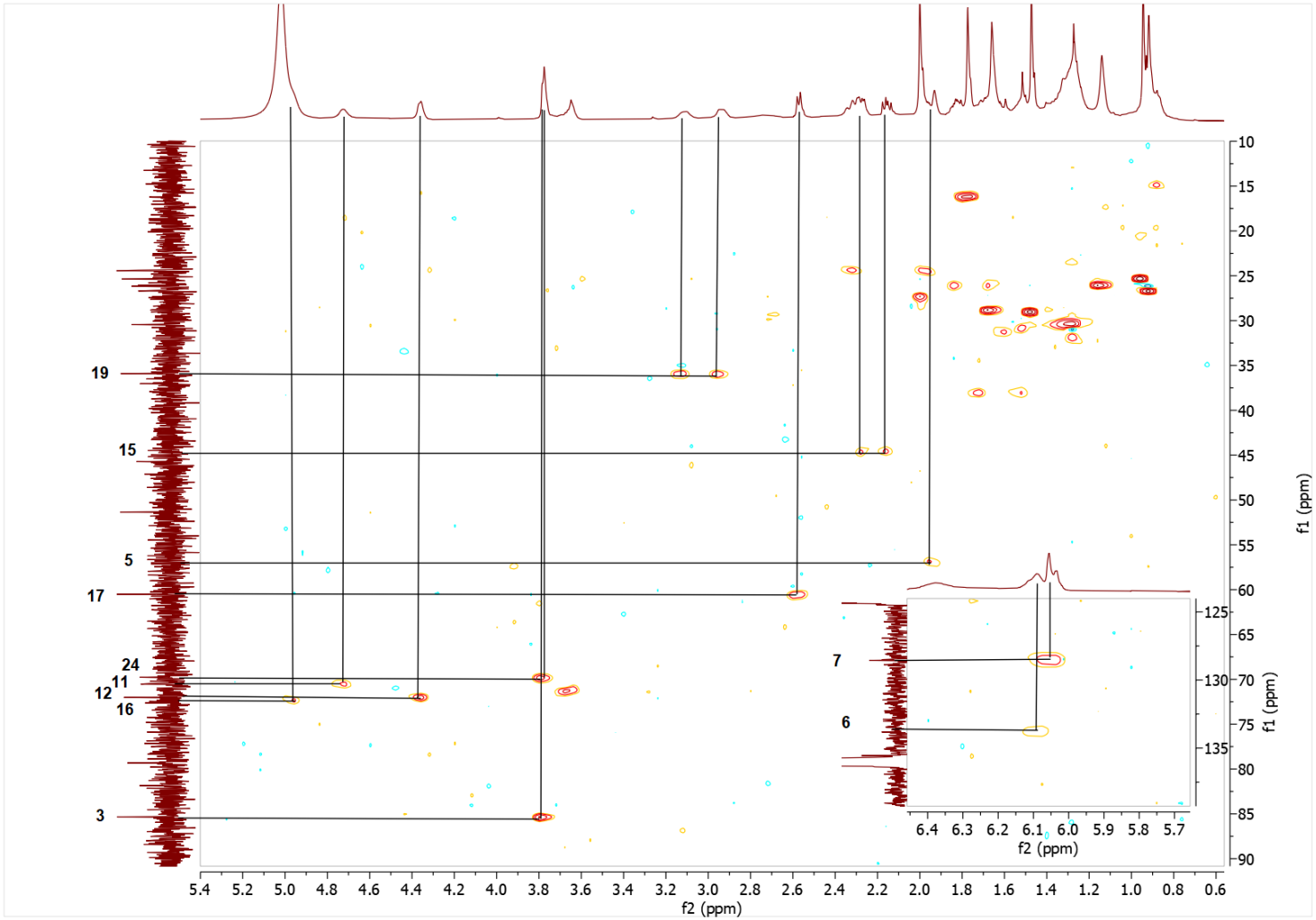

Spectrum 2.146. HSQC spectrum of compound **22**.

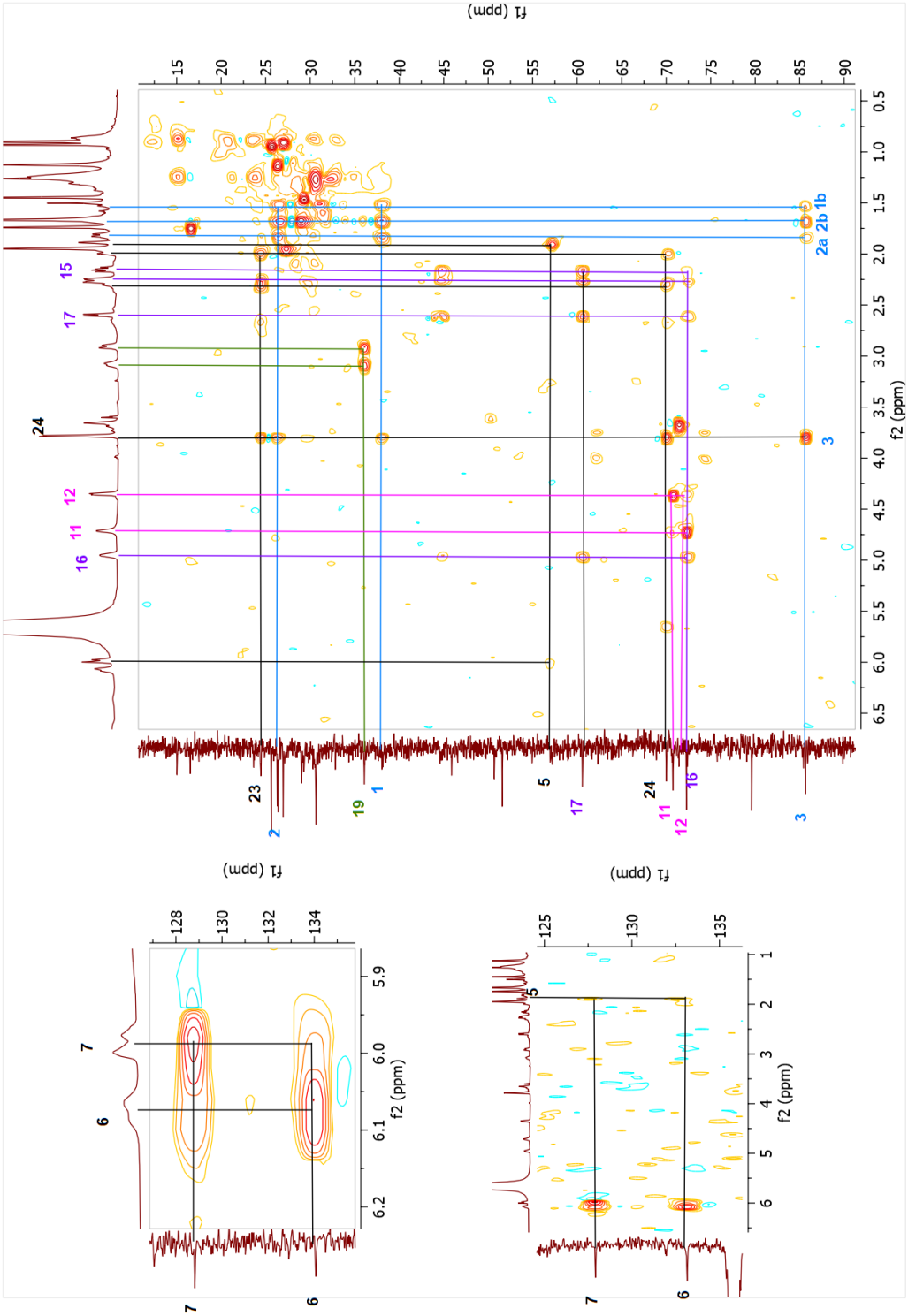

Spectrum 2.147. HSQC-TOCSY spectrum of compound **22**.

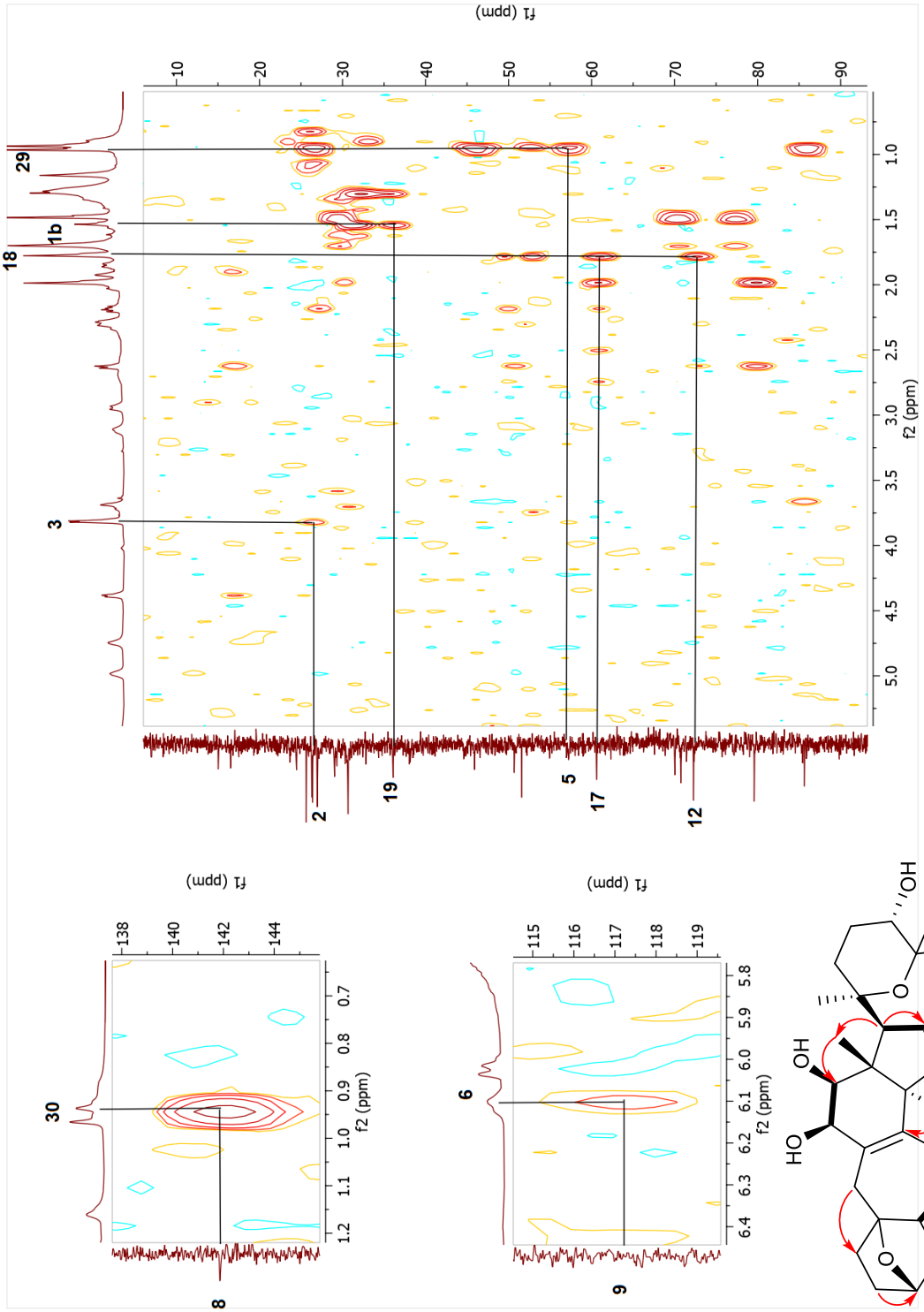

Spectrum 2.148. HMBC spectrum of compound **22**.

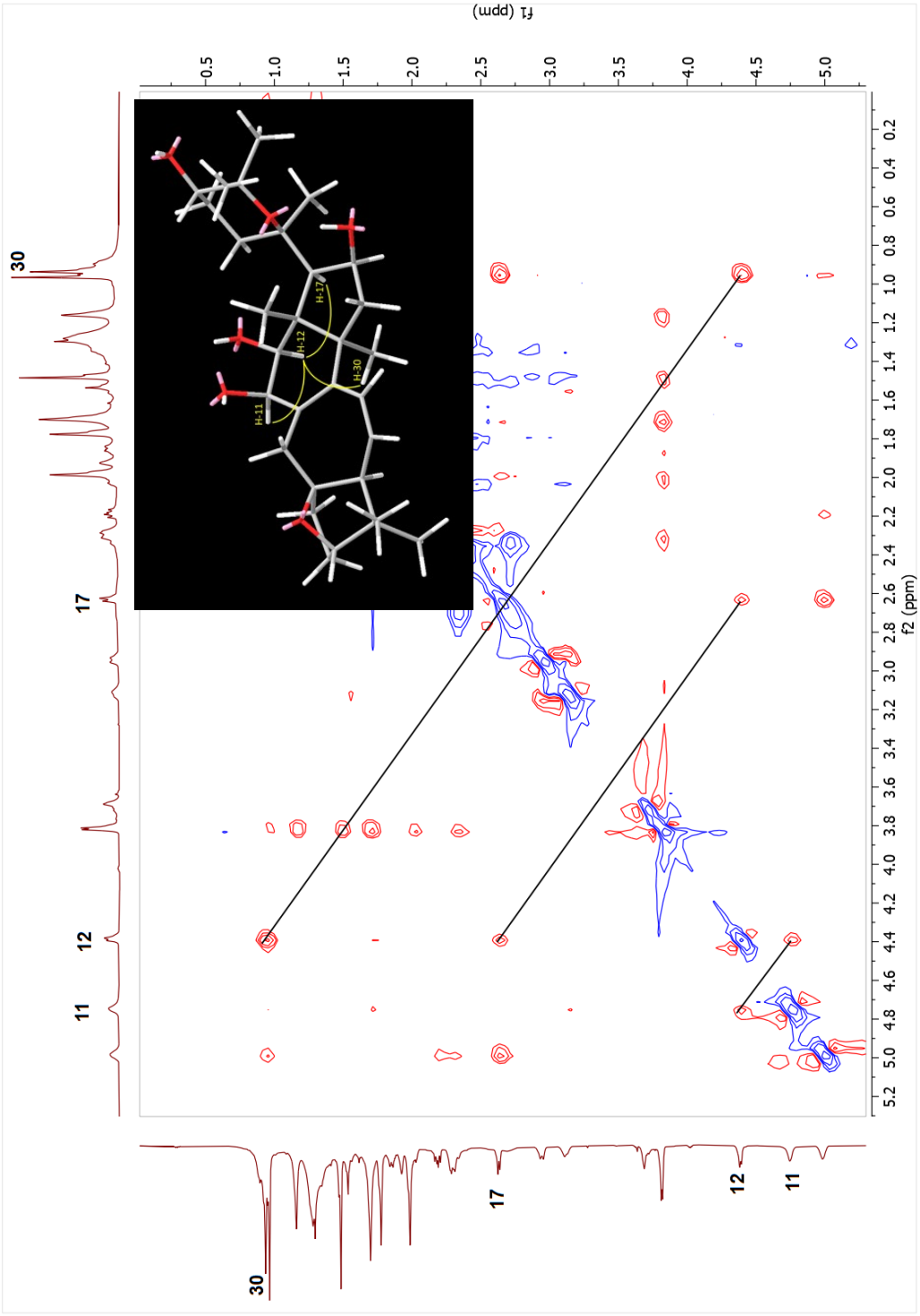

Spectrum 2.149. NOESY spectrum of compound **22**.

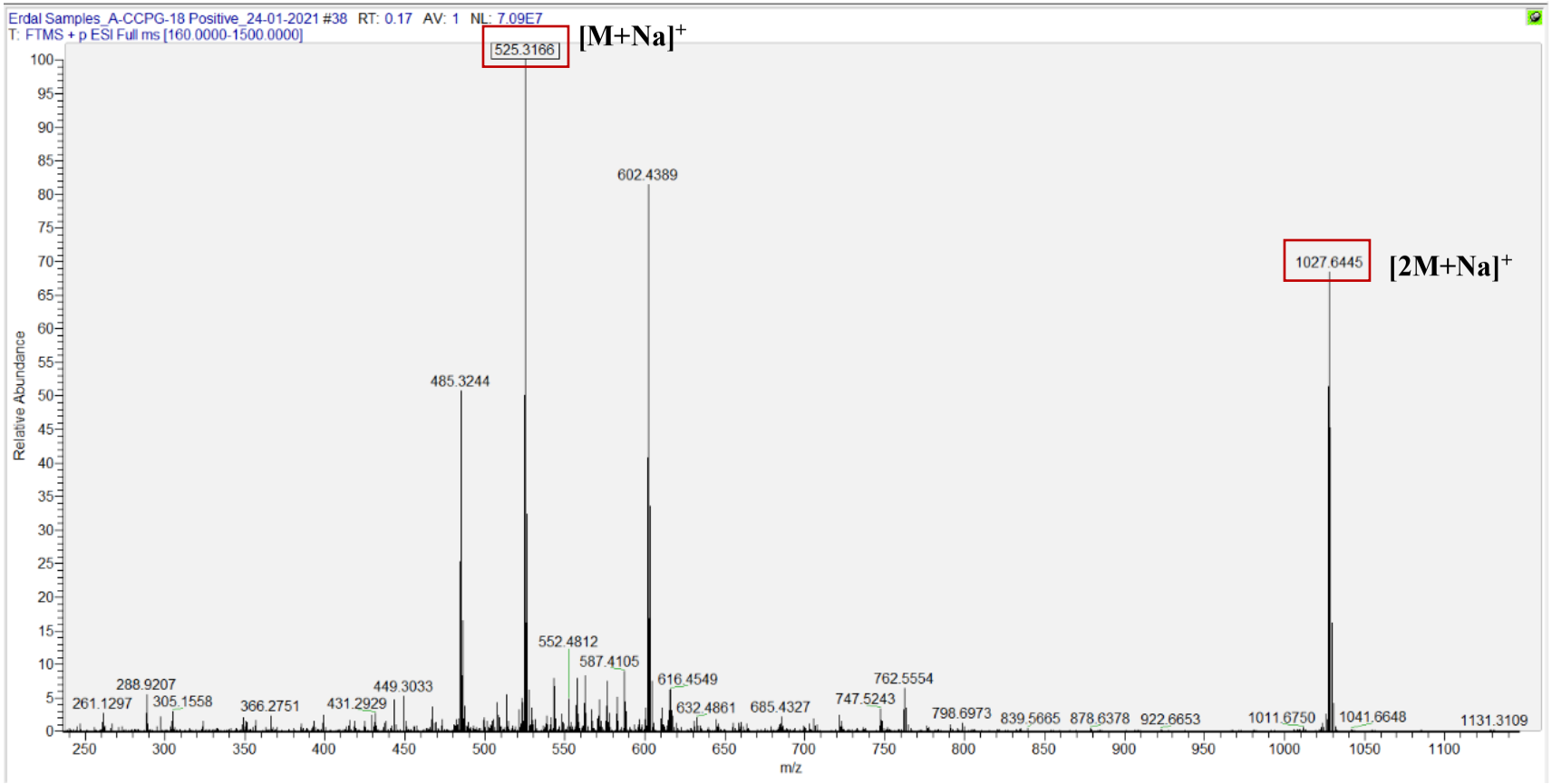

Spectrum 2.150. HR-ESI-MS spectrum of compound **22**.

2.3.3. Neuroprotective Activity of Biotransformation Products

The neuroprotective activities of isolated metabolites (except for **22** due to its scarce amount) were determined against H_2O_2-induced SH-SY5Y cell death. Compared to the control group, the compounds except **2**, **3**, **4**, **6**, **7**, **9**, **10**, **13**, **14**, **17**, and **20** did not exhibit promising neuroprotective activity (Table 2.23).

In addition to their protective effect against oxidative injury in SH-SY5Y, the selected compounds were also screened for their effect against 6-OHDA induced neurotoxicity in *in vitro* Parkinson's disease model. Despite the lower potency of compounds in this model compared to the H_2O_2-induced neurotoxicity model, the tested metabolites still showed a statistically significant protective effect, suggesting that they may act as general protective agents against neurotoxicity mediated by a different mechanism of action (Figure 2.30).

Table 2.23. Neuroprotective activity of metabolites against H_2O_2 toxicity. Data are presented as means ± S.D. (n = 3).

Metabolite	Concentration	Cell viability (%)	Metabolite	Concentration	Cell viability (%)
2	1 nM	56.22±1.83****	**12**	1 nM	36.18±1.92
	10 nM	61.36±3.72****		10 nM	46.24±1.84*
	100 nM	61.13±0.69****		100 nM	48.98±6.18**
	1000 nM	58.05±5.86****		1000 nM	42.36±1.97
3	1 nM	46.78±6.04	**13**	1 nM	51.46±7.85
	10 nM	46.72±2.08		10 nM	56.39±2.97*
	100 nM	50.93±0.24**		100 nM	58.08±12.10*
	1000 nM	65.85±2.29****		1000 nM	66.41±9.33**
4	1 nM	34.06±0.39	**14**	1 nM	60.80±4.43****
	10 nM	59.74±3.45****		10 nM	56.54±4.19****
	100 nM	56.28±3.32****		100 nM	39.88±2.70
	1000 nM	53.62±5.87****		1000 nM	34.05±1.34
5	1 nM	26.86±2.47	**15**	1 nM	36.95±3.03
	10 nM	25.06±3.60		10 nM	41.22±2.57
	100 nM	43.78±1.32		100 nM	43.53±5.26*
	1000 nM	42.50±5.72		1000 nM	37.04±0.51
6	1 nM	45.67±2.40	**16**	1 nM	41.96±2.26
	10 nM	46.02±5.91		10 nM	46.47±7.19
	100 nM	54.80±5.77***		100 nM	42.67±3.05
	1000 nM	52.05±1.33*		1000 nM	41.38±6.59
7	1 nM	42.64±3.93	**17**	1 nM	41.87±1.37
	10 nM	45.89±5.61		10 nM	42.70±2.28
	100 nM	55.61±13.27*		100 nM	62.77±7.89***
	1000 nM	48.95±3.92		1000 nM	72.54±13.30****
8	1 nM	36.61±11.01	**18**	1 nM	44.04±0.67
	10 nM	40.30±1.51		10 nM	42.03±0.76
	100 nM	36.63±2.69		100 nM	44.39±0.92
	1000 nM	40.24±12.93		1000 nM	38.07±4.77
9	1 nM	44.15±2.33	**19**	1 nM	38.04±1.89
	10 nM	46.16±3.15		10 nM	40.53±7.05
	100 nM	51.43±4.84*		100 nM	39.88±4.66
	1000 nM	70.51±0.84****		1000 nM	49.06±3.58
10	1 nM	51.08±8.54*	**20**	1 nM	56.82±1.94**
	10 nM	58.49±3.43***		10 nM	58.29±6.26**
	100 nM	74.71±3.31****		100 nM	70.62±6.93****
	1000 nM	68.10±4.80****		1000 nM	64.76±6.00****
11	1 nM	38.16±0.69	**21**	1 nM	46.98±1.60**
	10 nM	43.92±6.21		10 nM	44.72±2.41*
	100 nM	46.90±9.53		100 nM	38.72±3.05
	1000 nM	54.29±3.65**		1000 nM	35.74±1.35
H_2O_2	70 μM	37.93±1.95			

*p < 0.05, **p < 0.05, ***p < 0.001, ****p < 0.0001 significant difference from H_2O_2-treated cells.

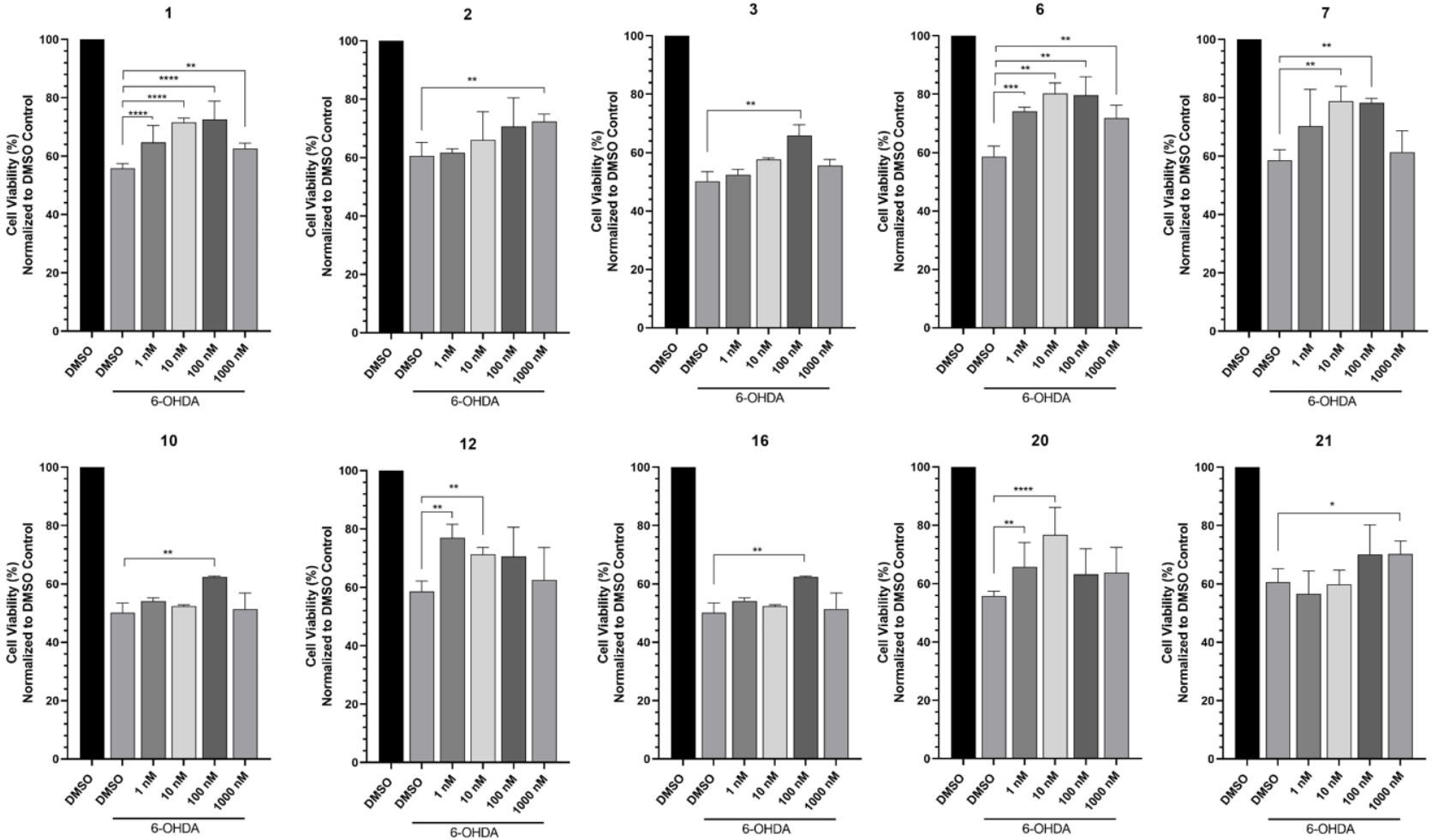

Figure 2.30. Neuroprotective activity of selected compounds against 6-OHDA toxicity. Error bars are the standard deviations (n = 3). p-Values were calculated with respect to 6-OHDA-treated cells (*$p < 0.05$, **$p < 0.01$, ***$p < 0.001$, ****$p < 0.0001$).

2.3.3.1. Selected Compounds Decreased H_2O_2-mediated Oxidative Stress

Excessive ROS was reported to cause severe cell damage and induce cell death[95]. Since H_2O_2 is well known to increase the level of ROS, we aimed to determine the effect of compounds on H_2O_2-mediated increased ROS levels.

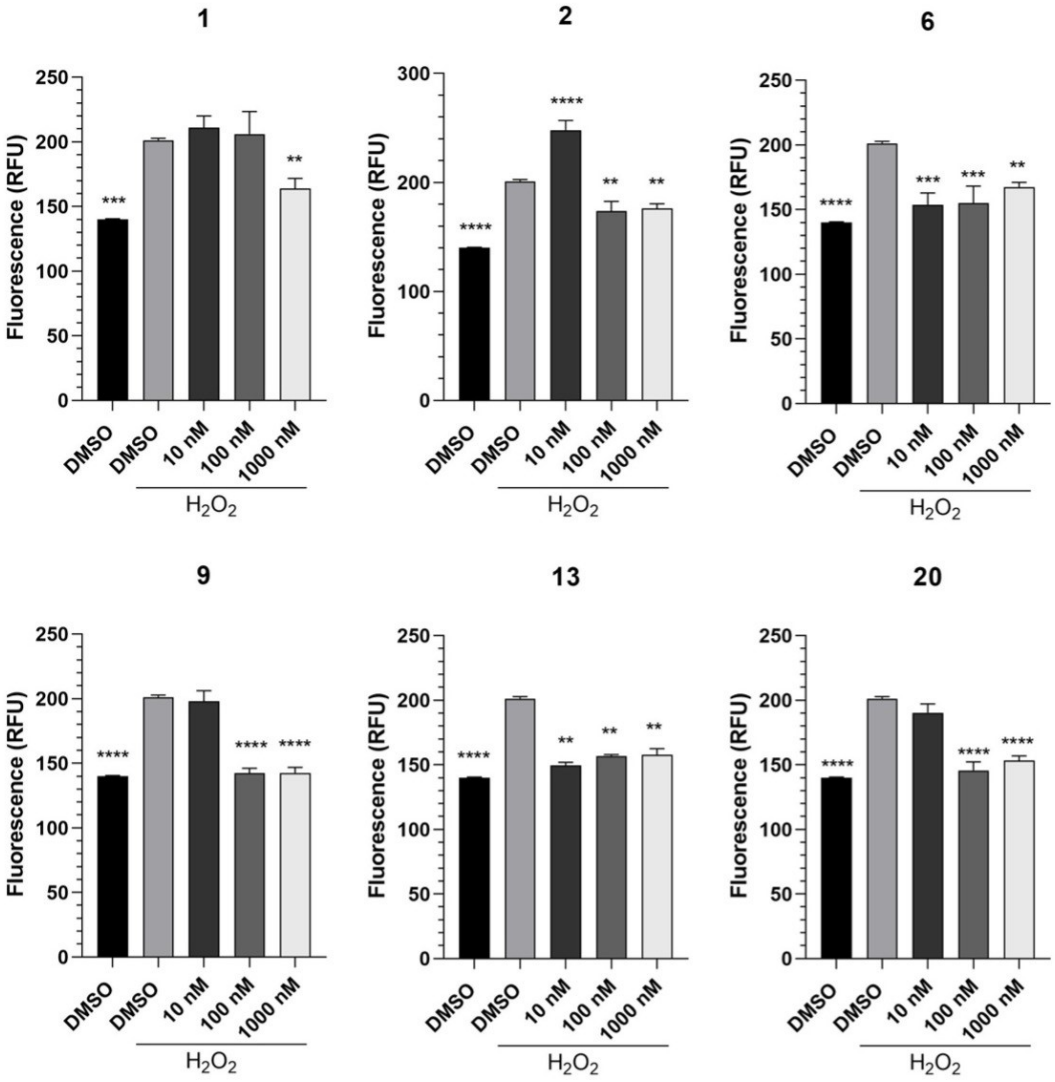

Figure 2.31. Selected metabolites abbreviated H_2O_2-induced oxidative stress in SH-SY5Y cells. Data are presented as means ± S.D. (n = 3).

Six molecules, including parent compound (**1**), were selected to detect their potential in rescuing H_2O_2-induced oxidative stress, considering their cell viability results, structure, and available quantity. Results showed that treatment with H_2O_2 significantly increased ROS levels compared to control. In line with the cell viability assay, all selected compounds reduced H_2O_2-induced ROS levels in cells (Figure 2.31). Parent **1** was the least potent, while **6** and **13** were the most effective compounds reducing ROS at all concentrations (Figure 2.31). Interestingly, **2** enhanced ROS production via H_2O_2 at 10 nM, but higher concentrations significantly decreased ROS level (Figure 2.31).

2.3.3.2. Selected Metabolites Prevent H_2O_2-induced Mitochondria Damage

Mitochondrial dysfunction is one of the most emerging pathological processes in neurodegenerative diseases[96]. Since mitochondrial membrane potential was reported as an indicator to detect mitochondrial dysfunction, we next evaluated effect of **1** and four selected compounds on mitochondrial membrane potential by using Mitotracker Red.

As expected, the fluorescence intensity significantly decreased after treatment with H_2O_2 treatment, which suggested that H_2O_2 could induce mitochondrial dysfunction. All selected compounds efficiently protected cells from H_2O_2 mediated mitochondrial damaged (Figure 2.32).

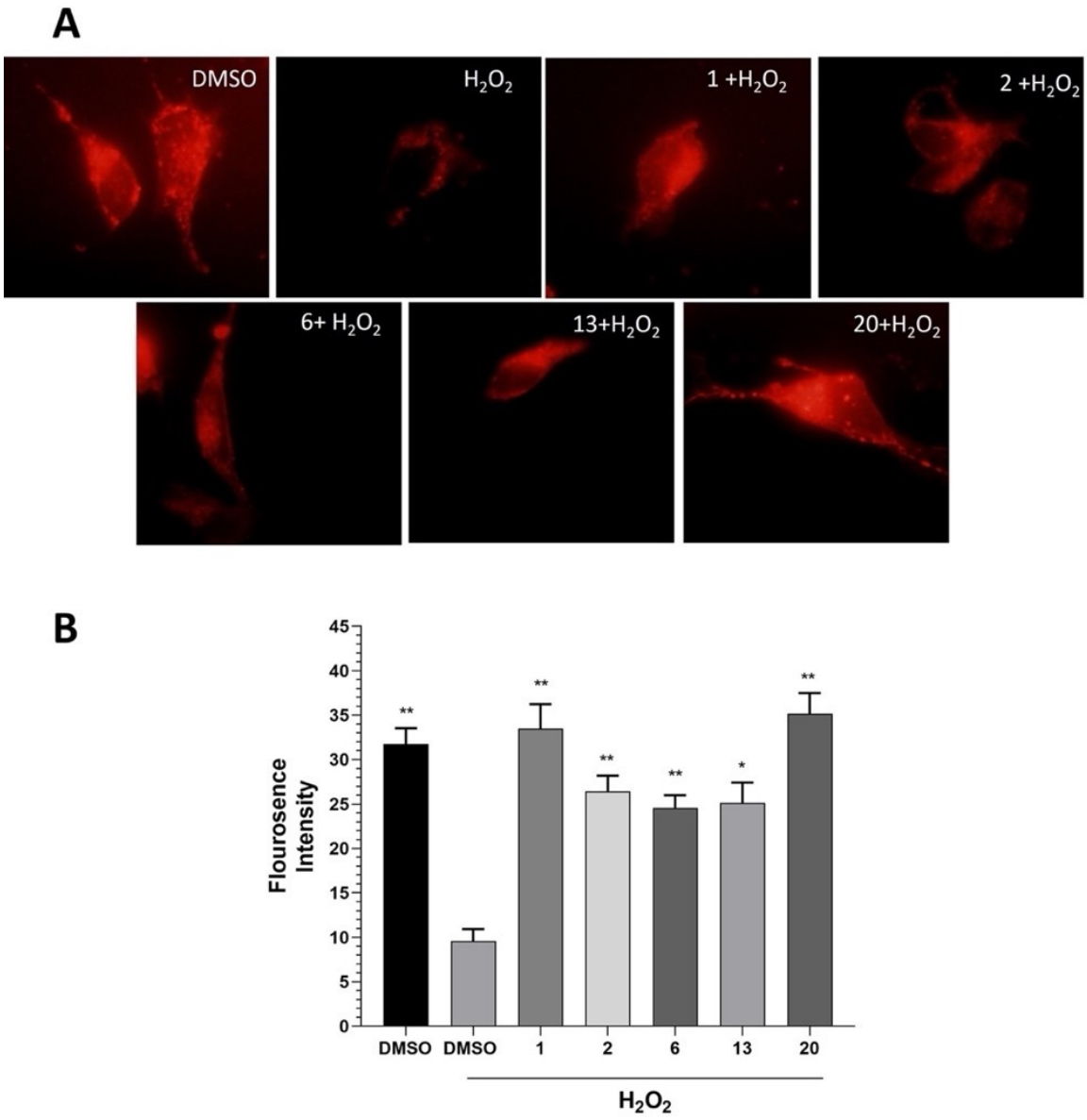

Figure 2.32. Selected metabolites protect SH-SY5Y cells from H_2O_2-induced mitochondrial damage. (A) Representative microscopy images of cells stained with MitoTracker Red. (B) Quantification of MitoTracker Red fluorescence intensities per cell volume (n = 30 cells). Data are presented as means ± S.E. (n = 30).

2.4. Discussion

In recent years, endophytic fungi have received great attention as a whole-cell catalyst because of their capability to produce enzymes necessary for their colonization. It is anticipated that the endophytic biocatalysts will match chemical reactions even as powerful as conventional chemical methods in near future[58,63–65]. Additionally, studies on fungal biotransformation of plant secondary metabolites with the plant's own endophytes are very limited. Our previous studies demonstrated that *Alternaria eureka* expresses P450 monooxygenase enzymes and effectively catalyzes various modifications on triterpenoid and steroid structures[49,73,84,91,92]. In this study, the biocatalysis of cyclocephagenol (**1**) by *A. eureka* yielded twenty-one metabolites (Figure 2.33)[97]. *A. eureka* was found to be capable of modifications including monooxygenation, dehydration, methyl migration, epoxidation, and ring expansion resulted in the formation of metabolites that would be difficult or impossible to prepare by conventional synthetic methods. Although fungal biotransformation has been used in the modification of natural products for a long time, demonstration of endophytic fungi's utilization in biotransformation is essential for the field not only for utilizing endophytes as potent catalysis systems but also for proving the potential of the plant's own microbiota for transformation studies.

The regioselective hydroxylation at C-12 position was the most prevalent reaction in the cycloartane skeleton. We suggest that *A. eureka* first catalyzes α- or β-hydroxylation at C-12, then performs further modifications. The other monooxygenation locations were identified as C-7 and C-11. Although hydroxylation at C-7 has been encountered with steroidal sapogenins[49,84,91,92], this modification is reported for the first time on the triterpenoid framework by *A. eureka*.

One of the most interesting biotransformation was the dihydroxylation at C-11 and C-12. Previously, 11α-hydroxy,12β-acetoxy steroids were obtained from the gorgonian *Isis hippuris*[98]. This is the first report of C-11 and C-12 dihydroxylated products obtained via microbial biotransformation. Additionally, 3(10)-epoxy formation and ring expansion modifications have been reported in the previous studies[73,75,99], whereas the 6,8-diene system is being reported for the first time in triterpenoid chemistry.

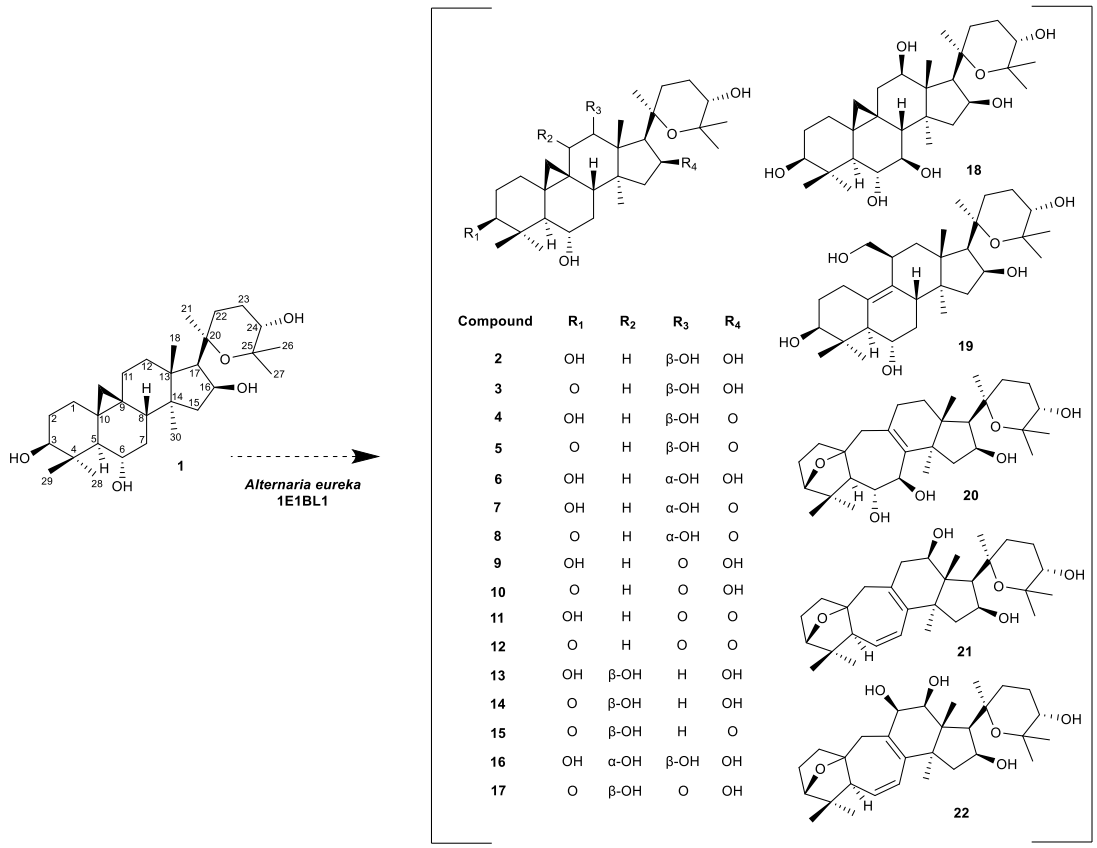

Compound	R_1	R_2	R_3	R_4
2	OH	H	β-OH	OH
3	O	H	β-OH	OH
4	OH	H	β-OH	O
5	O	H	β-OH	O
6	OH	H	α-OH	OH
7	OH	H	α-OH	O
8	O	H	α-OH	O
9	OH	H	O	OH
10	O	H	O	OH
11	OH	H	O	O
12	O	H	O	O
13	OH	β-OH	H	OH
14	O	β-OH	H	OH
15	O	β-OH	H	O
16	OH	α-OH	β-OH	OH
17	O	β-OH	O	OH

Figure 2.33. Biotransformation products of cyclocephagenol (**1**) by *A. eureka*

Natural products have the potential for the prevention and treatment of neurodegeneration. In recent years, cycloartane-type saponins, especially astragaloside IV and cycloastragenol, have been reported as a new class of neuroprotective agents[55,56]. Based on the promising bioactivity of cycloartane-types saponins, we first evaluated the neuroprotective activity of cyclocephagenol (**1**) against H_2O_2-induced SH-SY5Y cell death. Compared to cycloastragenol, the neuroprotective activity of **1** started at lower concentrations. Since the neuroprotective activity of cyclocephagenol was noteworthy, a biotransformation study on **1** was carried out to develop a molecule library and to investigate structure-activity relationships by *A. eureka*.

Among the oxygenated metabolites, **2** and **6** possessing hydroxy group at position 12 (12β and 12α, respectively) showed potent neuroprotective activity. While the most active concentration of **2** was 10 nM, the neuroprotection by **6** was observed at a higher concentration (100 nM). Also, the metabolite **13** possessing hydroxy group at position 11

demonstrated potent neuroprotective activity at higher concentrations (100 and 1000 nM). On the other hand, a dihydroxy group in ring C (**16**; 11α,12β-dihydroxy) led to a loss of neuroprotection suggesting that the hydroxylation pattern was critical for the activity.

The presence of ketone functionality at C-3 or C-16 (**3**: 3-oxo-12β-hydroxy, **4**: 16-oxo-12β-hydroxy, **7**: 16-oxo-12α-hydroxy) had no detrimental effect on neuroprotection compared to metabolite **2** and **6**. However, the co-presence of ketone group at C-3 and C-16 (**5**: 3,16-dioxo-12β-hydroxy, **8**: 3,16-dioxo-12α-hydroxy) diminished neuroprotective activity. Moreover, the oxidation at C-12 (**9**: 12-oxo, 1000 nM) improved neuroprotective activity whereas additional oxidation at C-16 (**11**: 12,16-dioxo) lessened neuroprotective activity. This finding suggested that the co-presence of ketone group at C-12 and C-16 affects the biological activity negatively. In contrast to metabolite **3** (3-oxo-12β-hydroxy), oxidation at position 3 improved neuroprotective activity in **14** (3-oxo,11β-hydroxy) and **10** (3,12-dioxo). Although metabolite **16** (11α,12β-dihydroxy) was not active, activity in **17** (3,12-dioxo, 11β-hydroxy) indicated that oxidation in C-12 was important for biological activity.

Compound **20** was one of the most potent compounds, while neuroprotection was considerably decreased in **21**, a dehydration product of **20**, revealing that conformational flexibility in the B ring was also crucial.

As a result of SAR studies, we conclude that i) monooxygenation at positions 11 (**13**) and 12 (**2** and **6**) is significant for bioactivity; ii) oxidation at C-12 (**9**, **10**, **17**) improves neuroprotective activity; iii) further increase of hydrophobicity (**5**, **8**, **11**, **12**) and hydrophilicity (**16**, **18**) diminishes bioactivity; iv) 3(10)β-epoxy-9,10-seco-cycloartane products formed by ring expansion and epoxidation reactions could be potential neuroprotective agents as long as they have conformational flexibility. Further studies revealed that selected compounds reduced the amount of ROS and preserved the integrity of the mitochondrial membrane.

Collectively, the biocatalyst potential of *A. eureka*, which plays an important role in expanding our cycloartane molecule library, has been demonstrated once again. In addition to chemical diversity, biotransformation provided several novel compounds having potent protective activity against H_2O_2- and 6-OHDA-induced neurotoxicity. Further studies are warranted to establish mechanism of action of the bioactive metabolites.

CHAPTER 3

BIOCATALYSIS OF CYCLOCEPHAGENOL AND ITS DERIVATIVES BY *CAMAROSPORIUM LABURNICOLA* TO OBTAIN TELOMERASE ACTIVATORS

3.1. Background

Within the scope of the 114Z958 – TÜBİTAK project, our group performed biotransformation studies on *Astragalus*-derived cycloartane triterpenoids (cycloastragenol, cyclocanthogenol, astragenol and 20(27)-octanor cycloastragenol) using *Astragalus* endophytic fungi to obtain more active telomerase activators than the commercially available cycloastragenol. Compounds shown in Figure 3.1 demonstrated high telomerase activation at very low doses and increased telomerase activation compared to the positive control cycloastragenol.

The major modifications leading to the increase in activity were the oxidation of C-3(OH), conversion of ring A to 7-membered lactone, and the formation of 3(4)-seco structures via cleavage of the ring A, catalyzed by *C. laburnicola*.

Another substantial modification was the hydroxylation of C-12 by the P450 monooxygenase system of *Alternaria eureka*. The compound A-CA-03, possessing the α-oriented hydroxyl group at C-12, was found to be one of the most effective compounds.

Based on our previous studies, we first focused on the bioactivity of cyclocephagenol (**1**), 12α-hydroxycyclocephagenol (**2**), and 12β-hydroxycyclocephagenol (**6**). To see the potential of compounds **1**, **2**, and **6** towards telomerase activation, a more economical preliminary experiment [hTERT (human Telomerase Reverse Transcriptase) protein expression] was conducted. All compounds increased hTERT protein expression; therefore, we further performed a modification study on these compounds utilizing *C. laburnicola*.

Later, we screened biotransformation products for their effects on telomerase activation by immunoblotting studies and PCR-based ELISA tests.

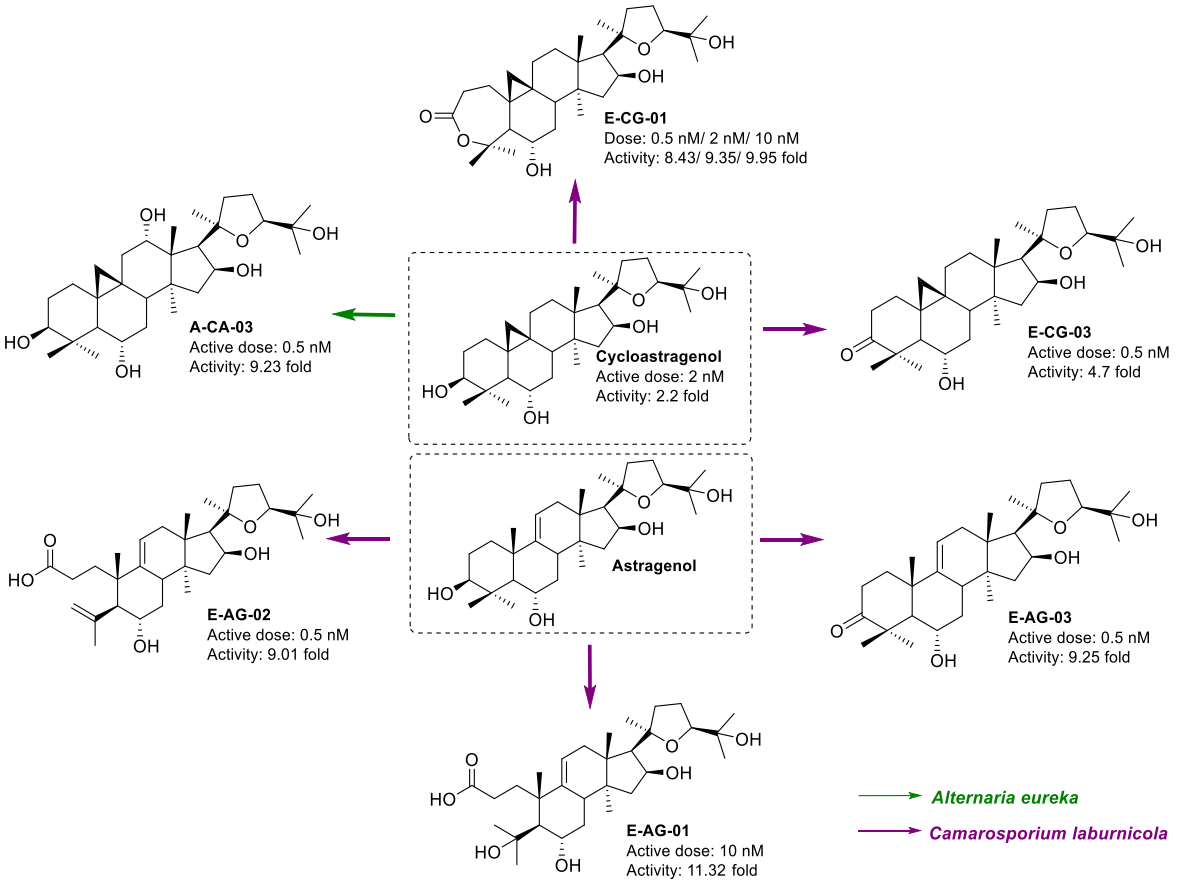

Figure 3.1. Telomerase activator compounds obtained within the scope of 114Z958-TÜBİTAK project and their bioactivity results. Telomerase activation was determined according to the control DMSO. The telomerase activation in the 0.5-300 nM range was evaluated, and the highest activities were shown accordingly.

The overriding reason for carrying out this study was to investigate whether the biotransformation of cyclocephagenol by *C. laburnicola* would produce telomerase activators as in cycloastragenol and astragenol. In addition, we also performed a biotransformation study on 12α-hydroxycyclocephagenol and 12β-hydroxycyclocephagenol

using *C. laburnicola* to obtain hybrid metabolites, possessing both hydroxylation at C-12 and modification at A-ring to increase the potency.

3.1.1. Telomer, Telomerase and Telomerase Activators

Telomeres are specialized structures consisting of TTAGGG tandem repeat sequences at the ends of chromosomes. They protect chromosome ends from fusion and degradation and shorten over time in dividing somatic cells[100–102]. Telomerase is a cellular "reverse transcriptase" (TERT, telomerase reverse transcriptase) enzyme that uses the relevant RNA component (Terc, telomerase RNA component) as a template and helps repair telomere ends by adding TTAGGG repeats[103]. The dynamic maintenance of telomeres by telomerase is closely related to the restricted proliferative lifespan of normal cells and the immortality of cancer cells. Because both normal and abnormal (such as cancer) cells must maintain genomic integrity, research in the field of telomeres and telomerase plays a crucial role in examining various areas such as aging, cancer, and pathogen-induced chronic degenerative diseases[104]. In addition, considering the ever-increasing aging population, regenerative medicine has focused on developing strategies for maintaining telomere length in recent years[105].

Telomerase activation is of great importance for the development of new anti-aging therapies. However, one of the main reasons for the delay in the expected explosion in this area has been speculation that telomerase activation will lead to cancer. This speculation is because telomerase is highly expressed in more than 90% of human cancer cell lines[106]. However, studies in the last 15 years have refuted these considerations: i) Telomerase-based therapies not only stopped the aging process in humans but also reversed it[107,108]; ii) Telomere shortening in human beings contributes to mortality in many age-related diseases[109]; iii) Telomerase is not an oncogene that causes cancer and does not cause cells to lose growth control and become cancerous[110]; iv) Short telomeres have been reported to cause cancer by causing telomeric dysfunction and chromosome instability[111].

Telomerase enzyme activators are shown to be promising agents for the healthy aging progression. Cycloastragenol is only biosynthesized in *Astragalus* species. As a very significant telomerase activator, it was discovered in 2004 by Geron Corp. Since 2007, it has been in the market as a new anti-aging dietary supplement with the trade name TA-65.

Telomere shortening is a consequence of the biological aging process and a risk factor for many age-related diseases. It has been shown to have a significant effect on many diseases, such as neurodegenerative diseases (Alzheimer's and Parkinson's diseases), macular degeneration, coronary artery disease, hypertension, and diabetes. Telomere-shortening-related diseases are not only age-related. Congenital dyskeratosis, AIDS, aplastic anemia, and pulmonary fibrosis are diseases caused by telomere dysfunction. Telomerase activation represents a potential goal for treating diseases associated with telomere loss. Therefore, *in vivo* telomerase activation has significant potential for treating many chronic and degenerative diseases. The use of cycloastragenol as a telomerase activator in regenerative medicine and degenerative diseases has been demonstrated by many studies[27–32,112–121]. Also, the entry of cycloastragenol and its derivatives into clinical trials for Alzheimer's disease (NCT number: 02531334) and metabolic syndrome (NCT number: 02530255) is an indication of the potential of telomerase activators towards degenerative diseases. In 2022, two new clinical studies were initiated using *Astragalus membranaceus* in cognitive impairment and parkinsonism (NCT number: 05578443 and 05506891, respectively).

Apart from cycloastragenol, studies on different telomerase activators have also taken place in the literature. One of these is epithalon, a synthetic tetrapeptide discovered by Russian scientist Vladimir Khavinson, produced by mimicking pineal gland protein epithalamine. Khavinson et al. (2003) demonstrated that epithalon could induce the expression of telomerase enzyme component, telomerase activity, and telomere elongation[122]. Also, a clinical study of epithalamine was conducted in older adults with the coronary disease for 15 years in Russia. Long-term treatment of epithalamine normalized the circadian rhythm of melatonin production and lipid and carbohydrate metabolism and improved life quality. Also, cardiovascular and respiratory failures were 2-fold lower in the epithalamine-treated group[123,124]. One disadvantage of epithalon and epithalamine is that intravenous injection is necessary because of the compounds' peptide nature and, thus,

stomach stability issues. However, epithalon or epithalamine has not been approved for use by the FDA.

Metformin (dimethyl biguanide) is currently preferred as a blood glucose-lowering agent to manage type 2 diabetes mellitus. In addition, metformin can effectively reduce the risk of many age-related diseases and conditions, including cardiometabolic disorders, neurodegeneration, cancer, chronic inflammation, and frailty. However, well-designed clinical trials are still warranted to enable the potential use of this therapeutic agent as a geroprotector. Also, this molecule is active at relatively higher concentrations[125,126].

In recent years, *Centella asiatica* extract has been reported as a telomerase activator by *in vitro* and *in vivo* studies. Tsoukalas et al. (2019) have reported that *Centella asiatica* extract had superior activity compared to TA-65 in peripheral blood mononuclear cells. However, this study did not directly compare TA-65's active constituent cycloastragenol, and *Centella asiatica* extract towards telomerase activation[127]. Until 2021, TA-65 has been on the market as the only natural product telomerase activator. Recently, *Centella asiatica* extract has been placed on the market as a dietary supplement with the trade name Reverse™. It was also shown that Reverse™ supplementation for three months increased telomerase activity via restored TERT expression in the brains of naturally aged rats[128].

Apart from these, many compounds have been reported to show telomerase activation. These compounds include oleanolic acid, quercetin, resveratrol, curcumin, and astragaloside IV. In addition, these compounds showed promising activity in age-related diseases, which may be related to their telomerase activation[52].

3.2. Materials and Methods

3.2.1. Microorganism and Starting Compound

Cyclocephagenol (**1**) was donated by Bionorm Natural Products, Ltd. (İzmir, Turkey). 12β-hydroxycyclocephagenol (**2**) and 12α-hydroxycyclocephagenol (**6**) were isolated in our

previous study (see Chapter 2). *C. laburnicola* used in this study was isolated from fresh and healthy leaves of *Astragalus angustifolius* (Figure 3.2). The original strain was deposited at the Bedir Laboratory with the deposit number 20131E4BL1[72]. All cultures were maintained on potato dextrose agar (PDA) slants and stored at 4 °C until use. Before biotransformation, the fungus was pre-cultivated on PDA in Petri dishes for 10 days at 25 °C.

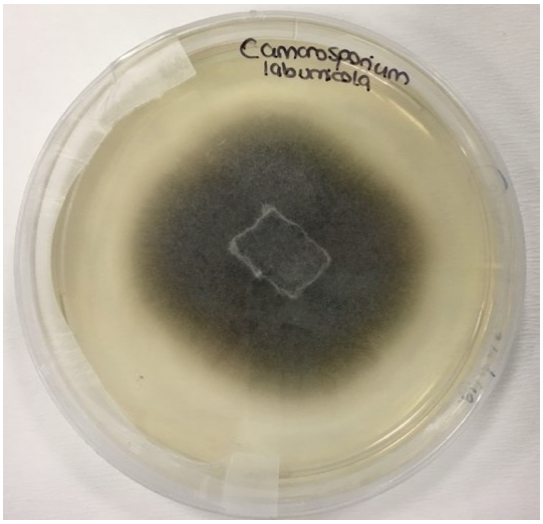

Figure 3.2. *Camarosporium laburnicola*

3.2.2. Microbial Transformation Procedure

Stock cultures stored at 4 °C in an agar slant were transferred to the fresh PDA medium and incubated at 25 °C for 10 days. Following incubation, Tween 80 (0.1%) was added to the fungi grown in the PDA medium and a spore solution was obtained by scraping with an inoculation loop. The spore suspension was inoculated to Potato Dextrose Broth (PDB). After three days of incubation, the substrate (20 mg/mL in DMSO) was dosed at 1% (v/v) of the medium. Preparative-scale biotransformation studies were performed employing 100 mg of **1** for 4 days, 30 mg of **2** for 30 days, and 30 mg of **6** for 30 days with *C. laburnicola* (25 °C and 180 rpm).

3.2.3. Extraction and Isolation

After an incubation period, the fungal mycelia were filtered on a Buchner funnel, and the filtrate was extracted with EtOAc (×3). The organic phase was evaporated under reduced pressure to dryness.

Compounds **23**-**25** were isolated from the EtOAc extract (120 mg) of *C. laburnicola* with **1** (Chromatogram 3.1). This extract was subjected to vacuum-liquid chromatography (VLC) loaded with reversed-phase silica gel (RP-C18, 30 g) to yield **23** (22.6 mg), **25** (9.2 mg), and one impure fraction (A) after elution with an ACN:H_2O gradient (40:60, 50:50, 60:40, 100:0). Fraction A (7.9 mg) was chromatographed on a silica gel column (10 g) using $CHCl_3$:MeOH gradient (100:0, 98:2, 97:3) to afford 29 fractions. Fractions from A22 to A26 (6.8 mg) were combined and re-chromatographed over a silica gel column (10 g) using $CHCl_3$:IPA gradient (99:1, 97:3) to afford **24** (2.3 mg) (Figure 3.3).

Chromatogram 3.1. Thin layer chromatogram of the EtOAc extract obtained from preparative scale biotransformation study of cyclocephagenol by *C. laburnicola* [Reverse phase C18 silica gel, Mobile phase: 70:30 (ACN: H_2O)].

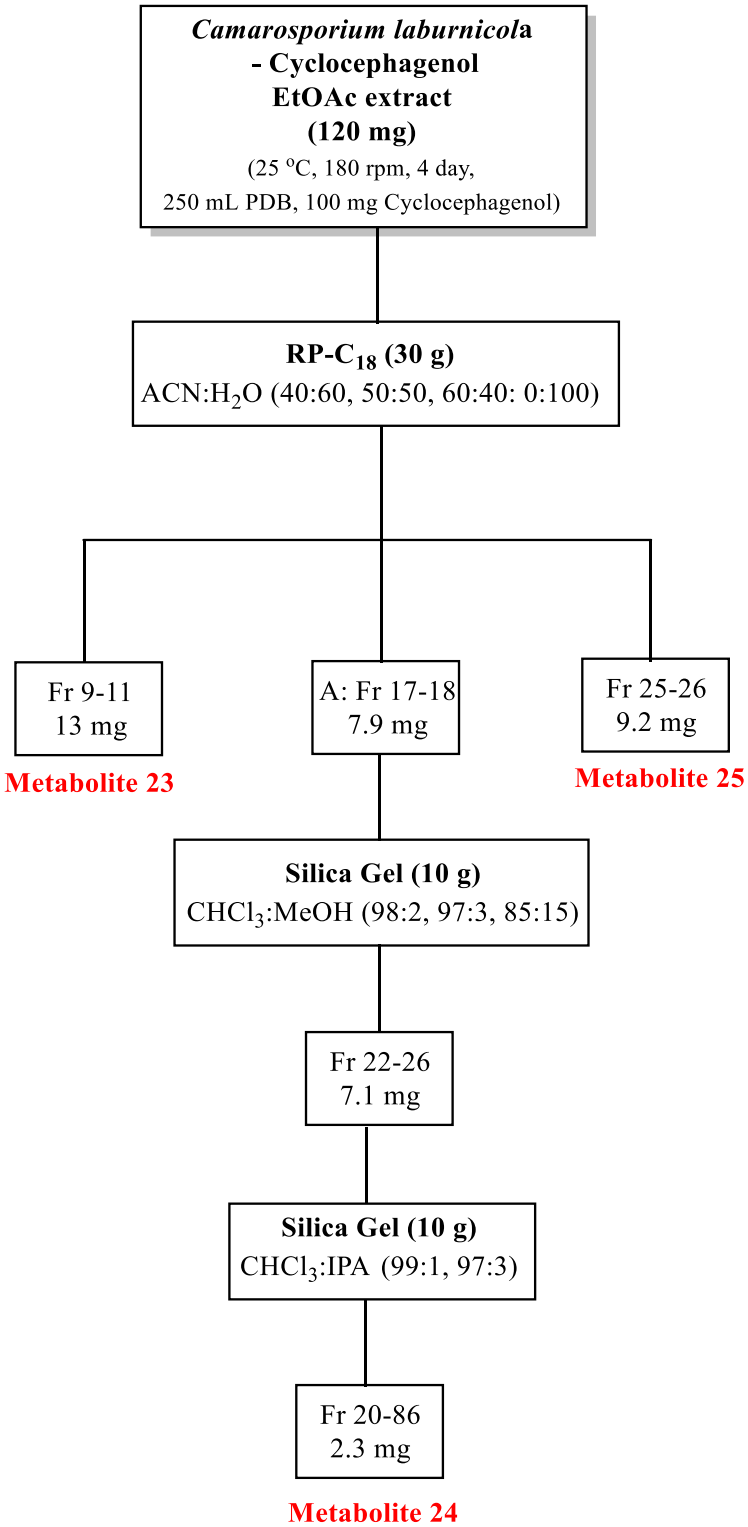

Figure 3.3. Isolation scheme of biotransformation products of cyclocephagenol by *C. laburnicola*

Compounds **26-29** were isolated from the EtOAc extract of **6** (241 mg) by *C. laburnicola* (Chromatogram 3.2). This extract was chromatographed on a silica gel column (33 g) using *n*-hexane:EtOAc:MeOH:H_2O (10:10:2:0, 10:10:3:0, 0:100:17.5:13.5) gradient to give four impure fractions (Fractions A-D). Each impure fraction was subjected to vacuum-liquid chromatography (VLC) loaded with reversed-phase silica gel (RP-C18, 20 g) to yield 2**6** (7.2 mg), **27** (3.7 mg), **28** (3.4 mg) and **29** (2 mg) (Figure 3.6).

However, 12β-hydroxycyclocephagenol couldn't be converted by *A. eureka* effectively. Therefore, isolation studies were not performed on the EtOAc extract of **2** by *C. laburnicola* (Figure 3.4).

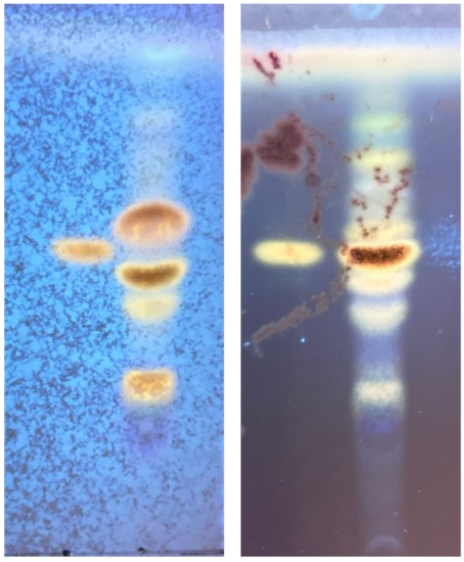

(6) Extract **(2) Extract**

Chromatogram 3.2. Thin layer chromatogram of the EtOAc extract obtained from preparative scale biotransformation study of 12α-hydroxycyclocephagenol and 12β-hydroxycyclocephagenol by *C. laburnicola* [Silica gel, Mobile phase: 100:17.5:13.5 (EtOAc:MeOH:H_2O)].

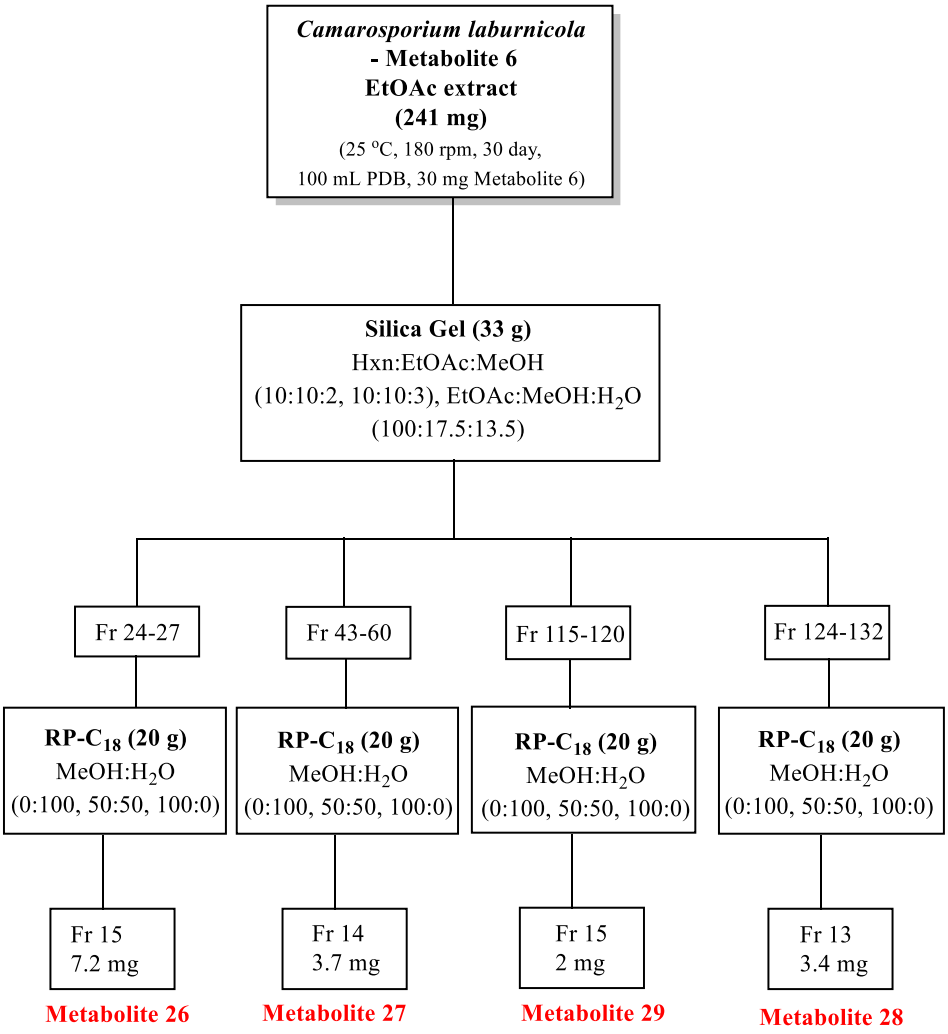

Figure 3.4. Isolation scheme of biotransformation products of metabolite **6** by *C. laburnicola*

3.2.4. Bioactivity Studies

3.2.4.1. Cell Line and Culture Conditions

Primary human epidermal keratinocyte cells (HEKn) (ATCC; PCS-200-010) were cultured in Dermal Cell Basal Media (ATCC; PCS-200-030) supplemented with Keratinocyte Growth Kit (ATCC; PCS-200-040) according to the manufacturer's

instructions at 37 °C under humidified 5% CO_2. HEKn cells were seeded at a density of 2500 to 5000 cells per cm^2 when they reached 70-80% confluency.

3.2.4.2. Immunoblotting Studies

Cells were seeded into 12 well plates for bioactivity studies. Metabolites were dissolved in DMSO to a final concentration of 5 mM. Then, metabolites were added to cells at final concentrations of 2, 10, 30, 100 and 300 nM. After the 24 h incubation time, cells were detached by trypsinization and harvested with 1X PBS in eppendorf. After that, the cell suspension was centrifuged for 3 min at 10000 g at 4 °C, and the supernatant was removed. The same process was repeated two times for 2 and 1 min. 1X PBS and 2X RIPA that involve 25X PIC (protein inhibitor cocktail) were used as lysis buffer. Samples were vortexed with 30 µL of PBS lysis buffer, 30 µL of RIPA lysis buffer was added, and samples were vortexed. Then samples were vortexed vigorously four times after every 5 min. Samples were centrifuged at 15500 g at 4 °C for 20 min, and the supernatant was transferred to clean eppendorf.

The total protein content of samples was determined by using BCA assay to equalize the protein quantity of samples for loading. 190 µL BCA solution (reagent A and B in 50:1 ratio) were added to 2 µL samples and 8 µL distilled water. Following incubation at 37 °C for 30 min, colorimetric absorbance was measured at 562 nm wavelength. Samples were prepared according to the data of the BCA assay, and 4X loading buffer was added to each with a final concentration of 1X. A dry bath was used to denature samples at 95 °C for 5 min.

Samples were run with 10% SDS gels. Firstly, they were run at 80 V for 30 min, then 140V was used to complete the running process. Following the running process, proteins on gels were transferred to PVDF (Polyvinylidene difluoride) membrane. A sandwich containing a sponge, two filter papers, gel, PVDF membrane, two filter papers, and a sponge sequentially was assembled in a transfer cassette for the transfer process at 300 mA for 90 min (in ice) or 40 mA overnight.

PVDF membranes, that proteins were transferred on, were treated with 5% milk for 1 h before blotting with primer antibodies. Antibodies were incubated for 1 h for GADPH (CST, 5174) antibody and overnight for hTERT antibody (Origene, TA301588). Then membranes were washed with wash buffer for 30 min, and appropriate secondary antibodies were used for 1 h. After the last washing step for 30 min, chemiluminescence images were taken using ECL with Vilber Lourmat Fx-7 imaging system. Images were edited in Image J program.

3.2.4.3. Telomerase Activity Assay

The identification of telomerase enzyme activity was performed in HEKn cells by TeloTAGGG Telomerase PCR Plus Kit (Sigma Aldrich, 12013789001) according to the supplier's instruction. The obtained data were presented as a fold change of DMSO used as a solvent control. Experiments were done in two biological experiments with two technical replicates. The experiment was conducted as below:

Step 1: Preparation of cell extracts

- 200 µL of lysing buffer (Solution 1) was used to suspend the pelleted cells and incubated them on ice for 30 min.
- After completion of the incubation period, the lysates were centrifuged at 16000 g for 20 min (2-8 ºC).
- The supernatant was carefully cooled and transferred to a clean eppendorf.

Step 2: Performing elongation/amplification

- The PCR reaction was designed for the samples group and the control group. For both the positive-negative sample and the sample to be investigated for activation, 25 µL of the reaction mixture and 5 µL of the internal standard solution were transferred into PCR tubes, or 30 µL of the prepared master mix was transferred into PCR tubes.
- PCR was performed according to Table 3.1.

Table 3.1. The PCR conditions

	Time	Temperature	Cycle
Primer Elongation	10-30 min	25 ºC	1
Telomerase inactivation	5 min	94 ºC	1
Amplification:			
Denaturation	30 s	94 ºC	
Annealing	30 s	50 ºC	30
Polymerization	90 s	72 ºC	
Final Extension	10 min	72 ºC	1
Final hold		4 ºC	

Step 3: Hybridization and photometric deduction

- For each sample, 10 µL of denaturation agent was added to nuclease-free 96-well plates.
- 2.5 µL of the amplified products were transferred to the plate and incubated at 15 to 25 °C for 10 min.
- According to the experimental flow chart, 100 µL Hybridization Buffer T was added to some of the samples and 100 µL Hybridization Buffer IS was added to others.
- After careful homogenization, 100 µL of the reaction mixture was transferred to the MP module coated with streptavidin. The MP module was carefully covered with a special coating paper.
- After the transfer was completed, the MP module was incubated at 37 °C for 2 h with shaking at 300 rpm.
- Once incubation was complete, hybridization solutions were carefully removed.
- Each well was washed three times in 1X Wash buffer (250 µL was added per well for each wash, and Wash buffer was carefully removed).
- The prepared Anti-DIG-HRP working solution was added to each well.
- The MP module was carefully covered with special covering paper and incubated at 15-25 °C for 30 min at 300 rpm with shaking.
- When incubation was complete, the solution was carefully removed from the well.

- Each well was washed five times in 1X Wash buffer (250 µL was added per well for each wash, and Wash buffer was carefully removed).
- 100 µL of room temperature warmed TMB substrate solution was added to each well.
- The MP module was carefully covered with special covering paper and incubated at 15-25 °C for 10-20 min at 300 rpm with shaking.
- At the end of incubation, the color change was terminated by adding the Termination agent without any removal.
- Within 30 min, the samples were measured with a microplate reader at 450 nm and 690 nm, the reference wavelength.

3.3. Results

3.3.1. Effect of Cyclocephagenol (1), 12β-hydroxycyclocephagenol (2) and 12α-hydroxycyclocephagenol (6) on hTERT Expression

As hTERT protein level is a preliminary indicator of probable telomerase activation, compounds **1**, **2**, and **6** were screened for their effects on hTERT expression by Western Blot. All three metabolites were found to increase the hTERT protein levels compared to the DMSO-treated control group. While **1** and **2** increased the hTERT protein levels in a dose dependent-manner, metabolite **6** enhanced hTERT protein levels at 10-, 30 and 100 nM concentrations (Figure 3.5).

Based on the strong activities of these metabolites, a biotransformation study on **1**, **2** and **6** were carried out to enrich our molecule library, obtain potent telomerase activators and investigate structure-activity relationships.

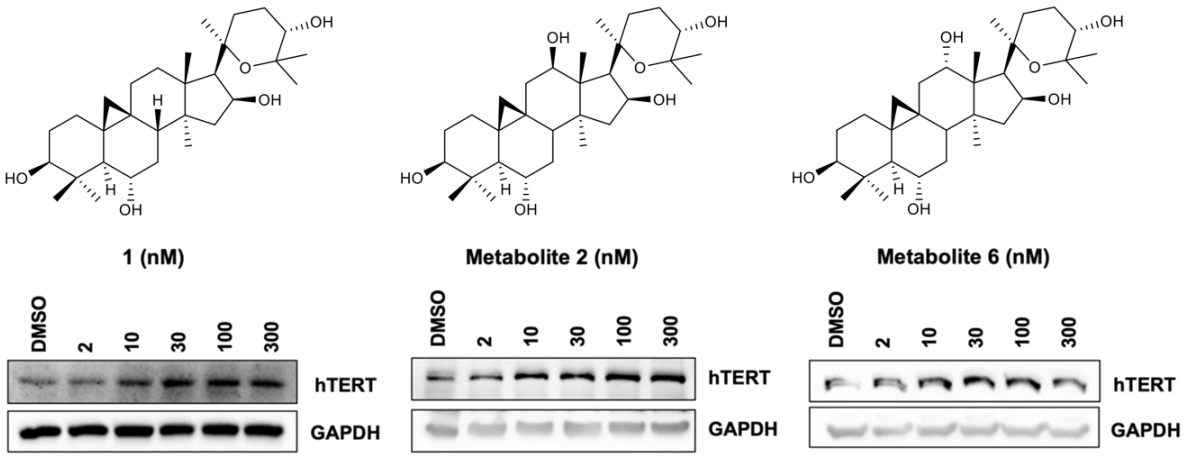

Figure 3.5. Effects of **1**, **2** and **6** on hTERT protein level.

3.3.2. Biotransformation of Cyclocephagenol (1) and 12α-hydroxycyclocephagenol (6) by *Camarosporium laburnicola*

The biotransformation of cyclocephagenol with the endophytic fungus *C. laburnicola* for four days afforded three metabolites (**23** – **25**), while the biotransformation studies performed on 12α-hydroxycyclocephagenol by *C. laburnicola* for 30 days yielded four metabolites (**26** – **29**).

The structures of the compounds were established by 1D-, 2D-NMR and HR-MS analyses. Comparison of the NMR data for **23** - **25** with those of **1** and **26** - **29** with those of **6** revealed the presence of the same partial structures for the B → E rings. These observations suggested A ring biotransformation occurred in metabolites **23** – **29**.

3.3.2.1. Structure Elucidation of Compound 23

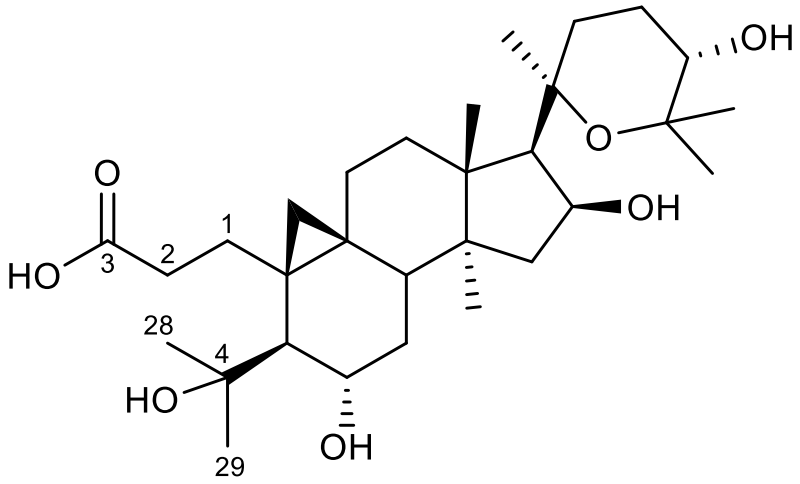

Figure 3.6. Chemical structure of compound **23**.

HR-ESI-MS spectrum of **23** showing a major ion peak at *m/z* 545.34691 ($[M+Na]^+$) indicated a molecular formula of $C_{30}H_{50}O_7$. In the ^{13}C-NMR spectrum, the oxymethine signal belonging to C-3 was lost, and a carboxyl signal was deduced from δ_C 176.0 resonance. In addition, a quaternary carbon adjacent to oxygen (δ_C 75.7) was noticed. When five out of six degrees of unsaturation accounted for the ring systems (rings B $\rightarrow$ E and the cyclopropane) was assessed with the presence of a carboxyl group, revealing an additional unsaturation, a cleavage for ring A was evident. In the HMBC spectrum, the long-distance correlation of the carbon at δ_C 75.7 to H-5, H_3-28 and H_3-29 justified the hydroxylation at C-4. Additionally, a downfield shift of H_2-2 signals (δ_H 2.96, m, H-2a; δ 2.60, m, H-2b) together with the long-distance correlation of the carboxyl signal with H-2 and H-1 proved the structure being 3(4)-seco-cyclocephagenol. Based on these results, the structure of **23** was established as 20,25-epoxy-6α,16β,24α-trihydroxy-3,4-secocycloartan-3-oic acid.

Table 3.2. The ^{13}C and ^{1}H NMR data of **23** (100/400 MHz, δ ppm, in C_5D_5N).

Position	δ_C (ppm)	δ_H (ppm), *J* (Hz)
1	31.9†	1.67 m, 2.71 m
2	32.9	2.60 m, 2.96 m
3	176.0	-
4	75.7	-
5	53.3	2.37 d (8.4)
6	71.1	4.05 dd (12.7, 5.6)
7	36.9	1.58 m, 1.79 m
8	46.8†	1.59 m
9	25.0	-
10	28.5	-
11	26.5	1.15 m, 2.30 m
12	34.2	1.68 m, 1.84 m
13	46.9†	-
14	45.3	-
15	48.7	1.77 m, 2.15 m
16	73.8	4.89 dd (13.4, 7.7)
17	60.9	2.06 d (7.7)
18	22.0	1.71 s
19	31.9†	0.59 d (4.4), 1.00 d (4.4)
20	78.8	-
21	28.5	1.55 s
22	26.4	1.24 m, 3.03 m
23	23.8	1.87 m, 2.16 m
24	68.4	3.66 brs
25	75.1	-
26	28.4	1.44 s
27	27.8	1.27 s
28	33.3	1.76 s
29	28.8	1.60 s
30	20.7	0.94 s

†Overlapped signals

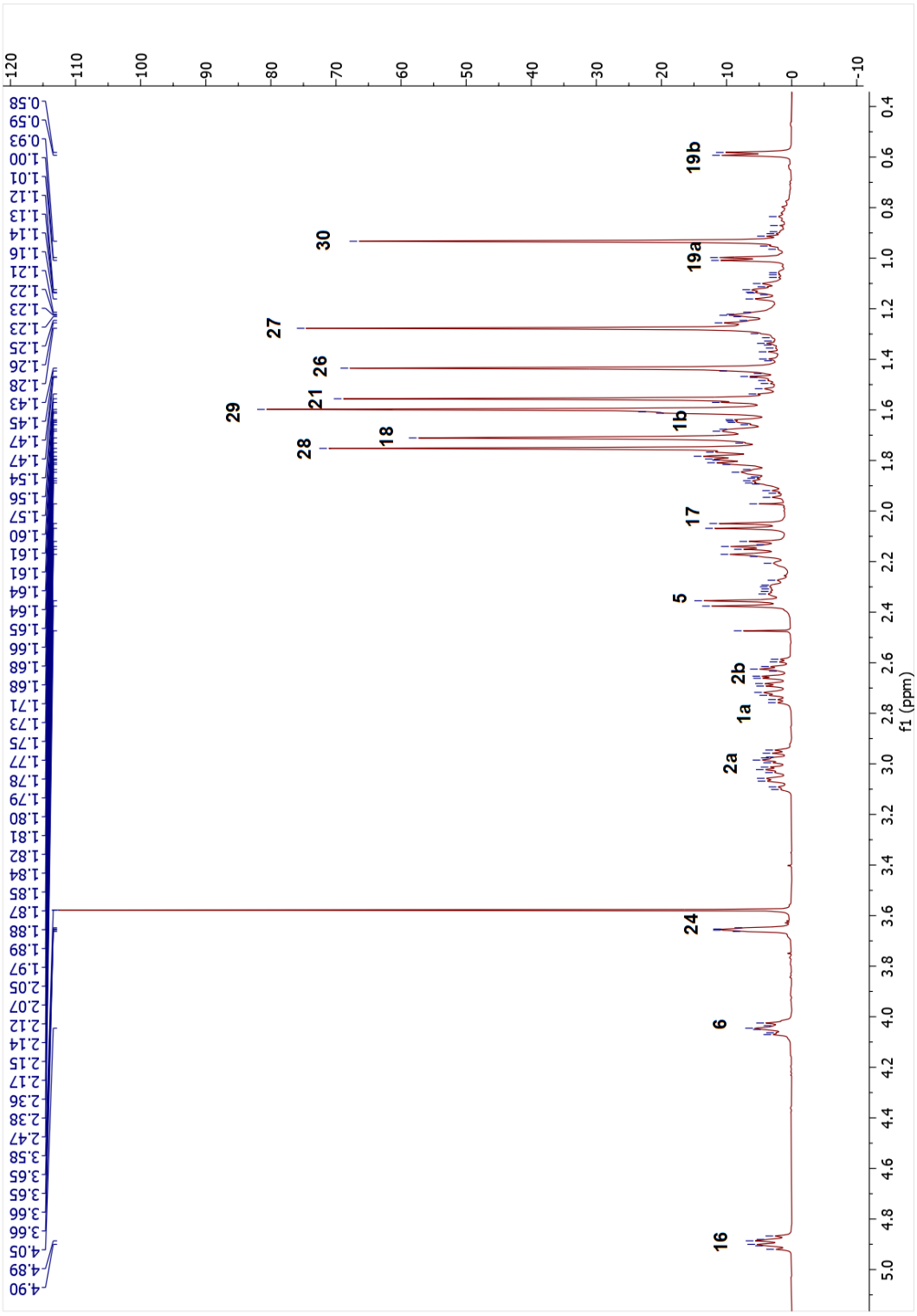

Spectrum 3.1. ^{1}H-NMR spectrum of compound **23**.

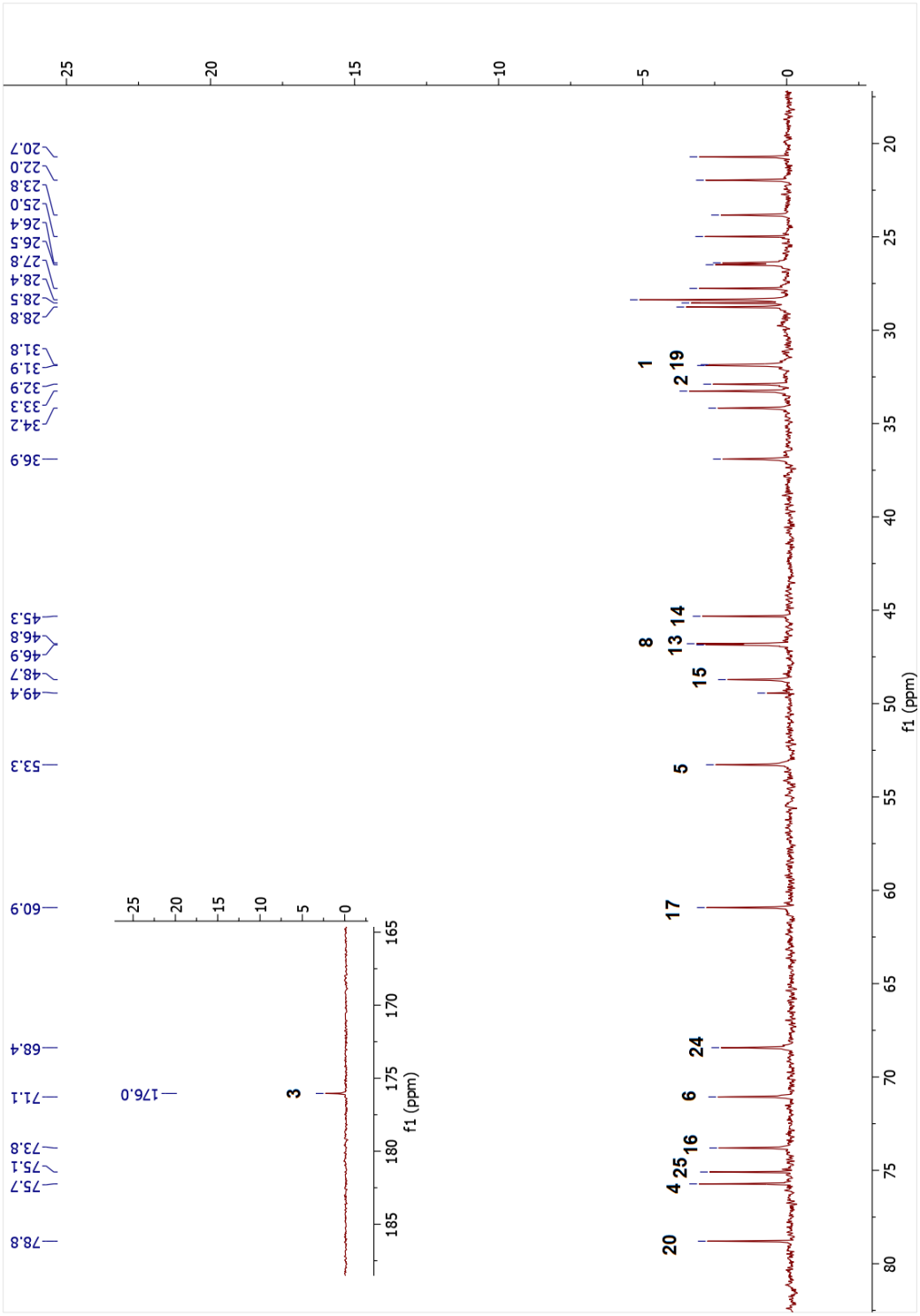

Spectrum 3.2. ^{13}C-NMR spectrum of compound **23**.

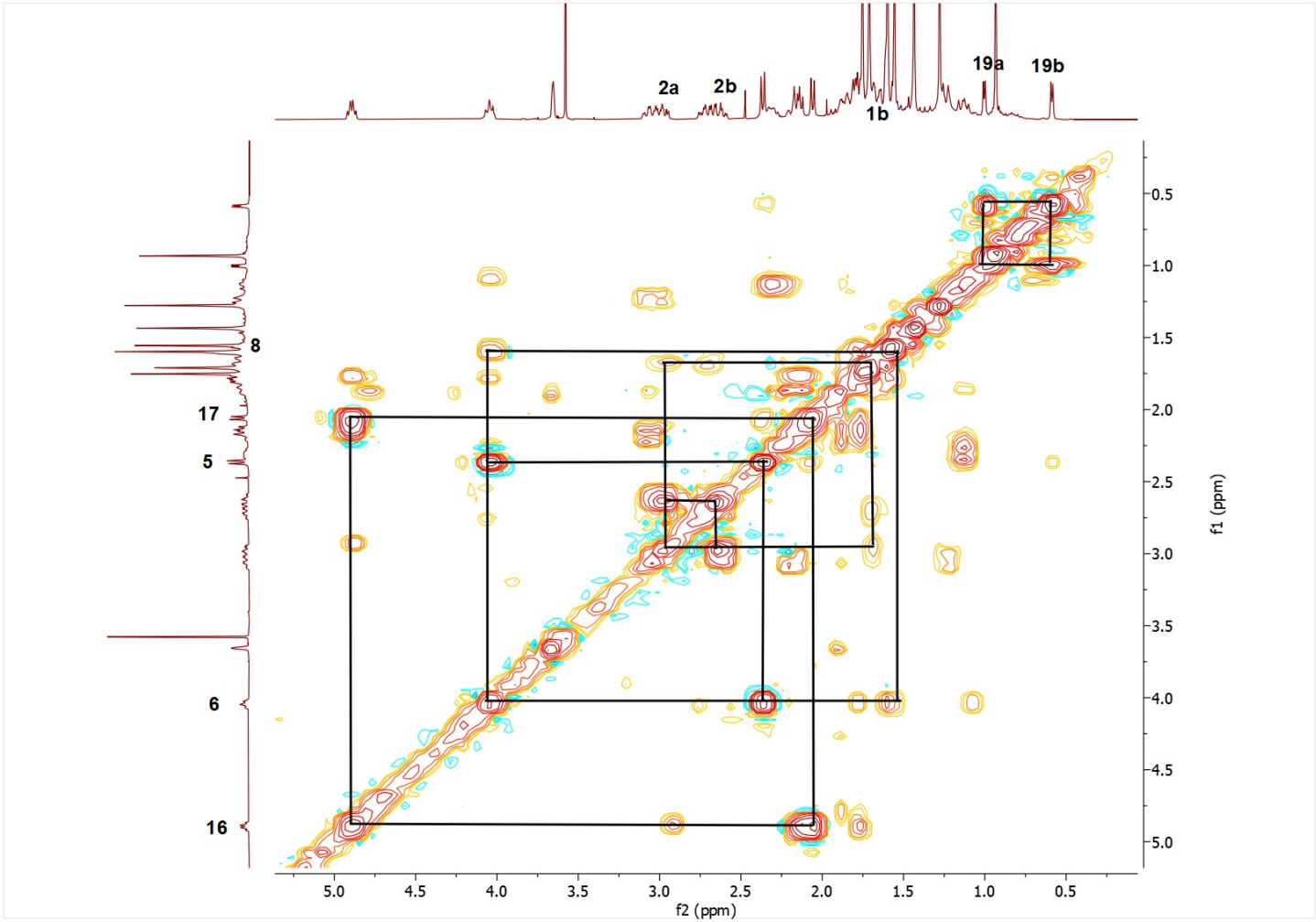

Spectrum 3.3. COSY spectrum of compound **23**.

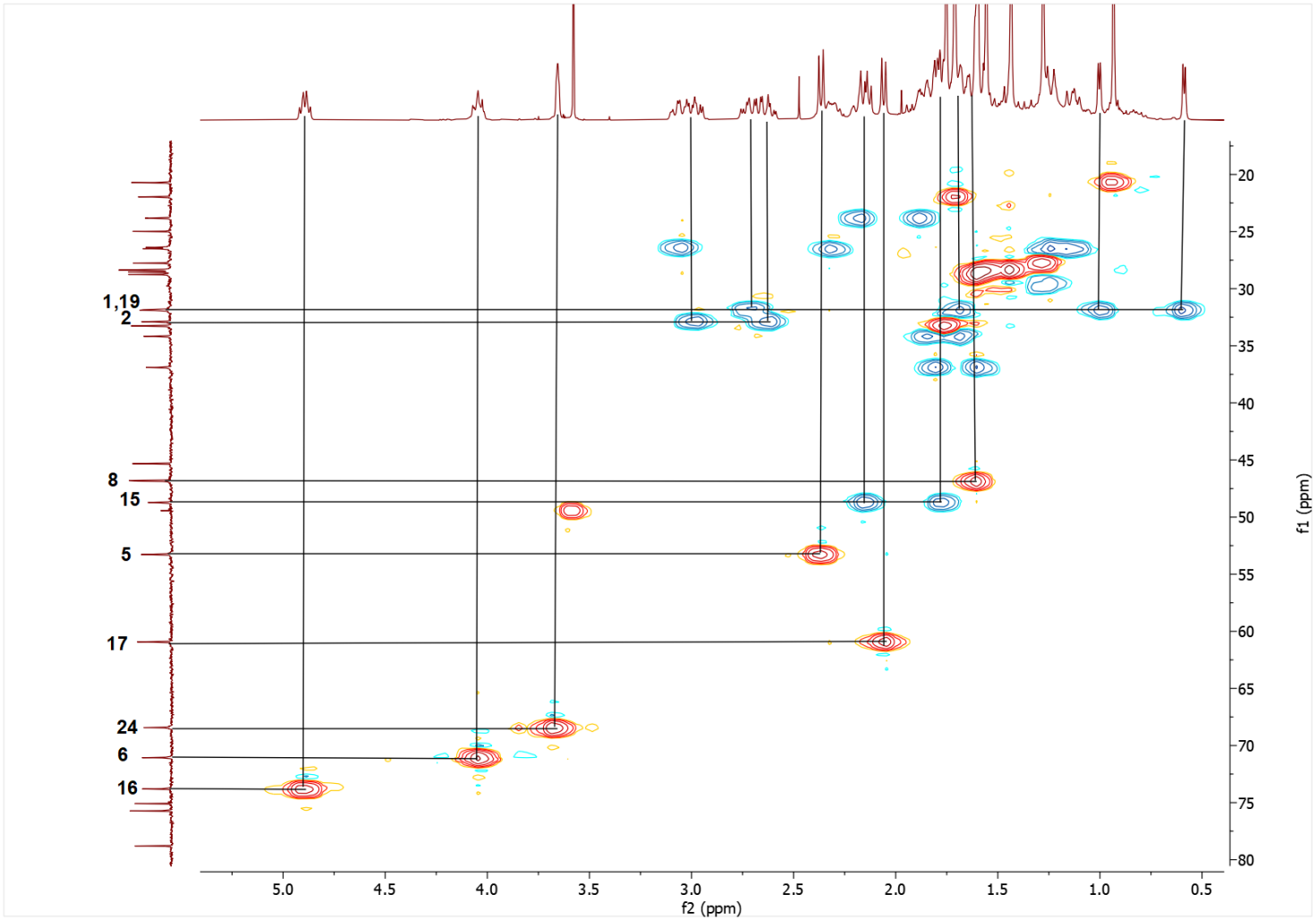

Spectrum 3.4. HSQC spectrum of compound **23**.

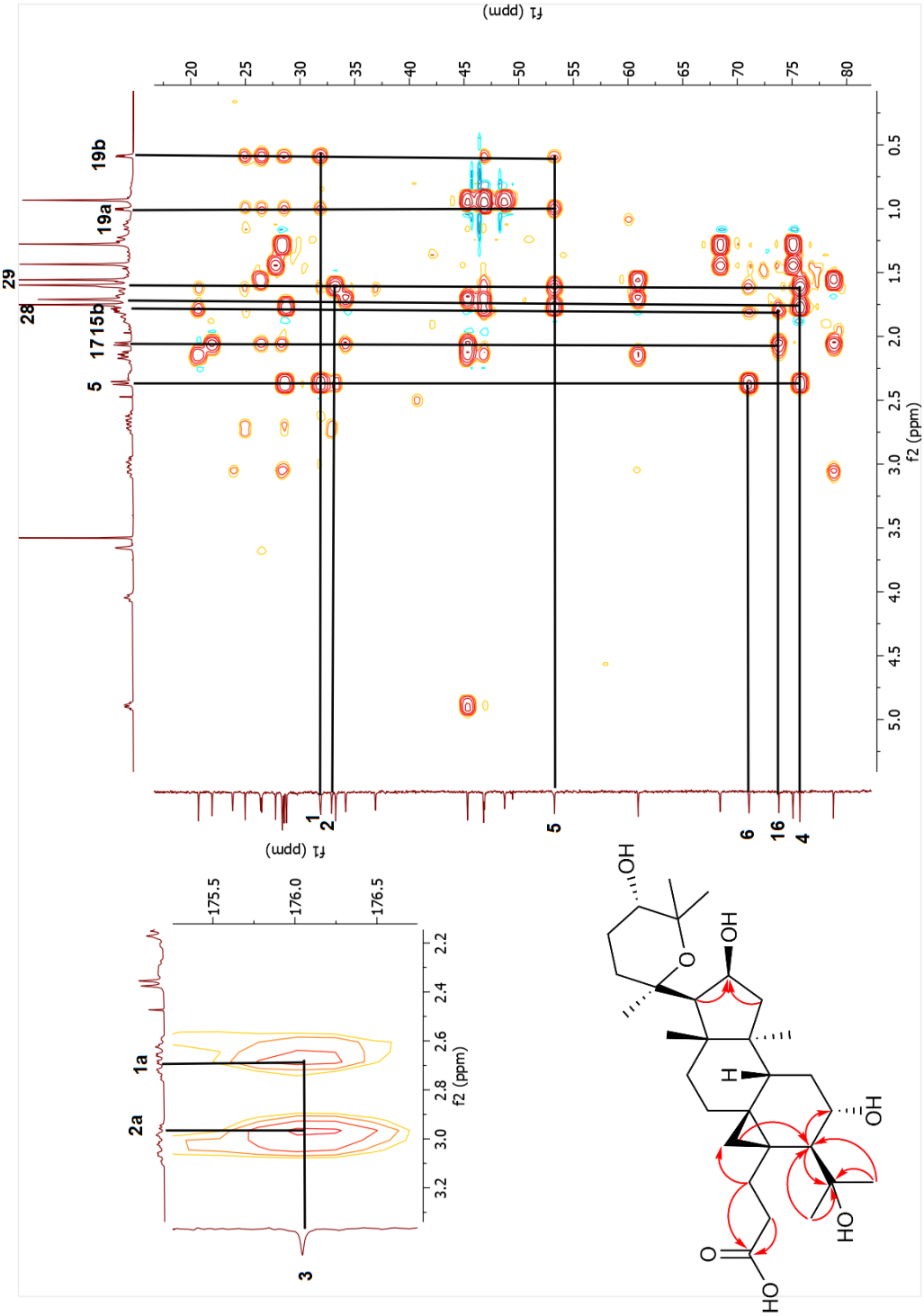

Spectrum 3.5. HMBC spectrum of compound **23**.

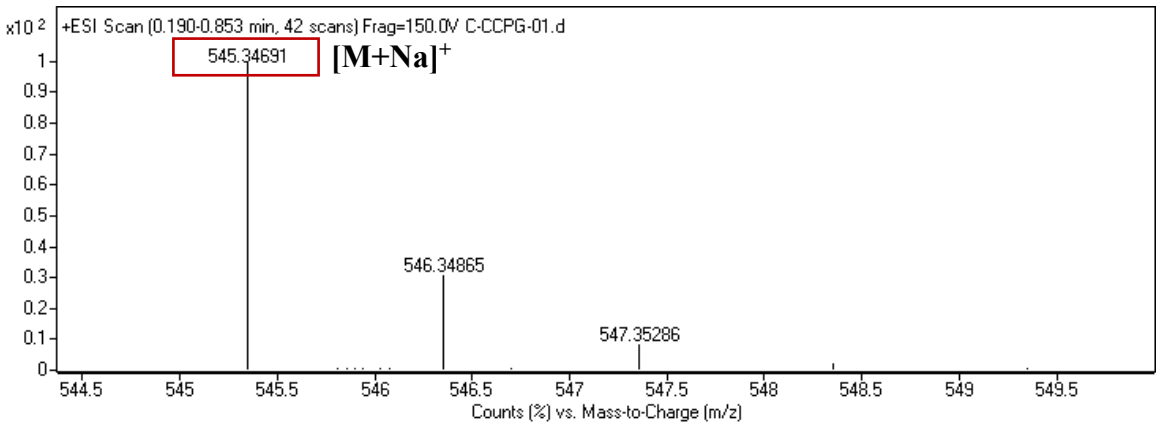

Spectrum 3.6. HR-ESI-MS spectrum of compound **23**.

3.3.2.2. Structure Elucidation of Compound 24

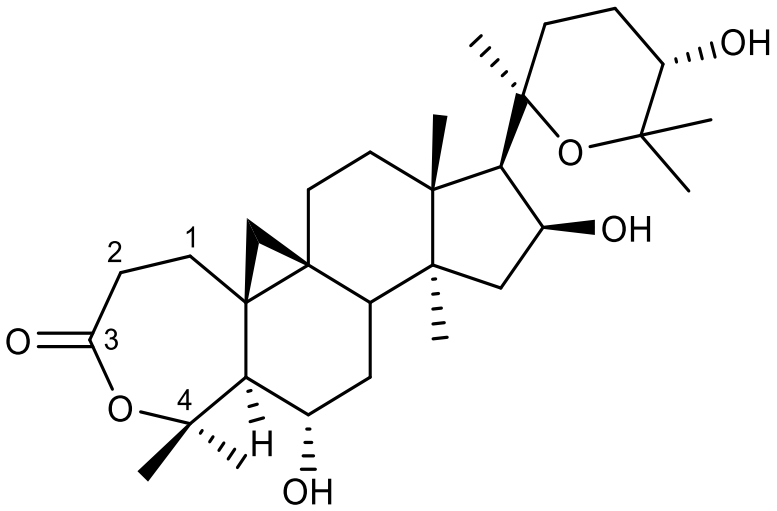

Figure 3.7. Chemical structure of compound **24**.

The molecular formula of **24** was established as $C_{30}H_{48}O_6$ by HR-ESI-MS analysis (*m/z* 527.33635 $[M + Na]^+$). From detailed inspection of 1D and 2D-NMR spectra, the carbonyl signal at 174.3 ppm and its long-range correlations with two methylene groups (H_2-2 and H_2-1) suggested a ring opening for **24** at first glance, as in **23**. However, an oxygenated quaternary carbon was observed at 85.6 ppm in the ^{13}C-NMR spectrum. In the HMBC

spectrum, its long-range correlations with two methyl groups (δ_H 1.71 and 1.49) implied that it was C-4. The downfield shift of C-4 resonance (9.9 ppm) compared to metabolite **23** (δ_C 75.7) and previously reported metabolites of our group[49,74] ascertained that C-4 was in a 7-membered lactone ring system. As a result, **24** was elucidated as 20,25-epoxy-6α,16β,24α-trihydroxycycloartan-3-olide.

Table 3.3. The ^{13}C and ^{1}H NMR data of **24** (125/500 MHz, δ ppm, in C_5D_5N).

Position	δ_C (ppm)	δ_H (ppm), *J* (Hz)
1	33.0	1.28 m, 1.95 m
2	34.3	2.60 m, 2.88 m
3	174.5	-
4	86.1	-
5	53.8	2.40 d (9.3)
6	71.6	3.66 m
7	37.9	1.51 m, 1.69 m
8	48.6	1.72 m
9	22.3	-
10	26.5	-
11	27.1	0.80 m, 2.02 m
12	34.6	1.74 m, 1.85 m
13	47.1	-
14	46.1	-
15	49.3	1.80 m, 2.15 m
16	74.4	4.68 dt (8.2, 4.2)
17	61.5	2.10 d (7.7)
18	22.5	1.70 s
19	31.8	0.53 d (5.0), 0.79 d (4.9)
20	79.5	-
21	29.1	1.60 s
22	27.1	1.26 m, 3.11 m
23	24.5	1.91 m, 2.21 m
24	69.1	3.70 brs
25	75.9	-
26	29.1	1.47 s
27	28.6	1.32 s
28	32.4	1.93 s
29	28.5	1.67 s
30	21.5	0.94 s

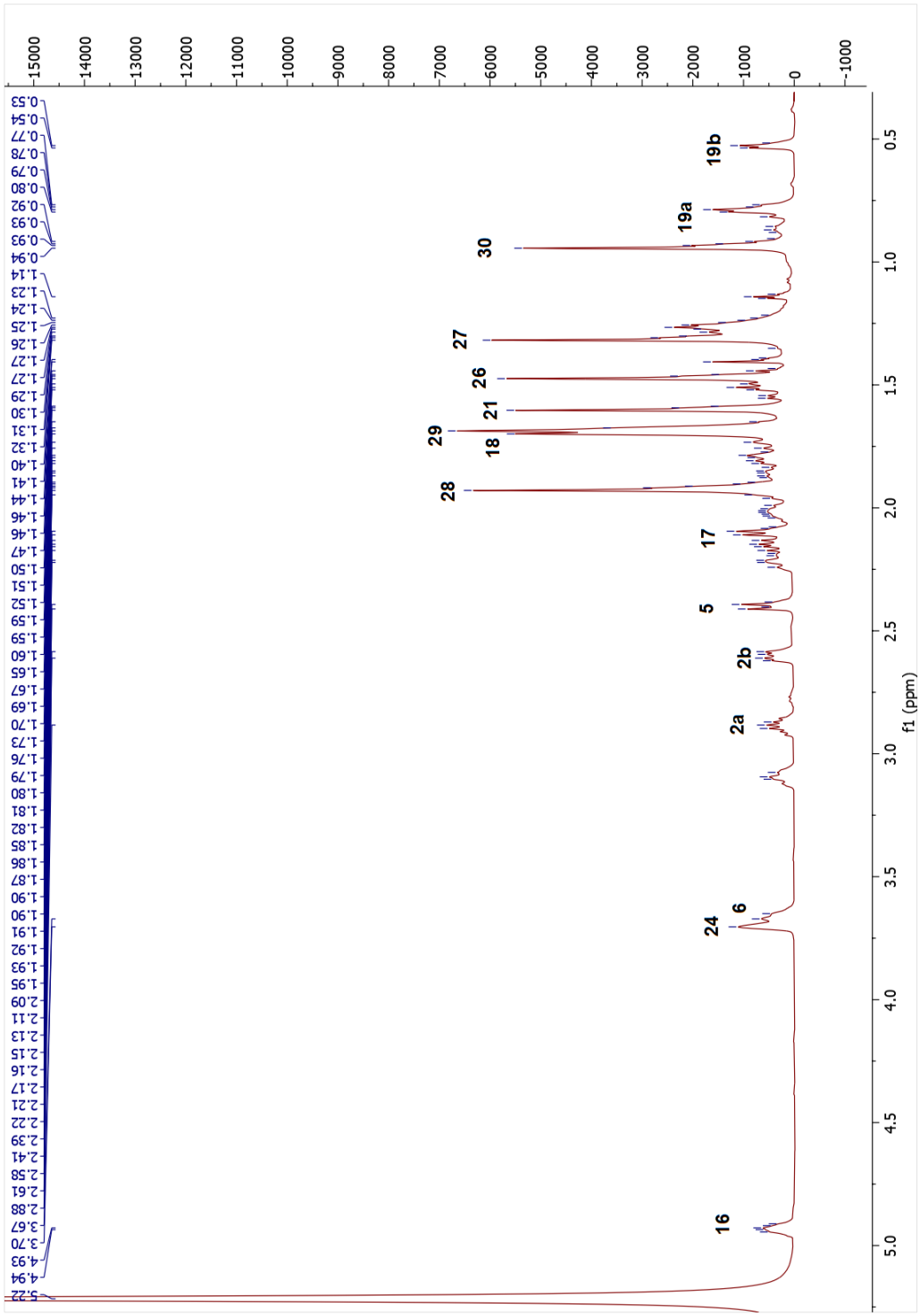

Spectrum 3.7. ^{1}H-NMR spectrum of compound **24**.

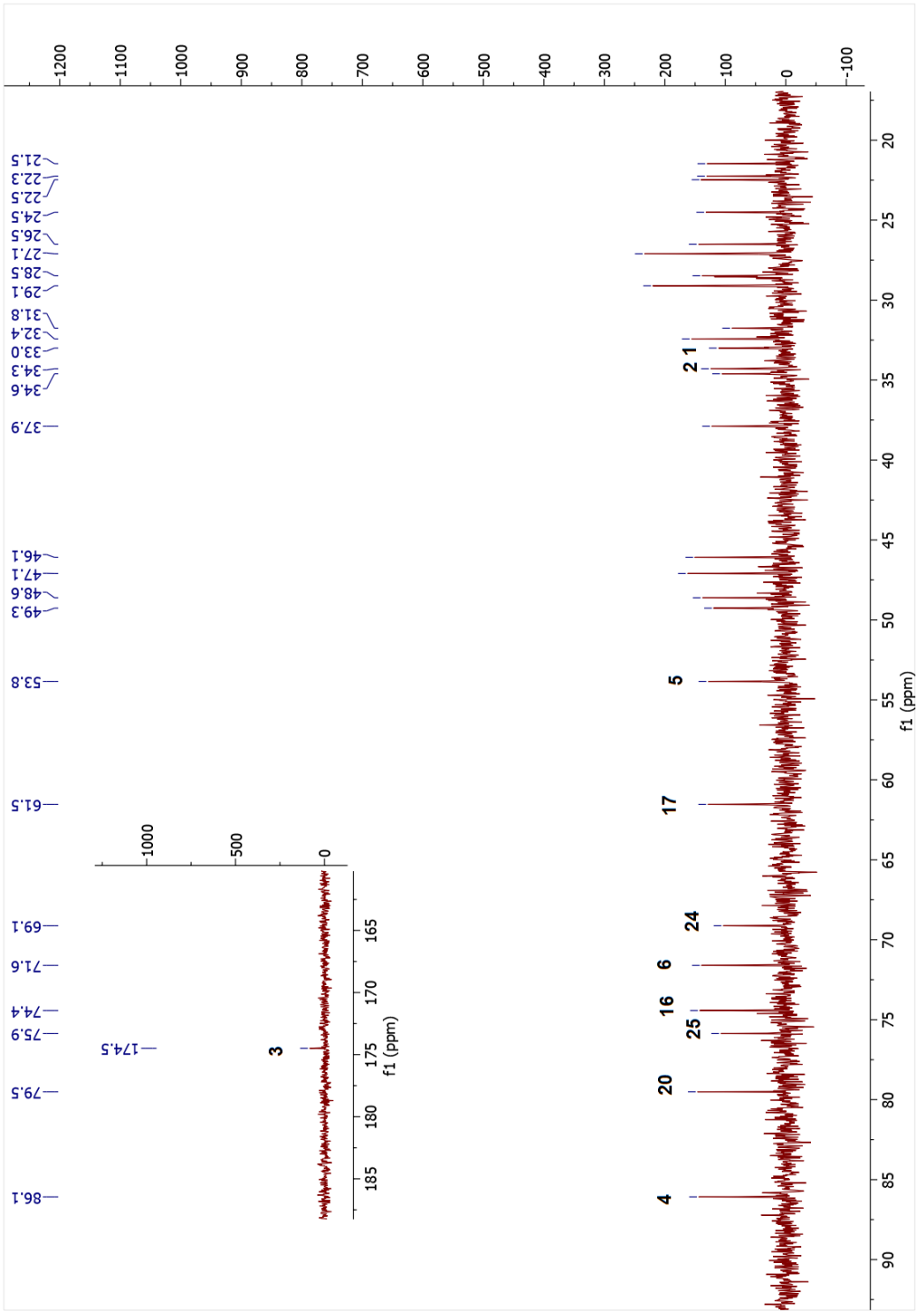

Spectrum 3.8. ^{13}C-NMR spectrum of compound **24**.

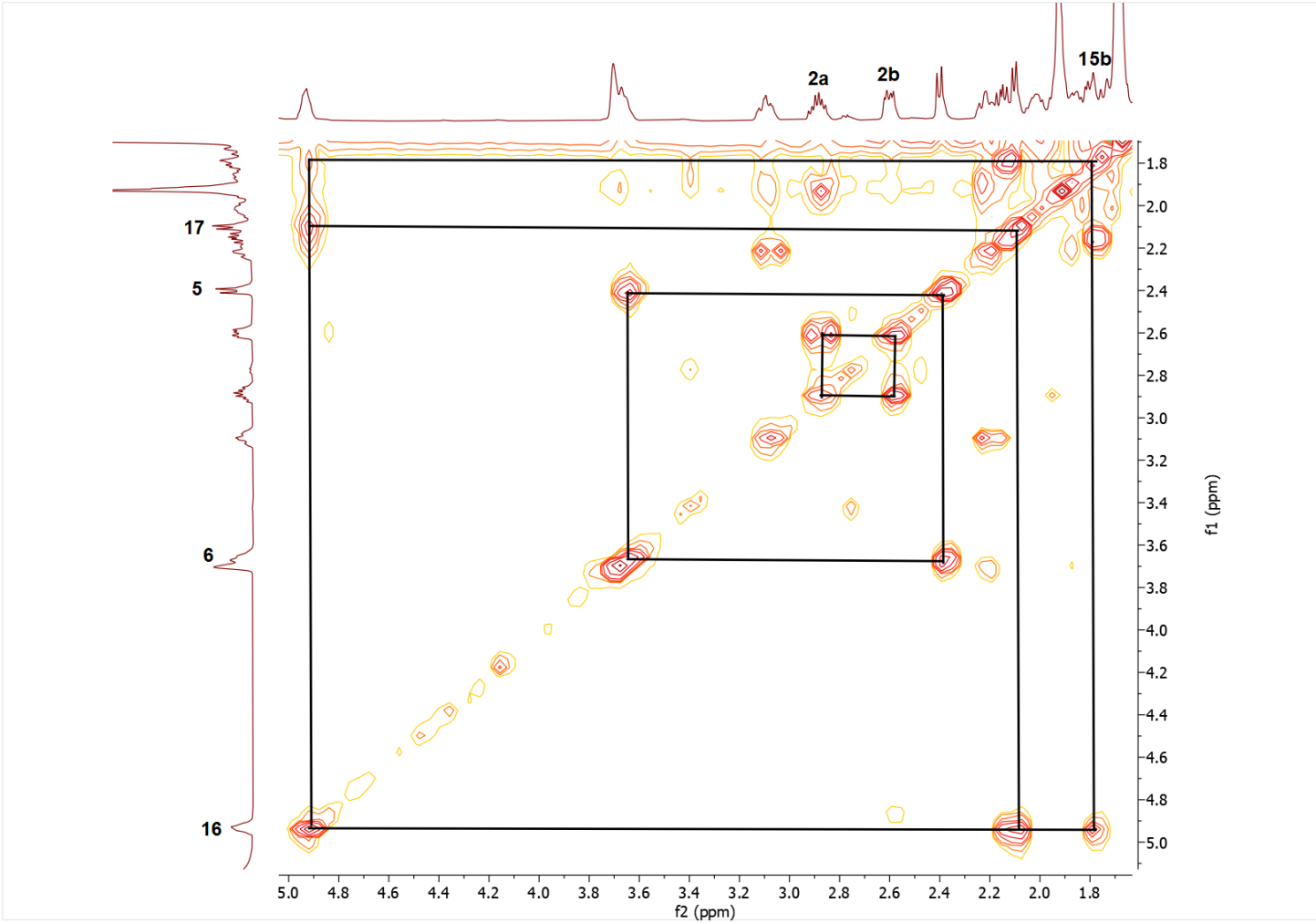

Spectrum 3.9. COSY spectrum of compound **24**.

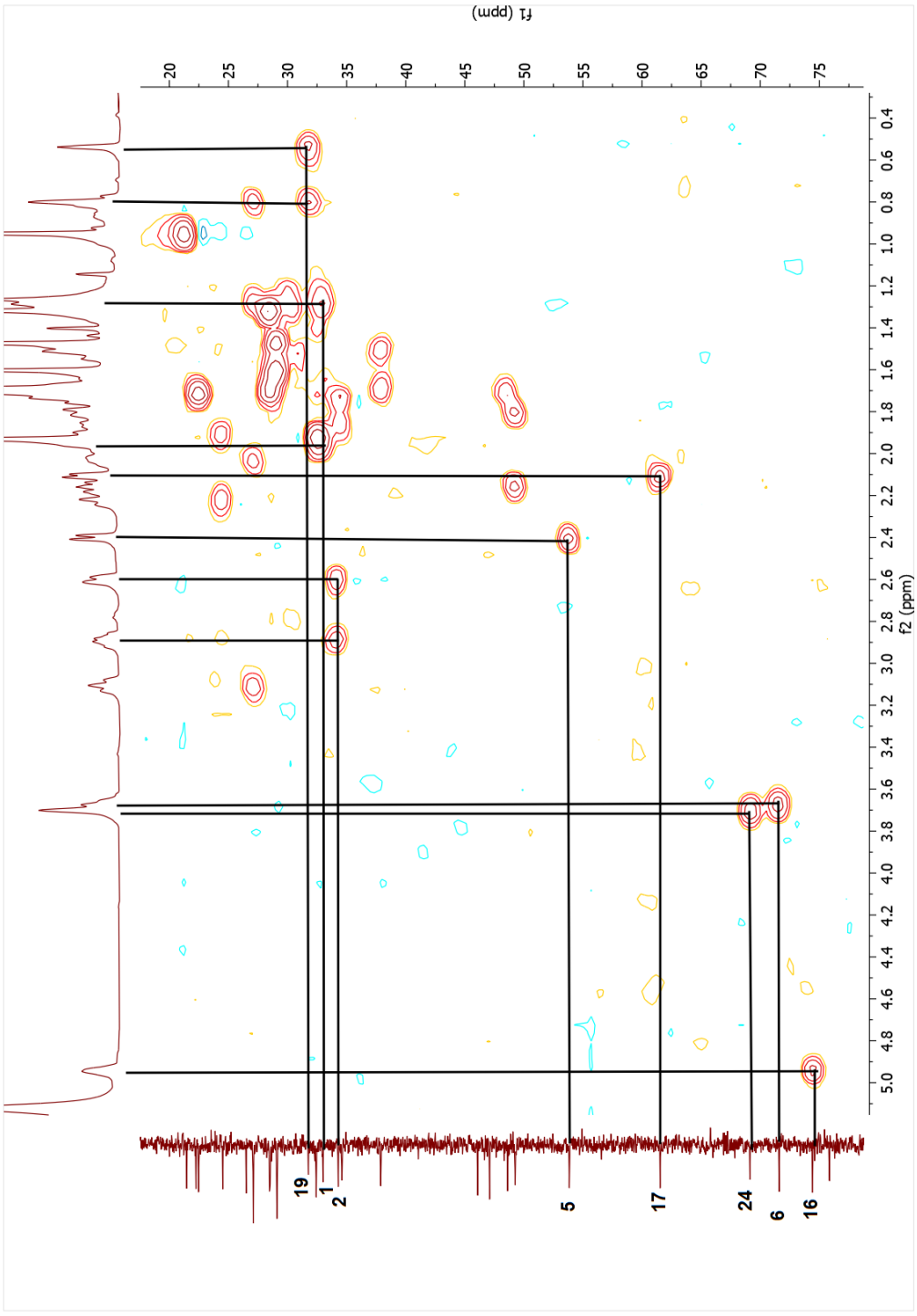

Spectrum 3.10. HSQC spectrum of compound **24**.

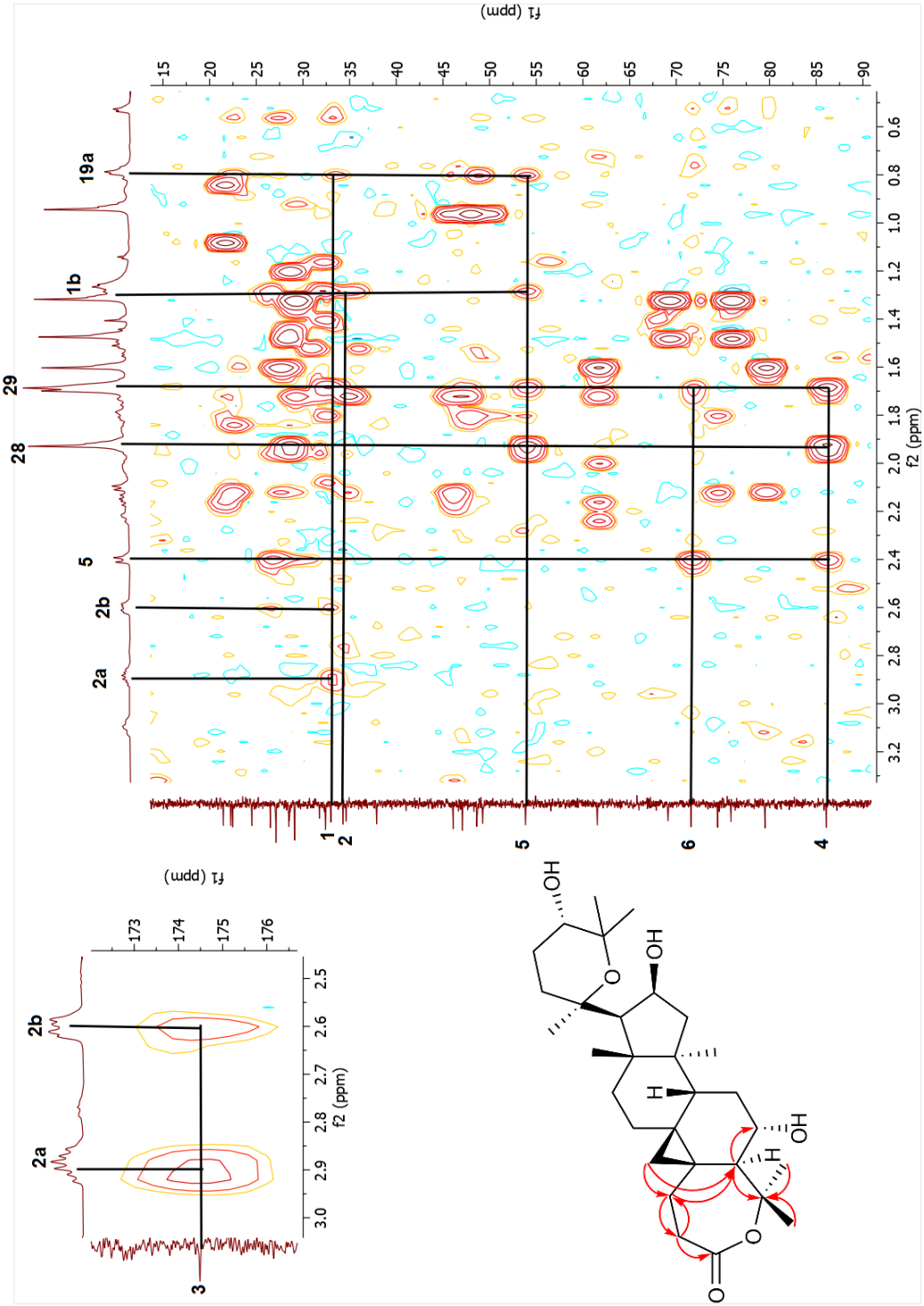

Spectrum 3.11. HMBC spectrum of compound **24**.

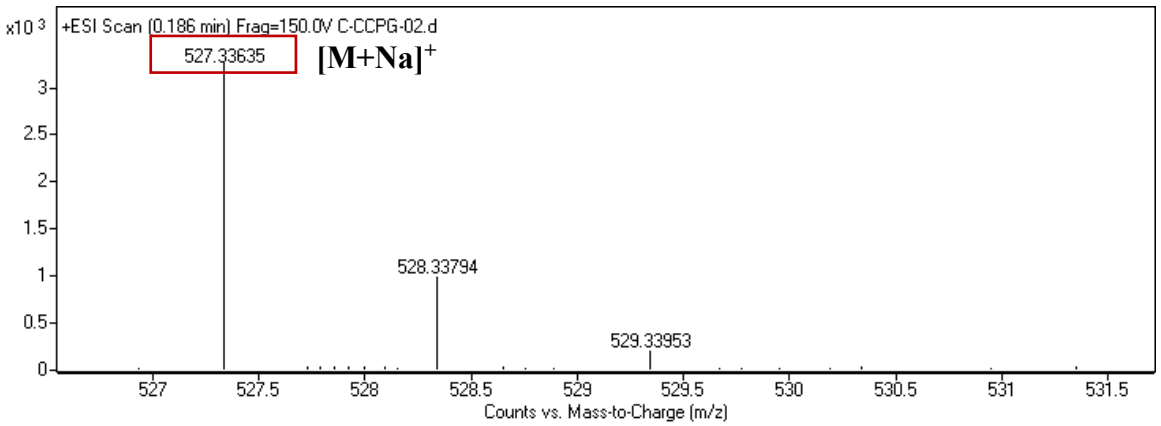

Spectrum 3.12. HR-ESI-MS spectrum of compound **24**.

3.3.2.3. Structure Elucidation of Compound 25

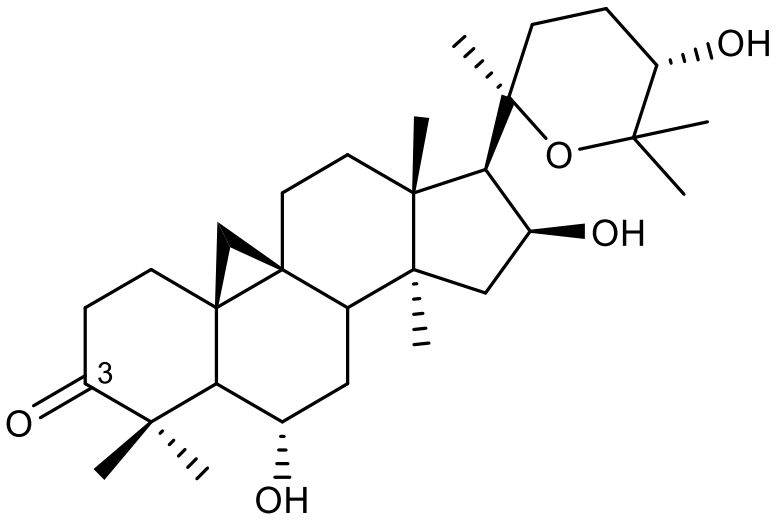

Figure 3.8. Chemical structure of compound **25**.

The metabolite **25** gave a molecular formula of $C_{30}H_{48}O_5$ based on the HR-ESI-MS data (*m/z* 511.33940 $[M + Na]^+$). Apart from the oxymethine signals of C-3, the characteristic signals of the starting molecule **1** were present for **25**. In the ^{13}C-NMR spectrum, the resonance at 216.6 ppm was obvious, implying a biotransformation of C-3 secondary alcohol

to a ketone via an oxidation reaction. Accordingly, this assumption was substantiated by long-range correlations between C-3 and H-5/H_3-28/H_3-29 in the HMBC spectrum. As a result, the structure of **25** was determined to be 20,25-epoxy-6α,16β,24α-trihydroxycycloartan-3-one.

Table 3.4. The ^{13}C and ^{1}H NMR data of **25** (100/400 MHz, δ ppm, in C_5D_5N).

Position	δ_C (ppm)	δ_H (ppm), *J* (Hz)
1	31.6	1.25 m, 1.96 m
2	35.6	2.43 ddd (14.3, 8.1, 6.8), 2.70 ddd (14.2, 8.6, 5.9)
3	216.6	-
4	50.3	-
5	53.3	2.18 d (9.7)
6	69.0	3.64 m
7	38.1	1.58 m, 1.71 m
8	47.8	1.86 m
9	20.9	-
10	28.1	-
11	26.0	0.91 m, 1.98 m
12	33.8	1.69 m, 1.82 m
13	46.5	-
14	45.7	-
15	48.1	1.79 m, 2.17 m
16	73.7	4.90 tdd (8.1, 5.4, 3.2)
17	60.7	2.07 d (7.3)
18	21.5	1.68 s
19	30.8	0.31 d (4.1), 0.64 d (4.2)
20	78.8	-
21	28.4	1.57 s
22	26.4	1.24 m, 3.08 td (13.5, 4.5)
23	23.8	1.87 m, 2.19 m
24	68.4	3.66 brs
25	75.1	-
26	28.4	1.44 s
27	27.8	1.28 s
28	28.4	1.74 s
29	20.1	1.42 s
30	20.4	0.92 s

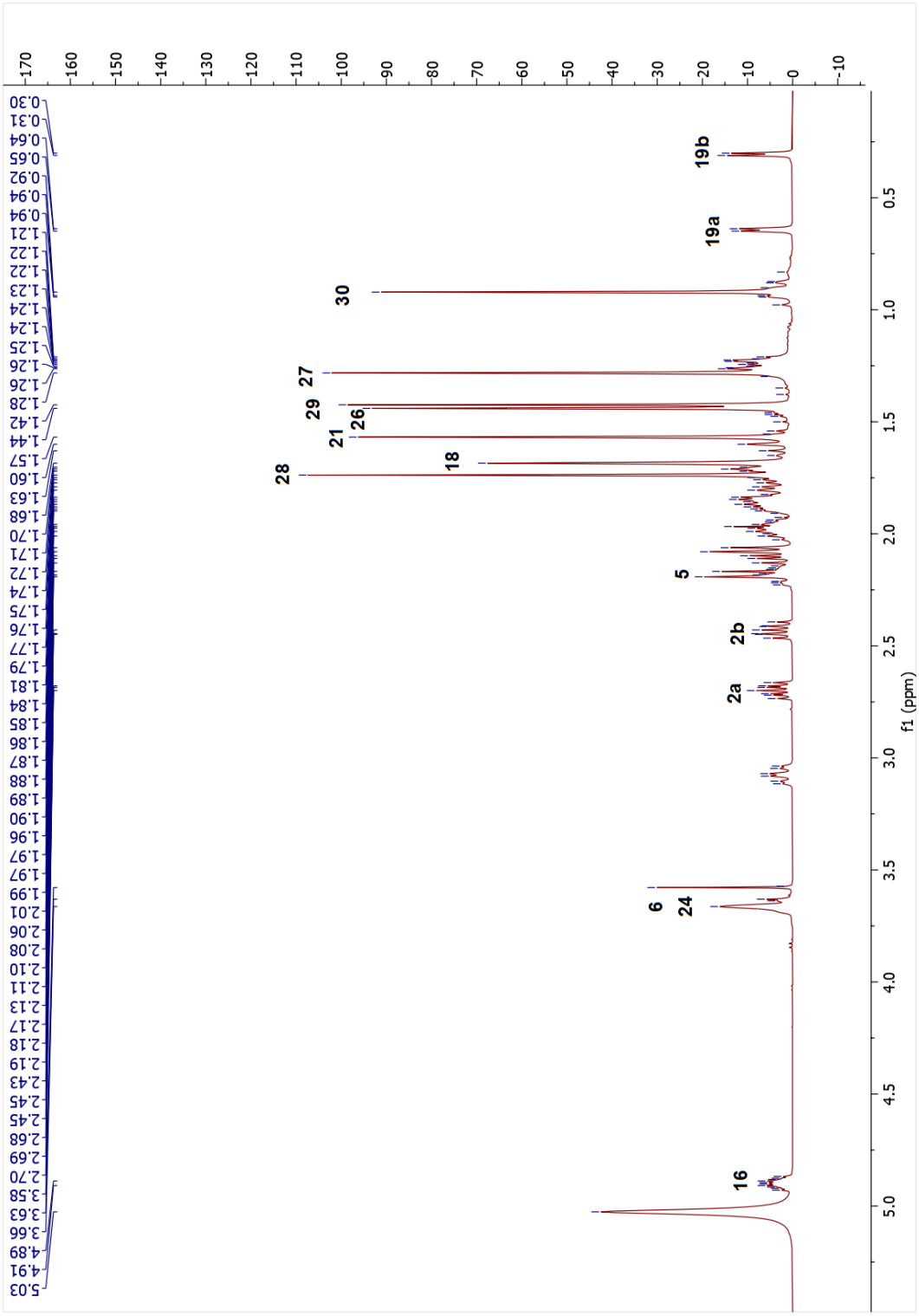

Spectrum 3.13. ^{1}H-NMR spectrum of compound **25**.

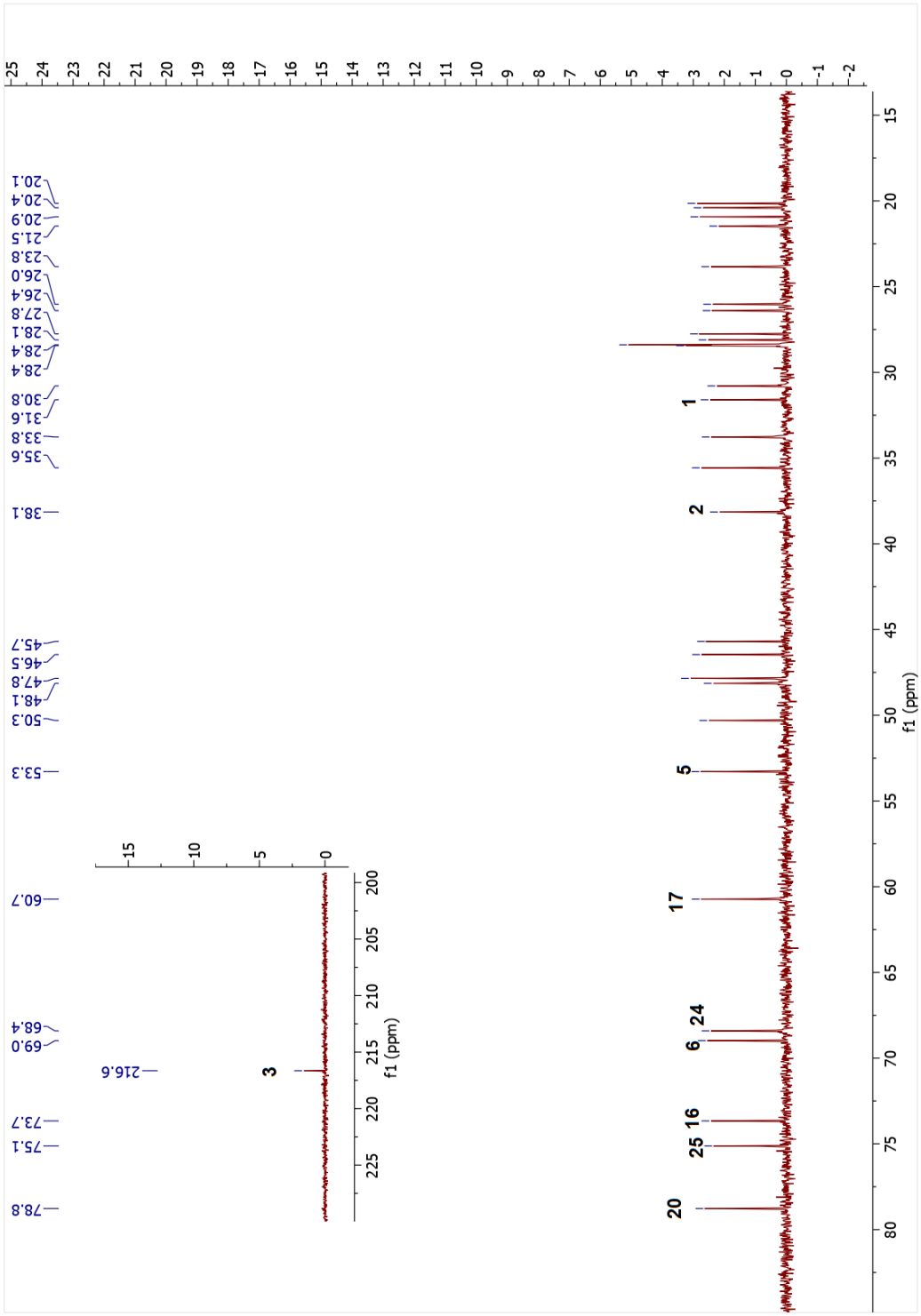

Spectrum 3.14. ^{13}C-NMR spectrum of compound **25**.

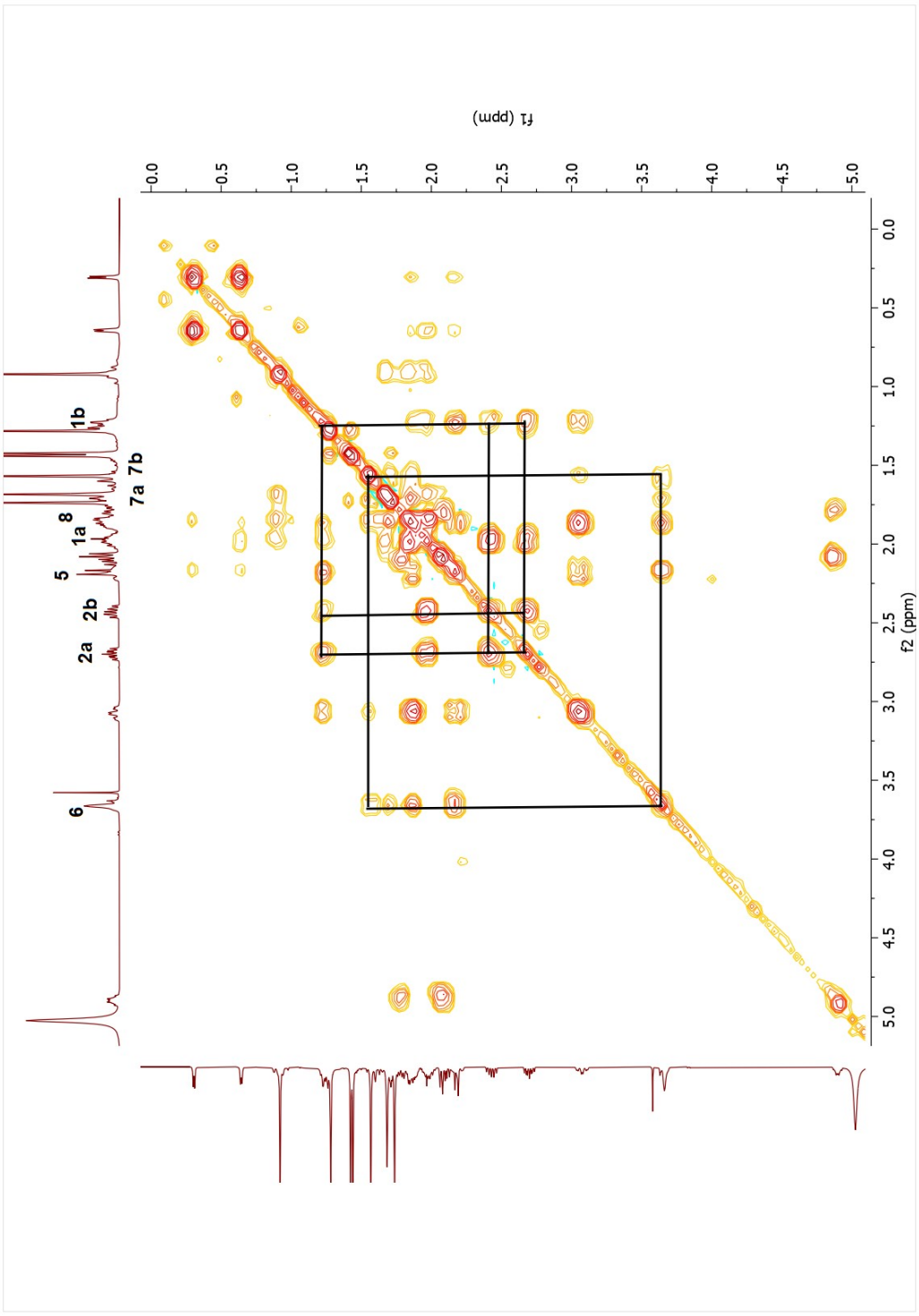

Spectrum 3.15. COSY spectrum of compound **25**.

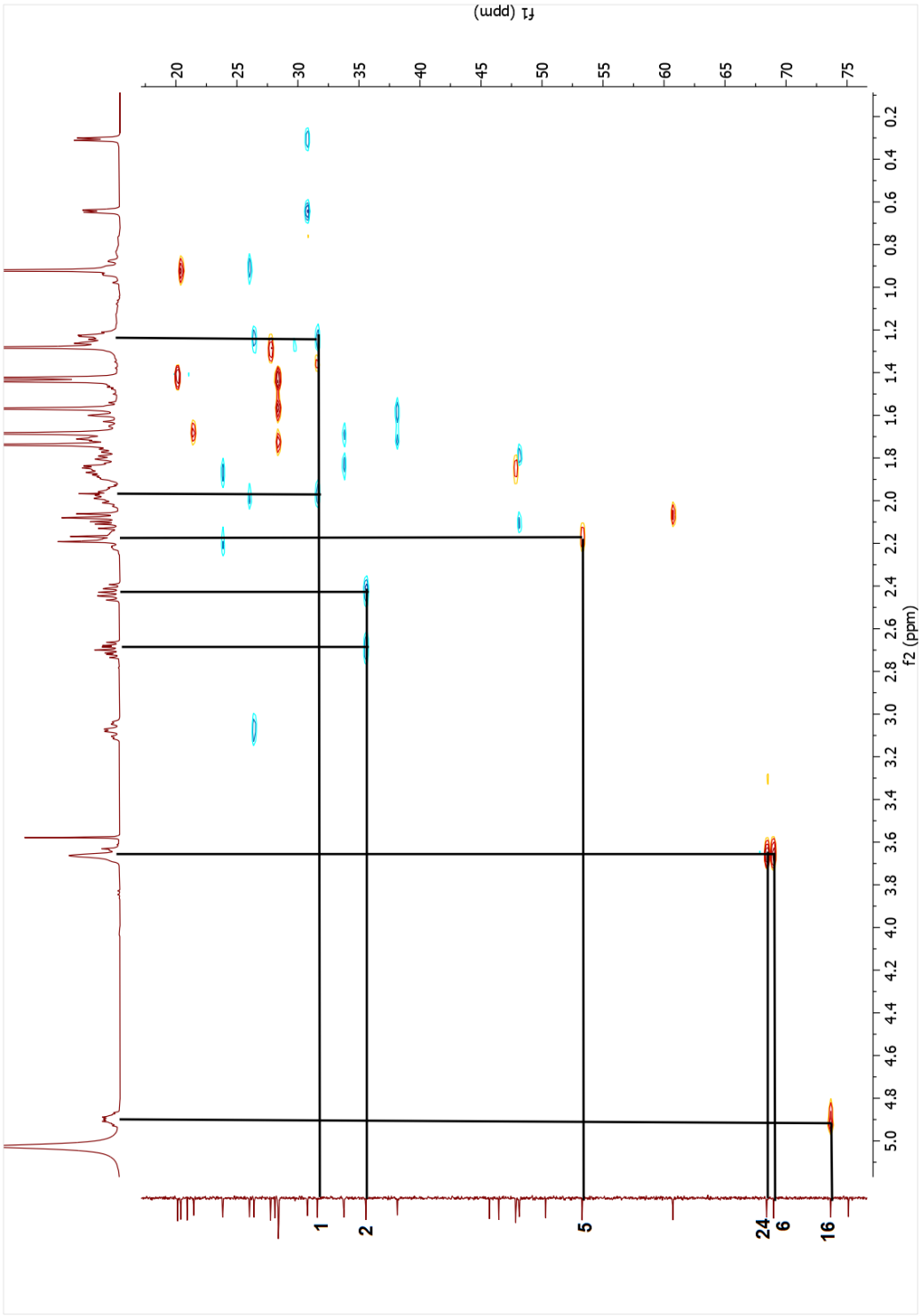

Spectrum 3.16. HSQC spectrum of compound **25**.

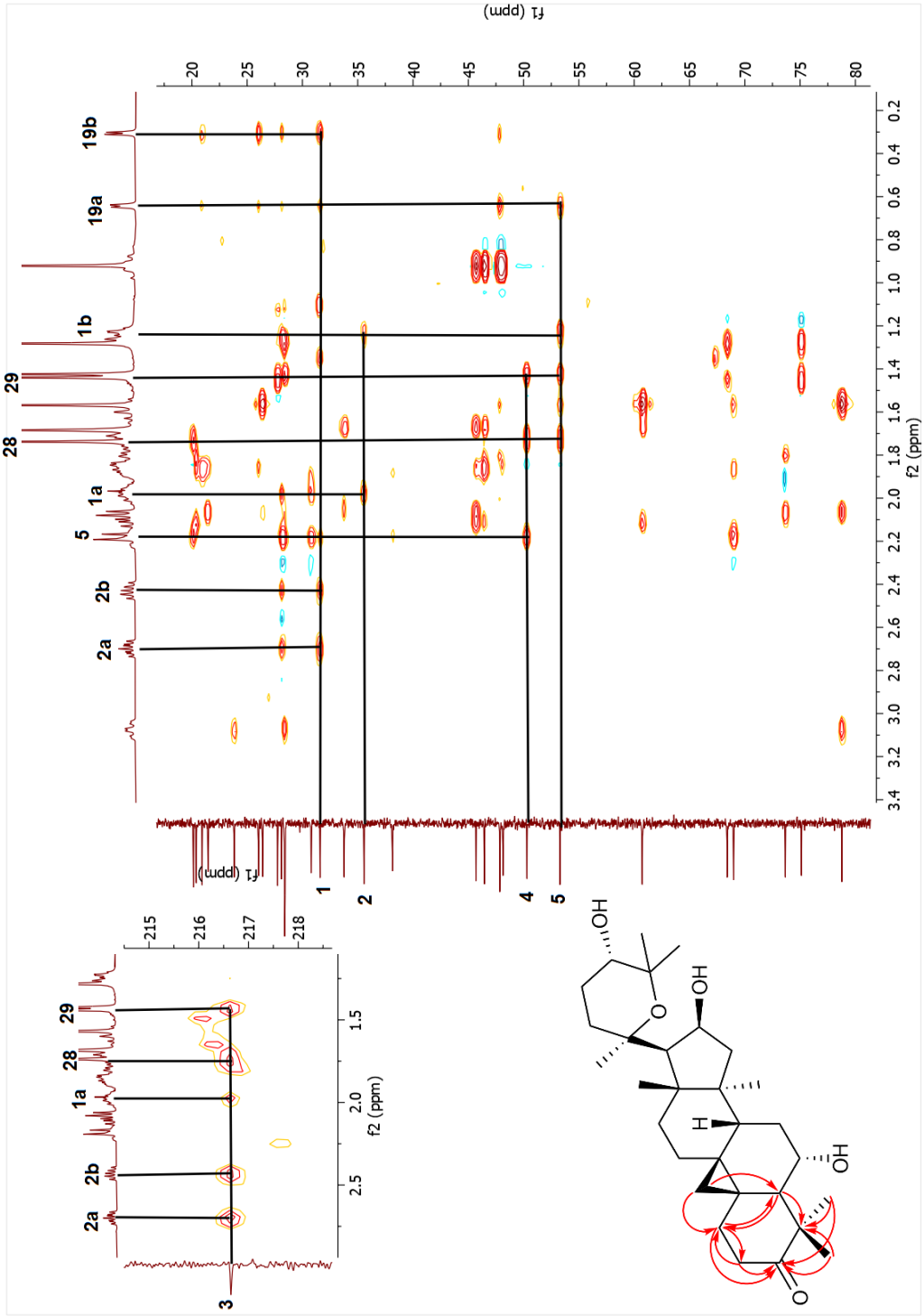

Spectrum 3.17. HMBC spectrum of compound **25**.

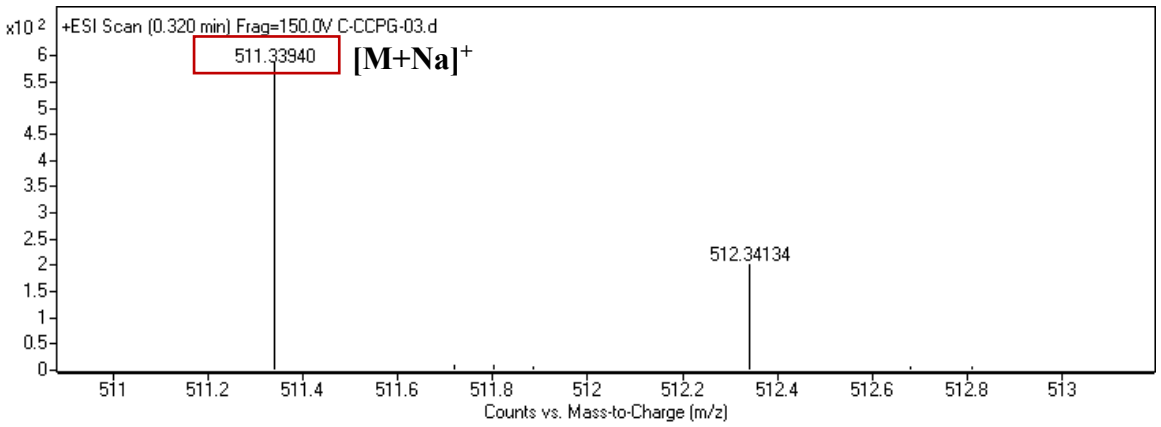

Spectrum 3.18. HR-ESI-MS spectrum of compound **25**.

3.3.2.4. Structure Elucidation of Compound 26

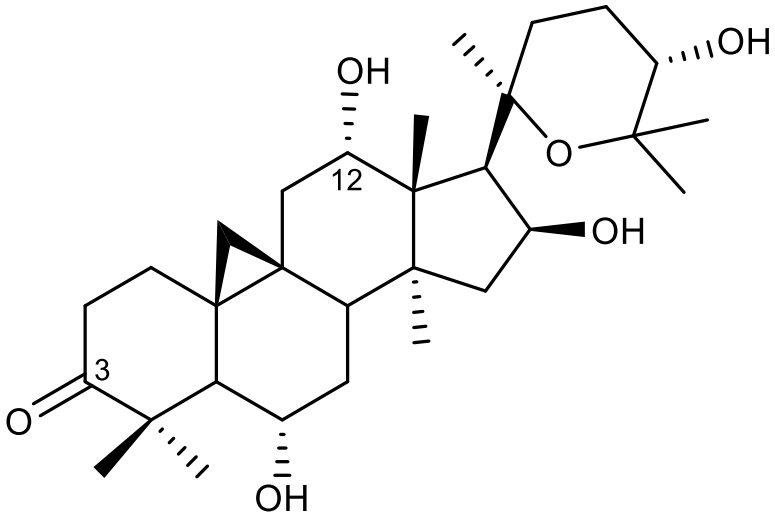

Figure 3.9. Chemical structure of compound **26**.

The metabolite **26**, the first metabolite of **6** (12α-hydroxycyclocephagenol), gave a molecular formula of $C_{30}H_{48}O_6$ based on the HR-ESI-MS data (*m/z* 503.33835 $[M - H]^-$). Apart from the proton and carbon resonances deriving from the ring A, the characteristic signals of **6** were present for **26**. In the ^{13}C-NMR spectrum, the resonance at 217.4 ppm was

obvious, implying a biotransformation of C-3 secondary alcohol to a ketone as in **25**. The long-range HMBC correlations from H_3-28 and H_3-29 (δ 1.78 and 1.50, respectively) to C-3 (δ 217.4) also verified the oxidation location. As a result, the structure of **26** was determined to be 20,25-epoxy-6α,12α,16β,24α-tetrahydroxycycloartan-3-one.

Table 3.5. The ^{13}C and ^{1}H NMR data of **26** (150/600 MHz, δ ppm, in C_5D_5N).

Position	δ_C (ppm)	δ_H (ppm), *J* (Hz)
1	32.3	1.38 m, 2.11 m
2	36.0	2.43 ddd (14.1, 8.4, 6.0), 2.77 m
3	217.4	-
4	51.0	-
5	54.0	2.29 d (9.8)
6	70.0	3.70 dd (9.9, 4.9)
7	39.1	1.75 (2H)
8	49.1	1.88 m
9	21.8	-
10	28.7	-
11	38.6	1.76 m, 2.38 m
12	74.5	4.26 ddd (9.2, 6.1, 2.6)
13	46.8	-
14	52.0	-
15	51.4	1.90 m, 2.19 dd (12.7, 7.9)
16	72.5	4.93 m
17	55.7	2.97 d (8.0)
18	21.2	1.71 s
19	31.4	0.48 d (4.2), 0.70 d (4.2)
20	79.9	-
21	27.8	1.99 s
22	29.4	2.13 dd (13.1, 3.7)
23	24.3	1.94 dd (14.0, 3.7), 2.34 t (3.4)
24	69.2	3.73 brs
25	76.3	-
26	29.1	1.57 s
27	28.7	1.39 s
28	29.3	1.78 s
29	20.7	1.50 s
30	22.6	1.28 s

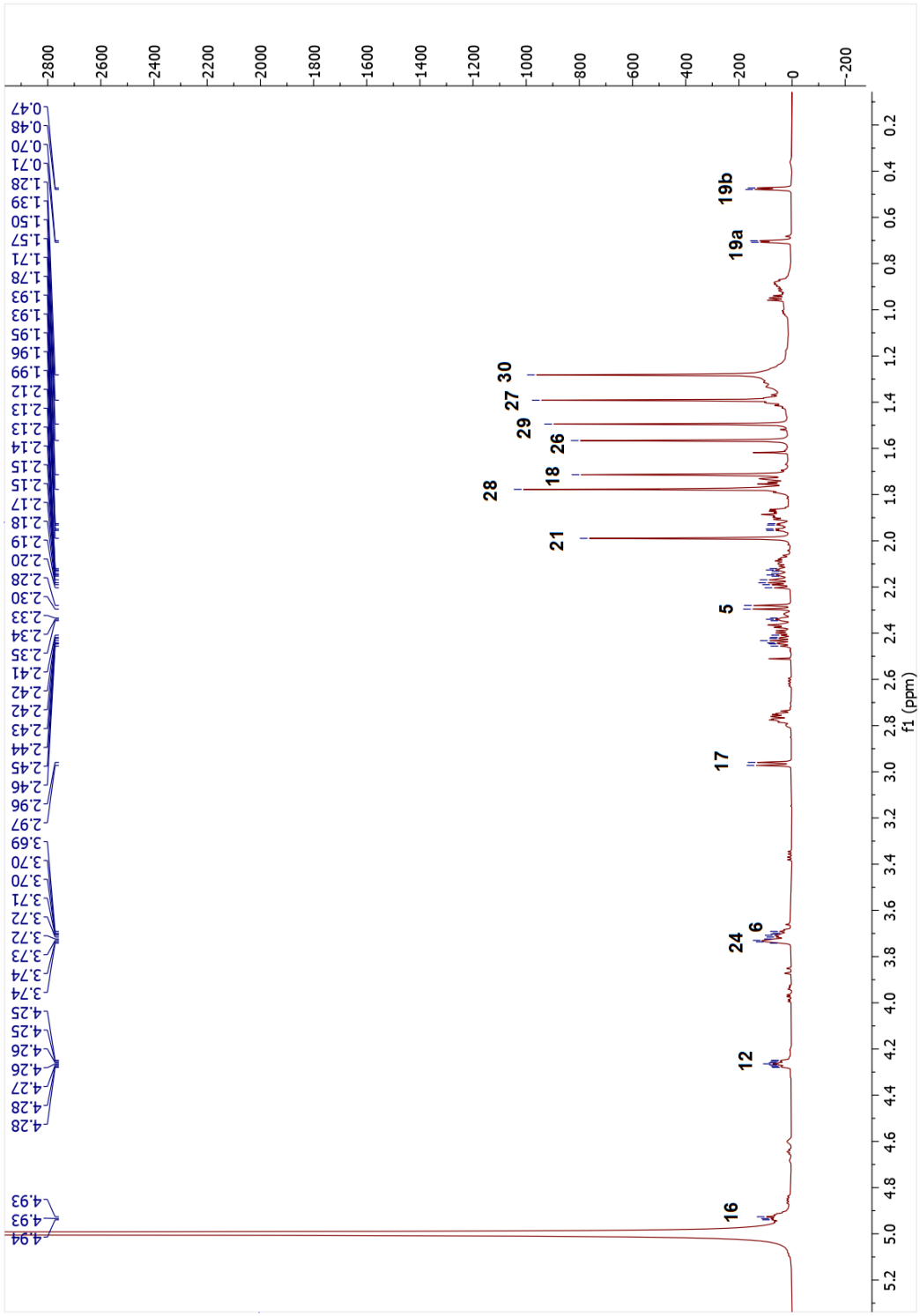

Spectrum 3.19. ^{1}H-NMR spectrum of compound **26**.

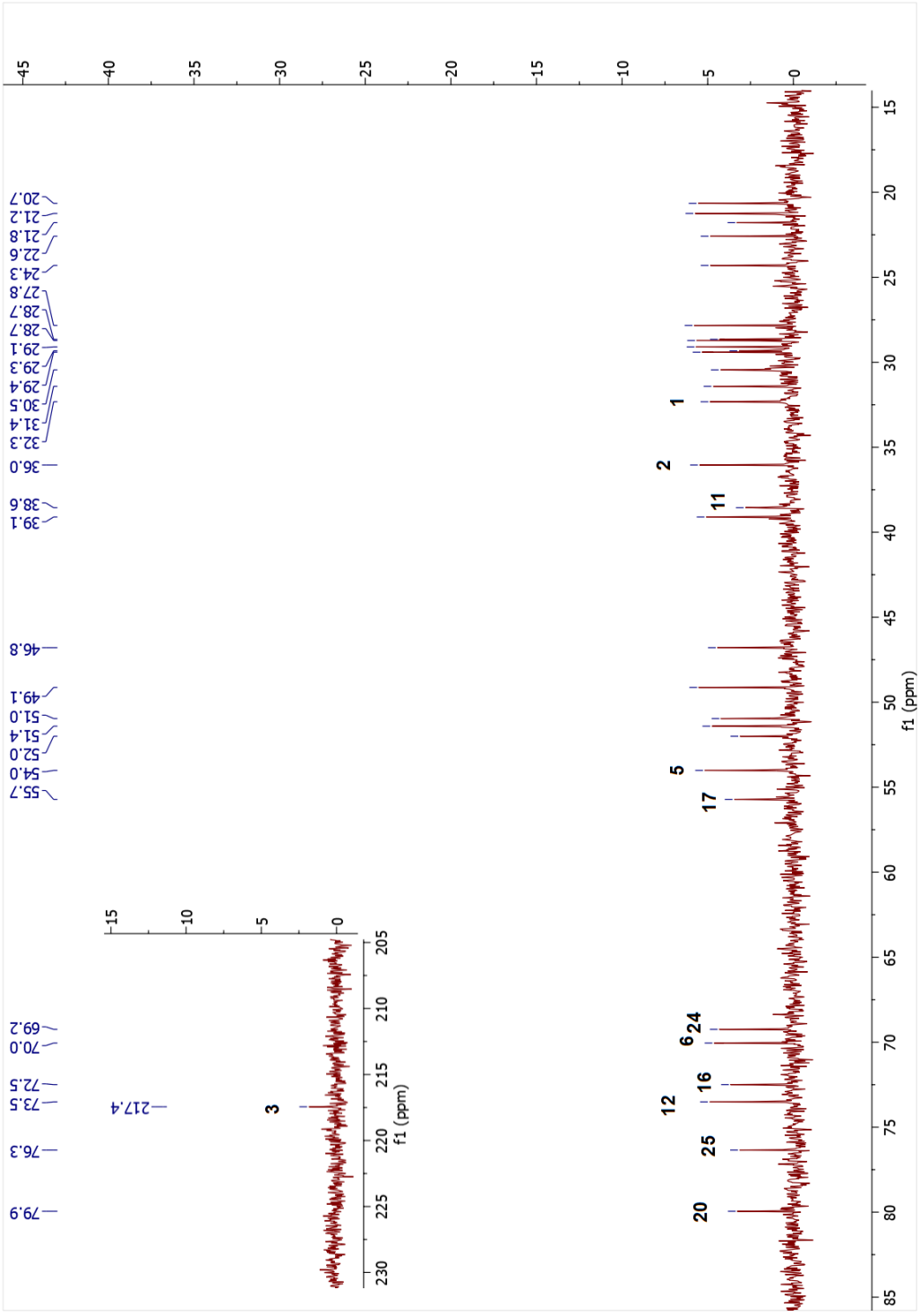

Spectrum 3.20. ^{13}C-NMR spectrum of compound **26**.

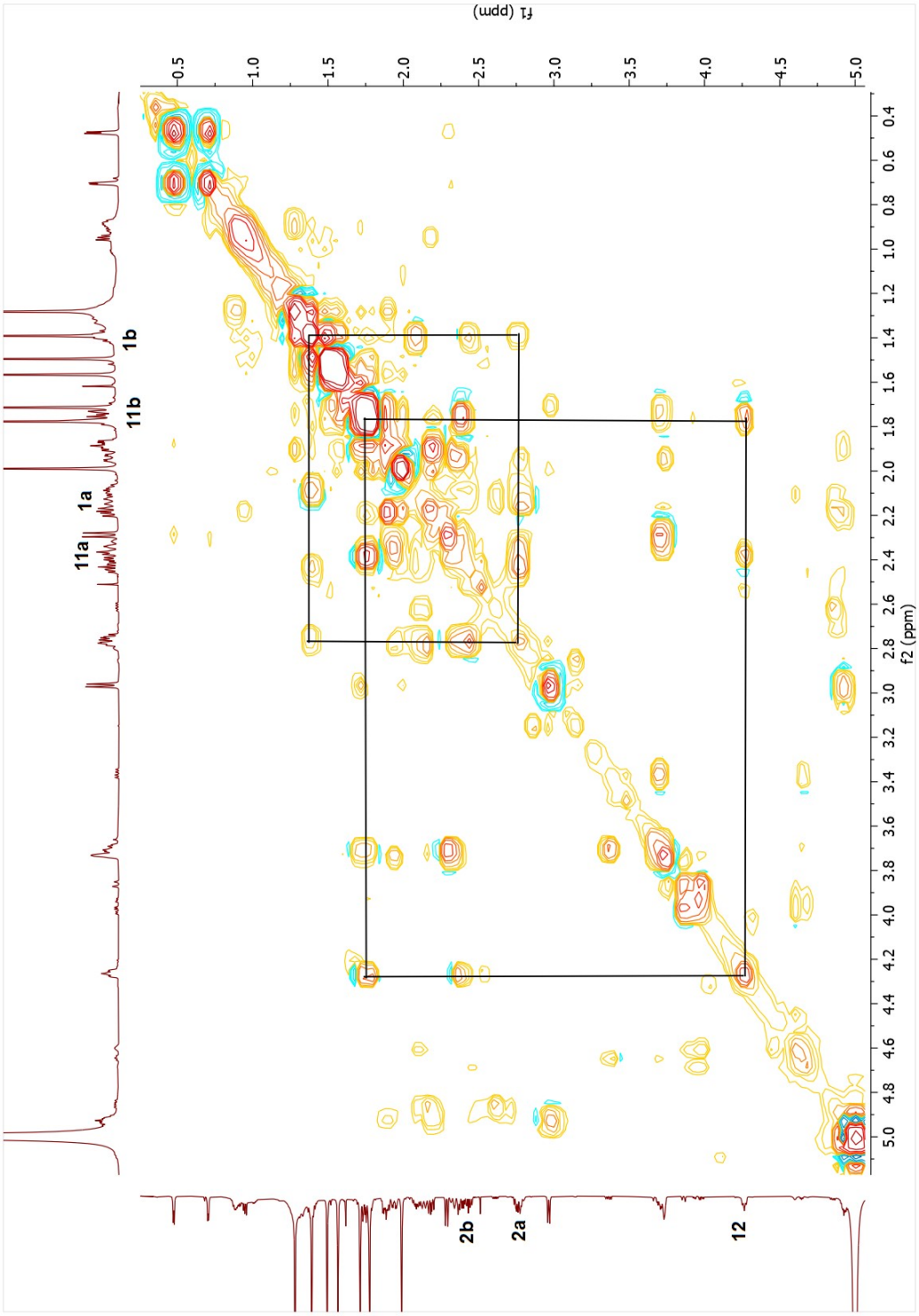

Spectrum 3.21. COSY spectrum of compound **26**.

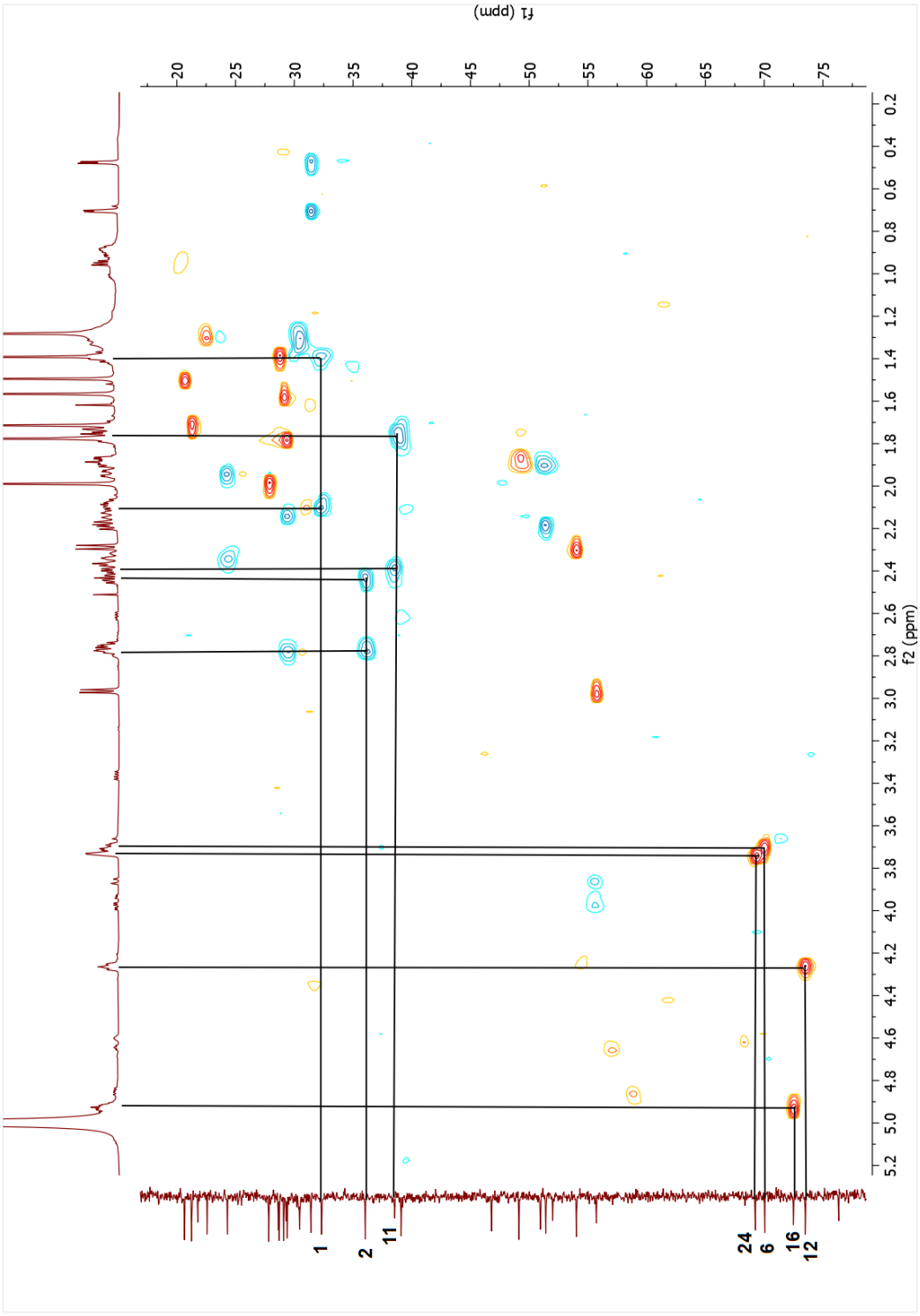

Spectrum 3.22. HSQC spectrum of compound **26**.

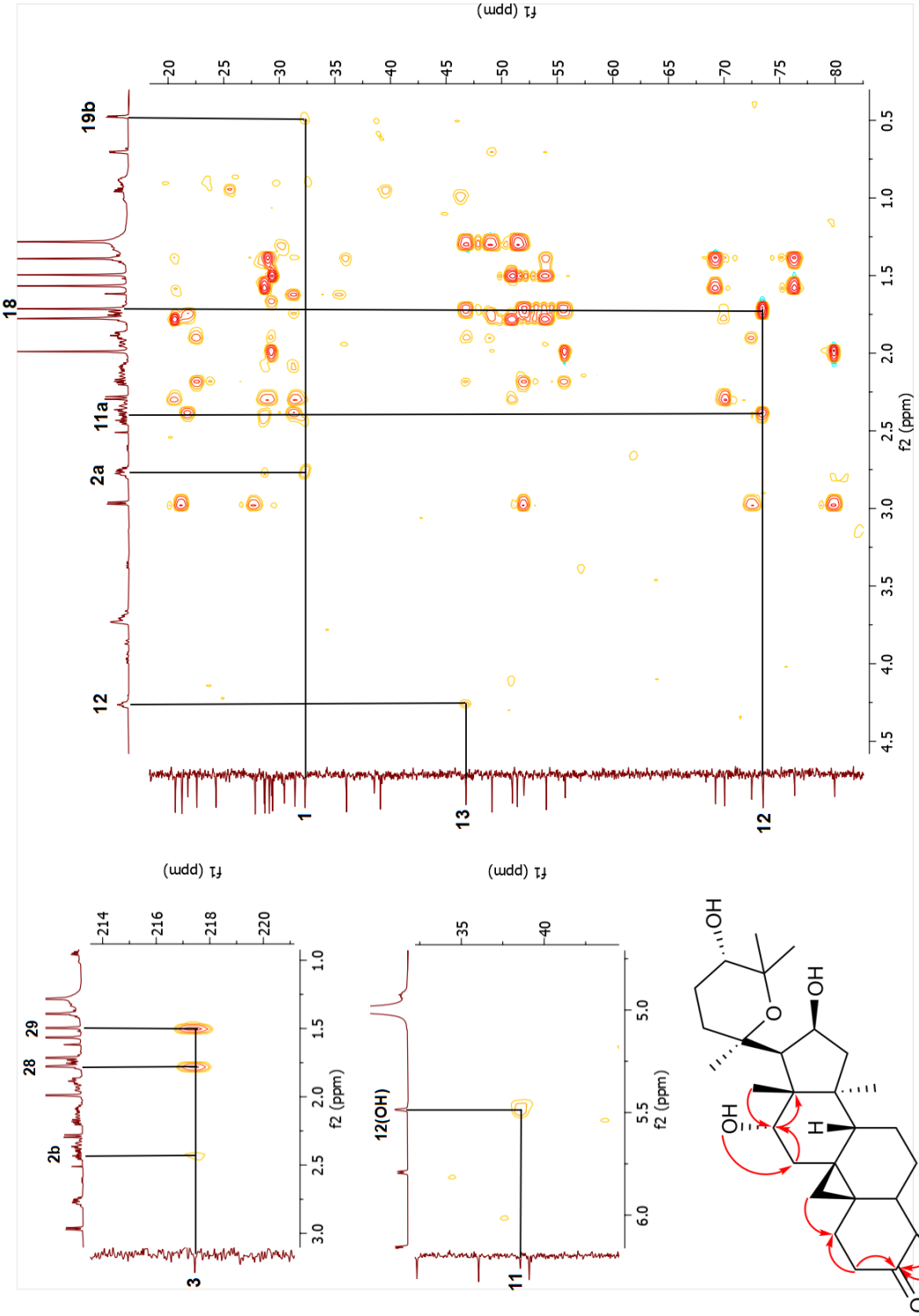

Spectrum 3.23. HMBC spectrum of compound **26**.

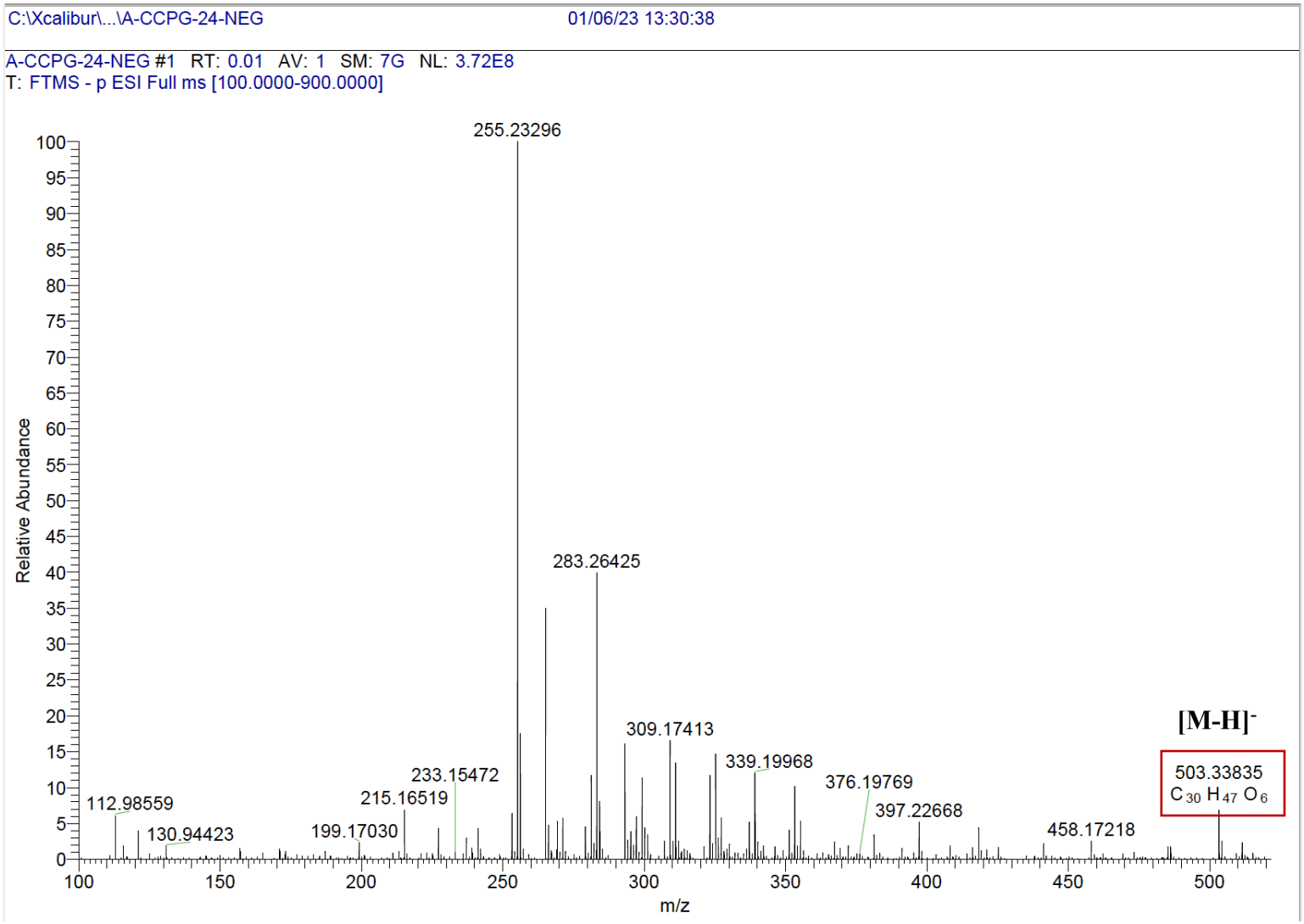

Spectrum 3.24. HR-ESI-MS spectrum of compound **26**.

3.3.2.5. Structure Elucidation of Compound 27

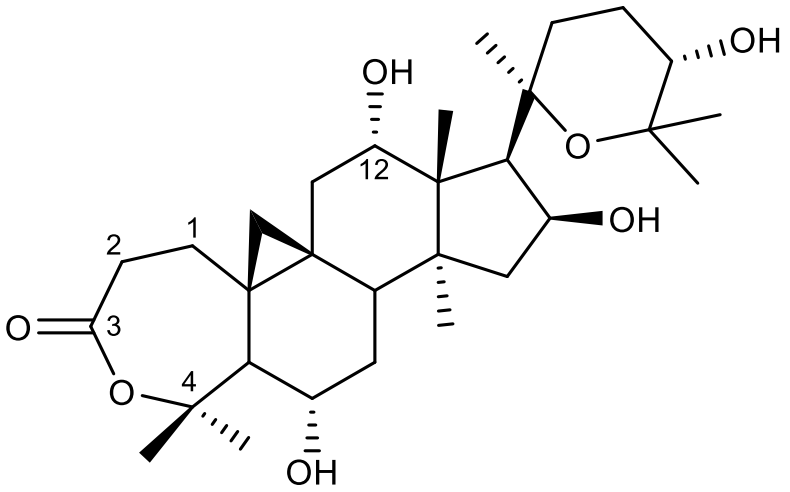

Figure 3.10. Chemical structure of compound **27**.

The HR-ESI-MS spectrum of **27** showed a major ion peak at *m/z* 519.33289 $[M - H]^-$ ($C_{30}H_{48}O_7$). Initial inspection of the ^{1}H-NMR spectrum of **27** revealed the absence of characteristic H-3 resonance. The HMBC spectrum showed a $^3J_{C\text{-}H}$ correlation between the H-1a signal (δ_H 1.42) and a carbonyl carbon at 173.6 ppm. From inspection of ^{13}C-NMR spectrum, an oxygenated quaternary carbon was observed at δ_C 85.3, which displayed long-range correlations with two methyl groups (δ_H 1.94 and 1.70) in the HMBC spectrum. Thus, the resonance of δ_C 85.3 was readily assigned to C-4. Comparing the chemical shifts and coupling constants with those of **24**, it was ascertained that **27** also had a 7-membered lactone ring system in ring A. As a result, **27** was elucidated as 20,25-epoxy-6α,12α,16β,24α-tetrahydroxycycloartan-3-olide.

Table 3.6. The ^{13}C and ^{1}H NMR data of **27** (100/400 MHz, δ ppm, in C_5D_5N).

Position	δ_C (ppm)	δ_H (ppm), *J* (Hz)
1	32.5	1.42 m, 1.99 m
2	33.6	2.58 dd (13.2, 5.1)
3	173.6	-
4	85.3	-
5	53.2	2.44 d (9.3)
6	70.9	3.70 m
7	37.4	1.62 m, 1.70 m
8	48.1	1.72 m
9	21.7	-
10	25.8	-
11	38.2	1.67 m, 2.35 dd (14.6, 5.8)
12	73.0	4.25 t (7.6)
13	51.0	-
14	46.0	-
15	51.0	1.89 m, 2.21 dd (12.5, 7.8)
16	71.9	4.93 m
17	54.9	2.96 d (8.1)
18	20.5	1.70 s
19	30.8	0.67 d (4.8), 0.84 d (4.9)
20	79.3	-
21	27.1	1.97 s
22	28.6	2.10 d (13.4), 2.78 t (12.2)
23	23.6	1.95 m, 2.35 m
24	68.5	3.72 brs
25	75.5	-
26	28.4	1.56 s
27	28.0	1.39 s
28	31.7	1.94 s
29	27.8	1.70 s
30	22.1	1.27 s

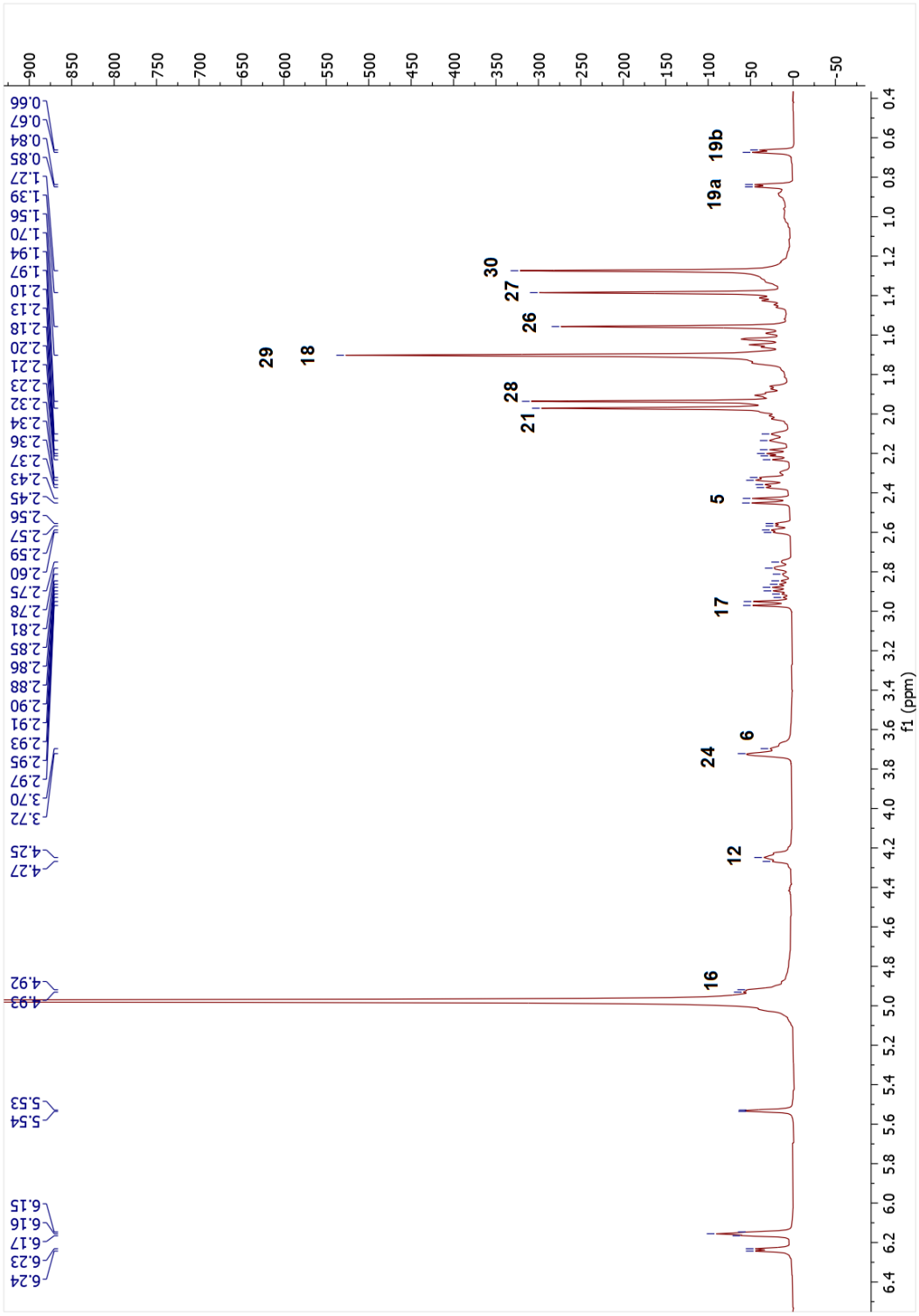

Spectrum 3.25. ^{1}H-NMR spectrum of compound **27**.

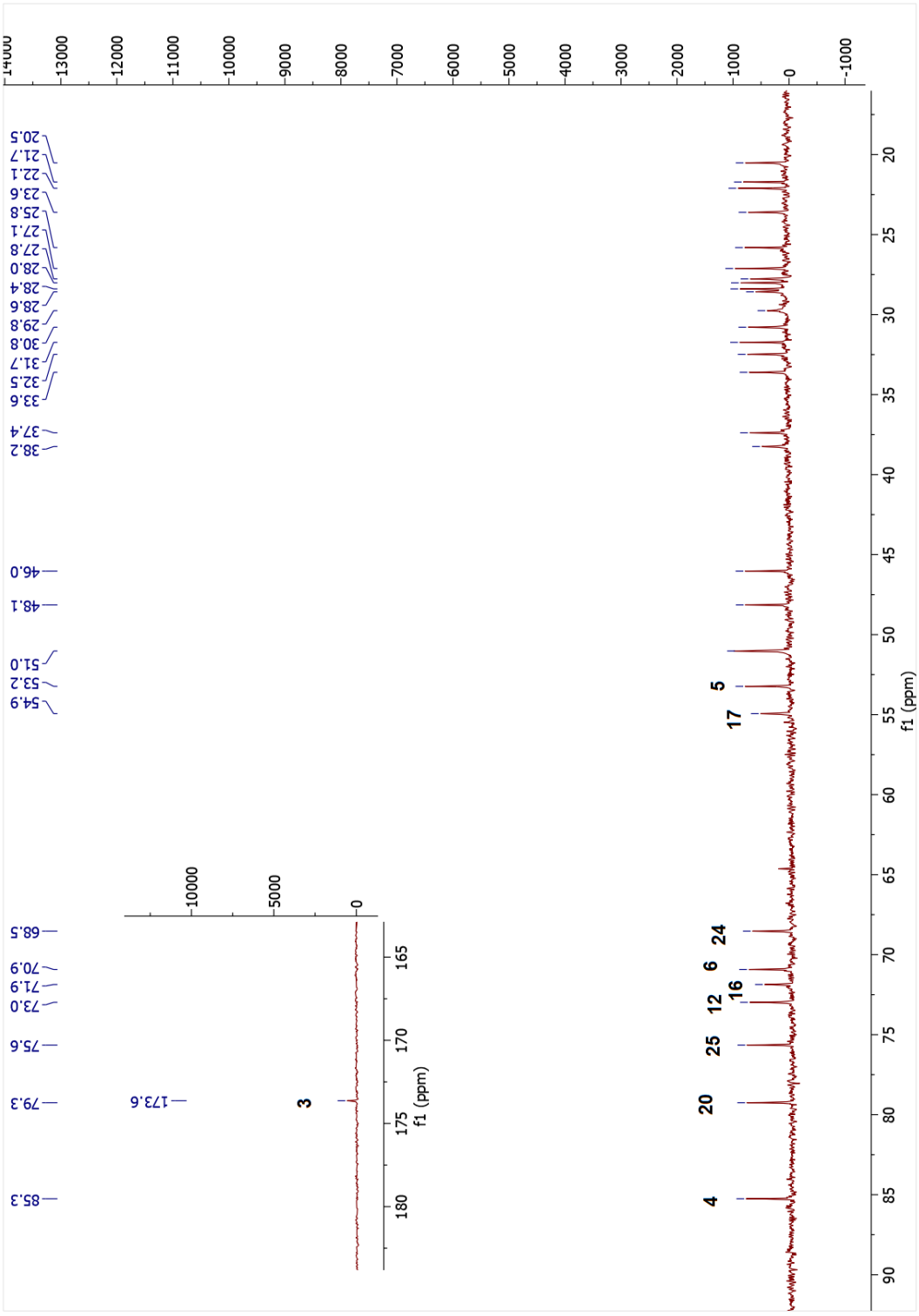

Spectrum 3.26. ^{13}C-NMR spectrum of compound **27**.

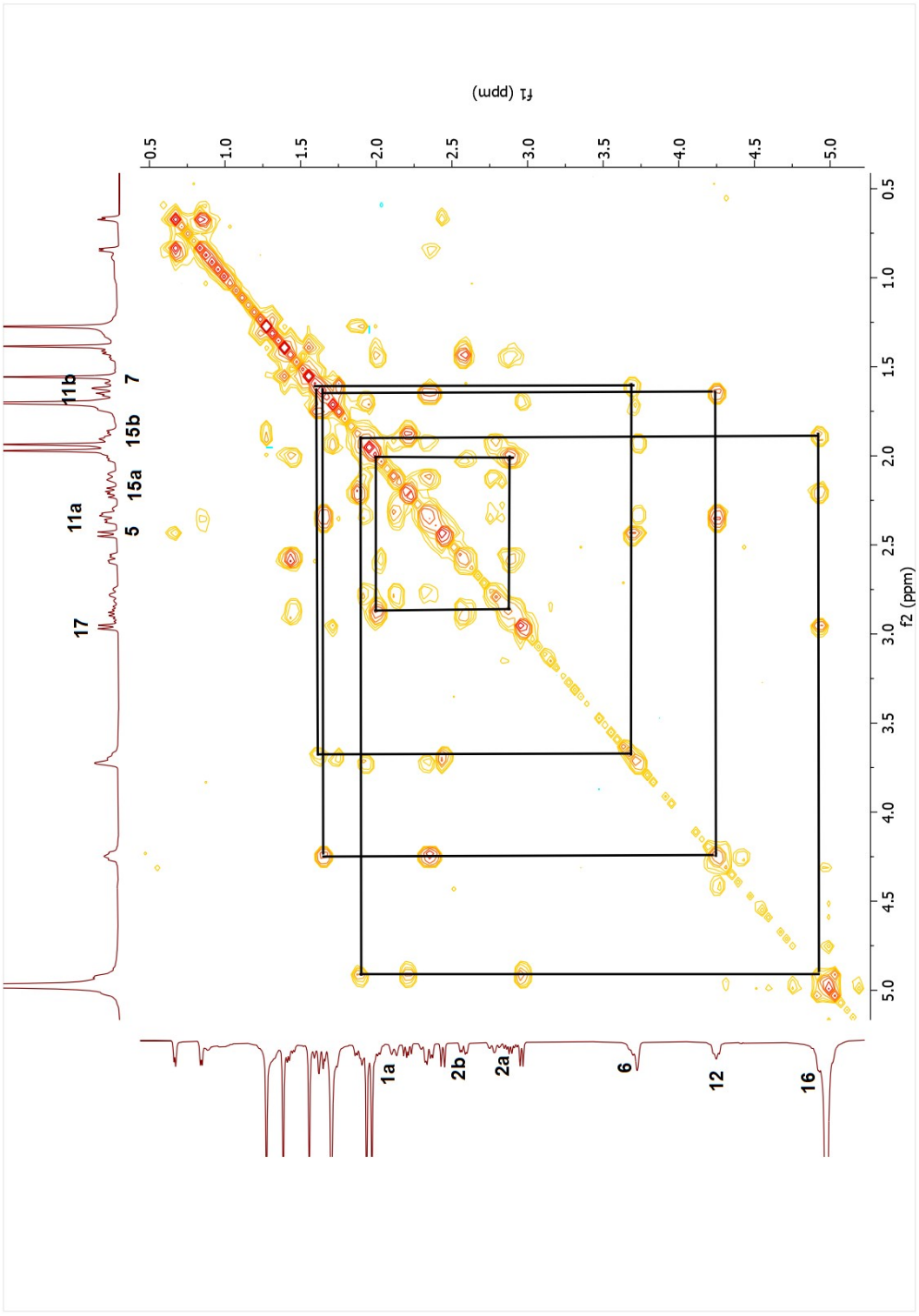

Spectrum 3.27. COSY spectrum of compound **27**.

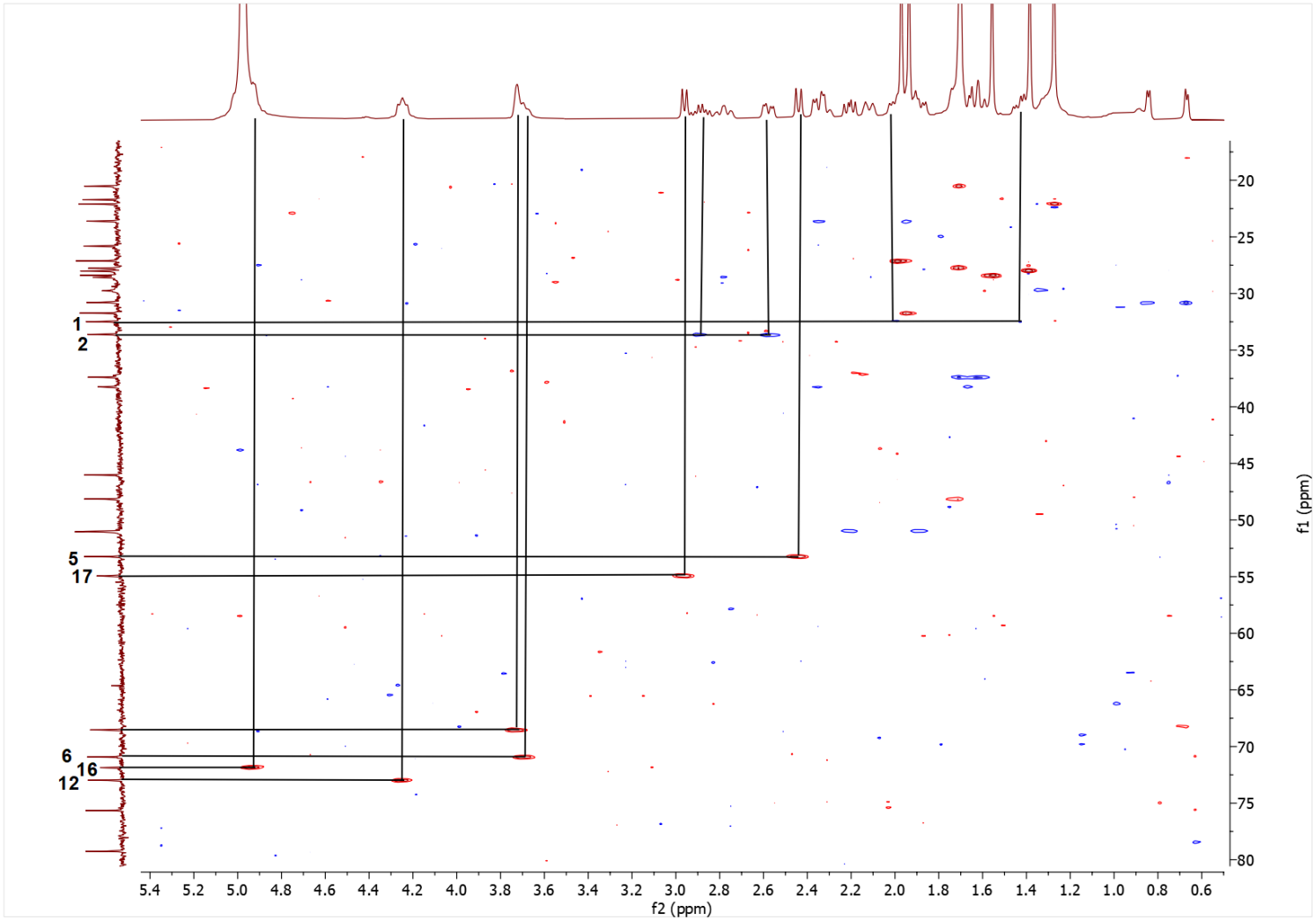

Spectrum 3.28. HSQC spectrum of compound **27**.

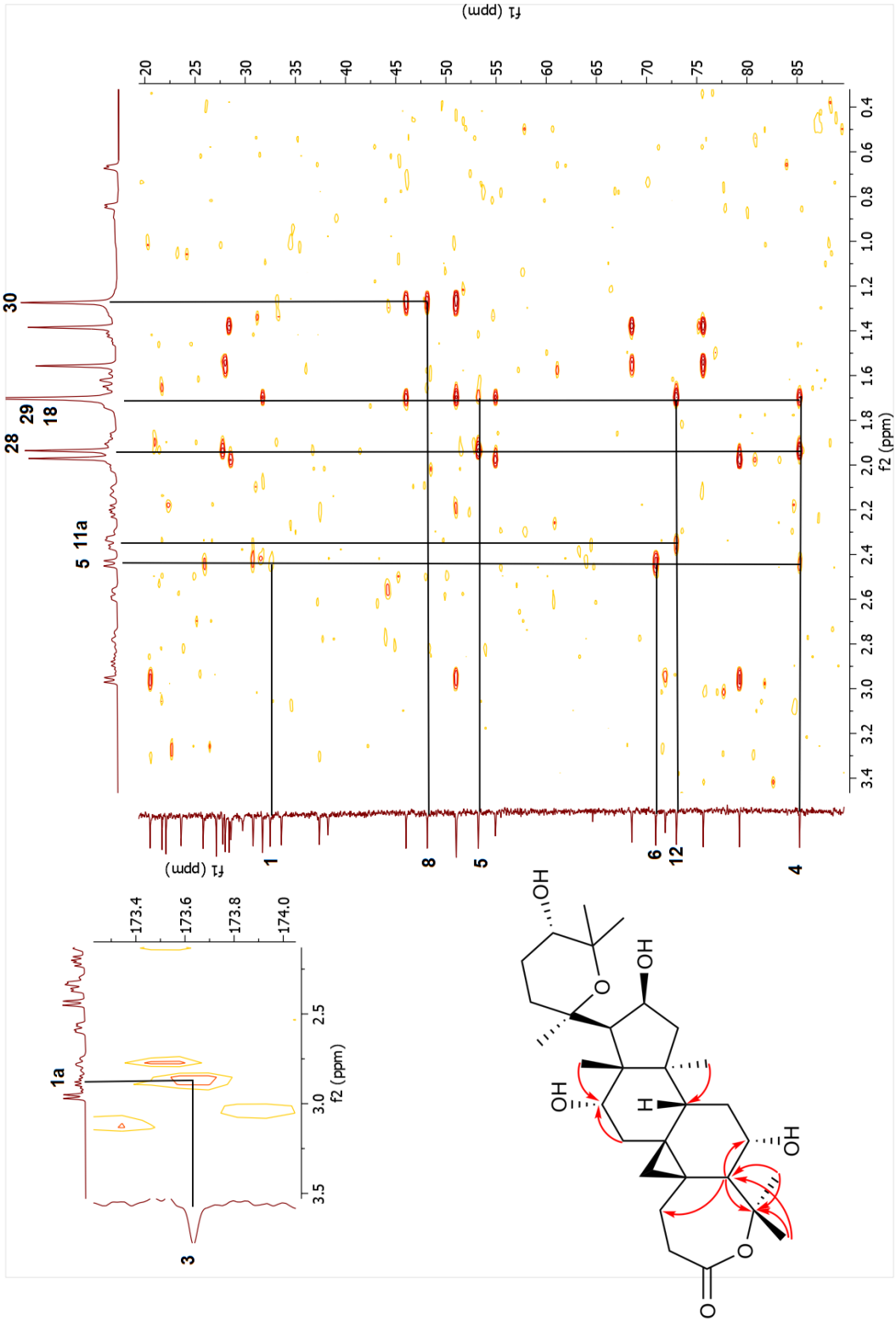

Spectrum 3.29. HMBC spectrum of compound **27**.

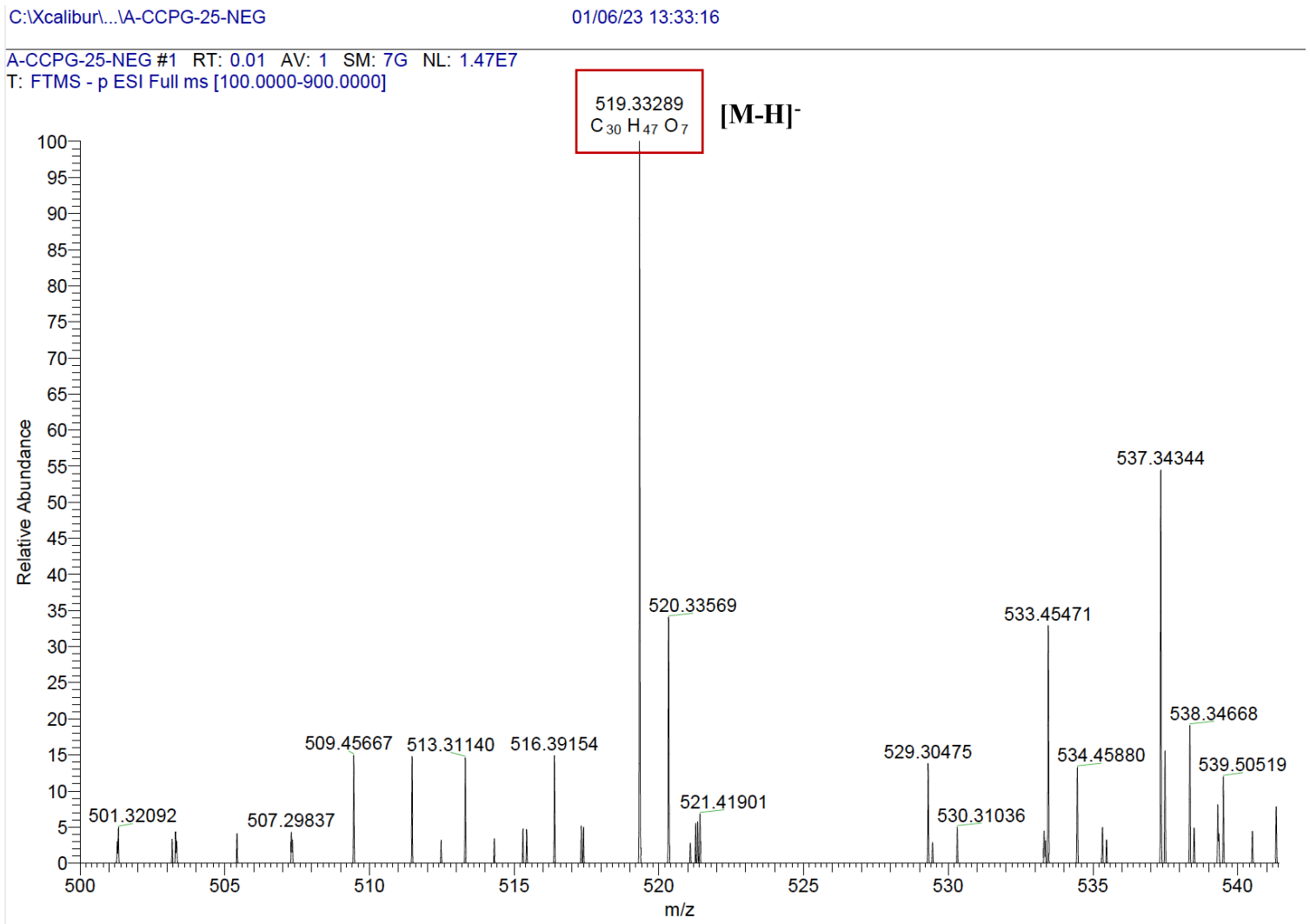

Spectrum 3.30. HR-ESI-MS spectrum of compound **27**.

3.3.2.6. Structure Elucidation of Compound 28

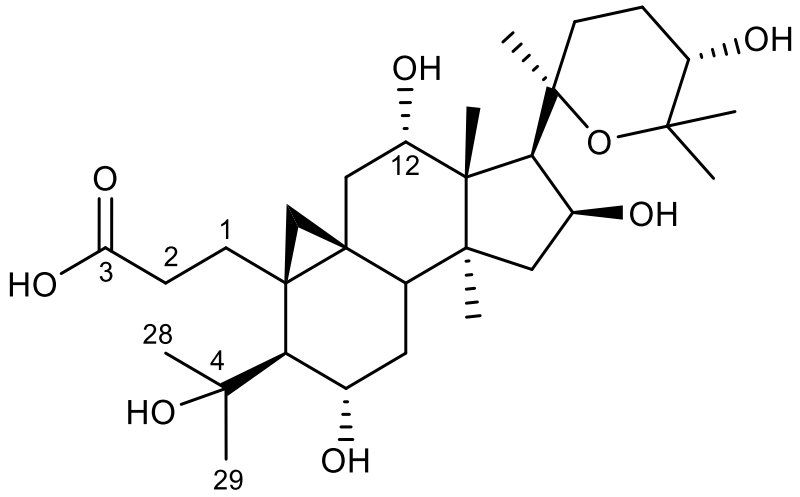

Figure 3.11. Chemical structure of compound **28**.

HR-ESI-MS spectrum of **28** showing a major ion peak at *m/z* 537.34344 ($[M - H]^-$) indicated a molecular formula of $C_{30}H_{50}O_8$. In the ^{13}C-NMR spectrum, the oxymethine signal belonging to C-3 was lost and a carboxyl signal was deduced from δ_C 179.5 resonance. In addition, a low-field carbon adjacent to oxygen (δ_C 76.4) was noticed. In the HMBC spectrum, the long-distance correlation of this carbon (δ_C 76.4) to H-5, H_3-28 and H_3-29 helped us to assign it as C-4. These data implied a ring cleavage in ring A, as in **23**. The resemblance of the spectral data of **28**, deduced from 1D- and 2D-NMR spectra, with those of **23** and **6** was evident for the characteristic 3(4)-seco structures with a carboxyl group at C-3 and hydroxyl functionality at C-4 establishing the structure of **23**. Based on these results, the structure of **28** was established as 20,25-epoxy-6α,12α,16β,24α-tetrahydroxy-3,4-secocycloartan-3-oic acid.

Table 3.7. The ^{13}C and ^{1}H NMR data of **28** (150/600 MHz, δ ppm, in C_5D_5N).

Position	δ_C (ppm)	δ_H (ppm), *J* (Hz)
1	33.0	1.82 m, 2.77 m
2	34.0	2.74 m, 3.00 m
3	179.5	-
4	76.4	-
5	54.2	2.45 d (8.3)
6	71.9	4.10 m
7	37.7	1.72 m, 1.85 m
8	47.8	1.67 m
9	29.2	-
10	25.7	-
11	38.7	2.04 dd (14.5, 8.4), 2.69 dd (14.5, 6.8)
12	74.0	4.28 t (7.9)
13	47.2	-
14	51.8	-
15	51.9	1.89 m, 2.23 dd (12.6, 7.7)
16	72.7	4.93 q (7.2)
17	55.7	2.97 d (8.3)
18	21.5	1.76 s
19	32.3	0.74 d (4.4), 1.06 d (4.4)
20	80.0	-
21	27.8	1.98 s
22	29.2	2.13 m, 2.78 m
23	24.3	1.93 m, 2.34 t (13.9)
24	69.3	3.73 brs
25	76.4	-
26	29.1	1.58 s
27	28.8	1.40 s
28	34.0	1.80 s
29	29.5	1.65 s
30	22.6	1.31 s

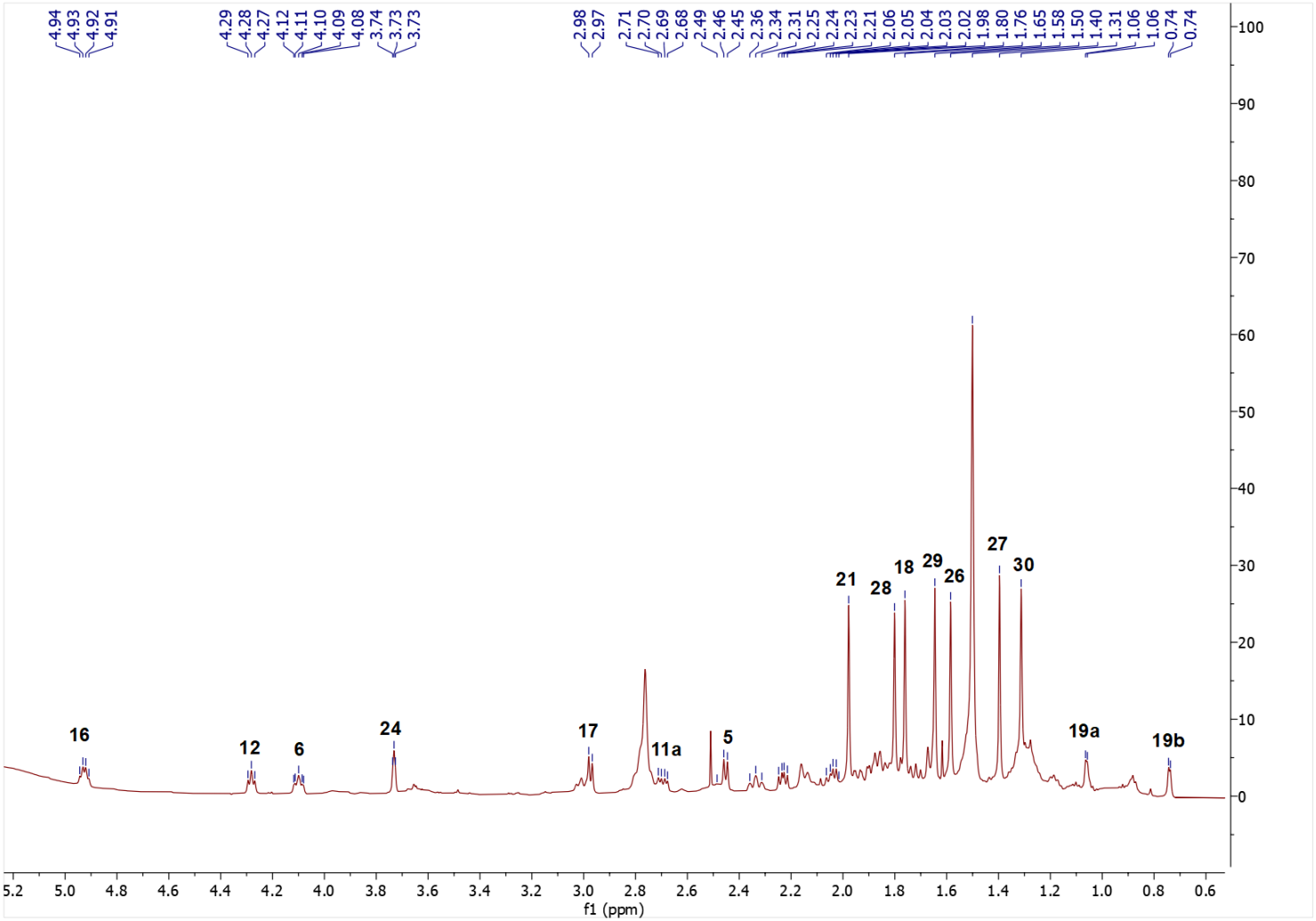

Spectrum 3.31. ^{1}H-NMR spectrum of compound **28**.

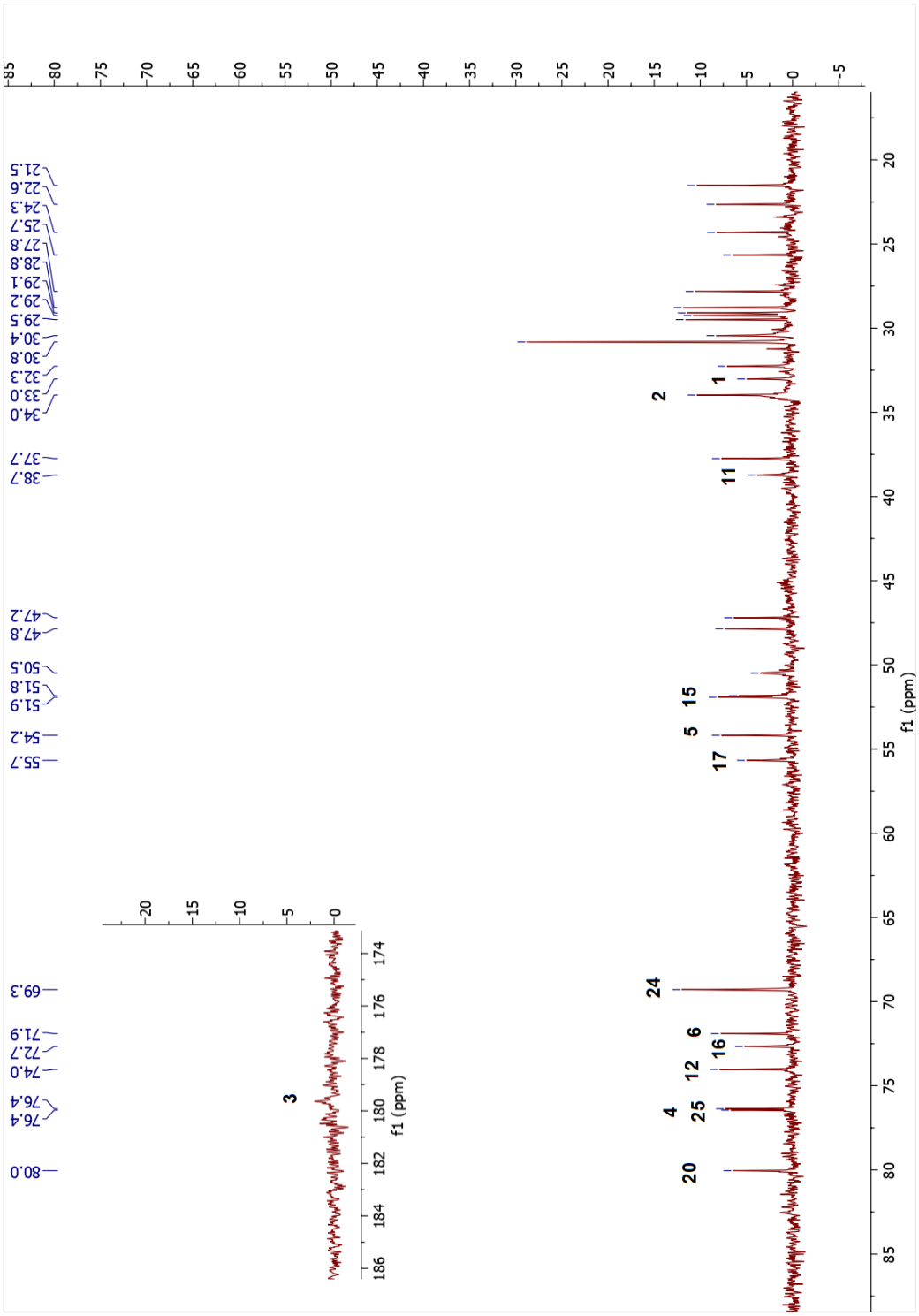

Spectrum 3.32. ^{13}C-NMR spectrum of compound **28**.

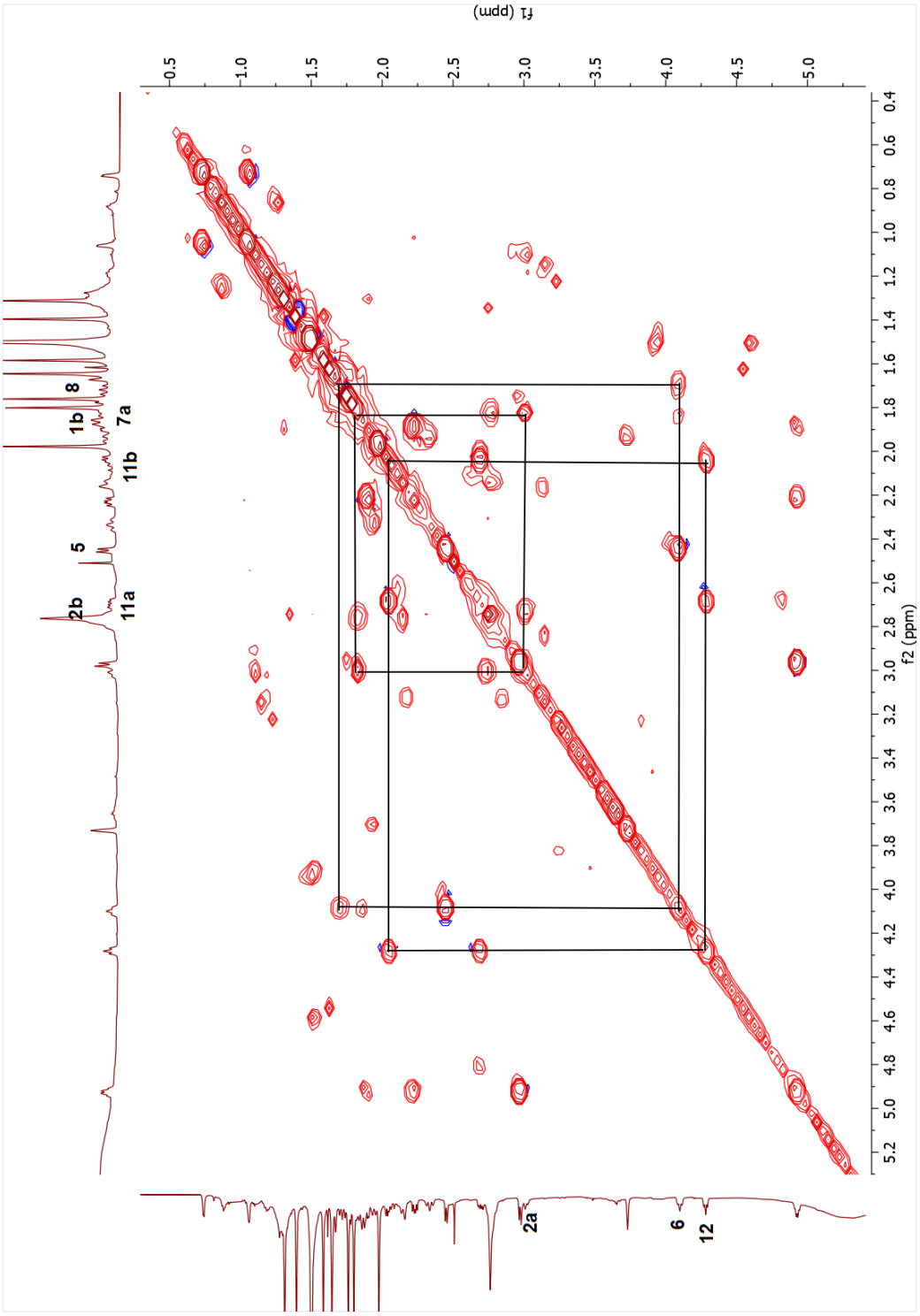

Spectrum 3.33. COSY spectrum of compound **28**.

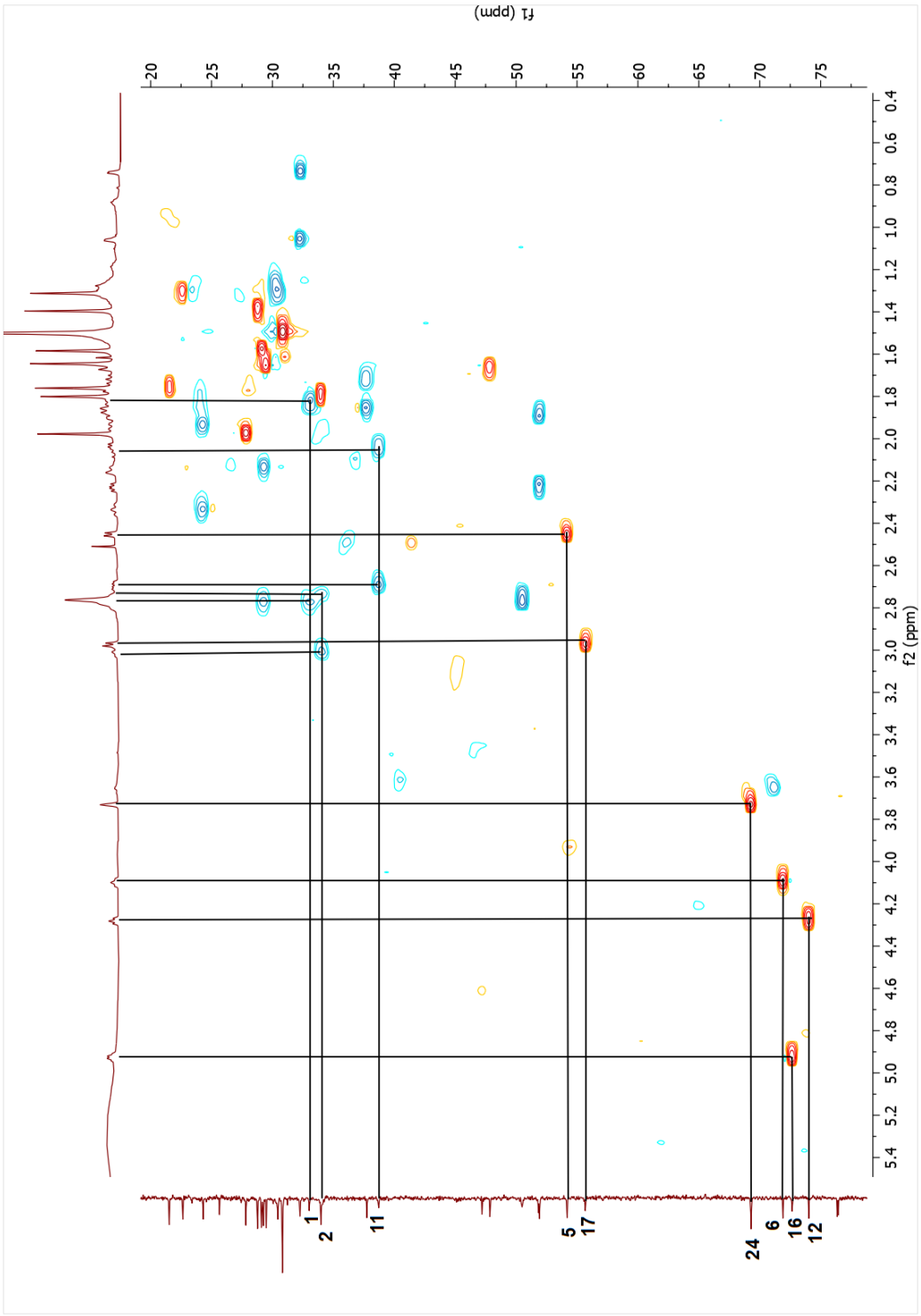

Spectrum 3.34. HSQC spectrum of compound **28**.

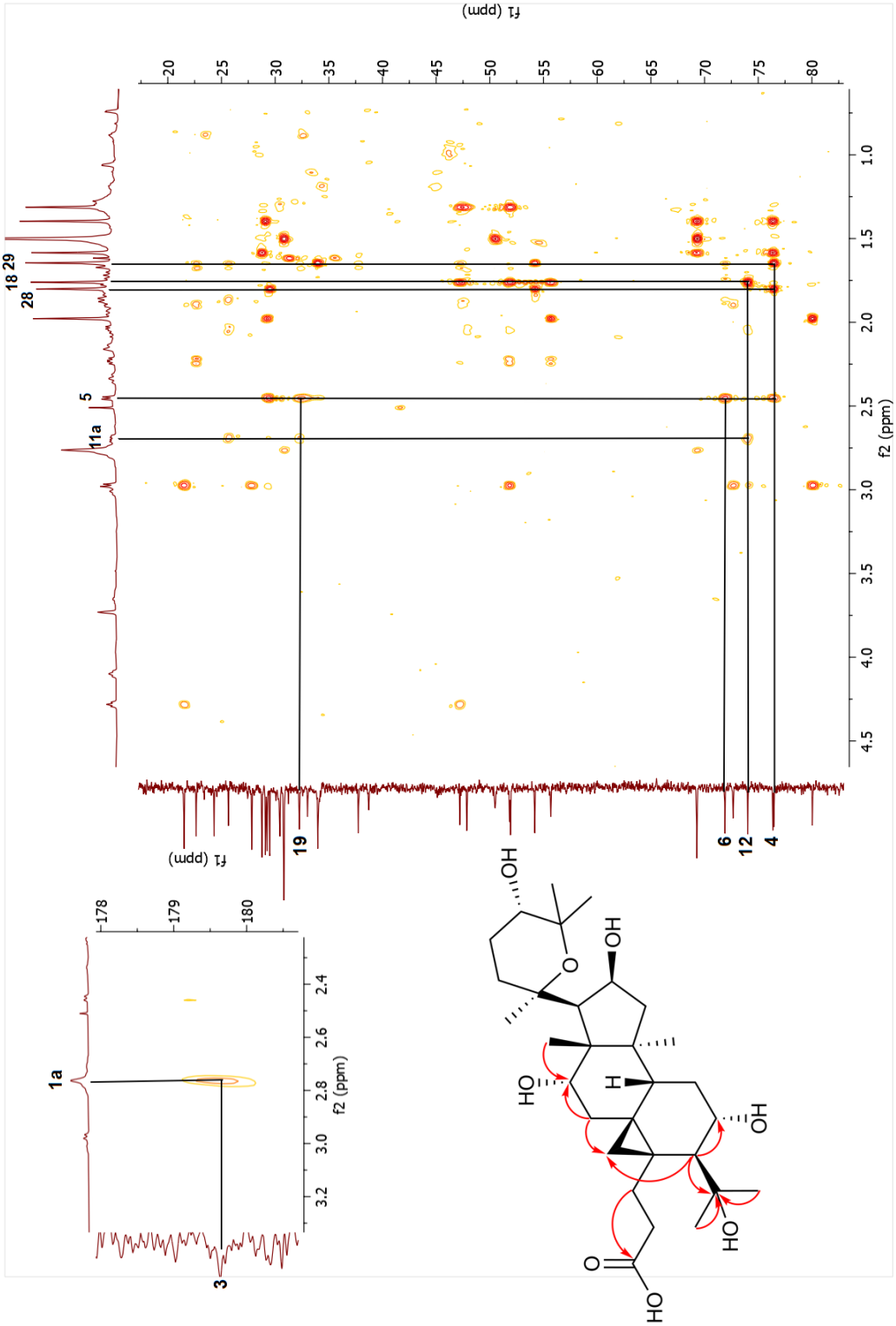

Spectrum 3.35. HMBC spectrum of compound **28**.

Spectrum 3.36. HR-ESI-MS spectrum of compound **28**.

3.3.2.7. Structure Elucidation of Compound 29

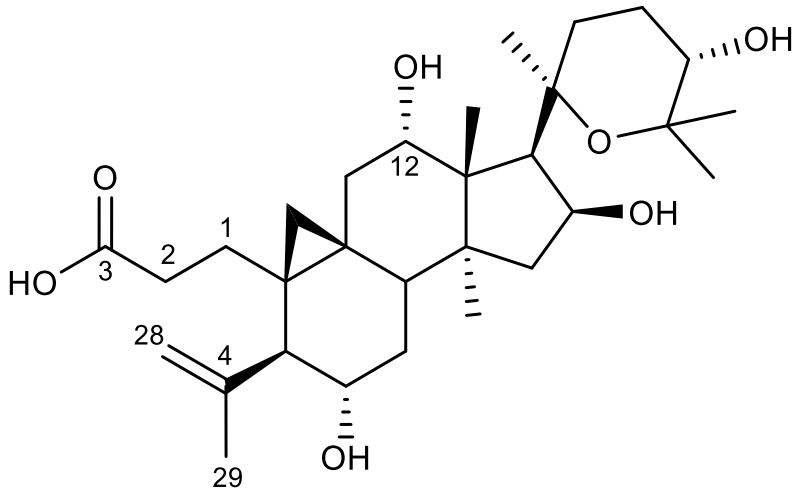

Figure 3.12. Chemical structure of compound **29**.

In the HR-ESI-MS spectrum of **29**, the major ion peak at *m/z* 519.33122 $[M - H]^-$ confirmed the molecular formula as $C_{30}H_{48}O_7$. The ^1H and ^{13}C-NMR spectra of **29** implied a ring cleavage as in compound **28**. The resonances observed at δ_H 5.21 and 5.09 suggested an exocyclic methylene group corresponding to carbon at δ_C 115.3 in the HSQC spectrum. In addition, one of the two methyl groups at C-4 disappeared, and the other one shifted to a low field ($\delta_{H\text{-}29}$ 1.89). The HMBC spectrum displayed cross-peaks from H-29 (δ_H 1.89) to C-28 (δ_C 115.3), C-4 (δ_C 147.1) and C-5 (δ_C 55.7). This indicated that an A-ring cleavage was followed by a dehydration reaction yielding a C-4(28) disubstituted double bond system. Accordingly, the COSY spectrum revealed a spin system of H-28a (δ_H 5.21) → H-28b (δ_H 5.09) → H_3-29 (δ_H 1.89), including an allylic coupling and justifying this assignment. Consequently, a new 3(4)-seco structure of 12α-hydroxycyclocephagenol with an isopropenyl group extending from C-5 was established. On the basis of these results, the structure of **29** was established as 20,25-epoxy-6α,12α,16β,24α-tetrahydroxy-3,4-secocycloartan-4(28)-en-3-oic acid.

Table 3.8. The ^{13}C and ^{1}H NMR data of **29** (150/600 MHz, δ ppm, in C_5D_5N).

Position	δ_C (ppm)	δ_H (ppm), *J* (Hz)
1	31.1	1.80 t (13.1), 2.53 m
2	33.1	2.70 m, 2.95 m
3	177.3	-
4	147.1	-
5	55.7	2.78 d (9.7)
6	69.3	3.64 m
7	36.7	1.65 m, 1.90 m
8	49.0	1.94 m
9	30.7	-
10	22.2	-
11	39.0	2.11 m, 2.73 m
12	73.4	4.28 t (7.7)
13	47.0	-
14	51.8	-
15	51.3	1.91 m, 2.21 dd (12.6, 7.9)
16	72.3	4.94 m
17	55.5	2.99 d (8.0)
18	21.2	1.75 s
19	32.4	0.63 d (4.4), 0.73 d (4.4)
20	79.8	-
21	27.7	1.99 s
22	29.1	2.13 m, 2.81 m
23	24.2	1.94 m, 2.34 t (14.0)
24	69.1	3.74 s
25	76.2	-
26	28.9	1.59 s
27	28.6	1.40 s
28	115.3	5.09 s, 5.21 s
29	20.7	1.89 s
30	22.3	1.33 s

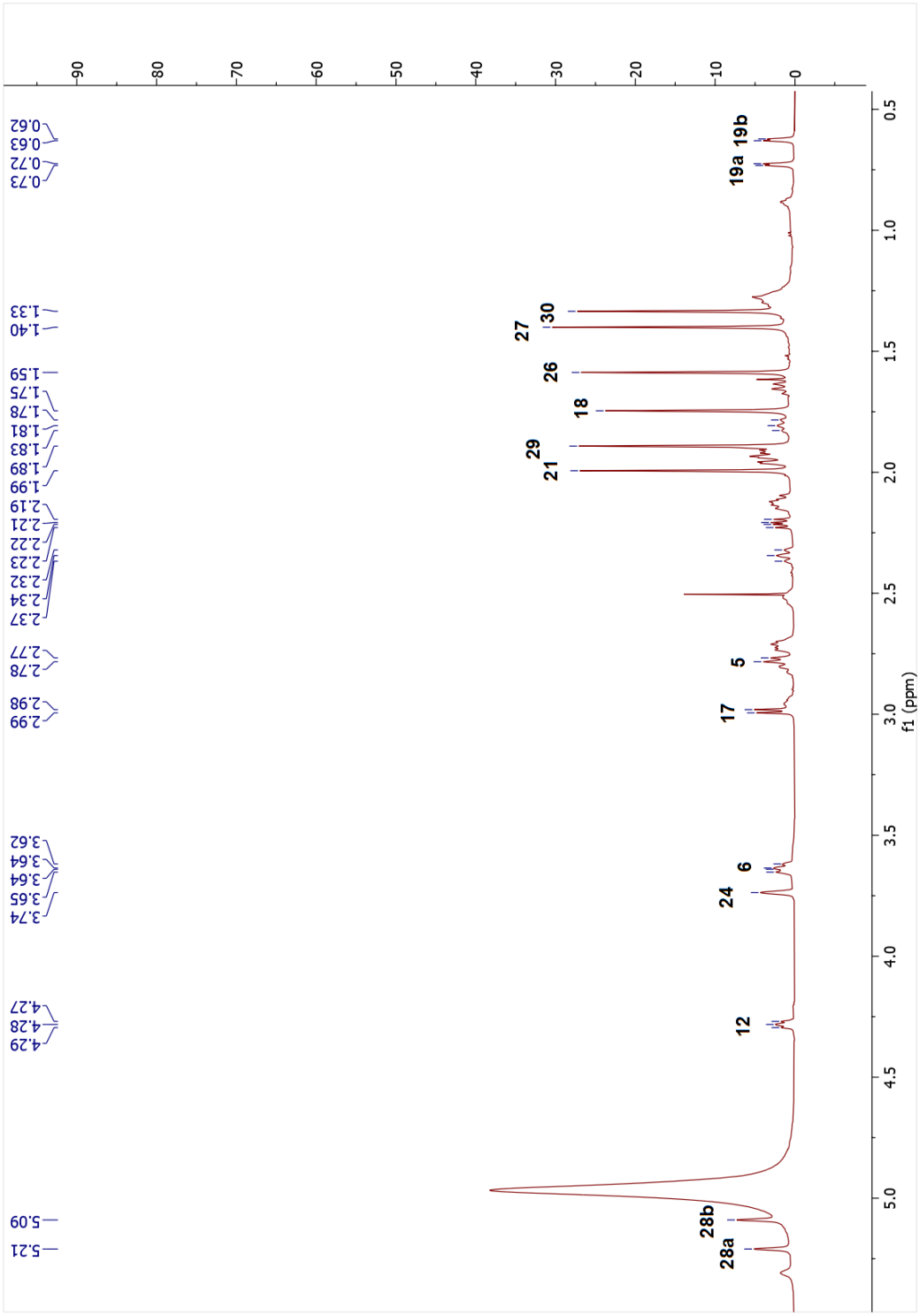

Spectrum 3.37. ^{1}H-NMR spectrum of compound **29**.

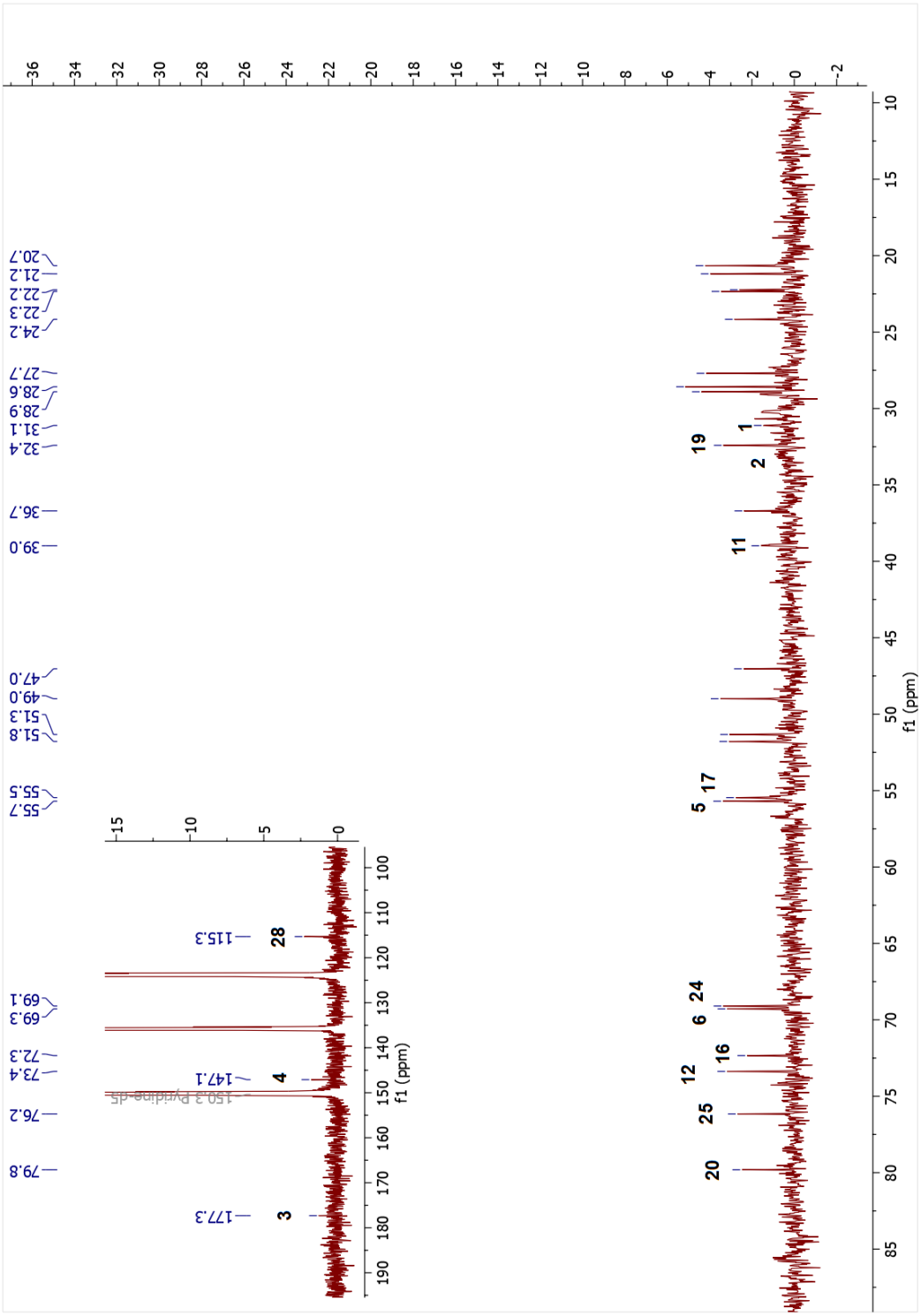

Spectrum 3.38. ^{13}C-NMR spectrum of compound **29**.

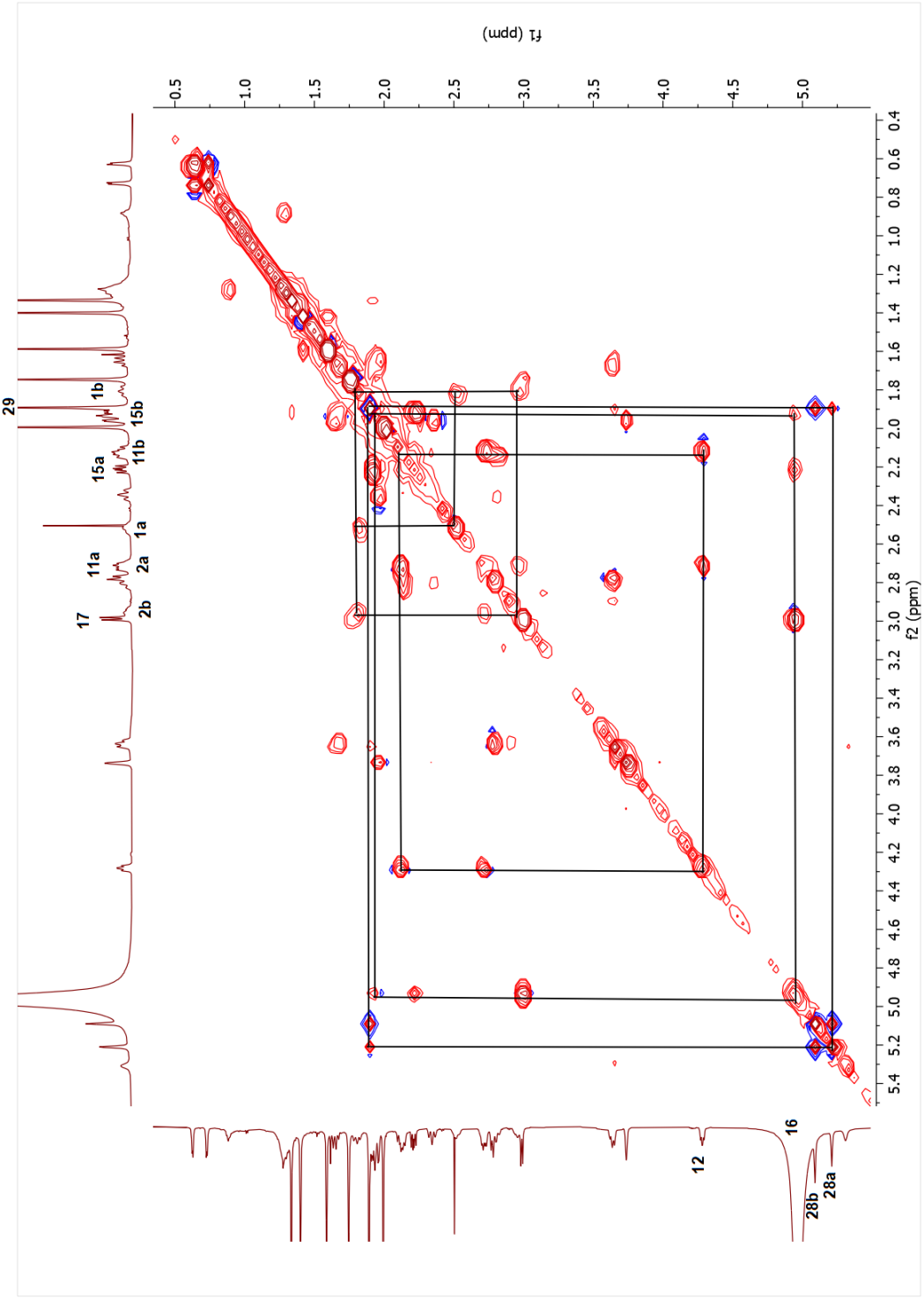

Spectrum 3.39. COSY spectrum of compound **29**.

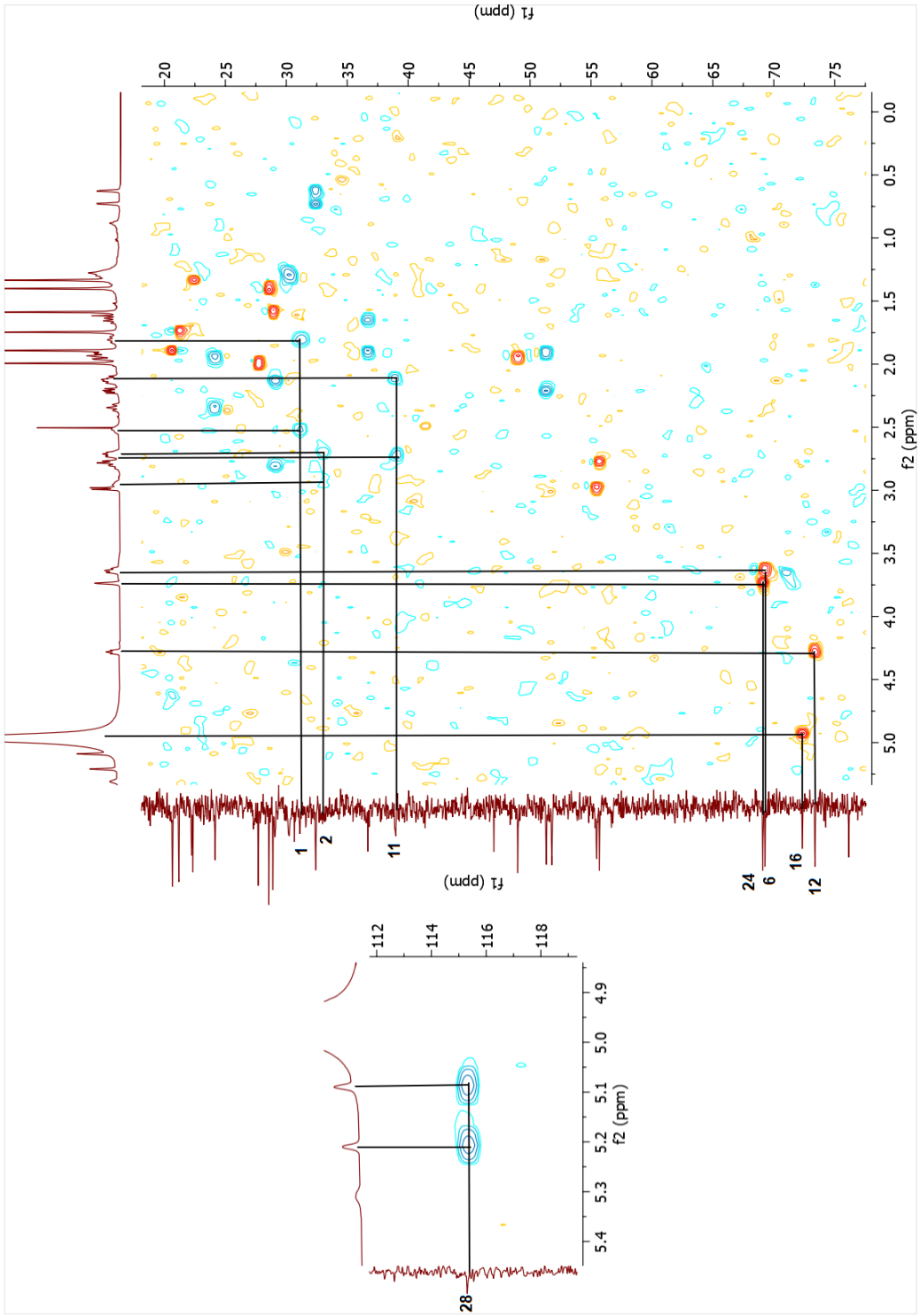

Spectrum 3.40. HSQC spectrum of compound **29**.

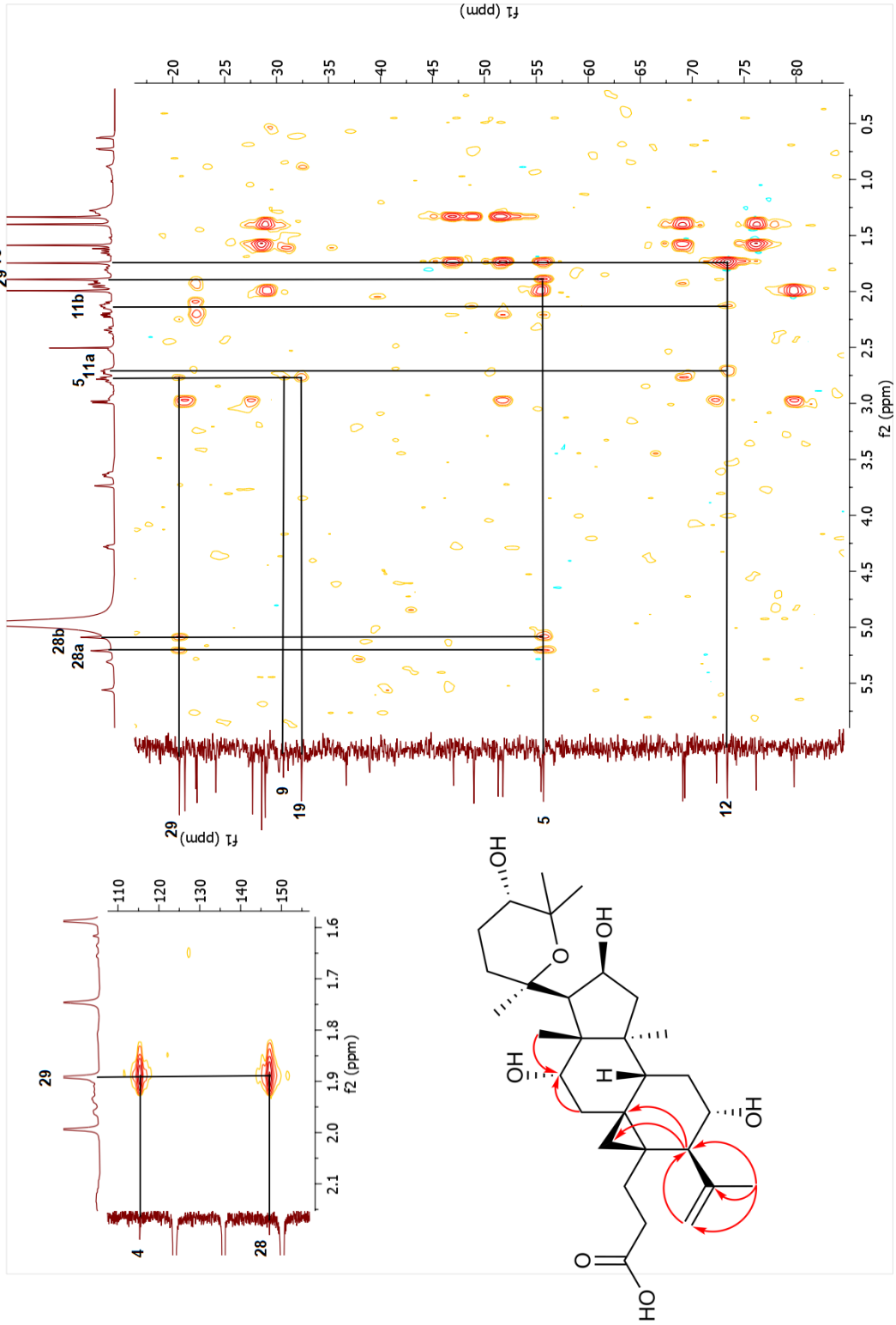

Spectrum 3.41. HMBC spectrum of compound **29**.

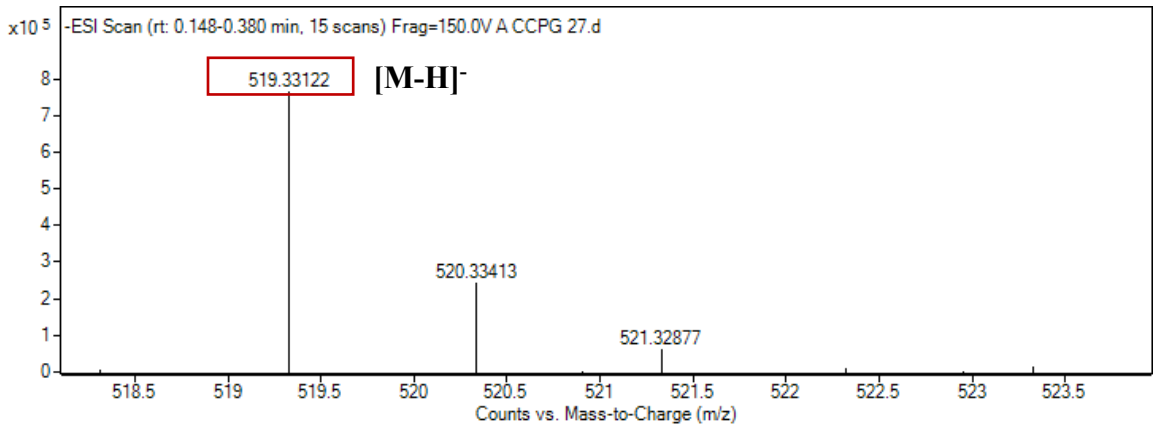

Spectrum 3.42. HR-ESI-MS spectrum of compound **29**.

3.3.3. Telomerase Activation by Cyclocephagenol and Its Derivatives

3.3.3.1. The Effects of Biotransformation Products on hTERT Protein Levels

In preliminary screening, Western blot experiments were performed to examine the effect of biotransformation products on hTERT protein level, which is a reverse transcriptase subunit of the telomerase enzyme. While metabolites **23** and **24** enhanced hTERT protein levels at lower concentrations as 2-, 10 and 30 nM, metabolites **26** and **29** increased this protein levels at 10-, 30 and 100 nM concentrations—besides, metabolite **25** increased hTERT protein levels in a dose-dependent manner (Figure 3.13).

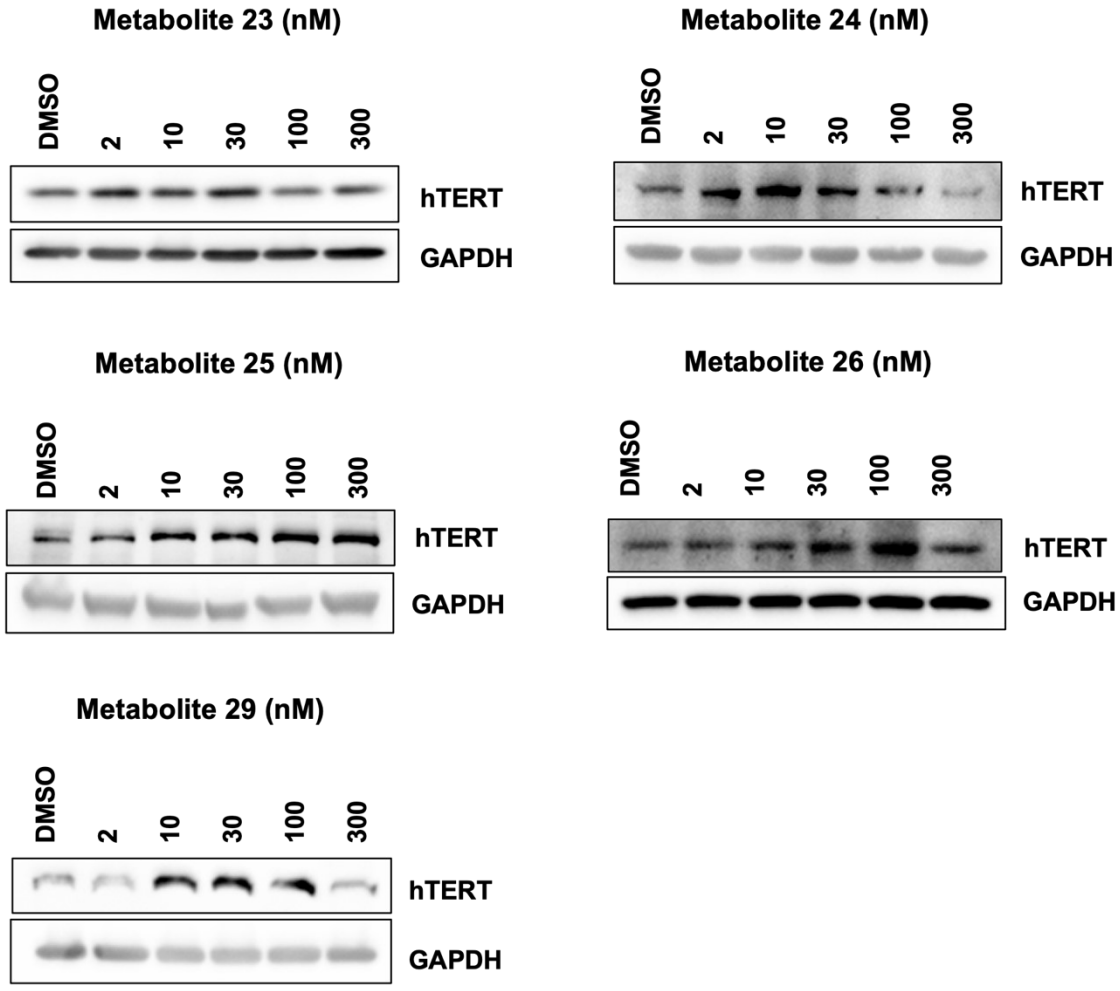

Figure 3.13. Effects of **23**, **24**, **25**, **26** and **29** on hTERT protein level.

3.3.3.2. Determination of Telomerase Enzyme Activity by Using TeloTAGGG Assay

After evaluating hTERT protein levels *via* Western Blot studies, the concentrations that increased protein levels were selected and investigated in terms of telomerase enzyme activity via ELISA assay.

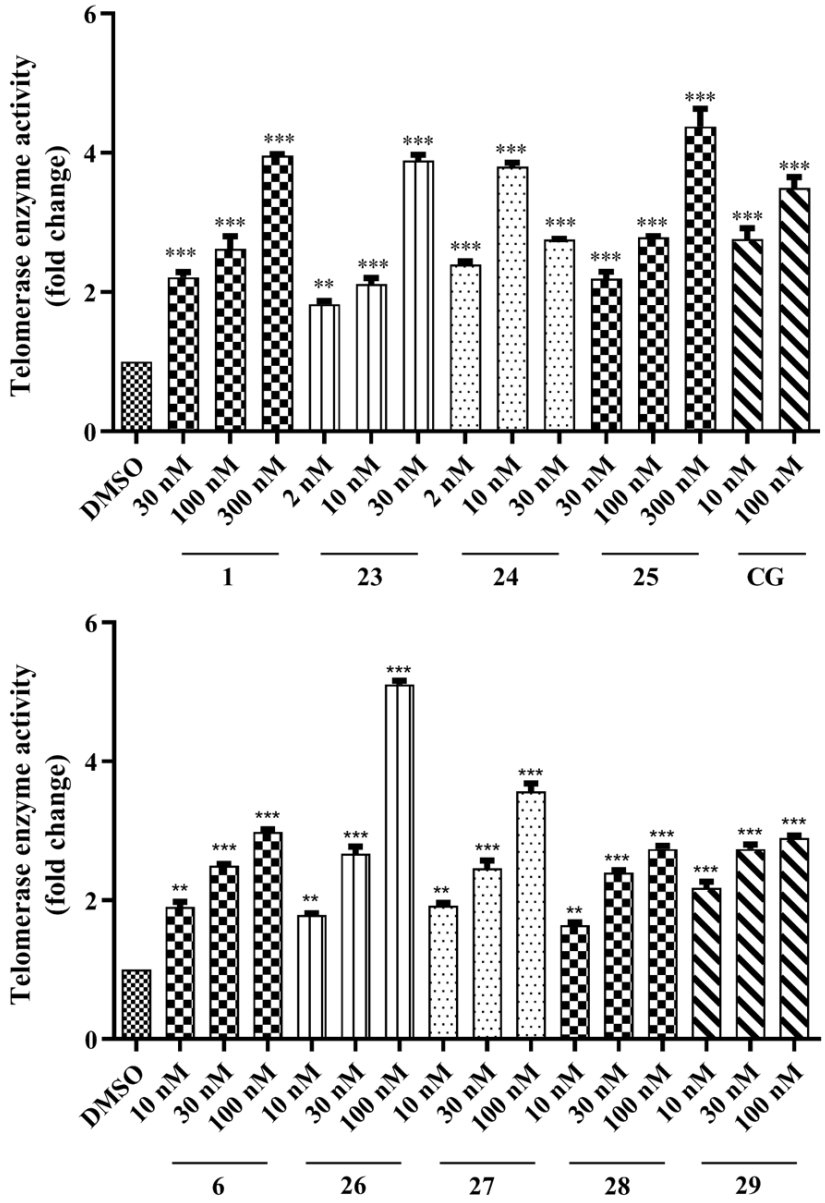

Figure 3.14. Telomerase activity of compounds **1**, **6**, **23**-**29** in cell lysates measured by TeloTAGGG Telomerase PCR Plus assay (Values are expressed as the fold change relative to the control DMSO).

Compared to the DMSO-treated control group, starting compounds and their derivatives exhibited promising telomerase activation (Figure 3.16). While cyclocephagenol (**1**) increased telomerase enzyme activity at the highest concentration (300 nM) by 3.95-fold compared to DMSO, metabolites **23**, **24** and **25** improved enzyme activity as 3.89-fold (30

nM), 3.81-fold (10 nM) and 4.38-fold (300 nM), respectively. Additionally, the active dose of metabolite **6** (2.98-fold) and its derivatives **26** (5.11-fold), **27** (3.57-fold), **28** (2.74-fold) and **29** (2.90-fold) were 100 nM. The positive control, cycloastragenol (CG), provided a 3.5-fold increase in telomerase activation at 100 nM (Figure 3.14).

3.4. Discussion

The fact that telomerase activators have the potential to be used not only in anti-aging therapies but also in regenerative medicine and degenerative diseases makes these activators very valuable[27,29–32,115,117,118]. One of the major reluctancy to apply telomerase activators in the field has been their probable potential inducing cellular transformation to initiate cancer. In recent years, studies on the discovery of telomerase activators and their molecular/mechanistic basis have increased with the demonstration that telomerase activation via small molecules does not cause cancer[106–111]. Cycloastragenol, as a pioneer molecule, plays a vital role in telomerase activation research. Indeed, a recent finding by Deng et al. (2022) reporting that cycloastragenol inhibits tumor growth *in vivo* was also entirely meaningful for the field[129].

Based on the telomerase activator potentials of cycloartanes and our previous studies[48–51], we decided to carry out biotransformation studies on cyclocephagenol (**1**), a novel cycloartane-type sapogenin from *Astragalus microcephalus*, and its 12-hydroxy derivatives. As there was no bioactivity data on cyclocephagenol and its derivatives in telomerase activation, we first evaluated the hTERT protein level of cyclocephagenol (**1**) and its 12-hydroxy derivatives (**2** and **6**) on HEKn cells. While cyclocephagenol (**1**) and **2** increased hTERT protein levels in a dose-dependent manner, metabolite **6** increased this protein levels at 10, 30 and 100 nM concentrations.

Since the hTERT protein levels of these compounds were notable, biotransformation studies were carried out on cyclocephagenol and its 12-hydroxy derivatives within the scope of this study. Biotransformation studies yielded seven new biotransformation products (Figure 3.16). Structural elucidations were accomplished through 1D-, 2D-NMR, and HR-

ESI-MS analysis. As in our previous study, *C. laburnicola* was found to catalyze oxidation, Baeyer-Villiger oxidation, ring opening, and dehydration reactions, respectively.

A biotransformation study on cyclocephagenol (**1**) resulted in the production of three compounds (**23**: 3(4)-seco, **24**: A-lacto, and **25**: 3-oxo), as in the biotransformation of cycloastragenol[48,50]. Interestingly, in the biotransformation study performed with 12α-hydroxycyclocephagenol, a dehydration reaction (**29**) was also achieved in addition to these modifications (**26**: 3-oxidation; **27**: lactone formation; **28**: 3(4)-ring cleavage). This modification was also observed in the biotransformation of astragenol in our previous studies[48,50]. From a chemistry point of view, we speculate that the 12-OH group makes hydrogen bonds with the carboxylic acid group at C-3 since they are both on the same face of the molecule, which allows the dehydratase enzyme to work on the isopropyl alcohol group. Figure 3.15a shows the MM2-minimized energy conformation of metabolite **28**, displaying possible hydrogen bonds between COOH at C-3 and OH at C-12, supporting our hypothesis.

In examining NMR data of biotransformation products, it was observed that cyclopropane protons shifted to the lower field in 3(4)-seco and lactone derivatives. This shift was about 0.43 ppm for H-19a and 0.25 ppm for H-19b for the 3(4)-seco derivatives, while both protons shifted to the low field of about 0.22 ppm for the lactone derivatives. The reason is thought to be the presence of electron-withdrawing groups on the A-ring (lactone and carboxylic acid). In addition, it was determined that the H-6 proton shifted to a lower field of ca. 0.30 ppm in the 3(4)-seco derivatives. This may be due to the hydrogen bond between the carboxylic acid at C-3 and the hydroxy group at C-4 (Figure 3.15b). By contrast, in metabolite **29**, the H-6 proton is shifted to the higher field of ca. 0.12 ppm. The carboxylic acid group at C-3 can make a hydrogen bond with the hydroxy group at C-4 and C-12. When energy minimization was performed with the Chem 3D program, we found that their energies were quite close (Figure 3.15). However, further analysis is required to explain this phenomenon.

In the case of 12β-hydroxycyclocephagenol, metabolite production was low, and most of the starting compound remained in the broth. Although 12β-hydroxycyclocephagenol increased the hTERT protein level compared to the control group, further studies were not performed due to the abovementioned yield issue.

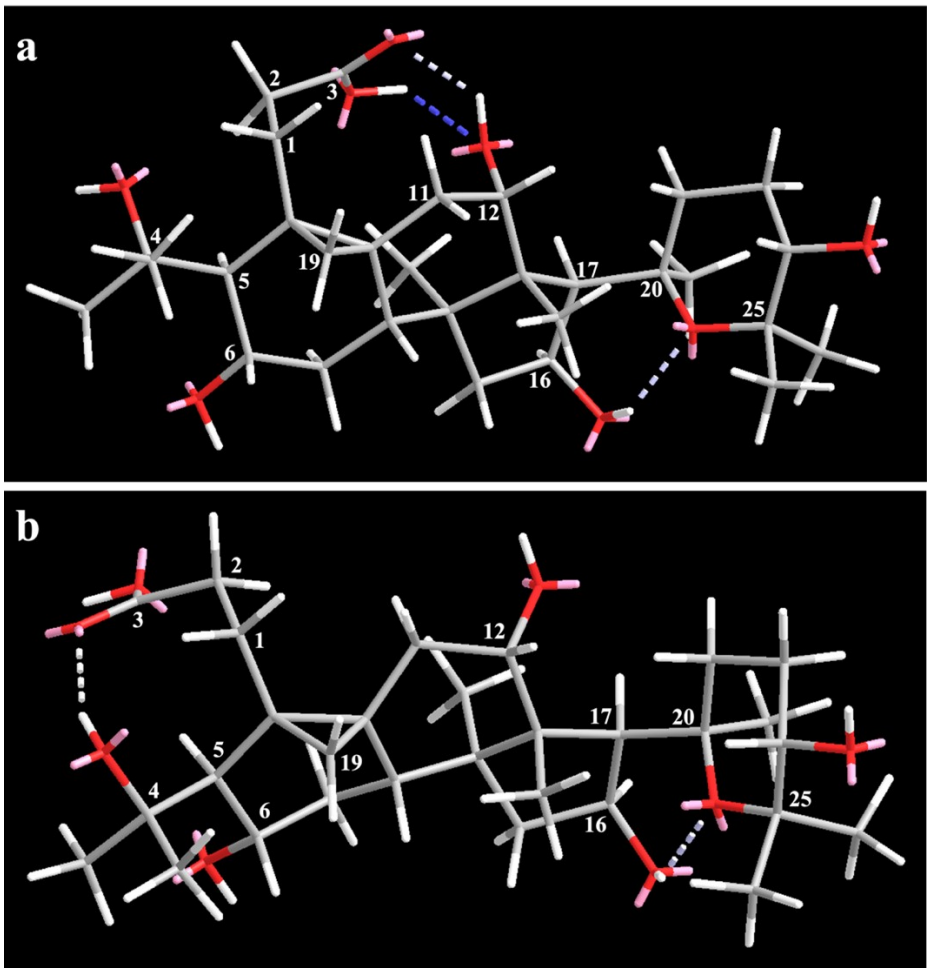

Figure 3.15. MM2 minimized energy conformation of metabolite **28** and possible intramolecular hydrogen bonds. a) Hydrogen bonds between carboxylic acid at C-3 and hydroxy group at C-12 (Minimized energy: 87.9472 kcal/mol); b) Hydrogen bonds between carboxylic acid at C-3 and hydroxy group at C-4 (Minimized energy: 85.6523 kcal/mol).

In the continuation, biotransformation products were screened for their effects on telomerase enzyme activation. Due to the high cost of the TeloTAGGG kit (Unit price: 2000 $), Western Blot analysis was used for the preliminary screening. The effect of metabolites on hTERT protein level was investigated by Western Blot in the dose range of 2 - 1000 nM. As a result, all metabolites were active compared to the DMSO-treated control group. The dose range for TeloTAGGG study was determined as 2-30 nM for metabolites **23** and **24**, while 30-300 nM range was chosen for **1** and **25**. Metabolites **6** and **27-29** were tested in the

10-100 nM dose range. Additionally, the most active doses of cycloastragenol (10 and 100 nM) were preferred as the positive control.

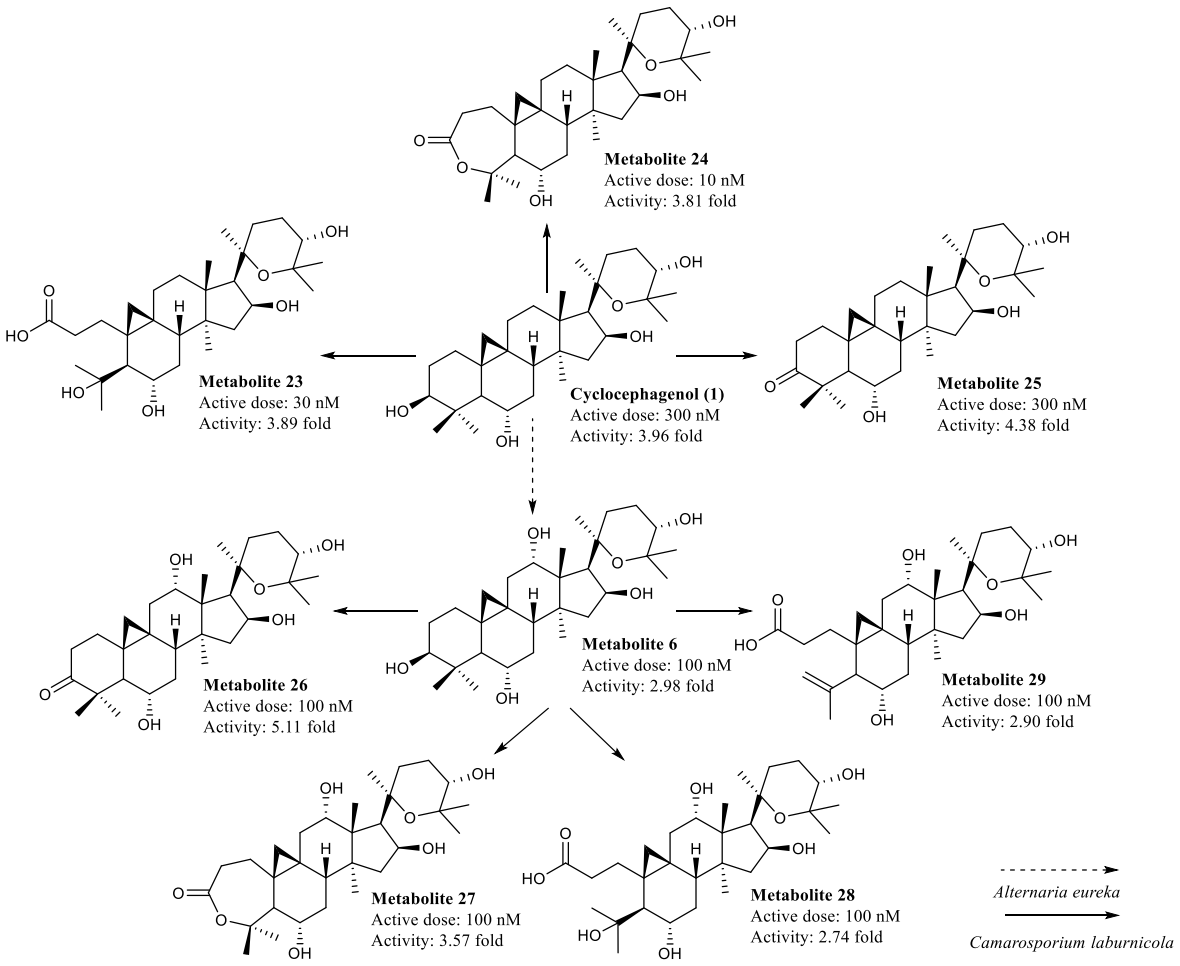

Figure 3.16. Telomerase activity of starting compounds (**1** and metabolite **6**) and their biotransformation products (**23** - **29**) obtained by *C. laburnicola*. Telomerase activation was determined according to the control DMSO. The telomerase activation in the 2-300 nM range was evaluated, and the highest activities were shown accordingly.

According to TeloTAGGG results, all molecules except metabolite **24** showed dose-dependent telomerase activation compared to the control. On the other hand, metabolite **24** showed a dose-dependent increase up to 10 nM and decreased at 30 nM. In addition, the effect of metabolites on hTERT protein level was consistent with TeloTAGGG results.

In the evaluation of the starting compounds (**1** and **6**), cyclocephagenol was found to be more active at a higher dose (3.96-fold at 300 nM). In comparison, metabolite **6** showed lower activity (2.98-fold) at 100 nM than cycloastragenol. The hydroxylation at C-12 caused a decrease in activity compared to our previous studies. When the biotransformation products of **1** were examined, it was determined that metabolites **23** (3.89-fold at 30 nM) and **24** (3.81-fold at 10 nM) showed similar activity with cyclocephagenol at lower doses. Metabolite **25** was found to be 4.38-fold active at 300 nM. In the case of biotransformation products of **6**, metabolites **26** (5.11-fold at 100 nM) and **27** (3.57-fold at 100 nM) showed higher activity than **6**, while metabolites **28** (2.74-fold at 100 nM) resulted in a decrease in activity. Also, metabolite **29** (2.90-fold at 100 nM) displayed similar telomerase activation with **6**.

Metabolites **25** (4.38-fold at 300 nM) and **26** (5.11-fold at 100 nM), possessing a ketone functionality at C-3, are noteworthy because they are the most active derivatives. While hydroxylation at C-12 decreased telomerase activation in metabolite **6** (2.98-fold at 100 nM) compared to **1** (3.96-fold at 300 nM), a more active metabolite was obtained at a lower dose when oxidation in C-3 occurred in **6** (**26**). When examining the 3-oxo derivatives from a chemical point of view, i) the hydrogen bond donor characteristic in C-3 has disappeared and has completely switched to the acceptor position, ii) the polarity has decreased relatively compared to the starting compound, iii) the chair conformation has changed in the A ring, resulting in a boat conformation. Although it is premature to infer a structure-activity relationship with a limited number of compounds, the copresence of oxidation at C-3 and monooxygenation at C-12 seems to be important in increasing telomerase activation.

Metabolites **24** and **27** are formed because of BVMO activity and contain seven-membered lactones in the A ring. Metabolite **24** provided a 3.81-fold telomerase activation at 10 nM, while metabolite **27** exhibited a 3.57-fold activation at a higher dose (100 nM). Contrary to 3-oxo derivatives, the hydroxylation at C-12 causes a decrease in activity in lactone derivatives. Lactone derivatives have similar properties with 3-oxo derivatives: i) a high electron density at the hydrogen bond acceptor position in the A ring, ii) partial boat conformation, iii) slightly more polar character than 3-oxo derivatives.

After lactone ring formation, a lactone hydrolase enzyme catalyzes a further step to yield 3(4)-seco metabolites (metabolites **23**, **28** and **29**). When these three molecules were

tested, it was observed that metabolite **23** showed similar activity to metabolite **1** at lower doses, but metabolites **28** and **29** did not provided an increase in telomerase activation. Metabolites **23** and **28** carrying hydroxy at C-4 showed 3.89-fold activation at 30 nM and 2.74-fold at 100 nM, respectively; metabolite **29** containing C-4(28) double bonds provided a 2.9-fold activation at a concentration of 100 nM. As with lactone derivatives, hydroxylation at C-12 caused a decrease in activity. Considering the general physicochemical properties of 3(4)-seco, its more polar and ionizable nature due to the presence of a carboxylic acid is significant, especially for water solubility and possible electrostatic interactions. The carboxylic acid formed in the A ring (C-3) and the hydroxylation at C-4 forming an electron-rich region might be the key feature for molecular interactions with biological macromolecules (membrane/nuclear receptors and/or proteins) at the cellular level.

Collectively, the tested cyclocephagenol derivatives also demonstrated potent telomerase activation compared to the positive control cycloastragenol (varying between 1.02- and 1.46-fold; Figure 3.16).

CHAPTER 4

OPTIMIZATION OF BIOTRANSFORMATION PROCESSES OF *CAMAROSPORIUM LABURNICOLA*

4.1. Background

Camarosporium laburnicola (Camarosporiaceae) is an endophyte belonging to the Ascomycota phylum and was first isolated from the dried branches of *Laburnum anagyroides* (yellow cluster) tree growing in Rostov region of Russia by Timur S. Bulgakov in 2014. In 2017, the taxonomic classification of this species and the characteristics of the fungus took place in the literature[130]. Since *C. laburnicola* was discovered recently, it has not been the subject of any work other than the taxonomic and phylogenetic studies carried out during its identification as a plant endophyte until today. Our group also isolated this endophytic fungus from *Astragalus angustifolius* plant within the scope of 114Z958-TÜBİTAK project, and the fungus was identified as *C. laburnicola* MFLU 15-1522 by the German Culture Collection (Leibniz Institute DSMZ). For this reason, it was an untouched organism, and the first studies for its potency as a biocatalyst were carried out by our group[48–50].

Within the 114Z958-TÜBİTAK project, we aimed to develop a compound library utilizing endophytic fungi to discover telomerase activators. For this reason, no effort has been made to increase metabolite production and/or to search for alternative methods for higher efficiency and productivity. The yields of these bioactive metabolites remained very low: 32% for E-CG-01, 2.8% for E-CG-03, 0.78% for E-AG-01, 2.12% for E-AG-02 and 1.15% for E-AG-03 (Figure 4.1). *C. laburnicola*, with mostly silent secondary metabolite pathways, providing narrow metabolite diversity as a biocatalyst, and its potential to afford bioactive transformation products, especially towards telomerase activation, were the overriding basis for selecting this fungus for further studies. Another fungus that expresses

similar enzymes that catalyze the formation of lactone on ring A and the subsequent ring opening reactions on the same ring is *Glomeralla fusarioides*. However, in addition to these modifications, hydroxylation at the C-11 position and epoxidation reactions at the C-9(11) position have also been observed in biotransformation studies with *G. fusarioides*.

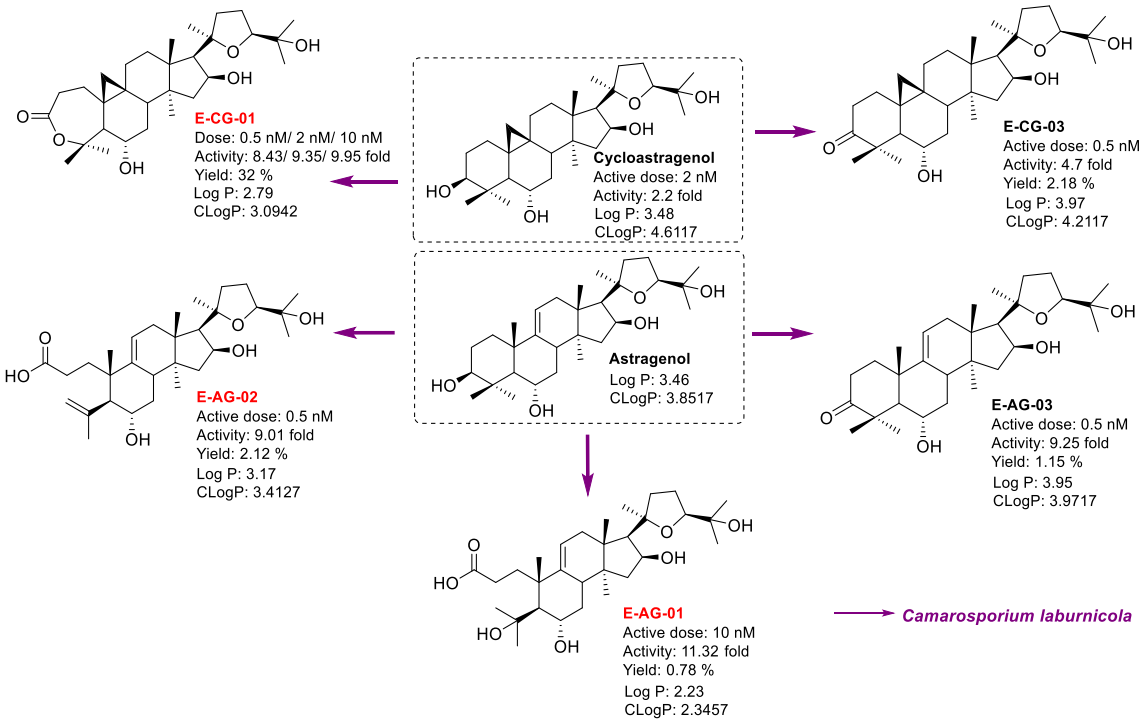

Figure 4.1. Telomerase activator compounds obtained by *C. laburnicol*a within the scope of 114Z958-TÜBİTAK project and their bioactivity results. Telomerase activation was determined according to the control DMSO. The telomerase activation in the 0.5-300 nM range was evaluated, and the highest activities were shown accordingly.

In our preliminary studies, it has been shown that *C. laburnicola* expresses alcohol dehydrogenase, BVMO, and lactone hydrolase enzymes very actively and processes our molecules towards a single pathway affording the production of three or four molecules. As mentioned in Chapter 3, these reactions produce potent telomerase activators, more potent than cycloastragenol. If the production of novel telomerase activators is the major target

involving large-scale studies, *C. laburnicola* is highly advantageous over alternative organisms from an industrial microbiology perspective.

When the potent molecules shown in Figure 4.1 are examined, 3-oxo, 3(4)-lacto and 3(4)-seco structures are more active than cycloastragenol. Although the synthesis of 3-oxo forms of cycloastragenol and astragenol is probable with chemical synthesis, it is not reasonable to obtain these forms in high yield due to the presence of extra secondary alcohol groups at C-6 and C-16 positions affording by-products. These side products decrease the yield and make the purification process difficult, causing additional costs and time loss. Moreover, using additional procedures with more chemicals means moving away from the applications of green chemistry. That reveals the importance of microbial processes.

The bioavailability of cycloastragenol and astragenol are known to be low (~ 5%). To increase the bioavailability of these molecules, ionizable functional groups (e.g., carboxylic acid and/or amino group) are needed to prepare salt forms. At this point, the derivatives E-AG-01 and E-AG-02 containing the carboxylic acid group are important. One of the reasons for preferring 3(4)-seco and 3(4)-lacto forms compared to 3-oxo forms is to increase the bioavailability. In addition, these metabolites obey Lipinski's rule of five. Lipinski's rule of five was derived from analysis of compounds in the World Drug Index database, which aims to identify properties important in making a drug orally active. Although there are exceptions, oral drugs tend to follow Lipinski's rule of five. Relevant factors were found to include numbers that are multiples of five: i) a molecular weight less than 500, ii) no more than 5 hydrogen bond donor groups, iii) no more than 10 hydrogen bond acceptor groups, iv) a calculated log P (clog P) value less than +5 (log P is a measure of a drug's hydrophobicity)[131]. When Figure 4.1. is examined, it is seen that all the metabolites have a molecular weight of approximately 500 and clog P values of less than 5. In addition, we can interpret that the clog P values of 3(4)-seco and 3(4)-lacto derivatives are considerably lower than the starting molecules, and they have a more hydrophilic character than starting compounds (cycloastragenol and astragenol).

Our potent molecules are of great importance for the market of telomerase activators, which have great growth potential in the future. In this regard, one of the most critical steps is completing subsequent R&D work for the large-scale production of potent molecules. Thus, we decided to optimize the microbial biotransformation process with *C. laburnicola* to

produce potent telomerase activators with higher efficiency, aiming: for E-CG-01 32% → 75%; for E-AG-01 0.78% → 50%; for E-AG-02 2.12% → 60%. For this purpose, optimization studies were carried out using the design of experiment strategies for important process parameters by using design of experiment approach.

4.1.1. Whole Cell Biotransformation

Biotransformation is divided into two classes according to the biocatalyst used. Microorganisms, plants, or mammalian cells perform biocatalysis in whole-cell systems, while isolated enzyme systems are used in the enzymatic biotransformation process[132]. The advantages and disadvantages of these processes are summarized in Table 4.1.

Table 4.1. Comparison of whole cell biotransformation and isolated enzymes[60,62].

Whole Cell Biotransformation		**Isolated Enzymes**	
Advantages	**Disadvantages**	**Advantages**	**Disadvantages**
Simple and low costs	Unwanted side reactions	Better reaction control (example: pH) No side reactions	Addition of cofactor or cofactor regeneration system is necessary
Cofactor regeneration employing by cell metabolism	Substrate uptake limitation Energy is required to transport substrate/product across the membrane	No limitation in substrate/product transport	Many enzymes are not commercially available in pure form Purification of enzymes is necessary
No enzyme isolation and purification	Substrate/product inhibition is possible	Higher substrate and product concentration tolerance	Stability problem

Whole-cell systems provide a stable environment for enzymes, and thus they can be used for extended periods. They are also advantageous in regenerating cofactors such as

NAD(P)H and ATP. These systems contain multiple enzymatic pathways; they provide optimum enzyme concentrations and energy levels, minimize activity loss, and allow multi-step transformations. They also offer a less costly process by eliminating the need to isolate and purify enzymes. Because of these advantages, whole-cell systems are preferred more than enzymatic systems in industrial processes[57,133,134].

Whole-cell biotransformation processes have been successfully applied to commercialize pharmaceuticals and pharmaceutical intermediates. Industrial applications of whole cell biotransformation include the production of hydrocortisone by using *Curvularia* sp. (applied by Schering AG, in 2006 acquired by Merck, Germany), pravastatin by using *Mucor hiemalis* (Daiichi Sankyo Inc., USA, and Bristol-Myers Squibb, USA), and 11α-hydroxyprogesterone using *Rhizopus* sp. (developed in the 1950s by Pharmacia & Upjohn later acquired by Pfizer Inc., USA) where mainly P450 monooxygenases are involved (Figure 4.2)[135]. Some other examples of all cell biotransformation processes used by the pharmaceutical industry are shown in Table 4.2.

Apart from the advantages of whole-cell systems and biotransformation studies, there are also disadvantages, such as by-product formation, complicated downstream processes, and low substrate conversion[62,132,136]. These challenges must be overcome to transition to industrial production with whole-cell systems[137]. At this point, although genetic engineering approaches offer a way out, recombinant organisms cannot be used much in industrial applications due to problems such as the long and challenging development processes of recombination, low productivity, and stabilization problems experienced on an industrial scale[42,138]. At this point, it should be considered that optimizing biotransformation processes is less costly than developing recombinant microorganisms.

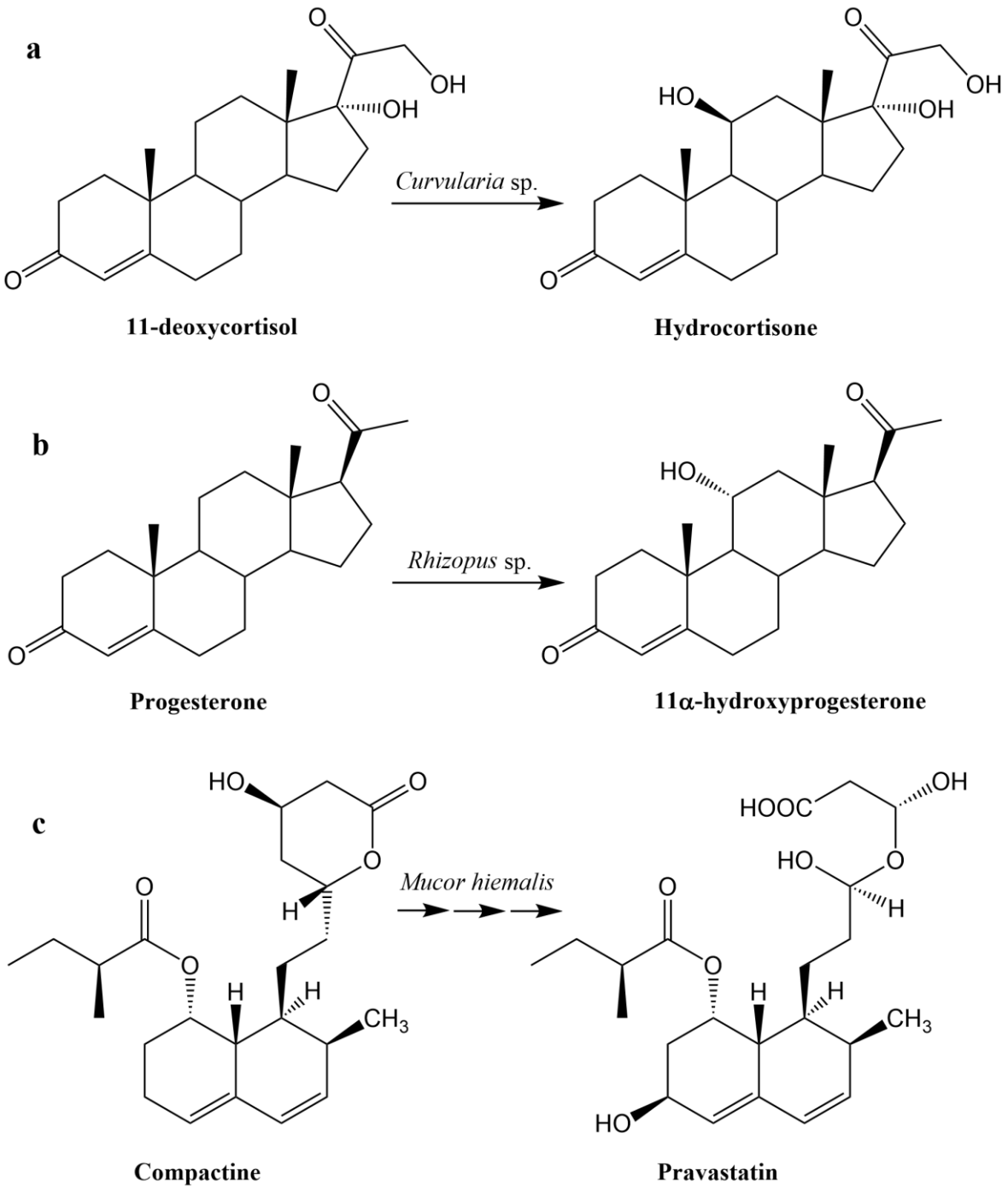

Figure 4.2. Examples of industrial application of whole cell biotransformation: a) 11β-hydroxylation of 11-deoxycortisol to hydrocortisone, b) hydroxylation of progesterone to 11α-hydroxyprogesteron; c) production of pravastatin by hydroxylation of compactin.

Table 4.2. Industrial applications of whole cell biotransformation for the preparation of pharmaceuticals and pharmaceutical intermediates[62,133].

Biotransformation Product → Final Product	**Indication**	**Reaction Type/Enzymes**	**Microorganism**
11 α-Hydroxyprogesterone → Cortisone	Anti-inflammation	Hydroxylation	*Rhizopus arrhius*
β-Hydroxyisobutyric acid → Captopril	Treatment for hypertension	Hydroxylation	*Candida rugosa*
β-Hydroxy-n-butyric acid → Carbapenem	Antibacterial	Hydroxylation	*Candida rugosa*
5-Methylpyrazine-2-carboxylic acid → Acipimox	Anti-lipolytic	Oxidation	*Pseudomonas putida*
5-Methylpyrazine-2-carboxylic acid → Glipicide	Anti-diabetic	Oxidation	*Pseudomonas putida*
Pyridyl-3-acetic acid → Risedronate	Treatment for osteoporosis	Oxidation	*Pseudomonas oleovorans*
(4S,6S)-Hydroxy-sulfone → Trusopt	Treatment for glaucoma	Reduction	*Neurospora crassa*
(R)-Ethyl-4,4-4-trifluoro-3-hydroxybutanoate → Belfoxatone	Anti-depressant	Reduction	Recombinant *E.coli*
D-4-Hydroxyphenyl glycine → Ampicillin/amoxycillin	Antibacterial	Hydrolysis	*Bacillus brevis*

(cont. on next page)

Table 4.2. cont.

Biotransformation Product → Final Product	**Indication**	**Reaction Type/Enzymes**	**Microorganism**
Phenylacetylcarbinol → Ephedrine	Treatment for asthma	Lyase	*Saccharomyces cerevisiae*
D-Aspartic acid → Apoxycillin	Antibacterial	Decarboxylation	*Pseudomonas dacunhae*
3,4-Dihydroxy-L-phenylalanind → L-DOPA	Treatment of Parkinsonism	Lyase (Tyrosine phenol lyase)	*Erwinia herbicola*
CDP-choline	Treatment of negative symptoms of schizophrenia	Multi-step under ATP generation	*Corynebacterium ammoniagenes*
Glutathione	Support the immune system	γ-Glutamylcysteine synthetase, glutathione synthetase	Recombinant *E. coli*
(S)-2,2-Dimethyl-cyclopro-panecarbox-amide → Cilastatin	Dehydropeptide inhibitor	Hydrolysis	*Comononas acidivoran*s and recombinant *E. coli*
D-Carnitine → L-Carnitine	Thyroid inhibitor	Multi-enzymatic pathway	*Agrobacterium* sp.
Nicotinamide	Treatment of pellagra	Hydrolysis/ Nitrile hydratase	*Rhodococcus rhodochrous*
(S)-Pipecolic acid → Incel	Anticancer	Hydrolysis	*Pseudomonas fluorescens*
CBZ-D-proline → Eletriptan	Treatment of migraine	Hydrolysis	*Arthrobacter* sp.

4.1.2. Optimization Strategies for Whole-Cell Biotransformation

Optimizing microbial biotransformation processes is of great importance in transferring studies from laboratory to industrial scale. Various factors affect microbial processes, including the composition of media components, pH, and temperature[139]. Two approaches are generally used in optimizing these processes, one factor at a time (OFAT) and design of experiment. In the OFAT approach, the limits of one variable are changed while the other variables are kept constant. This method requires a lot of workloads, takes time, and allows one-dimensional analysis, and it cannot generally guarantee that the optimum point has been determined[140,141].

As testing all possibilities is not practical, the OFAT approach may not be sufficient for microbial processes with many parameters. In addition to needing a lot of experimentation, optimum points can only be determined if the limits are chosen correctly. Since second and higher-order models can be developed, statistical experimental design approaches allow the optimum points to be determined accurately[142,143].

Plackett Burman Design (PBD) is a method used to eliminate parameters that are not effective in production reliably and practically without the need for many experiments[144]. PBD is very useful when the effects of many variables are studied, but only some of these variables are effective. This method allows us to determine the effects of n variables on the process by performing n+1 trials with a two-level fractional factorial design. Although this method ignores the interaction between parameters, it allows the reliable selection of a small number of effective parameters from many variables. PBD generally results in three or four significant factors. After that, significant factors are brought into the response surface methodology (RSM) for further optimization[140,143,145].

RSM is a combination of mathematical and statistical techniques used to develop new processes or optimize existing processes to reveal the interaction between parameters and the dual or individual effects of parameters on the process with a second or higher-order equation[146]. The application of RSM generally reduces the cost of expensive analysis methods and increases production yields. RSM is an effective tool applied in the optimization of medium compositions, conditions of enzymatic hydrolysis, and fermentation

processess[147]. The most common experimental designs using RSM are Central Composite Design (CCD) and Box-Behnken Design (BBD).

CCD is the most widespread method used to develop a quadratic model among RSM approaches. CCD consists of a factorial design (±1), an axial design in which experimental points are at a distance from its center (±α), and a central point (0). The axial point (α) and the number of trials at the center point increase the number of levels and give the experimental design flexibility. In addition, CCD allows one to know what effect the factors had on the response if one goes beyond or below the chosen levels of factors. The axial point and the number of trials at the center of the domain influence the accuracy of the estimation[148–151].

Design of experiment approaches have been used in microbial biotransformation studies, and some examples are summarized in Table 4.4. In these studies, a combination of PBD and CCD has been successfully applied to increase production yields by optimizing parameters.

Table 4.3. Case studies using design of experiment methodologies for optimization of biotransformation

Substrate	Product	Microorganism and Production Type	Screening Methodology and Parameters	Optimization Methodology and Parameters	Results	Ref.
R-(+)-limonene	R-(+)-α-terpinol	*Sphingobium* sp. Whole cell biotransformation in shake flask	PBD, Parameters: pH, biomass concentration, limonene concentration, temperature, agitation	CCD, Parameters: pH, limonene concentration, agitation	240 g/L limonene Fold increase: 2 times the highest concentration reported so far	Molina et al. (2019)[140]
β-aminopro-pionitrile	β-alanine	*Rhodococcus* sp. G20 Resting cell biotransformation in bioreactor	-	CCD Parameters: cells loading, substrate concentration, air flow rate	6.45 g/(Lh) β-alanine Fold increase: 40.6% increase in productivity	Liang et al. (2008)[147]
Root of *Dioscorea zingibenensis* C. H. Wright (DCW)	Diosgenin	*Fusarium* sp. CPCC 400226 Whole cell biotransformation in shake flask	PBD Parameters: glass bead addition, antifoam addition, surfactant addition, working volume, agitation, temperature, fermentation period, pH, inoculum size	CCD Parameters: temperature, fermentation period, antifoam addition	2.24% diosgenin Fold increase: 40.6% increase in productivity	Liu et al. (2021)[143]
Betulin	Betulinic acid	*Armillaria luteo-virens* Sacc. ZJUQH100-6 Whole cell biotransformation in shake flask	FFD Parameters: glucose concentration, pH, Tween 80, betulin concentration, stage of inoculation	CCD Parameters: Tween 80, botulin concentration	9.32% betulin Fold increase: 74.53% in comparison with non-optimized conditions	Liu et al. (2020)[152]
PBD: Plackett Burman Design, CCD: Central Composite Design, FFD: Fractional Factorial Design, OFAT: One Factor at a Time, BBD: Box Behnken Design						

(Cont. on next page)

Table 4.3. cont.

Substrate	Product	Microorganism and Production Type	Screening Methodology and Parameters	Optimization Methodology and Parameters	Results	Ref.
Phytosterol	Andro-stenedione	Mutant *Mycobacterium neoaurum* ZJUVN-08 Whole cell biotransformation in shake flask	FFD Parameters: inducer concentration, pH, substrate concentration, incubation time, molar ratio of hydroxypropyl-β-cyclodextrin/phytosterol	CCD Parameters: molar ratio of hydroxypropyl-β-cyclodextrin/phytosterol, substrate concentration	5.96 g/L androstenedione 94.69% conversion rate Fold increase: the maximum yield was nearly same with non-optimized (5.99 g/L), while phytosterol conversion rate increased by 10.66% compared to non-optimized.	Zhang et al. (2013)[146]
Agricultural lignocellulo-sic by-products	Biovanillin	*Enterobacter hormaechei* Solid state biotransformation in flask	OFAT Parameters: sugarcane baggase, wheat straw, rice straw, rice bran, corn cob	CCD Parameters: moisture content, inoculum size, pH, temperature, incubation time	0.476 g/100 g biovanillin Fold increase: 16.4-fold in comparison with non-optimized conditions	Mehmood et al. (2022)[153]
Glycyrrhizin	Monoglu-curonyl glycyrrheti nic acid	*Aspergillus niger* Whole cell biotransformation in shake flask	PBD Parameters: pH, temperature, glycyrrhizin concentration, inoculum size, peptone, $NaNO_3$, K_2HPO_4, $MgSO_4.7H_2O$, $FeSO_4$, cultivation time	BBD Parameters: $MgSO_4.7H_2O$, cultivation time, glycyrrhizin concentration	35.72% monoglucuronyl glycyrrhetinic acid Fold increase: not reported	Quan et al. (2015)[154]
(-)-cubebin	(-)-hinokinin	*Absidia coerulea* 3A9 Whole cell biotransformation in shake flask	PBD Parameters: $NaNO_3$, temperature, pH, seawater concentration, sucrose concentration	-	27.6% (-)-hinokinin Fold increase: not reported	de Souza et al. (2021)[155]
PBD: Plackett Burman Design, CCD: Central Composite Design, FFD: Fractional Factorial Design, OFAT: One Factor at a Time, BBD: Box Behnken Design						

(Cont. on next page)

Table 4.3. cont.

Substrate	Product	Microorganism and Production Type	Screening Methodology and Parameters	Optimization Methodology and Parameters	Results	Ref.
Caffeine	Theobro-mide	*Pseudomonas* sp. Resting cell biotransformation in shake flask	-	CCD Parameters: caffeine concentration, initial cell loading, pH OFAT used for furher optimization Parameters: effect of divalent metal ions, reaction temperature	1 g/L theobromide Fold increase: not reported	Retnadhas and Gummadi (2014)[156]
Limonene	Limonene-1,2-diol	*Colletotrichum nymphaeae* CBMA1 0864 Whole cell biotransformation in shake flask and bioreactor	-	CCD for shake flask Parameters: agitation, temperature, pH, inoculum concentration OFAT for bioreactor Parameters: agitation, air flow rate, type of substrate [R-(+)-limonene, S-(-)-limonene, citrus terpene]	Shake flask: 6.75 g/L limonene-1,2-diol Bioreactor: 7.11 g/L limonene-1,2-diol Volumetric productivity of bioreactor (98.78 mg/L.h) was higher than shake flask (35.16 mg/L.h). Fold increase: 1.69-fold increase in comparison with previous study[159]	Sales et al. (2019)[157]
Arabinose	L-arabitol	*Candida parapsilosis* Whole cell biotransformation in shake flask	PBD Parameters: Arabinose concentration, yeast extract, malt extract, $(NH_4)_2SO_4$, KH_2PO_4, temperature, rotation speed	CCD Parameters: rotation speed, temperature, arabinose concentration	14.3 g/L L-arabitol Fold increase: not reported	Kordowska-Wiater et al. (2013)[158]

PBD: Plackett Burman Design, CCD: Central Composite Design, FFD: Fractional Factorial Design, OFAT: One Factor at a Time, BBD: Box Behnken Design

4.2. Materials and Methods

4.2.1. Determination of Growth Curve for *Camarosporium laburnicola*

The isolate stocked on Potato Dextrose Agar (PDA, Merck, 1.10130.0500) at 4 °C was transferred to fresh PDA medium and incubated at 25 °C for ten days. Afterward, Tween 80 solution (0.1%) was added to petri dishes, and the spore solution was obtained by scraping it with an inoculation loop. After that, this solution was thoroughly mixed with a vortex. Erlenmeyer flasks (250 mL) containing 50 mL of Potato Dextrose Broth (PDB, HKM Culture Media, 021053) were prepared for dry weight determination. The spore suspension was inoculated at the medium's 2% (v/v). Each day, nutrient media of three Erlenmeyer flasks were filtered through the Buchner funnel. The cells remaining on the filter paper were dried at 50 °C until measuring a stable weight. The growth curve graph was obtained by changing the dry weight over time.

4.2.2. Optimization Studies

Stock cultures stored at 4 °C in an agar slant were transferred to the fresh PDA medium and incubated at 25 °C for 10 days. Following incubation, *C. laburnicola* was prepared for biotransformation studies according to the experimental set presented by Design Expert 12. Tween 80 solution was added to petri dishes and spore solution was obtained by scraping with an inoculation loop. Then, the spore solution was inoculated into the pH-adjusted PDB medium. Substrates, cycloastragenol (CG) and astragenol (AG) (Figure 4.3), were prepared in DMSO at concentrations of 10, 20 and 30 mg/mL. After inoculation, the substrate was dosed at 1% (v/v) of the medium in the determined substrate feeding time, and production continued under submerged culture.

The mycelium was removed from the nutrient medium for the biotransformation termination. The broth was extracted three times with EtOAc. The organic phase was evaporated using a rotary evaporator. Then, extracts were dissolved in tert-BuOH:H_2O (65:35), frozen at -80 °C, and lyophilized at -55 °C under vacuum.

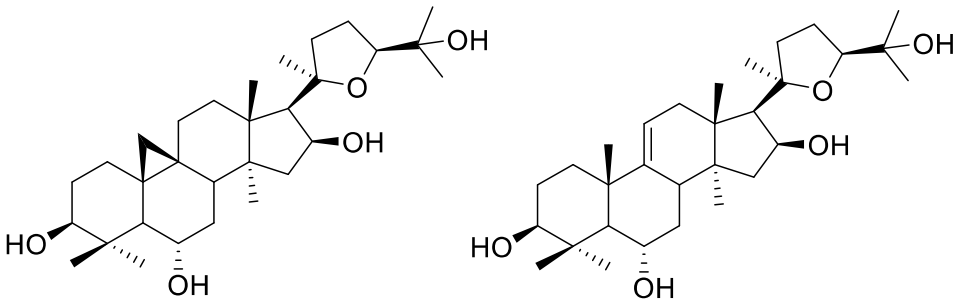

Figure 4.3. Structures of starting compounds.

4.2.2.1. Screening of Parameters by Plackett Burman Design

Plackett Burman Design (PBD) was used to screen all parameters that would affect the biotransformation study. The design was established with Design Expert 12 program for scanning nine parameters and two extra parameters (for overlooked parameters). A total of 15 experimental sets were formed. Each set was carried out in triplicate. The upper (+1), lower (-1), and center (0) values of the parameters were determined by considering our preliminary studies (Table 4.4). The target products (E-AG-01, E-AG-02 and E-CG-01) were followed qualitatively by using Thin Layer Chromatography (TLC) and quantitatively by High Performance Liquid Chromatography-Diode Array Detector (HPLC-DAD) method.

Table 4.4. Lower and upper values of factors that may affect biotransformation yield.

	Factor	**-1**	**0**	**+1**
1	Substrate feeding time (days)	3	4	5
2	Biotransformation time (days)	3	6	0
3	Temperature (°C)	20	25	30
4	pH	4.6	5.6	6.6
5	Working volume (mL)	30	50	70
6	Shaking speed (rpm)	150	180	210
7	The amount of inoculant (v/v %)	2	11	20
8	Substrate concentration (w/v %)	0.01	0.02	0.03
9	The amount of Tween 80 (v/v %)	0	0.1	0.2

4.2.2.2. Optimization of Parameters by Central Composite Design

Central Composite Design (CCD) is a method that allows parameters to be tested volumetrically (in a 3D plane) at five levels: center, extreme (low-high), and factorial (low-high). CCD allows one to decide whether the model is statistically significant by comparing the errors calculated at the center points and the differences between the other points. Thus, it determines whether the model can be used for prediction.

CCD was used for optimization studies, and experiment sets were designed on three parameters determined in PBD experiment sets. The biotransformation time, temperature and shaking speed parameters were entered into the program matrix with their lower and upper limits (Table 4.5). Constant parameters and their values are given in Table 4.6. Each set was carried out in triplicate. The target products (E-AG-01, E-AG-02 and E-CG-01) were followed by TLC and HPLC-DAD methods.

Table 4.5. Experimental values and coded levels of the independent variables used for the Central Composite Design.

Factor		**-1.68179**	**-1**	**0**	**+1**	**+1.68179**
1	Biotransformation time (day)	0.954622	3	6	9	11.0454
2	Temperature (°C)	16.591	20	25	30	33.409
3	Shaking speed (rpm)	129.546	150	180	210	230.454

Table 4.6. Parameters and their values kept constant in CCD experiment sets.

Factor	Value
Substrate feeding time (day)	3
pH	5.6
Working volume (mL)	50
Inoculant concentration (v/v %)	10
Substrate concentration (w/v %)	0.02
Tween 80 concentration (v/v %)	0.1

4.2.2.3. One Factor at a Time Studies

Because target yields cannot be achieved, additional experiments were planned to increase production yield. OFAT experiments were carried out by changing one of the parameters thought to be effective on biotransformation and keeping the others constant. The parameters altered in these trials were the biotransformation time and the incubation time of the fungus in PDA medium.

Time course study (biotransformation time): The working volume/total volume ratio (1:5) was kept constant, and a 1 L shake flask was used in this study. Optimum process conditions determined in the CCD model were applied (E-AG-01: 22 °C, 180 rpm; E-AG-02: 22 °C, 180 rpm, E-CG-01: 20 °C, 210 rpm). Each set was carried out in triplicate. Ten mL samples were taken every day for ten days.

The incubation time of fungus in PDA: Stock cultures stored at 4 °C were transferred to the fresh PDA medium and incubated at 25 °C for 6, 7, 8, 11 and 15 days. Petri dishes belonging to 5 different incubation times in PDA were inoculated into 1 L shake flasks containing 200 mL PDB medium. Biotransformation studies were carried out at 22 °C, at 180 rpm shaking speed for seven days. Each set was carried out in triplicate. Ten mL samples were taken every day for ten days.

4.2.3. Biotransformation Studies: 1 L Bioreactor

The Sartorius Biostat Q Plus stirred tank bioreactor system (Figure 4.4) in the IZTECH-BIYOMER Fermentation Technologies Laboratory was used for the scale-up studies. Refrigerated circulator systems (Polyscience, BS-SHK4450CH-1CE) were used to cool the bioreactor jackets.

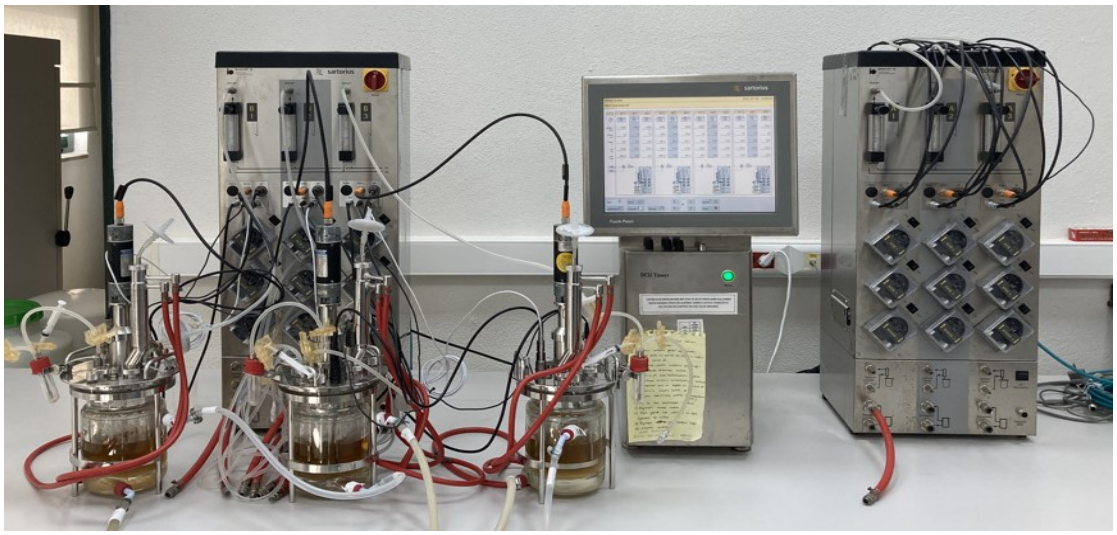

Figure 4.4. Sartorius Biostat Q Plus stirred tank bioreactor system

For sterilization, PDB medium was transferred into the bioreactor. The oxygen, pH and antifoam probes were attached. The inputs of the sampling unit, acid (1 N HCl, Isolab), base (1 N NaOH, AFG Scientific), and antifoam (10%, Silicone Antifoam, Sigma) flasks to the reactor were set up by silicone hoses. 0.22 µm PTFE filters (Sartorius and Sigma) were used at the exhaust outlet, aeration inlet, and outlets of acid and base bottles. Before sterilization, clamps were attached to all hoses except the exhaust outlet. The prepared system was autoclaved at 121 °C for 20 min.

The sterilized bioreactor system was connected to the control unit, and the system was left to cool. After the system cooled down to 30 °C, the jacket was connected to the

refrigerated circulator. The conditions determined by the optimization studies were applied to the bioreactor. The control unit was used to control and monitor the temperature, pH, aeration, and pO_2. A 10% spore suspension was inoculated. The substrate was prepared in DMSO (20 mg/mL) and dosed at 1% of the working volume after 72 h incubation. The dimensions and configurations of the bioreactors are presented in Table 4.7. In bioreactor studies, three different experiments were set up. In these experimental sets, the effects of aeration and pH (Table 4.8), the presence of microparticles (Table 4.9), and agitation speed (Table 4.10) on biotransformation efficiency were evaluated. Approximately 10 mL samples were taken from the bioreactor each day after substrate feeding. The sample was extracted three times with ethyl acetate (EtOAc). The EtOAc extracts were evaporated in a rotary evaporator and were prepared for HPLC analysis.

Table 4.7. Dimensions and configurations of the bioreactors

Dimensions and configurations	**1 L (Working volume: 600 mL)**	**1 L (Working volume: 750 mL)**
Number of impellers	2	2
Number of blades in each impeller	6	6
Number of baffles	4	4
D_t (cm)	14	14
D_{int} (cm)	11	11
D_i (cm)	4.5	4.5
D_s (cm)	4	4
Distance between two impellers	1	1.5
H_t (cm)	17	17
H_l (cm)	6.2	8
H_i (cm)	2.5	2.5
H_s (cm)	1	1
H_b (cm)	11	11
W_b (cm)	1	1
W_i (cm)	1	1

D_t, the diameter of the tank, D_{int}, the inner diameter of the tank, D_i, diameter of the blade, D_s, the diameter of the ring sparger, H_t, length of the tank, H_i, the distance between the impeller at the bottom and the bottom of the tank, H_l, height of the liquid, H_s, the length of the sparger to the bottom of the tank, H_b, height of the baffle, W_b, width of the baffle, W_i, width of the blade.

Table 4.8. Conditions used to evaluate effects of aeration and pH on biotransformation efficiency

Parameter	**Bioreactor A1**	**Bioreactor A2**	**Bioreactor A3**	**Bioreactor A4**
Temperature	20 °C	20 °C	20 °C	20 °C
pH	Controlled, pH was kept constant at 5.6.	No control, pH change was monitored.	Controlled, pH was kept constant at 5.6.	No control, pH change was monitored.
Working Volume	750 mL	600 mL	600 mL	600 mL
Aeration rate	1 vvm	-	-	1 vvm
Agitation speed	210 rpm	210 rpm	210 rpm	210 rpm

Table 4.9. Conditions used to evaluate the effect of microparticles on biotransformation efficiency

Parameter	**Bioreactor B1**	**Bioreactor B2**	**Bioreactor B3**
Temperature	20 °C	20 °C	20 °C
pH	No control, pH change was monitored.	No control, pH change was monitored.	No control, pH change was monitored.
Working Volume	600 mL	600 mL	600 mL
Aeration rate	1 vvm	1 vvm	1 vvm
Agitation speed	210 rpm	210 rpm	210 rpm
Microparticle concentration	-	1% Talcum	2.5% Talcum

Table 4.10. Conditions used to evaluate the effect of agitation speed on biotransformation efficiency

Parameter	**Bioreactor C1**	**Bioreactor C2**	**Bioreactor C3**
Temperature	20 °C	20 °C	20 °C
pH	No control, pH change was monitored.	No control, pH change was monitored.	No control, pH change was monitored.
Working Volume	600 mL	600 mL	600 mL
Aeration rate	1 vvm	1 vvm	1 vvm
Agitation speed	210 rpm	400 rpm	800 rpm
Microparticle concentration	2.5% Talcum	2.5% Talcum	2.5% Talcum

4.2.4. Biotransformation Studies: 5 L Shake Flasks

Stock cultures stored at 4 °C in an agar slant were transferred to the fresh PDA medium and incubated at 25 °C for ten days. Following incubation, 0.1% Tween 80 was added to the fungi grown in the PDA, and the spore solution was obtained by scraping the spores with an inoculation loop. The spore suspension was inoculated into the PDB medium. CG and AG were prepared in DMSO at 40 mg/mL concentrations. After inoculation, the substrate was dosed at 0.5% (v/v) of the medium after 72 h, and production continued under submerged culture. The conditions used in the shake flask experiment are given in Tables 4.11 and 4.12. Each set was carried out in triplicate. Ten mL samples were taken from the shake flasks each day after substrate feeding.

Figure 4.5. 5 L shake flasks used in microbial biotransformation studies.

Table 4.11. Conditions used in 5 L shake flasks studies.

Parameter	Flask A1	Flask A2	Flask A3	Flask A4
Working Volume	1000 mL	1000 mL	1000 mL	2000 mL
Inoculation	2% (v/v %)	5% (v/v %)	10% (v/v %)	2% (v/v %)
Temperature	CG: 20 °C AG: 22 °C	CG: 20 °C AG: 22 °C	CG: 20 °C AG: 22 °C	CG: 20 °C AG: 22 °C
Shaking Speed	CG: 210 rpm AG: 180 rpm	CG: 210 rpm AG: 180 rpm	CG: 210 rpm AG: 180 rpm	CG: 210 rpm AG: 180 rpm

Table 4.12. Conditions used in further studies to increase E-AG-02 concentration.

Parameter	Flask B1	Flask B2	Flask B3	Flask B4	Flask B5
Substrate feeding	Control, 5 mL AG on Day 0	5 mL AG and 10 mL of 2X PDB on Day 0	2 mL AG at Day 0, 1.5 mL at Day 1, 1.5 mL on Day 2	5 mL AG at Day 0, 1 mM cyclohexanone on Day 3	Production was terminated on Day 4, the broth was extracted, and EtOAc extract was fed into a fresh medium containing *C. laburnicola*.
Working volume: 1 L, inoculation: 2 %, temperature: 22 °C, working volume: 180 rpm, AG stock solution: 40 mg/mL in DMSO					

4.2.5. Biotransformation Studies: 7.7 L Bioreactor

A bioreactor system (manufactured by FEYAS in Kemalpaşa, İzmir, Turkey) was used for the scale-up studies (Figure 4.6). It was made of 316 L stainless steel. Refrigerated circulator systems (Polyscience, BS-SHK4450CH-1CE) were used to cool the bioreactor jacket. An air pump (BOYU, four output, 12W, 15L/min) was used to aerate the bioreactor.

For sterilization, PDB medium (5 L) was transferred into the bioreactor. The thermocouple was attached. The input of the sampling unit was set up with silicone hoses. 0.22 µm PTFE filters (Sartorius) were used at the exhaust outlet and aeration inlet. Before sterilization, clamps were attached to all hoses except the exhaust outlet. The prepared system was autoclaved at 121 °C for 20 min (Figure 4.7).

The sterilized bioreactor system was connected to the air pump, temperature monitor, and refrigerated circulator, and the system was left to cool. The optimized conditions (determined from 5 L and 250 mL shake flask studies) were applied to the bioreactor. A 2% spore suspension was inoculated to the bioreactor for CG. The substrate was prepared in DMSO or ethanol (EtOH) (40 mg/mL) and dosed at 0.5% of the working volume after 72 h incubation. The dimensions and configurations of the bioreactors used in these studies are presented in Table 4.13.

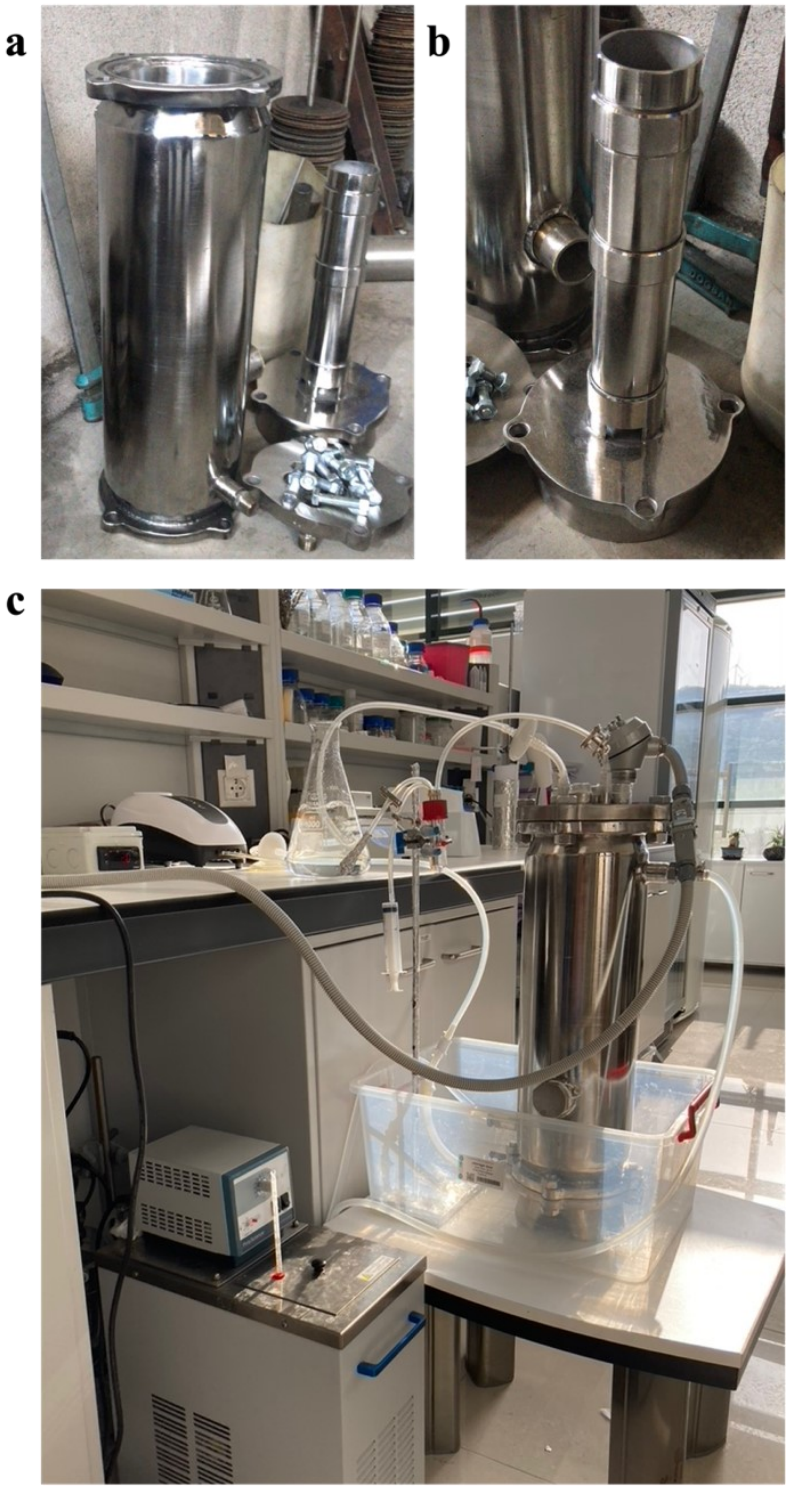

Figure 4.6. Bioreactor system (7.7 L).

Figure 4.7. Bioreactor ready for sterilization in the autoclave.

Table 4.13. Dimensions and configurations of the large-scale bioreactor.

Dimensions and configurations	**7.7 L (Working volume: 5 L)**
D_t (cm)	18
D_{int} (cm)	14
D_s (cm)	5.5
H_t (cm)	50
H_l (cm)	36
H_s (cm)	4
D_i (cm)	5
H_i (cm)	31

D_t, the diameter of the tank, D_{int}, the inner diameter of the tank, D_s, the diameter of the sparger, H_t, length of the tank, H_l, height of the liquid, H_s, the length of the sparger to the bottom of the tank, D_i, the diameter of the inner tube, H_i, the length of the inner tube.

In bioreactor studies, three different experiments were set up. In these experimental sets, the leak tightness of the system, contamination, proper aeration and mixing, growth of microorganisms, pH, and effective use of the substrate were evaluated. The conditions applied in the large-scale bioreactor studies are given in Table 4.14.

Approximately 10 mL samples were taken from the bioreactor each day after substrate feeding. The pH of the broth was measured, and values were recorded.

Table 4.14. Conditions used in large-scale bioreactor experiments

	Bioreactor D1	**Bioreactor D2**	**Bioreactor D3**
Temperature	20 °C	20 °C	20 °C
pH	No control, pH change was monitored.	No control, pH change was monitored.	No control, pH change was monitored.
Working Volume	5 L	5 L	5 L
Inner Tube	Used	Used	Not used
Aeration rate	1.9 L/min	1.9 L/min	1.9 L/min
Substrate	-	25 mL CG (40 mg/mL in DMSO)	25 mL CG (40 mg/mL in EtOH)

4.2.6. HPLC Analysis and Sample Preparation

Agilent Technologies 1200 Series was used for HPLC analysis. The device consists of a quadruple pump, automatic sample injection section, column furnace and diode array detector (DAD) equipment.

The conditions used for the analysis of the PBD experiment set were as follows:

Flow Rate: 1 mL/min

Column: Phenomenex-Kinetex 2.6u C18 100A 100x2.6mm ID

Guard column: SecurityGuard^{TM} ULTRA Cartridge UHPLC C18 4.6mm

Temperature: 25 °C

UV wavelength: 200, 205, 210, 215, 254, 360 nm

Injection volume: 20 µL

Solvents: A) Ultrapure Water (UPW) (0.1% Acetic Acid); B) Acetonitrile (ACN) (0.1% Acetic Acid); C) Methanol (MeOH).

Table 4.15. HPLC method used for the PBD experiment set.

Retention Time (min)	%A	%B	%C
0.0	50	50	0
2.0	50	50	0
7.0	10	90	0
9.0	10	90	0
9.01	0	0	100
12	0	0	100
12.01	50	50	0
18	50	50	0

The conditions used for the analysis of the CCD experiment set were as follows:

Flow Rate: 1 mL/min

Column: Phenomenex-Kinetex 2.6u C18 100A 100x2.6mm ID

Guard column: -

Temperature: 25 °C

UV wavelength: 200, 205, 210, 215, 254, 360 nm

Injection volume: 10 μL

Solvents: A) Ultrapure Water (UPW) (0.1% Acetic Acid); B) Acetonitrile (ACN) (0.1% Acetic Acid); C) Methanol (MeOH).

Table 4.16. HPLC method used for the CCD experiment set.

Retention Time (min)	%A	%B	%C
0.0	70	30	0
2.0	70	30	0
8.0	20	80	0
10.0	20	80	0
10.01	0	0	100
13	0	0	100
13.01	70	30	0
19	70	30	0

The conditions used for the analysis of the further experiments were as follows:

Flow Rate: 1 mL/min

Column: Phenomenex-Kinetex 2.6u C18 100A 100x2.6mm ID

Guard column: SecurityGuard^{TM} ULTRA Cartridge UHPLC C18 4.6mm

Temperature: 25 °C

UV wavelength: 200, 205, 210, 215, 254, 360 nm

Injection volume: 10 µL

Solvents: A) Ultrapure Water (UPW) (0.1% Acetic Acid); B) Acetonitrile (ACN) (0.1% Acetic Acid); C) Methanol (MeOH).

Table 4.17. HPLC method used for further analysis.

Retention Time (min)	%A	%B	%C
0.0	70	30	0
2.0	70	30	0
8.0	20	80	0
10.0	20	80	0
10.01	0	0	100
13	0	0	100
13.01	70	30	0
19	70	30	0

Sample Preparation:

Standard curves were generated for reference materials CG, E-CG-01, AG, E-AG-01 and E-AG-02 to evaluate the experimental results quantitatively. At this stage, 3-repetitive analyses were performed for seven concentrations selected between 1250 ppm and 25 ppm of the reference material and calibration curves were drawn.

The biotransformation extracts were prepared at a final concentration of 5000 ppm in MeOH and filtered using a 0.45 µm PTFE filter.

The amount of target metabolites (mg/L) was calculated, and the effect of the factors was evaluated according to these results.

4.2.7. Thin Layer Chromatography

In addition to analytical HPLC, thin layer chromatography was also used to monitor metabolite production. Twenty percent H_2SO_4 was sprayed on the plate developed in the mobile phase and the plate was heated at 110 °C for 2 min to visualize the spots of metabolites.

4.3. Results

4.3.1. Growth Curve of *Camarosporium laburnicola*

In order to determine the lower and upper limits of the substrate feeding time and biotransformation time, a growth curve was generated for *C. laburnicola* based on dry weight (Figure 4.8). In submerged culture conditions, the lag phase was completed on the 3rd day and the log phase was completed on the 8th day, and the fungal metabolism passed to the stationary phase.

In our preliminary studies with *C. laburnicola*, substrate feeding was performed on the 3rd day and the biotransformation studies lasted 4-10 days and the substrate was completely consumed in these conditions. From this point of view, we suggested that the reactions catalyzed by *C. laburnicola* occur during the growth phase. To confirm this observation, the lower limit was chosen as the 2nd day and the upper limit was selected as the 4th day as the substrate feeding time. The lower limit for the biotransformation time was determined as three days and the upper limit as nine days.

In addition, based on the growth curve graph, the μ_{max} and the doubling time were calculated as 0.059 h^{-1} and 11.67 h, respectively.

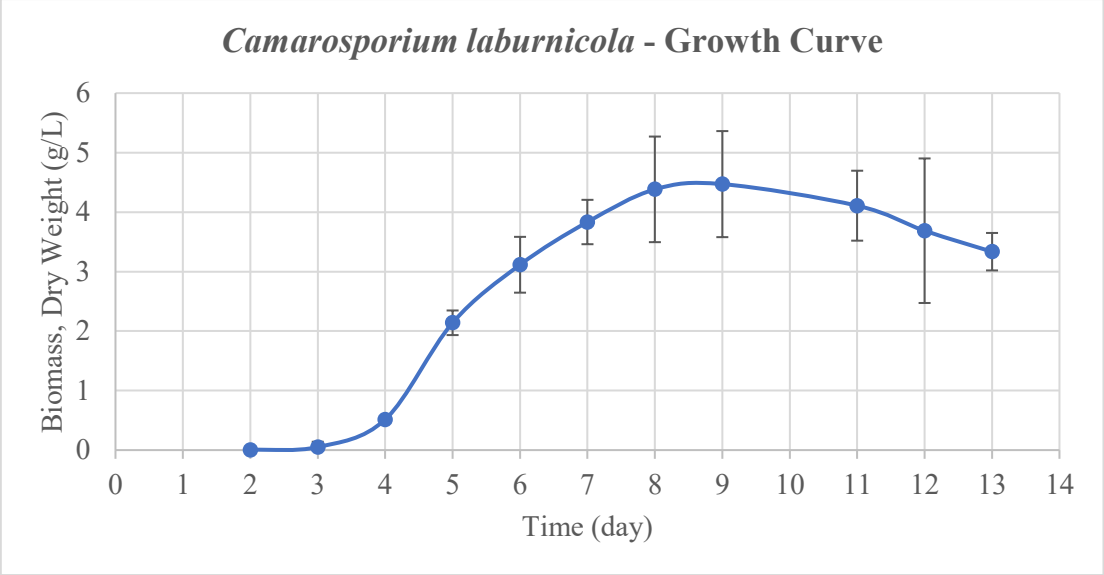

Figure 4.8. Growth curve for *C. laburnicola* based on dry weight.

4.3.2. TLC Mobile Phases for Reference Compounds

Mobile phases were optimized to compare the extracts obtained from the experimental sets. $CHCl_3$:MeOH:H_2O (90:10:0.1, 85:15:0.1) and *n*-hexane:EtOAc:MeOH (10:10:3) systems for silica gel plates, ACN:H_2O for reverse-phase silica gel plate (65:35) was used as mobile phase (Chromatogram 4.1).

In the reverse phase C18 silica gel plate, the R_f values of the substrates AG and CG and their 3-oxo derivatives (E-AG-03 and E-CG-03) were very close, but the resolution was good for the other derivatives (Chromatogram 4.1c). In the studies performed with a silica gel plate, the resolution of *n*-hexane:EtOAc:MeOH (10:10:3) system was higher for AG and its derivatives (Chromatogram 4.1d), and the R_f values of the three molecules (AG, E-AG-02, E-AG-04) were very close in the $CHCl_3$:MeOH:H_2O (90:10:0.1, 85:15:0.1) systems. For CG and its derivatives, the best resolution was achieved in $CHCl_3$:MeOH:H_2O (90:10:0.1, 85:15:0.1) systems (Chromatogram 4.1a).

As a result, *n*-hexane:EtOAc:MeOH (10:10:3) for AG and its derivatives and $CHCl_3$:MeOH:H_2O (90:10:0.1) for CG and derivatives were selected as the mobile phase for

the silica gel. ACN:H_2O (65:35) was preferred for AG, CG and their derivatives as mobile phase for reverse phase C18 silica gel. In addition, reverse phase C18 silica gel plate chromatograms provided preliminary data for developing the HPLC method.

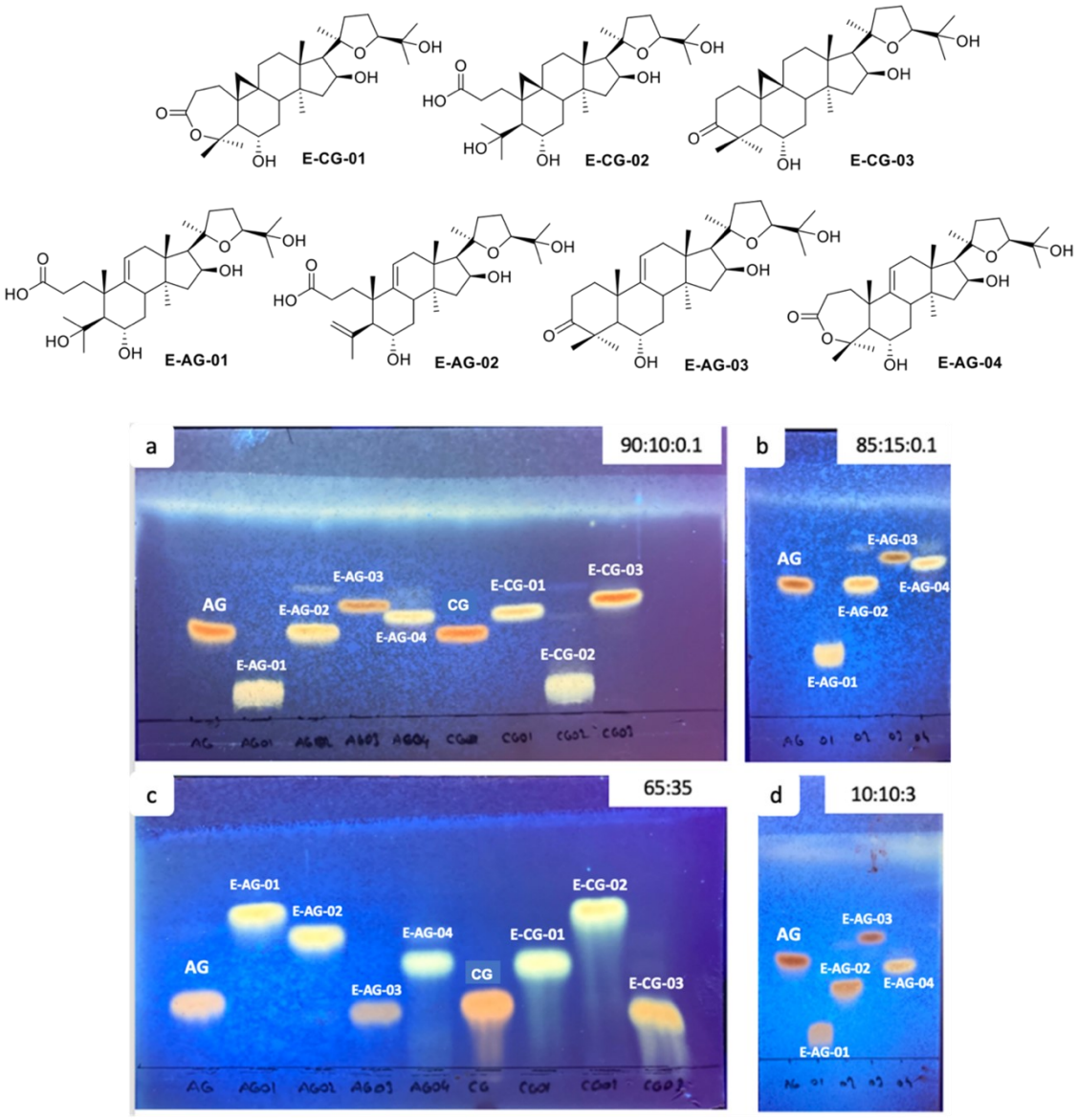

Chromatogram 4.1. TLC chromatograms of the reference compounds developed with the selected mobile phases: a) Silica gel, Mobile phase: 90:10:0.1 ($CHCl_3$:MeOH:H_2O); b) Silica gel, Mobile phase: 85:15:0.1 ($CHCl_3$:MeOH:H_2O); c) Reverse phase C18 silica gel, Mobile phase: 65:35 (ACN: H_2O), d) Silica gel, Mobile phase: 10:10:3 (*n*-hexane:EtOAc:MeOH).

4.3.3. HPLC Method Optimization and Standard Curves

The optimized TLC system was used to develop the HPLC method for the analysis of biotransformation extracts. ACN was preferred as the solvent because methanol causes high column back pressure. In the extracts, a guard column was used to prevent metabolites from the nutrient medium and/or the fungus's own metabolites from polluting and clogging the column. In our experiments, a back pressure of 180-200 bar was observed at a flow rate of 1 mL/min. Thus, this flow rate was chosen for the HPLC-DAD method.

E-AG-01 and E-AG-02 are carboxylic acid derivatives produced by ring-opening reactions at ring A. When ACN and UPW were used in analyzing these metabolites, tailing was observed in the peaks of the metabolites. For the symmetrical peaks, 0.1% HPLC-Quality acetic acid was added to the solvents to prevent the interaction of the free -OH groups in the column's stationary phase with the molecules, and the tail formation problem was solved (Chromatogram 4.2).

In this method, AG and its metabolites had retention times between 5.2 – 9.4 min, while CG and its metabolites had retention times between 5 – 9 min (Chromatogram 4.2).

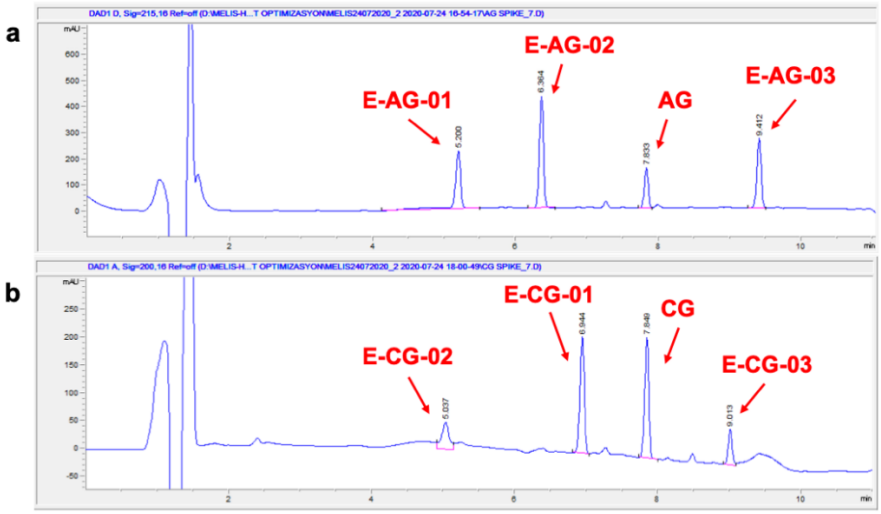

Chromatogram 4.2. HPLC chromatograms of spikes prepared with metabolites of AG and CG derivatives: a) AG and its derivatives, 215 nm; b) CG and its derivatives, 200 nm.

In method optimization studies, AG and its derivatives gave a higher response than CG and its derivatives. This difference is due to the presence of C-9(11) double bond on AG. The higher response of AG and its derivatives prevented obtaining a linear standard curve at 200 nm. On the other hand, CG and its derivatives gave inadequate responses at 205, 210 and 215 nm, and metabolite concentrations in the extracts remained below the detection limits. Therefore, 200 nm for CG and E-CG-01; 210 nm for E-AG-01; 215 nm for AG and E-AG-02 were used to generate standard curves (Figure 4.9).

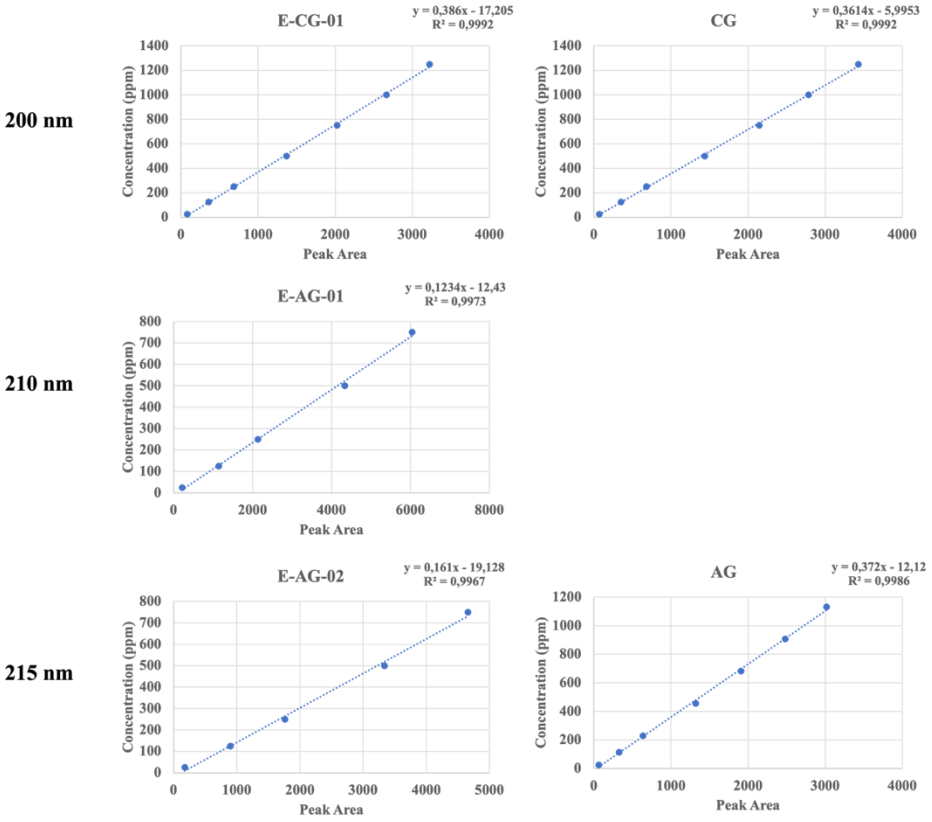

Figure 4.9. Standard curves of reference metabolites for PBD experiments.

Before the analyzes were performed for the CCD, the piece connecting the guard column to the main column was broken. For this reason, it was necessary to perform analyzes without a guard column, which led to the need for further method optimization.

In our preliminary experiments, the retention time of AG and its derivatives, especially the most polar metabolite, E-AG-01, was 2.4 min and the peaks interfered with other molecules entering the column in the extract due to the absence of a guard column (Chromatogram 4.3). When the analysis was performed by conditioning the column with a 30:70 (ACN:UPW) mobile phase to wash the unwanted metabolites from the column and then proceed to the analysis of the target molecules, smooth and symmetrical peaks were obtained for the target metabolites.

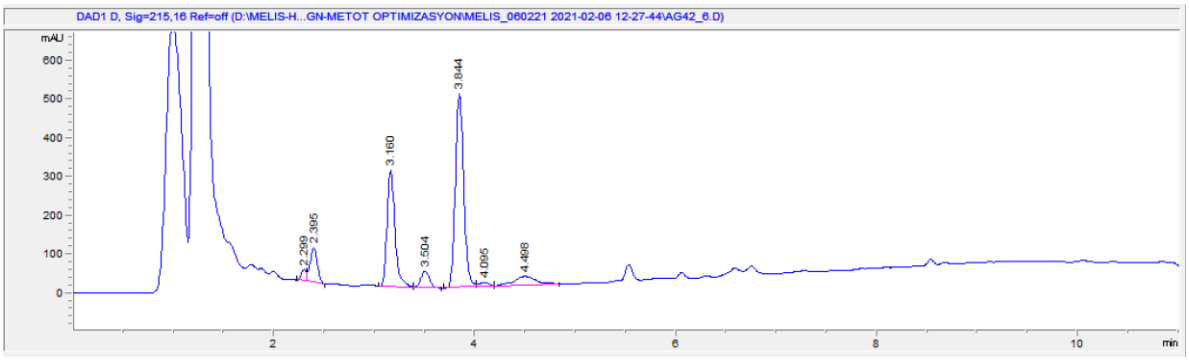

Chromatogram 4.3. HPLC chromatogram (215 nm) of the biotransformation extract of AG and its derivatives.

The second problem was that the back pressure was too high (350-400 bar) due to excessive loading on the column when 20 µL was injected, and a shoulder was observed on the peaks. This problem was solved by regenerating the column and reducing the injection volume (20 µL →10 µL).

In the second HPLC-DAD method, AG and its metabolites had a retention time of 6 to 9 min, while CG and its metabolites had a retention time of 6 to 7.5 min (Chromatogram 4.4). The standard curves generated for this method are given in Figure 4.10.

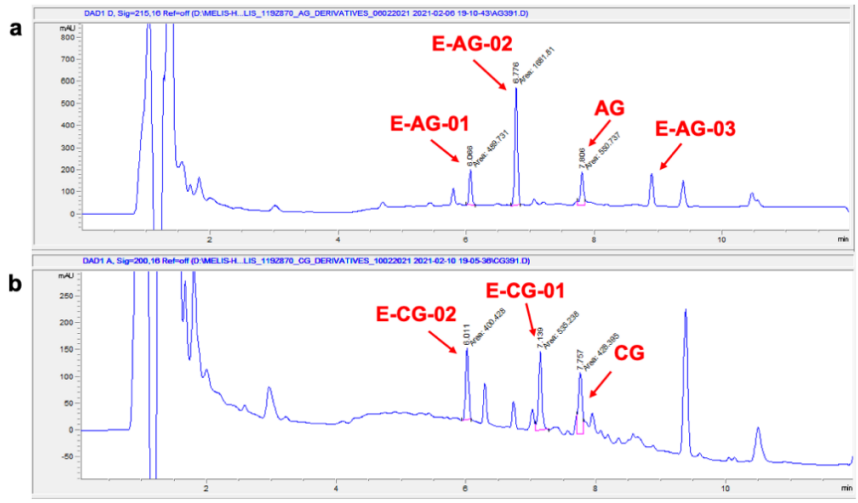

Chromatogram 4.4. HPLC chromatograms of biotransformation extracts of AG and CG derivatives: a) AG and derivatives, 215 nm; b) CG and its derivatives, 200 nm.

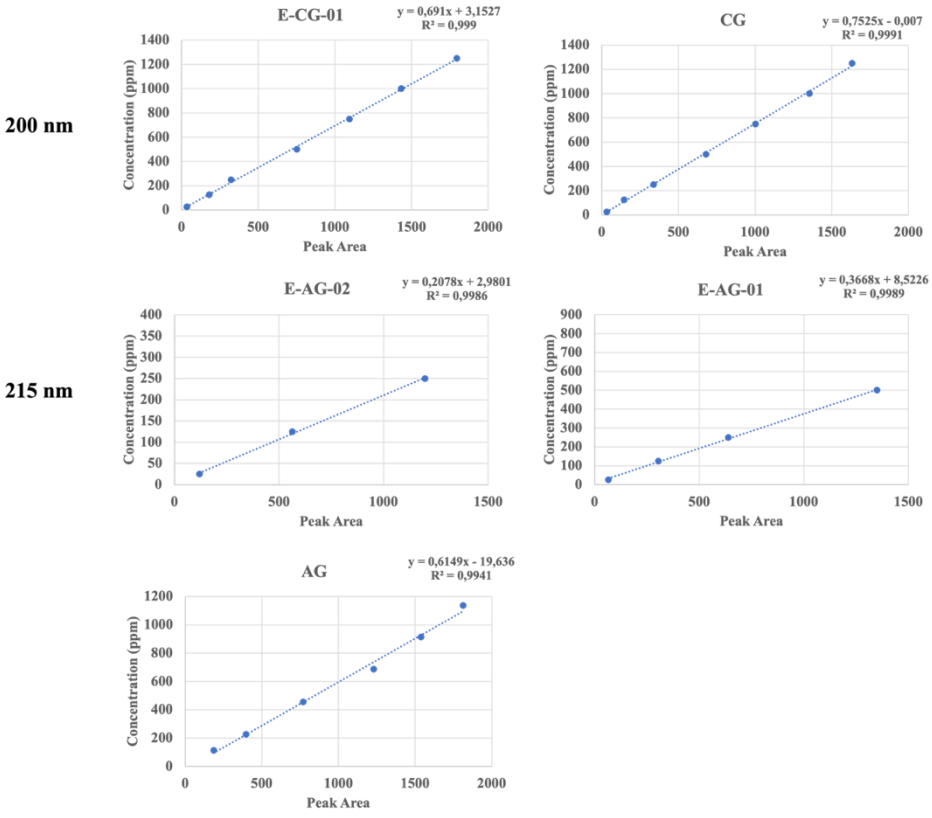

Figure 4.10. Standard curves of reference metabolites for CCD experiments.

The optimized method for CCD continued to be used without optimizing after the guard column was re-purchased. The resulting reference graphs are presented in Figure 4.11.

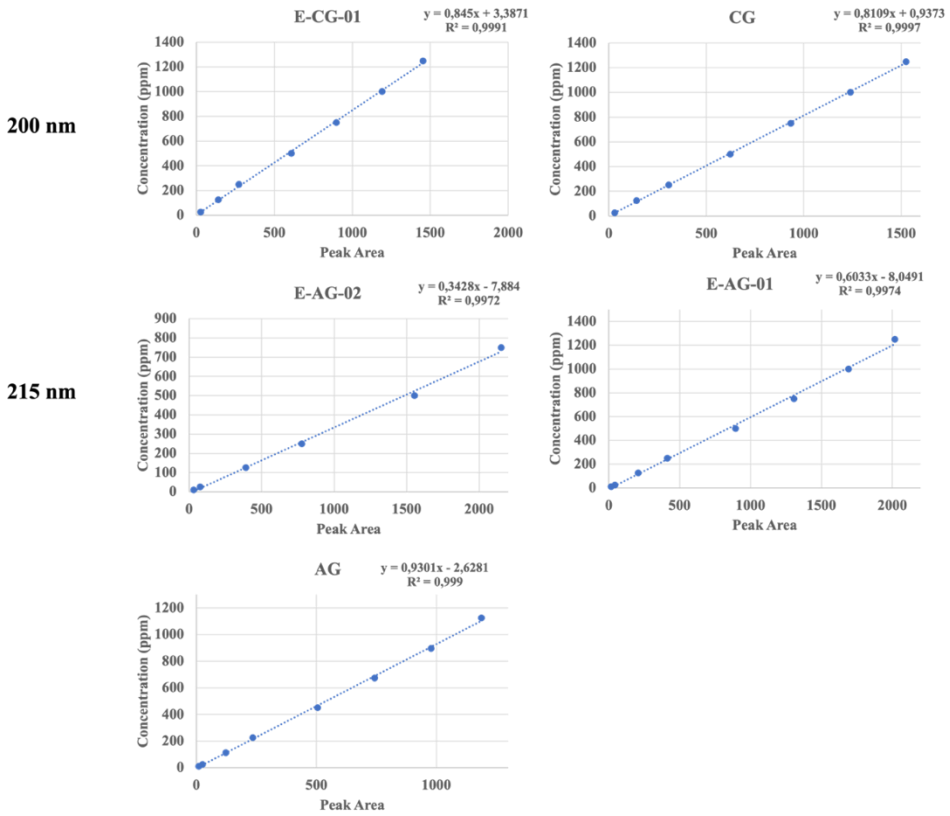

Figure 4.11. Standard curves of reference metabolites for further experiments

4.3.4. Results for Factor Screening by PBD

In this thesis study, the parameters thought to be effective on biotransformation were analyzed, and PBD was used in the first stage to subtract the parameters that were not statistically effective. The responses are expressed as mg/L of the target metabolite in the extracts. The statistical analysis was carried out using Design Expert 12. Parameter limits and responses are given in Table 4.18. The metabolite concentration in the extracts varied between 0 to 76.26 mg/L for E-CG-01, 0 to 41.64 mg/L for E-AG-01, and 0 to 63.26 mg/L

for E-AG-02. TLC and HPLC chromatograms of screening experiments are presented below (Chromatograms 4.5, 4.6, 4.7 and 4.8).

Table 4.18. Plackett-Burman Design and corresponding response measurements.

Exp. Code	Substrate feeding time	Biotrans. time	Temp.	pH	Working volume	Shaking speed	Inoculant	Substrate conc.	Tween 80	Dummy1	Dummy2	E-AG-01 (mg/L)	E-AG-02 (mg/L)
AG1	4	9	20	6.6	70	210	2	0.01	0	1	-1	14.80	41.50
AG2	2	9	30	4.6	70	210	20	0.01	0	-1	1	10.31	19.48
AG3	4	3	30	6.6	30	210	20	0.03	0	-1	-1	0.14	1.96
AG4	2	9	20	6.6	70	150	20	0.03	0.2	-1	-1	16.58	41.96
AG5	2	3	30	4.6	70	210	100	0.03	0.2	1	-1	0	0
AG6	2	3	20	6.6	30	210	20	0.01	0.2	1	1	6.38	8.60
AG7	4	3	20	4.6	70	150	20	0.03	0	1	1	1.39	10.13
AG8	4	9	20	4.6	30	210	2	0.03	0.2	-1	1	22.05	54.53
AG9	4	9	30	4.6	30	150	20	0.01	0.2	1	-1	0.28	2.62
AG10	2	9	30	6.6	30	150	2	0.03	0	1	1	0.10	1.68
AG11	4	3	30	6.6	70	150	2	0.01	0.2	-1	1	0	0
AG12	2	3	20	4.6	30	150	2	0.01	0	-1	-1	0	0.31
AG13	3	6	25	5.6	50	180	11	0.02	0.1	0	0	37.67	63.26
AG14	3	6	25	5.6	50	180	11	0.02	0.1	0	0	28.57	49.35
AG15	3	6	25	5.6	50	180	11	0.02	0.1	0	0	41.64	38.11

Exp. Code	Substrate feeding time	Biotrans. time	Temp.	pH	Working volume	Shaking speed	Inoculant	Substrate conc.	Tween 80	Dummy1	Dummy2	E-CG-01 (mg/L)
CG1	4	9	20	6.6	70	210	2	0.01	0	1	-1	32.33
CG2	2	9	30	4.6	70	210	20	0.01	0	-1	1	33.15
CG3	4	3	30	6.6	30	210	20	0.03	0	-1	-1	3.96
CG4	2	9	20	6.6	70	150	20	0.03	0.2	-1	-1	55.56
CG5	2	3	30	4.6	70	210	100	0.03	0.2	1	-1	0
CG6	2	3	20	6.6	30	210	20	0.01	0.2	1	1	25.25
CG7	4	3	20	4.6	70	150	20	0.03	0	1	1	34.08
CG8	4	9	20	4.6	30	210	2	0.03	0.2	-1	1	21.12
CG9	4	9	30	4.6	30	150	20	0.01	0.2	1	-1	10.44
CG10	2	9	30	6.6	30	150	2	0.03	0	1	1	36.57
CG11	4	3	30	6.6	70	150	2	0.01	0.2	-1	1	1.02
CG12	2	3	20	4.6	30	150	2	0.01	0	-1	-1	24.03
CG13	3	6	25	5.6	50	180	11	0.02	0.1	0	0	56.00
CG14	3	6	25	5.6	50	180	11	0.02	0.1	0	0	76.70
CG15	3	6	25	5.6	50	180	11	0.02	0.1	0	0	42.17

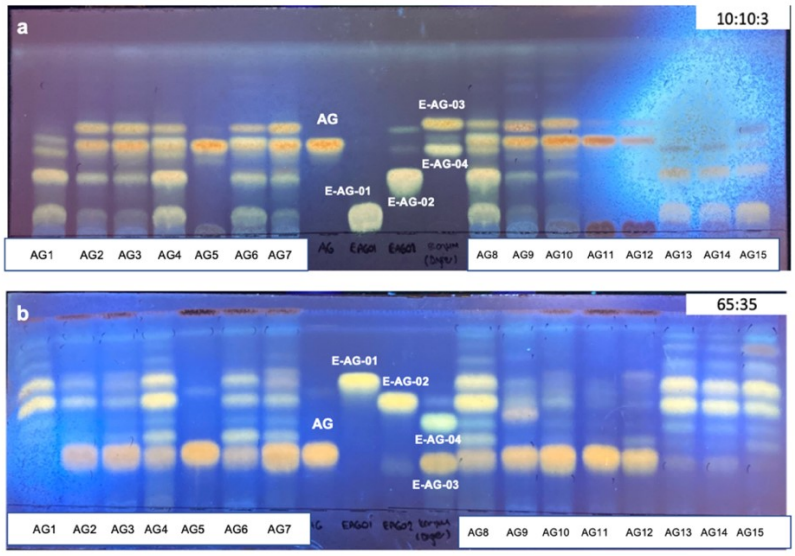

Chromatogram 4.5. Thin layer chromatograms of the extracts obtained for the PBD AG experiment set: a) Silica gel, Mobile phase: 10:10:3 (*n*-hexane:EtOAc:MeOH); b) Reverse phase C18 silica gel, Mobile phase: 65:35 (ACN: H_2O) (5000 ppm sample was prepared for each extract and each was spotted one time, 1 of 3 replicates was presented as a sample).

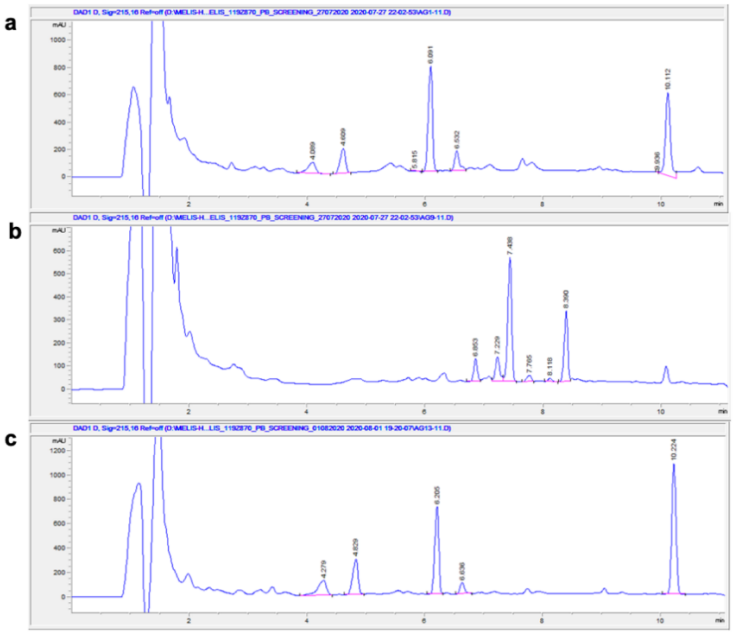

Chromatogram 4.6. Examples for the HPLC chromatograms (215 nm) of the extracts obtained for the PBD AG experiment set: a) AG1 coded sample; b) Example with code AG9; c) Example coded AG13 (1 out of 3 repetitions is presented as an example).

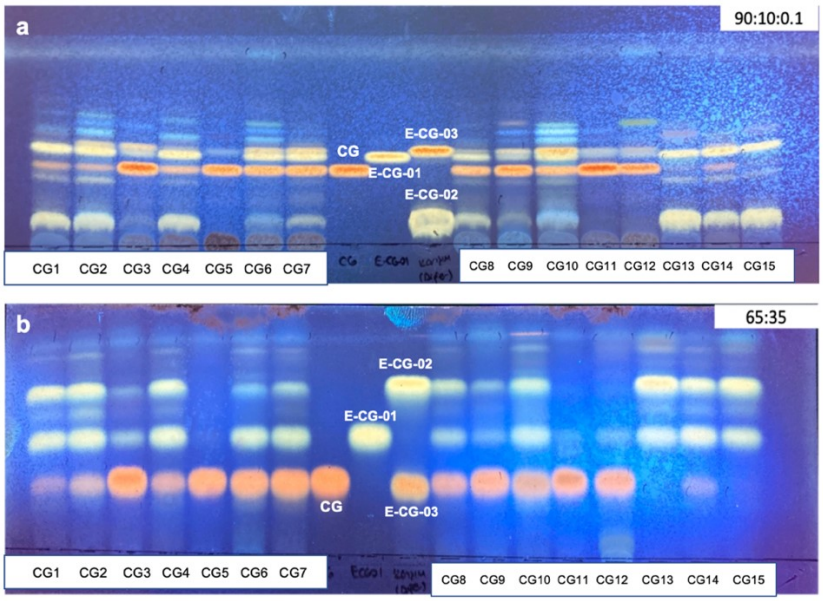

Chromatogram 4.7. Thin layer chromatograms of the extracts obtained for the PBD CG assay set: a) Silica gel, Mobile phase: 90:10:0.1 ($CHCl_3$:MeOH:H_2O); b) Reverse phase C18 silica gel, Mobile phase: 65:35 (ACN: H_2O) (5000 ppm sample was prepared for each extract, and each was spotted once, 1 of 3 replicates was presented as a sample).

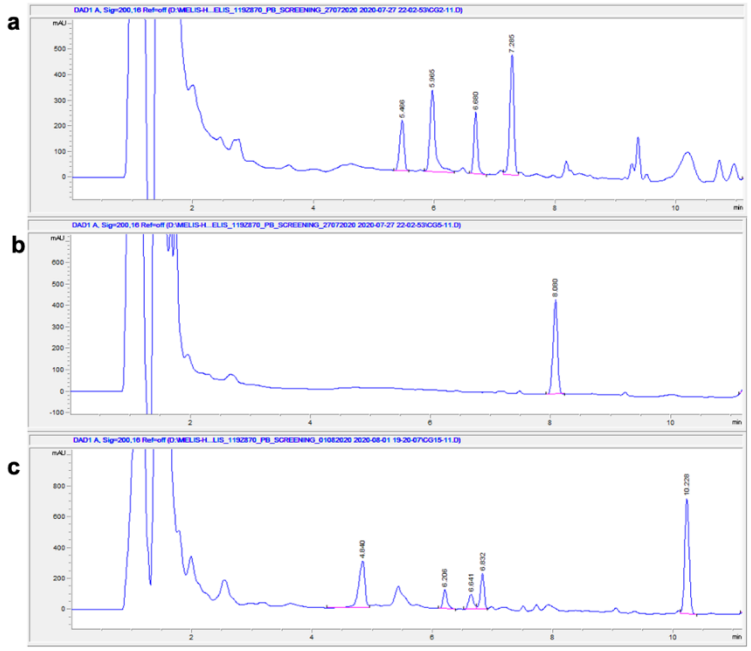

Chromatogram 4.8. Examples for the HPLC chromatograms (200 nm) of the extracts obtained for the PBD CG experiment set: a) CG2 coded sample; b) CG5 coded example; c) Example with code CG15 (1 out of 3 repetitions is presented as an example).

The percentage of contribution of the parameters to the individual E-AG-01 and E-AG-02 production are shown in Table 4.19 and Table 4.20. According to the results, three parameters with a statistically significant effect in the biotransformation process in a 90% confidence interval were: biotransformation time, temperature and shaking speed. The total effects of these three parameters were 73.89% for E-AG-01 and 76.76% for E-AG-02.

Table 4.19. The percentage of contribution of each process parameters on production of E-AG-01.

Term	Standardized Effect	Sum of Squares	% Contribution
Substrate Feeding Time	0.873705	2.29008	0.289382
Biotransformation Time	9.43596	267.112	33.7532
Temperature	-8.3956	211.458	26.7206
pH	0.659025	1.30294	0.164644
Working Volume	2.34572	16.5072	2.0859
Shaking Speed	5.9504	106.222	13.4225
Inoculant Concentration	-0.255587	0.195974	0.024764
Substrate Concentration	1.47481	6.52519	0.824544
Tween 80 Concentration	3.09277	28.6956	3.62607
Dummy 1	-4.29756	55.4072	7.00143
Dummy 2	1.39752	5.85922	0.74039

Table 4.20. The percentage of contribution of each process parameters on production of E-AG-02.

Term	Standardized Effect	Sum of Squares	% Contribution
Substrate Feeding Time	6.39249	122.592	2.68272
Biotransformation Time	23.5173	1659.19	36.3086
Temperature	-21.9371	1443.7	31.5931
pH	1.38255	5.73434	0.125487
Working Volume	7.16769	154.127	3.37283
Shaking Speed	11.6175	404.896	8.8605
Inoculant Concentration	-2.15631	13.949	0.305251
Substrate Concentration	6.3474	120.869	2.64501
Tween 80 Concentration	5.38484	86.9897	1.90363
Dummy 1	-8.89489	237.357	5.19417
Dummy 2	0.954201	2.7315	0.057744

The percentage of contribution of the parameters to the individual E-CG-01 production is shown in Table 4.21. According to the results, two parameters with a statistically significant effect in the biotransformation process in 90% confidence interval are: biotransformation time and temperature. The total effect of these two parameters was 48.76%.

Table 4.21. The percentage of contribution of each process parameters on production of E-CG-01.

Term	Standardized Effect	Sum of Squares	% Contribution
Substrate Feeding Time	-11.9371	427.483	11.5444
Biotransformation Time	16.8061	847.336	22.8828
Temperature	-17.8726	958.289	25.8791
pH	5.3095	84.5725	2.28393
Working Volume	5.79269	100.666	2.71853
Shaking Speed	-7.6475	175.453	4.7382
Inoculant Concentration	7.8919	186.846	5.04588
Substrate Concentration	4.17956	52.4061	1.41525
Tween 80 Concentration	-8.4557	214.496	5.79259
Dummy 1	-0.0302367	0.00274277	7.40701×10^{-5}
Dummy 2	4.14506	51.5446	1.39199

According to the results of the parameter screening, we moved on to optimization studies with the significant factors: biotransformation time, temperature, and shaking speed. The values of other factors that did not significantly affect metabolite production were kept constant in optimization studies.

4.3.5. Optimization of Parameters of Biotransformation Process

The CCD experiment was set to find the optimum values for significant parameters (biotransformation time, temperature, shaking speed). 2^3 full factorial CCD was selected to evaluate the individual and combined effects of biotransformation time, temperature, and

Table 4.22. Experiment set table with CCD optimization results.

Experiment Code	Biotransformation time	Temperature	Shaking Speed	E-AG-01 (mg/L)	E-AG-02 (mg/L)
AG1	3	20	150	16.86	18.85
AG2	9	20	150	29.26	48.85
AG3	3	30	150	0	0
AG4	9	30	150	0	0
AG5	3	20	210	18.85	18.84
AG6	9	20	210	36.56	44.39
AG7	3	30	210	0	0
AG8	9	30	210	2.78	2.63
AG9	1	25	180	5.21	4.50
AG10	11	25	180	21.18	37.73
AG11	6	17	180	14.12	26.02
AG12	6	33	180	0	0
AG13	6	25	130	13.08	31.42
AG14	6	25	230	23.15	45.05
AG15	6	25	180	11.36	24.61
AG16	6	25	180	12.49	26.64
AG17	6	25	180	35.27	57.42
AG18	6	25	180	31.78	54.10
AG19	6	25	180	27.50	54.00
AG20	6	25	180	34.14	62.18
Experiment Code	**Biotransformation time**	**Temperature**	**Shaking Speed**	**E-CG-01 (mg/L)**	
CG1	3	20	150	19.24	
CG2	9	20	150	32.13	
CG3	3	30	150	0	
CG4	9	30	150	0	
CG5	3	20	210	25.30	
CG6	9	20	210	24.90	
CG7	3	30	210	0	
CG8	9	30	210	1.76	
CG9	1	25	180	9.17	
CG10	11	25	180	23.24	
CG11	6	17	180	30.56	
CG12	6	33	180	0	
CG13	6	25	130	25.78	
CG14	6	25	230	18.27	
CG15	6	25	180	6.04	
CG16	6	25	180	4.71	
CG17	6	25	180	24.49	
CG18	6	25	180	19.32	
CG19	6	25	180	25.52	
CG20	6	25	180	20.82	

shaking speed. The CCD, in which three parameters were examined with 20 trials, includes 6 axial (end), 8 factorials, and 6 central points. The CCD matrix formed with the determined lower and upper limits is given in Table 4.22. In these trials, the lower and upper limits of the parameters, selected according to the PBD results, were used as 1-11 days for the biotransformation time, 17–33 °C for the temperature and 130-230 rpm for the shaking speed, so it was aimed to evaluate the effects in a wider range. The metabolite concentration in biotransformation extracts varied between 0 to 32.1 mg/L for E-CG-01; 0 to 34.1 mg/L for E-AG-01; 0 to 62.1 mg/L for E-AG-02.

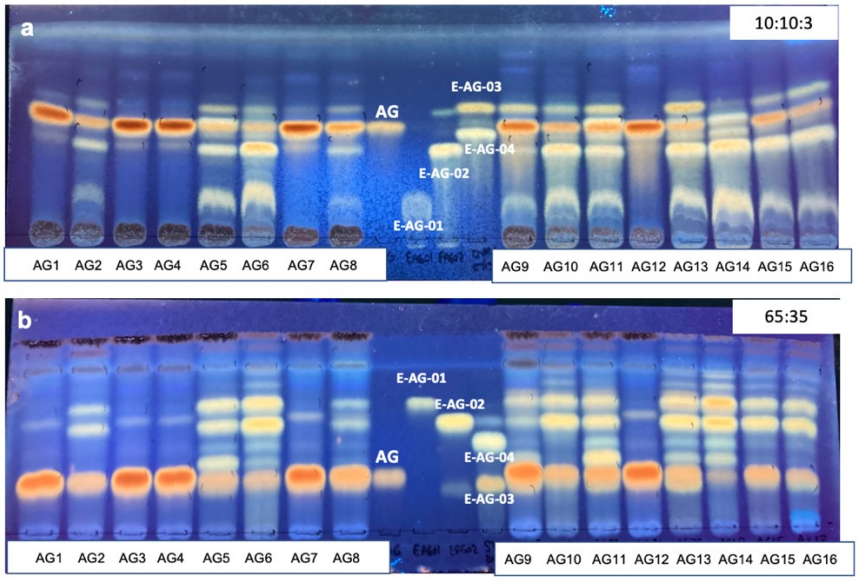

Chromatogram 4.9. Thin layer chromatograms of the extracts obtained for the CCD AG experiment set: a) Silica gel, Mobile phase: 10:10:3 (*n*-hexane:EtOAc:MeOH); b) Reverse phase C18 silica gel, Mobile phase: 65:35 (ACN: H_2O) (20000 ppm sample was prepared for each extract and each was spotted once, 1 out of 3 replicates was presented as a sample).

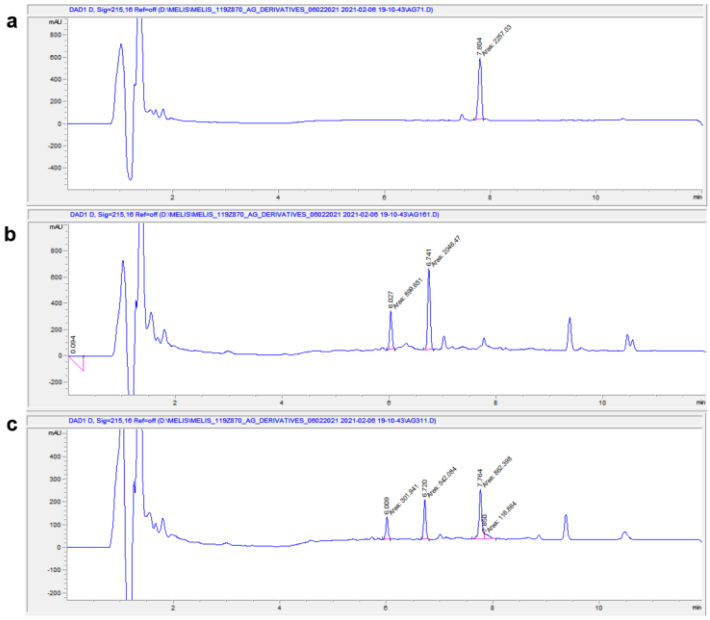

Chromatogram 4.10. Examples for the HPLC chromatograms (215 nm) of the extracts obtained for the CCD AG experiment set: a) AG3 coded sample; b) Example with code AG6; c) Example coded AG11 (1 out of 3 repetitions is presented as an example).

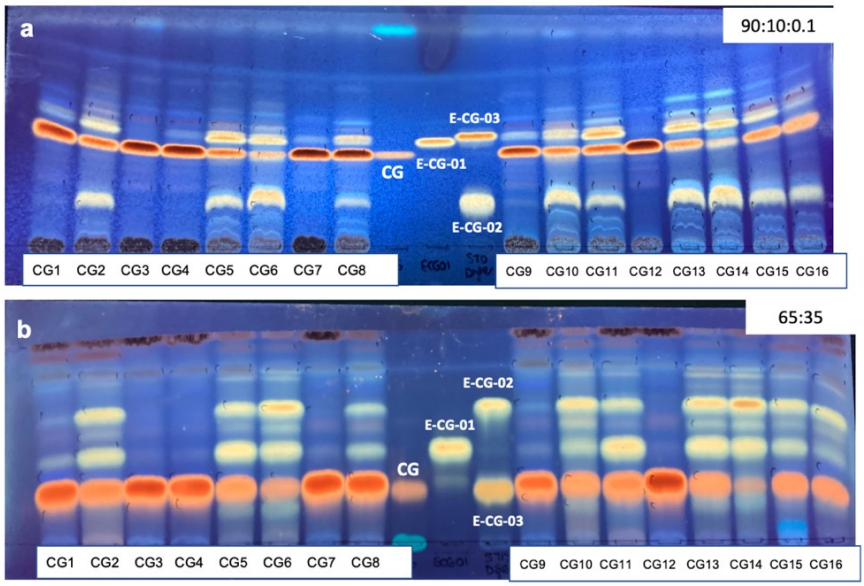

Chromatogram 4.11. Thin layer chromatograms of the extracts obtained for the CCD CG experiment set: a) Silica gel, Mobile phase: 90:10:0.1 ($CHCl_3$:MeOH:H_2O); b) Reverse phase C18 silica gel, Mobile phase: 65:35 (ACN: H_2O) (20000 ppm sample was prepared for each extract and each was spotted once, 1 out of 3 replicates was presented as a sample).

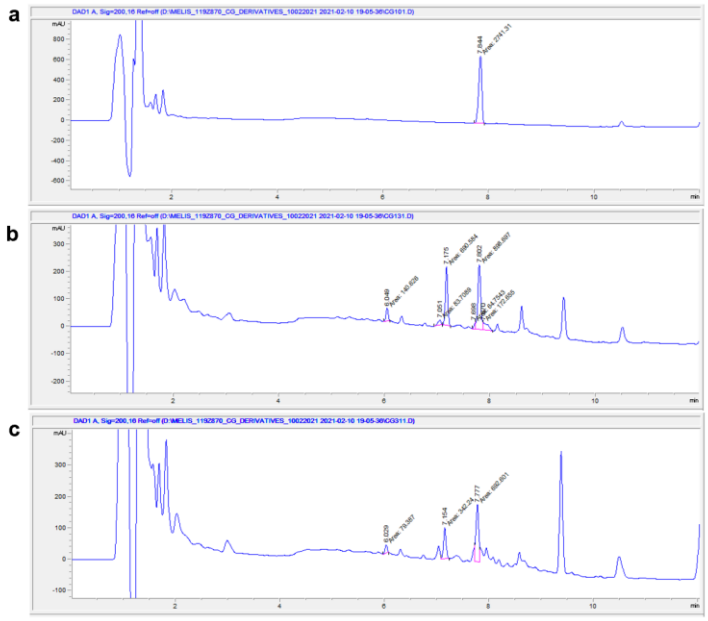

Chromatogram 4.12. Sample HPLC chromatograms (200 nm) of the extracts obtained for the CCD CG experiment set: a) CG4 coded sample; b) CG5 coded example; c) Example coded CG11 (1 out of 3 repetitions is presented as an example).

The results of the analysis of variance (ANOVA) for E-CG-01, E-AG-01 and E-AG-02 are given in Tables 4.23, 4.24 and 4.25. Variables with *p* values less than 0.05 in the 95% confidence interval were considered to have significant effects.

From model analysis, the R^2 values, F values and *p* values were used for evaluating the variables (Tables 4.23, 4.24 and 4.25). Models for each metabolite fitted the experimental data well, with close R^2 and adjusted R^2 values.

F and *p* values indicate that the models can be used to predict metabolite production. The p-values <0.0001 suggest that the F values of the models (E-CG-01: 12.84, E-AG-01: 33.62, E-AG-02: 78.80) are likely to occur by chance, with a very low probability of 0.01%.

According to ANOVA analyses, for E-CG-01 A (biotransformation time), B (temperature), C (agitation speed), A^2, B^2, ABC, A^2B, A^2C, AB^2; for E-AG-01 and E-AG-02 A, B, AB, A^2, B^2, C^2, A^2B are variables that have a statistically significant effect.

Table 4.23. ANOVA and regression results obtained with CCD experiment set of E-CG-01.

Source	Sum of Squares	df	Mean Square	F-value	p-value	
Model	6598.81	12	549.90	12.84	< 0.0001	significant
A-Biotransformation Time	482.73	1	482.73	11.27	0.0019	
B-Temperature	737.68	1	737.68	17.23	0.0002	
C-Shaking speed	231.37	1	231.37	5.40	0.0260	
AB	0.4907	1	0.4907	0.0115	0.9154	
AC	105.24	1	105.24	2.46	0.1260	
BC	3.63	1	3.63	0.0847	0.7727	
A^2	219.93	1	219.93	5.14	0.0297	
B^2	667.49	1	667.49	15.59	0.0004	
ABC	202.42	1	202.42	4.73	0.0365	
A^2B	292.38	1	292.38	6.83	0.0131	
A^2C	240.18	1	240.18	5.61	0.0235	
AB^2	226.06	1	226.06	5.28	0.0277	
Residual	1498.70	35	42.82			
Lack of Fit	182.29	2	91.14	2.28	0.1177	not significant
Pure Error	1316.42	33	39.89			
Cor Total	8097.51	47				

Std. Dev.	6.54	**R^2**	0.8149
Mean	16.99	**Adjusted R^2**	0.7515
C.V. %	38.51	**Predicted R^2**	0.7060
		Adeq Precision	10.8299

Model equation: E-CG-01 (mg/L) = 22.80 + 6.53 A – 7.34 B – 4.07 C – 0.1513 AB – 2.22 AC – 0.4124 BC – 2.69 A^2 – 4.46 B^2 + 3.07 ABC – 5.92 A^2B + 5.33 A^2C – 5.53 AB^2

Table 4.24. ANOVA and regression results obtained with CCD experiment set of E-AG-01.

Source	Sum of Squares	df	Mean Square	F-value	p-value	
Model	7990.61	8	998.83	33.62	< 0.0001	significant
A-Biotransformation Time	576.96	1	576.96	19.42	< 0.0001	
B-Temperature	299.11	1	299.11	10.07	0.0028	
C-Shaking speed	19.87	1	19.87	0.6687	0.4180	
AB	136.81	1	136.81	4.60	0.0376	
A^2	1516.41	1	1516.41	51.04	< 0.0001	
B^2	2728.84	1	2728.84	91.84	< 0.0001	
C^2	1148.21	1	1148.21	38.65	< 0.0001	
A^2B	501.62	1	501.62	16.88	0.0002	
Residual	1277.59	43	29.71			
Lack of Fit	65.90	6	10.98	0.3354	0.9138	not significant
Pure Error	1211.69	37	32.75			
Cor Total	9268.21	51				
Std. Dev.	5.45			**R^2**	0.8622	
Mean	16.14			**Adjusted R^2**	0.8365	
C.V. %	33.77			**Predicted R^2**	0.8101	
				Adeq Precision	15.0576	

Model equation: E-AG-01 (mg/L) = 32.09 + 3.81 A – 4.20 B + 0.7383 C- 2.45 AB – 6.35 A^2 – 8.53 B^2 – 5.79 C^2 – 7.18 A^2B

Table 4.25. ANOVA and regression results obtained with CCD experiment set of E-AG-02.

Source	Sum of Squares	df	Mean Square	F-value	p-value	
Model	25712.46	8	3214.06	78.80	< 0.0001	significant
A-Biotransformation Time	2940.10	1	2940.10	72.08	< 0.0001	
B-Temperature	1015.63	1	1015.63	24.90	< 0.0001	
C-Shaking speed	3.98	1	3.98	0.0977	0.7561	
AB	1129.18	1	1129.18	27.68	< 0.0001	
A^2	6639.09	1	6639.09	162.78	< 0.0001	
B^2	9808.81	1	9808.81	240.49	< 0.0001	
C^2	2980.76	1	2980.76	73.08	< 0.0001	
A^2B	739.42	1	739.42	18.13	0.0001	
Residual	1753.83	43	40.79			
Lack of Fit	162.92	6	27.15	0.6315	0.7041	not significant
Pure Error	1590.91	37	43.00			
Cor Total	27466.29	51				
Std. Dev.	6.39			**R^2**	0.9361	
Mean	27.12			**Adjusted R^2**	0.9243	
C.V. %	23.54			**Predicted R^2**	0.9134	
				Adeq Precision	22.1028	

Model equation: E-AG-02 (mg/L) = +57.07 + 8.59 A – 7.74 B + 0.3306 C – 7.03 AB – 13.30 A^2 – 16.16 B^2 – 9.33 C^2 – 8.71 A^2B

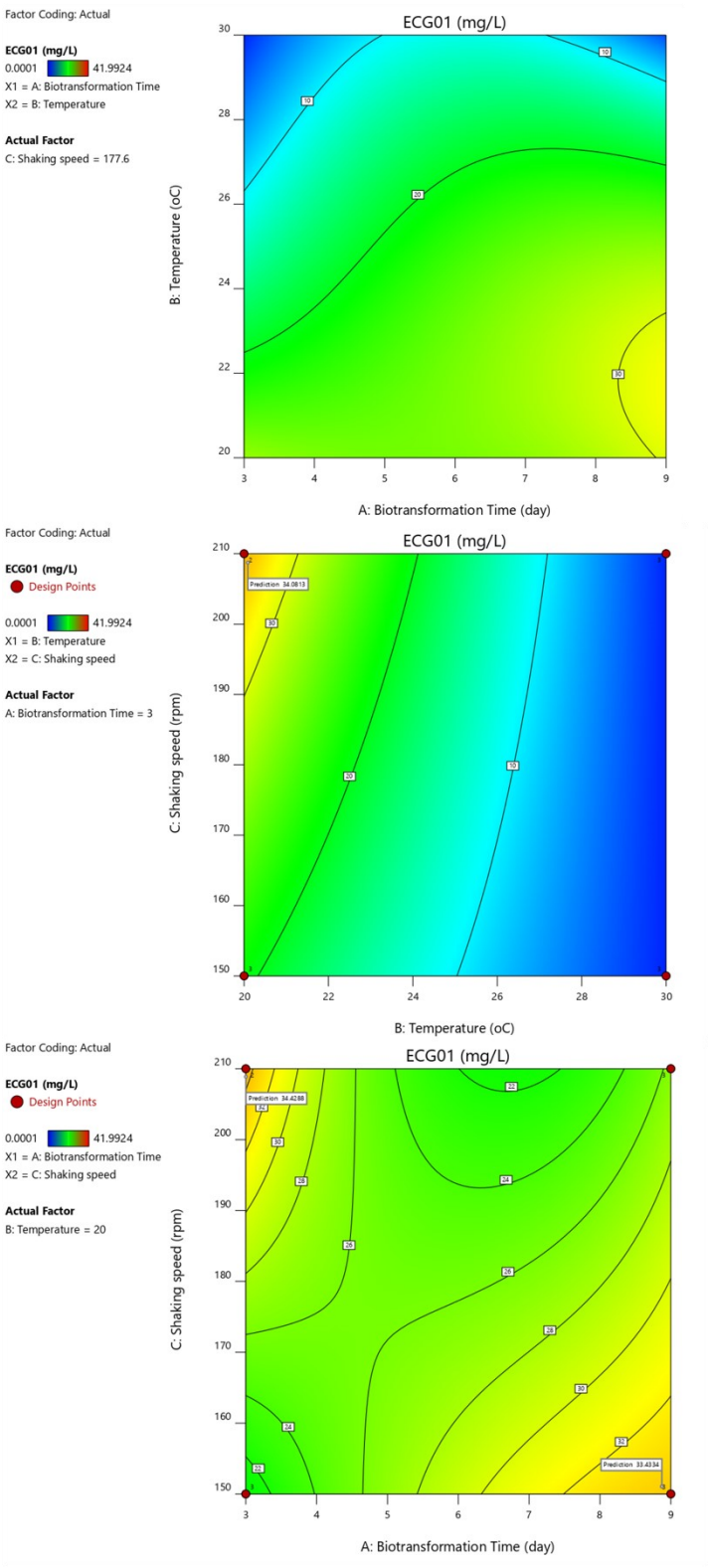

Figure 4.12. Contour plots for E-CG-01 as a function of temperature, biotransformation time and shaking speed.

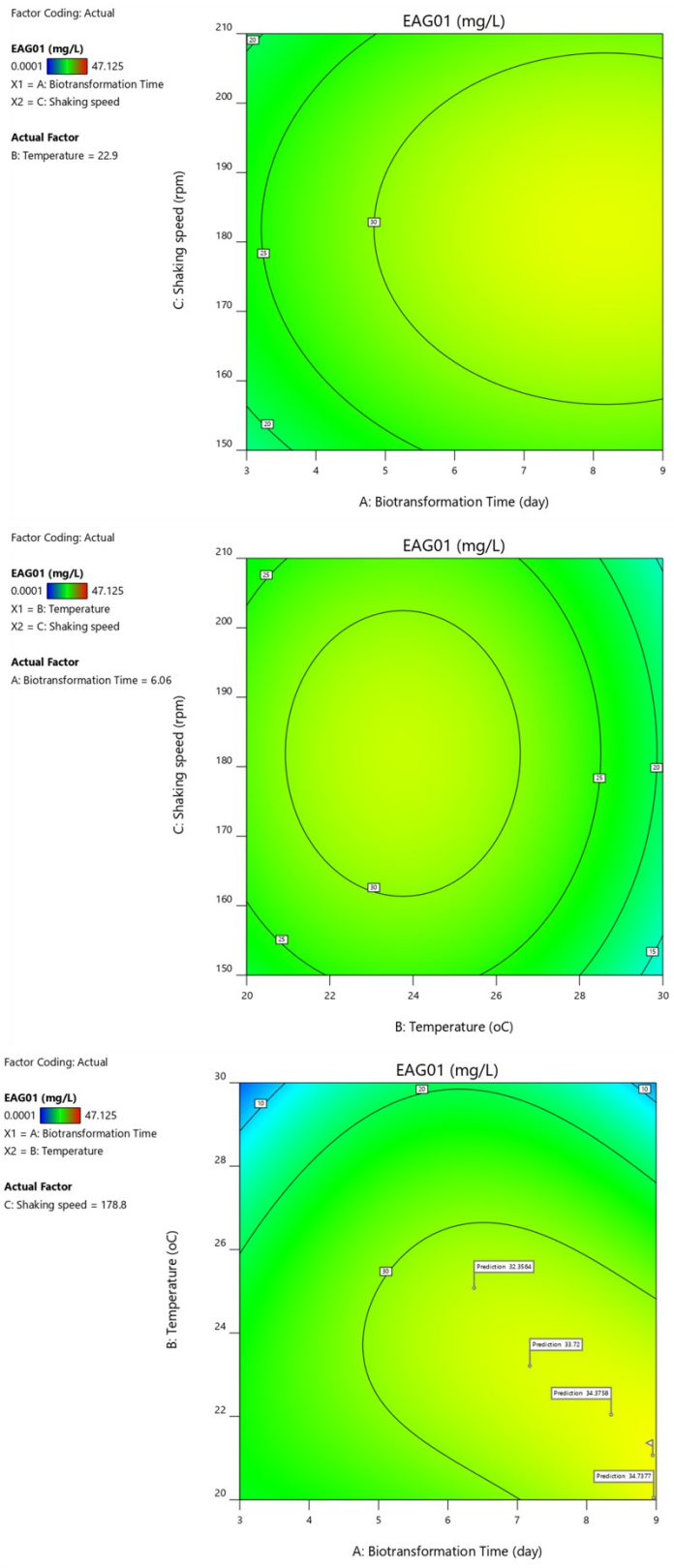

Figure 4.13. Contour plots for E-AG-01 as a function of temperature, biotransformation time and shaking speed.

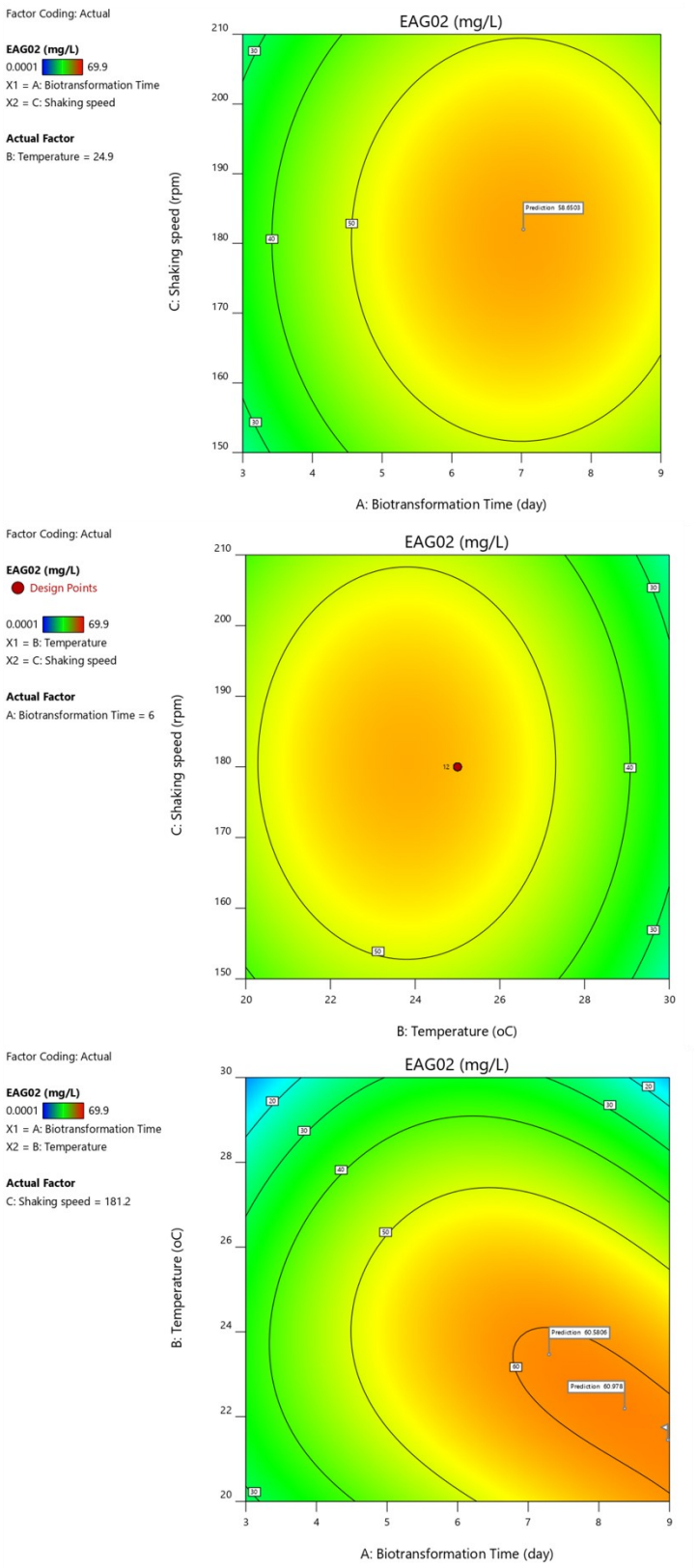

Figure 4.14. Contour plots for E-AG-02 as a function of temperature, biotransformation time and shaking speed.

The following results can be summarized for target molecules from the contour plots (Figures 4.12, 4.13 and 4.14);

- Temperature has a negative effect on the production efficiency of all three metabolites and the temperature should be kept between 20-23 °C,

- Interaction of the biotransformation time with the shaking speed influences the production yield of E-CG-01, high agitation speed and short biotransformation time or vice versa increases the yield (Figure 4.12),

- Long biotransformation time increases the production yield of AG derivatives (Figures 4.13 and 4.14),

- Central point of shaking speed (180 rpm) provides the highest yield in the production of AG derivatives (Figures 4.13 and 4.14).

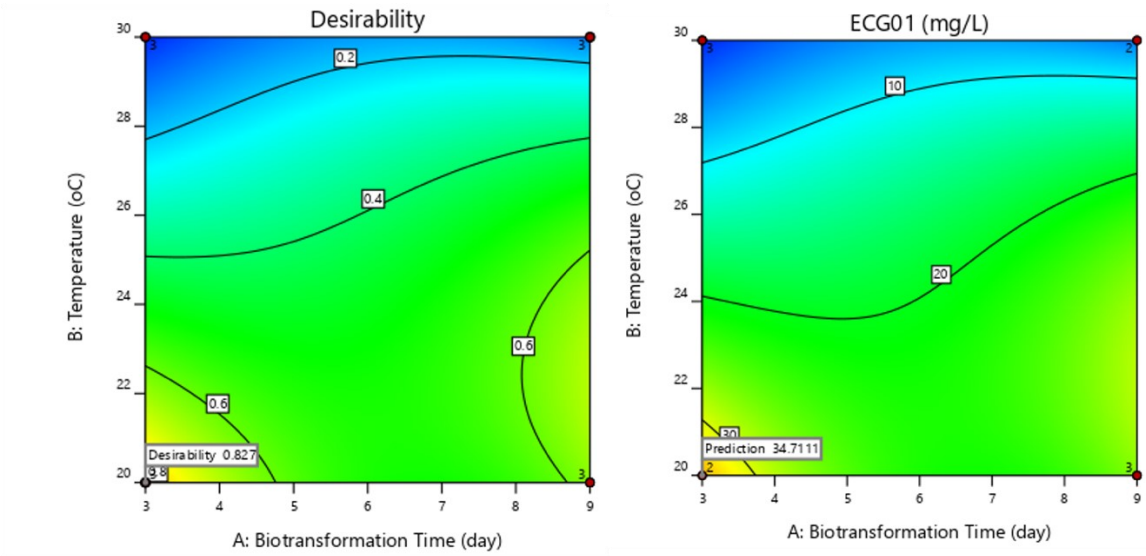

Figure 4.15. Contour plots which show the maximum production conditions of the E-CG-01 estimated by the CCD model (shaking speed 210 rpm).

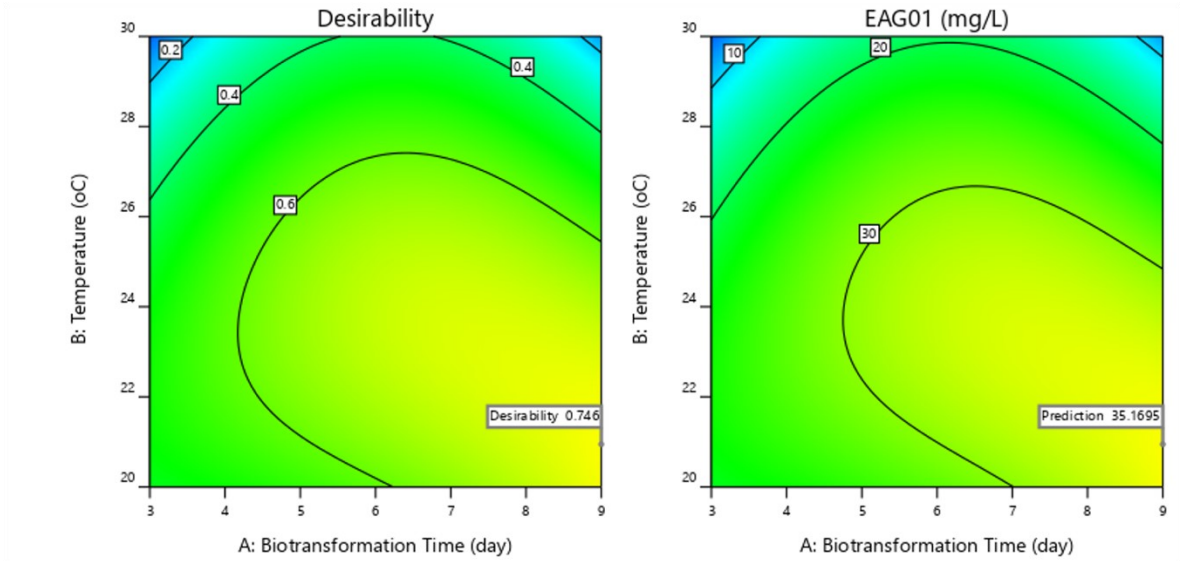

Figure 4.16. Contour plots which show the maximum production conditions of the E-AG-01 estimated by the CCD model (shaking speed 180 rpm).

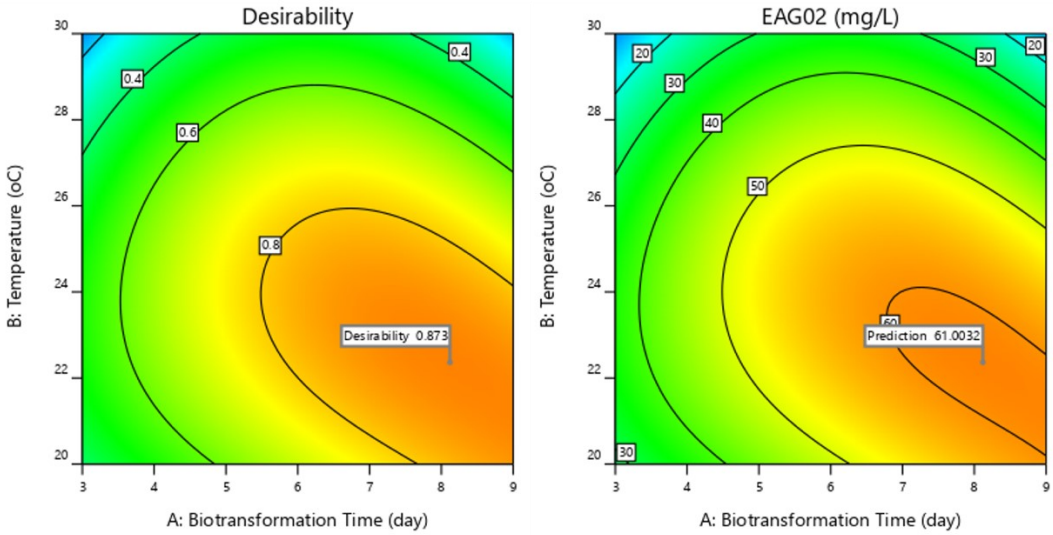

Figure 4.17. Contour plots which show the maximum production conditions of the E-AG-02 estimated by the CCD model (shaking speed 180 rpm).

The maximum production conditions of the target metabolites were determined from the contour plots obtained using the model equations produced with Design Expert 12 (Figures 4.15, 4.16 and 4.17). Table 4.26 summarizes optimized process conditions.

According to these results, E-CG-01 is predicted to be produced theoretically in 17% yield, E-AG-01 in 17.5% yield and E-AG-02 in 30.5% yield.

Table 4.26. Predicted conditions by CCD models to achieve maximum yields for E-CG-01, E-AG-01 and E-AG-02.

Metabolite	Concentration	Yield (%)	Target	Process Conditions
E-AG-01	35 mg/L	17.5	%0.78 → %50	22 ºC, 180 rpm, 9 day
E-AG-02	61 mg/L	30.5	%2.12 → %60	22 ºC, 180 rpm, 8 day
E-CG-01	34 mg/L	17	%32 → %75	20 ºC, 210 rpm, 3 day

4.3.6. Validation Studies

To validate CCD models, three experiments were selected. The level of selected parameters, the predicted values, the experimental results, and the highest and lowest acceptable values in the 95% confidence interval are given in Tables 4.27, 4.28 and 4.29. When the results of the validation experiments are examined, all trials are within the 95% confidence interval. In addition, all the experimental data were close to the predicted values. These results show that the models can predict the production of target metabolites.

Table 4.27. Validation experiments of CCD model for E-AG-01.

No	Biotrans. Time (day)	Temp. (ºC)	Shaking Speed (rpm)	E-AG-01 (Pred.) (mg/L)	E-AG-01 (Exp.) (mg/L)	95 % CI low (mg/L)	95 % CI high (mg/L)
1	3	20	210	17.28	10.16	5.42	29.13
2	8	22	180	34.15	35.47	22.74	45.56
3	6	22	180	31.54	31.62	20.08	43

Table 4.28. Validation experiments of CCD model for E-AG-02.

No	Biotrans. Time (day)	Temp. (ºC)	Shaking Speed (rpm)	E-AG-02 (Pred.) (mg/L)	E-AG-02 (Exp.) (mg/L)	95 % CI low (mg/L)	95 % CI high (mg/L)
1	3	20	210	19.44	13.03	5.54	33.33
2	8	22	180	60.85	59.19	47.48	74.22
3	6	22	180	55.89	57.43	42.46	69.32

Table 4.29. Validation experiments of CCD model for E-CG-01.

No	Biotrans. Time (day)	Temp. (ºC)	Shaking Speed (rpm)	E-CG-01 (Pred.) (mg/L)	E-CG-01 (Exp.) (mg/L)	95 % CI low (mg/L)	95 % CI high (mg/L)
1	3	20	210	34.71	35.19	18.64	50.79
2	8	22	180	29.06	40.92	15.36	42.76
3	6	22	180	25.59	24.29	11.84	39.34

4.3.7. One Factor at a Time Studies to Increase Yield of Target Metabolites

The targeted yields for E-AG-01, E-AG-02 and E-CG-01 molecules could not be reached in 250 mL flasks. Before moving on to bioreactor studies, two more experiments were conducted to increase the yields of target metabolites.

In the first experiment, the time-dependent variation of the concentrations of target metabolites was examined. According to Figure 4.18, the concentration of E-AG-01 reaches equilibrium after the 5^{th} day and is approximately 40 mg/L; the concentration of E-AG-02 is about 60 mg/L between 7-9 days and it starts to increase again (65 mg/L) from the 10^{th} day.

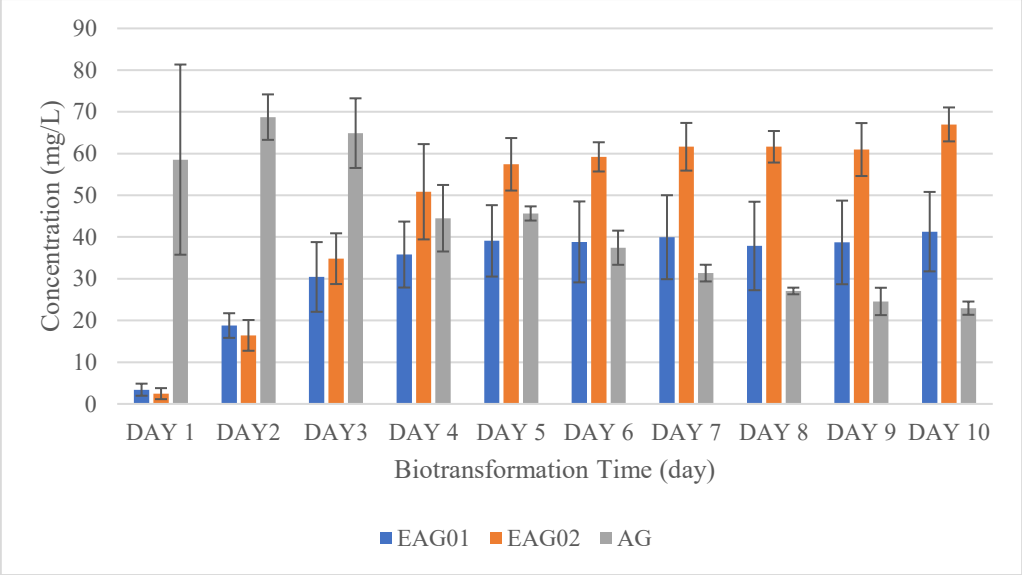

Figure 4.18. Time-course study for biotransformation of AG by *C. laburnicola*.

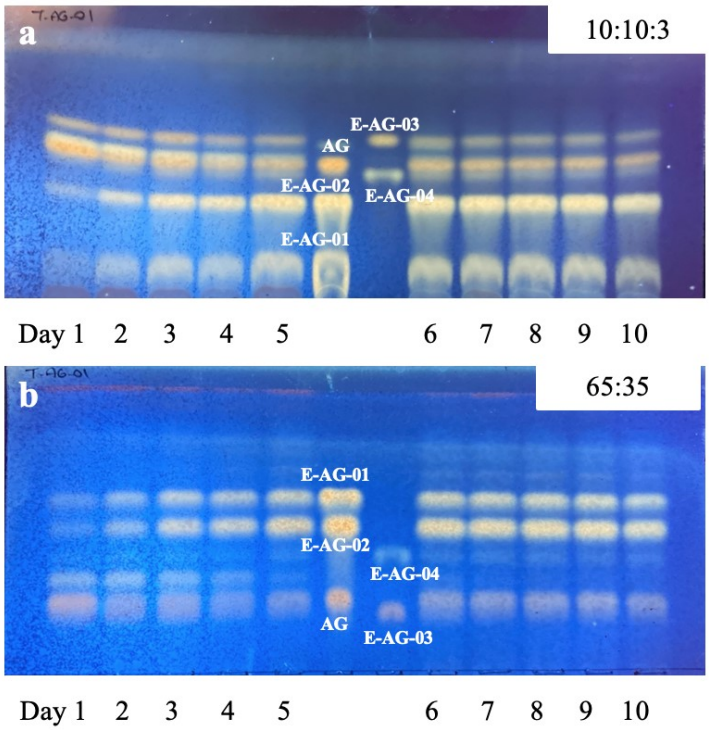

Chromatogram 4.13. Thin layer chromatograms of the time-course biotransformation study of AG; a) Silica gel, Mobile phase: 10:10:3 (*n*-hexane:EtOAc:MeOH); b) Reverse phase C18 silica gel, Mobile phase: 65:35 (ACN: H_2O) (5000 ppm sample was prepared for each extract and each was spotted one time, 1 out of 3 replicates was presented as a sample).

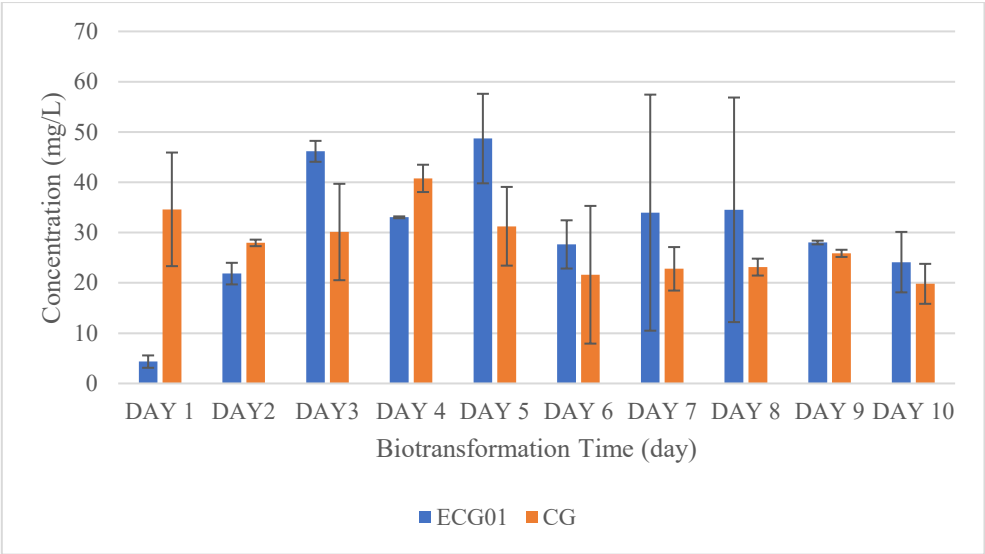

Figure 4.19. Time-course study for biotransformation of CG by *C. laburnicola.*

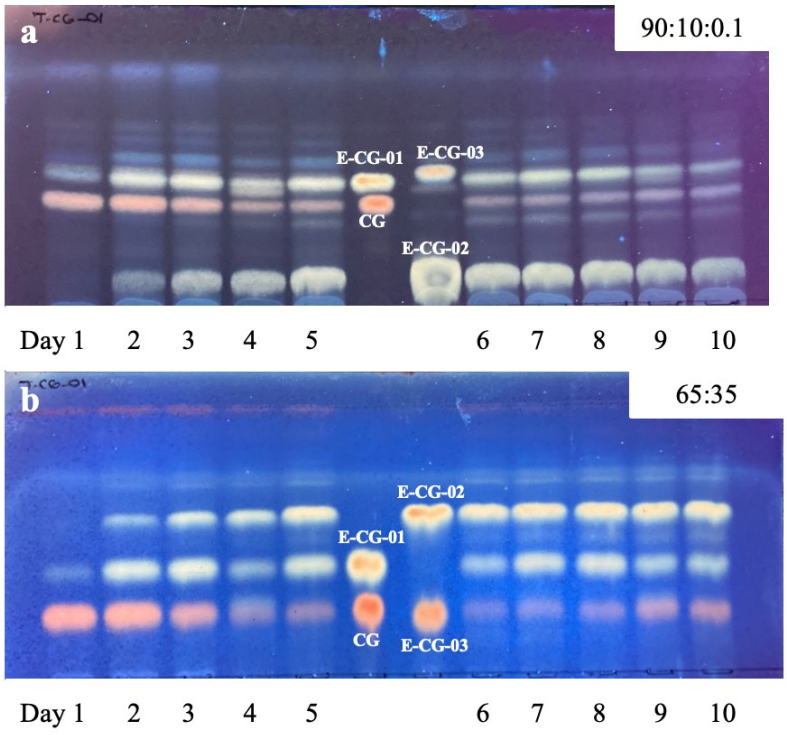

Chromatogram 4.14. Thin layer chromatograms of the time-course biotransformation study of CG: a) Silica gel, Mobile phase: 90:10:0.1 ($CHCl_3$:MeOH:H_2O); b) Reverse phase C18 silica gel, Mobile phase: 65:35 (ACN: H_2O) (5000 ppm sample was prepared for each extract and each was spotted once, 1 out of 3 replicates was presented as a sample).

The results of the time-course biotransformation study of CG by *C. laburnicola* are demonstrated in Figure 4.19 and Chromatogram 4.14. Based on Figure 4.19, the concentration of E-CG-01 increases until 3rd day and reaches the maximum concentration on Day 3 and Day 5 (45-50 mg/L). After the 5th day, the concentration of E-CG-01 begins to decrease.

From Chromatogram 4.14, it was observed that E-CG-01 transformed into the final product, E-CG-02, starting from the 5th day. For this reason, the conversion to E-CG-02 should be stopped by a chemical/genetic intervention or a change in the process conditions. For this reason, production should be terminated on the 3rd day, as predicted by the CCD model. Although substrate is not fully converted on the 3rd day, it is financially important to recover substrate at the end of production and include it in the subsequent processes.

The maximum concentrations and process conditions obtained from this study are presented in Table 4.30. This study is important in determining the biotransformation time and the effects of high-volume flask production on yield. In CCD studies, 1, 3, 6, 9 and 11 days were used as the biotransformation time. It was understood by this study whether there was a change in the interim days. Production yields were increased from 17.5% to 20% for E-AG-01, from 30.5% to 35% for E-AG-02, and from 17% to 23% for E-CG-01.

Table 4.30. Summary of time-course biotransformation study of AG and CG.

Metabolite	Concentration	Yield (%)	Target	Applied Process Conditions
E-AG-01	40 mg/L	20	%0.78 → %50	22 ºC, 180 rpm, 7 day
E-AG-02	70 mg/L	35	%2.12 → %60	22 ºC, 180 rpm, 10 day
E-CG-01	46 mg/L	23	%32 → %75	20 ºC, 210 rpm, 3 day

In the second experiment, the effect of the growing time of *C. laburnicola* in the petri dish on the biotransformation efficiency was investigated. According to Figures 4.20 and 4.21, using 11-day-old fungus for AG derivatives and 8-day-old fungus for E-CG-01 resulted in higher metabolite production. The process conditions and the yields of target metabolites are summarized in Table 4.31. Production yields were increased from 17.5% to 21% for E-

AG-01 and from 17% to 25% for E-CG-01. However, the production yield decreased from 30.5% to 28% for E-AG-02.

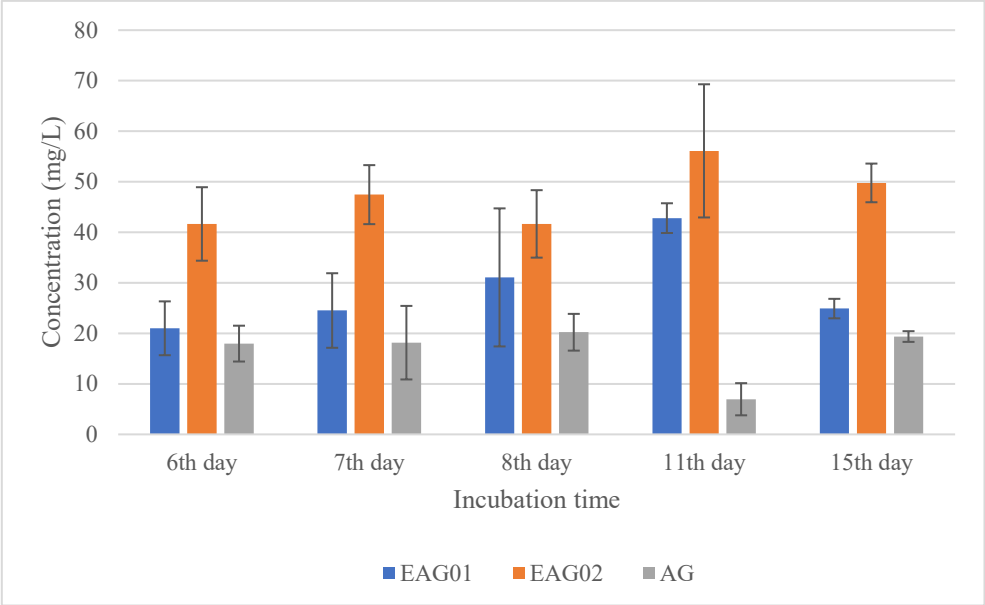

Figure 4.20. Effect of incubation time for biotransformation of AG by *C. laburnicola*.

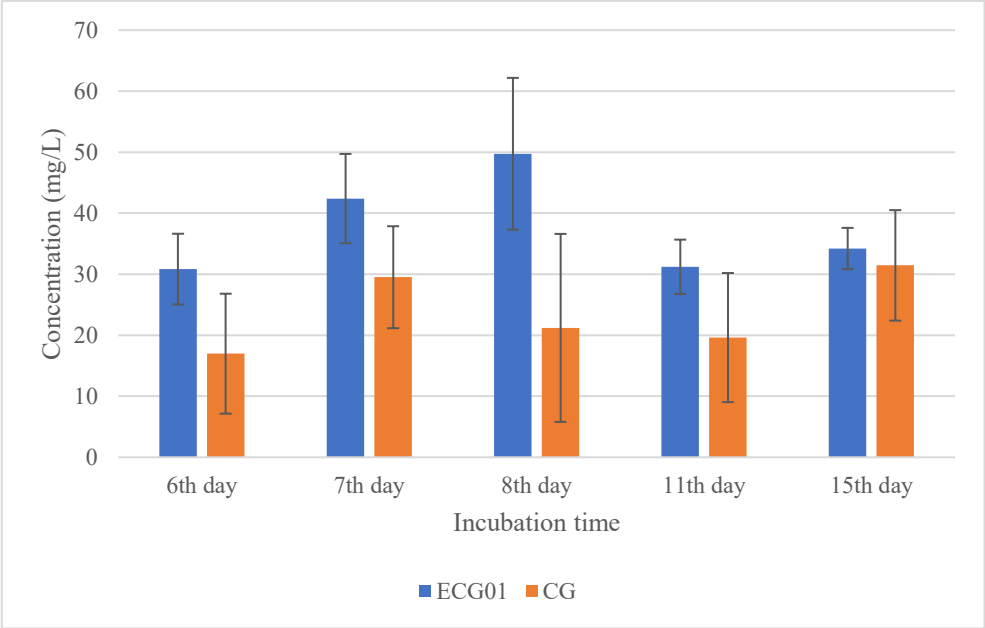

Figure 4.21. Effect of incubation time for biotransformation of CG by *C. laburnicola*.

Table 4.31. Summary of incubation time study for E-CG-01, E-AG-01 and E-AG-02.

Metabolite	Concentration	Yield (%)	Target	Applied Process Conditions
E-AG-01	42 mg/L	21	%0.78 → %50	22 ºC, 180 rpm, 7 day, 11-day-old fungus
E-AG-02	56 mg/L	28	%2.12 → %60	22 ºC, 180 rpm, 7 day, 11-day-old fungus
E-CG-01	50 mg/L	25	%32 → %75	22 ºC, 180 rpm, 7 day, 8-day-old fungus

4.3.8. Bioreactor Studies: 1 L

Scale-up studies were started using a 1 L volume bioreactor. Preliminary trials were carried out with CG substrate. In shake flasks productions, aeration and pH cannot be controlled. For this reason, four different productions were carried out to determine the effect of aeration and pH on microbial transformation by *C. laburnicola*. The process conditions used in these trials are presented in Table 4.8.

In Bioreactor A4, with the highest production of E-CG-01, aeration was applied, pH was not adjusted but recorded. The low yields in Bioreactors A1 and A3 might originate from constant pH values. On the other hand, the yield of E-CG-01 remained low, and there was no aeration in Bioreactor A2.

The time-dependent variation of pH and E-CG-01 concentration in Bioreactor A4 is given in Figure 4.22. According to this graph, E-CG-01 concentration increased while the pH decreased starting from day 2. From the 8^{th} to the 9^{th} day, E-CG-01 concentration decreased by approximately 5 mg/L, and pH and product concentration remained constant after day 9. In addition, E-CG-02, the final product of CG, was produced starting from day 5 (Chromatogram 4.15d). However, E-CG-02 formation could not be detected in Bioreactors A1, A2 and A3. In this experiment, a maximum concentration of 50 mg/L (25%) E-CG-01 was reached in Bioreactor A4. However, this value is below the target yield (75%) and is even lower than the initial yield (32%). For this reason, optimization studies were continued with different parameters.

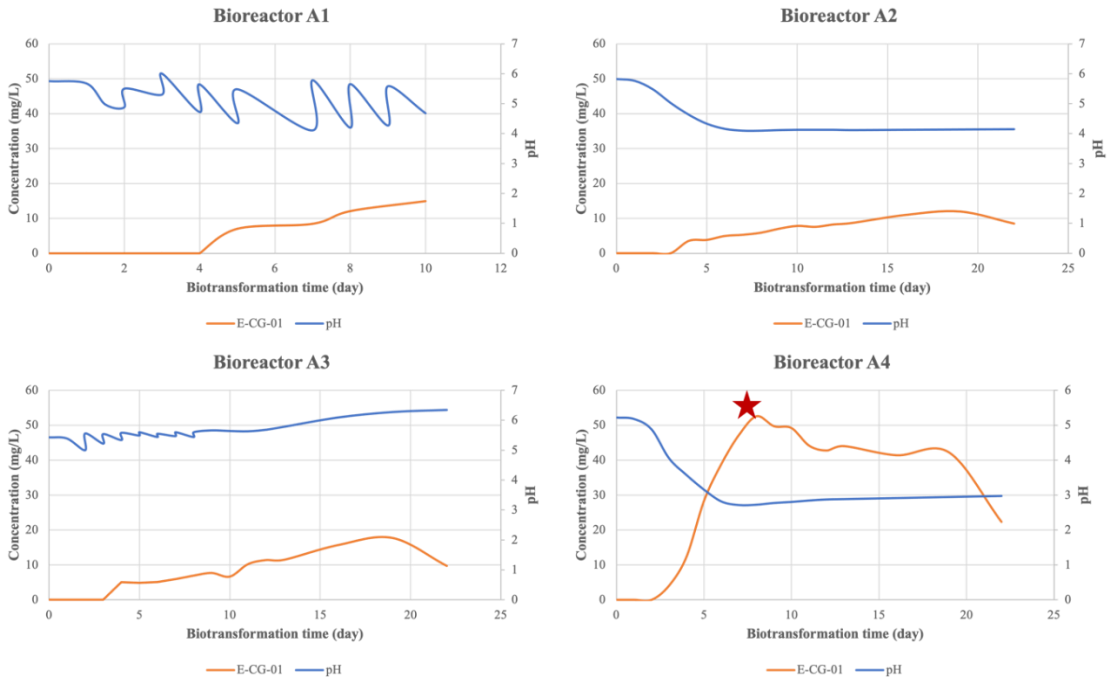

Figure 4.22. Time-dependent variation of pH and concentration of E-CG-01 in Bioreactors A1, A2, A3 and A4.

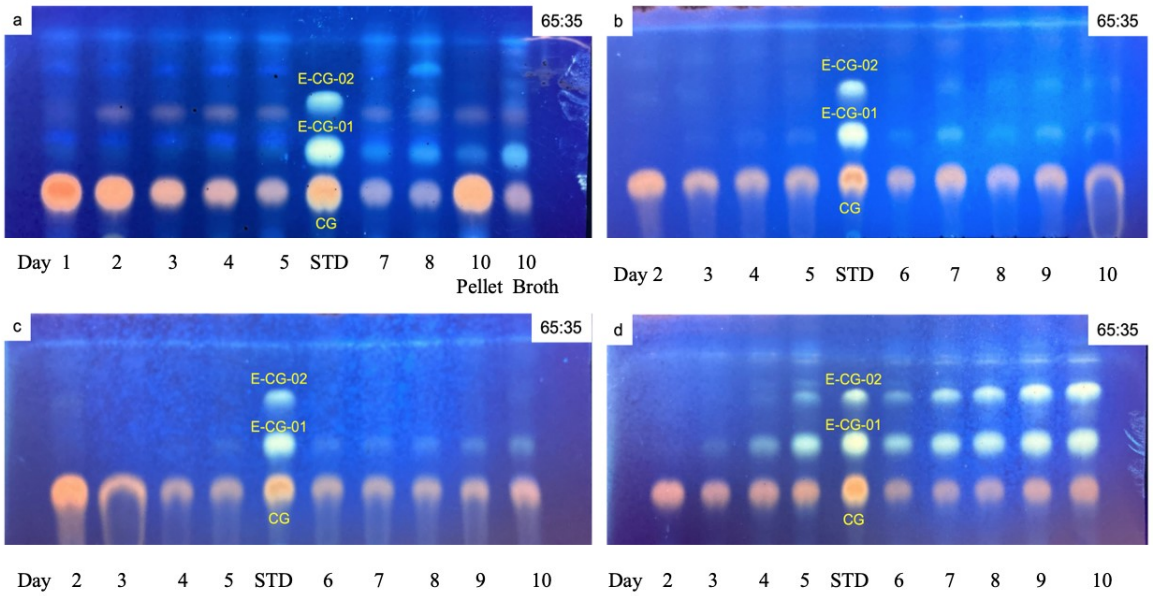

Chromatogram 4.15. Thin layer chromatograms of the preliminary bioreactor study performed on CG: a) Bioreactor A1, b) Bioreactor A2, c) Bioreactor A3, d) Bioreactor A4. [Reverse phase C18 silica gel, Mobile phase: 65:35 (ACN: H_2O)]. (5000 ppm sample was prepared for each extract, and each was spotted four times).

In the microbial transformation experiments carried out in the bioreactor, pellet formation of fungus was observed during production (Figure 4.23). Fungus developed pellet structures which attached to the metal and glass parts of the bioreactor instead of forming hyphal structures in submerged culture. This incident probably caused low production efficiency. To prevent this, it was decided to use microparticles (talcum, aluminum oxide, etc.)[160]. For this reason, an experiment was set to investigate the effect of talcum microparticles on pellet formation and E-CG-01 formation.

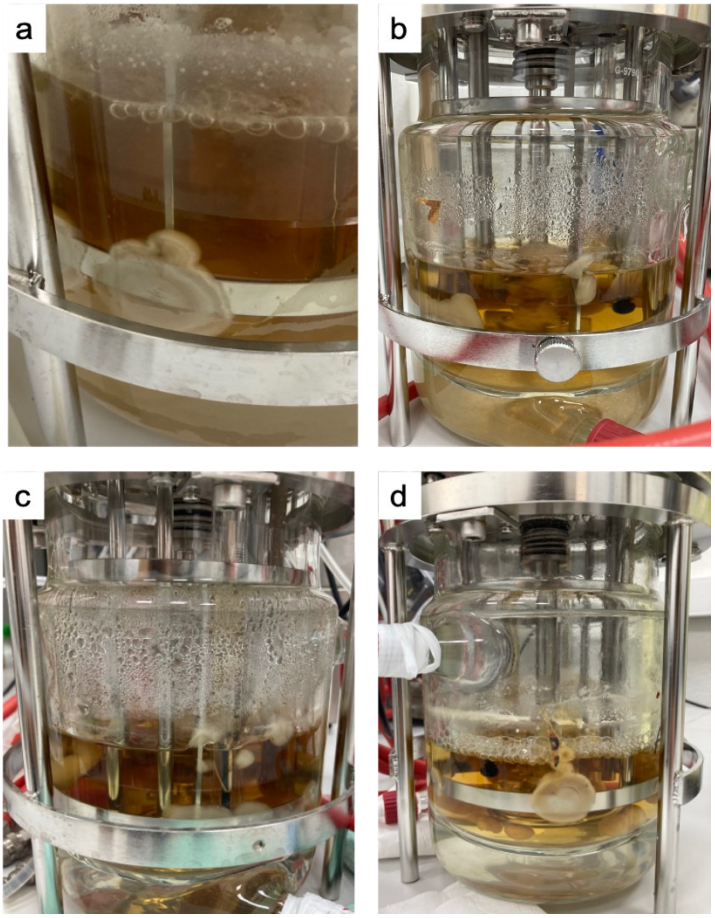

Figure 4.23. Preliminary bioreactor studies. A) Bioreactor A1, b) Bioreactor A2, c) Bioreactor A3, d) Bioreactor A4.

According to the results of the microparticle experiment set, a maximum of 58 mg/L E-CG-01 production was achieved using 2.5% talcum in PDB. Figure 4.24 demonstrated that

a lower E-CG-01 concentration (25 mg/L) was obtained in the control group (Bioreactor B1, Figure 4.24) compared to the previous production (Bioreactor A4, Figure 4.22). This deviation might originate from the fungus itself or the bioreactor. To be specific, fungal growth can cause blockage in spargers. Ineffective aeration may have affected the biotransformation efficiency. In this experiment, a maximum concentration of 58 mg/L (29%) E-CG-01 was reached in Bioreactor B3 (Figure 4.24). In addition, E-CG-02, the end product, was also measured in all bioreactors (Chromatogram 4.16).

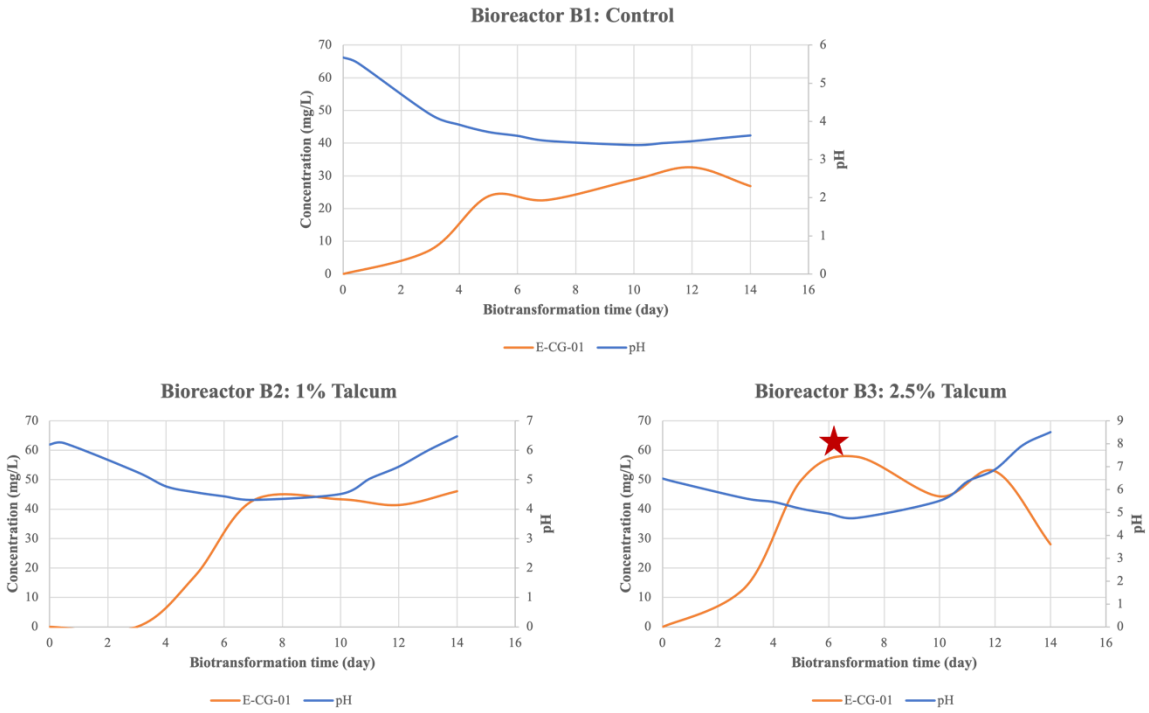

Figure 4.24. Time-dependent variation of pH and concentration of E-CG-01 in Bioreactors B1, B2 and B3.

It was observed that pellet formation could not be prevented in the microparticle-containing bioreactors (Figure 4.25). When the talcum was added to the nutrient medium, it was suspended by mixing. Two days after inoculation, there were no suspended microparticles in the medium, and big fungal pellets developed on glass/metal surfaces.

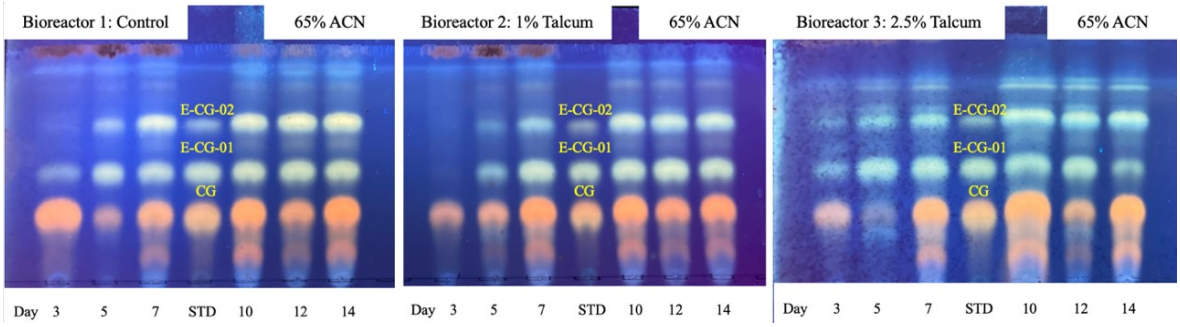

Chromatogram 4.16. Thin layer chromatograms of the microparticle study performed on CG. A) Bioreactor B1, b) Bioreactor B2, c) Bioreactor B3. [Reverse phase C18 silica gel, Mobile phase: 65:35 (ACN: H_2O)]. (5000 ppm sample was prepared for each extract, and each was spotted four times).

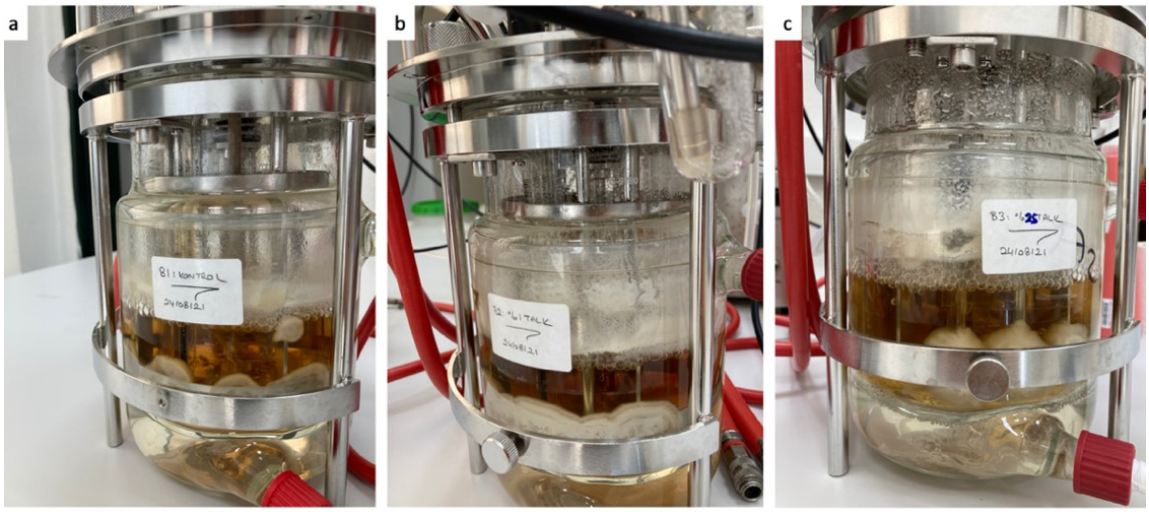

Figure 4.25. Bioreactor studies with microparticles. A) Bioreactor B1, b) Bioreactor B2 and c) Bioreactor B3.

Agitation speed is also used to prevent pellet formation[161,162]. For this reason, a new experimental set was designed to investigate the effect of different agitation speeds on pellet and product formation.

In this experiment, approximately 60 mg/L E-CG-01 was measured at 210 and 400 rpm. Even though the same conditions were used, the maximum E-CG-01 concentration was obtained on the 6th day in the microparticle experiment set. In contrast, it was reached on the 12th day in the agitation experiment set (Figure 4.26). This variation between productions has

not been explainable, and further studies are warranted. In addition, foam formation was increased by increasing agitation speed, and pellet formation couldn't be prevented in this experiment set (Figure 4.27).

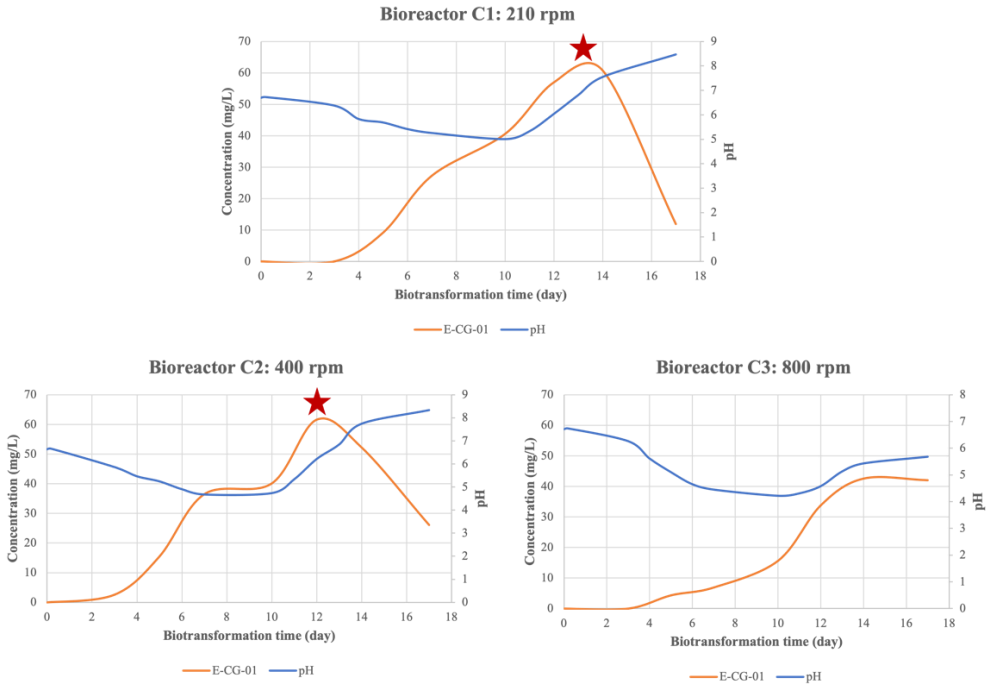

Figure 4.26. Time-dependent variation of pH and concentration of E-CG-01 in Bioreactors C1, C2 and C3.

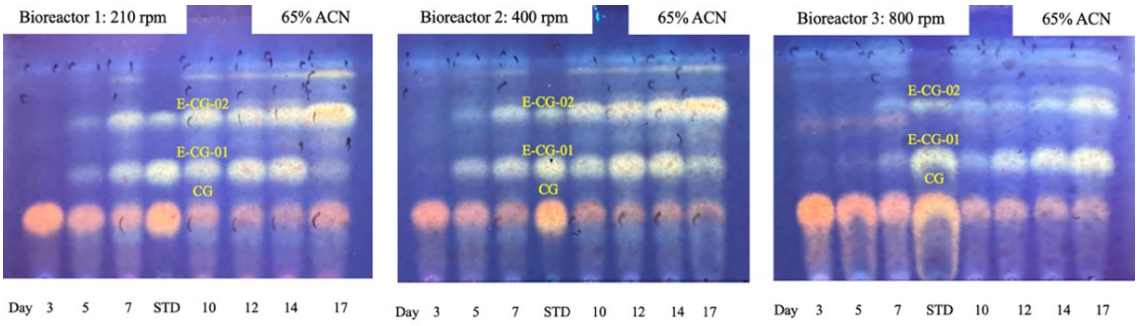

Chromatogram 4.17. Thin layer chromatograms of the agitation speed study performed on CG. A) Bioreactor C1, b) Bioreactor C2, c) Bioreactor C3. [Reverse phase C18 silica gel, Mobile phase: 65:35 (ACN: H_2O)]. (5000 ppm sample was prepared for each extract, and each was spotted four times).

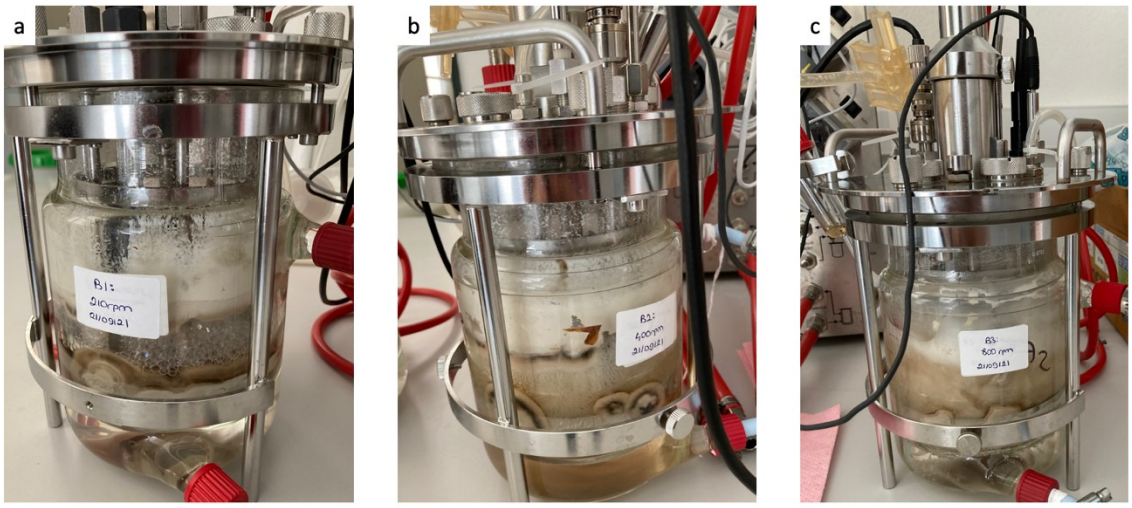

Figure 4.27. Bioreactor studies with different agitation speeds. A) Bioreactor C1, b) Bioreactor C2 and c) Bioreactor C3.

For E-CG-01, the maximum concentration was reached on the 3rd day of the optimization studies (250 mL shake flasks). In bioreactor studies, the maximum concentration of E-CG-01 was reached on day 12. This shows that the adaptation process of the fungus is quite long in the bioreactor resulting in low productivity.

Since we obtained higher efficiency in 5 L shake flask experiments in the preliminary studies, we decided to use 5 L flasks as part of scale-up experiments as an alternative to bioreactor systems. Thus 5 L shake flask experiments were designed before proceeding large-scale bioreactor step.

4.3.9. Microbial Biotransformation Studies in 5 L Shake Flaks

The time-dependent changes in the concentrations of target metabolites measured in 5 L flasks are given in Figures 4.28, 4.29 and 4.30.

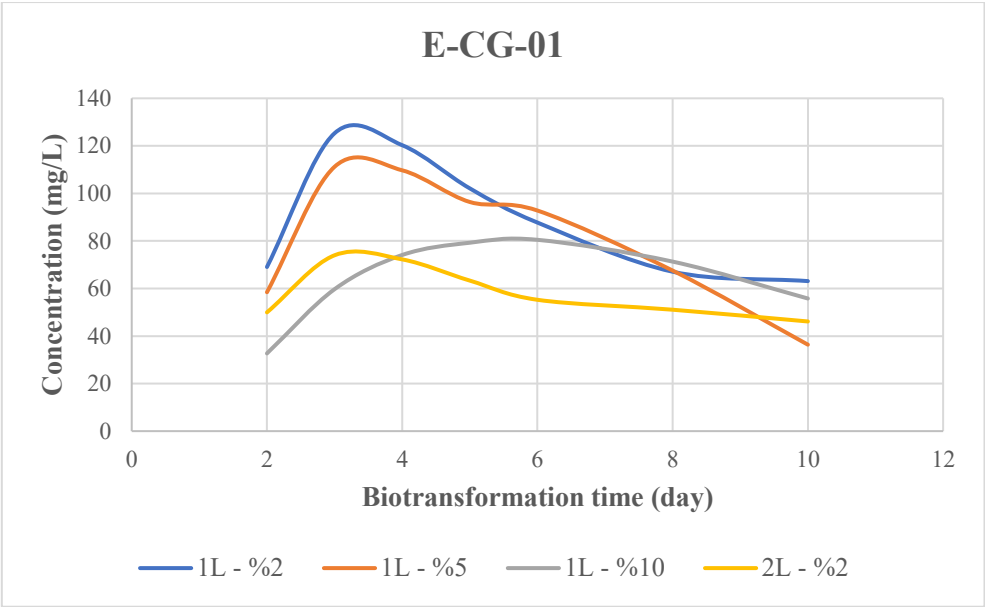

Figure 4.28. Time-dependent variation of E-CG-01 concentration in the production of 5 L shake flasks.

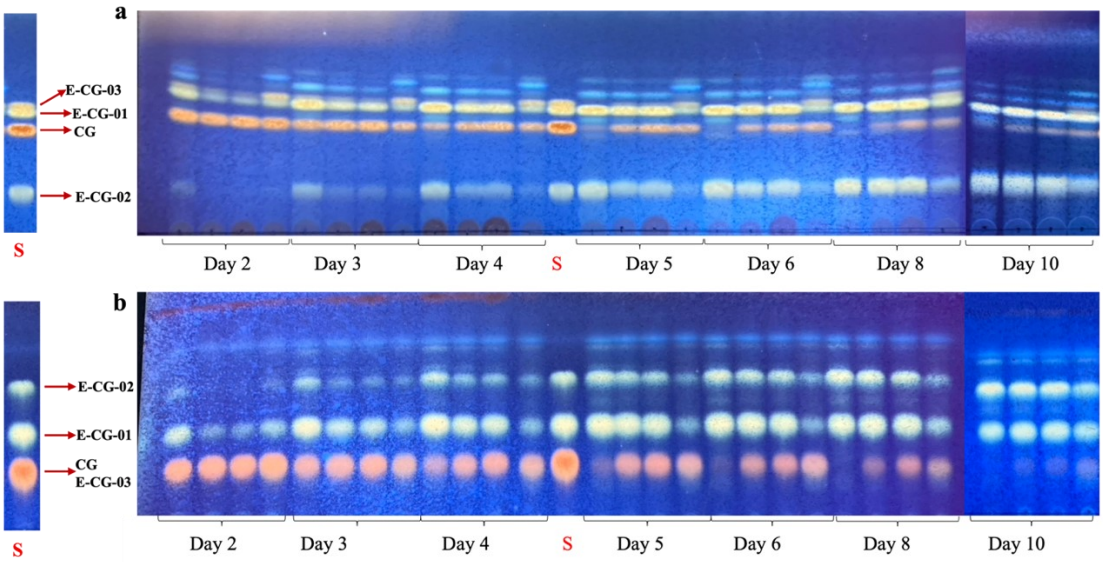

Chromatogram 4.18. Thin layer chromatogram of the 5 L shake flask study performed on CG, 1L – 2%, 1 L – 5%, 1 L – 10% and 2L- 2% for each day, respectively: a) Silica gel, Mobile phase: 90:10:0.1 ($CHCl_3$:MeOH:H_2O)] b) Reverse phase C18 silica gel, Mobile phase: 70:30 (ACN: H_2O).

The highest E-CG-01 concentration (125 mg/L) was found in the broth on day 3, and its concentration decreased starting from day 4 (Figure 4.29). The highest production efficiency was obtained in 1 L working and 2% inoculation volumes. According to the TLC analysis of day 3, there was still a non-transformed substrate (CG) in the broth, but the amount of E-CG-02, the end-product, was relatively low (Chromatogram 4.19). Termination of production on the 3rd day would provide high amounts of E-CG-01, and the remaining CG could be recovered.

When the graphs for E-AG-01 and E-AG-02 were examined, it was observed that the concentrations of the metabolites increased rapidly from day 2 to 4 and reached equilibrium after day 6 (Figures 4.29 and 4.30, Chromatogram 4.19). The highest concentrations for E-AG-01 and E-AG-02 were 86 mg/L and 55 mg/L, respectively. While the optimum condition for E-AG-01 was 1 L working and 2% inoculation volumes, the optimum condition for E-AG-02 was 1 L working and 10% inoculation volumes. The biotransformation time for AG metabolites was consistent with the optimization studies performed in 250 mL shake flasks.

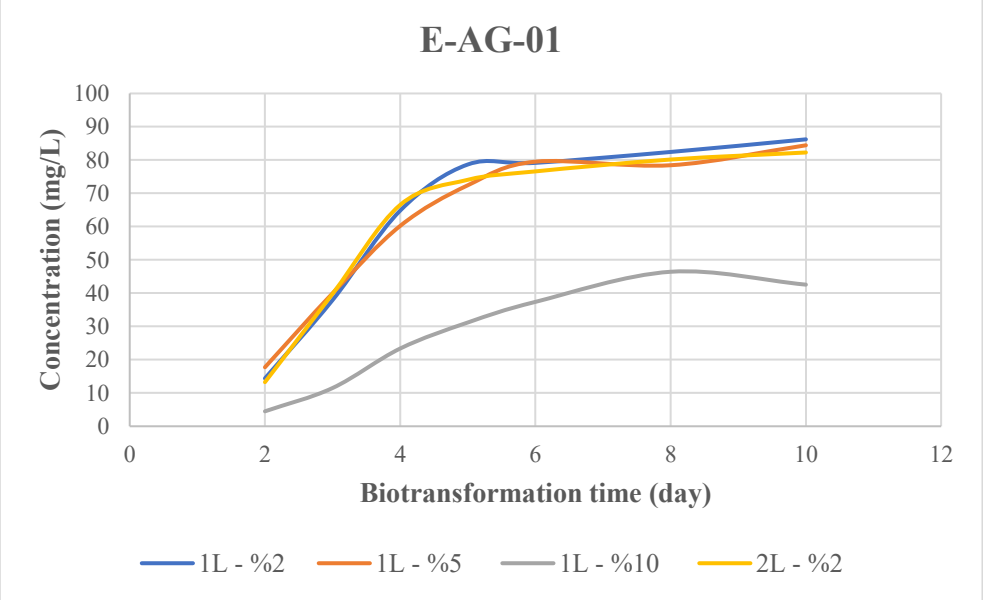

Figure 4.29. Time-dependent variation of E-AG-01 concentration in the production of 5 L shake flasks.

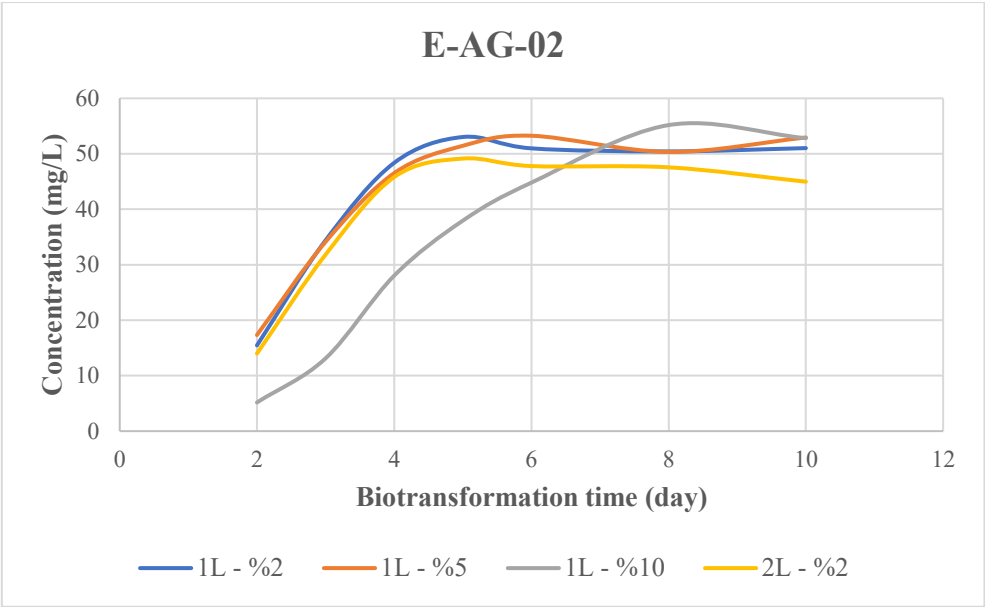

Figure 4.30. Time-dependent variation of E-AG-02 concentration in the production of 5 L shake flasks.

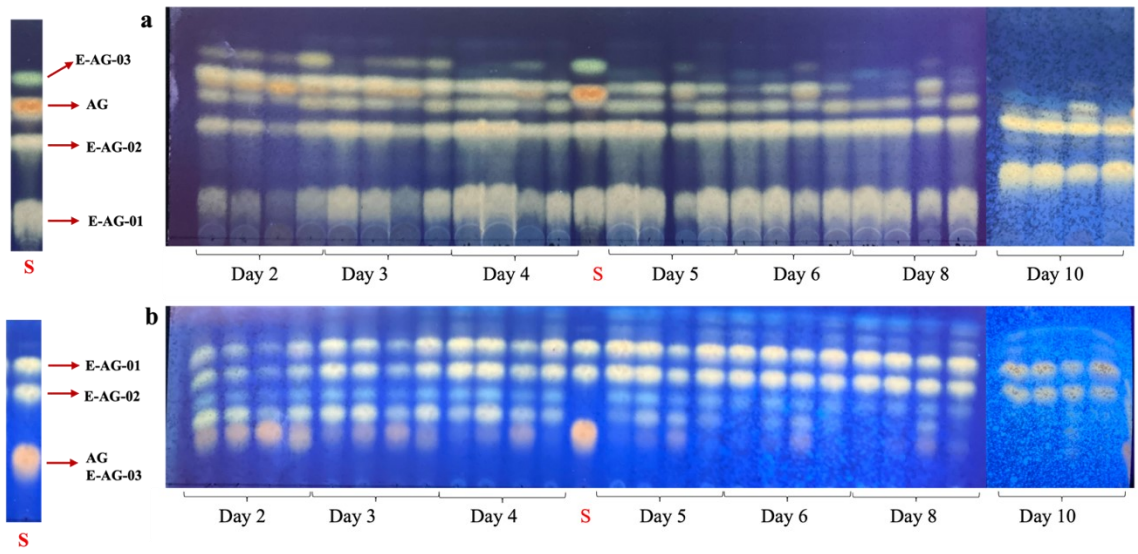

Chromatogram 4.19. Thin layer chromatogram of the 5 L shake flask study performed on AG, 1L – 2%, 1 L – 5%, 1 L – 10% and 2L- 2% for each day, respectively: a) Silica gel, Mobile phase: 10:10:3 (*n*-hexane:EtOAc:MeOH)] b) Reverse phase C18 silica gel, Mobile phase: 70:30 (ACN: H_2O)].

As a result of these studies, the target production yields for E-CG-01 and E-AG-01 were almost reached. The efficiency was increased 1.95-fold for E-CG-01, 55-fold for E-AG-01, and 13-fold for E-AG-02. To get to the target for E-AG-02, the yield should be increased 2-fold more.

An additional experiment set was planned to increase the E-AG-02 concentration (Table 4.12). According to the results, the highest concentration of E-AG-02 (81 mg/L) was obtained in Flask B4. The concentration of E-AG-01 (110 mg/L) also increased under these production conditions (Figures 4.31 and 4.32).

In Flask B4, cyclohexanone was used as a different source of xenobiotics. It has been reported that this compound is degraded using similar biotransformation reactions and microorganisms use it as a carbon source[163–165]. The dosing strategy in Flask B3 increased the E-AG-01 concentration but did not increase the E-AG-02 concentration. Adding a different substrate increased the yield of both AG metabolites (Figures 4.31 and 4.32). The strategy applied in Flask B5, stopping the production and feeding it back to the new medium after extraction, did not provide the expected increase in yield (Figure 4.33).

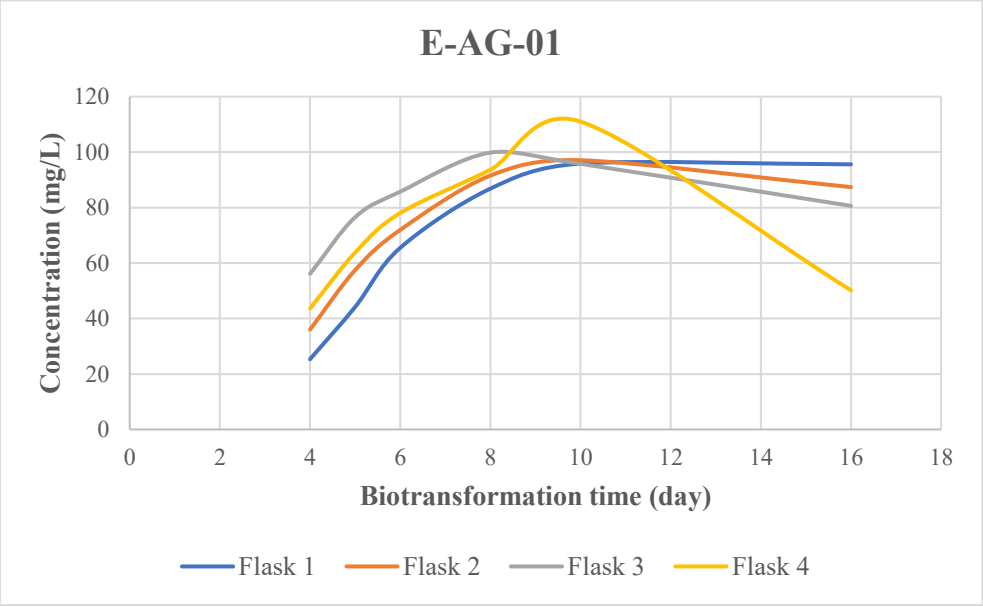

Figure 4.31. Time-dependent variation of E-AG-01 concentration in the further studies.

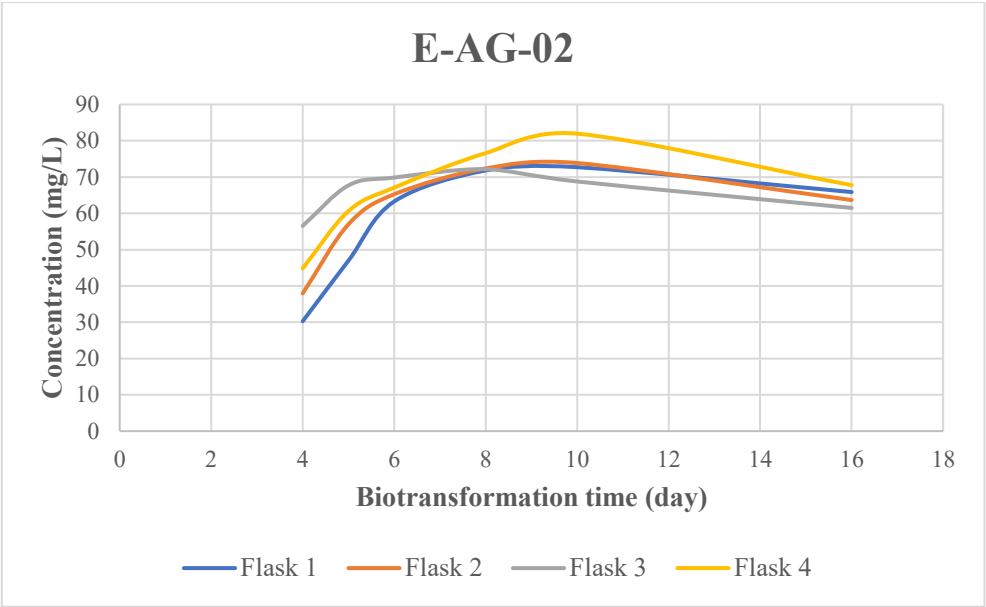

Figure 4.32. Time-dependent variation of E-AG-02 concentration in the further studies.

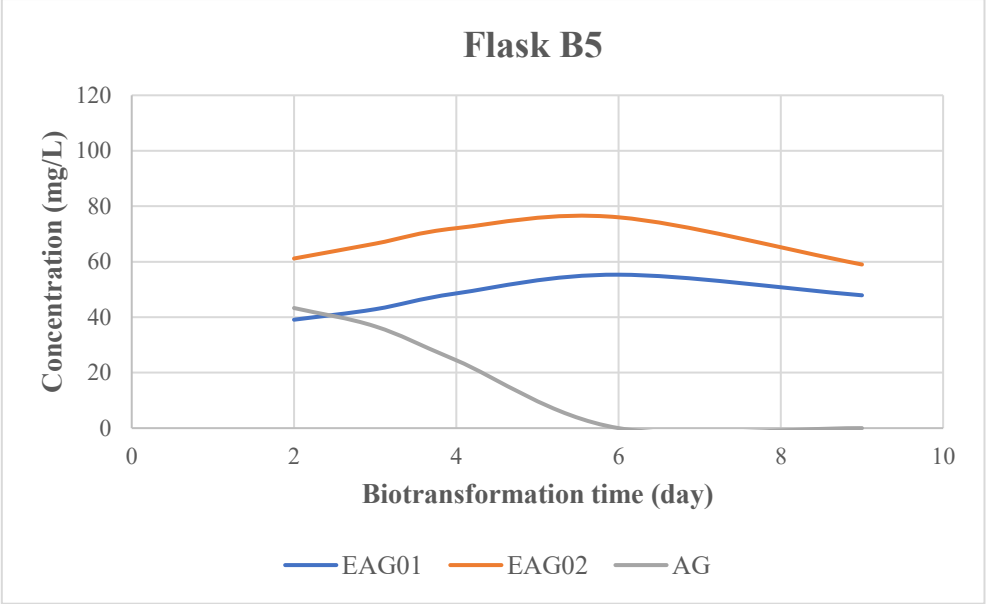

Figure 4.33. Time-dependent variation of AG, E-AG-01, and E-AG-02 concentration in the Shake Flask B5.

Table 4.32 summarizes the results of 5 L shake flask experiments. According to these results, the efficiency was increased 1.95-fold for E-CG-01, 70-fold for E-AG-01, and 19-fold for E-AG-02.

Table 4.32. Yields obtained at different production steps for target metabolites.

Target Metabolite	Initial Yield (%)	Targeted Yield (%)	Results of Optimization Studies in 250 mL flask (%)	Results of 5 L Flask (%)
E-CG-01	32	75	25	62.5
E-AG-01	0.78	50	21	55
E-AG-02	2.12	60	35	40.5

4.3.10. Bioreactor Studies: 7.7 L

In the preliminary bioreactor (1 L) studies, the highest concentration of E-CG-01 was measured as 60 mg/L on day 8. This shows that the adaptation process of the fungus is quite long in the bioreactor resulting in low productivity. Neither microparticle addition nor different agitation speed prevented the pellet formation. Also, it was observed that the microorganism could not use the substrate due to the formation of a substrate film layer on the upper parts of the bioreactors. In 5 L shake flask studies, hyphal growth was observed, and there was no large pellet formation. When we compared the yields of bioreactors and shake flask experiments, we concluded that inhibition of pellet formation positively affects the production yields. Considering that the mechanical mixing used in the stirred tank bioreactor damaged microorganisms and induced pellet formation, a different bioreactor design was evaluated for large-scale production.

Pneumatic bioreactors are cylindrical vessels with a gas inlet at the bottom. The gas inlet causes a turbulent stream to enable an optimum gas exchange. The mixing is done by gas sparging, requiring less energy than mechanical stirring. These bioreactors are advantageous systems for shear-sensitive productions[166].

The most used systems in pneumatic bioreactors are bubble column and airlift bioreactors. The difference is that the airlift bioreactor has an inner tube, while the bubble column bioreactor does not (Figure 4.34).

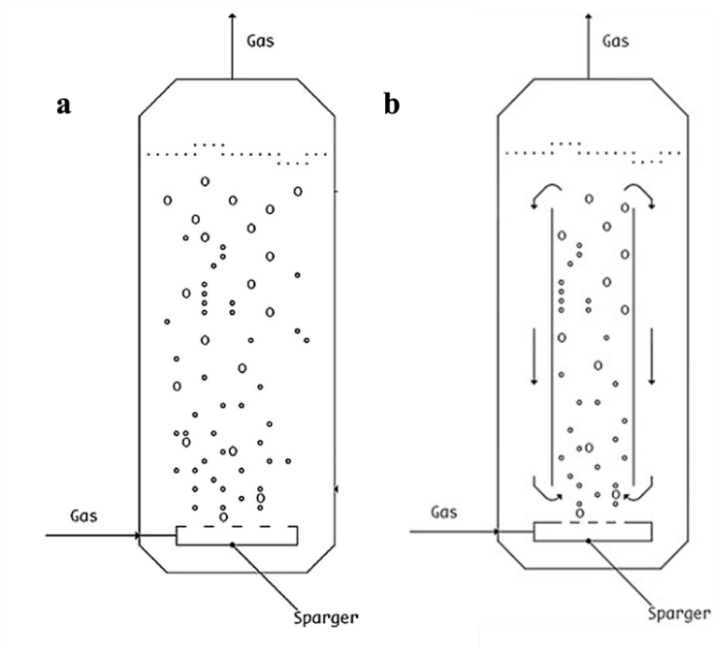

Figure 4.34. Principles of pneumatic bioreactors. a) Bubble column bioreactor, b) Airlift bioreactor[166].

In Bioreactor D1, *C. laburnicola* was produced for system control, and no substrate was added. The process conditions used in these trials are presented in Table 4.14. Since it was impossible to make an observation inside the system due to its stainless-steel structure with no window, the presence of microbial growth was checked by pH monitoring. The time-dependent variation of pH in Bioreactor D1 is given in Figure 4.35. According to this graph, pH decreased after day 4 and reached 3.52 on day 11. The decrease in pH indicated microbial growth, and this data was consistent with our results in our shake flask and 1 L bioreactor studies.

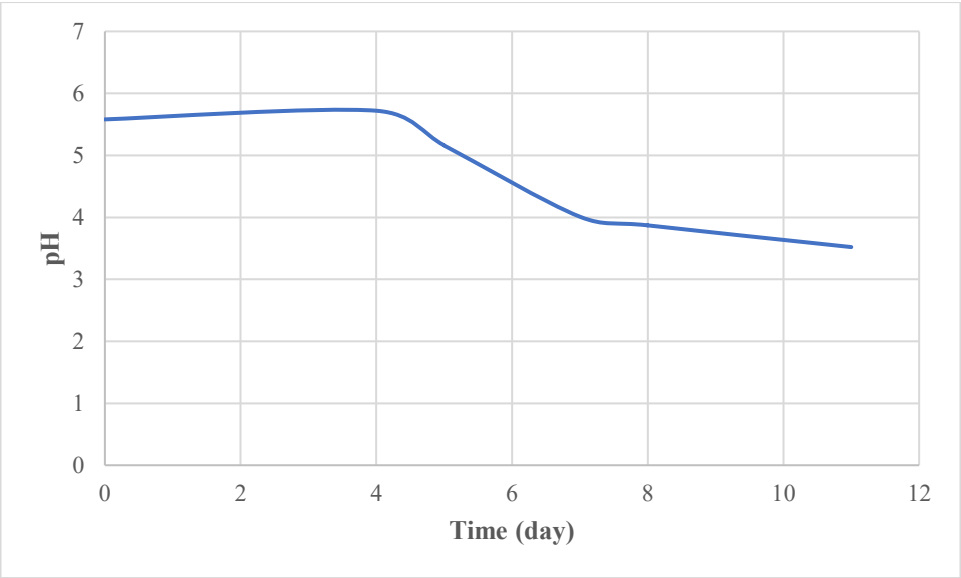

Figure 4.35. Time-dependent variation of pH in Bioreactor D1.

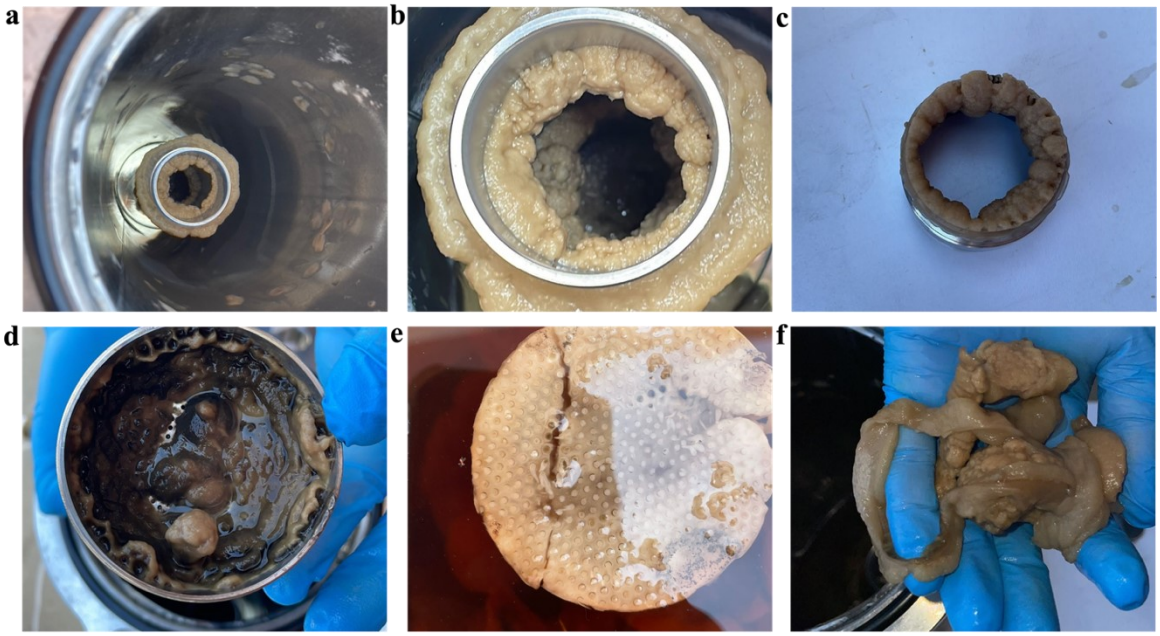

Figure 4.36. Pellet formation on the inner tube (a, b, c and f) and sparger (d and e) in Bioreactor D1.

Bioreactor D1 was terminated on day 11. A morphological examination was performed after opening the system, and there was no contamination trace inside. However,

pellet formations were observed around the inner tube, especially on the sparger. The color of the fungal pellets was like the color of young micelles. Cells interacting directly with the air around the sparger appeared to have the color of mature micelles (Figure 4.36). Although there was growth on the sparger, there was no backpressure problem during production.

In Bioreactor D2, CG was fed to the system. The water solubility of the AG and CG is relatively low. For this reason, these substrates are generally dissolved in DMSO and then fed to the medium. Since there was continuous shaking in 5 L shake flask studies, the substrate was quickly dispersed in the broth. In stirred tank bioreactor (1 L) studies, the substrate was distributed in the broth by mixing. The air supply was turned off to prevent foam formation and upward substrate transport. However, the formation of foam and a substrate film layer on the upper surface could not be prevented. The biggest challenge in the pneumatic mixing system is the inability to distribute substrate in the broth properly. Therefore, CG dissolved in DMSO was suspended in approximately 200 mL sterile medium to prevent precipitation while feeding into the bioreactor. However, CG has formed aggregates and precipitated over time. To avoid increasing broth volume, CG was fed to the system in this way. Also, three mL of antifoam solution was added to the system to break the foam. The foam was determined in the sample taken on day 1. For this reason, 2 mL of antifoam was added to the system. No foam was observed in the sample taken after the addition of antifoam. However, it was observed that there were CG aggregates in the sample taken. The production of E-CG-01 started on day 4. However, CG was not wholly depleted in samples taken for 10 days. Based on pH measurement and TLC analysis, production was terminated on day 10. When the bioreactor was opened, pellet formation was observed around the inner tube. It was also observed that the substrate remained above the broth (Figure 4.38).

The time-dependent variation of pH and E-CG-01 concentration in Bioreactor D2 is given in Figure 4.37. According to Figure 4.38, pH decreased from the 1st day of biotransformation, which indicates microbial growth. The highest E-CG-01 concentration (27 mg/L) was found in the broth on day 9. In addition, E-CG-02, the final product of CG, was produced starting from day 5 (Chromatogram 4.20).

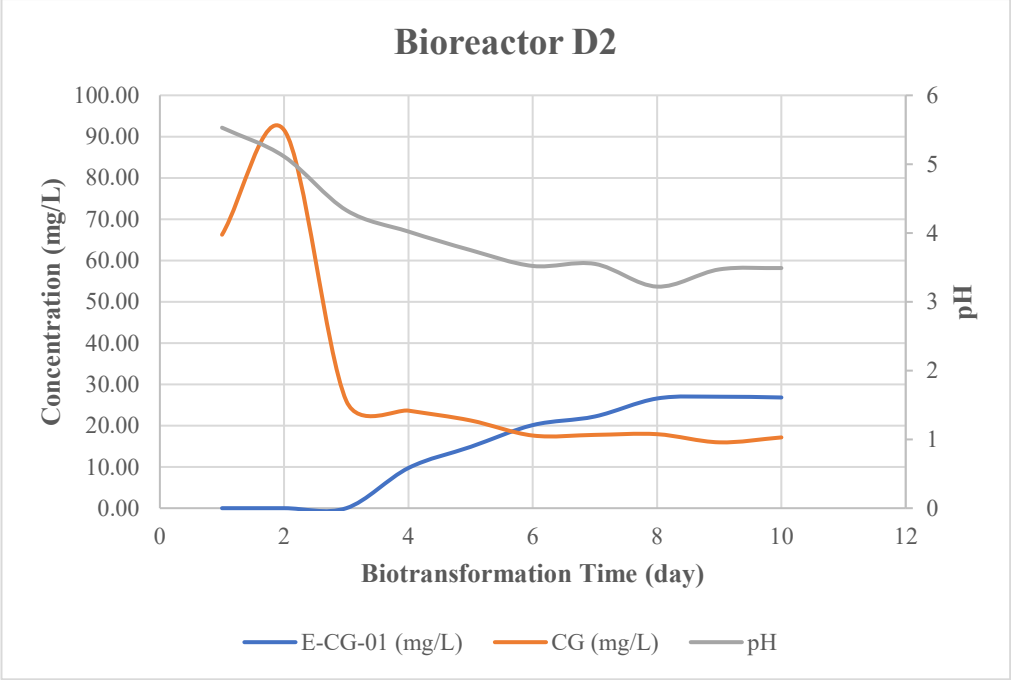

Figure 4.37. Time-dependent variation of pH and concentration of metabolites in Bioreactor D2.

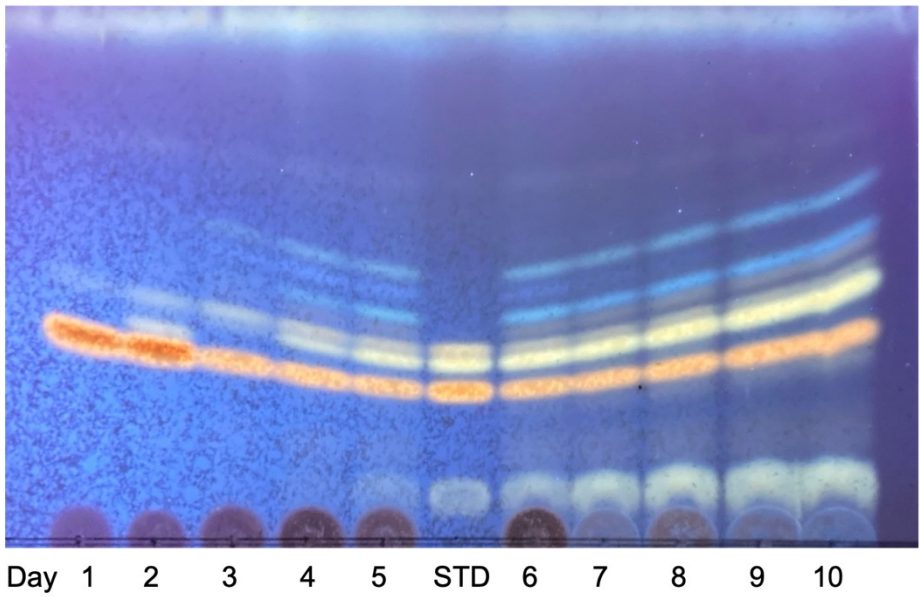

Chromatogram 4.20. Thin layer chromatogram of the Bioreactor D2 [Silica gel, Mobile phase: 90:10:0.1 ($CHCl_3$:MeOH:H_2O)].

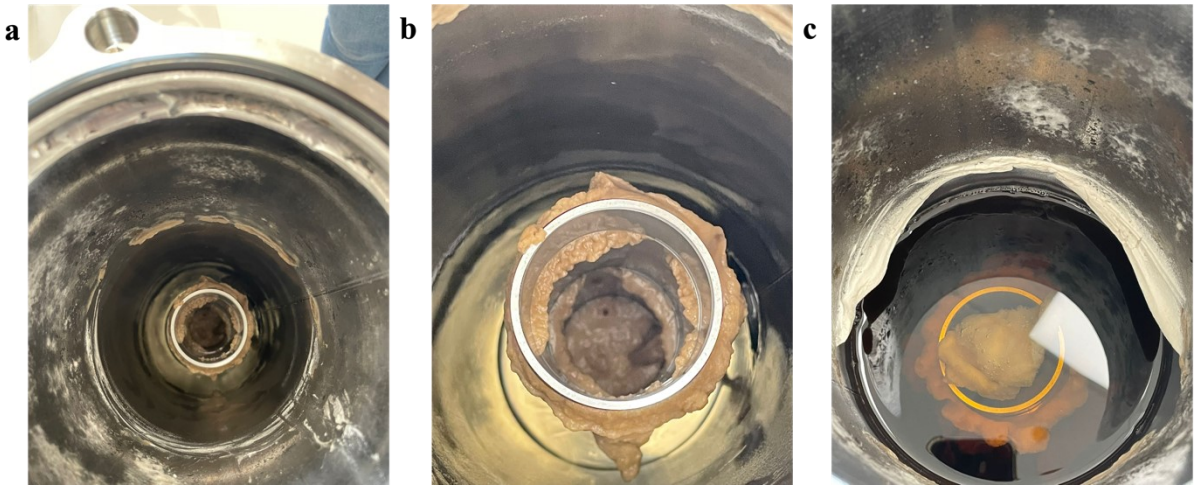

Figure 4.38. Pellet formation on the inner tube (a and b) and substrate remaining on the surface in Bioreactor D2.

In Bioreactor D3, it was planned to carry out production without an inner tube (as a bubble column bioreactor) and feed CG into the system by dissolving it in EtOH. This production aimed to prevent the formation of pellets by eliminating the surface on which the fungus adheres and ensuring that the substrate was effectively dispersed in the broth.

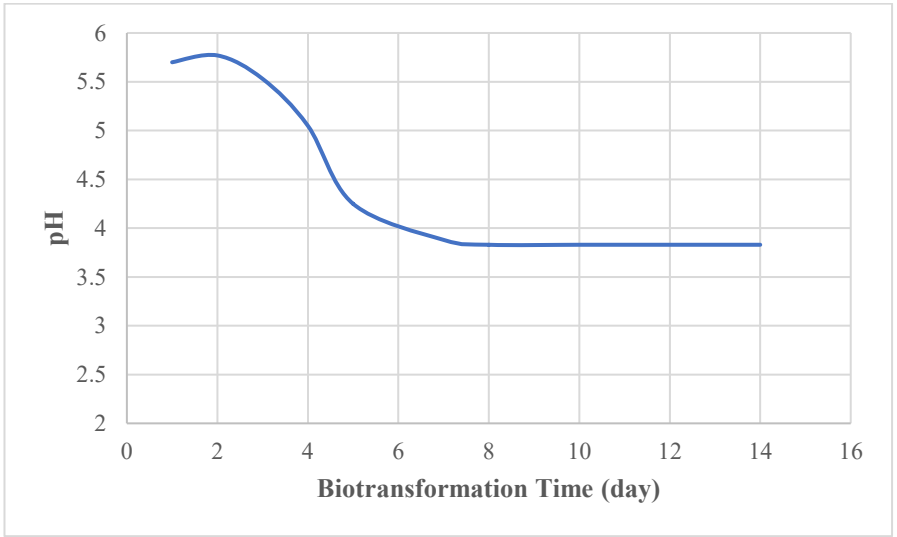

Figure 4.39. Time-dependent variation of pH in Bioreactor D3.

Unfortunately, the formation of E-CG-01 in Bioreactor D3 started on day 11, and E-CG-02 production was considerably less than in Bioreactor D2 (Chromatogram 4.21). In addition, the problems encountered in Bioreactors D1 and D2 (pellet and foam formation) still needed to be overcome.

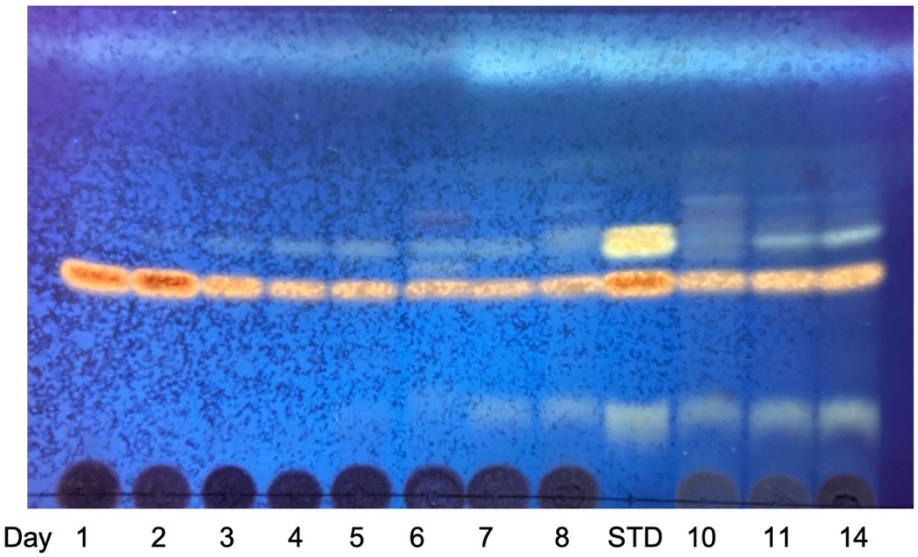

Chromatogram 4.21. Thin layer chromatogram of the Bioreactor D3 [Silica gel, Mobile phase: 90:10:0.1 ($CHCl_3$:MeOH:H_2O)].

4.4. Discussion

Whole cell biotransformation is an important tool in the production of pharmaceuticals due to their low cost (approx. ten times lower cost than purified enzymes), ability to catalyze cofactor-dependent reactions, and to catalyze multistep reactions with the combination of enzymes. In addition to these advantages, whole-cell biotransformation has disadvantages, such as low selectivity and undesirable side reactions. Fortunately, several strategies have been developed to avoid these disadvantages, such as synthetic biology and metabolic engineering toolboxes. In this way, industrial use of whole-cell biotransformation

is possible[62,136,167,168]. In addition to these strategies, process optimization with the design of experiment approach emerges as a lower-cost strategy[143,146,147].

A newly discovered fungus, *Camarosporium laburnicola*, has played an important role in producing potent telomerase activators by catalyzing the multistep enzymatic reaction in our previous studies[48,50]. However, increasing the production yields of the target metabolites is necessary for the transition to industrial production. In this context, the design of experiment approach was used to improve the yields of our target metabolites (32% → 75% for E-CG-01; 0.78% → 50% for E-AG-01; 2.12% → 60% for E-AG-02).

Initially, PBD was used to analyze the parameters thought to be effective on biotransformation and to subtract those that were not statistically effective. The parameters screened with PBD were temperature, pH, inoculant, substrate concentration, Tween 80 concentration, substrate feeding time, biotransformation time, working volume and shaking speed. Subsequently, CCD trials were carried out to find the optimum values for the three parameters (temperature, biotransformation time, and shaking speed), which were determined to be effective according to the PBD trials. 2^3 full factorial CCD was selected to evaluate the individual and combined effects of temperature, biotransformation time and shaking speed. In these trials, the lower and upper limits of the parameters were selected as 17-33 °C for the temperature, 1-11 days for the biotransformation time and 130-230 rpm for the shaking speed to evaluate the effects in a wider range.

The experiment results were interpreted through contour graphs obtained with the Design Expert 12 program. The optimum temperature and shaking speed for E-AG-01 and E-AG-02 were 22 °C and 180 rpm, respectively. As a result of the OFAT study for biotransformation time, the maximum production conditions were obtained on 7 days and 10 days for E-AG-01 and E-AG-02, respectively. Under these conditions, the maximum yield was 20% for E-AG-01 and 35% for E-AG-02. While E-AG-01 yield increased by 25.6-fold, E-AG-02 yield improved by 16.5-fold compared to non-optimized conditions. For E-CG-01, the maximum yield was reached at two conditions (22 °C, 180 rpm, 9 days, and 20 °C, 210 rpm, 3 days). Considering that time is an important parameter in industrial production, 20 °C, 210 rpm, 3 days were determined as the optimum conditions for maximum production. Although 23% efficiency was obtained in time-course studies, a 0.72-fold decrease was obtained compared to non-optimized conditions.

During the optimization studies, we observed that the fungus developed pellet structures. Growth of filamentous fungi can display dispersed or aggregated pellet structures in submerged culture[161,162]. Dispersed mycelia result in high biomass concentrations, highly viscous fermentation media, and restrictions in gas-liquid transfer, while complex pellets cause limitations in the mass transfer of substrates, products, and oxygen[169]. Therefore, the morphology of fungal growth is highly linked with process control and productivity and depends on the type of production[161,162,170]. For example, pellet formation increases lactic acid and fumaric acid production for *Rhizopus oryzae*[171], while filamentous growth enhances higher alpha-amylase productivity for *Aspergillus oryzae*[172]. Hence, processes should be designed based on the nature of filamentous fungi and desired products. The main factors that trigger pellet formation are electrostatics, hydrophobicity, and interactions between spore wall components. Since the surface of the fungus has a negative charge, pH and ionic strength of the medium can easily affect pellet formation. Several strategies were reported to prevent pellet formation, such as high agitation speed, adjustment of pH and medium composition, aeration rate, and bioreactor design[162,169,170,173]. Based on this information, we continued with bioreactor studies to solve the pellet problem, increase yield, and scale up.

Bioreactors provide a more controlled environment for microorganisms by controlling and interfering with pH, dissolved oxygen, and foam formation. Therefore, we carried out productions in 1 L bioreactors. In addition to the optimization studies of pH and aeration parameters, studies were also carried out for microparticle addition and agitation speed to prevent pellet formation. Unfortunately, this problem has not been overcome, and fungus exhibited pellet formation on the stainless-steel parts of the bioreactor. In addition to this, foam formation was also observed together with aeration. Foam formation led to the accumulation of starting compound on the upper side walls of the bioreactor and loss of starting compound. Although the maximum yield of E-CG-01 increased to 30%, productivity decreased (approx. 3-fold) compared to 250 mL shake flask studies. It has been reported that using different impellers can prevent pellet formation in mechanically stirred bioreactors[170]. However, we were not able to purchase different impellers due to funding issues. For this reason, we decided to carry out productions in 5 L shake flasks as an intermediate step before larger-scale bioreactor productions.

In the 5 L shake flask studies, two different working volumes (1 L and 2 L) and three different inoculant volumes (2%, 5% and 10%) were studied, considering our preliminary studies. Inoculation volume was found to be a non-significant parameter in PBD. Therefore, this parameter was not involved in optimization studies. However, as the scale is enlarged, the inoculation volume will also increase, and in parallel, it will cause an increase in cost. Furthermore, inoculum volume is directly correlated with pellet formation[162]. Hence, we decided to optimize inoculum volume at this stage. During production in 5 L flasks, the fungus formed filamentous structures. According to production yields, dispersed structures directly affected the production yield. As a result, we obtained a 62.5% yield for E-CG-01, 42.5% for E-AG-01 and 27.5% for E-AG-02. For E-CG-01 and E-AG-01, 2% inoculant and 1L working volume resulted in the maximum yield, while 10% inoculant and 1 L working volume gave the maximum yield for E-AG-02. However, we couldn't reach the targeted yield for E-AG-02. The reasons for low E-AG-02 concentration can be listed as follows: i) a decreased amount of carbon source in the environment, ii) stopping the biochemical reaction chain due to the reduction of the xenobiotic source (starting compound) in the environment, iii) *C. laburnicola* enters the stationary phase, slowing down the biotransformation reactions, which are considered part of primary metabolism. Adding a different xenobiotic to the broth was the most effective strategy among these approaches. As a result of this study, the yields of E-AG-01 and E-AG-02 increased to 55% and 40.5%, respectively.

At the last stage of scale-up studies, production trials were carried out in an pneumatic bioreactor. In this bioreactor system, mixing is done by aeration instead of using a mechanical stirrer. Aeration provides more moderate mixing and prevents shear stress in these systems. However, pellet formation was observed on the sparger and draft tube. In addition, the substrate was not sufficiently mixed, and a large amount of substrate accumulated on the upper side walls of the bioreactor as in a mechanical stirring bioreactor. The maximum yield of E-CG-01 was %14, and the productivity was lower than 1 L bioreactors.

C. laburnicola catalyzes oxidation, Baeyer-Villiger oxidation, ring opening and dehydration reactions, respectively. In the literature, there are examples of whole-cell systems that catalyze similar reactions on triterpenoids. Fungal biotransformation studies on pentacyclic triterpenoids form 3(4)-seco derivatives, whereas lactone formation is less common[174–180]. However, the yields were relatively low in fungal biotransformation studies.

Shen et al. (2022) reported a biotransformation study on ursane and oleanane-type triterpenoids using *Streptomyces olivaceus* CICC 23628, an actinobacterium. Although 3(4)-seco derivatives were obtained with high yield, hydroxylation reactions occurred afterward in this study[181]. There are biotransformation studies on tetracyclic triterpenoids only with *Glomerella fusarioides*. The study on eburicoic acid is the first example of an A-ring opening reaction[182]. In the biotransformation studies on cycloastragenol and astragenol, lactone and 3(4)-seco derivatives were obtained in low yield, and additional modifications at C-11 were observed[74]. Nevertheless, optimization of whole-cell biotransformation for yield increment was not performed in any of these studies.

In addition, our group also tested *C. laburnicola* on different molecular skeletons (ruscogenins, progesterone, gitoxigenin, betulin, glycyrrhetinic acid, madecassic acid, asiatic acid) and found that *C. laburnicola* biotransforms only cycloartane-type triterpenoids (cycloastragenol, astragenol, cyclocanthogenol, 20(27)-nor cycloastragenol, cyclocephagenol).

In this study, the biotransformation process of a whole cell system catalyzing oxidation – Baeyer Villiger oxidation – ring cleavage reactions was optimized for the first time. Although the targeted outputs could not be achieved in the bioreactor studies, the scale-up studies were concluded successfully in the shake flasks. As a result of this study, significant increases were obtained in the yield of target metabolites: 1.95-fold for E-CG-01, 70-fold for E-AG-01, and 19-fold for E-AG-02.

CHAPTER 5

EXTRACTION, ISOLATION AND CHARACTERIZATION OF THE ENZYMES FROM *CAMAROSPORIUM LABURNICOLA*

5.1. Background

In the 114Z958-TÜBİTAK project, *Camarosporium laburnicola*, an endophytic fungus isolated from *Astragalus* sp., has been determined as a potent biocatalyst that is involved in the production of potent telomerase activators. As a result of our biotransformation studies on different skeletons, we observed that *C. laburnicola* only makes modifications on the cycloartane skeletons. For this reason, we planned to carry out isolation and characterization studies of the enzymes of this fungus.

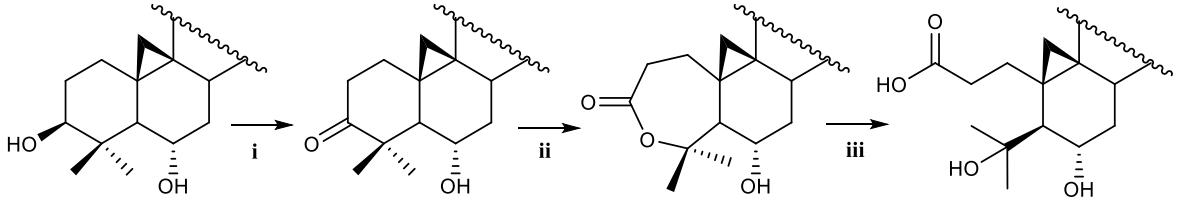

Figure 5.1. The proposed biochemical reaction chain for modifications occurring in the A ring. i) Dehydrogenase enzyme, ii) BVMO enzyme, iii) Lactone hydrolase enzyme.

Based on the TLC and HPLC analyses and the literature, we estimated that a sequential biochemical reaction chain produces the target metabolites by biotransformation

with *C. laburnicola*. The proposed reaction chain catalyzed proceeds as follows: i) Conversion of the secondary alcohol at C-3 to a ketone with a dehydrogenase enzyme; ii) Formation of the 7-membered lactone ring by the BVMO enzyme; iii) A lactone hydrolase opens this ring to give the 3(4)-seco ring A (Figure 5.1)[78,181,183–185].

5.1.1. Baeyer Villiger Monooxygenases

The Baeyer-Villiger reaction is expressed as the conversion of ketones to esters and cyclic ketones to lactones by using peracids as oxidants. This discovery by Adolf von Baeyer and his student Victor Villiger has gained an important place in synthetic organic chemistry. Since then, it has been used in many reactions, from the synthesis of steroids, antibiotics, and pheromones to the polymerization of monomers. The major advantages of Baeyer-Villiger oxidation are the ability to oxidize products containing only carbonyl groups, being tolerant to other functional groups, working with many oxidants, and being stable[78,186]. Despite these advantages, classical Baeyer-Villiger oxidation also has disadvantages such as low chemo-, regio- and enantioselectivity, narrow substrate range, the requirement to use organic peracids, unstable organic peracids, and high cost. Therefore, the interest in biological Baeyer Villiger monooxygenase (BVMO) applications has increased due to the preference for enzymatic/microbial systems over the use of strong acids within the scope of green chemistry applications[78,187–189].

The first discovery that Baeyer-Villiger reactions occur in biological systems was the identification of the 7-membered ring by the oxidation of cholestane in *Proactinomyces erythropolis* in 1948[190]. Biotransformation of progesterone with *Penicillium chrysogenum* and its conversion to testolactone with 70% efficiency is shown as the first evidence for lactone formation[191]. As a result of the biotransformation study of eburicoic acid with *Glomerella fusarioides*, the A-ring opened structure was the first example of A-ring degradation, and the mechanism of A-ring opening was explained with this example[182]. In biotransformation studies of cycloastragenol and astragenol molecules with *G. fusarioides* ATCC 9552, A-ring opening and lactone formation were also seen in biotransformation

studies conducted by our group[74,76]. Within the scope of our previous project (114Z958), one of the isolated endophytic fungi, namely *C. laburnicola,* produced the same metabolites as *G. fusarioides*. However, yields were higher than *G. fusarioides*, and less metabolite diversity was observed compared to *G. fusarioides*.

Many of the reported BVMO enzymes are found to be soluble in the cytoplasm, unlike P450 monooxygenase enzymes. BVMOs, which are under the class of flavin-dependent monooxygenases, are grouped according to their cofactors and the reactions they catalyze[78,187,192–194].

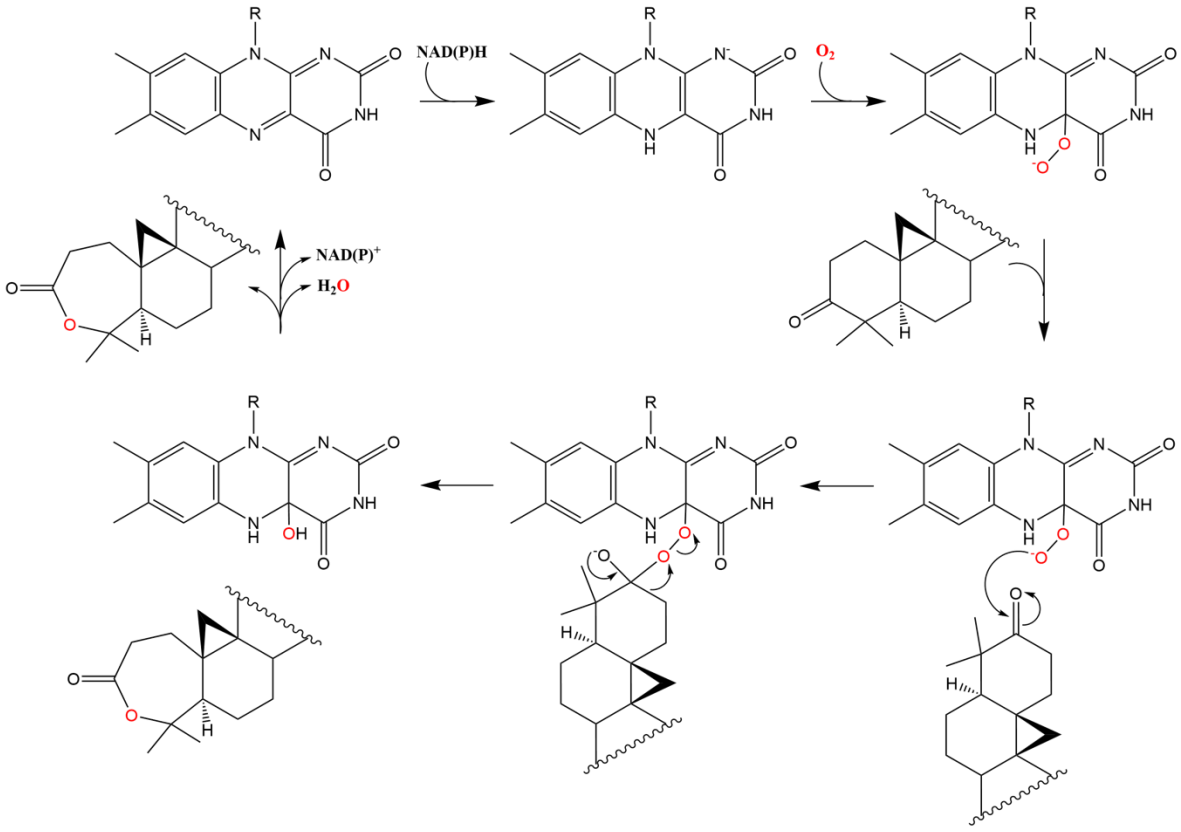

Figure 5.2. Catalytic mechanism of type I BVMOs[193].

Type 1 BVMO enzymes consist of a single polypeptide chain, tightly bound to flavin adenine dinucleotide (FAD), and use NADPH as a cofactor. It has the Rossmann motif (GxGxxG) indicating the binding site of these cofactors and carries the sequence

FXGXXXHXXXWP specific to the Type 1 BVMO class. During the BV oxidation reaction, the FAD cofactor remains tightly bound during catalysis. The reaction follows i) FAD is reduced by NADPH, which remains bound during catalysis, and molecular oxygen is used to generate a C4a-peroxyflavin intermediate, ii) peroxyanion-species performs a nucleophilic attack on the carbonyl carbon of the substrate, iii) the tetrahedral Criegee intermediate is formed and rearranged to yield the lactone and a hydroxyflavin species, iv) water is released from the flavin, the oxidized flavin species are produced, and the lactone and $NADP^+$ are released. Since $NADP^+$ is the rate-limiting step, $NADP^+$ remains bound during the cycle and leaves as the final group to facilitate efficient catalysis (Figure 5.2)[193,195].

Type 2 BVMO enzyme class contains flavin mononucleotide (FMN) and is NADH dependent. It does not have any fingerprint sequence as in the Type 1 class and generally consists of two different subunits. Another class is called Type O or atypical BVMO. This class is FAD dependent, using NADH or NADPH as cofactors[78,187,192].

Studies with BVMO enzymes focus on the isolation, characterization, and recombinant expression of new enzymes from different microorganisms[183,196–199]. Although many BVMOs have been identified to date, these enzymes are generally expressed in actinobacterium and filamentous fungi, and their genomic distribution appears to be quite specific in this sense[200]. Apart from these, BVMO enzymes have been investigated whether they are involved in primary or secondary metabolism in the cell, and it has been found that they are associated with both metabolisms. BVMO enzymes, which are involved in primary metabolism or catabolic pathways, provide a carbon source and degradation of xenobiotics[193]. A series of enzymes is thought to be involved in the degradation reactions involved in primary metabolism. Ketone structure is required for BVMO enzymes to form lactone/ester structures. For the degradation to take place, i) monooxygenases-hydroxylation, ii) dehydrogenase-ketone formation, iii) BVMO-lactone formation reactions are catalyzed[78,177,183,184]. They are also involved in secondary metabolism and have a crucial role in the biosynthesis of various secondary metabolites[193,200].

Although many BVMO enzymes perform Baeyer-Villiger oxidation, some BVMO enzymes have the ability to catalyze different reactions: Sulfoxidations, epoxidations, N-oxidations, and oxidations of selenium and boron-containing compounds[200].

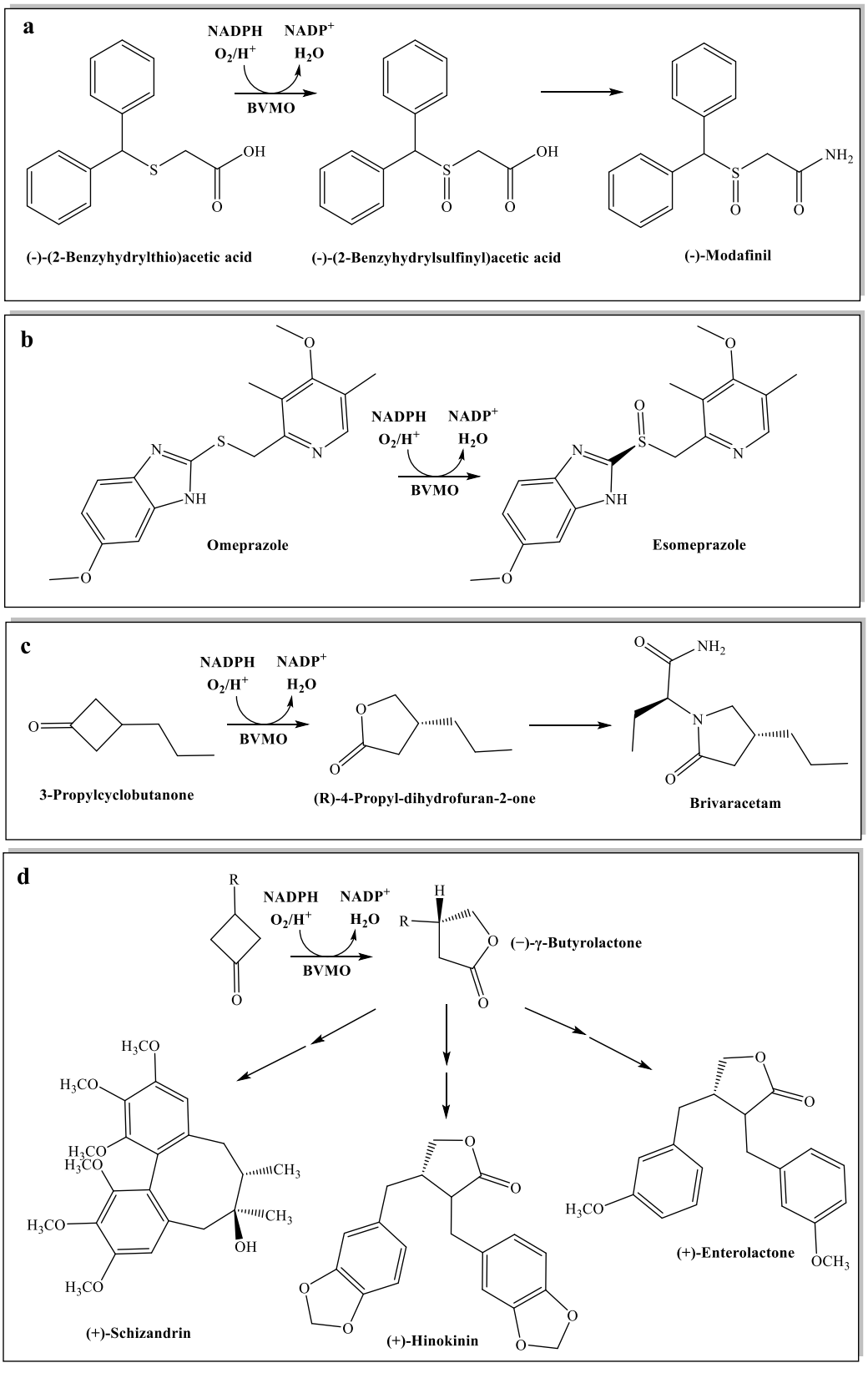

Figure 5.3. Examples of the application of BVMOs in the production of pharmaceuticals and pharmaceutical intermediates[42,201–204].

BVMO enzymes have many uses and can perform industrially important reactions. The first example is the production of β-amino acids. β-amino acids are of industrial importance as building blocks in producing β-peptides, alkaloids, terpenoids, and β-lactam antibiotics[205,206]. Another example is enantioselective sulfoxidation reactions, which make them very attractive to the organic chemical industry. For example, chiral β-hydroxysulfoxides are important building blocks in the production of benzoxathiepins, allyclic alcohols, and macrolides[207,208].

BVMO enzymes can contribute to the production of biologically active compounds by producing optically active compounds. One of them is that these enzymes are involved in the production of testolactone from different steroid starting molecules (dehydroepiandrostenedione, androstenedione, pregnenolone)[209]. Another example is the enantioselective sulfoxidation reaction catalyzed by the BVMOs in producing (-)-modafinil used in narcolepsy and other sleep disorders (Figure 5.3a)[201]. One of the promising examples is the synthesis of esomeprazole, a proton pump inhibitor, by BVMOs. At this point, we emphasize that esomeprazole is used in acid-related diseases and is a multibillion-dollar drug (Figure 5.3b)[202]. In recent years, the use of BVMOs has been patented in the production of brivaracetam, an antiepileptic agent (Figure 5.3c)[203]. Last but not least, the production of BVMO-mediated butyrolactones has the potential to be used as intermediates in the production of many natural products and bioactive molecules such as enterolactone (antitumoral), hinokinin (cytostatic) and schizandrin (antifungal) (Figure 5.3d)[42,204]. However, industrial applications of BVMO enzymes have not been encountered in the literature.

5.1.2. Alcohol Dehydrogenases

Alcohol dehydrogenases (ADHs), which belong to the oxidoreductase superfamily, catalyze the interconversion between alcohols and aldehydes or ketones with high stereoselectivity under mild conditions[210,211]. ADHs use a variety of different cofactors and can be divided into three classes based on their cofactor specificity: NAD(P), pyrollo-

quinoline quinone (PQQ), heme or cofactor F420, and flavin adenine dinucleotide (FAD)[212]. The NAD(P)-dependent ADHs are subclassed into three groups: short-chain ADHs, iron-activated ADHs, and zinc-dependent ADHs[212,213].

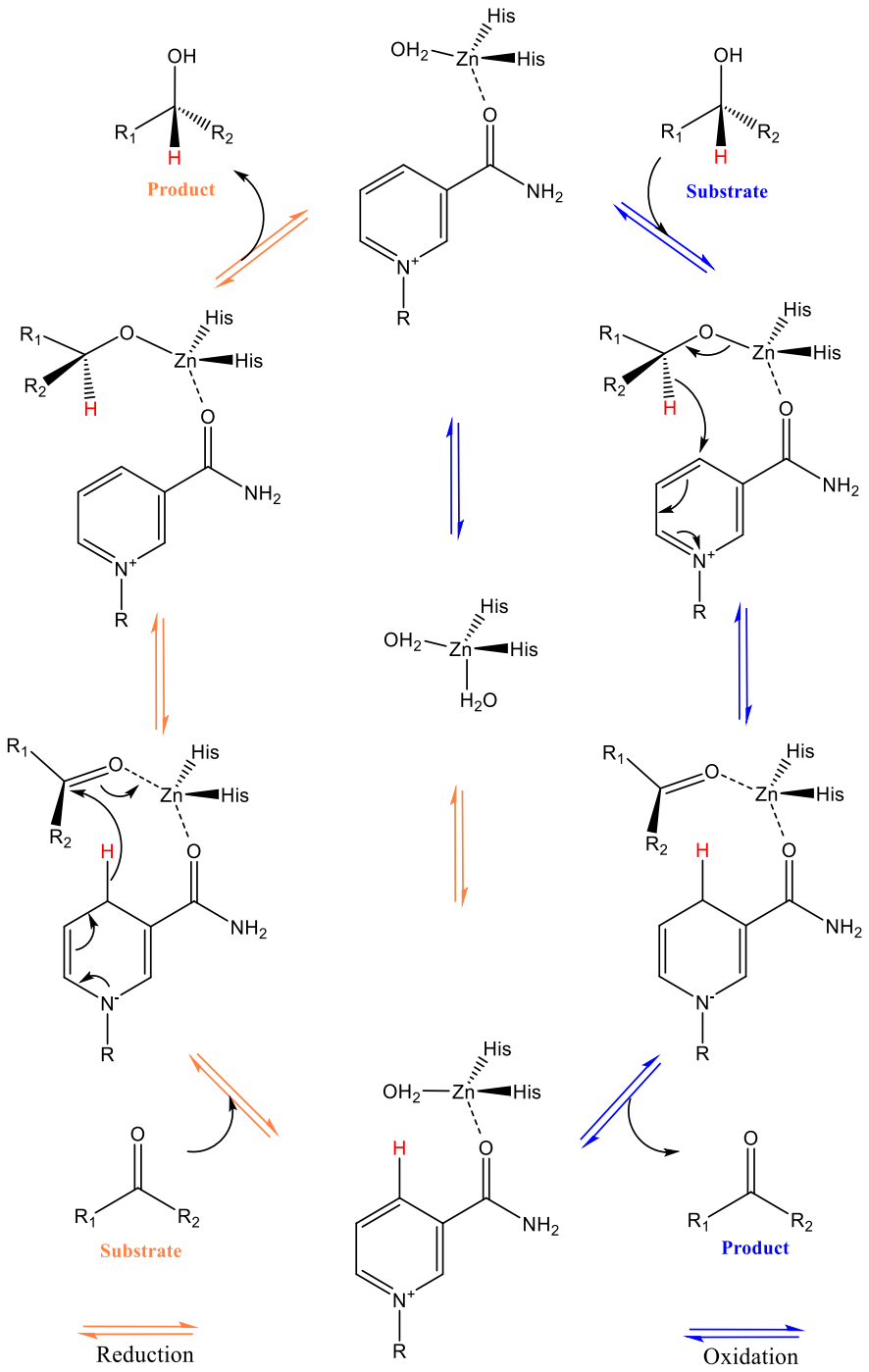

Figure 5.4. Catalytic mechanism of NADPH-dependent ADHs[214].

ADHs-mediated reactions are reversible. ADHs catalyze both the NAD(P)H-driven reduction of carbonyl compounds to the corresponding alcohol and the NAD(P)$^+$-driven oxidation of alcohols to their corresponding carbonyl products. The catalytic mechanism of ADH-catalyzed conversions involves i) binding the starting compound (alcohol or carbonyl compound) with nicotinamide cofactors to the enzyme active site, ii) a hydride transfer between the cofactor and the substrate. The mechanism of zinc-dependent ADHs is shown in Figure 5.4 as an example of the catalytic mechanisms of ADHs. Metal ions are involved in the coordination of the starting compounds in these enzymes[214,215].

ADHs are present in virtually all organisms. They can catalyze various substrates and are involved in a wide range of metabolic processes. Besides the scientific interest in ADHs, they are also attractive biocatalysts for industrial applications. In particular, their ability to catalyze chemo-, stereo- and regioselective reactions gives them significant potential for a range of applications in the food, pharmaceutical, and fine chemical industries[216].

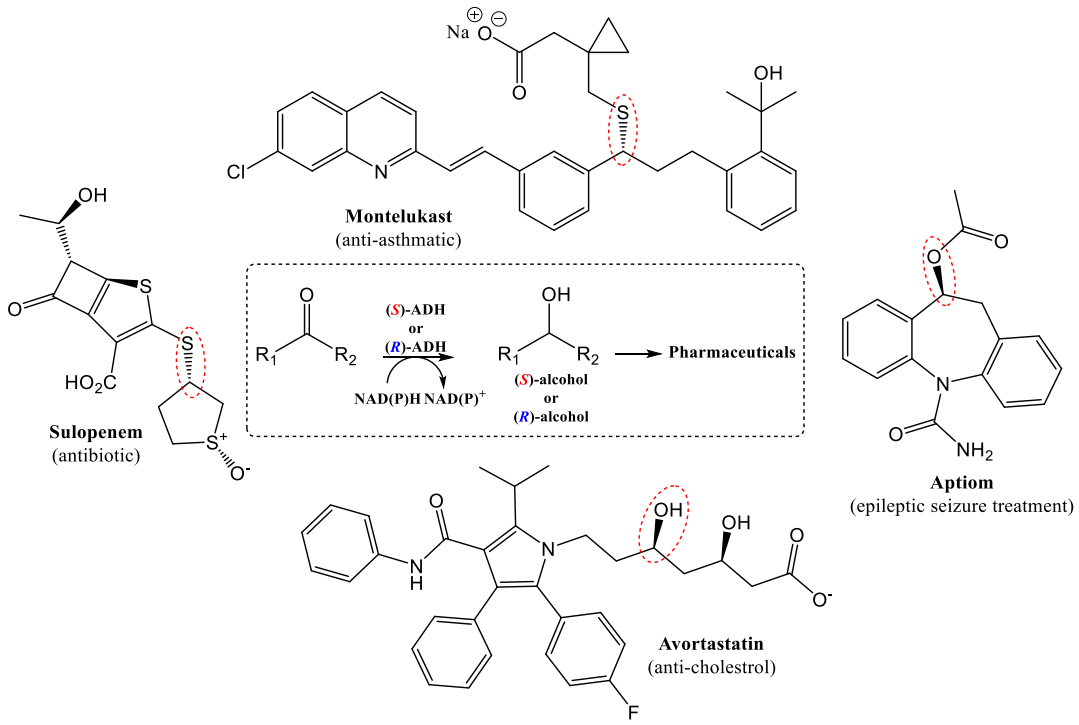

Figure 5.5. Major achievements in industrial scale production involving ADHs in the pharmaceutical production[210].

ADHs can be involved in synthesizing chiral products necessary to produce chiral drugs. After advances in the large-scale production of chiral drugs by ADH enzymes, pharmaceutical companies have started to prefer the use of ADH enzymes in producing chiral drugs, and ADH enzymes have taken place in the industry[217]. Examples of these productions are the synthesis of intermediates of atorvastatin, sulopenem, aptiom, and montelukast (Figure 5.5)[210].

Although ADHs have several catalytic advantages, the industrial application of ADHs is limited because of their commercial availability and the low water solubility of the substrates. Therefore, researchers have focused on developing robust enzymes with high catalytic efficiency, new anhydrous media to improve the solubility of substrates, and cofactor regeneration systems[42,218,219].

5.1.3. Lactone Hydrolases

Lactone hydrolases (LHs) catalyze the reversible or irreversible hydrolysis of lactone compounds and belong to the ester-hydrolyzing enzyme (esterase) family. These enzymes are involved in the synthesis and degradation pathways of various microorganisms. In addition, there are examples of the use of these enzymes for therapeutic purposes or alternative chemical processes[220–222].

Among the LHs, only studies on the detailed catalytic mechanisms of AHL hydrolases have been reported. AHL hydrolases have been reported to be metal-dependent enzymes. As with ADH enzymes, metals coordinate the substrate in AHL hydrolases. The reaction takes place as follows: i) AHL binds at the active site with its carbonyl carbon and oxygen (the leaving group), which are interacting with the zinc atoms; ii) hydroxide ion attacks the carbonyl carbon and leads to the formation of a tetrahedral intermediate; iii) collapse of the tetrahedral adduct leads to the expulsion of the oxygen leaving group; v) aspartate residue takes an alternative conformation to shuttle a proton from the carboxyl group to the leaving group oxygen; v) proton transfer results in the formation of the ring-

cleaved AHL product; vi) product release followed by regeneration of the enzyme completes the catalytic cycle (Figure 5.6)[223–225].

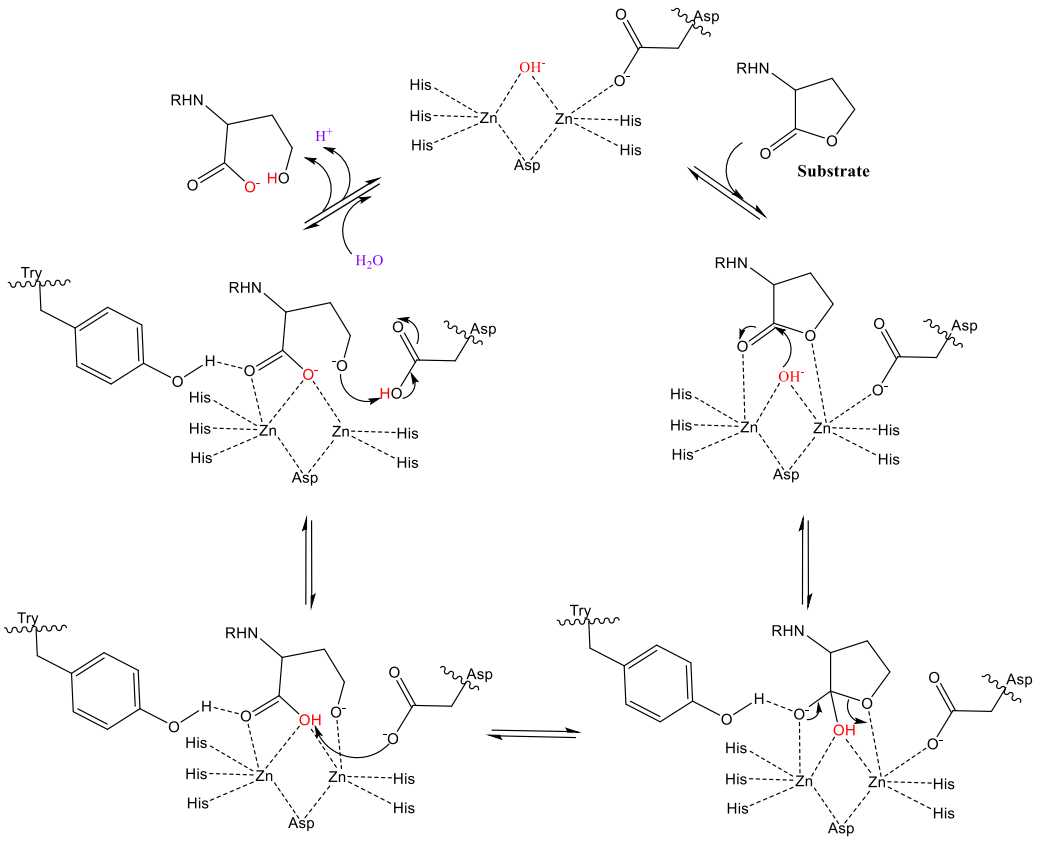

Figure 5.6. Catalytic mechanism of LHs[223–225].

One of the practices of LH is mycotoxin detoxification. Zearalenone (ZEN) is an estrogenic mycotoxin produced mainly by *Fusarium* species as a secondary metabolite in corn, wheat and other cereals. ZEN is a major contaminant in the food and feed industries and causes health problems for animals and humans. ZEN causes reproductive issues in livestock and shows DNA-binding activity and genotoxicity. While conventional methodologies for the detoxification of ZEN destroy the nutritional value of feeds, microbial or enzymatic detoxification could offer a practical and efficient method of ZEN decontamination without affecting the nutrient content of feeds (Figure 5.7)[226,227].

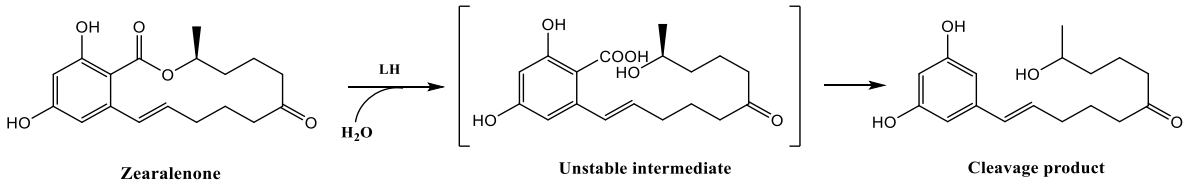

Figure 5.7. Detoxification mechanism of zearalenone by LH[227].

Some of the LHs are capable of degrading quorum sensing (QS) molecules [example: N-acyl-L-homoserine lactones, (AHLs)] that are one of the most noticeable communication systems of bacteria. AHLs and other QS molecules are responsible for virulence factors production, biofilm formation, antimicrobial sensitivity, and drug or multidrug resistance in the human pathogen *Pseudomonas aeruginosa*. Targeting QS molecules have been reported as a promising approach as potential protein therapeutics to prevent infection and biofouling (Figure 5.8)[228–230].

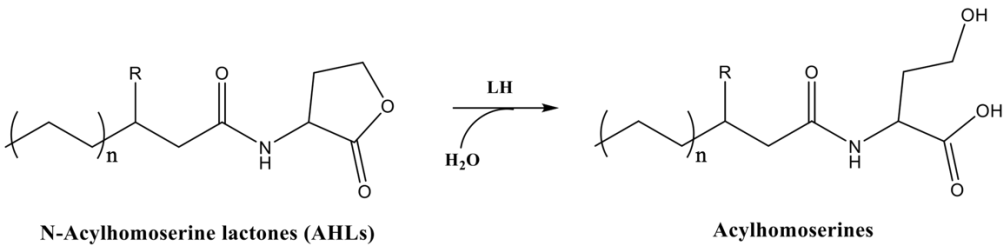

Figure 5.8. The general structure of AHLs and the cleavage of the lactone ring by LH[230].

Another application of LHs is the production of D-pantothenate, such as panthenyl alcohol, pantetheine, 4'-phosphopantetheine-S-sulfonate, and coenzyme A. They are widely used as a food and feed additive and for various pharmaceutical products. Conventionally, most D-pantothenate is produced from resolution DL-pantolactone using chemicals that are expensive, toxic, and often cause environmental problems. However, LHs, specifically D-lactonohydrolase, can catalyze the stereospecific hydrolysis of the racemic mixture of DL-pantolactone to produce D-pantothenic acid, which is used as a chiral material to be synthesized in D-pantothenate (Figure 5.9)[231–233].

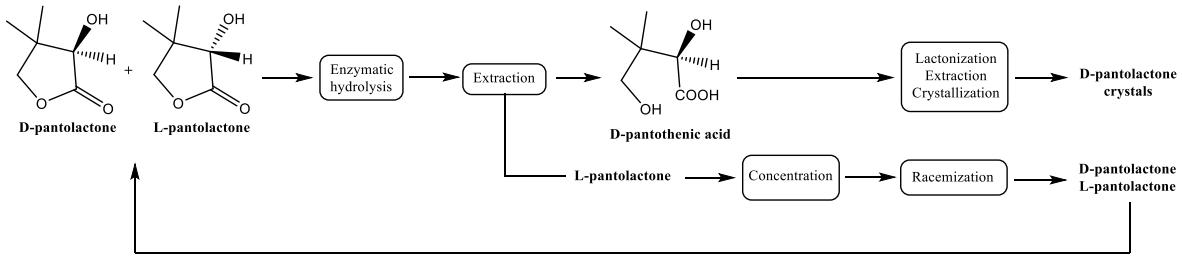

Figure 5.9. Enzymatic resolution processes for DL-pantolactone[220].

Dihydrocoumarin hydrolase (Figure 5.10a) is another example of LHs. This enzyme catalyzes the production of D-acetylthioisobutyrate intermediate (Figure 5.10b) for synthesizing a series of angiotensin-converting enzyme inhibitors. The same enzyme presents alternative process for the regioselective hydrolysis of methyl cetraxate to an antiulcer agent, cetraxate (Figure 5.10c)[220].

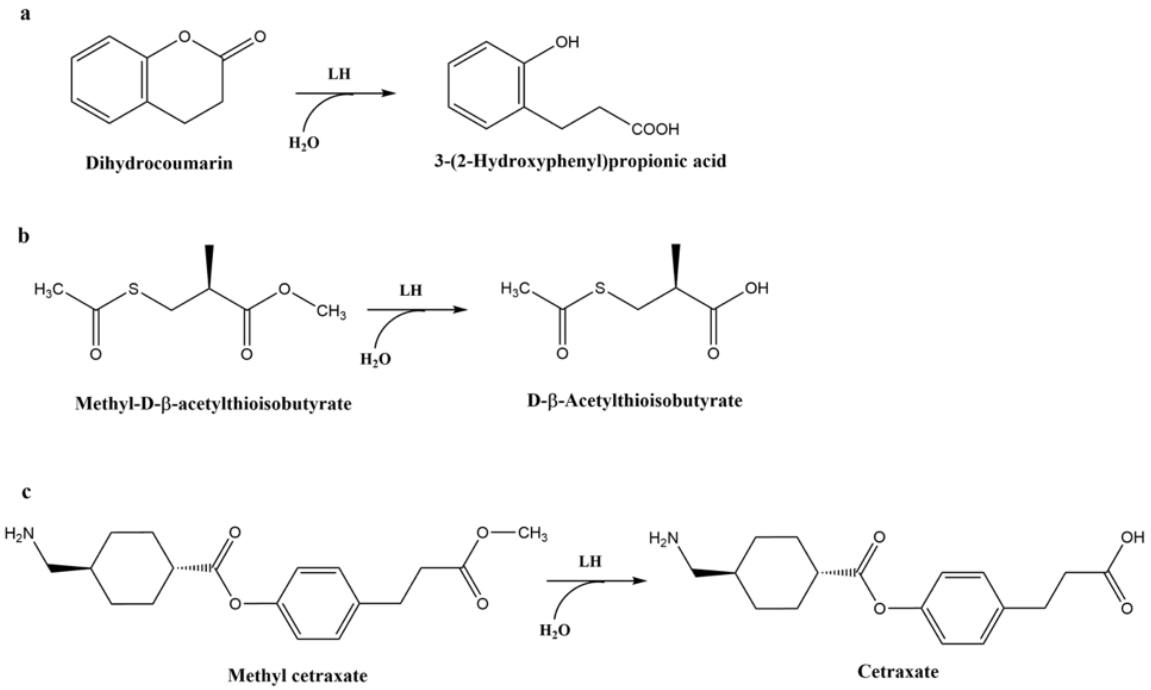

Figure 5.10. LHs catalyzing the stereospecific and/or regioselective hydrolysis[220].

5.2. Materials and Methods

5.2.1. Chemicals

Ammonium sulfate (Sigma – 31119), flavin adenine dinucleotide (FAD, Acros Organics – 347212500), phenylmethylsulfonyl fluoride (PMSF, Sigma – P7626), nicotinamide adenine dinucleotide phosphate sodium salt (NADPH, Cayman Chemicals – 9000743), nicotinamide adenine dinucleotide phosphate hydrate ($NADP^+$, Cayman Chemicals – 10004675), nicotinamide adenine dinucleotide sodium salt hydrate (NADH, Cayman Chemicals – 160078), nicotinamide adenine dinucleotide hydrate (NAD^+, Sigma, 43410), riboflavin 5′-monophosphate (FMN, ChemCruz-296265), sodium chloride (NaCl, Sigma – 31434), sodium phosphate dibasic anhydrous (Na_2HPO_4, Carlo Erba-480141), sodium phosphate monobasic monohydrate (NaH_2PO_4, Carlo Erba-480087), glycerol (Tekkim, FarmaGrade), isopropanol (IPA, Carlo Erba), dimethylsulphoxide (DMSO, Serva – 39757.02), BCA protein assay kit (Thermo Fischer Scientific, Pierce™ BCA Protein Assay Kit – 23225), Bradford reagent (Sigma, B6916), silica gel TLC plate (Merck – 105554), reversed phase C18 silica gel TLC plate (Merck – 105559), Trisma base (Sigma, T6066), tetramethyl ethylenediamine (TEMED, T7024), sodium dodecyl sulfate (SDS, Serva, 20760.01), ammonium persulfate (AP, Serva, 13376.02), sodium hydroxide (AFG Bioscience, 250938), 4x Laemli sample buffer (Biorad, 1610747), dithiothreitol (DTT, Fisher Bioreagents, BP172-5), Coomassie Brilliant Blue R250 (Bioshop, CBB250.5), PageRuler unstained protein ladder (Thermo, 26614), acrylamide/bis-acrylamide, 29:1, %30 (Serva, 10687), glycine (Carlo Erba, 453807), DEAE Sepharose Fast Flow (GE Healthcare, 17-0709-10), Phenyl Sepharose 6 Fast Flow (GE Healthcare, 17-0965-10), Q Sepharose Fast Flow (GE Healthcare, 17-0510-10), Sephacryl S200 (GE Healthcare, 17-0584-10), methanol (Honeywell, 24229), ethanol, (Honeywell, 32221), acetic acid (Sigma Aldrich, 27225), sodium acetate trihydrate (Isolab, 969.013) were used during thesis studies.

5.2.2. Buffers and Stock Solutions

Sodium Phosphate Buffer (NaP_i) (pH 7.4, 100 mM): 10.99 g Na_2HPO_4 and 3.12 g NaH_2PO_4 were dissolved in 1 L distilled water.

Sodium Phosphate Buffer (NaP_i) (100 mM, 100 mL): Na_2HPO_4 (0.2 M) and NaH_2PO_4 (0.2 M) were mixed according to the table below and 50 mL distilled water was added.

pH	Na_2HPO_4 (0.2 M)	NaH_2PO_4 (0.2 M)
6.0	6.15 mL	43.85 mL
6.4	13.25 mL	36.75 mL
7.0	30.5 mL	19.5 mL

Sodium Acetate – Acetic Acid Buffer (100 mM, 100 mL): Sodium acetate (0.2 M) and acetic acid (0.2 M) were mixed according to the table below.

pH	Sodium Acetate (0.2 M)	Acetic Acid (0.2 M)
5.0	70 mL	30 mL
5.4	86 mL	14 mL

Tris-HCl Buffer (1 M): 121.14 g Trisma base was dissolved in 800 mL distilled water. pH was adjusted to desired value using concentrated (1 M) hydrochloric acid. The final volume was made up to 1 L with distilled water.

Glycine-NaOH Buffer (pH 9.0, 100 mM): 0.75 g glycine and 0.07 g NaOH were dissolved in 100 mL distilled water.

Glycine-NaOH Buffer (pH 10.0, 100 mM): 0.75 g glycine and 0.26 g NaOH were dissolved in 100 mL distilled water.

4x Resolving Buffer (100 mL, pH 8.8 - 9.0): 1.5 M Tris HCl (18.17 g), 0.4% v/v TEMED (400 µl) and 0.4% w/v SDS (2 mL of 20% w/v SDS solution) were dissolved in 100 ml distilled water and pH of the solution was adjusted to 8.8-9.0.

4x Stacking Buffer (100 mL, pH 6.8): 0.5 M Tris HCl (6.06 g), 0.4% v/v TEMED (400 µl) and 0.4% w/v SDS (2 mL of 20% w/v SDS solution) were dissolved in 100 ml distilled water and pH of the solution was adjusted to 6.8.

10x Running Buffer (1000 mL): 30 g Trisma base, 144 g glycine and 10 g SDS were dissolved in 1000 ml distilled water.

Coomassie Brilliant Blue R250 Staining Solution (1000 mL): 1g of Coomassie Brilliant Blue R250 was dissolved in 300 mL methanol. Then 650 mL distilled water and 50 mL acetic acid was added to the solution.

Gel Fixation Solution (1000 mL): 500mL of methanol was added to 300 mL of distilled water. 100 mL of glacial acetic acid was added and the total volume was adjusted to 1000 mL with distilled water.

Destaining Solution 1 (1000 mL): 300mL of methanol was added to 500 mL of distilled water. 50 mL of glacial acetic acid was added and the total volume was adjusted to 1000 mL with distilled water.

Destaining Solution 2 (1000 mL): 50mL of methanol was added to 500 mL of distilled water. 70 mL of glacial acetic acid was added and the total volume was adjusted to 1000 mL with distilled water.

Ammonium Persulfate (AP) (%10 (w/v)): 1 g AP was dissolved in 10 mL distilled water. It was aliquoted and stored at -20°C.

Dithiothreitol (DTT) (500 mM): 77 g DTT was dissolved in 1 mL distilled water. It was aliquoted and stored at -20°C.

FAD (100 mM): 82.95 mg FAD was dissolved in 1 mL of 10 mM NaPi buffer (pH 7.4). It was aliquoted and stored at -20°C.

FMN (100 mM): 47.83 mg FMN was dissolved in 1 mL of 10 mM NaPi buffer (pH 7.4). It was aliquoted and stored at -20°C.

NADPH (50 mM): 41.67 mg NADPH was dissolved in 1 mL of 10 mM NaPi buffer (pH 7.4). It was aliquoted and stored at -20°C.

NADH (50 mM): 35.47 mg NADH was dissolved in 1 mL of 10 mM NaPi buffer (pH 7.4). It was aliquoted and stored at -20°C.

PMSF (100 mM): 17.42 mg PMSF was dissolved in 1 mL isopropanol. It was aliquoted and stored at -20°C.

NaCl (5 M): 73.05 g NaCl was dissolved in 250 mL distilled water.

Ammonium sulfate (AS, 4 M): 132.14 g AS was dissolved in 250 mL distilled water.

3-oxo-CG (E-CG-03*) (50 mM): 22.42 mg 3-oxo CG was dissolved in 1 mL DMSO. It was aliquoted and stored at -20°C.

CG (50 mM*): 24.5 mg 3CG was dissolved in 1 mL DMSO. It was aliquoted and stored at -20°C.

A-lacto-CG (E-CG-01*) (50 mM): 25.21 mg A-lacto-CG was dissolved in 1 mL DMSO. It was aliquoted and stored at -20°C.

**The starting compounds are available in our group's stocks.*

5.2.3. Methods

5.2.3.1. Extraction of Enzymes

To obtain cells for enzyme studies, stock cultures stored at 4 °C in an agar slant were transferred to the fresh PDA medium and incubated at 25 °C for ten days. Following incubation, Tween 80 solution (0.1%) was added to the fungi grown in the PDA medium, and a spore solution was obtained by scraping with an inoculation loop. The spore suspension (2%) was inoculated to PDB. After five days of incubation, vacuum filtration was used to separate the cells from the medium. Cell pellets were stored at -80°C until extraction studies.

Table 5.1. Contents of lysis solutions used in optimization studies.

Code of Solution/ Chemical Used (Final Concentration)	Buffer Type (50 mM, pH 7.4)	PMSF (0.5 mM)	FAD (0.1 mM)	NaCl (0.1 M)	Glycerol (10%)	Triton-X (0.1%)
Solution 1	NaPi	+	+	-	-	-
Solution 2	NaPi	+	+	+	+	-
Solution 3	NaPi	+	+	+	+	+
Solution 4	Tris-HCl	+	+	-	-	-
Solution 5	Tris-HCl	+	+	+	+	-
Solution 6	Tris-HCl	+	+	+	+	+

For extraction, the frozen cell pellet was ground in a mortar on ice, and the cell pellet was suspended with 3 mL of lysis buffer per gram of cells. After extraction, the cell lysate was centrifuged 6500 rpm for 15 min. Cell debris was removed, and further studies were performed with the supernatant.

Different lysis solutions were screened for extraction studies of enzymes with 5 g of cells. The contents of the solutions are given in Table 5.1.

5.2.3.2. Analytical Scale and Preparative Scale Ammonium Sulphate Precipitation Trials

An analytical ammonium sulphate (AS) precipitation test was performed to determine the appropriate AS concentration for further studies. Firstly, AS solution was added to 0.5 mL crude protein extract and dispersed by pipetting. After that, the sample was kept on ice for 10 min and centrifuged at 13000 rpm for 2 min. The resulting supernatant was transferred to the next tube, and AS was added to reach the subsequent concentration. This process was continued to obtain protein pellets precipitated at 1.5, 2.0, 2.5, 3.0 and 3.5 M AS concentrations. A hundred μL of buffer solution was added to dissolve the pellets used in activity studies.

The amount of AS required to obtain the intended final concentration was calculated. AS was added slowly to the protein extract mixed in a beaker on a magnetic stirrer at 4 °C. When all AS dissolved, the protein extract was removed from the magnetic stirrer and left to settle at 4 °C overnight. Centrifugation was performed at 5000 rpm for 1 h to separate the obtained precipitate from the supernatant. After the pellet was suspended in buffer solution, it was stored at -80 °C for further studies. The same procedures were repeated by calculating the AS required to reach the next AS concentration with the supernatant.

5.2.3.3. Desalting Procedure

Ultrafiltration units (10 kDa: Pall Scientific; 30 kDa: Amicon, Merck) and PD10 Desalting (GE Healthcare) columns were used for desalting.

PD10 column was conditioned with the appropriate buffer solution for the targeted enzyme. Then, 2.5 mL of protein extract was applied to the column. The first collected 2.5 mL was coded as waste. After all the extract entered the column, it was eluted with 3.5 mL of the same buffer solution. The column was washed with dH_2O and stored in 20% ethanol for further studies.

5.2.3.4. Chromatographic Processes

Ion exchange (DEAE Sepharose Fast Flow and Q Sepharose, GE Healthcare), hydrophobic interaction (Phenyl Sepharose 6 Fast Flow, GE Healthcare), and size exclusion resins (Sephacryl S200, GE Healthcare) were used in the chromatography studies. All chromatographic processes were carried out in a low-pressure liquid chromatography system at 4 °C. This system consists of a peristaltic pump (Schencen-LABV6/V6), a fraction collector (Biorad-Model 2110 Fraction Collector), and different sizes of columns [0.7 cm x 10 cm (Sigma-Aldrich), 2.5 x 10 cm (Sigma-Aldrich), 1 x 10 cm (GE Healthcare), 1 x 20 cm (GE Healthcare), 1.6 x 20 cm (GE Healthcare)] (Figure 5.11).

The degas treatment of the resin and the buffer solutions was carried out in an ultrasonic bath. A filter at the bottom of the selected column was wetted by adding distilled water. Then, the resin was added to the column. The column was conditioned with 5 column volumes (CV) of buffer solution. Elution was conducted with NaCl gradient for ion exchange chromatography, and AS or NaCl gradient for hydrophobic interaction chromatography. The mobile phase was fed to the system by a peristaltic pump. Fractions were collected with a fraction collector at 25 - 50% of the column volume. Bradford reagent was used to determine protein concentration in each fraction. An elution graph was drawn based on protein

concentrations, and an activity test was applied to selected peaks. From each fraction revealing protein content, a hundred µL of sampling was made. The samples were used for activity tests. According to the activity results, the fractions were combined and concentrated using the ultrafiltration unit.

Figure 5.11. Low-pressure liquid chromatography system installed for chromatographic processes.

5.2.3.5. Determination of Total Protein Amount

Bradford reagent and BCA Protein Assay were used to determine protein concentration.

Protein determination with BCA Protein Assay: 200 µL of BCA working solution (50:1, working solution 1: working solution 2) was applied to 10 µL protein extract. The 96-well plate was incubated at 37 °C for 30 min. The total amount of protein was calculated on the standard curve prepared with albumin by measuring the absorbance in the spectrophotometer at 562 nm.

Protein determination with Bradford reagent: 250 µL of Bradford reagent was applied to 5 µL of protein extract. The 96-well plate was incubated at room temperature for 5-45 min. The total protein amount was calculated on the standard curve prepared with albumin by measuring the absorbance in the spectrophotometer at 595 nm.

5.2.3.6. SDS-PAGE Analysis

The SDS-PAGE protocol was performed according to the Laemmli method (Laemmli, 1970). The mini gel system was used for this protocol (Biorad Mini-Protean Tetra Cell). The samples were run on a 12% gel. Gel contents are given in Table 5.2. The gels were run at 60 V for 40 min and then at 120 V until the process was complete.

Table 5.2. Solutions used in the preparation of resolving and stacking gels.

	Resolving Gel (for 10 mL)	**Stacking Gel (for 3 mL)**
Percentage of Gel	12 %	3.5 %
Acrylamide (30 %)	4 mL	0.35 mL
4x Resolving Gel Solution/ 4x Stacking Gel Solution	2.5 mL	0.75 mL
dH_2O	3.5 mL	1.9 mL
AP (10 %)	75 µL	25 µL

The gel was taken into a container for staining upon completion of the run. After washing three times with dH_2O to remove SDS, the gel was kept in a gel fixing solution for 30 min. It was then stained with Coomassie Brilliant Blue R250 solution for 1 h. After the dye was removed, the destaining solution 1 was added to the gel, and the solution was changed periodically until the gel background was clear. After removing the destaining solution 1, the gels were visualized and stored in destaining solution 2.

5.2.3.7. Activity Tests for Enzymes

Enzyme activity was determined by the analysis of product formation (E-CG-02 for LH, E-CG-03 for ADH, E-CG-01 for BVMO) using TLC. The reaction was initiated by adding the substrate (E-CG-01 for LH, CG for ADH, E-CG-03 for BVMO) to the reaction mixture (reaction solution, cofactors, protein extract/fraction). An equal volume of EtOAc was added to the reaction mixture to terminate the reactions. The EtOAc phase was used for TLC analyses. All reactions were carried out at 30 °C. One unit of enzymes was defined as the amount of enzymes needed to produce 1 nmol of metabolite (E-CG-03 for ADH, E-CG-01 for BVMO, E-CG-02 for LH) per minute.

5.2.3.8. Determination of Optimum pH for Enzymes

Activity test was performed in different buffer systems, sodium acetate-acetic acid (pH 5.0-5.4), sodium phosphate (pH 6.0-7.4), Tris-HCl (7.4-9.0) and glycine-NaOH (9.0-10.0) for 24 h at 30°C. An equal volume of EtOAc was added to the reaction mixture to terminate the reactions. EtOAc extracts were dried by using a vacuum concentrator. Then, activity measurement was performed for dried extract by HPLC-DAD methodologies. The highest activity was taken as 100%, and all results were calculated as relative activity.

5.2.3.9. HPLC Analysis and Sample Preparation

Agilent Technologies 1200 Series was used for HPLC analysis. The device consists of a quadruple pump, automatic sample injection section, column furnace and diode array detector (DAD) equipment. The conditions were as follows (Table 5.3):

Flow Rate: 1 mL/min

Column: Phenomenex-Kinetex 5u C18 100A 150x4.6mm ID

Temperature: 25 °C

UV wavelength: 200, 215, 254, 360 nm

Injection volume: 20µL

Solvents: A) Ultrapure Water (UPW) (0.1% Acetic Acid); B) Acetonitrile (ACN) (0.1% Acetic Acid); C) Methanol (MeOH).

Table 5.3. HPLC-DAD method.

Retention Time (min)	%A	%B	%C
0.0	70	30	0
2.0	70	30	0
8.0	20	80	0
10.0	20	80	0
10.01	0	0	100
13	0	0	100
13.01	70	30	0
20	70	30	0

Sample Preparation:

To quantitatively evaluate the experimental results, standard curves were generated for CG, E-CG-03, E-CG-01 and E-CG-02. At this stage, 3-repetitive analyses were performed for five concentrations selected between 500 ppm and 31.25 ppm of the reference material, and calibration curves were drawn.

EtOAc extracts were dissolved in 1 mL of HPLC-grade methanol and filtered using a 0.45 µm PTFE filter.

5.2.3.10. Thin Layer Chromatography

Thin layer chromatography was used to monitor metabolite production. Twenty percent H_2SO_4 was sprayed on the plate developed in the mobile phase and the plate was heated at 110 °C for 2 min to visualize the spots of metabolites.

5.3. Results

5.3.1. Determination of Extraction Conditions

The concentrations and total protein amount of the extracts obtained in the extraction studies are presented in Table 5.4. The solutions containing Triton-X (Solution 3 and 6) caused an increase in protein concentration. In addition, the NaPi buffer solution provided a higher amount of protein extraction than the Tris-HCl buffer solution. Also, solutions containing glycerol increased protein extraction efficiency. The use of Triton-X increased the extraction efficiency. However, it may affect the structure of target enzymes since product formation was significantly reduced.

Table 5.4. Protein concentrations and total protein amount of the extracts obtained with different lysis solutions

Sample	Protein Concentration (µg/mL)	Total Protein (mg)
Solution 1	828.4	19.5
Solution 2	1146.3	23.5
Solution 3	1261.5	27.8
Solution 4	671.1	16.1
Solution 5	871.1	17.9
Solution 6	1320.62	28.4

Activity tests of the protein extracts obtained with six different lysis solutions were performed with three substrates (E-CG-01, E-CG-03, CG) (Protein extract: 500 µg/mL, FAD: 0.1 mM, NADPH: 0.5 mM, Substrate: 0.5 mM). The results of the TLC analysis of the samples taken on days 1 and 4 of incubation are given in Chromatogram 5.1.

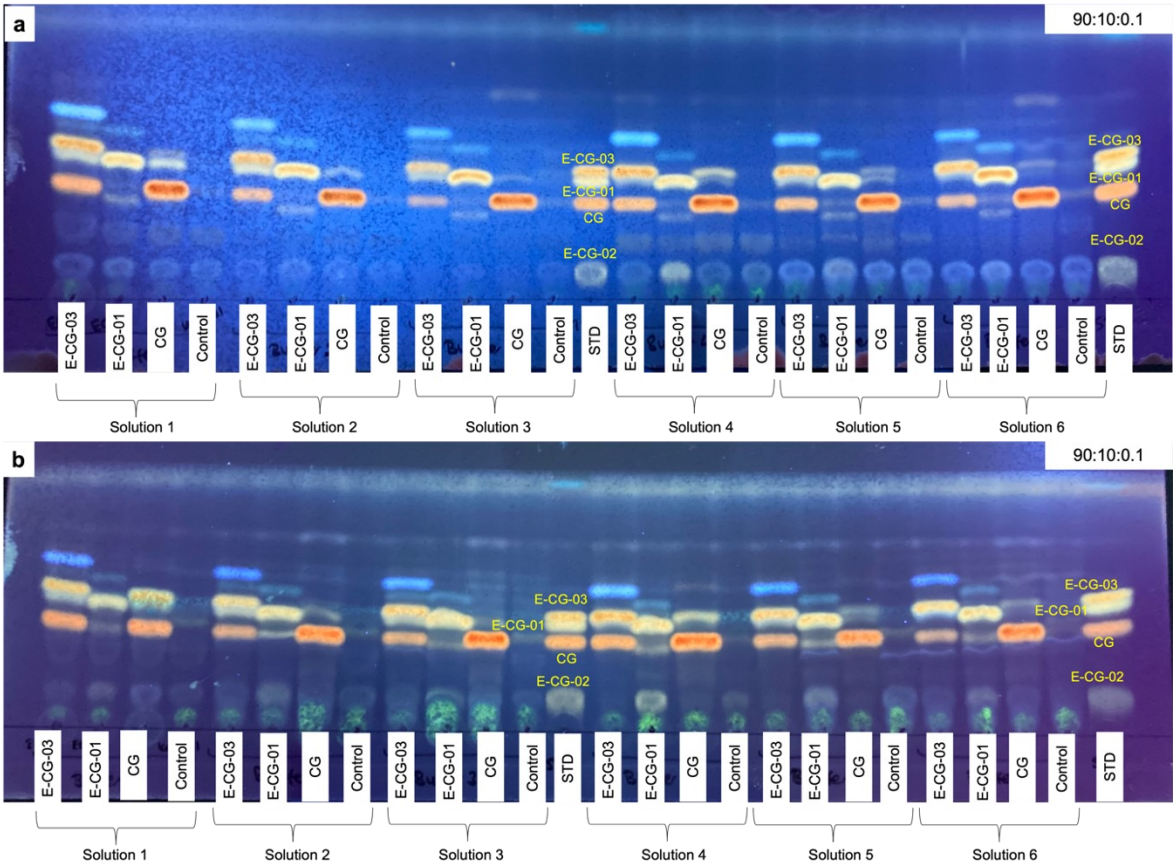

Chromatogram 5.1. Thin layer chromatograms of the substrate screening study. a) Incubation time: 24 h [Silica gel, Mobile phase: 90:10:0.1 ($CHCl_3$:MeOH:H_2O)]; b) Incubation time: 96 h [Silica gel, Mobile phase: 90:10:0.1 ($CHCl_3$:MeOH:H_2O)]. Control: Protein extract without addition of cofactor and substrate.

LH enzyme catalyzes the formation of E-CG-02 by hydrolyzing the lactone ring of E-CG-01 (Chromatogram 5.1). According to the results of the substrate screening, the proteins extracted with Solution 4 catalyzed more product formation than the other extracts.

For this reason, the Tris-HCl buffer solution (Solution 4) was decided to be used in further experiments on LH enzyme.

ADH enzyme takes place in the first step of the proposed biochemical reaction chain and catalyzes the conversion of CG to E-CG-03 (Chromatogram 5.1). While activity was observed in Solution 4 in the 1st day sample, Solution 1 provided higher conversion than the other solutions in the 4th day sample. For this reason, it was decided to study both solutions for further studies.

The protein extract with Solution 2 provided the highest conversion for the BVMO enzyme. As a result, it was determined that using NaPi buffer, glycerol, and NaCl is essential in BVMO extraction. When the activity results were considered for BVMO, a second active enzyme other than BVMO was remarkable. This enzyme is a bidirectional alcohol dehydrogenase enzyme, which works in the presence of NADPH and reduces the E-CG-03 (3-oxo) to the CG.

5.3.2. Determination of Cofactor Specificity of Enzymes

Activity test was performed for different cofactor combinations (Tables 5.5, 5.6 and 5.7) to determine the cofactor requirements of all enzymes.

Table 5.5. Substrate and cofactor combinations used in BVMO activity tests (Crude extract: 500 µg/mL)

Experiment	E-CG-03 (0.5 mM)	NADPH (0.5 mM)	NADH (0.5 mM)	FAD (0.1 mM)	FMN (0.1 mM)
1	+	+	-	+	-
2	+	-	+	+	-
3	+	+	-	-	+
4	+	-	+	-	+
5	+	-	-	-	-
6	-	-	-	-	-

According to the Chromatogram 5.2, BVMO enzyme showed activity in the presence of FAD and NADPH. In the presence of FMN and NADH, a minimal amount of substrate was converted to E-CG-01. Based on these data, it was decided to use FAD and NADPH in further studies. The ADH enzyme was found to perform the reduction reaction in the presence of NADH or NADPH.

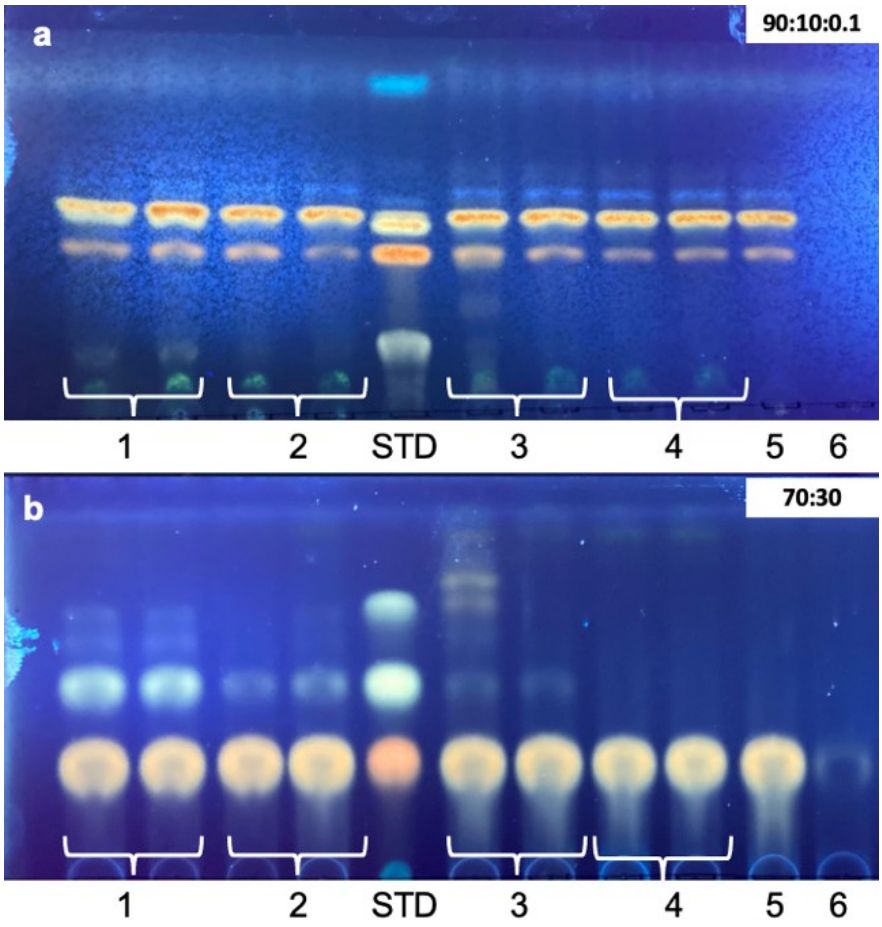

Chromatogram 5.2. Thin layer chromatograms of cofactor specificity study for BVMO: a) Silica gel, Mobile phase: 90:10:0.1 ($CHCl_3$:MeOH:H_2O); b) Reverse phase C18 silica gel, Mobile phase: 70:30 (ACN: H_2O).

There was precipitation in the extracts to be used for LH and ADH taken from the stock (-80 °C). For this reason, activity tests were performed on fractions separated as pellets and supernatant by using centrifugation.

The experiments set up to determine the cofactor specificity for LH are given in Table 5.6. According to the TLC results of LH activity test, LH enzyme was not cofactor dependent (Chromatogram 5.3b). When the pellet and supernatant were compared, there was no activity in the pellet, and product formation was observed in the supernatant fraction. Therefore, centrifugation was chosen as a preliminary purification step for isolating LH enzymes.

Table 5.6. Substrate and cofactor combinations used to determine cofactor specificity for LH enzyme

Experiment	Protein Extract/Fraction	E-CG-01 (0.5 mM)	NADPH (0.5 mM)	FAD (0.1 mM)
1	Crude extract	+	+	+
2	Crude extract	+	+	-
3	Crude extract	+	-	-
4	Crude extract	-	-	-
5	-	+	-	-
6	Crude extract (after melting, precipication was observed)	+	+	+
P	Pellet	+	+	+
S	Supernatant	+	+	+

The experiment set to determine the cofactor specificity for ADH is given in Table 5.7. First, it was confirmed that this enzyme is not FAD-dependent. Substrate conversion (from CG to E-CG-03) was observed with NADPH or $NADP^+$ as a cofactor, but higher product concentrations were observed with $NADP^+$ use compared to NADPH. Since the crude protein extract was used, NADPH – $NADP^+$ conversion was provided by other enzymes in the extract. Therefore, activity was also observed in the use of NADPH. So, we decided to continue with $NADP^+$ for further ADH studies. The activity was not as high as the crude extract compared to the pellet and supernatant fractions. Lower product formation was detected in the supernatant, while no activity was observed in the pellet (Chromatogram 5.3a).

Table 5.7. Substrate and cofactor combinations used to determine cofactor specificity for ADH enzyme

Experiment	Protein Extract/Fraction	CG (0.5 mM)	NADPH (0.5 mM)	FAD (0.1 mM)	$NADP^+$ (0.5 mM)
1	Crude extract	+	+	+	-
2	Crude extract	+	+	-	-
3	Crude extract	+	-	-	-
4	Crude extract	-	-	-	-
5	-	+	-	-	-
6	Crude extract	+	-	+	-
7	Crude extract	+	-	+	+
8	Crude extract	+	-	-	+
P	Pellet	+	+	-	+
S	Supernatant	+	+	-	+

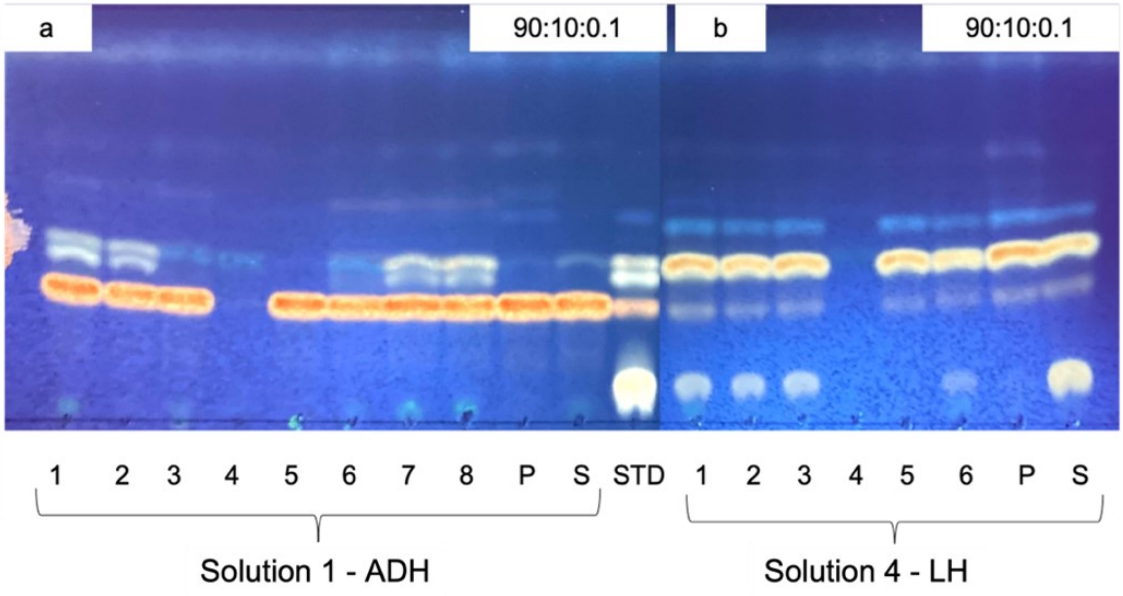

Chromatogram 5.3. Thin layer chromatograms of cofactor specificity study for ADH and LH (Incubation time: 24 h). a) ADH crude extract (500 µg/mL); b) LH crude extract (500 µg/mL) [Silica gel, Mobile phase: 90:10:0.1 ($CHCl_3$:MeOH:H_2O)].

5.3.3. Studies for Optimization and Purification of LH

The studies for the purification of the LH enzyme are described under the headings of optimization studies and purification studies.

5.3.3.1. Optimization Studies

Optimization studies for the LH enzyme are summarized in Table 5.8, and details are described below.

Table 5.8. Summary of optimization studies for LH.

Experiment Code	Sample	Methodology	Active Fraction
IEC-1	Crude Extract (53.26 mg)	Ion Exchange Chromatography Resin: DEAE Sepharose, 9 mL Column: 2.5 cm x 10 cm, Flow rate: 1 mL/min Starting Buffer: 50 mM Tris HCl (pH 7.4) Gradient Elution: 0 – 0.5 M NaCl	12.68 mg
AS Cut	Crude Extract (6.28 mg)	AS Precipitation Fractions: 1.5 M, 2.0 M, 2.5 M, 3.0 M, 3.5 M pellets	0.879 mg
HIC-1	IEC-1-FR10-14 (9.3 mg)	Hydrophobic Interaction Chromatography Resin: Phenyl Sepharose, 3 mL Column: 0.7 cm x 10 cm, Flow rate: 1 mL/min Starting Buffer: 50 mM Tris HCl (pH 7.4) + 1.5 M AS Gradient Elution: 1.5 M – 0 M AS	1.87 mg
SEC-1	HIC-1-FR28-33 (1.12 mg)	Size Exclusion Chromatography Resin: Sephacryl S200, 30 mL Column: 1.6 cm x 20 cm, Flow rate: 1.5 mL/min Starting Buffer: 50 mM Tris HCl (pH 7.4) + 150 mM NaCl Isocratic Elution: 150 mM NaCl	0.436 mg
IEC-2	Crude Extract (15 mg)	Ion Exchange Chromatography Resin: Q Sepharose, 3 mL Column: 0.7 cm x 10 cm, Flow rate: 1.5 mL/min Starting Buffer: 50 mM Tris HCl (pH 7.4) Gradient Elution: 0 – 1 M NaCl	2.503 mg
* The methods in “5.2.3.4. Chromatographic Processes” were used in the optimization steps.			

Ion Exchange Chromatography (IEC-1)

Optimization studies were started with ion exchange chromatography, and the weak ion exchange resin DEAE Sepharose was used in the first study. To clarify extract from the particles formed during the concentration step, centrifugation was performed at 5000 rpm for 15 min. The clarified extract (53.26 mg) was applied to the column. The protein profile of the fractions collected from the column is shown in Figure 5.12.

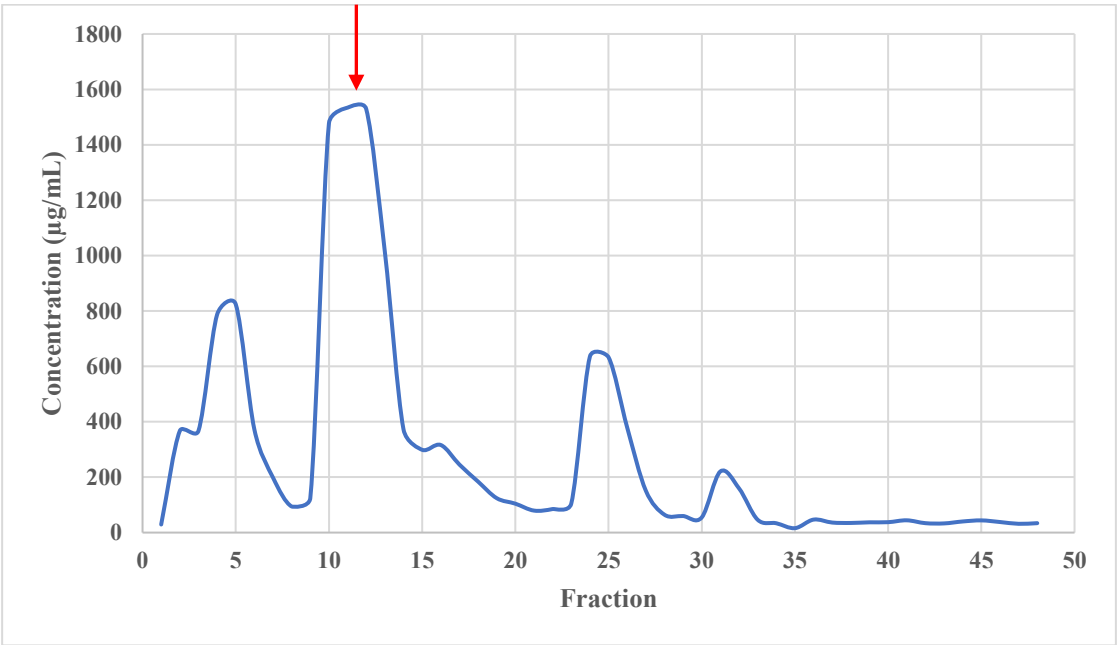

Figure 5.12. Separation of the LH crude extract on DEAE Sepharose (IEC-1).

According to Chromatogram 5.4, LH activity was observed for the fractions FR 10-20. The LH-rich fraction was eluted with 0.1-0.2 M NaCl. Fractions were combined and concentrated according to the activity results (Chromatogram 5.4) and the profile in Figure 5.12.

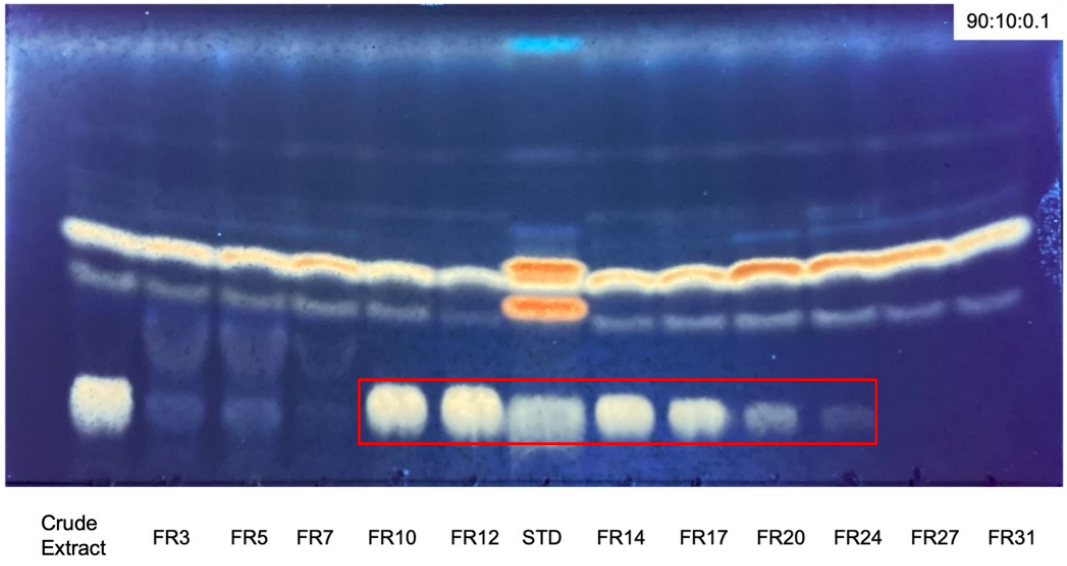

Chromatogram 5.4. Activity test results of the fractions obtained from IEC-1 (Incubation time: 12 h) [Silica gel, Mobile phase: 90:10:0.1 ($CHCl_3$:MeOH:H_2O)].

The active fraction (FR 10-14) was determined to be 12.68 mg (Table 5.9). According to the SDS-PAGE analysis, the protein profile of FR 10-14 was quite rich. However, most of the proteins (76%) that were not responsible for the activity were removed by ion exchange chromatography. In addition, an intense protein band around 30 kDa was observed in FR 10-14 (Figure 5.13).

Table 5.9. Combined fractions from IEC-1.

Fraction	Total Protein (µg)
1-2	1187.2
3-9	5819.9
10-14*	12679.4
15-18*	386.1
19-23*	288.6
24-28	2825.1
29-34	861.9

*Fractions with LH activity

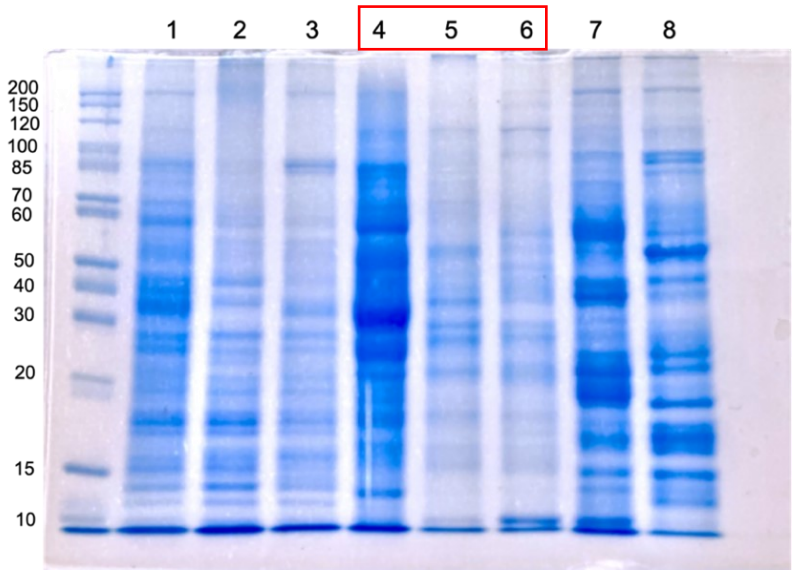

Figure 5.13. SDS-PAGE gel analysis of the fractions from IEC-1 (Gel percentage: 12%). 1) Crude extract (20 µg), 2) FR 1-2 (11.87 µg), 3) FR 3-9 (6.72 µg), 4) FR 10-14 (20 µg), 5) FR 15-18 (5.8 µg), 6) FR 19-23 (4.3 µg), 7) FR 24-28 (20 µg), 8) FR 29-34 (20 µg).

Analytical AS Precipitation (AS Cut)

In hydrophobic interaction chromatography, AS is used in concentrations ranging from 1.7 M to 0 M for protein elution. If there is a possibility of precipitation of the target protein at AS concentrations of 1.7 M and below, then this method should not be used. Therefore, the target protein's precipitation range should be analyzed using AS precipitation before hydrophobic interaction chromatography.

To test this method's usability for purification of LH, AS precipitation was performed with 1 mL of the LH crude extract (6283.8 µg/mL), and then activity tests were performed for the obtained fractions. The results are given in Table 5.10 and Chromatogram 5.5.

According to the activity test results, the precipitation was most intense for a 2.5 M fraction. For this reason, we decided to use a hydrophobic interaction resin and a 2.5 M AS concentration when precipitation is required in further steps. SDS-PAGE analysis of AS precipitation is presented in Figure 5.14. According to the gel image, partial isolation seems to be accomplished using AS.

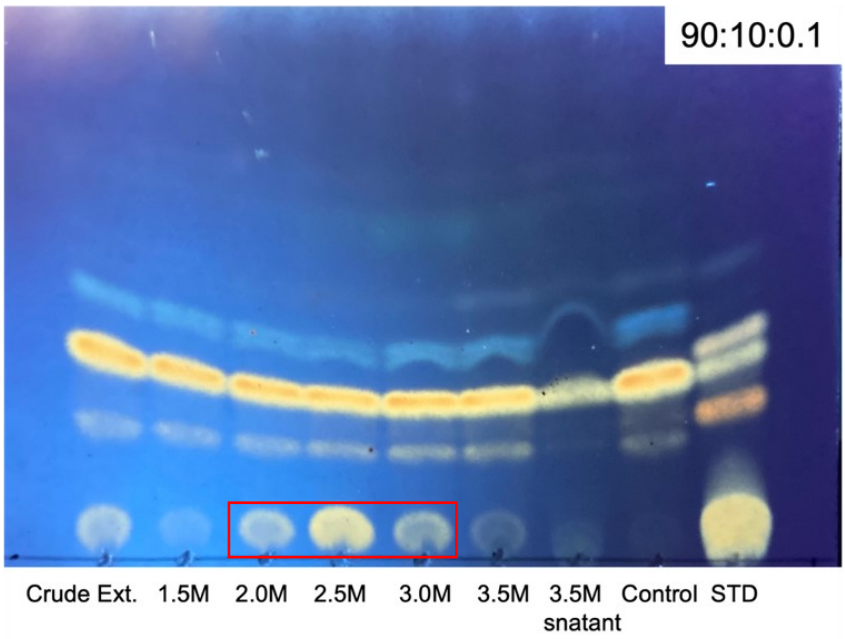

Chromatogram 5.5. Activity test results of the fractions obtained from analytical AS precipitation (Incubation time: 12 h, protein concentration: 250 µg/mL) [Silica gel, Mobile phase: 90:10:0.1 ($CHCl_3$:MeOH:H_2O)].

Table 5.10. Analytical AS precipitation for LH.

Fraction	Total Protein (mg)	Yield (%)
1.5 M Pellet	2.99	47.5
2.0 M Pellet	0.977	15.5
2.5 M Pellet	0.879	13.9
3.0 M Pellet	0.490	7.8
3.5 M Pellet	0.342	5.4
3.5 M Supernatant	0.380	6

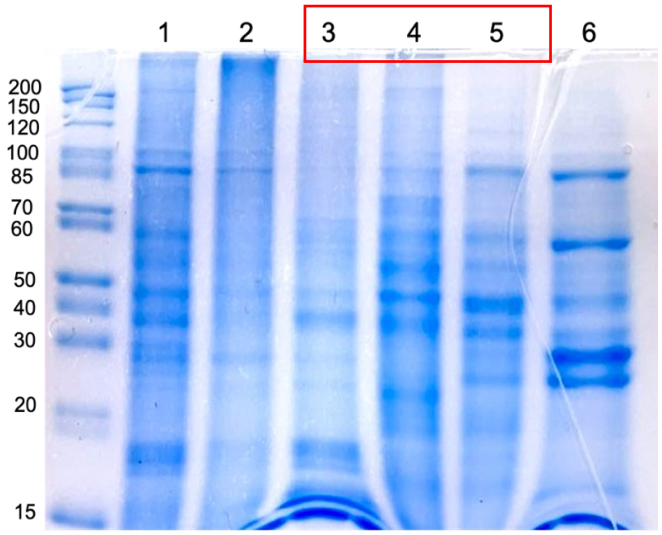

Figure 5.14. SDS-PAGE gel analysis of the fractions from AS precipitation (Gel percentage: 12%). 1) Crude extract (15 µg), 2) 1.5 M pellet (15 µg), 3) 2.0 M pellet (15 µg), 4) 2.5 M pellet (15 µg), 5) 3.0 M pellet (15 µg), 6) 3.5 M pellet (15 µg).

Hydrophobic Interaction Chromatography (HIC-1)

In hydrophobic interaction chromatography, proteins can irreversibly bind to the resin and remain in the column. For this reason, a preliminary trial was conducted with 2.5 mg of IEC-1-FR 10-14. The protein profile of the fractions collected from the column is shown in Figure 5.15.

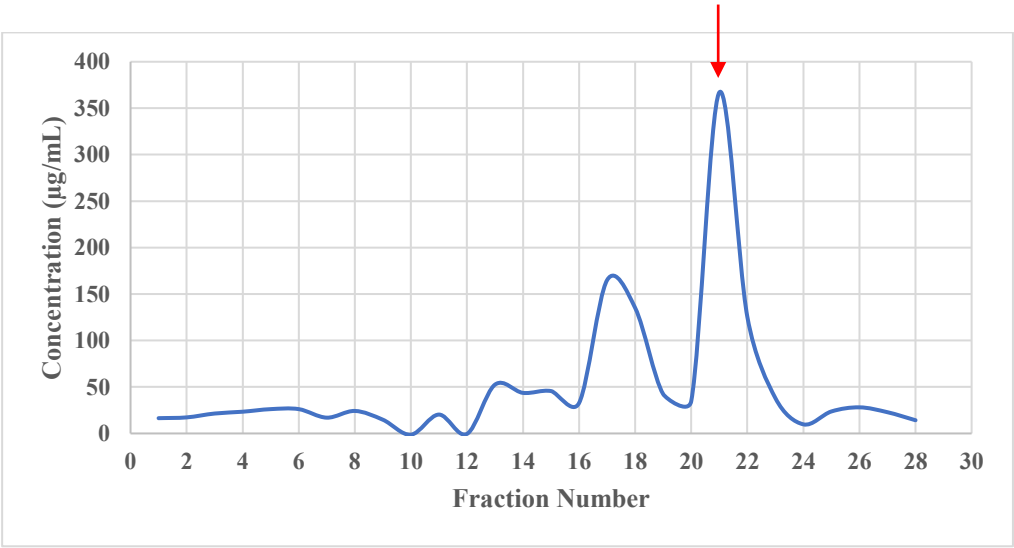

Figure 5.15. Separation of the IEC-1-FR 10-14 on Phenyl Sepharose (preliminary).

According to Chromatogram 5.6, LH-rich fraction was eluted at a low AS concentration. Therefore, we decided to apply a higher amount of protein to the same column using the same conditions.

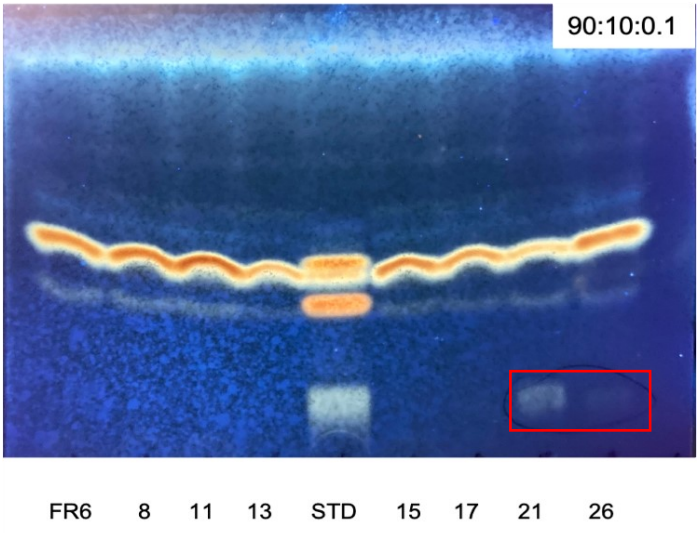

Chromatogram 5.6. Activity test result of the fractions obtained from preliminary HIC (Incubation time: 12 h) [Silica gel, Mobile phase: 90:10:0.1 ($CHCl_3$:MeOH:H_2O)].

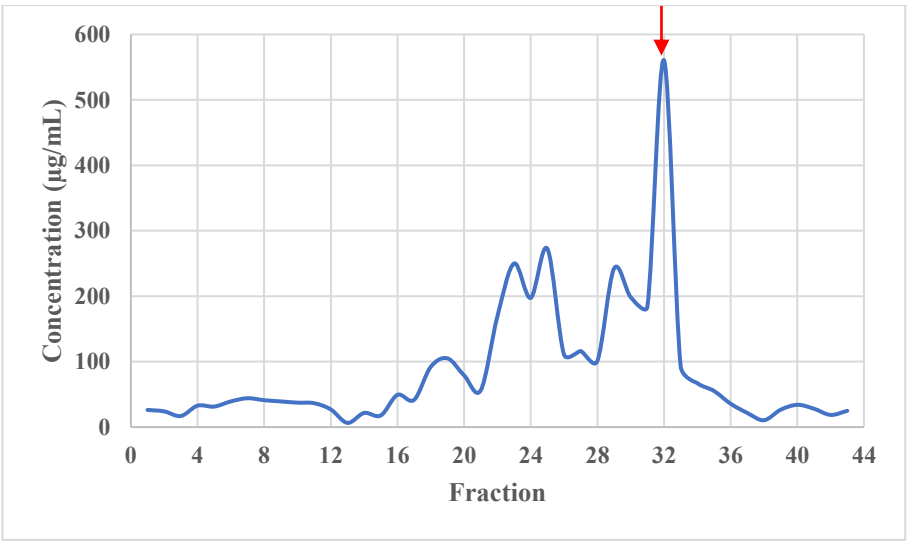

Figure 5.16. Separation of the IEC-1-FR 10-14 on Phenyl Sepharose (HIC-1).

For the preparative study, AS was added to the IEC-1-FR 10-14 (9.3 mg) at a final concentration of 1.5 M and applied to the column. Gradient elution from 1.5 to 0 M AS was performed for fractionation. The protein profile of the fractions collected from the column is shown in Figure 5.16.

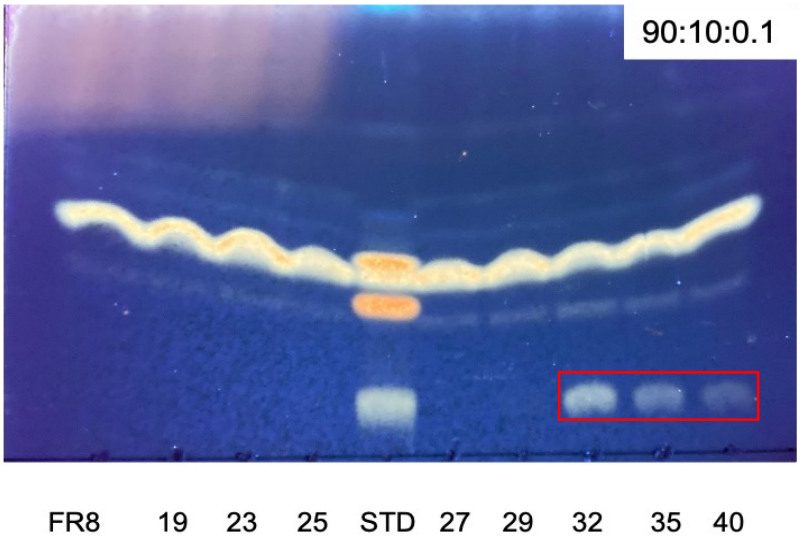

Chromatogram 5.7. Activity test results of the fractions obtained from HIC-1 (Incubation time: 12 h) [Silica gel, Mobile phase: 90:10:0.1 ($CHCl_3$:MeOH:H_2O)].

A similar protein profile was obtained in the preliminary and preparative trials (Figures 5.15 and 5.16). According to Chromatogram 5.7, LH activity was observed for the FR 32, 35 and 40. These fractions were combined and concentrated. Consequently, FR 28-33 displayed a higher activity compared to FR 34-38 and FR 39-43 (Chromatogram 5.8). Interestingly, the elution of LH continued in the washing step of the column (after FR 35) (Chromatogram 5.8). However, when looking at the protein amounts of active fractions (FR 28-33, FR 34-38 and FR 39-43), it was determined that most of LH was eluted from the column with 0 M AS before washing (FR 28-33: 1.87 mg) (Table 5.11).

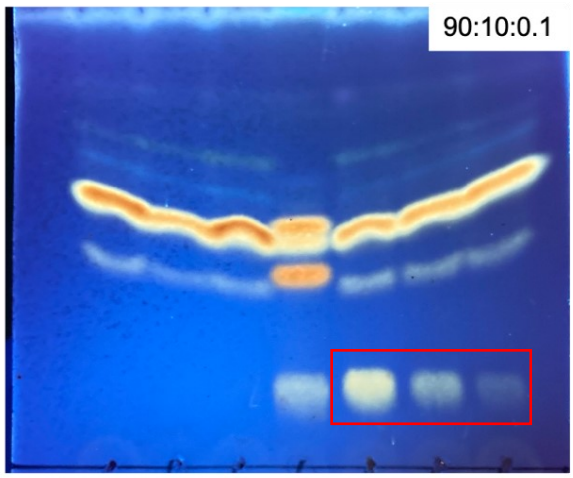

Chromatogram 5.8. Activity test results of the combined fractions obtained from HIC-1 (Incubation time: 12 h) [Silica gel, Mobile phase: 90:10:0.1 ($CHCl_3$:MeOH:H_2O)].

Table 5.11. Combined fractions from HIC-1.

Fraction	Total Protein (µg)
1-13	7.1
14-21	85.3
22-27	1124.5
28-33*	1872.5
34-38*	20.6

*Fractions with LH activity

Figure 5.17 demonstrates an intense band was observed in the range of 30-40 kDa in FR 22-27. However, LH activity was not detected in this fraction (Chromatogram 5.8). Five different protein bands were noticed in FR 28-33, where LH activity was found (Figure 5.17).

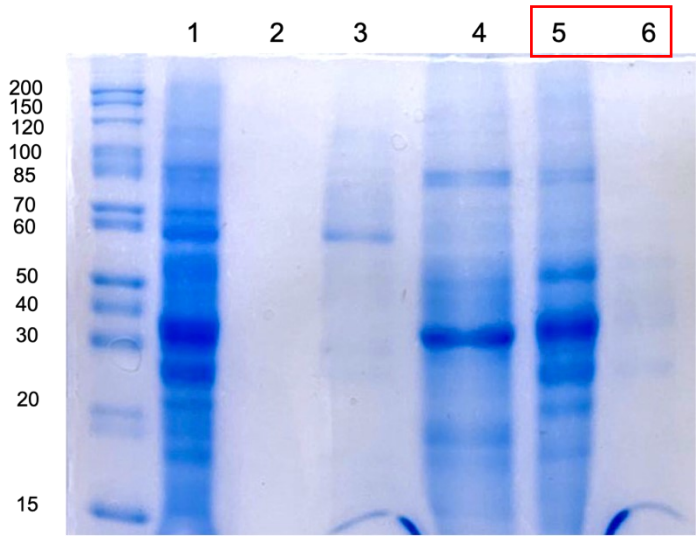

Figure 5.17. SDS-PAGE gel analysis of the combined fractions from HIC-1 (Gel percentage: 12%). 1) IEC-1-FR 10-14 (15 µg), 2) FR 1-13 (0.11 µg), 3) FR 14-27 (1.28 µg), 4) FR 22-27 (13.5 µg), 5) FR 28-33 (15 µg), 6) FR 34-38 (0.25 µg).

Size Exclusion Chromatography (SEC-1)

The active fraction (HIC-1-FR 28-33) (1.12 mg) was concentrated using an ultrafiltration unit and was submitted to the column. Isocratic elution was performed for fractionation. The protein profile of the fractions collected from the column is shown in Figure 5.18.

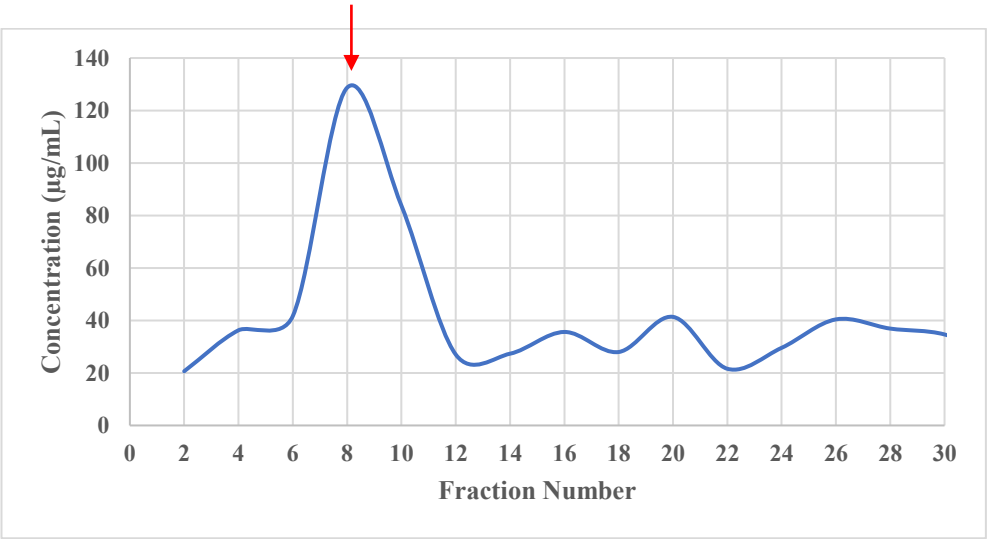

Figure 5.18. Separation of the HIC-1-FR 28-33 on Sephacryl S200 (SEC-1).

According to Chromatogram 5.9, LH activity was observed for the fractions FR 4-12. The combined fractions and protein amounts are given in Table 5.12.

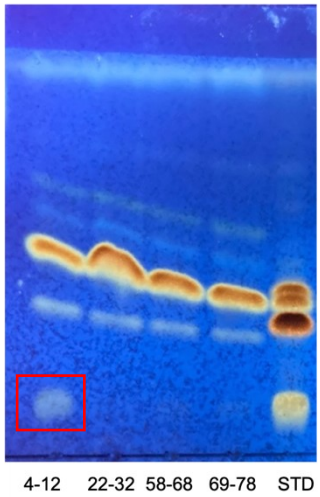

Chromatogram 5.9. Activity test results of the fractions obtained from SEC-1 (Incubation time: 23 h) [Silica gel, Mobile phase: 90:10:0.1 ($CHCl_3$:MeOH:H_2O)].

Table 5.12. Combined fractions from SEC-1.

Fraction	Total Protein (µg)
4-12*	436.48
22-32	32.49

* Fractions with LH activity

SDS-PAGE analysis was performed for the fractions obtained from LH optimization steps (Figure 5.19). The protein profile of SEC-1 fraction was very similar to HIC-1 fraction, and there was a protein band between 30-40 kDa. However, SEC did not provide further purification for LH enzyme. Flow rate can be optimized, or smaller volume fractions can be collected to increase the column's resolution and obtain separate protein peaks. Since a low amount of protein (218.24 µg) was obtained in the last purification step, a large-scale extraction and subsequent purification studies are necessary.

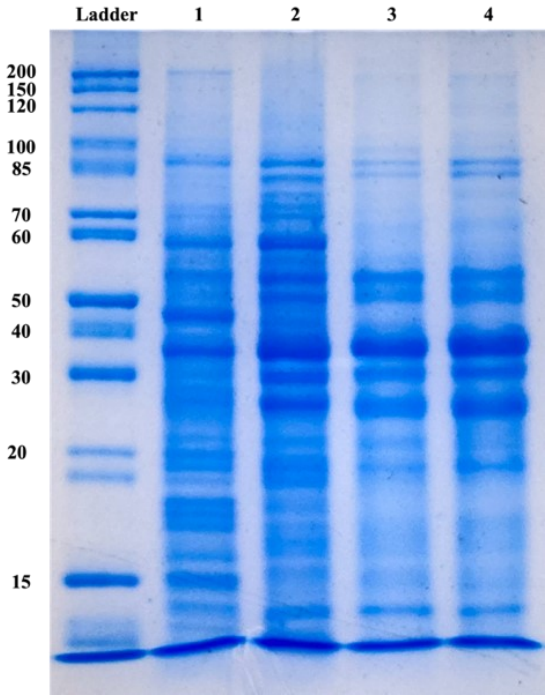

Figure 5.19. SDS-PAGE gel analysis of the fractions from LH purification steps (Gel percentage: 12%). 1) Crude extract (10 µg), 2) IEC-1-FR 10-14 (10 µg), 3) HIC-1-FR 28-33 (10 µg), 4) SEC-1-FR 4-12 (10 µg).

Ion Exchange Chromatography (IEC-2)

As an alternative to weak anion exchange resin, Q Sepharose (strong anion exchange resin) was tested for the purification of LH. A gradient elution from 0 to 1 M NaCl was performed for fractionation. The protein profile of the fractions collected from the column is shown in Figure 5.20.

According to Chromatogram 5.10, LH activity was observed for the fractions FR 28-34 and eluted with 0.2-0.3 M NaCl (Figure 5.20). Also, unlike previous steps, SDS-PAGE was performed on each fraction to determine the change in protein profile (Figure 5.21). According to Figure 5.21, four protein bands were observed in FR28. Other active fractions were more dilute than FR28, so protein bands are not clearly visible. FR 28-34 were combined and concentrated. The protein amount of FR 28-34 was 2.503 mg.

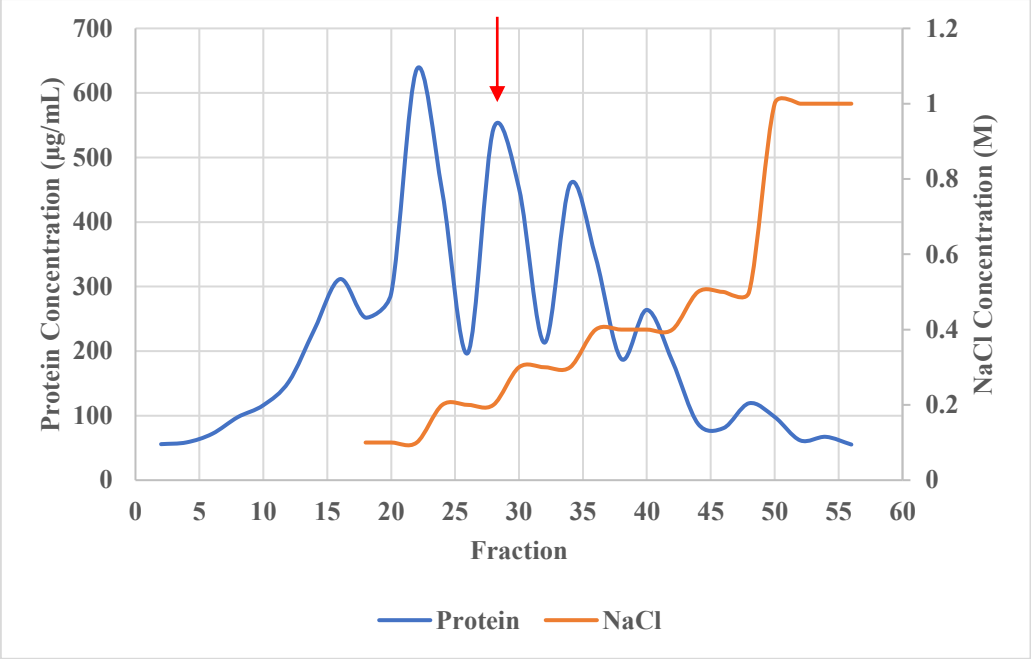

Figure 5.20. Separation of the LH crude extract on Q Sepharose Fast Flow (IEC-2).

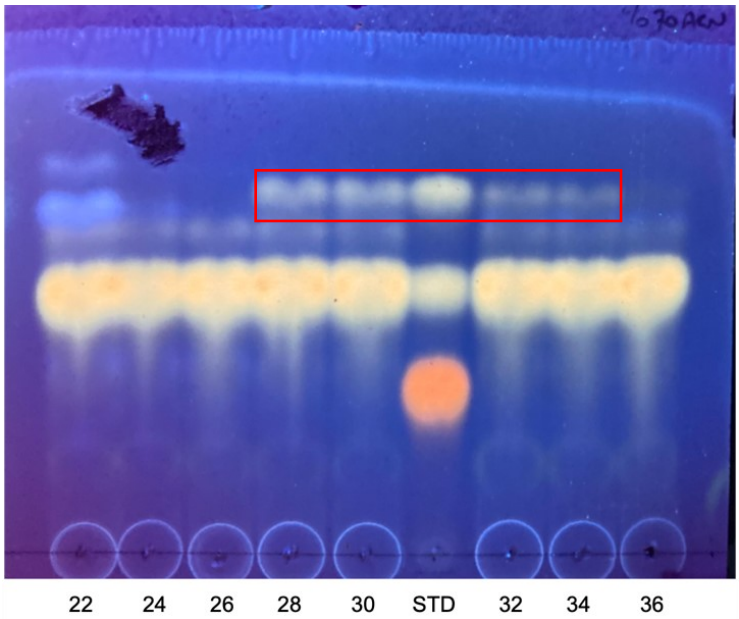

Chromatogram 5.10. Activity test results of the fractions obtained from IEC-2 (Incubation time: 15 h) [Reverse phase C18 silica gel, Mobile phase: 70:30 (ACN: H_2O)].

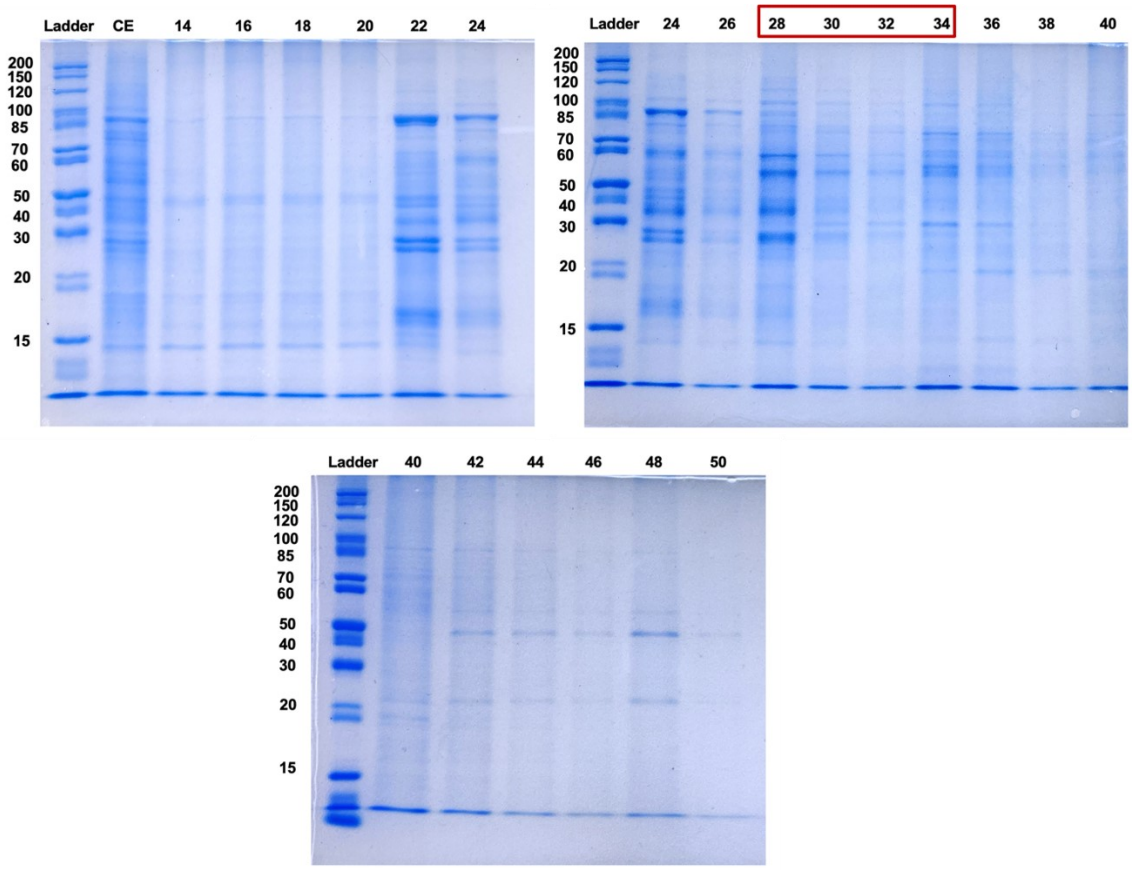

Figure 5.21. SDS-PAGE gel analysis of the fractions from IEC-2 (Gel percentage: 12%). The numbers indicate fractions and 15 µL of each fraction/crude extract was loaded onto the gel.

5.3.3.2. Purification Studies

Purification studies for the LH enzyme are summarized in Table 5.13, and details are explained below.

In line with the optimization studies, we decided to use Q Sepharose, which provides better separation, in the first step of the purification studies. The crude extract (215.21 mg) was applied to the column in 3 parts. A gradient elution from 0 to 1 M NaCl was performed for fractionation. The results of the first part as representative of all parts are presented in Figures 5.22, 5.23 and Chromatogram 5.11.

Table 5.13. Summary of purification studies for LH.

Experiment Code	Sample	Methodology	Active Fraction
IEC-1	Crude Extract (215.21 mg)	Ion Exchange Chromatography Resin: Q Sepharose, 10 mL Column: 1 cm x 20 cm, Flow rate: 1 mL/min Starting Buffer: 50 mM Tris HCl (pH 7.4) Gradient Elution: 0 – 1 M NaCl	46.39 mg
HIC-1	IEC-1-[FR50-54+FR-76-90+FR32-40] (46.21 mg)	Hydrophobic Interaction Chromatography Resin: Phenyl Sepharose, 3 mL Column: 0.7 cm x 10 cm, Flow rate: 1.5 mL/min Starting Buffer: 50 mM Tris HCl (pH 7.4) + 1.5 M AS Gradient Elution: 1.5 M – 0 M AS	1.087 mg
* The methods in "5.2.3.4. Chromatographic Processes" were used in the purification steps.			

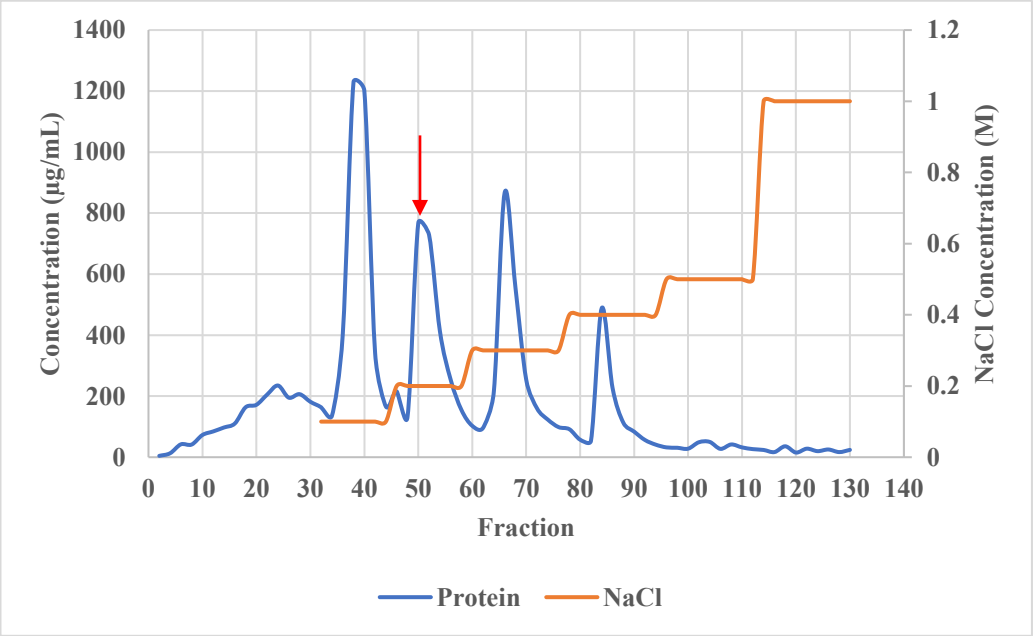

Figure 5.22. Separation of the LH crude extract on Q Sepharose (IEC-1).

A decrease in flow rate was encountered due to blockage in the Q Sepharose column. For this reason, the crude extract was applied to the column in three parts. As a result, 46.39 mg of the active fraction was obtained. In the SDS-PAGE analysis, it was observed that some proteins were enriched in the active fraction compared to the crude extract, in accordance with the optimization studies (Figure 5.23).

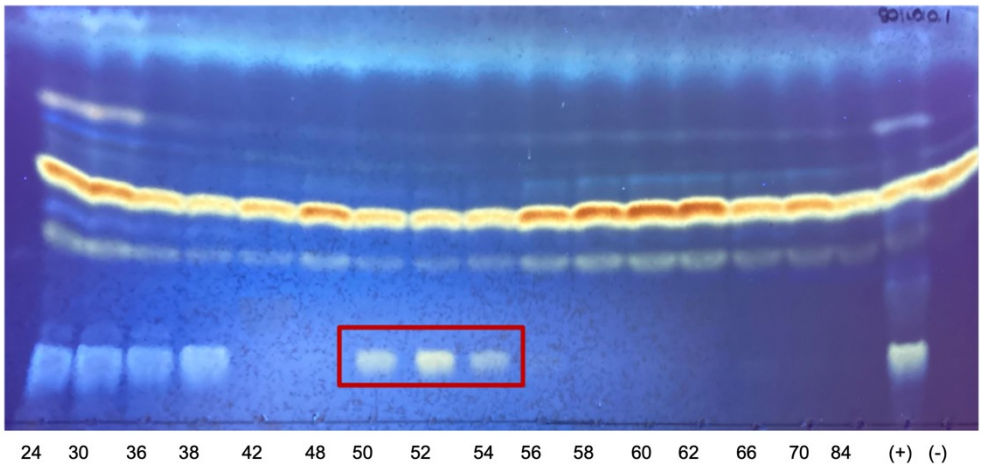

Chromatogram 5.11. Activity test results of the fractions obtained from IEC-1 (Incubation time: 14.5 h) [Silica gel, Mobile phase: 90:10:0.1 ($CHCl_3$:MeOH:H_2O)].

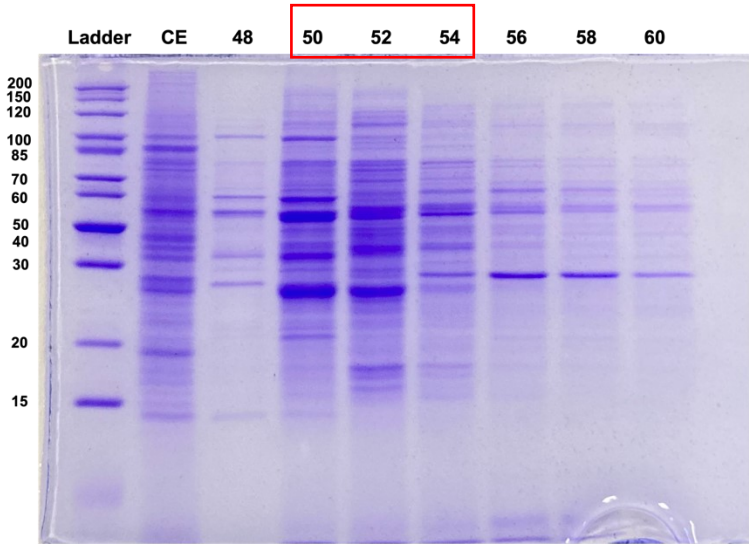

Figure 5.23. SDS-PAGE gel analysis of the fractions from IEC-1 (Gel percentage: 12%). The numbers indicate fractions and 15 µL of each fraction/crude extract was loaded onto the gel.

The active fractions (46.21 mg) were combined and loaded onto the Phenyl Sepharose column in 2 parts. The results of the first part are presented in Figures 5.24, 5.25 and Chromatogram 5.12. As in the optimization studies, the fractions exhibiting LH activity were eluted at 0 M AS concentration (Figure 5.24). In addition, protein elution was carried out using more elution buffer (50 mM Tris HCl, 10 CV) since the elution continued in the

washing step (Chromatogram 5.12). The protein amounts of the combined fractions of HIC-1 were as follows:

Part 1 - FR 98-102: 255.5 µg; FR 103-112: 22.19 µg

Part 2 - FR 92-98: 650.6 µg; FR 99-116: 158.3 µg.

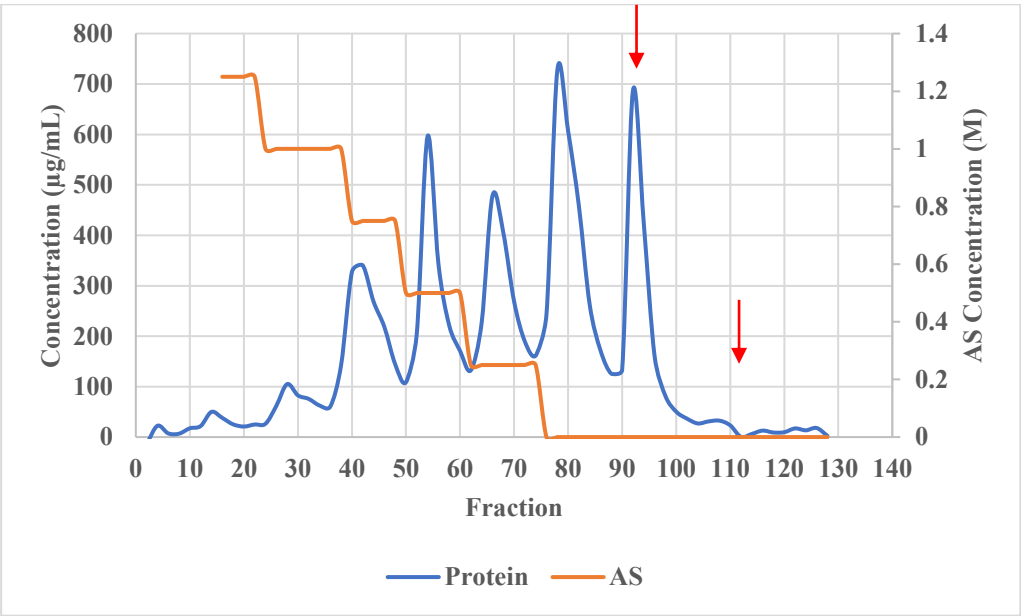

Figure 5.24. Separation of the IEC fractions from IEC-1 on Phenyl Sepharose (HIC-1).

SDS-PAGE gel images of the fractions belonging to the purification steps are given in Figure 5.25. Accordingly, the amount of protein just below 30 kDa was higher than the others as a result of hydrophobic interaction chromatography. When FR 99-116 is compared with other HIC fractions, it is seen that proteins below 30 kDa and 60 kDa are common. In the optimization studies, it was observed that the intensity of the protein in the range of 20-30 kDa increased with the purification steps. However, protein purity needs to be improved for protein identification.

A comparison of fractions obtained in optimization studies and purification studies is shown in Figure 5.25b. When SEC-1-FR 4-12 and HIC-1-FR 99-116 are compared, a more successful result was obtained when Q Sepharose and Phenyl Sepharose resins were used, compared to the DEAE Sepharose - Phenyl Sepharose - Sephacryl S200 strategy.

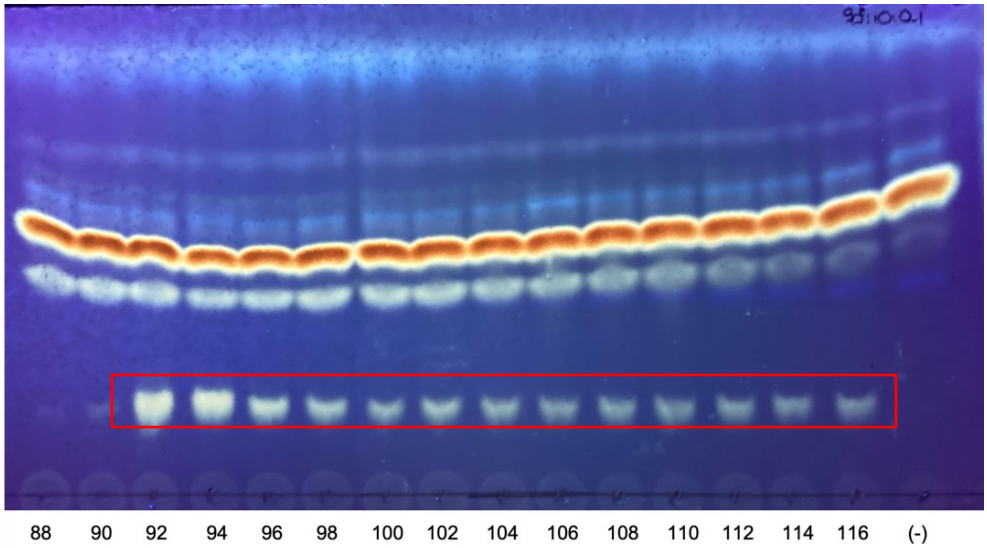

Chromatogram 5.12. Activity test results of the fractions obtained from HIC-1 (Incubation time: 15 h) [Silica gel, Mobile phase: 90:10:0.1 ($CHCl_3$:MeOH:H_2O)].

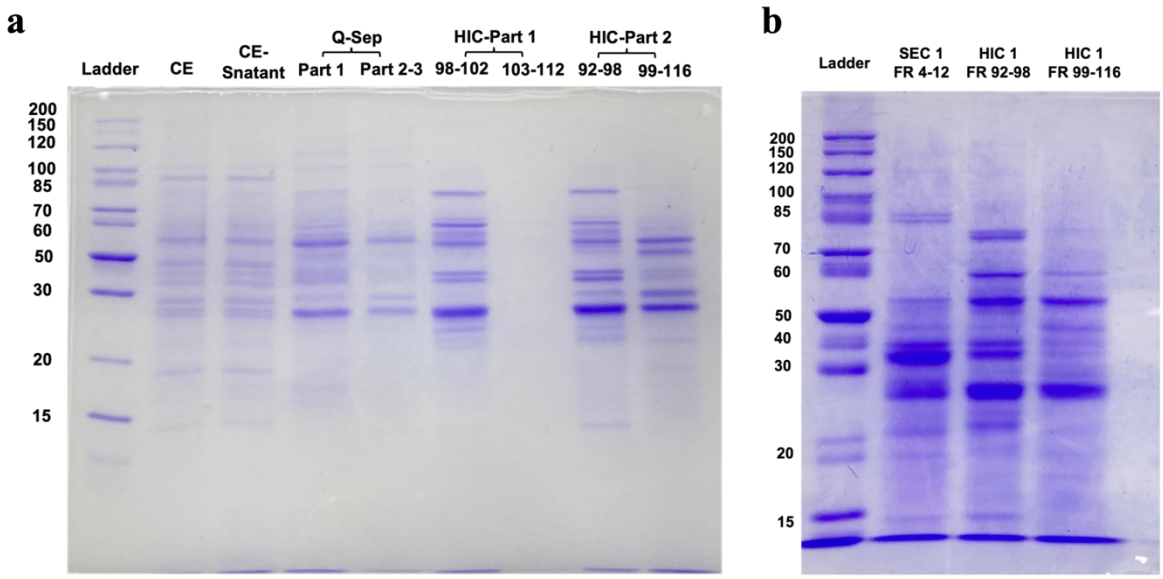

Figure 5.25. SDS-PAGE gel analysis of a) the combined fractions from purification studies, IEC-1 and HIC-1. b) Comparison of fractions from optimization (SEC-1-FR 4-12) and purification studies (HIC-1 fractions) (Gel percentage: 12%). 7.5 µg of protein was loaded onto each well.

5.3.4. Studies for Optimization and Purification of ADH

The studies for the purification of the ADH enzyme are described under the headings of optimization studies and purification studies.

5.3.4.1. Optimization Studies

Optimization studies for the ADH enzyme are summarized in Table 5.14 and details are explained below.

Table 5.14. Summary of optimization studies for ADH.

Experiment Code	Sample	Methodology	Active Fraction
IEC-1	Crude Extract (88.35 mg)	Ion Exchange Chromatography Resin: DEAE Sepharose, 10 mL Column: 2.5 cm x 10 cm, Flow rate: 1.25 mL/min Starting Buffer: 50 mM Tris HCl (pH 7.4) Gradient Elution: 0.1 – 0.5 M NaCl	16.66 mg
AS Cut	Crude Extract (6.05 mg)	AS Precipitation Fractions: 1.5 M, 2.0 M, 2.5 M, 3.0 M, 3.5 M pellets	1.5 M pellet: 1.088 mg 2.0 M pellet: 0.822 mg 2.5 M pellet: 0.801 mg
HIC-1	IEC-1-FR36-43 (11 mg)	Hydrophobic Interaction Chromatography Resin: Phenyl Sepharose, 3 mL Column: 0.7 cm x 10 cm, Flow rate: 1.5 mL/min Starting Buffer: 50 mM Tris HCl (pH 7.4) + 1.5 M AS Gradient Elution: 1.25 M – 0 M AS	FR 11-18: 0.869 mg FR 19-24: 1.547 mg
IEC-2	Crude Extract (4.28 mg)	Ion Exchange Chromatography Resin: Q Sepharose, 3 mL Column: 0.7 cm x 10 cm, Flow rate: 1.5 mL/min Starting Buffer: 50 mM Tris HCl (pH 7.4) Gradient Elution: 0.1 – 1 M NaCl	0.928 mg
* The methods in "5.2.3.4. Chromatographic Processes" were used in the optimization steps.			

Ion Exchange Chromatography (IEC-1)

In the first study, 88.35 mg of ADH extract was submitted to the DEAE Sepharose resin, and ADH enzyme was eluted with 0.1-0.2 M NaCl (Figure 5.26). Based on Chromatogram 5.13, the fraction with ADH activity was determined to be FR 36-43. Most non-target proteins (81%) were removed using DEAE Sepharose (Table 5.15). When the SDS-PAGE image of the fraction exhibiting ADH activity was analyzed, it was observed that there were many impurities in the fraction (Figure 5.27).

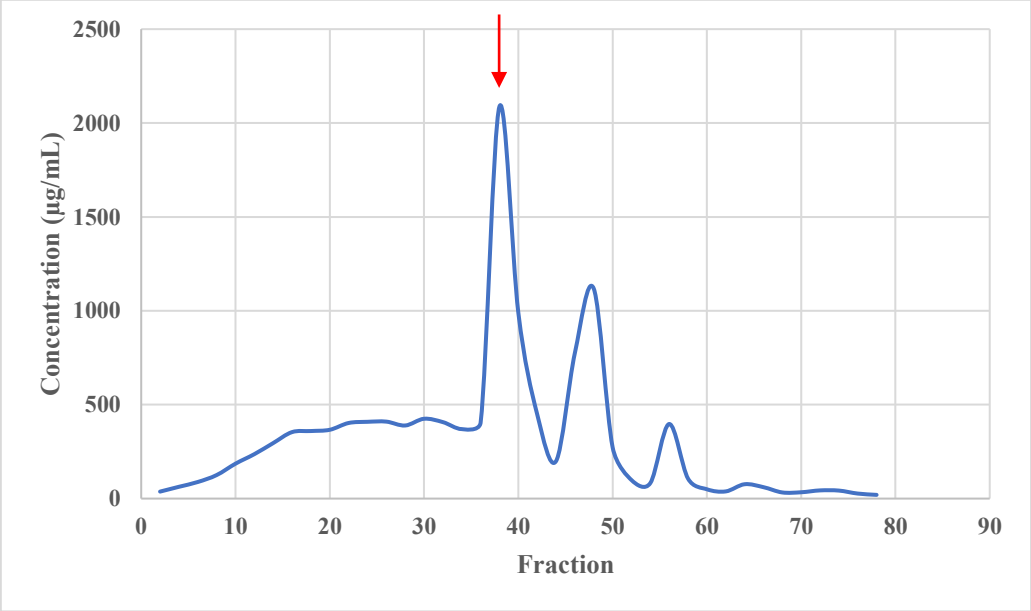

Figure 5.26. Separation of the ADH crude extract on DEAE Sepharose (IEC-1).

Table 5.15. Combined fractions from IEC-1.

Fraction	Total Protein (µg)
1-35	30288.1
36-43*	16660.425
44-53	9972.438
54-60	2805.38

* Fraction with ADH activity

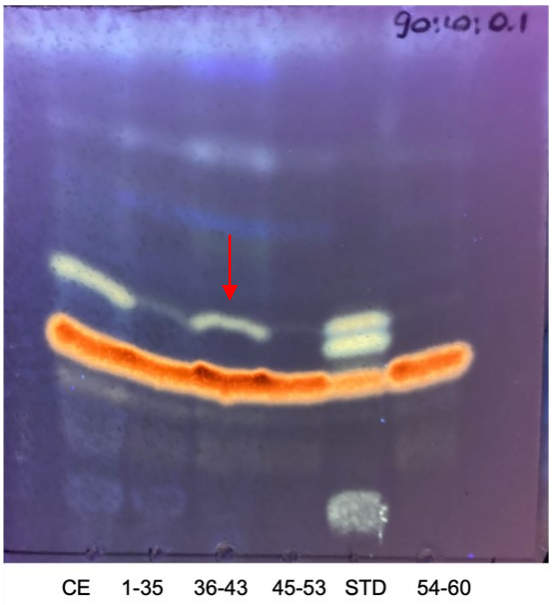

Chromatogram 5.13. Activity test results of the fractions obtained from IEC-1 (Incubation time: 20 h) [Silica gel, Mobile phase: 90:10:0.1 ($CHCl_3$:MeOH:H_2O)].

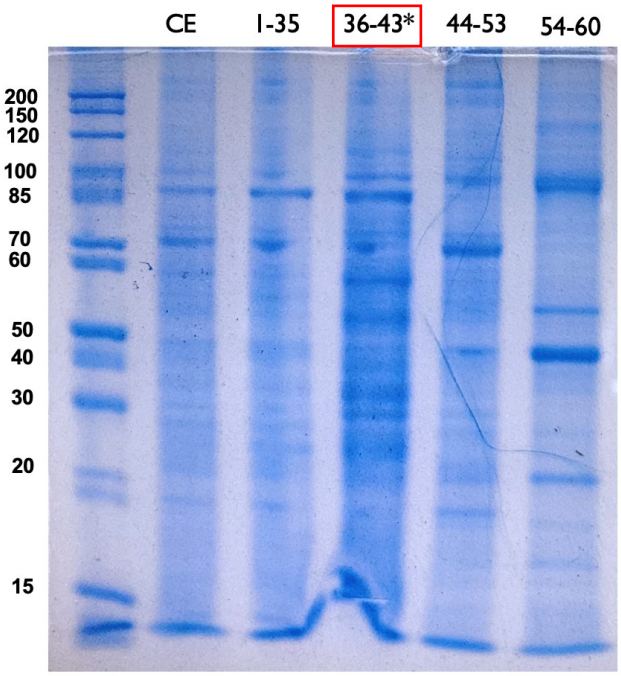

Figure 5.27. SDS-PAGE gel analysis of the fractions from IEC-1 (Gel percentage: 12%). 15 µg of protein was loaded onto each well.

Analytical AS Precipitation (AS Cut)

The analytical AS precipitation showed that the ADH enzyme precipitated at 1.5 M, 2.0 M, and 2.5 M AS concentrations (Chromatogram 5.14). ADH-rich fractions obtained by AS precipitation are approximately 45% of the total extract (Table 5.16). However, the SDS-PAGE result also showed that high purification did not occur (Figure 5.28). Although precipitation was observed at 1.5 M AS, the ADH activity of this fraction was less than the other active fractions (2.0 M and 2.5 M pellet). For this reason, we decided to attempt hydrophobic interaction chromatography.

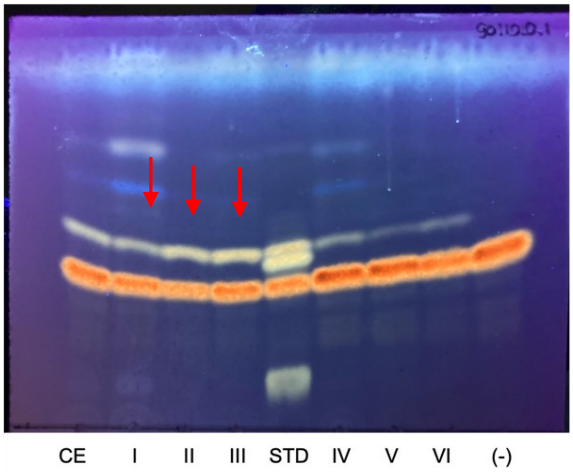

Chromatogram 5.14. Activity test results of the fractions obtained from analytical AS precipitation (Incubation time: 17 h, protein concentration: 500 µg/mL) [Silica gel, Mobile phase: 90:10:0.1 ($CHCl_3$:MeOH:H_2O)].

Table 5.16. Analytical AS precipitation for ADH.

Fraction	Total Protein (µg)	Yield (%)
1.5 M Pellet*	1088.1	18
2.0 M Pellet*	822.7	13.6
2.5 M Pellet*	801.2	13.2
3.0 M Pellet	525.4	8.68
3.5 M Pellet	370.8	6.13
3.5 M Supernatant	1146.3	19
* Fraction with ADH activity		

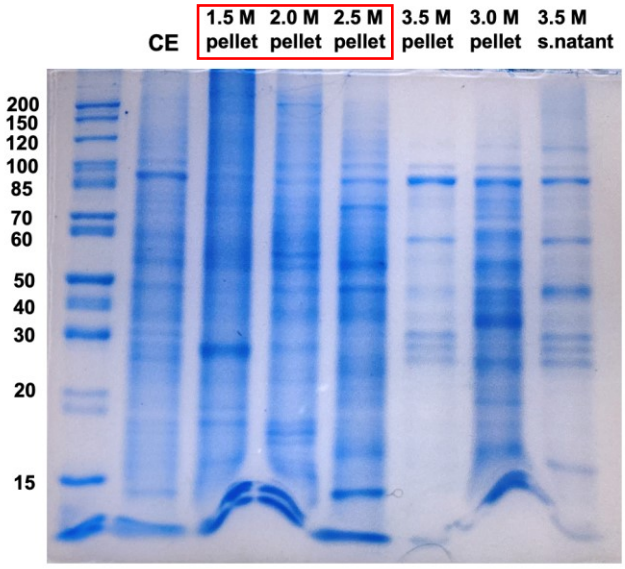

Figure 5.28. SDS-PAGE gel analysis of the fractions from AS precipitation (Gel percentage: 12%). 1) CE: Crude extract (15 µg), 2) 1.5 M pellet (15 µg), 3) 2.0 M pellet (15 µg), 4) 2.5 M pellet (15 µg), 5) 3.0 M pellet (2.82 µg), 6) 3.5 M pellet (3.96 µg).

Hydrophobic Interaction Chromatography

A preliminary study for hydrophobic interaction chromatography resulted in the elution of ADH enzyme with 1 M AS (Figure 5.29, Chromatogram 5.15). Therefore, Phenyl Sepharose resin was found suitable for the preparative study.

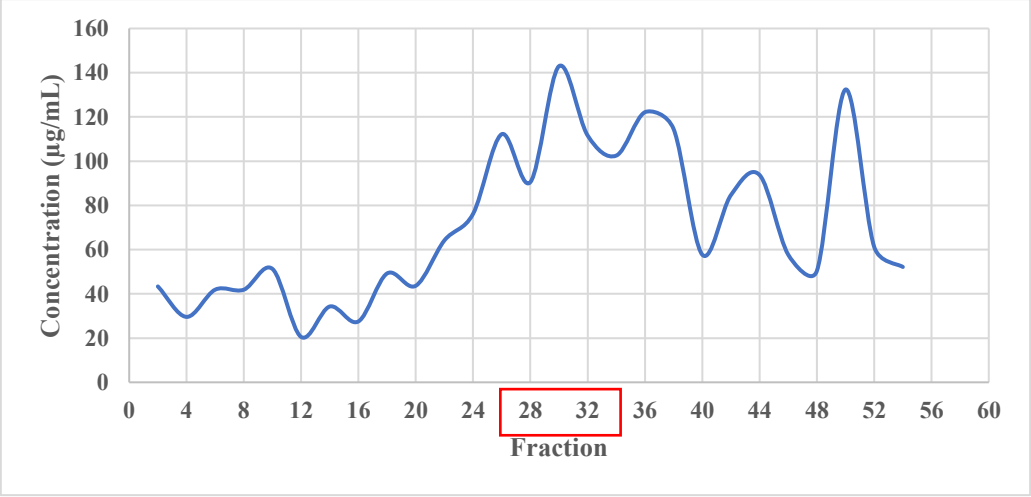

Figure 5.29. Separation of the IEC-1-FR 36-43 on Phenyl Sepharose (preliminary).

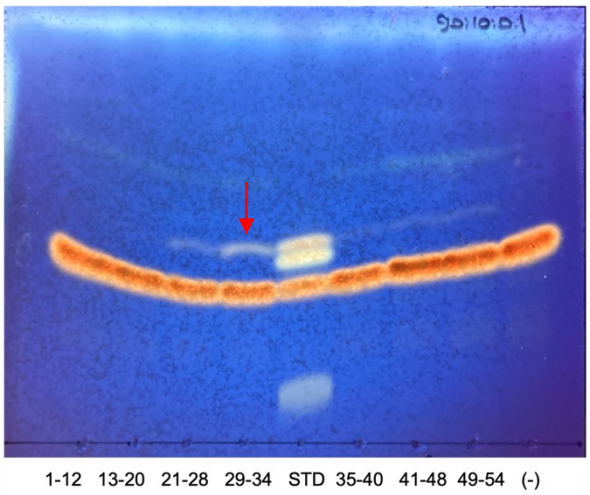

Chromatogram 5.15. Activity test results of the fractions obtained from preliminary HIC (Incubation time: 18 h) [Silica gel, Mobile phase: 90:10:0.1 ($CHCl_3$:MeOH:H_2O)].

The elution plot of the preparative hydrophobic interaction chromatography is presented in Figure 5.30. Fractions were combined based on the peaks in Figure 5.30 (Table 5.17).

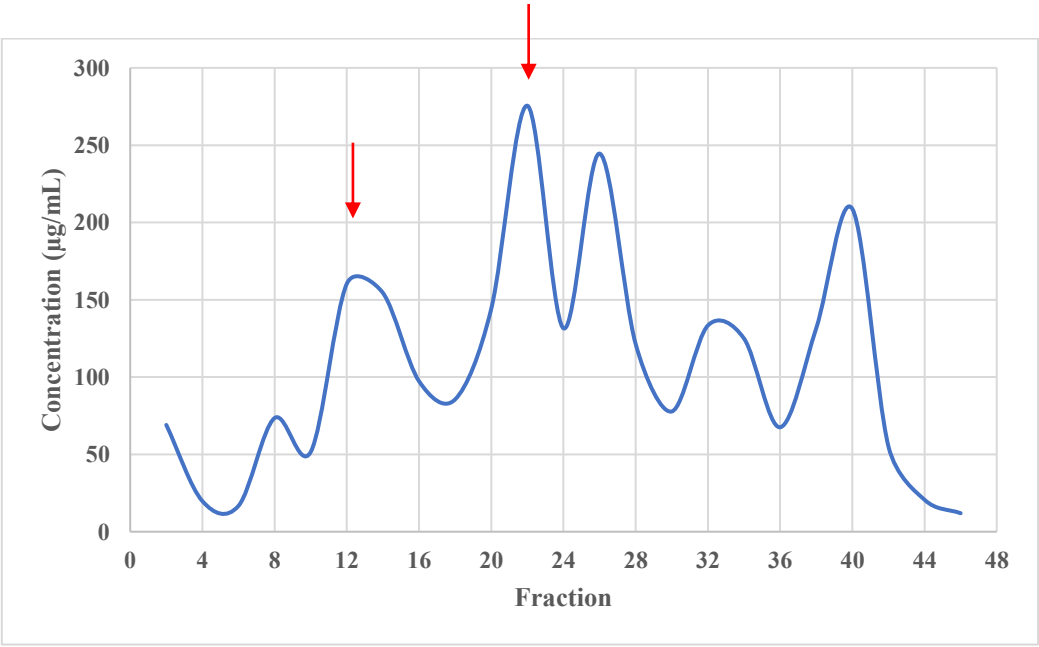

Figure 5.30. Separation of the IEC FR 36-43 on Phenyl Sepharose (HIC-1).

Table 5.17. Combined fractions from HIC-1.

Fraction	Total Protein (µg)
1-10	194.9011
11-18*	868.9975
19-24*	1546.592
25-30	883.3062
31-36	1070.591
37-46	1281.405

* Fraction with ADH activity

According to Chromatogram 5.16, two different fractions (FR 11-18 and FR 19-24) were determined to show ADH activity. The SDS-PAGE image showed that the protein profile of these fractions differed, but a band around 85 – 100 kDa was common (Figure 5.31).

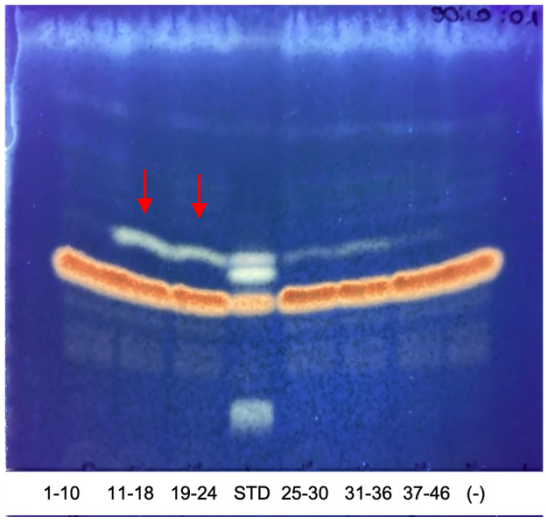

Chromatogram 5.16. Activity test results of the fractions obtained from HIC-1 (Incubation time: 14 h) [Silica gel, Mobile phase: 90:10:0.1 ($CHCl_3$:MeOH:H_2O)].

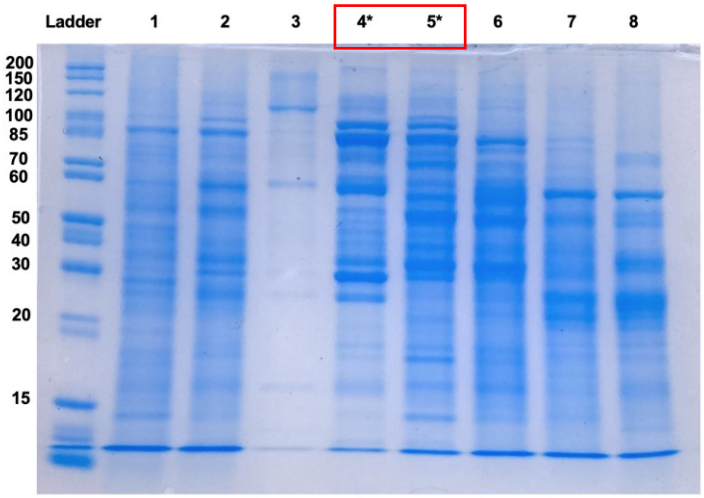

Figure 5.31. SDS-PAGE gel analysis of the fractions from HIC-1 (Gel percentage: 12%). 1) Crude extract (10 µg), 2) IEC-1-FR 36-43 (10 µg) 3) FR 1-10 (2.9 µg), 4) FR 11-18 (10 µg), 5) FR 19-24 (10 µg), 6) FR 25-30 (10 µg), 7) FR 31-36 (10 µg), 8) FR 37-46 (10µg)

Ion Exchange Chromatography

Q Sepharose was used as a strong anion exchanger in the last step of ADH optimization studies. When Figure 5.32 and Chromatogram 5.17 were examined together, it was determined that ADH was eluted at 0.1 M NaCl concentration.

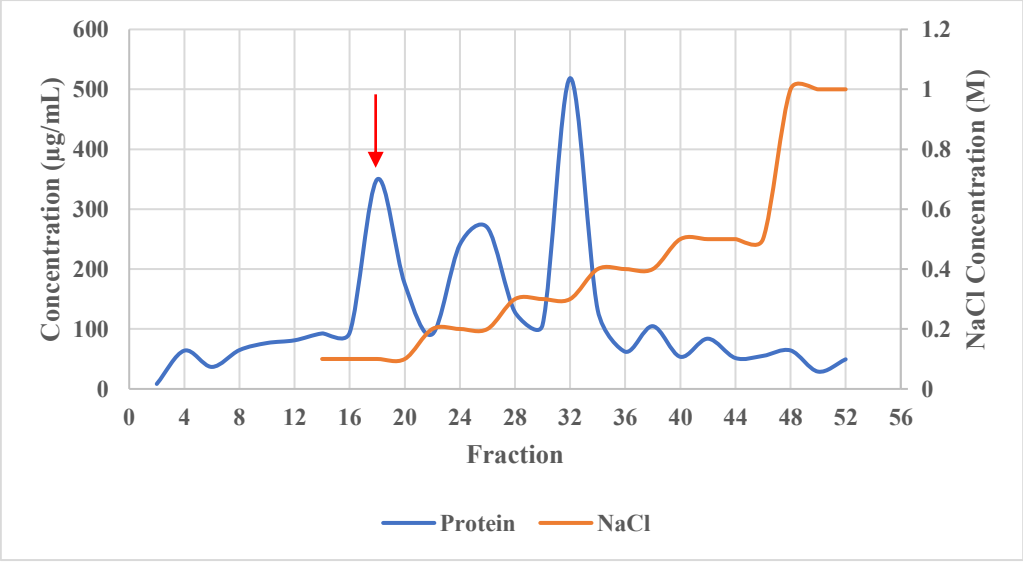

Figure 5.32. Separation of the ADH crude extract on Q Sepharose (IEC-2).

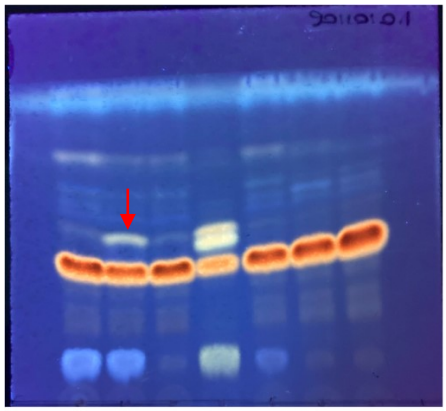

Chromatogram 5.17. Activity test results of the fractions obtained from IEC-2 (Incubation time: 19 h) [Silica gel, Mobile phase: 90:10:0.1 ($CHCl_3$:MeOH:H_2O)].

5.3.4.2. Purification Studies

Purification studies for the ADH enzyme are summarized in Table 5.18 and details are explained below.

Table 5.18. Summary of optimization studies for ADH.

Experiment Code	Sample	Methodology	Active Fraction
IEC-1	Crude Extract (202.52 mg)	Ion Exchange Chromatography Resin: DEAE Sepharose, 20 mL Column: 2.5 cm x 10 cm, Flow rate: 10 mL/min Starting Buffer: 50 mM Tris HCl (pH 7.4) Gradient Elution: 0.1 – 0.5 M NaCl	40.59 mg
HIC-1	IEC-1-FR 56-64 (39.9 mg)	Hydrophobic Interaction Chromatography Resin: Phenyl Sepharose, 5 mL Column: 1 cm x 10 cm, Flow rate: 1.75 mL/min Starting Buffer: 50 mM Tris HCl (pH 7.4) + 1.5 M AS Gradient Elution: 1.25 M – 0 M AS	6.179 mg
IEC-2	HIC-1-FR 26-31 (5.25 mg)	Ion Exchange Chromatography Resin: Q Sepharose, 3 mL Column: 0.7 cm x 10 cm, Flow rate: 1.5 mL/min Starting Buffer: 50 mM Tris HCl (pH 7.4) Gradient Elution: 0.1 – 0.4 M NaCl	1.31 mg
* The methods in "5.2.3.4. Chromatographic Processes" were used in the purification steps.			

In line with the optimization studies, we decided to use weak anion exchange resin (DEAE Sepharose), hydrophobic interaction resin (Phenyl Sepharose), and strong anion exchange resin (Q Sepharose), respectively, for purification studies. This study was started with 202.52 mg of crude extract.

In the first step, ADH activity was determined to be between FR 56-70 (Chromatogram 5.18). These fractions were eluted with 0.1 M and 0.2 M NaCl (Figure 5.33). However, in optimization studies with DEAE Sepharose, it was found that ADH enzyme was eluted with 0.1 M NaCl. Therefore, the fractions showing ADH activity were combined into two separate fractions (FR 56-64: 40.59 mg and FR 65-70: 44.43 mg). The reason why the elution continued with 0.2 M NaCl was peak tailing. For this reason, the second step continued with the FR 56-64, eluted with 0.1 M NaCl. SDS-PAGE gel image showed no clear separation in the protein profile as in the optimization studies (Figure 5.34).

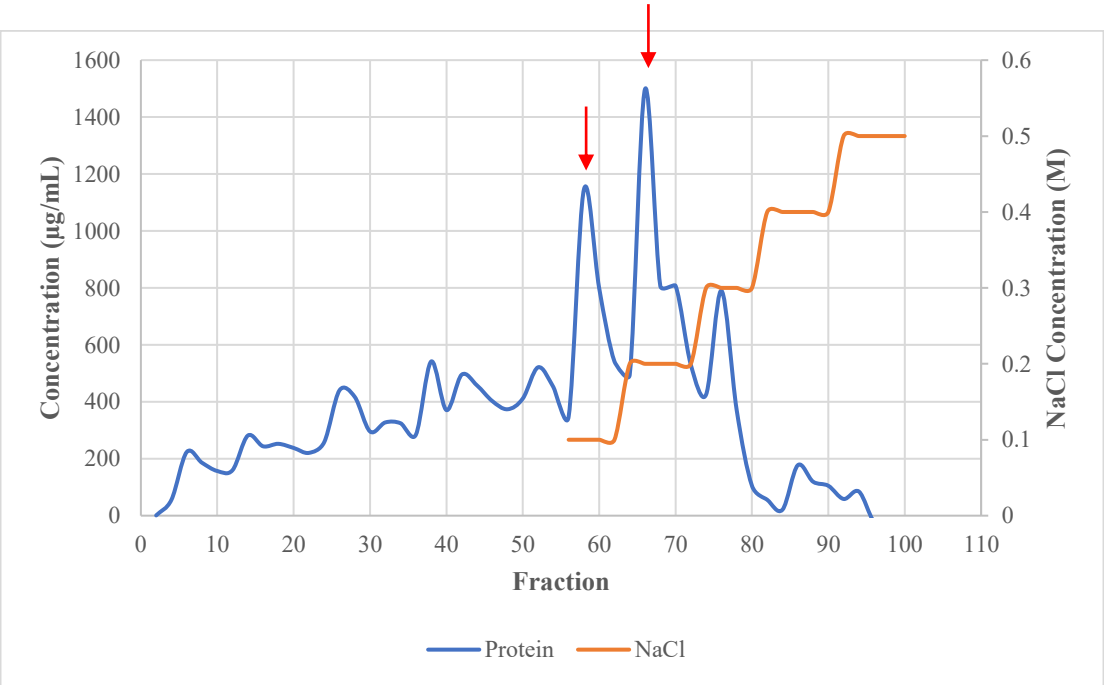

Figure 5.33. Separation of the ADH crude extract on DEAE Sepharose (IEC-1).

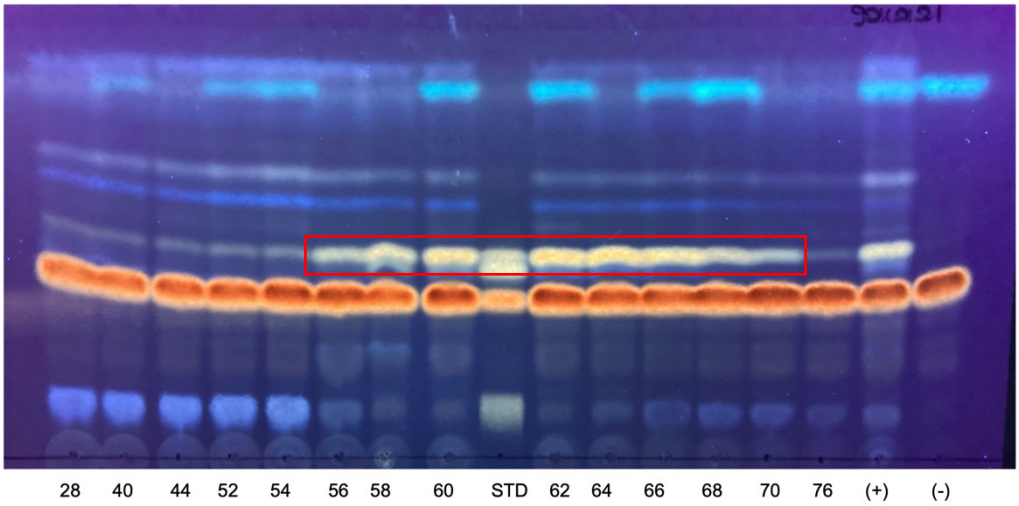

Chromatogram 5.18. Activity test results of the fractions obtained from IEC-1 (Incubation time: 12 h) [Silica gel, Mobile phase: 90:10:0.1 ($CHCl_3$:MeOH:H_2O)].

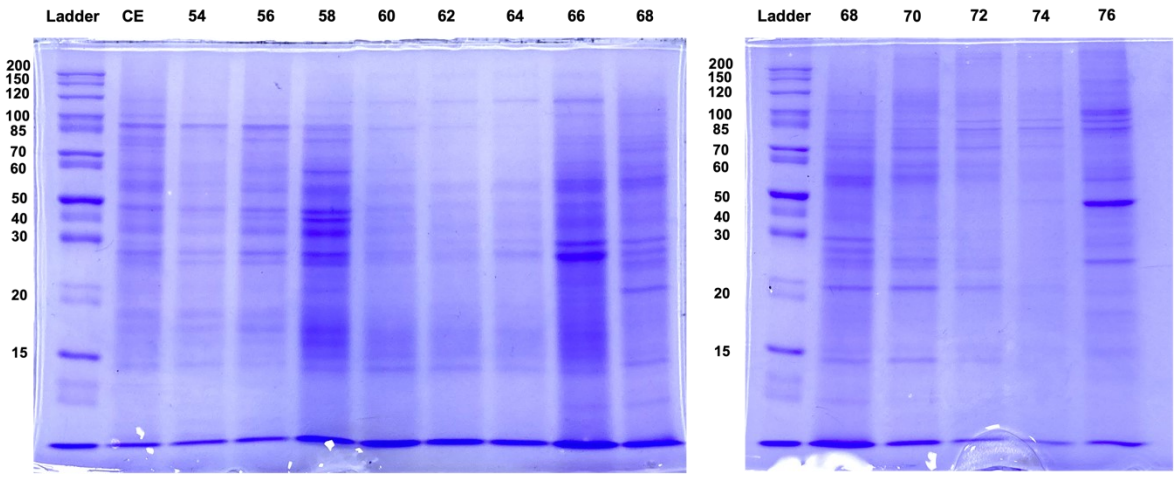

Figure 5.34. SDS-PAGE gel analysis of the fractions from IEC-1 (Gel percentage: 12%). The numbers indicate fractions and 15 µL of each fraction/crude extract was loaded onto the gel.

The results of the hydrophobic interaction chromatography used in the second step are presented in Figure 5.35 and Chromatogram 5.19. The results were consistent with the optimization studies. As a result of fractionation with Phenyl Sepharose, FR-26-31 was pooled together, and 6.179 mg of protein was obtained. When the gel image of FR 26-31 was

compared with other fractions, we observed that the protein around 85-100 kDa might belong to the ADH enzyme (Figure 5.36).

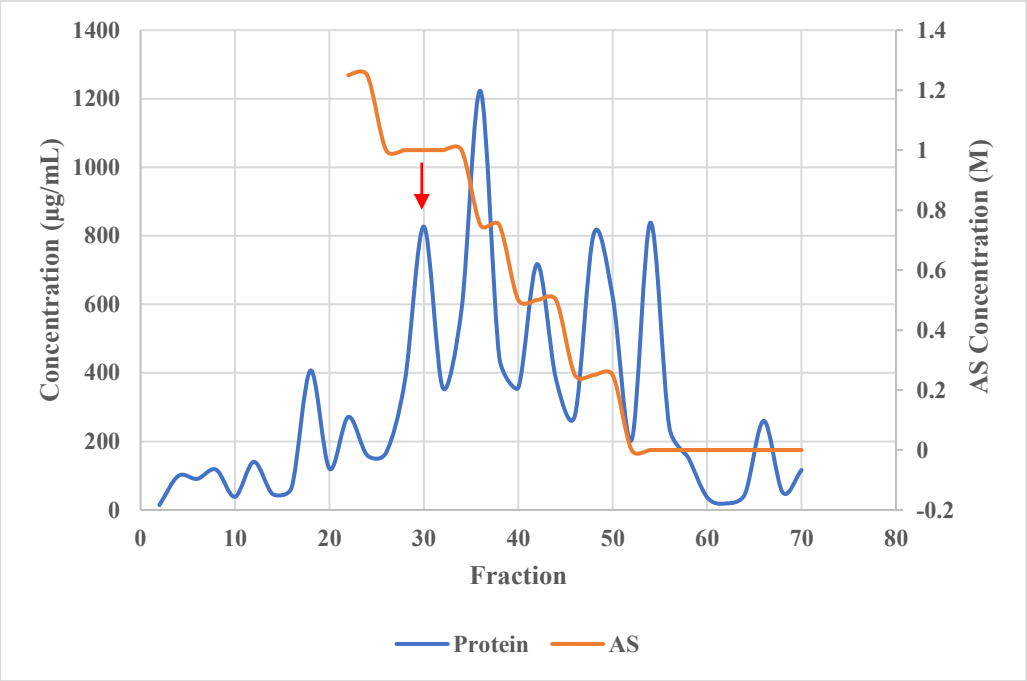

Figure 5.35. Separation of the IEC-1-FR 56-64 on Phenyl Sepharose (HIC-1).

Chromatogram 5.19. Activity test results of the fractions obtained from HIC-1 (Protein concentration: 500 µg/mL, Incubation time: 14 h) [Silica gel, Mobile phase: 90:10:0.1 ($CHCl_3$:MeOH:H_2O)].

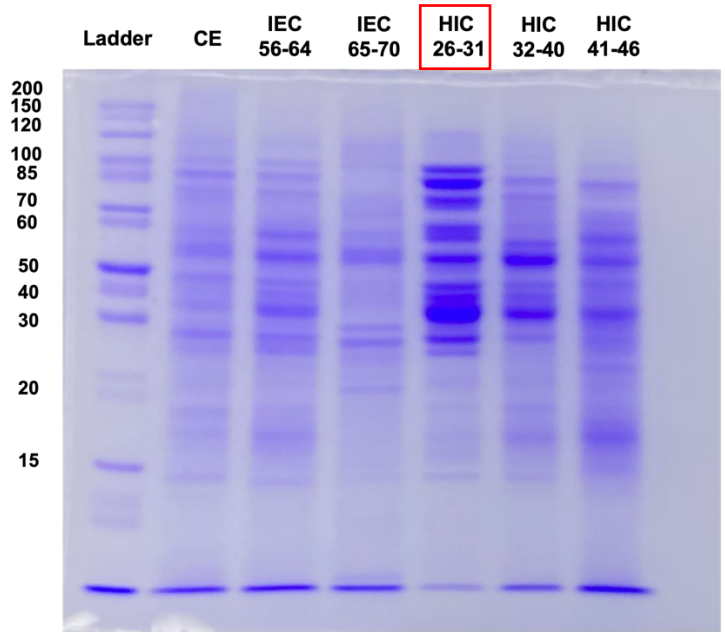

Figure 5.36. SDS-PAGE gel analysis of the combined fractions from IEC-1 and HIC-1 (Gel percentage: 12%). 7.5 µg of protein was loaded onto each well.

Q Sepharose resin was used in the third purification step, and a gradient of 0.1 M - 0.4 M NaCl was applied for elution (Figure 5.37).

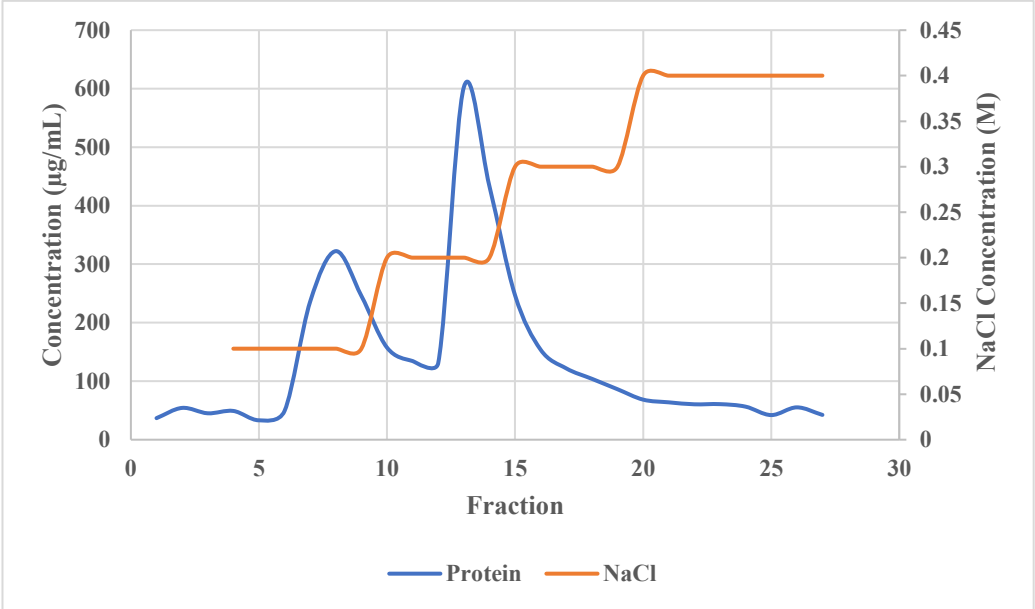

Figure 5.37. Separation of the LH crude extract on Q Sepharose (IEC-2).

According to the SDS-PAGE gel image, fractions with similar protein profiles were combined (Figure 5.38). The activity test result demonstrated that all three combined fractions had ADH activity (Chromatogram 5.20). The protein profiles of combined fractions differed from each other in terms of protein concentrations. Proteins in the 30-85 kDa range were in higher concentration in FR 13-14 than in FR 7-9 and FR 10-12 (Figure 5.38). When Chromatogram 5.20 and Figure 5.38 were examined, we focused on the idea that the band around 85 kDa could belong to the ADH enzyme.

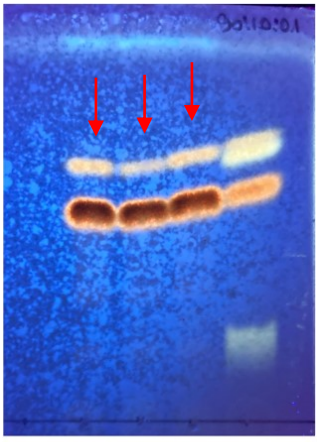

Chromatogram 5.20. Activity test results of the fractions obtained from IEC-2 (Incubation time: 12 h) [Silica gel, Mobile phase: 90:10:0.1 ($CHCl_3$:MeOH:H_2O)].

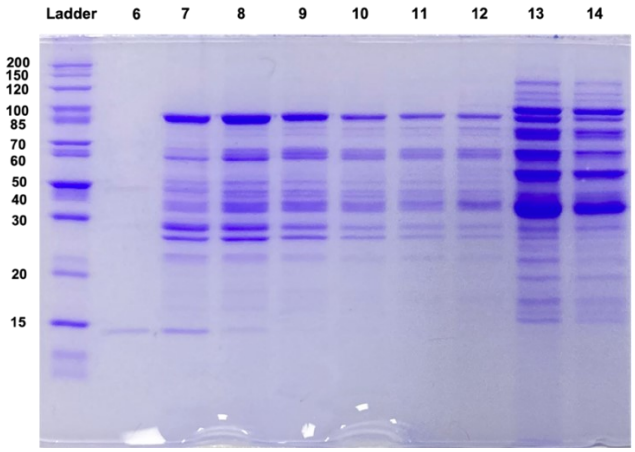

Figure 5.38. SDS-PAGE gel analysis of the fractions from IEC-2 (Gel percentage: 12%). The numbers indicate fractions and 15 µL of each fraction was loaded onto the gel.

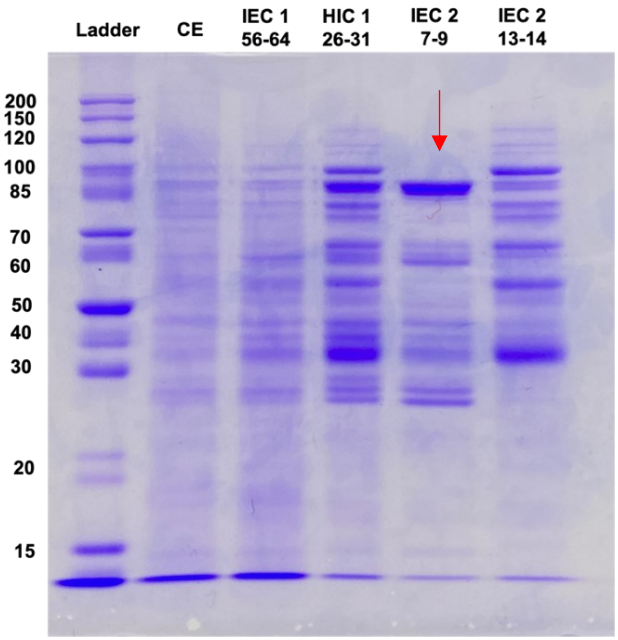

Figure 5.39. SDS-PAGE gel analysis of the fractions from ADH purification steps (Gel percentage: 12%). 7.5 µg of protein was loaded onto each well.

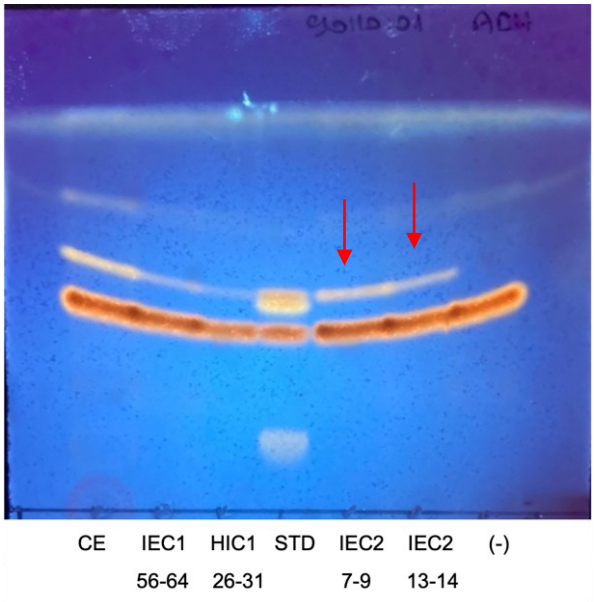

Chromatogram 5.21. Activity test results of the fractions obtained from ADH purification steps (Protein concentration: 250 µg/mL, Incubation time: 24 h) [Silica gel, Mobile phase: 90:10:0.1 ($CHCl_3$:MeOH:H_2O)].

The SDS-PAGE gel image of the ADH purification steps is presented in Figure 5.39, showing that the purification strategy applied was successful. Isolation from other proteins was achieved at each stage, and the concentration of the band around 85 kDa, thought to belong to the enzyme, was increased. The activities of the last two fractions (Chromatogram 5.21) and SDS-PAGE gel image (Figure 5.39) reinforce our assumption that the band at 85 kDa belongs to the ADH enzyme.

5.3.5. Studies for Optimization and Purification of BVMO

Optimization and purification studies for the BVMO enzyme are summarized in Table 5.19, and details are explained below.

Table 5.19. Summary of optimization and purification studies for BVMO.

Experiment Code	Sample	Methodology	Active Fraction
Preliminary AS Precipitation	Crude Extract (20 mg)	AS Precipitation Fractions: 50%, 70%, 80% and 90% pellets	-
Preparative AS Precipitation	Crude Extract (300 mg)	AS Precipitation Fractions: 40%, 60% and 80% pellets	80% Pellet: 8.82 mg
IEC-1	80% Pellet (8.82 mg)	Ion Exchange Chromatography Resin: DEAE Sepharose, 3 mL Column: 0.7 cm x 10 cm, Flow rate: 1 mL/min Starting Buffer: 50 mM NaPi (pH 7.4) Gradient Elution: 0 – 0.5 M NaCl	No active fraction
IEC-2	Crude Extract (53 mg)	Ion Exchange Chromatography Resin: DEAE Sepharose, 3 mL Column: 0.7 cm x 10 cm, Flow rate: 2 mL/min Starting Buffer: 50 mM NaPi (pH 7.4) + 10% glycerol Gradient Elution: 0.1 – 0.5 M NaCl	22.83 mg

cont. on next page

Table 5.19. cont.

SEC-1	IEC-1-FR1-30 (17.72 mg)	Size Exclusion Chromatography Resin: Sephacryl S200, 30 mL Column: 1.6 cm x 20 cm, Flow rate: 1.4 mL/min Starting Buffer: 50 mM NaPi (pH 7.4) + 500 mM NaCl Isocratic Elution: 500 mM NaCl	1.74 mg
IEC-3	Crude Extract (96 mg)	Ion Exchange Chromatography Resin: DEAE Sepharose, 12 mL Column: 2.5 cm x 10 cm, Flow rate: 4 mL/min Starting Buffer: 50 mM NaPi (pH 7.4) Gradient Elution: 0 – 0.5 M NaCl	25.94 mg
IEC-4	Crude Extract (25 mg)	Ion Exchange Chromatography Resin: Q Sepharose, 3 mL Column: 0.7 cm x 10 cm, Flow rate: 1.5 mL/min Starting Buffer: 50 mM NaPi (pH 7.4) Gradient Elution: 0 – 1 M NaCl	3.7 mg
HIC-1	IEC-3-FR27-29 (3.5 mg)	Hydrophobic Interaction Chromatography Resin: Phenyl Sepharose, 3 mL Column: 0.7 cm x 10 cm, Flow rate: 1.5 mL/min Starting Buffer: 50 mM NaPi (pH 7.4) + 1.5 M AS Gradient Elution: 1.5 M – 0 M AS	No active fraction
HIC-2	Crude Extract (20.7 mg)	Hydrophobic Interaction Chromatography Resin: Phenyl Sepharose, 3 mL Column: 0.7 cm x 10 cm, Flow rate: 1.5 mL/min Starting Buffer: 50 mM NaPi (pH 7.4) + 1.5 M AS Gradient Elution: 1.5 M – 0 M AS	No active fraction
HIC-3	Crude Extract (36.8 mg)	Hydrophobic Interaction Chromatography Resin: Phenyl Sepharose, 3 mL Column: 0.7 cm x 10 cm, Flow rate: 1.5 mL/min Starting Buffer: 50 mM NaPi (pH 7.4) + 1.5 M AS Gradient Elution: 1.5 M – 0 M NaCl	No active fraction
* The methods in "5.2.3.4. Chromatographic Processes" were used in the optimization and purification steps. ** All buffers used in these steps contain 0.1 mM FAD.			

AS Precipitation

Ammonium sulfate precipitation was tested in the first step for enzyme isolation. The precipitation was carried out with 50%, 70%, 80% and 90% AS using approximately 20 mg of protein. When the activity test was performed for the pellets, BVMO activity was not present (Chromatogram 5.22a). Also, ADH activity was found to be very low. These results suggested that a trace of ammonium sulfate could affect the reactions; therefore, the samples were processed with desalting procedures using a centrifugal filter unit (10kDa). After the

activity test, BVMO activity was still absent, whereas ADH activity was present (Chromatogram 5.22b).

The loss of BVMO activity was reported in fractionation and purification studies (AS, chromatographic studies). The FAD/FMN prosthetic group detached from the enzyme and caused a loss of activity[195]. Inorganic sulfate binds competitively to the cofactor binding site, leading to activity loss, mainly if the AS precipitation step is used[234]. Incubation with excess FAD/FMN was suggested to recover enzyme activity. For this reason, 80% and 90% pellets were incubated with 5 mM FAD for 1 h at 4°C and 30°C. Afterward, the activity test was performed, but BVMO activity was not recovered (Chromatogram 5.22c).

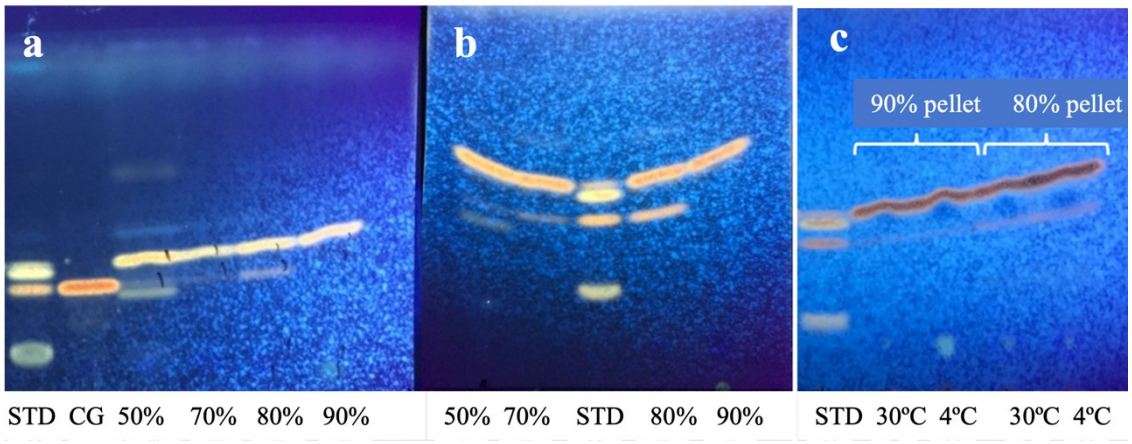

Chromatogram 5.22. Activity results of the pellets from AS precipitation a) no treatment, b) after ultrafiltration process and c) after FAD incubation [Silica gel, Mobile phase: 90:10:0.1 ($CHCl_3$:MeOH:H_2O)].

The effect of AS on BVMO activity was investigated by adding 1%, 5%, 10%, 20% and 40% to the protein extract. Activity results are shown in Chromatogram 5.23. According to the results, the activities of BVMO and ADH enzymes decreased using 1% AS and completely lost at 5%. In this case, the ultrafiltration process did not sufficiently remove the salt. For this reason, an experiment was set up for the desalting process by using PD10 desalting column.

The activity test results after the desalting process are shown in Chromatogram 5.24. The protein fraction was wholly removed from the AS salt when the PD10 column was used.

Sample B was tested to control whether there was activity loss due to PD10 column. When samples A and C were compared, the amount of protein used in sample C was 10% of sample A's, and its activity was still high. According to these results, AS precipitation decreases the protein load for further steps and concentrates the target enzyme. In sample C, ADH activity was present along with BVMO activity.

Chromatogram 5.23. Effect of different AS concentrations on BVMO activity (Incubation time: 24 h) [Silica gel, Mobile phase: 90:10:0.1 ($CHCl_3$:MeOH:H_2O)].

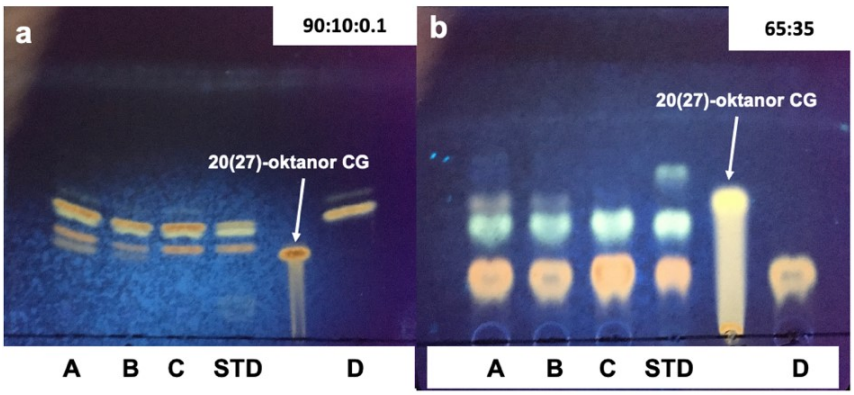

Chromatogram 5.24. Activity results after desalting by using PD10 column (Incubation time: 24 h). a) Silica gel, Mobil phase: 90:10:0.1 ($CHCl_3$:MeOH:H_2O); b) Reverse phase C18 silica gel, Mobile phase: 65:35 (ACN: H_2O). Sample A: Crude protein extract; Sample B: Crude extract eluted from PD10 column; Sample C: 80% pellet desalted with PD10; Sample D: Negative Control.

After overcoming the activity problem encountered after AS precipitation, preparative AS precipitation was performed with 300 mg of crude extract using 40%, 60% and 80% AS, respectively. According to Chromatogram 5.25, the BVMO activity was observed for the 60% and 80% fractions. Likewise, ADH was present in these fractions. There was no activity for both enzymes in the 40% pellet.

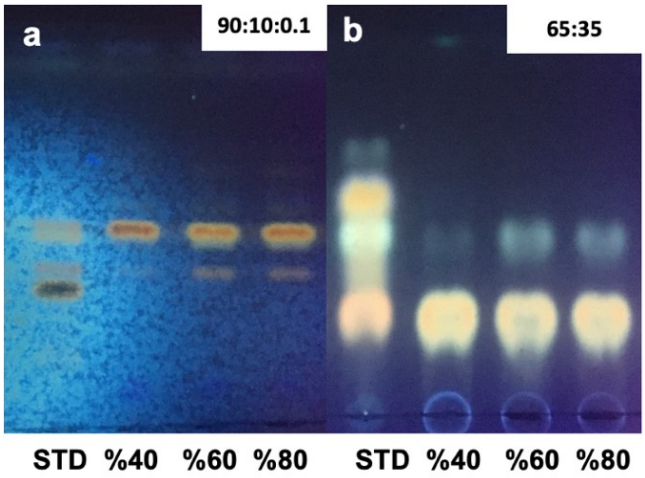

Chromatogram 5.25. Activity results of different AS fractions (Incubation time: 12 h). a) Silica gel, Mobile phase: 90:10:0.1 ($CHCl_3$:MeOH:H_2O); b) Reverse phase C18 silica gel, Mobile phase: 65:35 (ACN: H_2O).

Ion-Exchange Chromatography (IEC-1)

Following the AS precipitation, 80% pellet (8.82 mg) was applied to the DEAE Sepharose column. The fractions were combined based on the protein profile (Figure 5.40, Table 5.20). However, BVMO activity was not detected in these fractions (Chromatogram 5.26). In the SDS-PAGE gel analysis of the fractions (Figure 5.41), we noticed that the background turbidity in the crude extract was not observed in the fractions. Also, we observed that the partial isolation of proteins was accomplished in the combined fractions. However, interpretation of the protein bands was not possible since BVMO activity was not present.

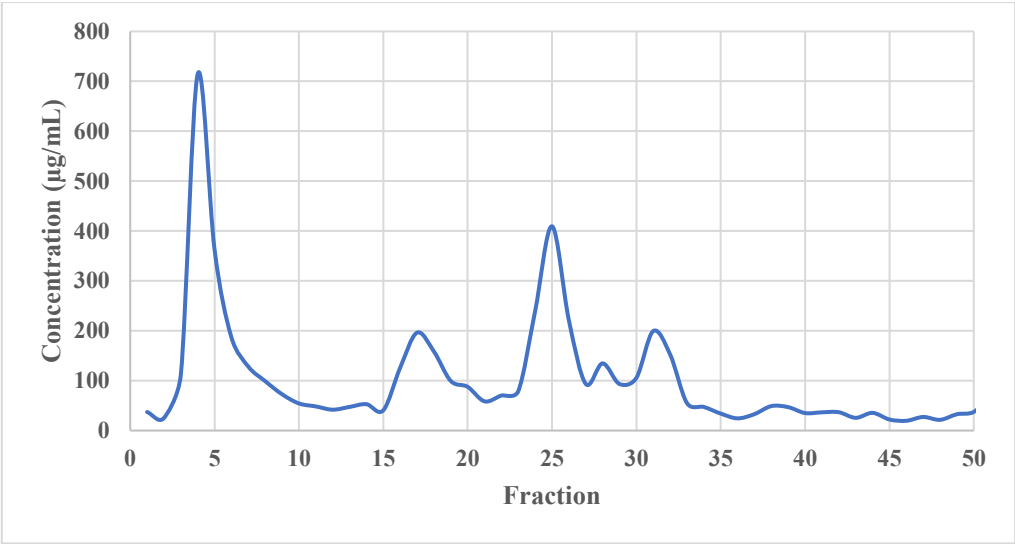

Figure 5.40. Separation of the BVMO fraction (80% pellet) on DEAE Sepharose (IEC-1).

Table 5.20. Combined fractions from IEC-1.

Fraction	Total Protein (µg)
2-10	1359
11-22	943.5
23-27	1033.4
28-36	786.9
39-49	132.7

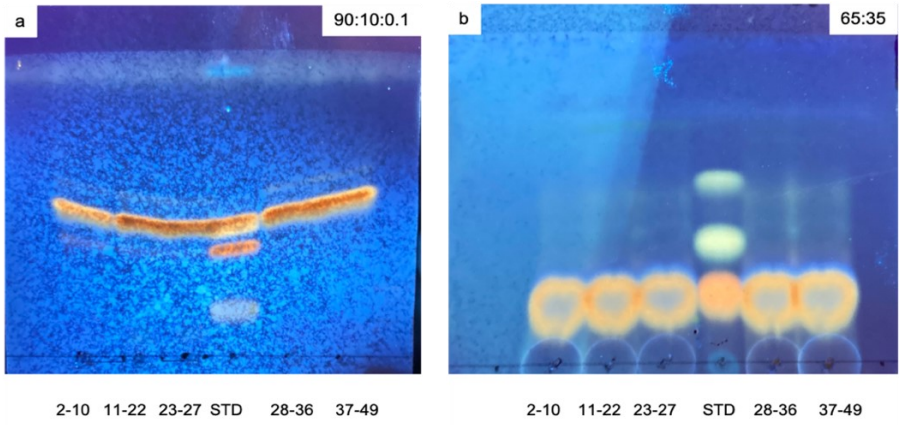

Chromatogram 5.26. Activity test result of the fractions IEC-1 (500 µg/mL of the fraction was used) (Incubation time: 48 h) a) Silica gel, Mobile phase: 90:10:0.1 ($CHCl_3$:MeOH:H_2O) b) Reversed phase C18 silica gel, Mobile phase: 65:35 (ACN: H_2O).

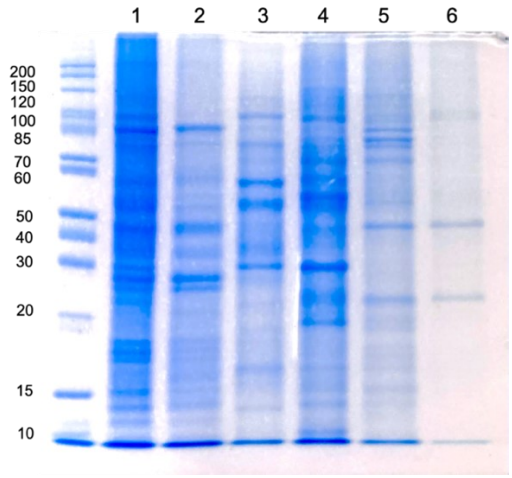

Figure 5.41. SDS-PAGE gel analysis of the fractions from IEC-1 (Gel percentage: 12%). 1) Crude extract (20 µg), 2) FR 1-10 (13.6 µg), 3) FR 11-22 (9.45 µg), 4) FR 23-27 (15.5 µg), 5) FR 28-36 (7.87 µg), 6) FR 39-49 (2 µg).

Ion-Exchange Chromatography (IEC-2)

As an alternative to AS precipitation, the BVMO crude extract (53 mg) was applied to the DEAE Sepharose resin without being concentrated. Since the lysis buffer for BVMO extraction contained 10% glycerol and 0.1 M NaCl, the column was conditioned with the same buffer.

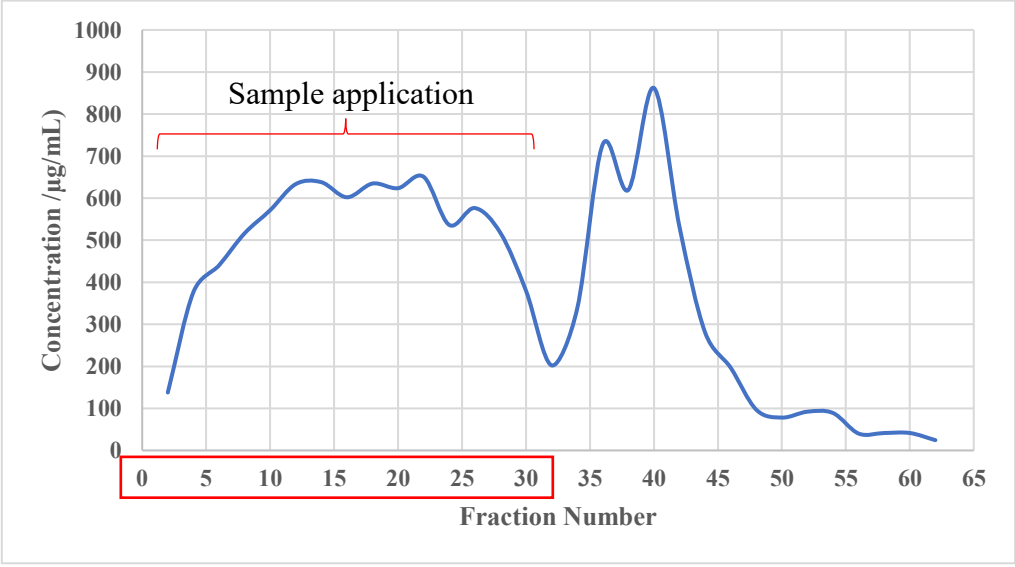

Figure 5.42. Separation of the BVMO crude extract on DEAE Sepharose (IEC-2).

According to Figure 5.42, there were unbound proteins that were eluted with the sample application. The activity test showed that the unbound proteins showed BVMO activity (Chromatogram 5.27). Subsequently, FR 1-30 (22.826 mg) were combined and concentrated.

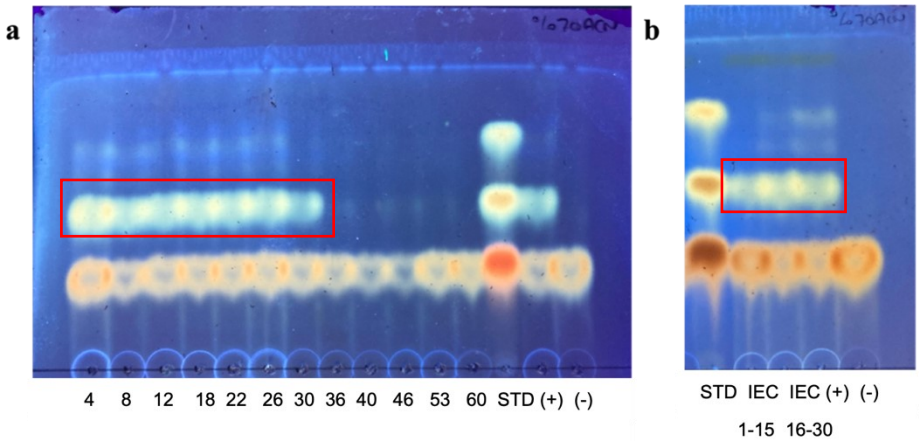

Chromatogram 5.27. Activity test results of a) the fractions, b) The combined fractions obtained from IEC-1 (Incubation time: 17 h) [Reverse phase C18 silica gel, Mobile phase: 70:30 (ACN: H_2O)].

Gel Filtration Chromatography (SEC-1)

The active fraction from ion exchange chromatography (IEC-1-FR 1-30: 17.72 mg) was applied to Sephacryl S200 resin. The protein profile of the collected fractions collected is shown in Figure 5.43. The combined fractions and protein amounts are presented in Table 5.21.

Table 5.21. Combined fractions from SEC-1.

Fraction	Total Protein (µg)
7-9	2855.88
10-12	3662.26
13-19*	1744.29

*Fractions with BVMO activity

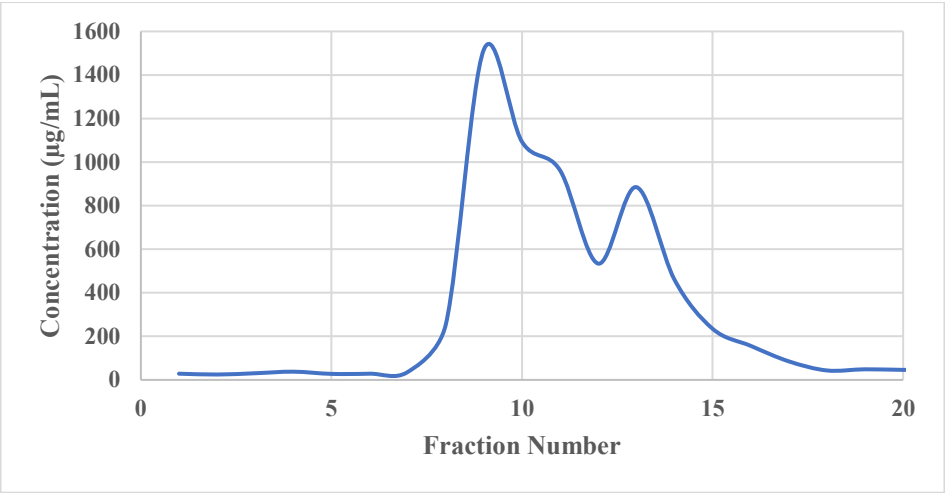

Figure 5.43. Separation of the IEC-1-FR 1-30 on Sephacryl S200 (SEC-1).

According to Chromatogram 5.28, BVMO activity was observed for FR 13-19. However, the activity was relatively low compared to the previous step. Figure 5.44 showed that protein load was reduced in the active fraction (SEC-1-FR 13-19) compared to the last IEC-1 step (IEC-1-FR 1-30). Since the protein profile of active (FR 13-19) and inactive (FR 10-12) fractions were similar, we could not determine which protein band belongs to the BVMO.

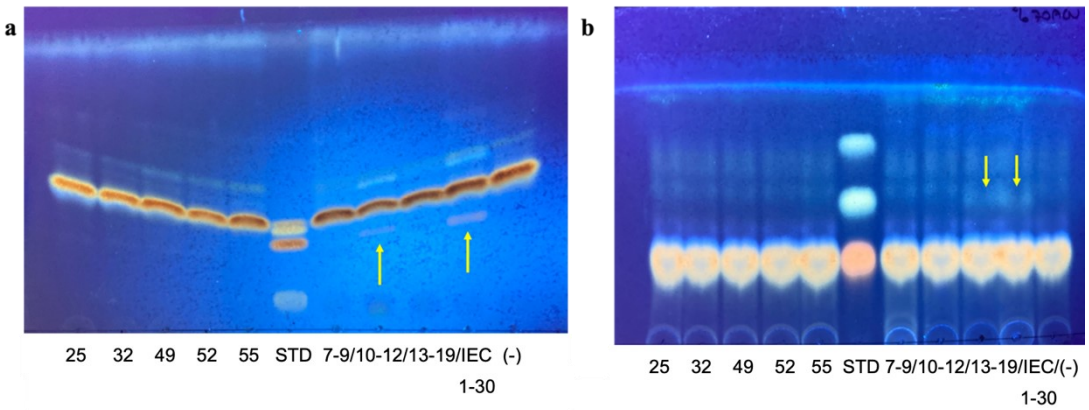

Chromatogram 5.28. Activity test results of the fractions and combined fractions obtained from SEC-1 (Incubation time: 20 h): a) [Silica gel, Mobile phase: 90:10:0.1 ($CHCl_3$:MeOH:H_2O)]; b) [Reverse phase C18 silica gel, Mobile phase: 70:30 (ACN: H_2O)].

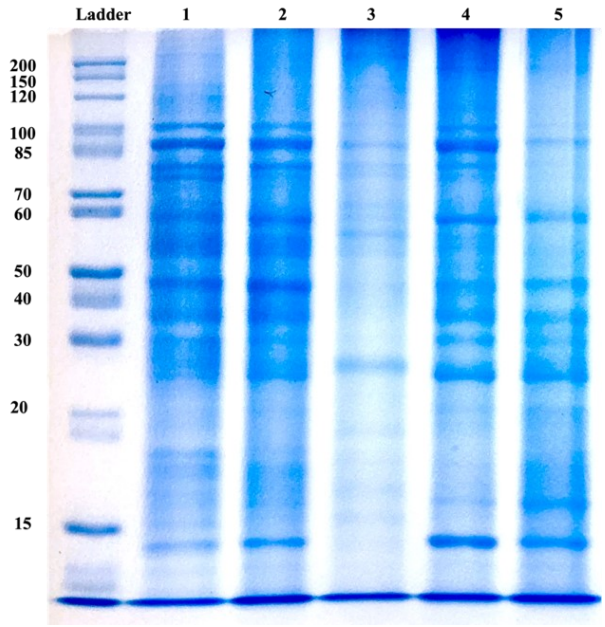

Figure 5.44. SDS-PAGE gel analysis of the fractions from IEC-2 and SEC-1 (Gel percentage: 12%). 1) Crude extract (15 µg), 2) IEC FR 1-30 (15 µg), 3) SEC FR 7-9 (15 µg), 4) SEC FR 10-12 (15 µg), 5) SEC FR 13-19 (15 µg).

Ion Exchange Chromatography (IEC-3)

Another ion exchange chromatography study was designed to understand whether glycerol influences the binding of proteins and to examine the effect of NaCl concentration between 0-100 mM on the elution of proteins. Therefore, enzyme extraction was performed without glycerol and NaCl, and the obtained extract was applied directly into the ion exchange column.

Unlike Experiment 1, BVMO activity was detected in the last fractions of the sample application (FR 16-27). Fractions were combined and concentrated according to the activity results (Chromatogram 5.29, Table 5.22) and the profile in Figure 5.46. The activity of FR 16-27 was higher than the collected fractions (Chromatogram 5.30). This may be because low salt (NaCl) concentration stabilizes the protein[235].

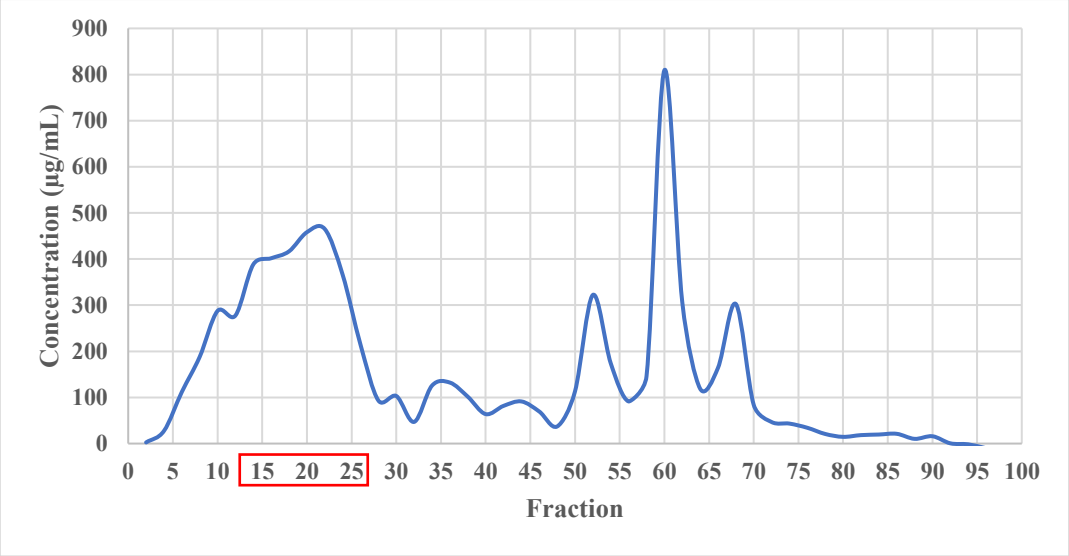

Figure 5.45. Separation of the BVMO crude extract on DEAE Sepharose (IEC-3).

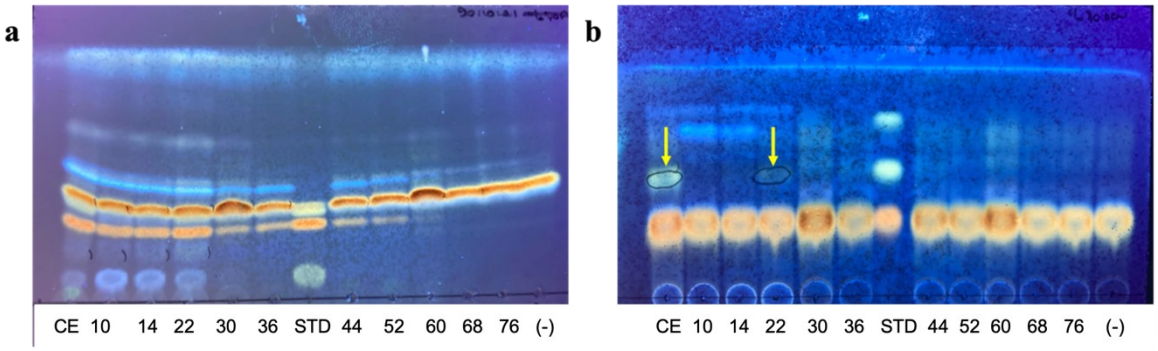

Chromatogram 5.29. Activity test results of the fractions obtained from IEC-3 (Incubation time: 17 h): a) Silica gel, Mobile phase: 90:10:0.1 ($CHCl_3$:MeOH:H_2O); b) Reverse phase C18 silica gel, Mobile phase: 70:30 (ACN: H_2O)

Table 5.22. Combined fractions from IEC-3.

Fraction	Total Protein (µg)
1-11	4431.43
12-15*	2408.39
16-27*	25943.23

*Fractions with BVMO activity

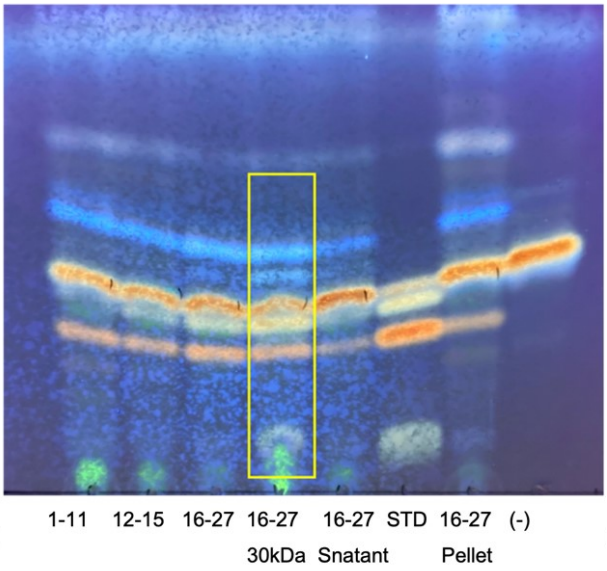

Chromatogram 5.30. Activity test results of the combined fractions obtained from IEC-3 (Incubation time: 72 h) [Silica gel, Mobile phase: 90:10:0.1 ($CHCl_3$:MeOH:H_2O)].

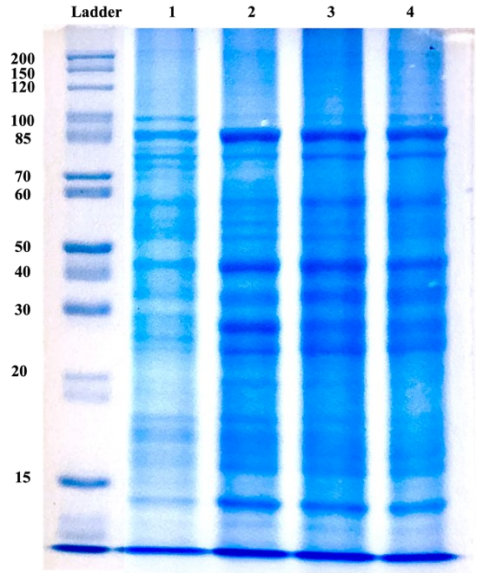

Figure 5.46. SDS-PAGE gel analysis of the fractions from IEC-3 (Gel percentage: 12%). 1) Crude extract (15 µg), 2) FR 1-11 (15 µg), 3) FR 12-15 (15 µg), 4) FR 16-27 (15 µg).

According to Figure 5.46, the intensities of the bands below 85 and 60 kDa were different when FR 1-11 and FR 16-27 were compared. One of these bands may belong to the BVMO enzyme.

Ion Exchange Chromatography (IEC-4)

In the previous step (IEC-3), the BVMO enzyme remained in the column but eluted from the column before applying the salt gradient. For this reason, a fractionation study was carried out using strong anion exchange resin instead of weak anion exchange resin. According to the results, we determined that the BVMO enzyme eluted with 0.1 M NaCl concentration (Figure 5.47, Chromatogram 5.31). When the active fraction was analyzed based on the SDS-PAGE gel image, an increment of concentration of some proteins was noticed (Figure 5.48).

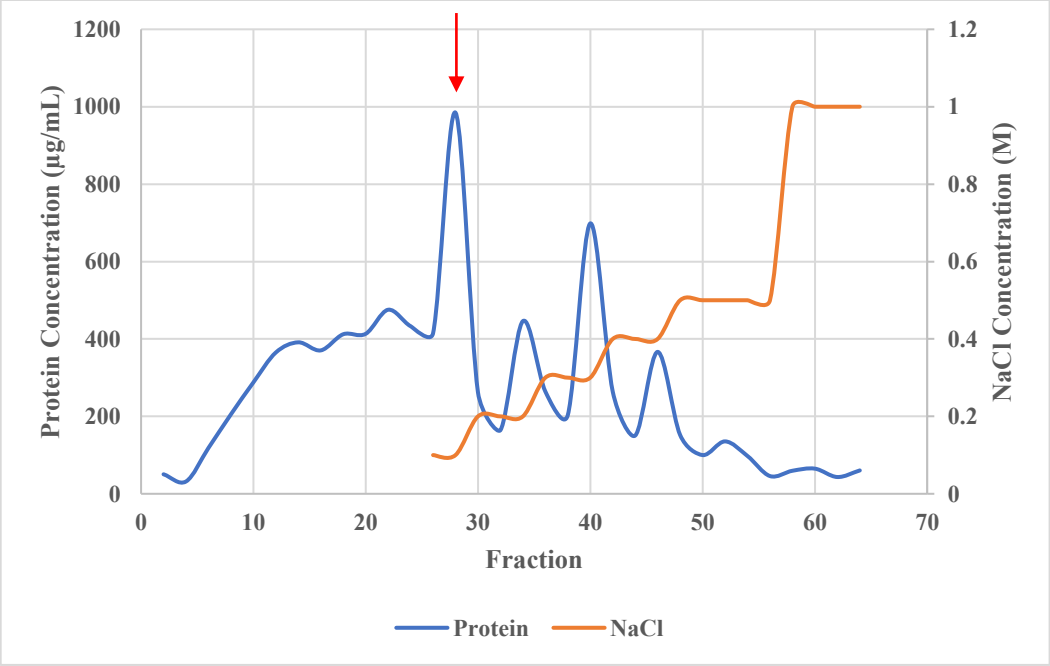

Figure 5.47. Separation of the BVMO crude extract on Q Sepharose (IEC-4).

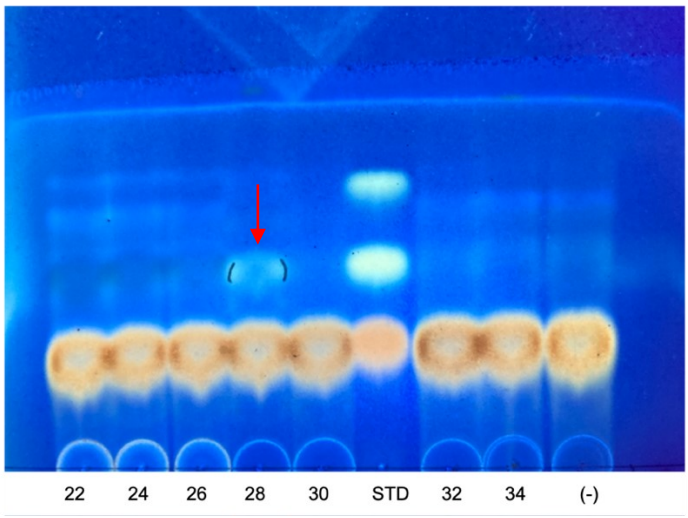

Chromatogram 5.31. Activity test results of the fractions obtained from IEC-4 (Incubation time: 14 h) [Reverse phase C18 silica gel, Mobile phase: 70:30 (ACN: H_2O)].

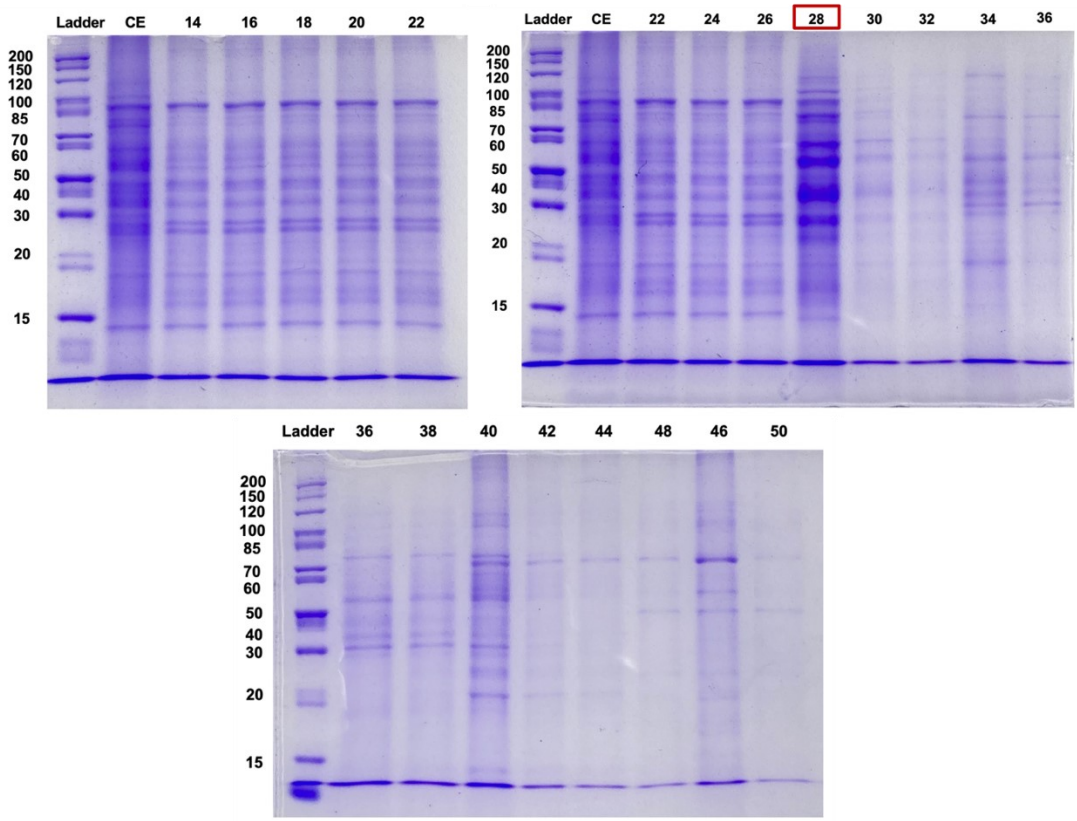

Figure 5.48. SDS-PAGE gel analysis of the fractions from IEC-4 (Gel percentage: 12%). The numbers indicate fractions and 15 µL of each fraction/crude extract was loaded onto the gel.

Hydrophobic Interaction Chromatography (HIC-1)

The active fraction (IEC-4-FR 27-29), obtained from fractionation on Q Sepharose (IEC-4), was applied to the Phenyl Sepharose resin. Since elution was performed using AS, the fractions were desalted using a PD10 column before the activity test. Although we obtained protein separation in the fractions (Figure 5.50), no fraction was found to be active (Chromatogram 5.32, Table 5.23).

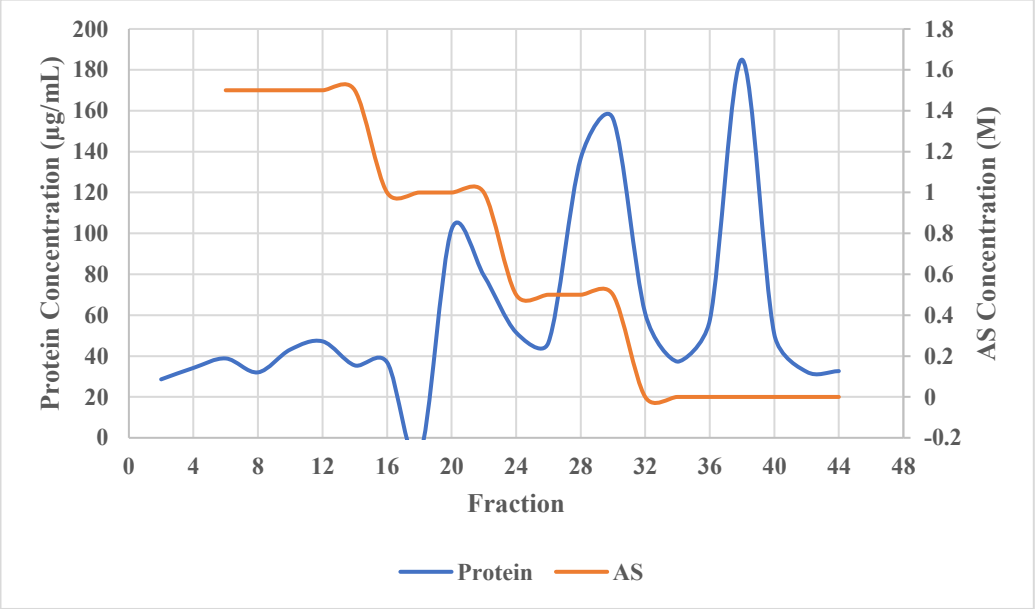

Figure 5.49. Separation of the IEC-3-FR 27-29 on Phenyl Sepharose (HIC-1).

Table 5.23. Combined fractions from HIC-1

Fraction	Total Protein (µg)
22-24	243.9991
28-30	598.2854
37-39	714.6762

*Fractions with BVMO activity

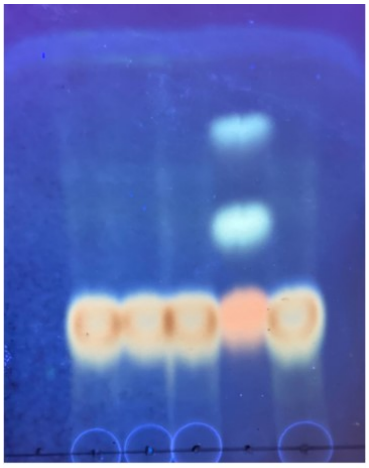

Chromatogram 5.32. Activity test results of the fractions obtained from HIC-1 (Incubation time: 12 h) [Reverse phase C18 silica gel, Mobile phase: 70:30 (ACN: H_2O)].

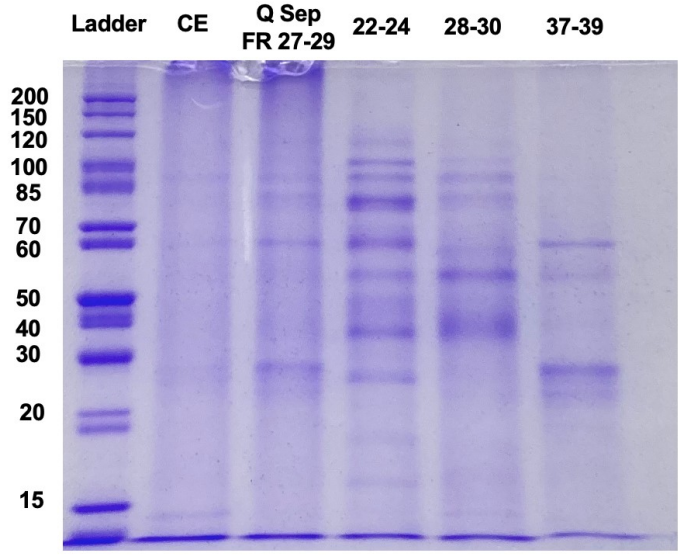

Figure 5.50. SDS-PAGE gel analysis of the combined fractions from IEC-1 and HIC-1 (Gel percentage: 12%). 5.5 µg of protein was loaded onto each well.

Hydrophobic Interaction Chromatography (HIC-2)

In second experiment with Phenyl Sepharose resin, HIC-1 conditions were repeated by using the BVMO crude extract with a higher amount of protein (20.9 mg). According to Figure 5.51, the fractions were combined, and desalted prior to activity test.

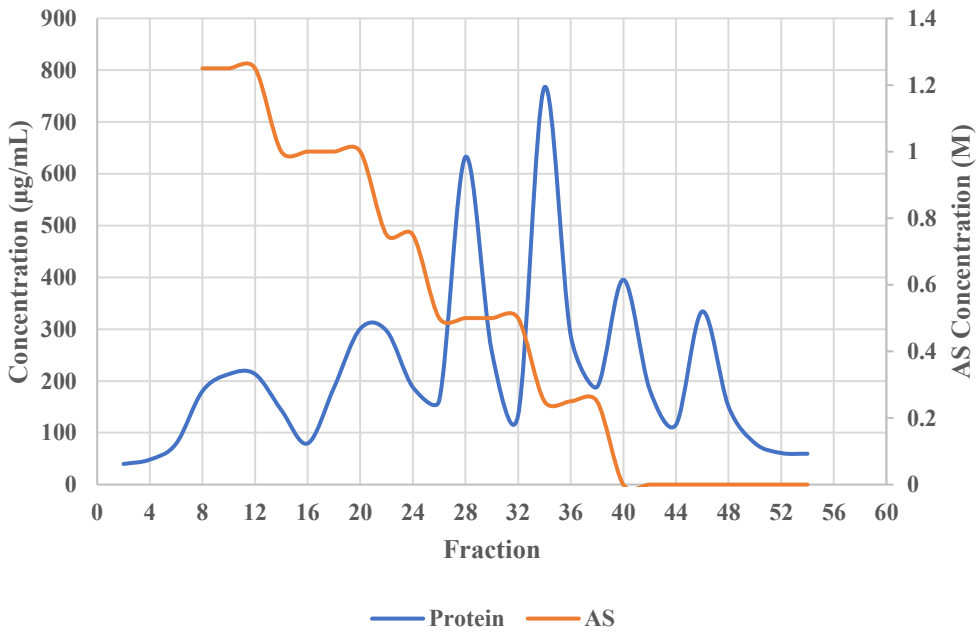

Figure 5.51. Separation of the BVMO crude extract on Phenyl Sepharose (HIC-2).

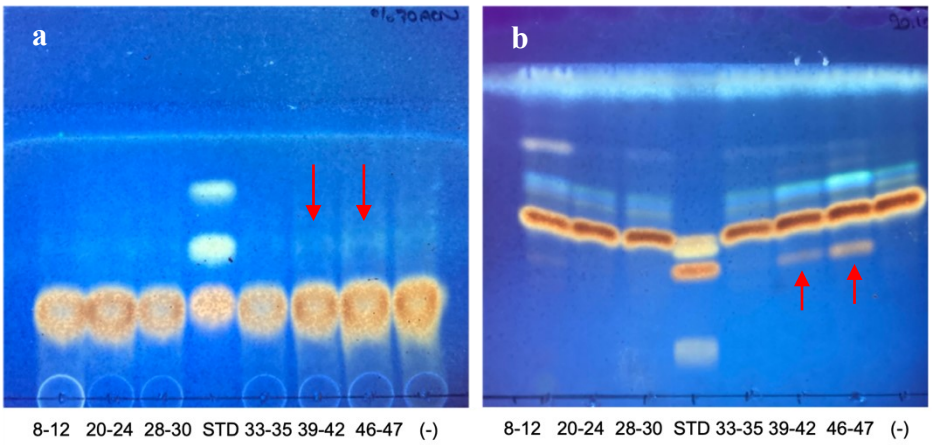

Chromatogram 5.33. Activity test results of the fractions obtained from HIC-2 (Incubation time: 13 h) a) Reverse phase C18 silica gel, Mobile phase: 70:30 (ACN:H_2O); b) Silica gel, Mobile phase: 90:10:0.1 ($CHCl_3$:MeOH:H_2O).

According to Chromatograms 5.33a and 5.33b, FR 39-42 and FR 46-47 showed BVMO activity and ADH activity. Therefore, the bands in the range of 20-30 kDa, which we

observe in Figure 5.52, may belong to the BVMO enzyme. Studies should continue to determine the activity clearly.

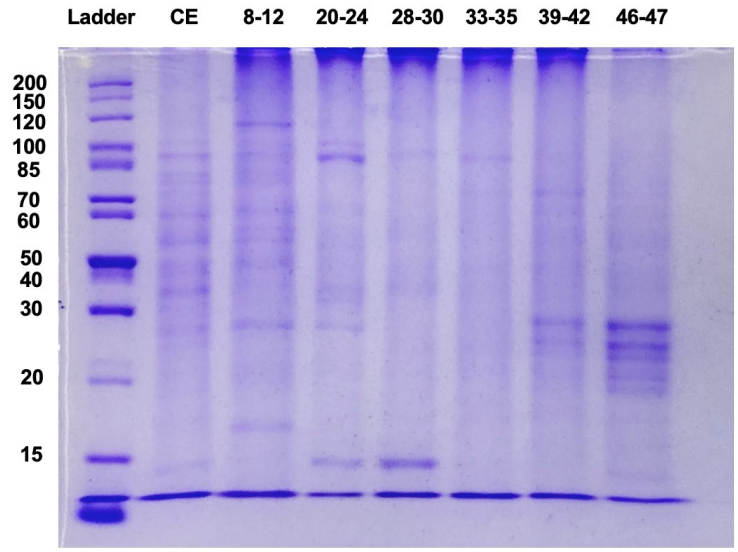

Figure 5.52. SDS-PAGE gel analysis of the combined fractions from HIC-2 (Gel percentage: 12%). 7.5 µg of protein was loaded onto each well.

Hydrophobic Interaction Chromatography (HIC-3)

NaCl was used as an alternative in hydrophobic interaction chromatography since ammonium sulfate caused a decrease in BVMO activity. 1.5 - 0 M NaCl gradient was preferred for elution. While applying the sample, some of the proteins were not bound to the column (Figure 5.53). It was understood that the concentration of NaCl must be greater than 1.5 M for the proteins to bind to the column. The activity test and SDS-PAGE results for the combined fractions are shown in Chromatogram 5.34 and Figure 5.54, respectively. Although BVMO activity was not present in Chromatogram 5.34, ADH activity was observed in all fractions except FR 56-63 and FR 66-71. According to Figure 5.54, the fractions' protein profiles are unclear. Additionally, an intense protein peak around 60 kDa was also noticed in Fr 1-24.

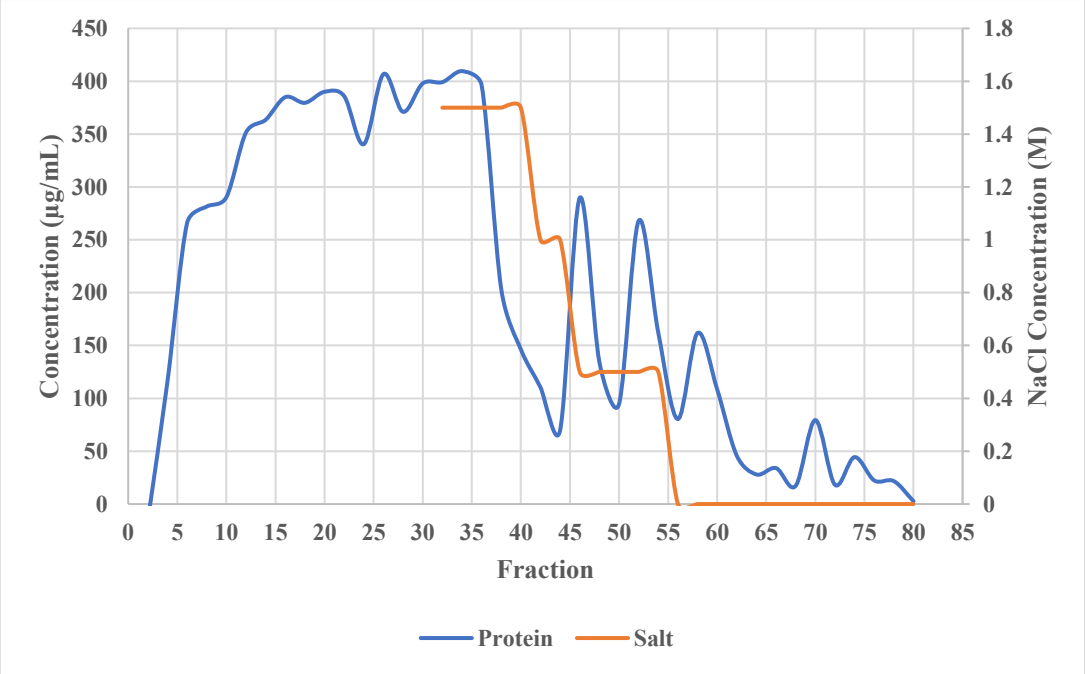

Figure 5.53. Separation of the BVMO crude extract on Phenyl Sepharose (HIC-3).

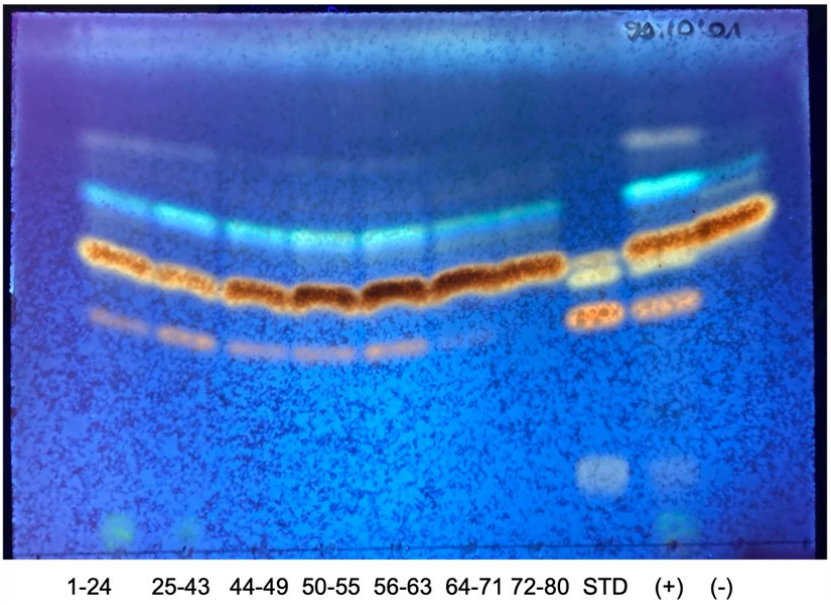

Chromatogram 5.34. Activity test results of the fractions obtained from HIC-3 (Incubation time: 20 h) [Silica gel, Mobile phase: 90:10:0.1 ($CHCl_3$:MeOH:H_2O)].

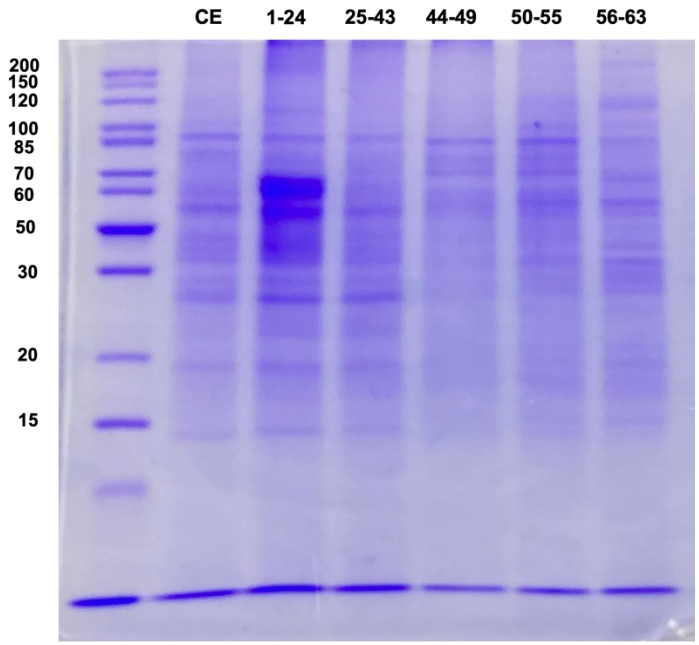

Figure 5.54. SDS-PAGE gel analysis of the combined fractions from HIC-3 (Gel percentage: 12%). 7.5 µg of protein was loaded onto each well.

5.3.6. Optimum pH Values for LH and ADH Enzymes

The activities of LH and ADH enzymes at different pH values are given in Figure 5.55 and Figure 5.56, respectively.

The optimum pH for LH was 7.4 and in Tris HCl buffer. A decrease in activity was detected between pH 8.0-9.0 in Tris HCl buffer. In addition, 60% activity was observed at pH 9, but no activity at pH 10.0 was observed in Glycine-NaOH buffer. The highest activity was obtained at 7.4 in Tris HCl buffer, while the activity decreased to 5% at 7.4 in Na phosphate buffer. This showed that Tris HCl is necessary for LH enzyme activity. The activity remained very low in Na acetate and Na phosphate buffers (Figure 5.55).

ADH enzyme showed at least 50% activity in all buffers except Na acetate (pH 5.0-5.4). While the highest activity was at pH 7.4 in Na phosphate, the maximum activity was observed at pH 8.5-9.0 in Tris-HCl. 80% of ADH activity at pH 10 in Glycine-NaOH buffer was remarkable. As a result, it was determined that the ADH enzyme work in a wide pH range (Figure 5.56).

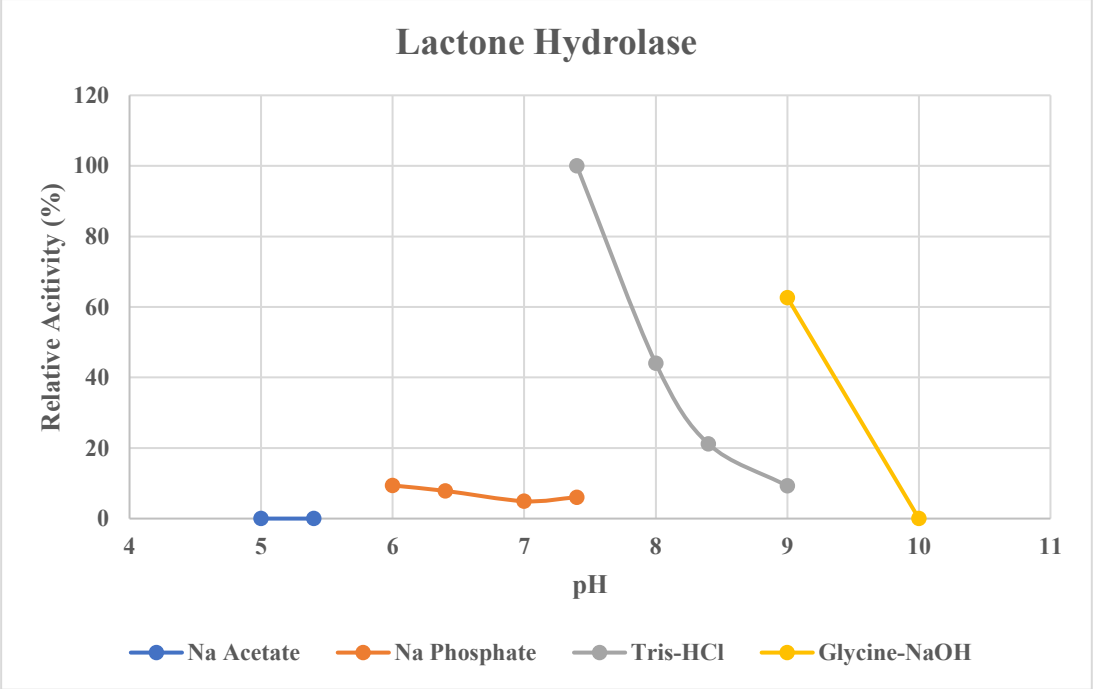

Figure 5.55. Effect of pH on the activity of LH.

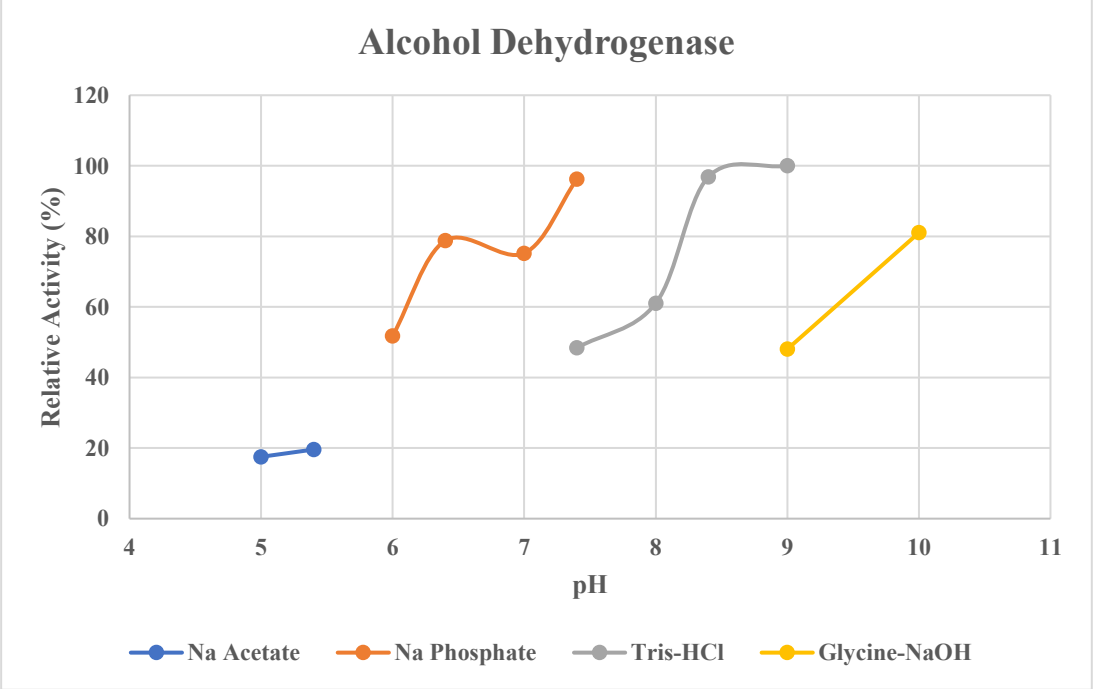

Figure 5.56. Effect of pH on the activity of LH.

5.4. Discussion

In the last part of this thesis, we performed studies on optimizing the isolation processes and characterization of enzymes responsible to produce telomerase activators from *C. laburnicola*. Since the genome sequence of *C. laburnicola* is unknown, it has yet to be possible to investigate the enzymes synthesized by this fungus, determine the similarities of these enzymes with the same enzyme class, or predict the properties of enzymes by computation. Also, no inference can be made about molecular weight or isoelectric point based on the literature, as the properties of enzymes vary according to the organism and the environment in which they are isolated. For this reason, enzyme extraction and purification methods from wild-type fungus were applied to obtain ADH, BVMO and LH enzymes.

ADH catalyzes the first step in the biotransformation of cycloartanes by oxidizing the secondary alcohol at C-3. We determined that ADH from *C. laburnicola* is $NADP^+$-dependent enzyme. In addition, we found that this enzyme can work in a wide pH range, but pH 8.4-9.0 were the optimum pH values.

Studies for the purification of ADH enzyme are presented in the purification table (Table 5.24). During the purification, an increase in the total enzyme activity was observed, probably because of the removal of contaminant proteins during column chromatography. According to Table 5.24, we achieved approximately 1.6-1.7-fold purification by DEAE Sepharose and Q Sepharose and 22-fold purification using Phenyl Sepharose compared to a previous step.

Table 5.24. Summary of purification of ADH from *C. laburnicola*.

Step	Total Protein (mg)	Total Volume (mL)	Total activity (U)	Specific activity (U/mg)	Purification fold
Crude Extract	206.43	365	37.37	0.18	1.00
DEAE Sepharose	40.59	61	12.68	0.31	1.73
Phenyl Sepharose	6.18	1	43.05	6.97	38.49
Q Sepharose	1.31	4.5	14.56	11.08	61.22
*U = nmol/min					

ADHs are better defined than BVMO and LH enzymes and have industrial use[210,211,216]. ADHs have been employed for synthesizing chiral alcohols since ADHs have broad substrate scope, excellent selectivity, and low impact on the environment[217,218]. Studies related to ADHs focused on improving the substrate scope and enantioselectivity of ADHs further and altering their enantio-preference using protein engineering techniques[218,236,237].

BVMO is involved in the second step by catalyzing the lactone formation in ring A using molecular oxygen in the biotransformation of cycloartanes. We have shown that BVMO from *C. laburnicola* was an FAD-containing and NADPH-dependent enzyme. For this reason, this enzyme may belong to Type I BVMO class[186,193]. Purification attempts for this enzyme resulted in activity loss at nearly every step. One of the problems encountered with BVMO enzymes is that they are unstable, and efforts have been made to obtain robust biocatalysts. Overriding reasons for the loss of activity seen in isolation studies have been reported, such as the loss of FAD/FMN group during purification[195], high or low ionic strength[235], and competition of some salts (such as AS) with its cofactor[234].

In the activity tests for the BVMO enzyme, a reduction reaction was detected in addition to lactone formation. Our first assumption was that when NADPH was present, the ADH enzyme used the substrate in the medium to reduce the ketone in the A ring (Figure 5.57). The second implication is that BVMO works in two directions. However, purified BVMO enzyme is needed to confirm these assumptions.

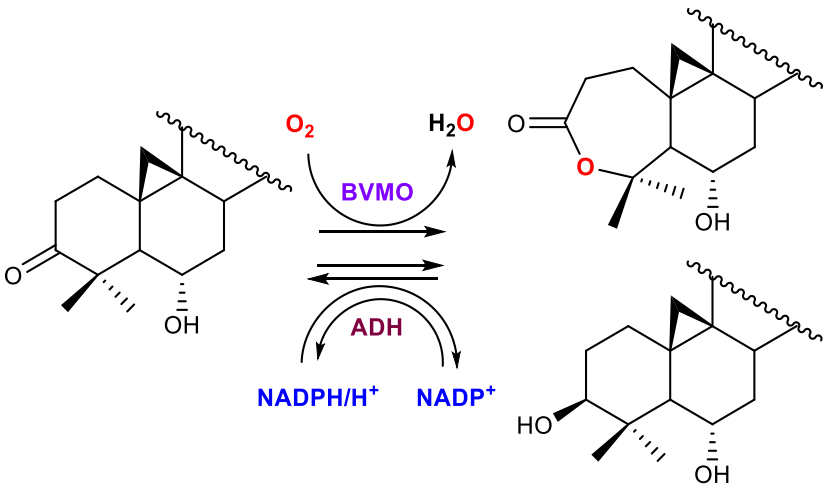

Figure 5.57. The reactions catalyzed by BVMO and ADH enzymes.

Studies on BVMO enzymes in the literature have focused on the discovery of new BVMO with genome mining studies[238,239], the development of cofactor regeneration systems for self-sufficient biocatalysts[240,241], the acquisition of stable BVMOs[242], the improvement of the properties of BVMO (enantio-, stereoselective, substrate specificity)[243,244] and development of screening process to detect BVMO activity[245–248]. The discovery of BVMO enzymes from wild-type microorganisms has been less frequent in the literature[163,235,249,250] with the development of recombinant DNA technology and bioinformatics tools.

Although there are studies on the BVMO-mediated whole-cell biotransformation of triterpenoids in the literature, no study has been reported regarding the isolation and characterization of enzyme systems. The discovery of steroid monooxygenases showing BVMO activity has been reported in studies on steroids[251–253]. However, steroid monooxygenases catalyze lactone formation in D-ring. Therefore, enzymes that form lactones in the A ring need to be investigated.

For the purification of BVMO, ion exchange chromatography can be used for enzyme isolation without causing loss of activity in the purification of BVMO enzyme. However, additional procedures are required for desalting in hydrophobic interaction chromatography and AS precipitation studies. Therefore, a purification study can be performed sequentially using ion exchange chromatography resins.

In BVMO purification studies, the activity was examined at each stage, as the molecular weight of the enzyme is unknown, like ADH and LH. We could only move on to the next step if there were an activity. However, we could not increase the concentration of BVMO in SDS-PAGE. As a solution, NATIVE-PAGE can be performed after the Q Sepharose-Phenyl Sepharose steps, and amino acid sequence analysis can be achieved by cutting the bands from the gel. Subsequently, we can compare the results with BVMO proteins in protein banks. However, this solution will be helpful if the obtained protein sequence is similar to the BVMO enzymes found in protein databases.

LH is involved in the third step and catalyzes the hydrolysis of the lactone ring, resulting in the formation of 3(4)-seco derivatives. As a result of our studies, we determined that the LH enzyme is not cofactor dependent and has an optimum pH of 7.4. In the purification study, the LH enzyme was purified 22.57 times using Q Sepharose and Phenyl Sepharose, respectively (Table 5.25).

Studies on LH enzymes have focused on the hydrolysis of N-acyl homoserine lactones[228–230] and the kinetic resolution of lactones[231,233]; however, purification studies are limited[221,254,255]. In addition, most microorganisms containing BVMO activity also have LH activity, resulting in a simultaneous degradation of the product of interest[221].

Table 5.25. Summary of purification of LH from *C. laburnicola*.

Step	Total Protein (mg)	Total Volume (mL)	Total activity (U)	Specific activity (U/mg)	Purification fold
Crude Extract	285.48	370	2446.53	8.57	1.00
Q Sepharose	46.39	13.25	1705.01	36.75	4.29
Phenyl Sepharose	0.91	1.25	175.35	193.46	22.57
*U = nmol/min					

We could not conduct studies to determine amino acid sequences in this study because the enzymes were not obtained in high purity. Carrying out these studies and investigating the similarities between the enzymes that catalyze the same reactions will add value to this study. In the continuation of this study, it is planned to obtain enzymes of sufficient purity. Afterward, it aimed to carry out enzyme kinetic studies to determine the catalytic properties of enzymes, determine the effects of various metals and salts on the activity, and determine the impact of temperature on the activity.

Since *C. laburnicola* biotransforms cycloartanes successfully, its enzymes caught our attention. In the continuation of this study, it is necessary to examine the activity of enzymes on diverse substrates to verify our opinion that these enzymes are quite selective towards cycloartane chemistry.

Collectively, ADH, BVMO and LH enzymes that catalyze modifications on A-ring of cycloartanes were biochemically studied for the first time.

CHAPTER 6

CONCLUSION

Endophytes have developed many unique features as a result of long evolutionary processes with the host organism. They are capable of producing a wide variety of enzymes necessary to maintain a stable symbiotic relationship with the host. The high biocatalytic potential of endophytes allows their survival and colonization in the host organism. In recent years, this group of microorganisms has attracted attention in biotransformation studies because of their ability to perform modifications in complex structures with a high degree of stereospecificity. Despite the high biocatalytic potential of these organisms, their use in biotransformation studies is still limited.

Potential of these organisms, our previous studies completed successfully resulted in the discovery of very effective telomerase activators, and the sector's interest in obtaining novel bioactive agents towards regenerative therapy and degenerative diseases have prompted us to carry out further studies on *Astragalus* endophytes and one of its major sapogenins, namely cyclocephagenol.

In this thesis, we first evaluated the potential of cyclocephagenol, an untouched lead compound from chemistry and bioactivity perspectives, for neuroprotection. The reason we focus on neurodegeneration is that a cycloastragenol-derived compound has entered clinical trials in Alzheimer's Disease. Cyclocephagenol exhibited a significant protective effect against H_2O_2-mediated cell death in SH-SY5Y cells, and its activity was greater than cycloastragenol. Thus, in the next step, biotransformation of cyclocephagenol with *A. eureka* was carried out to acquire novel derivatives to form a compound library and test them to deduce the structure-activity relationship. Accordingly, the biotransformation study with *A. eureka* afforded twenty-one new metabolites. When overall modifications are considered, this endophyte can catalyze hydroxylation, oxidation, epoxidation, ring opening-methyl migration, ring opening-B ring expansion, and dehydration reactions on the substrate. The reactions on cyclocephagenol once more emphasize the enzymatic richness and biocatalytic

potential of *A. eureka*. The subsequent bioactivity studies revealed that biotransformation products had statistically significant protective effects against the H_2O_2-induced neurotoxicity model, and the essential modifications for the neuroprotective activity were established successfully. As high ROS levels and disruption of mitochondrial membrane integrity have been related to neurotoxicity, selected compounds were further tested to observe their effects on ROS reduction and protection of the mitochondrial membrane. The selected compounds were noteworthy to reduce H_2O_2-mediated ROS levels and preserve the integrity of the mitochondrial membrane.

Based on potent telomerase activity of *C. laburnicola* biotransformation metabolites deriving from cycloastragenol and astragenol, we made a further attempt to discover new activators. To be sure, cyclocephagenol and its 12-hydroxy derivatives were good candidates for telomerase activation, a preliminary test was performed on hTERT protein level revealing that both compounds were notably active. Thus, in continuation, biotransformation studies were initiated with *C. laburnicola* to give seven new molecules. As in our previous studies, *C. laburnicola* catalyzed oxidation at C-3 and ring-opening reactions by Baeyer-Villiger oxidation on the cyclocephagenol and 12α-hydroxycyclocephagenol. When the compounds were tested by TeloTAGGG assay, it was found that cyclocephagenol and its metabolites had indeed more potency regarding telomerase activation compared to the positive control cycloastragenol (varying between 1.02- and 1.46-fold). Herein, we would like to determine the effects of hybrid molecules on telomerase activation since A-ring modified and 12-hydroxy derivatives of cycloastragenol showed higher activity in our previous studies. Although cyclocephagenol derivatives showed improved telomerase activation compared to the positive control, they were less active than previously identified cycloastragenol derivatives.

Recently, Yılmaz et al. (2022) have reported that cycloastragenol roles at the intersection of three major aging-related cellular pathways: NRF2, telomerase, and proteasome systems. They suggested that the proteasome activation by cycloastragenol is mediated by hTERT, and the improvement of telomerase activity and hTERT levels through cycloastragenol is driven by NRF2 system. Additionally, cycloastragenol reduced oxidative stress-induced ROS levels by increasing NRF2 nuclear localization and activity[256]. According to our results, the mechanism of cyclocephagenol to protect cells against H_2O_2-

mediated neurotoxicity might be similar to cycloastragenol[256]. To prove this deduction, further mechanistic studies are warranted for cyclocephagenol and its biotransformation products on the basis of this study.

In the third part of this thesis, independent from the first two, optimization studies were carried out to increase the production efficiency of previously identified potent telomerase activators, pending patent approval. Design of experiment methodology was used for factor screening and optimization studies. As a result of PBD experiments, it was determined that temperature, biotransformation time and shaking speed were influential in the production of target metabolites. CCD trials were performed with these three effective parameters (other parameters were fixed according to preliminary studies). Optimum conditions were determined for three metabolites according to CCD trials. We found that production yields were 25% for E-CG-01, 21% for E-AG-01, and 35% for E-AG-02.

After the optimization studies, we moved on to the scale-up studies. In the stirred-tank bioreactor (1 L) and airlift bioreactor (7.7 L) studies, the pellet formation problem was unavoidable, and the targeted yields could not be achieved. In 5 L shake flask studies, significant yield increases were obtained for our target metabolites: 1.95-fold for E-CG-01, 70-fold for E-AG-01, and 19-fold for E-AG-02. The biotransformation studies carried out within the scope of this thesis were carried out in submerged culture conditions. By considering the origin of the fungus (plant tissue), we believe that a further attempt should be made toward a solid-state culture of. *C. laburnicola*.

In the last step, studies were conducted to isolate the enzyme series (alcohol dehydrogenase, Baeyer Villiger monooxygenase, and lactone hydrolase), leading to the production of potent telomerase activators from *C. laburnicola*. As a result, the ADH enzyme was NADP-dependent and worked in a wide pH range; The BVMO enzyme was FAD-dependent and used the NADPH cofactor; It has been determined that the LH enzyme was not cofactor dependent and performed reaction at neutral pH. While the purification for the ADH and LH enzymes was completed to a large extent, the purification was not satisfactory for the BVMO enzyme due to the loss of activity.

As far as we ascertain from the literature, there has been no research focusing on the enzyme system modifying the A ring of triterpenoids. Thus, this is the first attempt to purify

and characterize the enzymes of this cascade reactions producing important bioactive metabolites.

Additionally, in whole-cell biotransformation studies with *C. laburnicola* on different aglycones (mostly sapogenins; unpublished data), it was observed that this fungus made modifications only on cycloartane skeleton. We speculate that familiarity of the endophytic fungus with the plant's (*Astragalus*) own secondary metabolites might have a role. On the contrary, *A. eureka* exhibited no such specificity. To shed light on this phenomenon, the substrate specificities of the fungi and their enzyme systems are supposed to be studied in detail, which we plan to focus in the near future.

We would like to emphasize that the overriding basis of carrying studies in the last two sections of this thesis was the need to obtain these compounds at large-scale for future therapeutic applications.

In conclusion, a few studies were reported on the biotransformation of plants' own secondary metabolites with their endophytes. In this study, it has been revealed that many complex and/or multi-step reactions can be catalyzed by the rich enzyme systems of endophytic fungi, and optimization studies can increase metabolite yields. As well, to form larger chemical libraries with broad diversity and improve bioactivities of the lead compounds, biotransformation using endophytic fungi and/or their enzymes has great potential.

REFERENCES

1. Bishayee, A.; Ahmed, S.; Brankov, N.; Perloff, M., Triterpenoids as Potential Agents for the Chemoprevention and Therapy of Breast Cancer. *Frontiers in Bioscience*. 2011.

2. Cárdenas, P. D.; Almeida, A.; Bak, S., Evolution of Structural Diversity of Triterpenoids. *Frontiers in Plant Science*. 2019.

3. Ren, Y.; Kinghorn, A. D., Natural Product Triterpenoids and Their Semi-Synthetic Derivatives with Potential Anticancer Activity. *Planta Medica* **2019**, *85* (11–12).

4. Xu, R.; Fazio, G. C.; Matsuda, S. P. T., On the Origins of Triterpenoid Skeletal Diversity. *Phytochemistry*. 2004.

5. Alqahtani, A.; Hamid, K.; Kam, A.; Wong, K. H.; Abdelhak, Z.; Razmovski-Naumovski, V.; Chan, K.; Li, K. M.; Groundwater, P. W.; Li, G. Q., The Pentacyclic Triterpenoids in Herbal Medicines and Their Pharmacological Activities in Diabetes and Diabetic Complications. *Current Medicinal Chemistry* **2013**, *20* (7).

6. Hamid, K.; Alqahtani, A.; Kim, M.-S.; Cho, J.-L.; Cui, P.; Li, C.; Groundwater, P.; Li, G., Tetracyclic Triterpenoids in Herbal Medicines and Their Activities in Diabetes and Its Complications. *Current Topics in Medicinal Chemistry* **2015**, *15* (23).

7. Mamedova, R. P.; Isaev, M. I., Triterpenoids from Astragalus Plants. *Chemistry of Natural Compounds* **2004**, *40* (4), 303–357.

8. Yang, L. P.; Shen, J. G.; Xu, W. C.; Li, J.; Jiang, J. Q., Secondary Metabolites of the Genus Astragalus: Structure and Biological-Activity Update. *Chemistry and Biodiversity*. 2013.

9. Pistelli, L. F., Secondary Metabolites of Genus Astragalus: Structure and Biological Activity. *Studies in Natural Products Chemistry* **2002**, *27* (PART H).

10. Kurt, M. Ü., Method Development for Pilot Production of Astragaloside VII / Astragaloside VII Molekülünün Pilot Üretimine Yönelik Metotların Geliştirilmesi, Izmir Institute of Technology, İzmir, 2019.

11. Bedir, E., Pharmacognostical Studies on Cycloartane Triterpene Saponins of Some Astragalus Species. PhD Thesis, Hacettepe University, Ankara, 1998.

12. Gülcemal, D.; Aslanipour, B.; Bedir, E., Secondary Metabolites from Turkish Astragalus Species. In *Plant and Human Health, Volume 2*; 2019.

13. Schaller, H., The Role of Sterols in Plant Growth and Development. *Progress in Lipid Research*. 2003.

14. Çaliş, I.; Yürüker, A.; Taşdemir, D.; Wright, A. D.; Sticher, O.; Luo, Y. de; Pezzuto, J. M., Cycloartane Triterpene Glycosides from the Roots of Astragalus Melanophrurius. *Planta Medica* **1997**, *63* (2).

15. Yesilada, E.; Bedir, E.; Çaliş, I.; Takaishi, Y.; Ohmoto, Y., Effects of Triterpene Saponins from Astragalus Species on in Vitro Cytokine Release. *Journal of Ethnopharmacology* **2005**, *96* (1–2).

16. Bedir, E.; Pugh, N.; Calis, I.; Pasco, D. S.; Khan, I. A., Immunostimulatory Effects of Cycloartane-Type Triterpene Glycosides from Astragalus Species. *Biological and Pharmaceutical Bulletin* **2000**, *23* (7), 834–837.

17. Özipek, M.; Dönmez, A. A.; Çaliş, I.; Brun, R.; Rüedi, P.; Tasdemir, D., Leishmanicidal Cycloartane-Type Triterpene Glycosides from Astragalus Oleifolius. *Phytochemistry* **2005**, *66* (10).

18. Gariboldi, P.; Pelizzoni, F.; Tatò, M.; Verotta, L.; El-Sebakhy, N.; Asaad, A. M.; Abdallah, R. M.; Toaima, S. M., Cycloartane Triterpene Glycosides from Astragalus Trigonus. *Phytochemistry* **1995**, *40* (6).

19. Uner, G.; Tag, O.; Erzurumlu, Y.; Kirmizibayrak, P. B.; Bedir, E., Identification of a Noncanonical Necrotic Cell Death Triggered via Enhanced Proteolysis by a Novel Sapogenol Derivative. *Chemical Research in Toxicology* **2020**, *33* (11), 2880–2891.

20. Radwan, M. M.; El-Sebakhy, N. A.; Asaad, A. M.; Toaima, S. M.; Kingston, D. G. I., Kahiricosides II-V, Cycloartane Glycosides from an Egyptian Collection of Astragalus Kahiricus. *Phytochemistry* **2004**, *65* (21 SPEC. ISS.).

21. Khushbaktova, Z. A.; Agzamova, M. A.; Syrov, V. N.; Radchenko, N. v.; Mirsalikhova, N. M.; Umarova, F. T., Influence of Cycloartanes from Plants of the Genus Astragalus and Their Synthetic Analogs on the Contractive Function of the Myocardium and the Activity of Na,K-ATPase. *Chemistry of Natural Compounds* **1995**, *30* (4).

22. Sevimli-Gür, C.; Onbailar, I.; Atilla, P.; Genç, R.; Akar, N.; Deliloğlu-Gürhan, I.; Bedir, E., In Vitro Growth Stimulatory and in Vivo Wound Healing Studies on Cycloartane-Type Saponins of Astragalus Genus. *Journal of Ethnopharmacology* **2011**, *134* (3).

23. Nalbantsoy, A.; Nesil, T.; Erden, S.; Çalış, İ.; Bedir, E., Adjuvant Effects of Astragalus Saponins Macrophyllosaponin B and Astragaloside VII. *Journal of ethnopharmacology* **2011**, *134* (3), 897–903.

24. Genç, R.; Yakuboğullari, N.; Nalbantsoy, A.; Çöven, F.; Bedir, E., Adjuvant Potency of Astragaloside Vii Embedded Cholesterol Nanoparticles for H3N2 Influenza Vaccine. *Turkish Journal of Biology* **2020**, *44* (5).

25. Yakuboğulları, N.; Genç, R.; Çöven, F.; Nalbantsoy, A.; Bedir, E., Development of Adjuvant Nanocarrier Systems for Seasonal Influenza A (H3N2) Vaccine Based on Astragaloside VII and Gum Tragacanth (APS). *Vaccine* **2019**, *37* (28).

26. Harley, C. B.; Chin, A. C.; Akama, T.; Ip, N. Y.; Wong, Y.; Miller-Martini, D. M., Compositions and Methods for Increasing Telomerase Activity. US7846904B2, 2004.

27. Harley, C. B.; Liu, W.; Blasco, M.; Vera, E.; Andrews, W. H.; Briggs, L. A.; Raffaele, J. M., A Natural Product Telomerase Activator as Part of a Health Maintenance Program. *Rejuvenation Research* **2011**, *14* (1).

28. Liu, T.; Ullenbruch, M.; Choi, Y. Y.; Yu, H.; Ding, L.; Xaubet, A.; Pereda, J.; Feghali-Bostwick, C. A.; Bitterman, P. B.; Henke, C. A.; Pardo, A.; Selman, M.; Phan, S. H., Telomerase and Telomere Length in Pulmonary Fibrosis. *American Journal of Respiratory Cell and Molecular Biology* **2013**, *49* (2).

29. le Saux, C. J.; Davy, P.; Brampton, C.; Ahuja, S. S.; Fauce, S.; Shivshankar, P.; Nguyen, H.; Ramaseshan, M.; Tressler, R.; Pirot, Z.; Harley, C. B.; Allsopp, R., A Novel Telomerase Activator Suppresses Lung Damage in a Murine Model of Idiopathic Pulmonary Fibrosis. *PLoS ONE* **2013**, *8* (3).

30. Dow, C. T.; Harley, C. B., Evaluation of an Oral Telomerase Activator for Early Age-Related Macular Degeneration - A Pilot Study. *Clinical Ophthalmology* **2016**, *10*.

31. Harley, C., Telomerase Therapeutics for Degenerative Diseases. *Current Molecular Medicine* **2005**, *5* (2).

32. Jäger, K.; Walter, M., Therapeutic Targeting of Telomerase. *Genes*. 2016.

33. Bedir, E.; Calis, I.; Dunbar, C.; Sharan, R.; Buolamwini, J. K.; Khan, I. A., Two Novel Cycloartane-Type Triterpene Glycosides from the Roots of Astragalus Prusianus. *Tetrahedron* **2001**, *57* (28), 5961–5966.

34. Bedir, E.; Calis, I.; Aquino, R.; Piacente, S.; Pizza, C., Cycloartane Triterpene Glycosides from the Roots of Astragalus Brachypterus and Astragalus Microcephalus. *Journal of natural products* **1998**, *61* (12), 1469–1472.

35. Horo, I.; Bedir, E.; Perrone, A.; Özgökçe, F.; Piacente, S.; Alankuş-Çalışkan, Ö., Triterpene Glycosides from Astragalus Icmadophilus. *Phytochemistry* **2010**, *71* (8–9), 956–963.

36. Djimtombaye, B. J.; Alankuş-Çalişkan, Ö.; Gülcemal, D.; Khan, I. A.; Anil, H.; Bedir, E., Unusual Secondary Metabolites from Astragalus Halicacabus Lam. *Chemistry and Biodiversity* **2013**, *10* (7).

37. Gülcemal, D.; Alankuş-Çalışkan, Ö.; Perrone, A.; Özgökçe, F.; Piacente, S.; Bedir, E., Cycloartane Glycosides from Astragalus Aureus. *Phytochemistry* **2011**, *72* (8), 761–768.

38. Karabey, F.; Khan, I. A.; Bedir, E., Cycloartane-Type Glycosides from Astragalus Schottianus. *Phytochemistry Letters* **2012**, *5* (2), 320–324.

39. Aslanipour, B.; Gülcemal, D.; Nalbantsoy, A.; Yusufoglu, H.; Bedir, E., Cycloartane-Type Glycosides from Astragalus Brachycalyx FISCHER and Their Effects on Cytokine Release and Hemolysis. *Phytochemistry Letters* **2017**, *21*, 66–73.

40. Bhatti, H. N.; Khera, R. A., Biological Transformations of Steroidal Compounds: A Review. *Steroids* **2012**, *77* (12), 1267–1290.

41. Bureik, M.; Bernhardt, R.; Bureik, M.; Bernhardt, R., Steroid Hydroxylation: Microbial Steroid Biotransformations Using Cytochrome P450 Enzymes. *Modern Biooxidation* **2007**, *155*, 176.

42. Carballeira, J. D.; Quezada, M. A.; Hoyos, P.; Simeó, Y.; Hernaiz, M. J.; Alcantara, A. R.; Sinisterra, J. v., Microbial Cells as Catalysts for Stereoselective Red–Ox Reactions. *Biotechnology advances* **2009**, *27* (6), 686–714.

43. Donova, M. v; Egorova, O. v., Microbial Steroid Transformations: Current State and Prospects. *Applied microbiology and biotechnology* **2012**, *94* (6), 1423–1447.

44. Fernandes, P.; Cruz, A.; Angelova, B.; Pinheiro, H. M.; Cabral, J. M. S., Microbial Conversion of Steroid Compounds: Recent Developments. *Enzyme and microbial technology* **2003**, *32* (6), 688–705.

45. Kar, S.; Sanderson, H.; Roy, K.; Benfenati, E.; Leszczynski, J., Green Chemistry in the Synthesis of Pharmaceuticals. *Chemical Reviews* **2021**.

46. Urlacher, V. B., Catalysis with Cytochrome P 450 Monooxygenases. *Handbook of Green Chemistry: Online* **2010**, 1–25.

47. Borges, K. B.; de Souza Borges, W.; Durán-Patrón, R.; Pupo, M. T.; Bonato, P. S.; Collado, I. G., Stereoselective Biotransformations Using Fungi as Biocatalysts. *Tetrahedron: Asymmetry* **2009**, *20* (4), 385–397.

48. Küçüksolak, M.; Ekiz, G.; Duman, S.; Yılmaz, S.; Ballar-Kırmızıbayrak, P.; Bedir, E., Telomerase Activators Derived from Astragalus Sapogenins via Biotransformation with the Recently Discovered Endophytic Fungus Camarosporium Laburnicola. In *67th International Congress and Annual Meeting of the Society for Medicinal Plant and Natural Product Research (GA) in cooperation with the French Society of Pharmacognosy AFERP*; © Georg Thieme Verlag KG, 2019; Vol. 85.

49. Duman, S.; Ekiz, G.; Yılmaz, S.; Yusufoglu, H.; Kırmızıbayrak, P. B.; Bedir, E., Telomerase Activators from 20 (27)-Octanor-Cycloastragenol via Biotransformation by the Fungal Endophytes. *Bioorganic Chemistry* **2021**, *109*, 104708.

50. Ekiz, G.; Yllmaz, S.; Yusufoglu, H.; Klrmlzlbayrak, P. B.; Bedir, E., Microbial Transformation of Cycloastragenol and Astragenol by Endophytic Fungi Isolated from Astragalus Species. *Journal of Natural Products* **2019**, *82* (11).

51. Bedir, E.; Ballar Kırmızıbayrak, P.; Ekiz, G.; Yılmaz, S.; Duman, S.; Küçüksolak, M., Production Method of Telomerase Activators and Telomerase Activators Obtained by This Method. EP3664810A2;EP3664810A4;TR201714942A2;US2021369738A1;WO2019070219A2;WO2019070219A3, 2019.

52. Kuru, G.; Üner, G.; Bedir, E., Is Telomerase a Hidden Player? Therapeutic Potential of Natural Telomerase Activators against Age-Related Diseases. *Phytochemistry Reviews* **2022**.

53. Rahman, M. H.; Bajgai, J.; Fadriquela, A.; Sharma, S.; Trinh, T. T.; Akter, R.; Jeong, Y. J.; Goh, S. H.; Kim, C. S.; Lee, K. J., Therapeutic Potential of Natural Products in Treating Neurodegenerative Disorders and Their Future Prospects and Challenges. *Molecules*. 2021.

54. K. Poddar, M.; Chakraborty, A.; Banerjee, S., Neurodegeneration: Diagnosis, Prevention, and Therapy. In *Oxidoreductase*; 2021.

55. Liu, X.; Zhang, J.; Wang, S.; Qiu, J.; Yu, C., Astragaloside IV Attenuates the H_2O_2-Induced Apoptosis of Neuronal Cells by Inhibiting α-Synuclein Expression via the P38 MAPK Pathway. *International Journal of Molecular Medicine* **2017**, *40* (6).

56. Ikram, M.; Jo, M. H.; Choe, K.; Khan, A.; Ahmad, S.; Saeed, K.; Kim, M. W.; Kim, M. O., Cycloastragenol, a Triterpenoid Saponin, Regulates Oxidative Stress, Neurotrophic Dysfunctions, Neuroinflammation and Apoptotic Cell Death in Neurodegenerative Conditions. *Cells* **2021**, *10* (10).

57. Adams, J. P.; Collis, A. J.; Henderson, R. K.; Sutton, P. W., Biotransformations in Small-Molecule Pharmaceutical Development. *Practical methods for biocatalysis and biotransformations* **2010**, *182*.

58. Borges, W. de S.; Borges, K. B.; Bonato, P. S.; Said, S.; Pupo, M. T., Endophytic Fungi: Natural Products, Enzymes and Biotransformation Reactions. *Current Organic Chemistry* **2009**, *13* (12), 1137–1163.

59. Illanes, A.; Cauerhff, A.; Wilson, L.; Castro, G. R., Recent Trends in Biocatalysis Engineering. *Bioresource technology* **2012**, *115*, 48–57.

60. Leresche, J. E.; Meyer, H.-P., Chemocatalysis and Biocatalysis (Biotransformation): Some Thoughts of a Chemist and of a Biotechnologist. *Organic process research & development* **2006**, *10* (3), 572–580.

61. Simić, S.; Zukić, E.; Schmermund, L.; Faber, K.; Winkler, C. K.; Kroutil, W., Shortening Synthetic Routes to Small Molecule Active Pharmaceutical Ingredients Employing Biocatalytic Methods. *Chemical Reviews* **2021**, *122* (1), 1052–1126.

62. Lam, K. S., Application of Whole-Cell Biotransformation in the Pharmaceutical Industry. In *Biocatalysis for the Pharmaceutical Industry: Discovery, Development, and Manufacturing*; 2009.

63. Pimentel, M. R.; Molina, G.; Dionísio, A. P.; Maróstica Junior, M. R.; Pastore, G. M., The Use of Endophytes to Obtain Bioactive Compounds and Their Application in Biotransformation Process. *Biotechnology research international* **2011**, *2011*.

64. Wang, Y.; Dai, C.-C., Endophytes: A Potential Resource for Biosynthesis, Biotransformation, and Biodegradation. *Annals of Microbiology* **2011**, *61* (2), 207–215.

65. Ludwig-Müller, J., Plants and Endophytes: Equal Partners in Secondary Metabolite Production? *Biotechnology letters* **2015**, *37* (7), 1325–1334.

66. Kusari, S.; Singh, S.; Jayabaskaran, C., Biotechnological Potential of Plant-Associated Endophytic Fungi: Hope versus Hype. *TRENDS in Biotechnology* **2014**, *32* (6), 297–303.

67. Nisa, H.; Kamili, A. N.; Nawchoo, I. A.; Shafi, S.; Shameem, N.; Bandh, S. A., Fungal Endophytes as Prolific Source of Phytochemicals and Other Bioactive Natural Products: A Review. *Microbial pathogenesis* **2015**, *82*, 50–59.

68. Zheng, Y.-K.; Qiao, X.-G.; Miao, C.-P.; Liu, K.; Chen, Y.-W.; Xu, L.-H.; Zhao, L.-X., Diversity, Distribution and Biotechnological Potential of Endophytic Fungi. *Annals of Microbiology* **2016**, *66* (2), 529–542.

69. Zaferanloo, B.; Quang, T. D.; Daumoo, S.; Ghorbani, M. M.; Mahon, P. J.; Palombo, E. A., Optimization of Protease Production by Endophytic Fungus, Alternaria Alternata, Isolated from an Australian Native Plant. *World Journal of Microbiology and Biotechnology* **2014**, *30* (6).

70. Chaichanan, J.; Wiyakrutta, S.; Pongtharangkul, T.; Isarangkul, D.; Meevootisom, V., Optimization of Zofimarin Production by an Endophytic Fungus, Xylaria Sp. Acra L38. *Brazilian Journal of Microbiology* **2014**, *45* (1).

71. Soca-Chafre, G.; Rivera-Orduña, F. N.; Hidalgo-Lara, M. E.; Hernandez-Rodriguez, C.; Marsch, R.; Flores-Cotera, L. B., Molecular Phylogeny and Paclitaxel Screening of Fungal Endophytes from Taxus Globosa. *Fungal Biology* **2011**, *115* (2).

72. Ekiz, G., Research on Bioactive Secondary Metabolite Profile of Septofusidium Berolinense and Biotransformation of Cycloartane Type Saponins by Endophytic Fungi. PhD Thesis, Ege University, İzmir, 2016.

73. Ekiz, G.; Duman, S.; Bedir, E., Biotransformation of Cyclocanthogenol by the Endophytic Fungus Alternaria Eureka 1E1BL1. *Phytochemistry* **2018**, *151*, 91–98.

74. Bedir, E.; Kula, C.; Öner, Ö.; Altaş, M.; Tağ, Ö.; Öngen, G., Microbial Transformation of Astragalus Sapogenins Using Cunninghamella Blakesleeana NRRL 1369 and Glomerella Fusarioides ATCC 9552. *Journal of Molecular Catalysis B: Enzymatic* **2015**, *115*, 29–34.

75. Feng, L.; Ji, S.; Qiao, X.; Li, Z.; Lin, X.; Ye, M., Biocatalysis of Cycloastragenol by Syncephalastrum Racemosum and Alternaria Alternata to Discover Anti-Aging Derivatives. *Advanced Synthesis & Catalysis* **2015**, *357* (8), 1928–1940.

76. Kuban, M.; Öngen, G.; Khan, I. A.; Bedir, E., Microbial Transformation of Cycloastragenol. *Phytochemistry* **2013**, *88*, 99–104.

77. Yang, W. Z.; Ye, M.; Huang, F. X.; He, W. N.; Guo, D. A., Biocatalysis of Cycloastragenol by Filamentous Fungi to Produce Unexpected Triterpenes. *Advanced Synthesis and Catalysis* **2012**, *354* (2–3).

78. Leisch, H.; Morley, K.; Lau, P. C. K., Baeyer-Villiger Monooxygenases: More than Just Green Chemistry. *Chemical Reviews*. 2011.

79. Masullo, M.; Pizza, C.; Piacente, S., Ruscus Genus: A Rich Source of Bioactive Steroidal Saponins. *Planta Medica* **2016**, *82* (18).

80. Huang, Y. L.; Kou, J. P.; Ma, L.; Song, J. X.; Yu, B. Y., Possible Mechanism of the Anti-Inflammatory Activity of Ruscogenin: Role of Intercellular Adhesion Molecule-1 and Nuclear Factor-KB. *Journal of Pharmacological Sciences* **2008**, *108* (2).

81. Bouskela, E.; Cyrino, F. Z. G. A.; Marcelon, G., Possible Mechanisms for the Inhibitory Effect of Ruscus Extract on Increased Microvascular Permeability Induced by Histamine in Hamster Cheek Pouch. *Journal of Cardiovascular Pharmacology* **1994**, *24* (2).

82. Bouskela, E.; Cyrino, F. Z. G. A.; Marcelon, G., Effects of Ruscus Extract on the Internal Diameter of Arterioles and Venules of the Hamster Cheek Pouch Microcirculation. *Journal of Cardiovascular Pharmacology* **1993**, *22* (2).

83. Özçinar, Ö.; Tağ, Ö.; Yusufoglu, H.; Kivçak, B.; Bedir, E., Biotransformation of Ruscogenins by Cunninghamella Blakesleeana NRRL 1369 and Neoruscogenin by Endophytic Fungus Neosartorya Hiratsukae. *Phytochemistry* **2018**, *152*, 1–9.

84. Özçınar, O.; Tağ, O.; Yusufoglu, H.; Kivçak, B.; Bedir, E., Biotransformation of Neoruscogenin by the Endophytic Fungus Alternaria Eureka. *Journal of natural products* **2018**, *81* (6), 1357–1367.

85. Chen, N. D.; Zhang, J.; Liu, J. H.; Yu, B. Y., Microbial Conversion of Ruscogenin by Gliocladium Deliquescens NRRL1086: Glycosylation at C-1. *Applied Microbiology and Biotechnology* **2010**, *86* (2).

86. Lamm, A. S.; Chen, A. R. M.; Reynolds, W. F.; Reese, P. B., Steroid Hydroxylation by Whetzelinia Sclerotiorum, Phanerochaete Chrysosporium and Mucor Plumbeus. *Steroids* **2007**, *72* (9–10).

87. Hunter, A. C.; Rymer, S. J.; Dedi, C.; Dodd, H. T.; Nwozor, Q. C.; Moghimi, S. M., Transformation of Structurally Diverse Steroidal Analogues by the Fungus Corynespora Cassiicola CBS 161.60 Results in Generation of 8β-Monohydroxylated Metabolites with Evidence in Favour of 8β-Hydroxylation through Inverted Binding in the 9α-Hydroxylase. *Biochimica et Biophysica Acta - Molecular and Cell Biology of Lipids* **2011**, *1811* (12).

88. Faramarzi, M. A.; Badiee, M.; Yazdi, M. T.; Amini, M.; Torshabi, M., Formation of Hydroxysteroid Derivatives from Androst-4-En-3,17-Dione by the Filamentous Fungus Mucor Racemosus. *Journal of Molecular Catalysis B: Enzymatic* **2008**, *50* (1).

89. Holland, H. L.; Chenchaiah, P. C.; Thomas, E. M.; Mader, B.; Dennis, M. J., Microbial Hydroxylation of Steroids. 9. Epoxidation of Δ 6 -3-Ketosteroids by Rhizopus Arrhizus ATCC 11145, and the Mechanism of the 6β Hydroxylase Enzyme . *Canadian Journal of Chemistry* **1984**, *62* (12).

90. Liu, J.; Tang, W.; Chen, R.; Dai, J., Microbial Transformation of 14-Anhydrodigoxigenin by Alternaria Alternata. *Chemistry and Biodiversity* **2015**, *12* (12).

91. Karakoyun, Ç.; Küçüksolak, M.; Bilgi, E.; Doğan, G.; Çömlekçi, Y. E.; Bedir, E., Five New Cardenolides Transformed from Oleandrin and Nerigoside by Alternaria Eureka 1E1BL1 and Phaeosphaeriasp. 1E4CS-1 and Their Cytotoxic Activities. *Phytochemistry Letters* **2021**, *41*, 152–157.

92. Bedir, E.; Karakoyun, Ç.; Doğan, G.; Kuru, G.; Küçüksolak, M.; Yusufoğlu, H., New Cardenolides from Biotransformation of Gitoxigenin by the Endophytic

Fungus Alternaria Eureka 1E1BL1: Characterization and Cytotoxic Activities. *Molecules* **2021**, *26* (10), 3030.

93. Bedir, E.; Calis, I.; Zerbe, O.; Sticher, O., Cyclocephaloside I: A Novel Cycloartane-Type Glycoside from Astragalus Microcephalus. *Journal of natural products* **1998**, *61* (4), 503–505.

94. Kitagawa, I.; Wang, H. K.; Takagi, A.; Fuchida, M.; Muira, I.; Yoshikawa, M., Saponin and Sapogenol. XXXIV. Chemical Constituents of Astragali Radix, the Root of Astragalus Membranaceus Bunge. (1). Cycloastragenol, the 9,19-Cyclolanostane-Type Aglycone of Astragalosides, and the Artifact Aglycone Astragenol. *Chemical and Pharmaceutical Bulletin* **1983**, *31* (2).

95. Ryter, S. W.; Hong, P. K.; Hoetzel, A.; Park, J. W.; Nakahira, K.; Wang, X.; Choi, A. M. K., Mechanisms of Cell Death in Oxidative Stress. *Antioxidants and Redox Signaling*. 2007.

96. Wang, Y.; Xu, E.; Musich, P. R.; Lin, F., Mitochondrial Dysfunction in Neurodegenerative Diseases and the Potential Countermeasure. *CNS Neuroscience and Therapeutics*. 2019.

97. Küçüksolak, M.; Üner, G.; Ballar-Kırmızıbayrak, P.; Bedir, E., Neuroprotective Metabolites via Fungal Biotransformation of a Novel Sapogenin, Cyclocephagenol. *Scientific Reports* **2022**, *12* (1), 1–15.

98. Shen, Y. C.; Prakash, C. V. S.; Chang, Y. T., Two New Polyhydroxysteroids from the Gorgonian Isis Hippuris. *Steroids* **2001**, *66* (9), 721–725.

99. Chen, C.; Ni, Y.; Jiang, B.; Yan, S.; Xu, B.; Fan, B.; Huang, H.; Chen, G., Anti-Aging Derivatives of Cycloastragenol Produced by Biotransformation. *Natural product research* **2021**, *35* (16), 2685–2690.

100. de Lange, T., Shelterin: The Protein Complex That Shapes and Safeguards Human Telomeres. *Genes and Development*. 2005.

101. Blackburn, E. H., Switching and Signaling at the Telomere. *Cell*. 2001.

102. Allsopp, R. C.; Vaziri, H.; Patterson, C.; Goldstein, S.; Younglai, E. v.; Futcher, A. B.; Greider, C. W.; Harley, C. B., Telomere Length Predicts Replicative Capacity of Human Fibroblasts. *Proceedings of the National Academy of Sciences of the United States of America* **1992**, *89* (21).

103. de Jesus, B. B.; Schneeberger, K.; Vera, E.; Tejera, A.; Harley, C. B.; Blasco, M. A., The Telomerase Activator TA-65 Elongates Short Telomeres and Increases Health Span of Adult/Old Mice without Increasing Cancer Incidence. *Aging Cell* **2011**, *10* (4).

104. Dagarag, M.; Evazyan, T.; Rao, N.; Effros, R. B., Genetic Manipulation of Telomerase in HIV-Specific CD8 + T Cells: Enhanced Antiviral Functions Accompany the Increased Proliferative Potential and Telomere Length Stabilization . *The Journal of Immunology* **2004**, *173* (10).

105. Molgora, B.; Bateman, R.; Sweeney, G.; Finger, D.; Dimler, T.; Effros, R. B.; Valenzuela, H. F., Functional Assessment of Pharmacological Telomerase Activators in Human T Cells. *Cells* **2013**, *2* (1).

106. Andrews, N. P.; Fujii, H.; Goronzy, J. J.; Weyand, C. M., Telomeres and Immunological Diseases of Aging. *Gerontology*. 2010.

107. Prescott, J. C.; Blackburn, E. H., Telomerase: Dr Jekyll or Mr Hyde? *Current Opinion in Genetics and Development* **1999**, *9* (3).

108. Funk, W. D.; Wang, C. K.; Shelton, D. N.; Harley, C. B.; Pagon, G. D.; Hoeffler, W. K., Telomerase Expression Restores Dermal Integrity to in Vitro-Aged Fibroblasts in a Reconstituted Skin Model. *Experimental Cell Research* **2000**, *258* (2).

109. Cawthon, R. M.; Smith, K. R.; O'Brien, E.; Sivatchenko, A.; Kerber, R. A., Association between Telomere Length in Blood and Mortality in People Aged 60 Years or Older. *Lancet* **2003**, *361* (9355).

110. Harley, C. B., Telomerase Is Not an Oncogene. *Oncogene* **2002**, *21* (4).

111. Thomas, M.; Yang, L.; Hornsby, P. J., Formation of Functional Tissue from Transplanted Adrenocortical Cells Expressing Telomerase Reverse Transcriptase. *Nature Biotechnology* **2000**, *18* (1).

112. Ip, F. C. F.; Ng, Y. P.; An, H. J.; Dai, Y.; Pang, H. H.; Hu, Y. Q.; Chin, A. C.; Harley, C. B.; Wong, Y. H.; Ip, N. Y., Cycloastragenol Is a Potent Telomerase Activator in Neuronal Cells: Implications for Depression Management. *NeuroSignals* **2014**, *22* (1).

113. Fauce, S. R.; Jamieson, B. D.; Chin, A. C.; Mitsuyasu, R. T.; Parish, S. T.; Ng, H. L.; Ramirez Kitchen, C. M.; Yang, O. O.; Harley, C. B.; Effros, R. B., Telomerase-Based Pharmacologic Enhancement of Antiviral Function of Human CD8 + T Lymphocytes . *The Journal of Immunology* **2008**, *181* (10).

114. Wang, J.; Wu, M. L.; Cao, S. P.; Cai, H.; Zhao, Z. M.; Song, Y. H., Cycloastragenol Ameliorates Experimental Heart Damage in Rats by Promoting Myocardial Autophagy via Inhibition of AKT1-RPS6KB1 Signaling. *Biomedicine and Pharmacotherapy* **2018**, *107*.

115. Wang, J.; Liu, Y.; Xia, Q.; Xia, Q.; Wang, B.; Yang, C.; Liang, J.; Liu, X., Potential Roles of Telomeres and Telomerase in Neurodegenerative Diseases. *International Journal of Biological Macromolecules*. 2020.

116. Li, M.; Li, S. chun; Dou, B. kai; Zou, Y. xiang; Han, H. zhen; Liu, D. xiang; Ke, Z. ji; Wang, Z. fei., Cycloastragenol Upregulates SIRT1 Expression, Attenuates Apoptosis and Suppresses Neuroinflammation after Brain Ischemia. *Acta Pharmacologica Sinica* **2020**, *41* (8).

117. Wu, J.; Zeng, Z.; Li, Y.; Qin, H.; Zuo, C.; Zhou, C.; Xu, D., Cycloastragenol Protects against Glucocorticoid-Induced Osteogenic Differentiation Inhibition by Activating Telomerase. *Phytotherapy Research* **2021**, *35* (4).

118. Liu, J.; Gao, D.; Dan, J.; Liu, D.; Peng, L.; Zhou, R.; Luo, Y., The Protective Effect of Cycloastragenol on Aging Mouse Circadian Rhythmic Disorder Induced by D-Galactose. *Journal of Cellular Biochemistry* **2019**, *120* (10).

119. Cao, Y.; Xu, L.; Yang, X.; Dong, Y.; Luo, H.; Xing, F.; Ge, Q., The Potential Role of Cycloastragenol in Promoting Diabetic Wound Repair in Vitro. *BioMed Research International* **2019**, *2019*.

120. Yu, Y.; Wu, J.; Li, J.; Liu, Y.; Zheng, X.; Du, M.; Zhou, L.; Yang, Y.; Luo, S.; Hu, W.; Li, L.; Yao, W.; Liu, Y., Cycloastragenol Prevents Age-Related Bone Loss: Evidence in D-Galactose-Treated and Aged Rats. *Biomedicine and Pharmacotherapy* **2020**, *128*.

121. Salvador, L.; Singaravelu, G.; Harley, C. B.; Flom, P.; Suram, A.; Raffaele, J. M., A Natural Product Telomerase Activator Lengthens Telomeres in Humans: A Randomized, Double Blind, and Placebo Controlled Study. *Rejuvenation Research* **2016**, *19* (6).

122. Khavinson, V. K.; Bondarev, I. E.; Butyugov, A. A., Epithalon Peptide Induces Telomerase Activity and Telomere Elongation in Human Somatic Cells. *Bulletin of Experimental Biology and Medicine* **2003**, *135* (6).

123. Korkushko, O. v.; Khavinson, V. K.; Shatilo, V. B.; Antonyk-Sheglova, I. A., Peptide Geroprotector from the Pituitary Gland Inhibits Rapid Aging of Elderly People: Results of 15-Year Follow-Up. *Bulletin of Experimental Biology and Medicine* **2011**, *151* (3).

124. Korkushko, O. v.; Khavinson, V. K.; Shatilo, V. B.; Antonyuk-Shcheglova, I. A., Geroprotective Effect of Epithalamine (Pineal Gland Peptide Preparation) in Elderly Subjects with Accelerated Aging. *Bulletin of Experimental Biology and Medicine* **2006**, *142* (3).

125. Zajda, A.; Huttunen, K. M.; Sikora, J.; Podsiedlik, M.; Markowicz-Piasecka, M., Is Metformin a Geroprotector? A Peek into the Current Clinical and Experimental Data. *Mechanisms of Ageing and Development*. 2020.

126. Piskovatska, V.; Stefanyshyn, N.; Storey, K. B.; Vaiserman, A. M.; Lushchak, O., Metformin as a Geroprotector: Experimental and Clinical Evidence. *Biogerontology*. 2019.

127. Tsoukalas, D.; Fragkiadaki, P.; Docea, A. O.; Alegakis, A. K.; Sarandi, E.; Thanasoula, M.; Spandidos, D. A.; Tsatsakis, A.; Razgonova, M. P.; Calina, D., Discovery of Potent Telomerase Activators: Unfolding New Therapeutic and Anti-Aging Perspectives. *Molecular Medicine Reports* **2019**, *20* (4).

128. TSOUKALAS, D.; BUGA, A. M.; DOCEA, A. O.; SARANDI, E.; MITRUT, R.; RENIERI, E.; SPANDIDOS, D. A.; ROGOVEANU, I.; CERCELARU, L.; NICULESCU, M.; TSATSAKIS, A.; CALINA, D., Reversal of Brain Aging by Targeting Telomerase: A Nutraceutical Approach. *International Journal of Molecular Medicine* **2021**, *48* (5).

129. Deng, G.; Zhou, L.; Wang, B.; Sun, X.; Zhang, Q.; Chen, H.; Wan, N.; Ye, H.; Wu, X.; Sun, D.; Sun, Y.; Cheng, H., Targeting Cathepsin B by Cycloastragenol Enhances Antitumor Immunity of CD8 T Cells via Inhibiting MHC-I Degradation. *Journal for ImmunoTherapy of Cancer* **2022**, *10* (e004874).

130. Tibpromma, S.; Hyde, K. D.; Jeewon, R.; Maharachchikumbura, S. S. N.; Liu, J. K.; Bhat, D. J.; Jones, E. B. G.; McKenzie, E. H. C.; Camporesi, E.; Bulgakov, T. S.; Doilom, M.; de Azevedo Santiago, A. L. C. M.; Das, K.; Manimohan, P.; Gibertoni, T. B.; Lim, Y. W.; Ekanayaka, A. H.; Thongbai, B.; Lee, H. B.; Yang, J. B.; Kirk, P. M.; Sysouphanthong, P.; Singh, S. K.; Boonmee, S.; Dong, W.; Raj, K. N. A.; Latha, K. P. D.; Phookamsak, R.; Phukhamsakda, C.; Konta, S.; Jayasiri, S. C.; Norphanphoun, C.; Tennakoon, D. S.; Li, J.; Dayarathne, M. C.; Perera, R. H.; Xiao, Y.; Wanasinghe, D. N.; Senanayake, I. C.; Goonasekara, I. D.; de Silva, N. I.; Mapook, A.; Jayawardena, R. S.; Dissanayake, A. J.; Manawasinghe, I. S.; Chethana, K. W. T.; Luo, Z. L.; Hapuarachchi, K. K.; Baghela, A.; Soares, A. M.; Vizzini, A.; Meiras-Ottoni, A.; Mešić, A.; Dutta, A. K.; de Souza, C. A. F.; Richter, C.; Lin, C. G.; Chakrabarty, D.; Daranagama, D. A.; Lima, D. X.; Chakraborty, D.; Ercole, E.; Wu, F.; Simonini, G.; Vasquez, G.; da Silva, G. A.; Plautz, H. L.; Ariyawansa, H. A.; Lee, H.; Kušan, I.; Song, J.; Sun, J.; Karmakar, J.; Hu, K.; Semwal, K. C.; Thambugala, K. M.; Voigt, K.; Acharya, K.; Rajeshkumar, K. C.; Ryvarden, L.; Jadan, M.; Hosen, M. I.; Mikšík, M.; Samarakoon, M. C.; Wijayawardene, N. N.; Kim, N. K.; Matočec, N.; Singh, P. N.; Tian, Q.; Bhatt, R. P.; de Oliveira, R. J. V.; Tulloss, R. E.; Aamir, S.; Kaewchai, S.; Marathe, S. D.; Khan, S.; Hongsanan, S.; Adhikari, S.; Mehmood, T.; Bandyopadhyay, T. K.; Svetasheva, T. Y.; Nguyen, T. T. T.; Antonín, V.; Li, W. J.; Wang, Y.; Indoliya, Y.; Tkalčec, Z.; Elgorban, A. M.; Bahkali, A. H.; Tang, A. M. C.; Su, H. Y.; Zhang, H.; Promputtha, I.; Luangsa-ard, J.; Xu, J.; Yan, J.; Ji-Chuan, K.; Stadler, M.; Mortimer, P. E.; Chomnunti, P.; Zhao, Q.; Phillips, A. J. L.; Nontachaiyapoom, S.; Wen, T. C.; Karunarathna, S. C., Fungal Diversity Notes 491–602: Taxonomic and Phylogenetic Contributions to Fungal Taxa. *Fungal Diversity* **2017**, *83* (1).

131. Patrick, G. L., Pharmacokinetics and Related Topics. In *An Introduction to Medicinal Chemistry*; 2009.

132. Hilterhaus, L.; Liese, A., Applications of Reaction Engineering to Industrial Biotransformations. In *Biocatalysis for the Pharmaceutical Industry*; 2009.

133. Ishige, T.; Honda, K.; Shimizu, S., Whole Organism Biocatalysis. *Current Opinion in Chemical Biology*. 2005.

134. Sanchez, S.; Demain, A. L., Enzymes and Bioconversions of Industrial, Pharmaceutical, and Biotechnological Significance. *Organic process research & development* **2011**, *15* (1), 224–230.

135. Girhard, M.; Urlacher, V. B., Biooxidation with Cytochrome P450 Monooxygenases. In *Modern Oxidation Methods*; 2005.

136. Faber, K., *Biotransformations in Organic Chemistry: A Textbook*; Springer, 2011.

137. Pollard, D. J.; Woodley, J. M., Biocatalysis for Pharmaceutical Intermediates: The Future Is Now. *TRENDS in Biotechnology* **2007**, *25* (2), 66–73.

138. de Carvalho, C. C. C. R., Whole Cell Biocatalysts: Essential Workers from Nature to the Industry. *Microbial Biotechnology*. 2017.

139. Nagata, Y.; Chu, K. H., Optimization of a Fermentation Medium Using Neural Networks and Genetic Algorithms. *Biotechnology Letters* **2003**, *25* (21).

140. Molina, G.; Pessôa, M. G.; Bicas, J. L.; Fontanille, P.; Larroche, C.; Pastore, G. M., Optimization of Limonene Biotransformation for the Production of Bulk Amounts of α-Terpineol. *Bioresource Technology* **2019**, *294*.

141. Sanjivkumar, M.; Silambarasan, T.; Balagurunathan, R.; Immanuel, G., Biosynthesis, Molecular Modeling and Statistical Optimization of Xylanase from a Mangrove Associated Actinobacterium Streptomyces Variabilis (MAB3) Using Box-Behnken Design with Its Bioconversion Efficacy. *International Journal of Biological Macromolecules* **2018**, *118*.

142. Wahid, Z.; Nadir, N., Improvement of One Factor at a Time through Design of Experiments. *World Applied Sciences Journal* **2013**, *21* (SPECIAL ISSUE1).

143. Liu, W.; Xiang, H.; Zhang, T.; Pang, X.; Su, J.; Liu, H.; Ma, B.; Yu, L., Development of a New Bioprocess for Clean Diosgenin Production through Submerged Fermentation of an Endophytic Fungus. *ACS Omega* **2021**, *6* (14).

144. Plackett, R. L.; Burman, J. P., The Design of Optimum Multifactorial Experiments. *Biometrika* **1946**, *33* (4).

145. Srinivas, M. R. S.; Chand, N.; Lonsane, B. K., Use of Plackett–Burman Design for Rapid Screening of Several Nitrogen Sources, Growth/Product Promoters, Minerals and Enzyme Inducers for the Production of Alpha-Galactosidase by Aspergillus Niger MRSS 234 in Solid State Fermentation System. *Bioprocess Engineering* **1994**, *10* (3).

146. Zhang, X. Y.; Peng, Y.; Su, Z. R.; Chen, Q. H.; Ruan, H.; He, G. Q., Optimization of Biotransformation from Phytosterol to Androstenedione by a Mutant Mycobacterium Neoaurum ZJUVN-08. *Journal of Zhejiang University: Science B* **2013**, *14* (2).

147. Liang, L. Y.; Zheng, Y. G.; Shen, Y. C., Optimization of β-Alanine Production from β-Aminopropionitrile by Resting Cells of Rhodococcus Sp. G20 in a Bubble Column Reactor Using Response Surface Methodology. *Process Biochemistry* **2008**, *43* (7).

148. Riswanto, F. D. O.; Rohman, A.; Pramono, S.; Martono, S., Application of Response Surface Methodology as Mathematical and Statistical Tools in Natural Product Research. *Journal of Applied Pharmaceutical Science* **2019**, *9* (10).

149. Mohamad Said, K. A.; Mohamed Amin, M. A., Overview on the Response Surface Methodology (RSM) in Extraction Processes. *Journal of Applied Science & Process Engineering* **2016**, *2* (1).

150. Bezerra, M. A.; Santelli, R. E.; Oliveira, E. P.; Villar, L. S.; Escaleira, L. A., Response Surface Methodology (RSM) as a Tool for Optimization in Analytical Chemistry. *Talanta*. 2008.

151. Ait-Amir, B.; Pougnet, P.; el Hami, A., Meta-Model Development. In *Embedded Mechatronic Systems*; 2015; Vol. 2.

152. Liu, J.; Fu, M. L.; Chen, Q. H., Biotransformation Optimization of Betulin into Betulinic Acid Production Catalysed by Cultured Armillaria Luteo-Virens Sacc ZJUQH100-6 Cells. *Journal of Applied Microbiology* **2011**, *110* (1).

153. Mehmood, T.; Saleem, F.; Javed, S.; Nawaz, S.; Sultan, A.; Safdar, A.; Ullah, A.; Waseem, R.; Saeed, S.; Abbas, M.; Bilal, M.; Ahmad, M. M.; Firyal, S., Biotransformation of Agricultural By-Products into Biovanillin through Solid-State Fermentation (SSF) and Optimization of Different Parameters Using Response Surface Methodology (RSM). *Fermentation* **2022**, *8* (206), 1–14.

154. Quan, Y.; Wang, L.; Liu, Y.; Cong, J.; Xie, S.; Wu, X., Optimization of Fermentation Medium for Glycyrrhizin Biotransformation to Monoglucuronyl-Glycyrrhetinic Acid by Plackett-Burman and Box-Behnken Design. *Korean Chemical Engineering Research* **2015**, *53* (3).

155. de Souza, J. M.; Santos, M. F. C.; Pedroso, R. C. N.; Pimenta, L. P.; Siqueira, K. A.; Soares, M. A.; Dias, G. M.; Pietro, R. C. L. R.; Ramos, H. P.; Silva, M. L. A.; Pauletti, P. M.; Veneziani, R. C. S.; Ambrósio, S. R.; Braun, G. H.; Januário, A. H., Optimization of (–)-Cubebin Biotransformation to (–)-Hinokinin by the Marine Fungus Absidia Coerulea 3A9. *Archives of Microbiology* **2021**, *203* (7).

156. Retnadhas, S., Optimization of Process Conditions for Biotransformation of Caffeine to Theobromine Using Induced Whole Cells of Pseudomonas Sp. *Journal of Bioprocessing & Biotechniques* **2014**, *04* (06).

157. Sales, A.; Pastore, G. M.; Bicas, J. L., Optimization of Limonene Biotransformation to Limonene-1,2-Diol by Colletotrichum Nymphaeae CBMAI 0864. *Process Biochemistry* **2019**, *86*.

158. Kordowska-Wiater, M.; Kubik-Komar, A.; Targoński, Z., Application of Response Surface Methodology for the Optimization of Arabinose Biotransformation to Arabitol by Candida Parapsilosis. *Central European Journal of Biology* **2013**, *8* (9).

159. Sales, A.; Afonso, L. F.; Americo, J. A.; de Freitas Rebelo, M.; Pastore, G. M.; Bicas, J. L., Monoterpene Biotransformation by Colletotrichum Species. *Biotechnology Letters* **2018**, *40* (3).

160. Coban, H. B.; Demirci, A., Enhancement and Modeling of Microparticle-Added Rhizopus Oryzae Lactic Acid Production. *Bioprocess and Biosystems Engineering* **2016**, *39* (2).

161. Žnidaršič, P.; Pavko, A., The Morphology of Filamentous Fungi in Submerged Cultivations as a Bioprocess Parameter. *Food Technology and Biotechnology* **2001**, *39* (3).

162. Veiter, L.; Rajamanickam, V.; Herwig, C., The Filamentous Fungal Pellet—Relationship between Morphology and Productivity. *Applied Microbiology and Biotechnology*. 2018.

163. DONOGHUE, N. A.; NORRIS, D. B.; TRUDGILL, P. W., The Purification and Properties of Cyclohexanone Oxygenase from Nocardia Globerula CL1 and Acinetobacter NCIB 9871. *European Journal of Biochemistry* **1976**, *63* (1).

164. Griffin, M.; Trudgill, P. W., The Metabolism of Cyclopentanol by Pseudomonas N.C.I.B. 9872. *The Biochemical journal* **1972**, *129* (3).

165. Iwaki, H.; Hasegawa, Y.; Wang, S.; Kayser, M. M.; Lau, P. C. K., Cloning and Characterization of a Gene Cluster Involved in Cyclopentanol Metabolism in Comamonas Sp. Strain NCIMB 9872 and Biotransformations Effected by Escherichia Coli-Expressed Cyclopentanone 1,2-Monooxygenase. *Applied and Environmental Microbiology* **2002**, *68* (11).

166. Prado Barragán, L. A.; Figueroa, J. J. B.; Rodríguez Durán, L. V.; Aguilar González, C. N.; Hennigs, C., Fermentative Production Methods. In *Biotransformation of Agricultural Waste and By-Products: The Food, Feed, Fibre, Fuel (4F) Economy*; 2016.

167. Tufvesson, P.; Lima-Ramos, J.; Nordblad, M.; Woodley, J. M., Guidelines and Cost Analysis for Catalyst Production in Biocatalytic Processes. *Organic Process Research and Development* **2011**, *15* (1).

168. Rossino, G.; Robescu, M. S.; Licastro, E.; Tedesco, C.; Martello, I.; Maffei, L.; Vincenti, G.; Bavaro, T.; Collina, S., Biocatalysis: A Smart and Green Tool for the Preparation of Chiral Drugs. *Chirality* **2022**, *34* (11), 1–16.

169. Grimm, L. H.; Kelly, S.; Krull, R.; Hempel, D. C., Morphology and Productivity of Filamentous Fungi. *Applied Microbiology and Biotechnology*. 2005.

170. Gibbs, P. A.; Seviour, R. J.; Schmid, F., Growth of Filamentous Fungi in Submerged Culture: Problems and Possible Solutions. *Critical Reviews in Biotechnology*. 2000.

171. Liao, W.; Liu, Y.; Chen, S., Studying Pellet Formation of a Filamentous Fungus Rhizopus Oryzae to Enhance Organic Acid Production. In *Applied Biochemistry and Biotechnology*; 2007; Vol. 137–140.

172. Carlsen, M.; Spohr, A. B.; Nielsen, J.; Villadsen, J., Morphology and Physiology of an α-Amylase Producing Strain of Aspergillus Oryzae during Batch Cultivations. *Biotechnology and Bioengineering* **1996**, *49* (3).

173. Papagianni, M., Advances in Citric Acid Fermentation by Aspergillus Niger: Biochemical Aspects, Membrane Transport and Modeling. *Biotechnology Advances*. 2007.

174. Fu, S. bin; Yang, J. S.; Cui, J. L.; Meng, Q. F.; Feng, X.; Sun, D. A., Multihydroxylation of Ursolic Acid by Pestalotiopsis Microspora Isolated from the Medicinal Plant Huperzia Serrata. *Fitoterapia* **2011**, *82* (7).

175. Fu, S. bin; Feng, X.; Meng, Q. F.; Cai, Q.; Sun, D. A., Two New Echinocystic Acid Derivatives Catalyzed by Filamentous Fungus Gliocladium Roseum CGMCC 3.3657. *Natural Product Research* **2019**, *33* (13).

176. Fu, S. bin; Yang, J. S.; Cui, J. L.; Meng, Q. F.; Feng, X.; Sun, D. A., Multihydroxylation of Ursolic Acid by Pestalotiopsis Microspora Isolated from the Medicinal Plant Huperzia Serrata. *Fitoterapia* **2011**, *82* (7).

177. Shirane, N.; Hashimoto, Y.; Ueda, K.; Takenaka, H.; Katoh, K., Ring-A Cleavage of 3-Oxo-Olean-12-En-28-Oic Acid by the Fungus Chaetomium Longirostre. *Phytochemistry* **1996**, *43* (1).

178. Fu, S.; Meng, Q.; Yang, J.; Tu, J.; Sun, D. A., Biocatalysis of Ursolic Acid by the Fungus: Gliocladium Roseum CGMCC 3.3657 and Resulting Anti-HCV Activity. *RSC Advances* **2018**, *8* (29).

179. Zhu, Y.; Shen, P.; Wang, J.; Jiang, X.; Wang, W.; Raj, R.; Ge, H.; Wang, W.; Yu, B.; Zhang, J., Microbial Transformation of Pentacyclic Triterpenes for Anti-Inflammatory Agents on the HMGB1 Stimulated RAW 264.7 Cells by Streptomyces Olivaceus CICC 23628. *Bioorganic and Medicinal Chemistry* **2021**, *52*.

180. Akihisa, T.; Nishino, H.; Takamine, Y.; Yoshizumi, K.; Tokuda, H.; Kimura, Y.; Ukiya, M.; Nakahara, T.; Yokochi, T.; Ichiishi, E., Microbial Transformations of Two Lupane-Type Triterpenes and Anti-Tumor-Promoting Effects of the Transformation Products. *Journal of Natural Products* **2002**, *65* (3).

181. Shen, P.; Zhou, J.; Jiang, X.; Ge, H.; Wang, W.; Yu, B.; Zhang, J., Microbial-Catalyzed Baeyer−Villiger Oxidation for 3,4-Seco- Triterpenoids as Potential HMGB1 Inhibitors. *ACS Omega* **2022**, *7*, 18745–18751.

182. Laskin, A. I.; Grabowich, P.; de Lisle Meyers, C.; Fried, J., Transformations of Eburicoic Acid. V. Cleavage of Ring A by the Fungus Glomerella Fusarioides. *Journal of Medicinal Chemistry* **1964**, *7* (4).

183. Kadow, M.; Saß, S.; Schmidt, M.; Bornscheuer, U. T., Recombinant Expression and Purification of the 2,5-Diketocamphane 1,2-Monooxygenase from the Camphor Metabolizing Pseudomonas Putida Strain NCIMB 10007. *AMB Express* **2011**, *1* (1).

184. Jakubovska, J.; Meškys, R., Characterization of 1,8-Cineole Degradation Encoding Operon from Rhodococcus Sp. TMP1. *Chemija* **2016**, *27* (1).

185. Shirane, N.; Hashimoto, Y.; Ueda, K.; Takenaka, H.; Katoh, K., Ring-A Cleavage of 3-Oxo-Olean-12-En-28-Oic Acid by the Fungus Chaetomium Longirostre. *Phytochemistry* **1996**, *43* (1).

186. Fürst, M. J. L. J.; Gran-Scheuch, A.; Aalbers, F. S.; Fraaije, M. W., Baeyer-Villiger Monooxygenases: Tunable Oxidative Biocatalysts. *ACS Catalysis*. 2019.

187. Kamerbeek, N. M.; Janssen, D. B.; van Berkel, W. J. H.; Fraaije, M. W., Baeyer-Villiger Monooxygenases, an Emerging Family of Flavin-Dependent Biocatalysts. *Advanced Synthesis and Catalysis*. 2003.

188. Mihovilovic, M.; Rudroff, F.; Grotzl, B., Enantioselective Baeyer-Villiger Oxidations. *Current Organic Chemistry* **2005**, *8* (12).

189. Kayser, M. M., "Designer Reagents" Recombinant Microorganisms: New and Powerful Tools for Organic Synthesis. *Tetrahedron*. 2009.

190. TURFITT, G. E., The Microbiological Degradation of Steroids; Fission of the Steroid Molecule. *The Biochemical journal* **1948**, *42* (3).

191. Fried, J.; Sabo, E. F., Synthesis of 17 α -Hydroxy Corticosterone and Its 9α -Halo Derivatives from 11-EPI-17α - Hydroxycorticosterone. *Journal of the American Chemical Society*. 1953.

192. Alphand, V.; Fraaije, M. W.; Mihovilovic, M. D.; Ottolina, G., Second Generation Baeyer-Villiger Biocatalysts. In *Modern Biocatalysis: Stereoselective and Environmentally Friendly Reactions*; 2009.

193. Tolmie, C.; Smit, M. S.; Opperman, D. J., Native Roles of Baeyer-Villiger Monooxygenases in the Microbial Metabolism of Natural Compounds. *Natural Product Reports*. 2019.

194. Mascotti, M. L.; Juri Ayub, M.; Furnham, N.; Thornton, J. M.; Laskowski, R. A., Chopping and Changing: The Evolution of the Flavin-Dependent Monooxygenases. *Journal of Molecular Biology* **2016**, *428* (15).

195. Malito, E.; Alfieri, A.; Fraaije, M. W.; Mattevi, A., Crystal Structure of a Baeyer-Villiger Monooxygenase. *Proceedings of the National Academy of Sciences of the United States of America* **2004**, *101* (36).

196. Kirschner, A.; Altenbuchner, J.; Bornscheuer, U. T., Cloning, Expression, and Characterization of a Baeyer-Villiger Monooxygenase from Pseudomonas Fluorescens DSM 50106 in E. Coli. *Applied Microbiology and Biotechnology* **2007**, *73* (5).

197. van Bloois, E.; Dudek, H. M.; Duetz, W. A.; Fraaije, M. W., A Stepwise Approach for the Reproducible Optimization of PAMO Expression in Escherichia Coli for Whole-Cell Biocatalysis. *BMC Biotechnology* **2012**, *12*.

198. Mascotti, M. L.; Ayub, M. J.; Dudek, H.; Sanz, M. K.; Fraaije, M. W., Cloning, Overexpression and Biocatalytic Exploration of a Novel Baeyer-Villiger Monooxygenase from Aspergillus Fumigatus Af293. *AMB Express* **2013**, *3*.

199. Bisagni, S.; Smuš, J.; Chávez, G.; Hatti-Kaul, R.; Mamo, G., Cloning and Expression of a Baeyer-Villiger Monooxygenase Oxidizing Linear Aliphatic Ketones from Dietzia Sp. D5. *Journal of Molecular Catalysis B: Enzymatic* **2014**, *109*.

200. de Gonzalo, G.; Mihovilovic, M. D.; Fraaije, M. W., Recent Developments in the Application of Baeyer-Villiger Monooxygenases as Biocatalysts. *ChemBioChem*. 2010.

201. Riva, S.; Fassi, P.; Allegrini, P.; Razzetti, G., Process for the Preparation of (-) Modafinil. US20070087422A1, 2005.

202. Huisman, G. W.; Collier, S. J., On the Development of New Biocatalytic Processes for Practical Pharmaceutical Synthesis. *Current Opinion in Chemical Biology*. 2013.

203. SHUAIJIANG, J.; KE, W.; LIKAI, Y.; RENMING, Y.; MENGXIN, W.; JIANGANG, W.; XIAOYONG, L., Baeyer-Villiger Monooxygenase and Application Thereof in Brivaracetam Synthesis. CN114480315A, 2022.

204. Rudroff, F.; Rydz, J.; Ogink, F. H.; Fink, M.; Mihovilovic, M. D., Comparing the Stereoselective Biooxidation of Cyclobutanones by Recombinant Strains Expressing Bacterial Baeyer - Villiger Monooxygenases. *Advanced Synthesis and Catalysis* **2007**, *349* (8–9).

205. Rehdorf, J.; Mihovilovic, M. D.; Bornscheuer, U. T.; Mihovilovic, M. D., Exploiting the Regioselectivity of Baeyer-Villiger Monooxygenases for the Formation of β-Amino Acids and β-Amino Alcohols. *Angewandte Chemie - International Edition* **2010**, *49* (26).

206. Kostichka, K.; Thomas, S. M.; Gibson, K. J.; Nagarajan, V.; Cheng, Q., Cloning and Characterization of a Gene Cluster for Cyclododecanone Oxidation in Rhodococcus Ruber SC1. *Journal of Bacteriology* **2001**, *183* (21).

207. Pellissier, H., Use of Chiral Sulfoxides in Asymmetric Synthesis. *Tetrahedron*. 2006.

208. Legros, J.; Dehli, J. R.; Bolm, C., Applications of Catalytic Asymmetric Sulfide Oxidations to the Syntheses of Biologically Active Sulfoxides. *Advanced Synthesis and Catalysis*. 2005.

209. Beneventi, E.; Ottolina, G.; Carrea, G.; Panzeri, W.; Fronza, G.; Lau, P. C. K., Enzymatic Baeyer-Villiger Oxidation of Steroids with Cyclopentadecanone Monooxygenase. *Journal of Molecular Catalysis B: Enzymatic* **2009**, *58* (1–4).

210. Koesoema, A. A.; Standley, D. M.; Senda, T.; Matsuda, T., Impact and Relevance of Alcohol Dehydrogenase Enantioselectivities on Biotechnological Applications. *Applied Microbiology and Biotechnology*. 2020.

211. Bartsch, S.; Brummund, J.; Köpke, S.; Straatman, H.; Vogel, A.; Schürmann, M., Optimization of Alcohol Dehydrogenase for Industrial Scale Oxidation of Lactols. *Biotechnology Journal* **2020**, *15* (11).

212. Reid, M. F.; Fewson, C. A., Molecular Characterization of Microbial Alcohol Dehydrogenases. *Critical Reviews in Microbiology* **1994**, *20* (1).

213. Cao, Y.; Liao, L.; Xu, X. W.; Oren, A.; Wang, C.; Zhu, X. F.; Wu, M., Characterization of Alcohol Dehydrogenase from the Haloalkaliphilic Archaeon Natronomonas Pharaonis. *Extremophiles* **2008**, *12* (3).

214. de Miranda, A. S.; Milagre, C. D. F.; Hollmann, F., Alcohol Dehydrogenases as Catalysts in Organic Synthesis. *Frontiers in Catalysis* **2022**, *2* (900554).

215. Zhou, J.; Xu, G.; Ni, Y., Stereochemistry in Asymmetric Reduction of Bulky-Bulky Ketones by Alcohol Dehydrogenases. *ACS Catalysis*. 2020.

216. Zheng, Y. G.; Yin, H. H.; Yu, D. F.; Chen, X.; Tang, X. L.; Zhang, X. J.; Xue, Y. P.; Wang, Y. J.; Liu, Z. Q., Recent Advances in Biotechnological Applications of Alcohol Dehydrogenases. *Applied Microbiology and Biotechnology*. 2017.

217. Rosenthal, K.; Lütz, S., Recent Developments and Challenges of Biocatalytic Processes in the Pharmaceutical Industry. *Current Opinion in Green and Sustainable Chemistry*. 2018.

218. Zhang, R.; Xu, Y.; Xiao, R., Redesigning Alcohol Dehydrogenases/Reductases for More Efficient Biosynthesis of Enantiopure Isomers. *Biotechnology Advances*. 2015.

219. Wang, S.; Meng, X.; Zhou, H.; Liu, Y.; Secundo, F.; Liu, Y., Enzyme Stability and Activity in Non-Aqueous Reaction Systems: A Mini Review. *Catalysts*. 2016.

220. Shimizu, S.; Kataoka, M.; Honda, K.; Sakamoto, K., Lactone-Ring-Cleaving Enzymes of Microorganisms: Their Diversity and Applications. *Journal of Biotechnology* **2001**, *92* (2).

221. van der Vlugt-bergmans, C. J. B.; van der Werf, M. J., Genetic and Biochemical Characterization of a Novel Monoterpene ε-Lactone Hydrolase from Rhodococcus Erythropolis DCL14. *Applied and Environmental Microbiology* **2001**, *67* (2).

222. Honda, K.; Kataoka, M.; Shimizu, S., Functional Analyses and Application of Microbial Lactonohydrolases. *Biotechnology and Bioprocess Engineering* **2002**, *7* (3).

223. Kim, M. H.; Choi, W. C.; Kang, H. O.; Lee, J. S.; Kang, B. S.; Kim, K. J.; Derewenda, Z. S.; Oh, T. K.; Lee, C. H.; Lee, J. K., The Molecular Structure and Catalytic Mechanism of a Quorum-Quenching N-Acyl-L-Homoserine Lactone Hydrolase. *Proceedings of the National Academy of Sciences of the United States of America* **2005**, *102* (49).

224. Momb, J.; Wang, C.; Liu, D.; Thomas, P. W.; Petsko, G. A.; Guo, H.; Ringe, D.; Fast, W., Mechanism of the Quorum-Quenching Lactonase (AiiA) from Bacillus Thuringiensis. 2. Substrate Modeling and Active Site Mutations. *Biochemistry* **2008**, *47* (29).

225. Fast, W.; Tipton, P. A., The Enzymes of Bacterial Census and Censorship. *Trends in Biochemical Sciences*. 2012.

226. Yu, X.; Tu, T.; Luo, H.; Huang, H.; Su, X.; Wang, Y.; Wang, Y.; Zhang, J.; Bai, Y.; Yao, B., Biochemical Characterization and Mutational Analysis of a Lactone Hydrolase from Phialophora Americana. *Journal of Agricultural and Food Chemistry* **2020**, *68* (8).

227. Takahashi-Ando, N.; Kimura, M.; Kakeya, H.; Osada, H.; Yamaguchi, I., A Novel Lactonohydrolase Responsible for the Detoxification of Zearalenone' Enzyme Purification and Gene Cloning. *Biochemical Journal* **2002**, *365* (1).

228. Bergonzi, C.; Schwab, M.; Naik, T.; Daudé, D.; Chabrière, E.; Elias, M., Structural and Biochemical Characterization of AaL, a Quorum Quenching Lactonase with Unusual Kinetic Properties. *Scientific Reports* **2018**, *8* (1).

229. Rémy, B.; Plener, L.; Decloquement, P.; Armstrong, N.; Elias, M.; Daudé, D.; Chabrière, É., Lactonase Specificity Is Key to Quorum Quenching in Pseudomonas Aeruginosa. *Frontiers in Microbiology* **2020**, *11*.

230. Kusada, H.; Zhang, Y.; Tamaki, H.; Kimura, N.; Kamagata, Y., Novel N-Acyl Homoserine Lactone-Degrading Bacteria Isolated from Penicillin-Contaminated Environments and Their Quorum-Quenching Activities. *Frontiers in Microbiology* **2019**, *10* (MAR).

231. Kataoka, M.; Shimizu, K.; Sakamoto, K.; Yamada, H.; Shimizu, S., Optical Resolution of Racemic Pantolactone with a Novel Fungal Enzyme, Lactonohydrolase. *Applied Microbiology and Biotechnology* **1995**, *43* (6).

232. Liu, Z.; Sun, Z., Cloning and Expression of D-Lactonohydrolase CDNA from Fusarium Moniliforme in Saccharomyces Cerevisiae. *Biotechnology Letters* **2004**, *26* (24).

233. Tang, Y. X.; Sun, Z. H.; Hua, L.; Lv, C. F.; Guo, X. F.; Wang, J., Kinetic Resolution of DL-Pantolactone by Immobilized Fusarium Moniliforme SW-902. *Process Biochemistry* **2002**, *38* (4).

234. Isupov, M. N.; Schröder, E.; Gibson, R. P.; Beecher, J.; Donadio, G.; Saneei, V.; Dcunha, S. A.; Mcghie, E. J.; Sayer, C.; Davenport, C. F.; Lau, P. C.; Hasegawa, Y.; Iwaki, H.; Kadow, M.; Balke, K.; Bornscheuer, U. T.; Bourenkov, G.; Littlechild, J. A., The Oxygenating Constituent of 3,6-Diketocamphane Monooxygenase from the CAM Plasmid of Pseudomonas Putida: The First Crystal Structure of a Type II Baeyer-Villiger Monooxygenase. *Acta Crystallographica Section D: Biological Crystallography* **2015**, *71*.

235. van der Werf, M. J., Purification and Characterization of a Baeyer-Villiger Mono-Oxygenase from Rhodococcus Erythropolis DCL14 Involved in Three Different Monocyclic Monoterpene Degradation Pathways. *Biochemical Journal* **2000**, *347* (3).

236. Nealon, C. M.; Musa, M. M.; Patel, J. M.; Phillips, R. S., Controlling Substrate Specificity and Stereospecificity of Alcohol Dehydrogenases. *ACS Catalysis*. 2015.

237. Sheldon, R. A., Recent Advances in Green Catalytic Oxidations of Alcohols in Aqueous Media. *Catalysis Today* **2015**, *247*.

238. Ceccoli, R. D.; Bianchi, D. A.; Carabajal, M. A.; Rial, D. v., Genome Mining Reveals New Bacterial Type I Baeyer-Villiger Monooxygenases with (Bio)Synthetic Potential. *Molecular Catalysis* **2020**, *486*.

239. Fraaije, M. W.; Wu, J.; Heuts, D. P. H. M.; van Hellemond, E. W.; Spelberg, J. H. L.; Janssen, D. B., Discovery of a Thermostable Baeyer-Villiger Monooxygenase by Genome Mining. *Applied Microbiology and Biotechnology* **2005**, *66* (4).

240. Mallin, H.; Wulf, H.; Bornscheuer, U. T., A Self-Sufficient Baeyer-Villiger Biocatalysis System for the Synthesis of ε-Caprolactone from Cyclohexanol. *Enzyme and Microbial Technology* **2013**, *53* (4).

241. Bornadel, A.; Hatti-Kaul, R.; Hollmann, F.; Kara, S., A Bi-Enzymatic Convergent Cascade for e-Caprolactone Synthesis Employing 1,6-Hexanediol as a 'Double-Smart Cosubstrate.' *ChemCatChem* **2015**, *7*, 2442–2445.

242. Fürst, M. J. L. J.; Boonstra, M.; Bandstra, S.; Fraaije, M. W., Stabilization of Cyclohexanone Monooxygenase by Computational and Experimental Library Design. *Biotechnology and Bioengineering* **2019**, *116* (9).

243. Kirschner, A.; Bornscheuer, U. T., Directed Evolution of a Baeyer-Villiger Monooxygenase to Enhance Enantioselectivity. *Applied Microbiology and Biotechnology* **2008**, *81* (3).

244. Butinar, L.; Mohorčič, M.; Deyris, V.; Duquesne, K.; Iacazio, G.; Claeys-Bruno, M.; Friedrich, J.; Alphand, V., Prevalence and Specificity of Baeyer-Villiger Monooxygenases in Fungi. *Phytochemistry* **2015**, *117*.

245. Bisagni, S.; Summers, B.; Kara, S.; Hatti-Kaul, R.; Grogan, G.; Mamo, G.; Hollmann, F., Exploring the Substrate Specificity and Enantioselectivity of a Baeyer-Villiger Monooxygenase from Dietzia Sp. D5: Oxidation of Sulfides and Aldehydes. *Topics in Catalysis* **2014**, *57* (5).

246. Sicard, R.; Chen, L. S.; Marsaioli, A. J.; Reymond, J. L., A Fluorescence-Based Assay for Baeyer-Villiger Monooxygenases, Hydroxylases and Lactonases. *Advanced Synthesis and Catalysis* **2005**, *347* (7–8).

247. Dudek, H. M.; Popken, P.; van Bloois, E.; Duetz, W. A.; Fraaije, M. W., A Generic, Whole-Cell-Based Screening Method for Baeyer-Villiger Monooxygenases. *Journal of Biomolecular Screening* **2013**, *18* (6).

248. Saß, S.; Kadow, M.; Geitner, K.; Thompson, M. L.; Talmann, L.; Böttcher, D.; Schmidt, M.; Bornscheuer, U. T., A High-Throughput Assay Method to Quantify Baeyer-Villiger Monooxygenase Activity. In *Tetrahedron*; 2012; Vol. 68.

249. Kamerbeek, N. M.; Moonen, M. J. H.; van der Ven, J. G. M.; van Berkel, W. J. H.; Fraaije, M. W.; Janssen, D. B., 4-Hydroxyacetophenone Monooxygenase from Pseudomonas Fluorescens ACB. A Novel Flavoprotein Catalyzing Baeyer-Villiger

Oxidation of Aromatic Compounds. *European Journal of Biochemistry* **2001**, *268* (9).

250. Hasegawa, Y.; Nakai, Y.; Tokuyama, T.; Iwaki, H., Purification and Characterization of Cyclohexanone 1,2-Monooxygenase from Exophiala Jeanselmei Strain Kufi-6N. *Bioscience, Biotechnology and Biochemistry* **2000**, *64* (12).

251. Leipold, F.; Rudroff, F.; Mihovilovic, M. D.; Bornscheuer, U. T., The Steroid Monooxygenase from Rhodococcus Rhodochrous; A Versatile Biocatalyst. *Tetrahedron Asymmetry* **2013**, *24* (24).

252. Itagaki, E., Studies on Steroid Monooxygenase from Cylindrocarpon Radicicola ATCC 11011: Purification and Characterization. *Journal of Biochemistry* **1986**, *99* (3).

253. Miyamoto, M.; Matsumoto, J.; Iwaya, T.; Itagaki, E., Bacterial Steroid Monooxygenase Catalyzing the Baeyer-Villiger Oxidation of C21-Ketosteroids from Rhodococcus Rhodochrous: The Isolation and Characterization. *Biochimica et Biophysica Acta (BBA)/Protein Structure and Molecular* **1995**, *1251* (2).

254. SHIMIZU, S.; KATAOKA, M.; SHIMIZU, K.; HIRAKATA, M.; SAKAMOTO, K.; YAMADA, H., Purification and Characterization of a Novel Lactonohydrolase, Catalyzing the Hydrolysis of Aldonate Lactones and Aromatic Lactones, from Fusarium Oxysporum. *European Journal of Biochemistry* **1992**, *209* (1).

255. Kataoka, M.; Nomura, J. I.; Shinohara, M.; Nose, K.; Sakamoto, K.; Shimizu, S., Purification and Characterization of a Novel Lactonohydrolase from Agrobacterium Tumefaciens. *Bioscience, Biotechnology and Biochemistry* **2000**, *64* (6).

256. Yılmaz, S.; Bedir, E.; Ballar-Kırmızıbayrak, P., The Role of Cycloastragenol at the Intersection of NRF2/ARE, Telomerase, and Proteasome Activity. *Free Radical Biology and Medicine* **2022**, *188*, 105–116.

VITA

Melis KÜÇÜKSOLAK

Education:

Ph.D., Bioengineering, GPA: 3.93/4.00, Izmir Institute of Technology, İzmir –Turkey, 2022

BSc, Bioengineering, GPA: 3.72/4.00, Ege University, İzmir –Turkey, 2014

Professional & Research Experience and Scholarship:

2017- : Research Assistant, Department of Bioengineering, Izmir Institute of Technology

2020-2022: TÜBİTAK, Project No: 119Z870, Scholarship Student

2016-2019: TÜBİTAK, 2211/A National PhD Scholarship Program

2015-2017: TÜBİTAK, Project No: 114Z958, Scholarship Student

Selected Publications and Conference Papers:

- **Küçüksolak, M.**; Üner, G.; Ballar-Kırmızıbayrak, P.; Bedir, E. **2022**. Neuroprotective Metabolites via Fungal Biotransformation of a Novel Sapogenin, Cyclocephagenol. *Scientific Reports*, 12 (1), 1-15.
- **Küçüksolak, M.**; Üner, G.; Ballar-Kırmızıbayrak, P.; Bedir, E. **2022**. Oral Presentation: Novel Neuroprotective Metabolites Produced via Biotransformation of Cyclocephagenol by *Alternaria eureka* 1E1BL1. *70th International Congress and Annual Meeting of GA*, Thessaloniki, Greece.
- Karakoyun, Ç.; **Küçüksolak, M.**; Bilgi, E.; Doğan, G.; Çömlekçi, Y. E.; Bedir, E. **2021**. Five New Cardenolides Transformed from Oleandrin and Nerigoside by *Alternaria eureka* 1E1BL1 and *Phaeosphaeria* sp. 1E4CS-1 and Their Cytotoxic Activities. *Phytochemistry Letters*, *41*, 152–157.
- **Küçüksolak, M.**; Ekiz, G.; Duman, S.; Yılmaz, S.; Ballar-Kırmızıbayrak, P.; Bedir, E. **2019**. Poster Presentation: Telomerase Activators Derived from *Astragalus* Sapogenins via Biotransformation with the Recently Discovered Endophytic Fungus *Camarosporium laburnicola*. *67th International Congress and Annual Meeting of the Society for GA*, Innsbruck, Austria.